A Study on Evolution of N-bearing Complex Organic Molecules towards Glycine

SUZUKI TAIKI

Doctor of Philosophy

Department of Astronomical Science
School of Physical Sciences
SOKENDAI (The Graduate University for Advanced Studies)

Doctoral thesis for the degree of Doctor of Philosophy

A Study on Evolution of N-bearing Complex Organic Molecules towards Glycine

Taiki Suzuki

Department of Astronomical Science

SOKENDAI (Graduate University for Advanced Studies),

2017

Acknowledgement

This work would be never completed without helpful support and discussions with my supervisors, Dr.Ohishi, Dr.Saito, and Dr.Hirota, who led me to the field of radio astronomy. I would like to show my greatest appreciation to them. Especially I want to greatly thank to my main supervisor, Dr.Ohishi, for his kindly supports for my study and fruitful discussions throughout doctoral and master course in SOKENDAI. A large part of this work is also based on the experience of study with chemical network simulation in Bordeaux University. Dr.Wakelam helped me my study and my daily life issues. I also appreciate Drs. Majumdar and Ruaud while my stays in Bordeaux not only as a researcher but also as good friends.

I am grateful to all the staff members of the SOKENDAI, Nobeyama Radio Observatory, and the National Astronomical Observatory of Japan (NAOJ), and the Arizona Radio Observatory for their support throughout our observations. I want to thank to students in SOKENDAI for scientific discussion and enjoyable life.

Finally, I want to thank my family, especially my father and mother, who brought me up with both financial and mental support.

INDEX

Abstract

Abstract

Origin of life is one of the oldest mysteries for the mankind. According to a recent theory, complex organic materials might have been delivered to the primordial Earth by comets, and contributed to the chemical evolution leading to life. Therefore, the chemical evolution in the interstellar medium could be the very first stage of chemical evolution leading to life. In this thesis, I studied chemical evolution and chemical differences in hot cores via both observations and theoretical studies, especially focusing on N-bearing species, which can be related to the simplest amino acid, glycine.

I conducted a survey observation of CH_2NH, one of glycine precursors. As a result, I successfully detected CH_2NH toward eight hot core sources, including four new detections. Not only some well-known complex organic molecules, such as CH_3OH and CH_3OCH_3 but also N-bearing species, such as CH_2CHCN and NH_2CHO, were simultaneously detected. I found that chemical compositions are very different among the hot core sources. For instance, NGC6334F showed lower fractional abundances of CH_2NH and other N-bearing species than those in G10.47+0.03 by a factor of ten. Such differences would be reconciled by different evolutionary stages or different physical conditions of hot cores. I suggested two hypothesis to explain the chemical differences of the sources.

First, CH_2NH-rich sources might be in the early phase of the evolution. G10.47+0.03, one of the CH_2NH-rich sources, showed weak emission of hydrogen recombination line, and past high spatial resolution observation toward Orion KL "Hot Core" could not detect recombination lines inside it. On the other hand, NGC6334F and W51 e1/e2, where N-bearing species are not so rich, showed strong emission of a hydrogen recombination line emission, which would trace evolved HII region inside their hot cores. In this case, different fractional abundances might be explained by different strength of UV from central stars. If UV radiation is strong, molecules would be efficiently destroyed.

A second hypothesis is related to temperature structures inside the hot cores. According to a past study, G10.47+0.03 showed the highest gas kinetic temperature among the observed sources. If high temperature regions are limited inside NGC6334F and W51 e1/e2, CH_2NH and other species would be adsorbed on interstellar grains in their envelope.

To test above hypotheses, I conducted chemical network simulations. I used the dataset

of KIDA (Wakelam et al. 2015), and some grain surface reactions were added taken from Garrod (2013). I assumed that physical evolution starts from a stage of the diffuse cloud will form a dense core via a gravitational collapse. Complex organic molecules are formed in this cold phase on the grains. The gas kinetic temperature is assumed to rise after a birth of a star; then frozen solid-phase species are evaporated. Following that, evaporated species react with each other in the gas phase. These gas phase species in this stage are observed.

With our simulation, first of all, I revealed the formation paths to possible glycine precursors, CH_2NH and CH_3NH_2 with this modeling. I found that the hydrogenation processes to HCN is the most efficient way to produce CH_3NH_2. Then CH_3NH_2 is evaporated from grains after a birth of a star. On the other hand, CH_2NH is very poor on grains since CH_2NH is quickly converted to CH_3NH_2 via a hydrogenation process. I found that CH_2NH is formed in the gas phase via radical-radical reactions rather than direct evaporation from grains. This process starts with the evaporation of saturated molecules such as CH_3OH and NH_3, and they are destroyed to form radicals in the gas phase. Finally, NH and CH_3 radicals will efficiently form CH_2NH.

I also tested the hypotheses with this chemical model. First, I tested the effect of UV radiation. While grains would be destroyed by strong UV radiation in the vicinity of a star, UV radiation would be attenuated by grains outside of HII regions. Considering these effects and assuming a central B0 type star (T=30000 K), I found that gas phase species would be destroyed within 0.001 pc from an edge of HII regions, and the effect of UV is negligible further outside of this distance due to the strong attenuation by grains. The simulation results assuming UV radiation from well evolved HII regions succeeded to explain the observed abundances of CH_2NH toward NGC6334F and W51 e1/e2. These results agree with our observational results that strong hydrogen recombination lines were detected towards NGC6334F and W51 e1/e2. However, our simulation results under cases with different UV strength could not explain the different abundances of other detected species since they are destroyed more quickly than CH_2NH.

Second, I tested a possibility that different temperatures in hot cores may lead to the different chemical compositions. My model calculations suggested that N-bearing species such as CH_2NH and CH_2CHCN tend to be converted to other species on grains at or below 120 K after adsorption process, due to the longer timescale than 200 K case. On the other hand, CH_3OH, which did not show the correlation with CH_2NH, is not destructed on grains under 120 K. Therefore, the difference of the temperature among sources would be a possible explanation for the different CH_2NH abundance.

Finally, I discussed the formation process to glycine. I extended the work by Garrod (2013) by adding newly suggested formation processes to glycine and the latest gas phase reactions by KIDA. I confirmed that "CH_2NH_2 + HOCO" process, which was claimed by Garrod (2013), would be the most dominant formation process to glycine. However, while Garrod (2013) assumed that HOCO is formed by hydrogen subtraction processes from HCOOH, I found a more efficient formation path to the HOCO radical. I discussed the importance of suprathermal hydrogen, H*, which can penetrate high activation barrier with its excess energy given by UV photons. In this case, H* can react with a ubiquitous species, CO_2. I found that H* may accelerate the formation of HOCO via the reaction of "CO_2 + H*". As a result, glycine abundance would be strongly enhanced.

Since our simulations showed that CH_3NH_2 can be sufficiently formed on grains during the gravitationally collapse from the diffuse cloud phase, the reaction of "CH_2NH_2 + HOCO" would form glycine efficiently in any star-forming regions. If glycine is sufficiently formed on grains, the aggregation of grains will form comets containing glycine inside. Such comets would have provided glycine to our primordial Earth and other exoplanets.

To further investigate this scenario, our next important step would be to achieve the first detection of interstellar glycine. Our simulations suggested that the UV photons from the central stars rather decreased glycine abundance since the destruction rates overcome the producing rates. It would be preferable to search for glycine in regions where UV radiation from central stars is well attenuated. The chemical simulations predicted that formation path of CH_2NH_2 would be hydrogen subtraction processes from CH_3NH_2, which would be abundant on the grains. Therefore, CH_3NH_2 would be a good compass to the first detection of glycine.

Chapter 1. Introduction

1. Introduction

1.1. Origin of Life

Why does human beings exist on the Earth? Origin of life is one of the oldest mystery for the mankind. The topic had been discussed by philosophers and theologians from much before the scientific revolution, when the concept of the modern science was established. In this section, I will describe the history of thought regarding origin of life.

1.1.1. Spontaneous Generation Theory

In the prehistoric age, it was believed that life has emerged by spontaneous generation. According to this scenario, not only bacteria, but also other insects and animals have emerged from inanimate matter such as mud and dust. There were two conflicting views to discuss spontaneous generation theory: materialism and idealism. From the stand point of materialism, life would have emerged via interactions of materials without mysterious power. On the other hand, idealism claimed that life has spiritual soul and is distinguished from other inanimate materials.

It was Platon and his disciple Aristoteles, who strongly influenced the proceeding thought of idealism in the medieval Europe. Platon convinced that biotic materials themselves, which compose animals or plants body, are not "life", and such biotic materials are activated by immortal soul. Aristoteles reflected this idea to his theory. He thought that all life, like mosquito, lions, and even human beings, emerged from inanimate materials.

In the medieval Europe, science is governed by religious ideology under the domination of the Roman empire. Theologians thought that the God had created everything. The representative theologians, such as Augustinus and Thomas Aquinas, combined spontaneous

generation theory to their doctrine. They claimed that it was the God who gave the soul to inanimate material, leading to the spontaneous generation of life.

René Descartes opposed the widely accepted idea at that time and tried to explain the origin of life from materialism perspective. He thought that origin of life should be explained by the natural process of materials without the spiritual soul. Although there were two views of the spontaneous generation of life, spiritual source, and natural process, no one doubted the spontaneous generation theory itself until the middle of the 17th century.

1.1.2. Experiments of Spontaneous Generation

Along with the progress of the biological studies, the foundation of spontaneous generation theory got unsettled. The critical paradigm shift was brought by the experiment by Louis Pasteur. He poured broth into two flasks, and one flask was sterilized and sealed, and the other one was sterilized but kept open. Nothing has emerged in the former flasks, while microorganisms grew in the latter flasks. In this experiment, he disproved the spontaneous generation theory, and argued that past observations of spontaneous generation could be explained as contaminations caused by outside micro organisms.

1.2. Evolution from Organic Materials to Life

In this section, I will review a widely accepted modern hypothesis to explain how the today's biological diversity was brought on the Earth, where no life would have existed just after its formation. At the end of the section, the importance of chemical composition of the primordial Earth will be emphasized.

1.2.1. Origin of Species

In the 18th century, most scientists still believed that all species were created by the God one by one. The importance of the evolution was realized by Charles Darwin. He argued in his book "On the Origin of Species" that different trait of organisms lead to differential survival and reproduction rate. As the results, the favorable trait for the organisms will be inherited to the next generation. He named this process as natural "selection" comparing artificial selection, which was well known at that time. He predicted the existence of the Last Universal Common Ancestor (LUCA), and the continuous small accumulation of favorable mutation of organisms was selected to survive by natural selection. Therefore, the speciation process is explained as the results of adaptation process of organisms to the different environment. As time goes on, due to the progress of geology, radiometric dating, and the detections of new fossils, his theory is widely supported.

1.2.2. DNA

The natural selection process would have existed even before the birth of LUCA. In the early Earth, there would have been primordial soup, which contained a variety of organic molecules. Since there were no bacteria to consume these organics at that time, they would survive long time to react with each other to be more complex. One day, a certain molecule would have got a capability to replicate itself. Biologists deduce that even before the origin of life, there would have been a competition to get available organisms among molecules which could replicate themselves. These species with the capability of self-replication would something like deoxyribonucleic acid (DNA), which is known to be composed of a sugar called deoxyribose, a phosphate group, and one of four nitrogen-containing nucleobases either cytosine, guanine, adenine, or thymine.

Currently, the diversity of species on the Earth is understood by means of DNA. The sequences of these nucleobases preserve the information regarding the synthesis of protein from amino acids, which govern the growth from the embryogenesis and growth of organisms. Further, the sequence of nucleobases is copied to produce germ cells. The occasional random error during the replication of information of DNA changes the genetic information of the organisms, which lead to the evolution and speciation as the results of natural selection.

1.2.3. Origin of Organic Materials

Diverse organic molecules would have existed in the primordial soup even before the formation of DNA or protein. Amino acids are essential biotic molecules which contain both the amino (-NH_2) and the carboxyl (-COOH) functional groups. Biologically, the carbon atom attached to the carboxyl functional group is called "α carbon", and then if there are more carbon atoms attached to α carbon, they are referred to as β carbon, γ carbon, in order. The most simplest amino acid is glycine (NH_2-CH_2-COOH). The replacement of the hydrogen atom attached at the α carbon of glycine to other side chain group (-R) will form variety of α-amino acids. For instance, if the H atom is replaced to the methyl functional group (-R is CH_3 in this case) will form α-alanine (NH_2-CH(CH_3)-COOH). There is a structural isomers for complex amino acids, like NH_2-CH_2-CH_3-COOH for α-alanine. Such amino acids, which has amino functional group attached to the β carbon, are referred as β-amino acids. For terrestrial life, α-amino acids are vital component of protein, which form muscles, cells and other tissues. Since α-amino acids except for glycine have chiral carbon atom, there are two enantiomers called L-amino acids and D-amino acids. Their structures are mirror images of each other like a right hand (D: dextro-rotatory) and a left hand (L: levo-rotatory). They cannot be overlapped with the other by means of rotation.

It is intriguing that only L-amino acids are selected in the terrestrial life.

Another interesting compound regarding the origin of life would be polyhydroxylated compounds (polyols), like sugars, sugar alcohols and sugar acids. Sugar is classified as molecules with more than two carbon atoms together with one formyl (-CHO) or carbonyl (-CO) functional group. They are components of nucleic acids (RNA, DNA) and cell membranes, and also play a role as a source of energy.

How were these organic materials supplied to the Earth? A. I. Oparin suggested the famous scenario that complex organic molecules are formed via chemical evolution of abiotic simple organic materials. If the life has emerged in the primordial soup, its chemical composition will be essential to study the possible chemical evolution on the Earth at that time.

1.3. Synthesis of Organic Molecules

Studies to synthesize organic materials on the primordial Earth condition date back to 1950s. Miller (1953) conducted the very famous experiment - Miller's experiment. He succeeded to form glycine, α-alanine and β-alanine, via electric discharge of H_2, H_2O, NH_3, and CH_4 gas mixture. It was the first experiment that synthesized organic materials from "inorganic material", which was against the "common sense" at that time. The selection of reducing atmosphere for the pre-requirements reflected on the formation scenario of the Earth at that time. It was believed that the Earth was formed relatively slowly with the cold interior, and it would take a time to have modern volcanic gas, containing CO_2, H_2O, and N_2. Through the interactions of H_2 gas provided from the Universe and materials provided by colliding planetesimals, Urey (1952) claimed that H_2O, NH_3, CH_4, and H_2 would be a dominant atmospheric composition in the primordial Earth.

However, since then, the atmospheric composition in the primordial Earth was reconsidered by geological studies. The formation model via planetary collisions would have melted the Earth's surface, causing so-called magma ocean, where the silicate portions of the Earth was melted either wholly or partially (Tonks & Melosh 1993). This process, beneath magma, which was supersaturated in greenhouse gasses such as H_2O or CO_2 under high pressure, would have delivered H_2O and CO_2 to the surface. The lower pressure close to the surface would make a bubble of exsolved volatiles from the delivered magma (Elkins-Tanton 2008, and the references therein). This vaporization process would have vitally changed the chemical composition of the primordial Earth. Elkins-Tanton (2008) argued that very small fractions of initial volatile contents ($\sim$0.01 wt.%) could produce the atmosphere in excess of 100 bars, via their simulation. In contrast to the primordial atmosphere, which was obtained from a remnant of the gaseous nebula, the atmosphere produced by the degassing process from the magma is called as "secondary atmosphere". According to the geological and theoretical studies, the degassing process would have occurred within as short as several million years (Walker 1977; Elkins-Tanton 2008).

Thus, the Miller's experiment should be revised under the composition of the secondary atmosphere. The pressure of oxygen (fugacity) of a magma is one of the critical parameters which determines both mineral saturation and molecular species of the gas. To deduce the oxidation state of the secondary atmosphere, Trail (2011) used Hadean zircon. Since zircon is an exceptionally durable mineral and is known to crystallize in the first 500 Myr of Earth history, zircon is an ideal mineral for the investigation of the ancient atmosphere. Through their analysis, Trail (2011) concluded that outgassing of Earth's interior at that time would not be reducing species such as CH_4, NH_3, H_2, but dominated by CO_2, H_2O, and SO_2. If the secondary atmosphere was not reducing but rather neutral, is it possible to synthesize sufficient organic compounds through electronic discharge? Miller (1983) conducted discharging experiments under different gas composition, and demonstrated that

CO or CO_2 dominant gas mixture required the same amount of H_2 gas to produce amino acids. However, it was doubtful if early Earth could maintain sufficient H_2 gas over a long period, without escaping to the space. They also showed that discharge of CH_4 gas can produce a variety of essential amino acids in proteins like aspartic acids, glutamic acids, the combination of H_2 and CO or CO_2 only produce the simplest amino acid, glycine. If electric discharge process was the dominant source for prebiotic molecules towards life, further processes to make different amino acids would be necessary. Chyba & Sagan (1992) argued that if the CO_2 dominant ($[H_2]/[CO_2] \sim 0.1$) atmosphere was assumed, the amount of synthesized organic molecules per year (kg year^{-1}) would decrease by a factor of 100.

1.4. Exogenous Delivery of Organic Molecules

If the discharge is not an efficient way to synthesize organic materials, exogenous delivery is an another candidate for the origin of organic materials. In the 1960s, Oró (1961) first suggested a scenario that carbon compounds would have been accumulated by cometary matter. He argued that comets and asteroids, fallen over the period of heavy bombardment prior to 3.8 Gyr, might be a major source of organic compounds at that time. Interplanetary dust particles (IDPs), whose mass range is 10^{-12} to 10^{-6} g, would be an another candidate for the source of organics. They are so small that gently decelerated in the upper atmosphere to avoid pyrolysis. Since then the importance of the exogenous delivery of organic compounds has been discussed.

To evaluate how much organics can survive the cometary impact and be accumulated on the primordial Earth, Chyba et al. (1992) calculated the temperature during the impact considering the comet-asteroid interaction with the atmosphere, surface impact, and resulting organic pyrolysis. They argued that averaged comets would experience the temperature of 40000 K. If the rate of pyrolysis with an activation energy E is given

by the rate of the Arrhenius law, whose rate is proportional to the Boltzmann factor of $\exp(E/k_BT)$, almost all species cannot survive under such a high temperature. Through the calculation of temperature during the impact from the final velocity, they found that only the comets with the final velocity of lower than 10 km s $^{-1}$ can provide HCN (whose activation barrier for pyrolysis is 1800 K) and thus could have delivered organic molecules. They estimated the amount of organic molecules would be 10^6 to 10^7 kg per year.

However, subsequent studies re-evaluated the importance of comets. Blank et al. (1998) claimed that high shock pressure will suppress the reaction rate of pyrolysis. They applied the Boltzmann factor of $\exp((E + PV)/k_BT)$. With this modification, the reaction rate at 7000 K and 100 GPa is similar to that of 900 K and 1 atm, giving organics more opportunities to survive the shock. Further, Pierazzo & Chyba (1999) pointed out that the oblique impacts would generate lower peak temperatures. They calculated the surviving fraction of five amino acids as a function of the angle of the impact, considering their kinetic parameters. The survivability of amino acids weighted over the range of possible impact angles, in the 2 km size and 10 km projectile, are ∼10% and ∼1%, respectively. At that time, it was a remarkable result that certain amino acids would have survived even large cometary impact.

On the other hand, IDPs are sufficiently gently decelerated in the upper atmosphere to avoid being heated to have their organic molecules to be pyrolyzed. At 4 Gyr ago, Earth would have been accreting $\sim 2\times 10^8$ kg yr^{-1} of organics from IDPs (Chyba & Sagan 1997). Chyba & Sagan (1997) compared the production rates of organics in the primordial Earth via various origins and argued that IDP is the most efficient way to produce organics to the Earth surface, under CO_2 dominant ($[H_2]/[CO_2] \sim 0.1$) atmosphere.

1.5. Preceeding Studies of Biotic Molecules in Extraterrestrial Objects

1.5.1. Organic Compounds in the Comets and Meteorite

There is some direct evidence that extraterrestrial objects contain these important biotic molecules. A well-studied example of exogenous delivery of organic materials would be the Murchison meteorite, which fell into Victoria, Australia, in 1969. Many authors have reported the detection of not only common amino acids such as glycine, alanine, and glutamic acids, but also exotic ones in the Earth like isovaline and pseudleucine (e.g., Engel & Nagy 1982; Engel & Macko 1997, and the references therein) Cooper et al. (2001) reported the detection of sugars, sugar alcohol, and sugar acids.

There were studies not only meteorite fallen into the Earth, but also the composition of comets in the solar system. In 2006, NASA ' s Stardust spacecraft brought back samples from comet 81P/Wild 2 to the Earth. With the sample, Elsila et al. (2009) claimed the detection of glycine in the comet, showing the δ^{13}C of 29 %, which is apparently different from the terrestrial one. Further, the chemical composition of the coma of comet 67P/Churyumov-Gerasimenko was investigated by the ROSINA mass spectrometer (Altwegg et al. 2016). They reported methylamine, ethylamine, and glycine, confirming the results of the Stardust mission. Since Altwegg et al. (2016) did not use any sample preparation, and the possibility of contamination from the terrestrial source was clearly excluded.

1.5.2. The Homochirality and Interstellar Circular Polarization

The origin of the homochirality of biological molecules has been another long lasting puzzle. If organic compounds required for life arrived from the Universe, the exogenous delivery scenario may be a key for this problem. In laboratories, it has been demonstrated

that sufficient enantiomeric excess can be produced from a racemic material using circularly polarized (CP) light at UV wavelength (Bonner 1991). A possible good source for the CP would be high-mass star-forming regions. Bailey et al. (1998) detected circular polarization in the Orion OMC-1 at the infrared wavelength. They used a Mie-scattering model and argued that similar amount of CP at UV wavelength would be produced. The effect of CP as the origin of homochirality is supported by proceeding detections of CP in other star-forming regions and the enantiomeric excess in the meteorites. Recently, Kwon et al (2013) detected larger and stronger CP towards the NGC6334 region. The discovery of an excess L-amino acids in the Murchison meteorite was reported (e.g., Engel & Nagy 1982; Engel & Macko 1997), which supports the scenario that the homochirality of biological molecules is caused by the exogenous phenomena.

1.6. Astronomical Observations towards Star Forming Regions

The interstellar medium (ISM), where more than 190 molecules ranging from simple linear molecules to complex organic molecules (hereafter COMs) were detected, show chemically rich environment. Astronomers usually regard the species with more than six atoms as COMs. Not only O-bearing species, CH_3OH, CH_3OCH_3, $HCOOCH_3$, but also N-bearing species such as CH_3CH_2CN and CH_2CHCN are known COMs. In 2016, a chiral molecule propylene oxide (CH_3CHHCH_2O) was detected towards Sgr B2 (N) molecular cloud in absorption (McGuire et al. 2016). This detection implies that molecules can get sufficient complexity, and it will accelerate surveys of other chiral molecules, like amino acids.

From this point of view, many observations were conducted to search for prebiotic molecules in the ISM, which might turn into the "Seeds of Life" when delivered to a planetary surface. Especially, a great attention was paid to amino acids, essential building

blocks of terrestrial life; many surveys were made unsuccessfully to search for the simplest amino acid, glycine (NH_2CH_2COOH), towards Sgr B2 and other high-mass star forming regions (e.g., Brown et al. 1979; Snyder et al. 1983; Combes et al. 1996). In 2003, Kuan et al. (2003) claimed the first detection of glycine, however, several follow-up observations concluded denied the detection (e.g., Jones et al. 2007). The difficulty of the past glycine surveys would be originated from potential weakness of glycine lines and low sensitivities of telescopes used for the surveys.

1.7. Purpose of This Study

Since simple species have gathered astronomical interests rather than COMs so far, our knowledge of chemical evolution is limited to well-known COMs. The formation processes of abundant COMs such as CH_3OH and $HCOOCH_3$ have been discussed through experimental and theoretical studies, and are thought to be formed by chemical processes on grain surface (thermal hopping and tunneling effect), and then supplied to the gas via evaporation (e.g., Watanabe et al. 2002; Garrod 2008). Therefore it is commonly thought that other COMs would also be formed on interstellar grains, and then supplied to the gas via evaporation process. However, despite the importance regarding the origin of life, our knowledge on formation process of N-bearing COMs are limited. In order to understand very first possible steps to the origin of life, chemical evolution of N-bearing COMs in the Universe would be inevitable.

A difficulty associated with studies of COMs is that the small number of sources where various COMs are detected. In order to expand our knowledge on COM evolution, COM surveys would be necessary. So far, various COMs were detected towards birthplaces of high-mass stars, which are usually called “hot cores”. The survey observations of COMs towards such high-mass star-forming regions would provide us with important opportunities

to investigate the chemical evolution of COMs in the Universe.

Currently, many observations and theoretical studies showed the existence and formation process of complex O-bearing molecules. On the other hand, the knowledge on N-bearing species, which are related to pre-biotic molecules, are still limited. Among such molecules, if the simplest amino acid, glycine, can be formed in the Universe, it would be the next essential step in tackling the problem of origin of life. In this thesis, through the combination of observations and theoretical modeling studies, I will discuss the formation process of glycine and other N-bearing species. I will also show the condition of potential glycine-rich sources towards the first detection of interstellar glycine by ALMA.

Since glycine has not been detected in the ISM, its precursors would be essential in searching for good candidate sources for glycine surveys. In Chapter 2, I present the results of survey observations of CH_2NH, which is suggested to be a precursor of glycine. The results implied that the abundances of not only N-bearing species but also other N-bearing species are different among sources. I also present a hypothesis to explain the different abundances of N-bearing species from the source properties. A hypothesis to explain chemical difference in hot cores will also be discussed in this Chapter. In Chapter 3, I will investigate the formation process of observed species by means of chemical modeling. I will suggest the most efficient formation paths for observed species, including glycine precursors CH_2NH and CH_3NH_2. In addition, the hypothesis in Chapter 2 will be discussed based on our chemical modeling. In Chapter 4, the formation process to glycine will be discussed with our updated chemical model, which is based on Garrod (2013). I will discuss the importance of suprathermal hydrogen for the first time. Our conclusions are summarized in Chapter 5.

Chapter 2.
CH_2NH survey

2. CH_2NH Survey

The large part of the description about CH_2NH survey was already published and can be found in Suzuki et al. (2016). Further, the details of simultaneously detected COMs in my survey are presented in this thesis for the first time.

2.1. Introduction

Formation processes of glycine have been studied by many researchers. There are some theoretical and laboratory studies that have demonstrated that glycine is formed on icy grain surface from methylamine (CH_3NH_2) and CO_2 under UV irradiation (Holtom et al. 2005). It is suggested that CH_3NH_2 can be formed from abundant species, CH_4 and NH_3, on icy dust surface (Kim & Kaiser 2011). Alternatively, methanimine (CH_2NH) would be related to the formation of CH_3NH_2. Another possible route to form these species is hydrogenation to HCN on the dust surface, as investigated both in experimentally and theoretically (Woon 2002; Theule et al. 2011). These issues also have been discussed in details by Majumdar et al. (2013) where they identified CH_2NH_2 as another possible precursor for glycine formation.

$$HCN \xrightarrow{2H} CH_2NH$$

$$CH_2NH \xrightarrow{2H} CH_3NH_2$$

Theule et al. (2011) mentioned that the hydrogenation process to CH_2NH might be much quicker compared to that of HCN. It is also suggested that CH_2NH may be formed in the gas phase reactions among radicals (Turner et al. 1999; Halfen et al. 2013). Halfen et al. (2013) showed that the excitation temperatures of CH_2NH and CH_3NH_2 are different, suggesting different formation paths for CH_2NH and CH_3NH_2. If this is the case, CH_2NH might not be a direct precursor to CH_3NH_2.

CH_2NH is related to another formation path to glycine; if H atom and HCN are added to CH_2NH on the grain surface, aminoacetonitrile (NH_2CH_2CN) would be formed (Danger et al. 2011). NH_2CH_2CN yields glycine via hydrolysis (Peltzer et al. 1984). These formation processes are shown in Figure 1.

Such precursor candidate molecules were reported in the ISM. First detection of CH_2NH was made towards Sgr B2 (Godfrey et al. 1973). CH_2NH was confirmed towards Sgr B2 by many authors, and in particular, Halfen et al. (2013) reported 27 transitions of CH_2NH towards Sgr B2. Dickens et al. (1997) reported new detections of CH_2NH in three high-mass star forming regions, W51 e1/e2, Orion KL, and G34.3+0.15. Recently, Qin et al. (2010) reported the detection of CH_2NH towards G19.61-0.23 through a line survey with the Sub-Millimeter Array. The past results of CH_2NH surveys are summarized in Table 1. Further CH_3NH_2 was detected towards Sgr B2 (Kaifu et al. 1974) and Orion KL (Fourikis et al. 1974). Isokoski et al. (2013) conducted a line survey towards G31.41+0.3, and reported detection of CH_3NH_2. NH_2CH_2CN was detected towards Sgr B2 (Belloche et al. 2008).

Investigation of glycine formation processes described in Figure 1 would be an important step to know how "seed of life" is formed from ubiquitous species. One of the ways to discuss the formation processes would be to compare actual CH_2NH abundances in various physical conditions with the chemical modelings. However, the small number of CH_2NH sources makes it difficult to discuss the connections of different physical conditions and CH_2NH chemistry. The survey observations of possible glycine precursors will help not only to discuss the physical condition where CH_2NH is rich, but also to plan promising future glycine surveys with ALMA.

In this section, we extended the CH_2NH survey conducted by Dickens et al. (1997) towards high-mass and low-mass star forming regions, and report four new CH_2NH sources. Our new detection of CH_2NH sources enabled us to discuss the connection of CH_2NH

chemistry and their physical properties. The observational method will be described in section 2.2 (Observation Procedure); our results will be described in section 2.3 (Results); we will compare the evolutionary stages of the CH_2NH sources in section 2.4 (Discussion). We will also discuss the formation path to CH_2NH in the discussion section. We will summarize our work in section 2.5 (Conclusion). The detailed description of the CH2NH survey is separately published in Suzuki et al. (2016).

2.2. Observation Procedure

2.2.1. NRO 45 m telescope

We conducted survey observations of CH_2NH with the 45 m radio telescope at the Nobeyama Radio Observatory (NRO), National Astronomical Observatory of Japan in April, May, and December 2013.

At NRO, we used the TZ receiver (Nakajima et al. 2013) in the dual polarization mode. The 4_{04}-3_{13} transition of CH_2NH at 105 GHz was observed. The SAM45 spectrometer was used for the backend with a frequency resolution of 122 kHz, corresponding to a velocity resolution of 0.35 km s^{-1} at 105 GHz. The system temperature ranged from 150 to 300 K. The main beam efficiency ($\eta_{\rm mb}$) was 0.37 for more than 90 GHz and 0.41 for less than 90 GHz, and the beam size (FWHM) was linearly decreased from 20.6" at 80 to 15.5" at 106 GHz. Observations were performed in the position switching mode. The pointing accuracy was checked by observing nearby SiO masers, and the pointing error was typically 5", but 10" under windy condition. We were able to obtain other molecular lines between 103 and 107 GHz simultaneously, and for some objects transitions between 105 and 108 GHz, and between 92 and 95 GHz were observed in the USB and LSB, respectively.

2.2.2. SMT telescope

We also used the Sub-Millimeter Radio Telescope (SMT), Arizona Radio Observatory in October 2013. With the SMT telescope, the CH_2NH lines, 1_{11}-0_{00}, 4_{14}-3_{13}, and 4_{23}-3_{22} at 225, 245, and 255 GHz regions, respectively, were observed. We used the 1 mm ALMA SBS SIS receiver in the dual polarization mode. The system temperature was between 250 and 400 K. The main beam efficiency was 0.74. The beam sizes (FWHM) ranged from 35" to 40" depending on the observing frequencies. The position switching mode was employed. The pointing accuracy was checked using the Venus, and its accuracy was kept within 10". We used the Forbes Filters as the spectrometer with a frequency resolution of 250 kHz, which is equivalent to a velocity resolution of 0.29 km s^{-1}. Since the Forbes Filter has 512 channels, the observed frequency range covered 128 MHz wide at 225 GHz. For the transitions in 245 and 255 GHz, we split the Forbes filter into two 256 channel sets, and two lines were observed simultaneously.

2.2.3. Source Selection

To select our target sources, we noted that CH_3OH is well known to be formed via hydrogenation process to CO on the grain surface (CO $\rightarrow$ H_2CO $\rightarrow$ CH_3OH). If the formation processes of COMs are related to the grain surface reactions, CH_3OH-rich sources would be good target sources. Thus, our sources were selected from "The Revised Version of Class I Methanol Maser Catalog" (Val'tts et al. 2012), which is available on the Internet: (http://www.asc.rssi.ru/mmI/), and from CH_3OH maser sources (Minier & Booth 2002). We also took into account the results of survey observations of complex organic molecules towards hot core sources by Ikeda et al. (2001). Hot cores are high-mass star forming regions traced by the high temperature and dense molecular gas, which are sometimes associated with HII regions. Further, we also selected two famous low-mass star forming

regions where complex molecules have been observed. These sources for our survey are summarized in Table 3.

In this table, W3(H_2O), Orion KL, NGC6334F, G10.47+0.03, G19.61-0.23, G31.41+0.3, W51 e1/e2, and DR21(OH) are molecule-rich sources (Ikeda et al. 2001). G75.78+0.34 and Cep A were selected from the CH_3OH maser catalogs. The above sources are high-mass star-forming regions.

2.2.4. Observed Species

I could obtain wide range of spectra simultaneously in the CH_2NH surveys. As the results, several transitions of COMs were observed simultaneously. Here I summarize the observed COMs and their previous studies.

CH_3OH

CH_3OH is one of the well-known species in the ISM. Since the first detection by Ball et al. (1970), CH_3OH was detected toward various high-mass and low-mass star-forming regions, circumstellar shell. Extragalactic methanol masers were reported since the first detections by Sinclair et al. (1992). Recently, CH_3OH was confirmed in a protoplanetary disk (TW Hya) via high-resolution observation by ALMA (Walsh et al. 2016). In addition to these detections in the gas phase, solid phase CH_3OH is also detected (e.g., Sandford et al. 1993). The detection of CH_3OH in Comet Hale-Bopp (1995 O1) would imply that CH_3OH formed in interstellar nebula remains in cometary nuclei (Ikeda et al. 2002).

CH_3OCH_3

CH_3OCH_3 was first detected by Snyder et al. (1974). It is known that CH_3OCH_3 is one of the abundant species in hot cores (Ikeda et al. 2001) and hot corinos such as IRAS16293-2422 (Cauzax et al. 2003; Bottinelli et al. 2004). Brouillet et al. (2013) conducted mapping observation of CH_3OCH_3 toward Orion KL, and claimed that the distribution is quite similar to that of $HCOOCH_3$, suggesting these species would trace the same environment.

CH_3COCH_3

Currently, CH_3COCH_3 sources are limited to hot molecular cores. Its first detection was made by Combes et al. (1987), which was confirmed by Snyder et al. (2002). Recently, new detections of CH_3COCH_3 were reported toward other star-forming regions, Orion KL (Friedel et al. 2005; Peng et al. 2013), G24.78+0.08 (Codella et al. 2013), and W51 North region (Rong et al. 2016).

$HCOOCH_3$

Since the first detection of $HCOOCH_3$ (Brown et al. 1975), $HCOOCH_3$ has been found towards star forming regions (e.g., Bisschop et al. 2007). Its isotopologues, $H^{13}COOCH_3$ and $HCOO^{13}CH_3$ were reported by Favre et al. (2014). The first excited state of $HCOOCH_3$ is also observed towards Orion KL and W51 e2 (Kobayashi 2007; Demyk et al. 2008).

CH_2CHCN

CH_2CHCN was first detected toward Sgr B2 by Gardner & Winnewisser (1975). CH_2CHCN has been detected towards various environment in the Universe, such as Orion (Schilke et

al. 1997), dark clouds (Matthews et al. 1983), circumstellar enverope of red giants (Agúndez et al. 2008).

CH_3CH_2CN

CH_3CH_2CN was first detected toward Orion Molecular Cloud and Sgr B2 (Johnson et al. 1977). Following that CH_3CH_2CN was reported in hot corinos of low-mass protostars such as IRAS 16293-2422, NGC1333-IRAS 2A, and NGC 1333-IRAS 4A (Cauzax et al. 2003; Taquet et al. 2015). The ^{13}C isotopologues of CH_3CH_2CN were detected in Orion IRc2 and Sgr B2(N) (Demyk et al. 2007; Muller et al. 2008).

NH_2CHO

NH_2CHO was detected in various environment in the Universe. Since its first detection by Rubin et al. (1971) towards Sgr B2, NH_2CHO has been detected towards several high-mass star forming regions (Bisschop et al. 2007), hot corinos (Kahane et al. 2013), shock regions in L1157-B1 and B2 (Mendoza et al. 2014), and comets (Biver et al. 2014). The detection of NH_2CHO in the comets indicates that NH_2CHO could be delivered to the early Earth and be related to the chemistry to the origin of life. Since NH_2CHO contains the peptide bond, NH_2CHO could be the starting point for the prebiotic synthesis of both metabolic and genetic species: amino acids, nucleic acid bases, acyclonucleosides, sugars, amino sugars, and carboxylic acids in the primordial Earth.

CH_2NH and CH_3NH_2

CH_3NH_2 is a notable species in the context of origin of life, since it has been demonstrated that CH_3NH_2 would react with CO_2 on the interstellar ice surface to form glycine under UV radiation field (Holtom et al. 2005). There were few report on the detections of CH_2NH

and CH_3NH_2. Altwegg et al. (2016) reported the detection of CH_3NH_2 in the comet 67P/Churyumov-Gerasimenko. In addition, both CH_2NH and CH_3NH_2 have been observed towards high-mass star-forming regions. First detection of CH_2NH was made towards Sgr B2 (Godfrey et al. 1973). CH_2NH was confirmed towards Sgr B2 by many authors, and in particular, Halfen et al. (2013) reported 27 transitions of CH_2NH towards Sgr B2. Since then, the number of CH_2NH sources was extended by the proceeding surveys towards high-mass star-forming regions (Dickens et al. 1997; Suzuki et al. 2016). Recently, Qin et al. (2010) reported the detection of CH_2NH towards G19.61-0.23 through a line survey with the Sub-Millimeter Array. Further CH_3NH_2 was detected towards Sgr B2 (Kaifu et al. 1974) and Orion KL (Fourikis et al. 1974).

2.3. Results

We detected CH_2NH lines towards eight high-mass star-forming regions as shown in Figure 2. Among them, Orion KL, W51 e1/e2, G34.3+0.15, and G19.61-0.23 were known as CH_2NH sources in the past surveys (Dickens et al. 1997; Qin et al. 2010). However, we report the detection of the 4_{04}-3_{13} transition for the first time. Other sources, NGC6334F, G10.47+0.03, G31.41+0.3, and DR21(OH), are new CH_2NH sources. The observing results of all COMs including CH_2NH are summarized in Tables 4 through 12.

Figure 2 shows detected 4_{04}-3_{13} line of CH_2NH with the NRO 45 m telescope towards the eight high-mass star-forming regions. The dotted lines correspond to the rest frequency of the 4_{04}-3_{13} transition (105.794062 GHz). Two other CH_2NH lines (4_{14}-3_{13} and 4_{23}-3_{22}) were detected with the SMT telescope towards G10.47+0.03 and G31.41+0.3. We note that the 4_{04}-3_{13} line towards G10.47+0.03 and G31.41+0.3 show comparable intensities to that of Orion KL. Figure 3 shows the CH_2NH lines observed towards G10.47+0.03 and G31.41+0.3 with the NRO 45 m telescope and the SMT telescope. In this figure, the vertical solid line

corresponds to the systemic radial velocity of each source, shown in Table 3. The difference of radial velocities among the three observed transitions, 4_{04}-3_{13}, 4_{14}-3_{13}, and 4_{23}-3_{22}, are within 0.25 km s^{-1}. On the other hand, we did not detect the 1_{11}-0_{00} transition towards G31.41+0.3. All of the observed spectra are shown in Figure 4.

In the other sources (Cep A, W3(H_2O), DR21(OH), G75.78+0.34, NGC2264 MM3 IRS1, NGC1333 IRAS4B, and IRAS16293-2422), no CH_2NH transitions were detected. We briefly summarize their properties here. Cep A is a high-mass star-forming region which harbors several radio continuum sources including several HII regions. These complex components are spatially unresolved in our beam. W3(H_2O) is an H_2O maser source with which HII regions are associated. G75.78+0.34 is known to contain at least two ultra compact (UC) HII regions ionized by B0-B0.5 ZAMS stars and possibly Hyper-Compact HII regions. NGC2264 MMS3 IRS1 is a dense core associated with a small star cluster, where $HCOOCH_3$ emission was reported (Sakai et al. 2007). NGC1333 IRAS4B and IRAS16293-2422 are class 0 low-mass protostars where complex organic molecules have been reported. It is known that IRAS16293-2422 has three components named A1, A2, and B, which are unresolved in our beam. Outflow activities are confirmed in A2 and B (Loinard et al. 2013). Complex organic molecules such as methyl formate ($HCOOCH_3$) and glycolaldehyde (CH_2OHCHO) were detected towards IRAS16293-2422 (Jørgensen et al. 2012). Since NGC1333 IRAS4B is located 30" away from IRAS4A, enabling us to separate them with our beam. $HCOOCH_3$ is detected towards NGC1333 IRAS4B (Sakai et al. 2006).

2.3.1. Derivation of Abundance

In this subsection we will describe the methodologies in deriving fractional abundances of COMs. In sources where more than two transitions are available, we calculated column densities (N_{rot}) of COMs using the rotation-diagram method described in Turner (1991),

and the following equation was employed:

$$\log \frac{3kW}{8\pi^3 \nu S d^2 g_{\rm I} g_{\rm K}} = \log \frac{N_{\rm rot}}{Q(T_{\rm rot})} - \frac{E_{\rm u}}{k} \frac{\log e}{T_{\rm rot}} \tag{1}$$

where W is the integrated intensity, S is the intrinsic line strength, d is the permanent electric dipole moment, $g_{\rm I}$ and $g_{\rm K}$ are the nuclear spin degeneracy and the K-level degeneracy, respectively, N is the column density, $Q_{\rm rot}$ is the rotational partition function, $E_{\rm u}$ is the upper level energy, and $T_{\rm rot}$ is the rotation temperature. $g_{\rm I}$ and $g_{\rm K}$ are unity for CH_2NH because CH_2NH is an asymmetric top with no identical H atoms. The column density is derived from the interception of a diagram, and its slope will give us the excitation temperature. In this derivation, the source size of 10" was assumed. The rotation diagrams are shown in Figures 4 through 11. The derived abundances are summarized in Table 13.

The assumption of rotation diagram method that observed transitions are optically thin is not always correct. Also, the source size may have large uncertainty. A more accurate way to derive abundances is to use the least squares fitting method. If the column density and excitation temperature are given, the brightness temperature can be calculated with the following formula:

$$T_{\rm B} = (J(T_{\rm ex}) - J(T_{\rm bb}))(1 - \exp(-\tau))\eta_{\rm mb}(\frac{\Theta_{\rm Source}}{\Theta_{\rm beam}})^2, \tag{2}$$

where

$$J(T) = \frac{{\rm h}\nu}{k} \frac{1}{\exp(\frac{{\rm h}\nu}{kT}) - 1} \tag{3}$$

$$\tau = 1.248 \times 10^{-13} \frac{S d^2 N_{\rm rot} f(T, E_{\rm u})}{Q(T_{\rm ex}) \Delta v} \tag{4}$$

$$f(T, E_{\rm u}) = \exp(\frac{{\rm h}\nu}{kT} - 1) \times \exp(-E_{\rm u}/kT) \tag{5}$$

$T_{\rm bb}$ is the brightness temperature of the cosmic background radiation (2.7 K), $\eta_{\rm mb}$ is the main beam efficiency, $\Theta_{\rm Source}$ is the source size, and $\Theta_{\rm beam}$ is the beam size.

Thus, if more than three transitions are available, the best-estimated source size, the column density, and the excitation temperatures, which make the χ^2 minimum, can be derived via utilizing the Marquard method:

$$\chi^2(N, T, \Theta) = \sum_i (Ta^*(i) - Tcalc(N, T, \Theta, i))^2 \tag{6}$$

"i" represents the number of observed transitions. In this method, $Tcalc(N, T, \Theta, i)$ is theoretically predicted brightness temperature of a certain transition number "i" via the equation (2), under a given column density of N, the excitation temperature of $T_{\rm ex}$, and the source size of Θ. In the equation (6), squares of substructions of observed Ta*(i) values from corresponding predicted $Tcalc(N, T, \Theta, i)$ values are calculated for all "i", and the $\chi^2(N, T, \Theta)$ is given as their sum. The initial column density and the excitation temperature are assumed from the rotation diagram method. When the rotation temperature is high, it would be reasonable to assume that such species would exist in a compact hot component rather than in an envelope. If actual source size is compact, the column density under 10" source size would underestimate an actual value. Therefore, the initial column density for the Marquard method was given by multiplying the factor of $(\frac{10"}{\Theta_{continuum}})^2$ to the $N_{\rm rot}$, where $\Theta_{continuum}$ is the size of continuum emission:

$$N_{\rm initial} = N_{\rm rot} \times (\frac{10"}{\Theta_{continuum}})^2 \tag{7}$$

The derived abundances are summarized in Table 14.

2.3.2. G10.47+0.03

The antenna temperature of the 4_{04}-3_{13} transition is about 0.1 K, which is very strong among our sources. The linewidth is 8 km s^{-1} which is typical in this source. Various complex molecules, like $HCOOCH_3$, CH_3OCH_3, CH_3COCH_3, CH_3CHO, were detected. In addition to these species, HCOOH and c-C_2H_4O were also reported by Ikeda et al. (2001). In our survey, N-bearing molecules such as CH_3CH_2CN, CH_2CHCN, NH_2CHO were confirmed with sufficient signal to noise ratios. Three CH_2NH lines were observed with the NRO 45 m and the SMT telescopes. Unfortunately, due to lack of time, we could not observe by the SMT the 1_{11}-0_{00} line at 225 GHz whose upper energy level is 10.8 K. I calculated the column density and excitation temperature using the rotation diagram method for observed COMs (Figure 4). Assuming a source size of 10", I obtained the following column densities and excitation temperatures: 2.7±0.4×10^{17} cm^{-2} and 184±20 K for CH_3OH, 7.1 ±1.9×10^{15} cm^{-2} and 60 ±40 K for $HCOOCH_3$, 3.0 ±0.8×10^{15} cm^{-2} and 126 ±21 K for CH_3OCH_3, 4.2 ±0.9×10^{14} cm^{-2} and 16±2 K for CH_3CHO, 5.7 ±0.8×10^{15} cm^{-2} and 119 ±61 K for NH_2CHO, 2.3 ±0.3×10^{16} cm^{-2} and 398±209 K for CH_3CH_2CN, 1.9 ±0.1×10^{16} cm^{-2} and 383 K for CH_2CHCN, 4.7 ±1.6×10^{15} cm^{-2} and 84±54 K for CH_2NH, and 1.4 ±0.4×10^{15} cm^{-2} and 61 ±42 K for CH_3NH_2. Among our new detections, G10.47+0.03 is a CH_2NH abundant source.

Using the above as initial values, I obtained the best-estimated values of the column densities, excitation temperatures, and the source sizes by the least square fitting method. In this case, I found the source sizes, column densities, and the excitation temperatures of, respectively, 3.2±0.2", 2.6 ±0.4×10^{18} cm^{-2}, and 106 ±20 K for CH_3OH, 1.6±0.3", 1.1 ±0.4×10^{18} cm^{-2} and 151±78 K for $HCOOCH_3$, 1.9±0.4", 7.6±0.4×10^{17} cm^{-2} and 94±17 K for CH_3OCH_3, 2.1±0.4", 7.6±4.1×10^{17} cm^{-2} and 63±39 K for NH_2CHO, 1.3±0.1", 8.5 ±2.2×10^{17} cm^{-2} and 169±26 K for CH_3CH_2CN, 1.0±0.1", 1.7 ±0.3×10^{18} cm^{-2} and 230

±47 K for CH_2CHCN.

For CH_2NH and CH_3NH_2, the column densities were obtained by assuming a source size of 1.3", which corresponds to the continuum source size. In this case, the column density of CH_2NH and CH_3NH_2 are 2.8±1.0×10^{17} cm^{-2} and 8.0±2.1×10^{16} cm^{-2}. It is reported that the distribution of $(CH_3)_2CO$ is very similar to that of CH_3CH_2CN in Orion KL (Peng et al. 2013). Thus, I employed the source size of 1.3" and the excitation temperature of 170 K, which is the same one as that of CH_3CH_2CN in this source. If I use the 9(0,9)-8(1,8)EE and 9(1,9)-8(0,8)EE transitions, which showed the best S/N ratios, the column density of $(CH_3)_2CO$ is 3.8±1.9×10^{16} cm^{-2} for a source size of 10"and 2.2±1.1×10^{18} cm^{-2} for a source size of 1.3".

2.3.3. Orion KL

Orion KL is the closest high-mass star forming region and famous for its rich interstellar chemistry. It is well known that a component called "Orion Compact Ridge" is located at (α(2000), δ(2000))=(05^h 32^m 46.5^s, -05° 24' 30.0"), about 7" away from the "Hot Core". In our 16" beam size, lines from these components are observed simultaneously. O-bearing molecules like CH_3OCH_3, CH_3CHO, CH_3OH, $(CH_3)_2CO$, and N-bearing molecules like CH_3CH_2CN, CH_2CHCN, CH_2NH, and $H^{13}CCCN$ were detected. Assuming a source size of 10", I obtained the column densities, and the excitation temperatures of, respectively, 4.3±0.3×10^{17} cm^{-2} and 172±8 K for CH_3OH, 3.4±1.0 ×10^{16} cm^{-2} and 80±43 K for $HCOOCH_3$, 4.3±0.3×10^{16} cm^{-2} and 91±7 K for CH_3OCH_3, 3.5±0.8×10^{14} cm^{-2} and 28±8 K for CH_3CHO, 9.9±1.2×10^{15} cm^{-2} and 146±28 K for CH_3CH_2CN, 3.1±0.2×10^{15} cm^{-2} and 97±7 K for CH_2CHCN, 5.5±0.7 ×10^{15} cm^{-2} and 88±18 K for CH_2NH. The spatial distributions of several detected species are known in the past papers. If I calculate corresponding source sizes from the reported spatial distributions of these species, I get

5.2" for CH_3OH (Peng et al. 2012), 2.8" for CH_3CH_2CN and $(CH_3)_2CO$ (Peng et al. 2013), CH_3OCH_3 (Brouillet et al. 2013), 3.5" for $HCOOCH_3$ (Favre et al. 2011). Peng et al. (2013) claimed that the spatial distribution of CH_3CH_2CN and $(CH_3)_2CO$ are overlapped on the position of Hot Core, whose radial velocity is $\sim$5 km s^{-1}. Although the detailed distributions of CH_2CHCN and NH_2CHO are not well investigated, Blake et al. (1987) claimed that CH_2CHCN would be in Hot Core rather than Compact Ridge from the line shapes and their radial velocities. Thus, I employed a source size of 2.8" for CH_2CHCN considering the distribution of CH_3CH_2CN. The distributions of CH_3OH, $HCOOCH_3$, CH_3OCH_3 are overlapped on the Compact Ridge, whose radial velocity is $\sim$8 km s^{-1} with a narrower line width than the Hot Core species. The column densities and the excitation temperatures under above source sizes were estimated using the least squares method. As the results, I obtained the column densities, and the excitation temperatures of, respectively, $2.3\pm0.1\times10^{18}$ cm^{-2}, and 192±18 K for CH_3OH, $1.5\pm0.2\times10^{17}$ cm^{-2} and 44±3 K for $HCOOCH_3$, $6.5\pm0.9\times10^{17}$ cm^{-2} and 178±24 K for CH_3OCH_3, $1.7\pm0.6\times10^{17}$ cm^{-2} and 63±6 K for CH_3CH_2CN, $4.8\pm2.0\times10^{16}$ cm^{-2} and 122±50 K for CH_2CHCN, and $6.0\pm1.7\times10^{16}$ cm^{-2} and 84±54 K for CH_2NH.

2.3.4. NGC6334F

NGC6334F is known as an active star-forming region with its narrow line width. $HCOOCH_3$, CH_3OCH_3, CH_3COCH_3, and CH_3OH were detected. N-bearing species such as CH_2NH, CH_2CHCN and CH_3CH_2CN were detected, while their emissions were not so strong as those in G10.47+0.03. The survey conducted by Ikeda et al. (2001) also reported O-bearing molecules ($HCOOCH_3$, CH_3OCH_3, CH_3OH, HCOOH and c-C_2H_4O). Assuming the source size of 10", I obtained the column densities, and the excitation temperatures of, respectively, $3.1\pm0.5\times10^{17}$ cm^{-2} and 201±24 K for CH_3OH, $1.5\pm 0.4\times10^{17}$ cm^{-2}

and 313± 575 K for $HCOOCH_3$, 4.4±1.0×10^{15} cm^{-2} and 101±21 K for CH_3OCH_3, 1.5±0.4×10^{14} cm^{-2} and 20±5 K for CH_3CHO, 6.5±1.7×10^{14} cm^{-2} and 50±30 K for NH_2CHO, 3.4±0.7×10^{14} cm^{-2} and 83±30 K for CH_3CH_2CN, and 2.3±1.1×10^{15} cm^{-2} and 27±13 K for CH_3NH_2, respectively, using the rotation diagram method. The low exicitation temperatures of CH_3CHO shows that this species would be in the envelope of the hot core.

The observed energy ranges are too limited to apply the rotation diagram method for $(CH_3)_2CO$ and CH_2CHCN. Since the distribution of CH_3CH_2CN is similar to that of CH_2CHCN and $(CH_3)_2CO$ in Orion KL, they would be synthesized in a similar environment. I assumed the excitation temperatures to be 80 K for these species, referring to that of CH_3CH_2CN. As the results, the column densities were obtained to be 2.9±1.0×10^{14} cm^{-2} for CH_2CHCN and 3.4±1.4×10^{15} cm^{-2} for $(CH_3)_2CO$, respectively.

The least squares fitting method was employed to correct the effect of optically thick emissions. The initial source size was assumed to be 3.5" from the source size of continuum emission (Hernández-Hernández et al. 2014). Then I obtained the source sizes, the column densities, and the excitation temperatures of, respectively, 3.8±0.5", 2.6±0.4×10^{18} cm^{-2} and 116±37 K for CH_3OH, 1.9±0.1", 1.1±0.4×10^{18} cm^{-2} and 101±10 K for $HCOOCH_3$, 4.5±1.5", 7.6±0.4×10^{17} cm^{-2} and 82±14 K for CH_3OCH_3. The column density of CH_3NH_2 was calculated assuming the source of 3.5". For the other species, I fixed the source size to be 3.5" due to the lack of enough number of emission lines. CH_3CH_2CN shows the excitation temperature of 58±23 K and the column density of 8.5±2.2×10^{17} cm^{-2}. For CH_2CHCN and $(CH_3)_2CO$, NH_2CHO and CH_3NH_2, their column densities were 2.4±0.8×10^{16} cm^{-2}, 2.8±1.1×10^{17} cm^{-2}, 5.3±1.3×10^{15} cm^{-2} and 1.4±1.6×10^{16} cm^{-2}, respectively, asumming the source size of 3.5". The rotation temperature of CH_2NH was fixed to 40 K, which is a typical excitation temperature of HCOOH whose dipole moment is close to CH_2NH, and, column density was obtained to be 2.7±1.6×10^{15} cm^{-2}.

2.3.5. W51 e1/e2

Various complex molecules like $(CH_3)_2CO$, CH_3CHO, CH_3OCH_3, CH_3CH_2CN, CH_2NH were detected towards W51 e1/e2, as reported in Ikeda et al. (2001). The linewidth is typically 7 km s^{-1}. Assuming a source size of 10", I obtained the column densities, and the excitation temperatures of, respectively, $2.8\pm0.7\times10^{17}$ cm^{-2} and 222±46 K for CH_3OH, $5.0\pm0.6\times10^{15}$ cm^{-2} and 131±24 K for CH_3OCH_3, $3.3\pm1.9\times10^{13}$ cm^{-2} and 10±3 K for CH_3CHO, $4.8\pm3.2\times10^{14}$ cm^{-2} and 27±23 K for NH_2CHO, and $1.1\pm0.2\times10^{14}$ cm^{-2} and 179±140 K for CH_3CH_2CN using the rotation diagram method. The low excitation temperature of CH_3CHO implies that they would be in the envelope of the source. Thus, their distributions would be extended. NH_2CHO also showed the low excitation temperature of 27 K, however, we note that the observed energy range is so limited for this species to determine an accurate excitation temperature. For $HCOOCH_3$, the excitation temperature was not determined (4277±48777 K). In the rotation diagram of $HCOOCH_3$, low energy transitions showed large scattering in the distribution of the plots. This result would be due to the assumption of rotation diagram that all transitions are optically thin.

The CH_2CHCN and $(CH_3)_2CO$ were fixed in the least squares method due to the limited energy levels of the observed transitions. The initial source size was assumed to be 2", considering two ∼1.1" size components of the continuum emission in the observed region (Hernández-Hernández et al. 2014). The initial excitation temperature of $HCOOCH_3$ was set to be 200 K referring to that of CH_3OH. I obtained the source sizes, the column densities, and the excitation temperatures of, respectively, 3.1±0.3", $3.7\pm0.4\times10^{18}$ cm^{-2} and 246±50 K for CH_3OH, 1.6±0.2", $2.0\pm0.6\times10^{18}$ cm^{-2} and 69±16 K for $HCOOCH_3$, 2.7±0.8", $3.9\pm3.2\times10^{17}$ cm^{-2} and 95±28 K for CH_3OCH_3, 1.6±1.0", $9.8\pm7.5\times10^{16}$, and 39±37 K for CH_3CH_2CN. With the least squares method, the best source size to reproduce the observed CH_2NH transitions was 10". This is because if compact source sizes were

assumed, the 1(1,1)-0(0,0) and 4(1,4)-3(1,3) transitions, referred by Dickens et al. (1997), tend to be optically thick and the predicted Ta*values were weaker than observed ones. Therefore, it may be likely that a spatial distribution of CH_2NH in W51 e1/e2 is extended.

The abundances under compact source size for $(CH_3)_2CO$, NH_2CHO, and CH_2CHCN were derived by assuming that the source size is the same as the continuum emission size of 2", and assuming the excitation temperatures obtained by the rotation diagram method. As the results, column densities for $(CH_3)_2CO$, NH_2CHO, and CH_2CHCN were, respectively, $1.7\pm0.8\times10^{17}$, $2.0\pm0.8\times10^{16}$ and $1.4\pm0.5\times10^{16}$ cm^{-2}.

2.3.6. G31.41+0.03

G31.41+0.3 is known as a molecular rich source. Isokoski et al. (2013) reported a result of submillimeter line survey in this source, and complex molecules, CH_3OH, H_2CO, C_2H_5OH, $HCOOCH_3$, CH_3OCH_3, CH_3CN, HNCO, NH_2CHO, C_2H_5CN, CH_2CO, HCOOH, CH_3CHO, and CH_3CCH were detected. In addition to G10.47+0.03, G31.41+0.3 also showed high antenna temperature of the $4_{04} - 3_{13}$ transition of CH_2NH ($\sim$0.1 K). Similar to G10.47+0.03, many O-bearing molecules like CH_3OH, $HCOOCH_3$ and NH_2CHO were also reported. As shown in Table 8, several transitions of N-bearing molecules (e.g., CH_3CH_2CN, CH_2CHCN, and CH_2NH) were observed, but they tend to be weaker by a factor of a few than in the case for G10.47+0.3. Three CH_2NH transitions were observed towards this object with the NRO 45m and the SMT telescopes. The 1_{11}-0_{00} line was not detected, which was expected to be strong if the excitation temperature is lower.

Assuming the source size of 10", I obtained the column densities, and the excitation temperatures of, respectively, $1.1\pm0.2\times10^{17}$ cm^{-2} and 217±37 K for CH_3OH, $3.6\pm1.4\times10^{15}$ cm^{-2} and 33±18 K for $HCOOCH_3$, $9.6\pm1.3\times10^{14}$ cm^{-2} and 62±15 K for

NH_2CHO, and 8.5±8.2×10^{14} cm^{-2} and 28±17 K for CH_2NH using the rotation diagram method. The excitation temperature of CH_3CH_2CN was negative if it was derived from the rotation diagram. This result would be due to the assumption of rotation diagram that all transitions are optically thin. An excitation temperature of 60 K was assumed for CH_2CHCN and $(CH_3)_2CO$, from the analysis of CH_3CH_2CN with the least squares fitting method described in the next paragraph,, and the column densities are 3.7±2.4×10^{14} cm^{-2} and 3.6±1.4×10^{15} cm^{-2}. An excitation temperature of 10 K was assumed for CH_3CHO and the column density was derived to be 2.5±1.5×10^{14} cm^{-2}.

The excitation temperatures, the column densities were also estimated with the least squares method. The rotation diagram method for CH_3CH_2CN gave the negative excitation temperature and this result would be unrealistic. Therefore, for CH_3CH_2CN, different initial column densities and the excitation temperatures were tested under 1-5×10^{17} cm^{-2}, and 100-200 K with the least squares method. As a result, I obtained the source sizes, the column densities, and the excitation temperatures of, respectively, 1.8±0.1", 3.8±0.6×10^{18} cm^{-2}, and 185±51 K for CH_3OH, 2.6±1.1", 1.1±1.7×10^{17} cm^{-2}, and 41±35 K for $HCOOCH_3$, 3.4±2.2", 1.9±2.7×10^{17} cm^{-2}, and 76±12 K for CH_3OCH_3, 1.8±0.3", 3.0±1.5×10^{16} cm^{-2}, and 41±18 K for NH_2CHO, 1.7±0.6", 3.5±1.7×10^{17} cm^{-2}, and 62±44 K for CH_3CH_2CN. Most of the transition of CH_3CH_2CN were actually optically thin under 3.5×10^{17} cm^{-2} and 62 K, and it was impossible to derive accurate values by rotation diagram method. The numbers of observed transition were not enough for CH_2CHCN, CH_2NH, and $(CH_3)_2CO$. If their source size was fixed to be the continuum size of 1.7", their column densities of CH_2CHCN, CH_2NH, and $(CH_3)_2CO$, respectively, are 1.3±0.8×10^{16}, 3.1±3.0×10^{16}, and 2.3±1.0×10^{16} cm^{-2}.

2.3.7. G34.3+0.2

CH_3OH, CH_3OCH_3, CH_3CH_2CN, CH_2CHCN, $HCOOCH_3$, and CH_2NH were detected. In Ikeda et al. (2001), c-C_2H_4O, C_2H_5CN, C_2H_5OH, $HCOOCH_3$ were also reported. As for CH_2NH, Dickens et al. (1997) reported the 4_{14}-3_{13} transition whose upper level energy is close to that of the 4_{04}-3_{13} line. Thus, we estimated the column density of CH_2NH solely based on our data.

Assuming a source size of 10", I obtained the column densities, and the excitation temperatures of, respectively, $1.2\pm0.3\times10^{17}$ cm^{-2} and 196±42 K for CH_3OH, $5.6\pm0.9\times10^{16}$ cm^{-2} and 331±362 K for $HCOOCH_3$, $1.7\pm0.4\times10^{15}$ cm^{-2} and 117±72 K for CH_3OCH_3, and $5.7\pm1.0\times10^{14}$ cm^{-2} and 167±83 K for CH_3CH_2CN, and $1.4\pm0.8\times10^{14}$ cm^{-2} and 25±10 K for CH_2CHCN using the rotation diagram method. The excitation temperature of $HCOOCH_3$ was not determined from rotation diagram. This would be becuse some transitions are optically thick and led to scattering of plots in rotation diagram. The column deisity and excitation temperature for $HCOOCH_3$ will be discussed with the least squares method below. Considering the very low excitation temperature of CH_3CHO in other sources, CH_3CHO would exist in the envelope of the hot cores. Therefore its abundance was derived to be $5.2\pm2.0\times10^{14}$ cm^{-2} assuming the excitation temperature of 10 K. $(CH_3)_2CO$ and NH_2CHO abundances were derived under the excitation temperatures of 60 K, considering that the excitation temperatures of CH_3CH_2CN and $HCOOCH_3$ derived with the least squares method are not so high, as described in the latter part of this subsection. The abundance of CH_2NH was derived to be $7.1\pm4.2\times10^{14}$ cm^{-2} assuming an excitation temperature of 40 K, which is the typical excitation temperature of HCOOH (Ikeda et al. 2001).

The least squares method was applied for CH_3CH_2CN, $HCOOCH_3$, and CH_3CH_2CN. As the results, the source sizes, the column densities, and the excitation temperatures

are, respectively, 2.3±0.3", 3.2±0.5×10^{18} cm^{-2}, 98±27 K for CH_3OH, 1.3±0.4", 2.4±1.3×10^{18} cm^{-2}, 48±29 K for $HCOOCH_3$, and 1.4±0.4", 3.3±2.4×10^{16} cm^{-2}, 49±39 K for CH_3CH_2CN. Most of the observed transitions of $HCOOCH_3$ and CH_3CH_2CN with lower energy levels tend to be optically thick, resulting in strongly overestimated excitation temperatures with rotation diagram method. The least squares method was not applied for CH_2CHCN and CH_3OCH_3, due to lack of enough number of observed transitions. In Table 14, abundances under compact source sizes for $(CH_3)_2CO$, CH_3OCH_3, NH_2CHO, CH_2CHCHN, and CH_2NH were simply derived by compensating an effect of beam dilution.

2.3.8. G19.61-0.23

Qin et al. (2010) conducted a line survey towards this source, and many organic molecules (e.g., CH_3OH, $HCOOCH_3$, C_2H_5OH, NH_2CHO, HNCO, CH_3CN, CH_3CH_2CN,...) were reported. Among them, the first detection of CH_2NH was made. Although we observed a relatively small number of strong lines for this source, some CH_2CHCN, CH_3CH_2CN, and CH_3OH lines were detected. We made marginal detection of the 4_{04}-3_{13} transition of CH_2NH. Due to the lack of enough observed transitions, molecular abundances for this source were calculated from the rotation diagrams assuming a continuum source size of 2.5". CH_3OH shows the excitation temperature and the column density of 131±68 K and 3.5±3.3×10^{16}cm^{-2}, and NH_2CHO shows 78±57 K and 5.8±2.2×10^{14}cm^{-2}. The excitation temperatures of CH_2CHCN and CH_3CH_2CN were fixed at 60 K from the relatively lower excitation temperature of NH_2CHO for this source. As the results, their abundances are 5.3±3.0×10^{14}cm^{-2} for CH_2CHCN and 1.4±1.0×10^{14}cm^{-2} for CH_3CH_2CN. CH_2NH abundances assuming the excitation temperature of 40 K, referring to that of HCOOH (Ikeda et al. 2001) whose dipole moment is close to that of CH_2NH, was 9.4±6.5×10^{15}cm^{-2}.

2.3.9. DR21(OH)

DR21(OH) is a relatively line poor star-forming region among our new CH_2NH objects. The observed O-bearing species are CH_3OH and $HCOOCH_3$. This result agrees with that of Ikeda et al. (2001). Although CH_3CH_2CN and CH_2CHCN were not detected, we succeeded in detecting weak CH_2NH transition. If we assume the excitation temperature of CH_2NH to be 40 K, referring to that of HCOOH (Ikeda et al. 2001) whose dipole moment is close to CH_2NH, the column density is estimated to be $2.7\pm2.1\times10^{14}$ cm^{-2} under a source size of 10". Although the excitation temperatures for CH_3OH and $HCOOCH_3$ are highly uncertain due to lack of sufficient number of data, the column densities are $4.6\pm1.0\times10^{15}cm^{-2}$ for CH_3OH and $1.1\pm0.7\times10^{15}cm^{-2}$ assuming the excitation temperature of 150 K.

2.3.10. Other Sources

CH_2NH was not detected with sufficient S/N ratio towards G75.78+0.34, W3(H2O), and Cep A. Among them, O-bearing molecules, $HCOOCH_3$ and CH_3OH, were detected towards W3 (H_2O), but none of the N-bearing molecules were detected. The analysis via the rotation diagram method with four transitions observed toward W3 (H_2O) gave the column density of CH_3OH to be $6.7\pm8.4\times10^{16}cm^{-2}$. The column density for $HCOOCH_3$ assuming the excitation temperature of 150 K is $2.7\pm2.0\times10^{15}cm^{-2}$. For G75.78+0.34 and Cep A, COMs were not detected.

2.4. Discussion

As presented in Figure 12, the observed CH_2NH abundances are different by a factor of about 20. What characteristics cause such a large difference among CH_2NH abundances? In this section, we will discuss three hypotheses to explain the different CH_2NH abundances

in terms of distance, kinetic temperatures, and evolutionary phase of sources.

2.4.1. Chemical Properties of CH_2NH-rich sources

Before the detailed discussions of physical properties, it would be useful to discuss chemical properties of CH_2NH-rich sources. The observed fractional abundances for COMs are summarized in Figure 12, based on Tables 14 and 13. In these histograms, the fractional abundances under the compact source sizes are basically presented. However, the fractional abundances under the source size of 10" are shown for DR21(OH) and W3(H_2O), since only hydrogen column densities estimated under extended CO emission are available. The fractional abundances of CH_3CHO for all sources and CH_2NH for W51 e1/e2 were also estimated under the source size of 10" since they would have extended distributions.

To clarify the correlations of the CH_2NH fractional abundance and those of other COMs, they are plotted in Figure 13. In the following discussion, I discuss if there is a correlation between CH_2NH and other species presented as "y", with the correlation coefficient below:

$$r(CH_2NH, species\ y) = \frac{\sum^{n}_{source\ i}(X_{source\ i,CH_2NH} - \overline{X_{CH_2NH}})(X_{source\ i,species\ y} - \overline{X_{species\ y}})}{\sqrt{\sum(X_{source\ i,CH_2NH} - \overline{X_{CH_2NH}})^2 \sum (X_{source\ i,species\ y} - \overline{X_{species\ y}})^2}}, \quad (8)$$

where n is the total number of the observed sources, and $X_{source\ i,species\ y}$ and $\overline{X_{species\ y}}$, respectively, represent a fractional abundance for a certain source "i", and averaged fractional abundance of a certain species "y" among all sources. r is close to unity if the correlation is strong and negative values of r mean negative correlation. r=0 corresponds to the case where there is no correlation.

According to Figure 13, there would be correlations between CH_2NH and CH_3CH_2CN, CH_2CHCN, and $(CH_3)_2CO$. The high correlation coefficient of 0.97 supports that there is

a correlation between CH_3CH_2CN and CH_2NH. CH_2CHCN, CH_3OCH_3, and $(CH_3)_2CO$ showed the moderate correlation coefficients of 0.67, 0.70, and 0.71, respectively. For $(CH_3)_2CO$, we need to be careful due to the number of limited observed transitions. For the case of Orion KL, it should be taken into account that our beam observed the "Hot Core" and the "Compact Ridge" components simultaneously; the former is known to be rich in N-bearing molecules while the latter is rich in O-bearing species. If the data of Orion KL is excluded, the correlation coefficient between CH_2NH and CH_3OCH_3 is 0.29, while CH_2NH and CH_3CH_2CN, CH_2CHCN, still showed the high correlation coefficient of 0.95, 0.99. NH_2CHO has somewhat moderate correlation coefficient of 0.53. I note that this correlation coefficient is as high as 0.97 if Orion KL is excluded in the calculation.

On the other hand, Figure 13 suggested that fractional abundances of CH_3OH and $HCOOCH_3$ are not so correlated to that of CH_2NH. For instance, in NGC6334F, while the fractional abundances of CH_2NH is lower than that in Orion KL by almost a factor of 10, the fractional abundances of CH_3OH and $HCOOCH_3$ are comparable to that in Orion KL. The correlation coefficients for CH_3OH and $HCOOCH_3$ showed low values of 0.34 and 0.40, respectively. If the data point of Orion KL is excluded, the correlation coefficients for CH_3OH and $HCOOCH_3$ showed negative values of -0.09 and -0.35, respectively.

Therefore, it would be likely that the fractional abundances of CH_2NH are correlated with those of CH_3CH_2CN and CH_2CHCN, and they may have similar production and/or destruction processes. On the other hand, fractional abundances of CH_2NH would not be related to those of CH_3OH and $HCOOCH_3$, indicating that they are formed and/or destroyed in different ways.

2.4.2. Different Distance

First of all, we will discuss the possibility that the difference of CH_2NH abundances is simply due to different beam filling factors originating from the different distances to the sources. Actually, the beam averaged CH_2NH column densities would be high for closer sources since they are less affected by beam dilution. However, the difference depending on the source sizes was small when we compared their fractional abundances of CH_2NH. In Figure 14, we plotted the fractional abundances of CH_2NH against the distance to the sources. It would be difficult to find the correlation between fractional abundances of CH_2NH and the distances in Figure 14. The difference of CH_2NH fractional abundances would be due to source properties rather than just an effect of beam dilution.

2.4.3. Different Evaporation Temperature

The second possibility is that the different temperatures of CH_2NH sources might contribute to CH_2NH abundances. Theule et al. (2011) demonstrated that CH_2NH can be formed via the hydrogenation process to HCN on the dust surface (Figure 1). If CH_2NH is produced on dust surface, gas phase CH_2NH abundance would be lower until source temperature gets high enough to sublimate species from dust surface. Hernández-Hernández et al. (2014) reported rotation temperatures of CH_3CN, which is often used as a tracer of the kinetic temperature, towards 17 sources including G10.47+0.03, NGC6334F, W51 e2, and W3(H_2O). The reported temperatures were 499 K for G10.47+0.03, 408 K for NGC6334F, 314 K for W51 e2, and 182 K for W3(H_2O). It is notable that W3(H_2O), where CH_2NH was not detected, has a lower temperature than CH_2NH sources and G10.47+0.03 showed the highest temperature. Thus, this scenario would be convincing when the desorption temperature of CH_2NH is high.

One easy way to roughly estimate desorption temperature would be to use the Clausius-Clapeyron equation (2) and the ideal gas law (3), described below:

$$\log_{10} \mathrm{P} = 4.559(1 - (\mathrm{T}/\mathrm{T_B})) \tag{9}$$

$$\mathrm{P} = 8.314\mathrm{nT} \tag{10}$$

where $\mathrm{T_B}$ is the boiling point under the standard state, T is the sublimation temperature under the interstellar gas pressure P, and n is the number density of the species. We have to be cautious that the desorption temperature derived in this method is an approximated value, and it would have an uncertainty in two reasons. First, the Clausius-Clapeyron equation is applicable for the phase transition between pure solid or liquid and gas. However, the actual interstellar molecules would be far from pure material, which are physisorbed on H_2O ice. In spite of the difference of the physical condition, the Clausius-Clapeyron equation succeeds to reproduce the commonly accepted sublimation temperature of H_2O (from 90 to 100 K) and CO (from 15 to 18 K) in the ISM, assuming the density from 1×10^5 to 1×10^7 cm^{-3}. Second, since the boiling point for CH_2NH is not measured, we had to use theoretically predicted value of 215($\pm$15) K from a chemical database (http://www.chemspider.com/).

If we use the CH_2NH fractional abundance of 3.1×10^{-8} (the value observed in G10.47+0.03) and the molecular hydrogen number density of 10^7 cm^{-3}, the CH_2NH number density n is 0.31 cm^{-3}. In our calculation, we assume the initial T values of from 20 K to 200 K (=$\mathrm{T_0}$) and the P is obtained from the equation (2), then, next desorption temperature, $\mathrm{T_1}$ is obtained with the equation (3). In these iterations between equations (9) and (10), we are able to determine the final T value when the difference of successive temperatures reaches within 1 K. As a result, we found that the estimated desorption temperature of 40 K is quite low compared to the gas temperatures of star-forming regions.

We also calculated the desorption temperature in terms of the equilibrium of

microscopic accretion and desorption process, which may better approximate the interstellar situation. The accretion rate R_{acc}(i) (cm^{-3} s^{-1}) and the desorption time scale t_{evap} (s) for the species i are described in Hasegawa et al. (1992) as shown below:

$$R_{\rm acc}(i) = \sigma_d < v(i) > n_{\rm gas}(i) n_d \tag{11}$$

$$t_{\rm evap} = \nu_0^{-1} \exp(E_D / kT_{\rm dust}), \tag{12}$$

$$\text{where } \nu_0 = (2 n_s E_D / \pi^2 m)^{1/2}. \tag{13}$$

σ_d, <v(i)>, n_{gas}(i), n_{dust}(i), n_d, E_D, n_s, m, respectively, represent the cross section of the dust, averaged velocity of the gas species under a certain temperature, the gas and the dust surface phase number density of the species, the dust number density, the desorption energy, the surface density of the site ($\sim 1.5 \times 10^{15}$cm^{-2}), and the mass of the molecule (4.83×10^{-23} g for CH_2NH). Using the desorption time scale t_{evap}, the desorption rate R_{des}(i) (cm^{-3} s^{-1}) is given by $t_{evap}^{-1} n_{dust}$(i). The desorption temperature is defined as the temperature which makes R_{des}(i) and R_{acc}(i) equal. Assuming a grain radius of 1×10^{-5} cm^{-1}, a physical cross section of 3.14×10^{-10} cm^{-2} is used for the σ_d. In Ruaud et al. (2015), the E_D for CH_2NH is assumed to be the same as CH_3OH (5530 K). Although the mass of CH_3OH and CH_2NH are similar, this assumption may overestimate the desorption temperature for CH_2NH, since OH group in CH_3OH can strongly interact with H_2O molecules in the interstellar ice. Thus, if we use the desorption temperature of CH_3OH, we would be able to estimate the upper limit to the desorption temperature for CH_2NH.

We used our simulation results described in Chapter 3 of this thesis, to estimate the number density of CH_2NH (n_{gas} and n_{dust}) just before the warm-up of the core. Under a molecular hydrogen number density of 1×10^7 cm^{-3}, n_{gas} (CH_2NH) and n_{dust} (CH_2NH) are roughly 1×10^{-7} cm^{-3} and 1×10^{-4} cm^{-3}. The mass of grain per unit volume (g cm^{-3}), M_{grain}, is given as the below equation with a gas-to-dust mass ratio of 0.01:

$$M_{grain} = n_{gas} \times m(H_2) \times 0.01,$$

where $m(H_2)$=3.34×10^{-24} kg is a mass for hydrogen molecule. A mass of single grain can be estimated as:

$M_{singlegrain} = \frac{4}{3}\pi r_{grain}^3 \times \rho$,

where r_{grain} and ρ are, respectively, a radius and a mass density of grains. Then, the dust number density n_d is given as $M_{grain}/M_{singlegrain}$. I obtained n_d to be 4.73×10^{-5} cm^{-3} assuming a grain radius of 1×10^{-5} cm, and a typical mass density for grain of 3 g cm^{-3}.

Then, the upper limit to the desorption temperature can be calculated to be 100 K. If the desorption temperature for CH_2NH is as high as 100 K, gas phase abundance of CH_2NH would be very low in the outer part of the cloud. In this case, CH_2NH-rich sources may be limited to "hot" sources, where sufficiently high temperature regions are evolved inside.

However, this explanation may not be enough to explain the chemical properties of CH_2NH-rich sources. According to the Clausius-Clapeyron equation, the evaporation temperature of CH_3OH is 60 K to 80 K. Even if we calculate the evaporation temperature of CH_3OH via equilibrium of microscopic accretion and desorption process, the evaporation temperature is also ∼100 K. Therefore, if CH_2NH is depleted due to the different gas temperature, CH_3OH would be also depleted.

The other view point to explain the different CH_2NH abundance, and the correlation between CH_3CH_2CN and CH_2CHCN rather than CH_3OH in terms of different temperature would be the destruction process on the grains. The laboratory experiment by Theule et al. (2011) demonstrated that CH_2NH would be converted to CH_3NH_2 via hydrogenation process on grains:

$HCN + 2H \rightarrow CH_2NH$

$CH_2NH + 2H \rightarrow CH_3NH_2$

From the similarity of this process, if CN bond is susceptible to the hydrogenation process, CH_2CHCN and CH_3CH_2CN are also likely to be converted to $CH_3CH_2CH_2NH_2$, although theoretical and experimental studies have not been available currently. If this is the case, while saturated species such as CH_3OH and CH_3NH_2 would be built on grains, the origin of unsaturated species such as CH_2NH and CH_2CHCN may be gas phase reactions rather than grain surface reactions. Their formation paths will be discussed in detail in Chapter 3.

Even after the source temperature gets so high that most of frozen species can evaporate, a part of evaporated and/or newly formed species in gas phase reactions can be adsorbed on grains. For these adsorbed species, the timescale to stay on grains before evaporation would strongly depend on the temperature of grains. The timescale for evaporation would be longer in relatively low temperature sources and hydrogenation processes would be efficient in such sources. Since unsaturated species are suspectible to hydrogenation process than saturated species, the correlation of CH_2CHCN and CH_3CH_2CN with CH_2NH may be explained by destruction processes due to hydrogenation processes. Therefore, if we assume that CH_2NH is destroyed in the sources where gas temperature is relatively low and suspectible to hydrogenation process, it may possible to explain the different CH_2NH abundances and chemical properties of CH_2NH-rich sources simultaneously.

2.4.4. Different Evolutionary Phase

The third hypothesis is that the different CH_2NH abundances are related to the evolutionary phases of HII regions inside a hot core. In the ISM, it is well-known that star formation starts in a cold pre-stellar core. The gas temperature gradually rises when a protostar is formed inside the core, and finally frozen species on the dust are evaporated into

the gas phase when the dust temperature gets high enough. As we have already mentioned, some of our sources are known to have high gas temperatures. Followed by that, CH_2NH will be gradually photo-dissociated due to strong UV field in the vicinity of an evolved HII region inside the core. In this case, the CH_2NH-rich sources can be explained as less evolved HII regions than the other sources, as is shown below.

The hydrogen recombination lines, which are originated from HII regions, would be good tools to study the evolutionary state of an HII region. We compared in Figure 15 the strength of a recombination line, H54β, among five CH_2NH sources. The observed line properties are summarized in Table 15. In G10.47+0.03 and G31.41+0.3, the observed H54β line is very weak or below 3 sigma level. For Orion KL, it is well known that recombination lines are originated from the foreground HII region; Plambeck et al. (2013) reported that recombination lines were not detected inside the Hot Core of Orion KL. Our results suggest that top three CH_2NH-rich sources would possess less evolved HII regions, while the H54β line is prominent towards W51 e1/e2 and NGC6334F. These sources are considered to have more evolved HII regions, supporting our scenario. We also note that past observational results also agree with this scenario. Cesaroni et al. (2010) claimed that G10.47+0.03 contains two deeply embedded Hyper Compact HII regions in the positions of the hot core while no detectable HII region is present in G31.41+0.3. Although it is difficult to compare directly with our observations, Jiménez-Serra et al. (2011) detected H40α, H34α, and H31α towards Cep A. Cep A would possess an evolved HII region inside and the dissociation process might result in the non-detection of CH_2NH. Considering above, the difference of the evolutionary phase would be the second plausible reason to explain the different CH_2NH abundances.

However, I note that this scinario cannot explain the chemical property that CH_2NH is correlated with CH_3CH_2CN, CH_2CHCN rather than CH_3OH and $HCOOCH_3$. Since UV

radiation would equally destroy single bands of these species, it would be reasonable to assume that they are simultaneously decrease.

2.5. Summary

The main results of this section can be summarized as follows:

1. We conducted the survey observations of CH_2NH towards high-mass star-forming regions; CH_2NH were detected in eight sources. Among them, the first detections were made in four objects, G10.47+0.03, G31.41+0.3, DR21(OH), and NGC6334F. However, CH_2NH was not detected towards low-mass star-forming regions.

2. We calculated the column densities and fractional abundances or their upper limits in our sources. The fractional abundances range from $\sim 10^{-9}$ to $\sim 10^{-8}$. We also found that Orion KL and G10.47+0.03 have higher CH_2NH abundances than other sources by almost one order of magnitude.

3. We found the correlations between the fractional abundances of CH_2NH and CH_3CH_2CN, CH_2CHCN. On the other hand, CH_3OH and $HCOOCH_3$ showed no correlation with CH_2NH.

4. The difference of CH_2NH abundances might be explained by different temperatures in hot cores, which enable frozen species on grains to evaporate into gas phase. Another hypothesis would be related to the evolutionary phase of HII region: If HII regions are fully evolved, CH_2NH would be destroyed by strong UV radiation. These possibilities will be discussed in the Section 4.

Chapter 3. Astrochemical Modeling of the Evolution of COMs

3. Astrochemical Modeling of the Evolution of COMs

3.1. Purpose

In this section, we test the connection between the different chemical compositions among sources and their evolutionary phase by means of the chemical modelling. I will use not only the observed abundances of CH_2NH, but also other observed COMs.

3.2. The Nautilus Chemical Model

To simulate the abundance of various COMs in hot cores, the NAUTILUS gas-grain chemical model (Semenov et al. 2010; Reboussin et al. 2014) was used with the similar physical model used in Garrod (2013), where a collapse phase is followed by a static warm-up phase. This chemical model computes the time evolution of species in three-phases, gas-phase, grain surface, and inert grain mantle (Ruaud et al. 2015). The gas-phase chemistry is described by the public network kida.uva.2014 (Wakelam et al. 2015). During collisions with grains, species from the gas-phase can be physisorbed on the surfaces. They can then diffuse, react and be evaporated through thermal and non-thermal processes. In the following subsections, I summarize important processes in the chemical model used in this thesis. All details about the model can also be found in Ruaud et al. (2015).

3.2.1. Basic Equations

In this subsection, I describe basic equations of our three phase model. The detailed description is also found in Ruaud et al. (2016). The equation to determine the gas-phase, grain surface, and grain mantle concentrations of the i-th species, denoted as $n(i)$, $n^s(i)$, and $n^m(i)$ [cm^{-3}], respectively, are:

$$\left.\frac{\mathrm{d}n(i)}{\mathrm{d}t}\right|_{\mathrm{tot}} = \sum_l \sum_j k_{lj} n(l) n(j) + k_{\mathrm{diss}}(j) n(j)$$

$$+k_{\mathrm{des}}(i) n_s(i) - k_{\mathrm{acc}}(i) n(i) - k_{\mathrm{diss}}(i) n(i) - n(i) \sum_l k_{ij} n(j), \tag{14}$$

$$\left.\frac{\mathrm{d}n_s(i)}{\mathrm{d}t}\right|_{\mathrm{tot}} = \sum_l \sum_j k^s_{lj} n_s(l) n_s(j) + k^s_{\mathrm{diss}}(j) n_s(j)$$

$$+k_{\mathrm{acc}}(i) n(i) + k^m_{\mathrm{swap}}(i) n_m(i) + \left.\frac{\mathrm{d}n_m(i)}{\mathrm{d}t}\right|_{m\to s} - n_s \textstyle\sum_j k^s_{ij} n_s(j)$$

$$-k_{\mathrm{des}}(i) n_s(i) - k^s_{\mathrm{diss}}(i) n_s(i) - k^s_{\mathrm{swap}}(i) n_s(i) - \left.\frac{\mathrm{d}n_s(i)}{\mathrm{d}t}\right|_{s\to m}, \tag{15}$$

and

$$\left.\frac{\mathrm{d}n_m(i)}{\mathrm{d}t}\right|_{\mathrm{tot}} = \sum_l \sum_j k^m_{lj} n_m(l) n_m(j) + k^m_{\mathrm{diss}}(j) n_m(j) + k^m_{\mathrm{swap}}(i) n_s(i) + \left.\frac{\mathrm{d}n_s(i)}{\mathrm{d}t}\right|_{s\to m}$$

$$-n_m \sum_j k^m_{ij} n_m(j) - k^m_{\mathrm{diss}}(i) n_m(i) - k^m_{\mathrm{swap}}(i) n_m(i) - \left.\frac{\mathrm{d}n_m(i)}{\mathrm{d}t}\right|_{m\to s}. \tag{16}$$

where k_{lj}, k^s_{lj}, and k^m_{lj}, are the gas-phase reaction rates [$\mathrm{cm^3 s^{-1}}$] between species i and j in the gas phase, on the grain, and in the mantle, respectively. $k_{\mathrm{acc}}(i)$ and $k_{\mathrm{des}}(i)$ [$\mathrm{s^{-1}}$] are the accretion and desorption rate coefficients [$\mathrm{s^{-1}}$], respectively. k_{diss}, k^s_{diss}, and k^m_{diss} are the sum of the dissociation rate coefficients in the gas phase, on the grain surface, and in the mantle. These dissocistion processes include (1) direct cosmic ray processes, (2) secondary UV photons induced by cosmic-rays and (3) the standard interstellar UV photons, as described in the following subsections in detail. $\left.\frac{\mathrm{d}n_m(i)}{\mathrm{d}t}\right|_{s\to m}$ and $\left.\frac{\mathrm{d}n_m(i)}{\mathrm{d}t}\right|_{m\to s}$, respectively, represent indivisual transfer rate of species i from the surface to mantle and vice versa. These terms are calculated as below:

$$\left.\frac{\mathrm{d}n_m(i)}{\mathrm{d}t}\right|_{s\to m} = \alpha_{\mathrm{gain}} \frac{n_s(i)}{n_{s,\mathrm{tot}}} \frac{\mathrm{d}n_{s,\mathrm{gain}}}{\mathrm{d}t}, \tag{17}$$

and,

$$\left.\frac{\mathrm{d}n_m(i)}{\mathrm{d}t}\right|_{m\to s} = \alpha_{\mathrm{gain}}\frac{n_m(i)}{n_{m,\mathrm{tot}}}\frac{\mathrm{d}n_{s,\mathrm{loss}}}{\mathrm{d}t}, \tag{18}$$

where $\frac{\mathrm{d}n_{s,\mathrm{gain}}}{\mathrm{d}t}$ and $\frac{\mathrm{d}n_{s,\mathrm{loss}}}{\mathrm{d}t}$ are, respectively, the overall rate of gain and loss of surface material:

$$\frac{\mathrm{d}n_{s,\mathrm{gain}}}{\mathrm{d}t} = \sum_i [\sum_l \sum_j k^s_{lj} n_s(l) n_s(j) + k^s_{\mathrm{diss}}(j) n_s(j) + k_{\mathrm{acc}}(i) n(i)], \tag{19}$$

and,

$$\frac{\mathrm{d}n_{s,\mathrm{loss}}}{\mathrm{d}t} = \sum_i [n_s(i) \sum_j k^s_{lj} n_s(j) + k_{\mathrm{des}}(i) n_s(i) + k^s_{\mathrm{diss}}(i) n_s(i)], \tag{20}$$

α_{gain} and α_{loss} are defined as follows:

$$\alpha_{\mathrm{gain}} = \frac{\sum_i N_s(i)}{2N_{\mathrm{site}}} \tag{21}$$

and,

$$\alpha_{\mathrm{loss}} = \begin{cases} \frac{\sum_i N_m(i)}{\sum_i N_s(i)} & \text{if} \quad \sum_{\mathrm{i}} \mathrm{N_m(i)} < \sum_{\mathrm{i}} \mathrm{N_s(i)} \\ 1 & \text{if} \quad \sum_{\mathrm{i}} \mathrm{N_m(i)} > \sum_{\mathrm{i}} \mathrm{N_s(i)} \end{cases} \tag{22}$$

$$\tag{23}$$

where $N_m = n_m(i)/n_{\mathrm{dust}}$ and $N_s = n_s(i)/n_{\mathrm{dust}}$ are, respectively, the concentlation of species i on the grain surface and in the mantle under the grain number density $\mathrm{n_{dust}}$.

The terms of $\left.\frac{\mathrm{d}n_m(i)}{\mathrm{d}t}\right|_{s\to m}$ and $\left.\frac{\mathrm{d}n_m(i)}{\mathrm{d}t}\right|_{m\to s}$ represent a way to renewal of the grain surface materials. The exchange of molecules by their physical motion is accounted by k^s_{swap} and $\mathrm{k}^m\mathrm{swap}$ [s^{-1}]. The swapping rate from the mantle to surface is:

$$k^m_{\rm swap}(i) = \begin{cases} \frac{1}{t^m_{\rm hop}(i)} & \text{if} \quad {\rm N_{lay,m}} < 1 \\ \frac{1}{t^m_{\rm hop}(i) N_{\rm lay,m}} & \text{if} \quad {\rm N_{lay,m}} > 1 \end{cases} \tag{24}$$

$$\tag{25}$$

where $N_{\rm lay,m} = \sum_i N_m(i)/N_{\rm site}$ is the number of mantle layers under the site density on the grain $\rm N_{site}$. The timescale of thermal hopping $t^m_{\rm hop}(i)$, is given as below:

$$t^m_{\rm hop} = \nu_0^{-1} \exp(E^m_{\rm diff}/kT_d), and \tag{26}$$

$$\nu_0 = (2 n_s E_D/\pi^2 m)^{1/2}, \tag{27}$$

where $E^m_{\rm diff}$ is deduced from the desorption energy $\rm E_D$ by multiplying a factor of 0.8, as was employed in Ruaud et al. (2016).

The evaporation time scale $\rm t_{evap}$, the evaporation rate $\rm R_{evap}$, and the accretion rates are given as the following formula:

$$t_{\rm des} = \nu_0^{-1} \exp(E_D/kT_d), \tag{28}$$

$$k_{\rm des} = t^{-1}_{\rm des}, and \tag{29}$$

$$R_{\rm acc}(i) = \sigma_d < v(i) > n_d, \tag{30}$$

where σ_d is the geometrical gas-dust cross section, $< v(i) >$ is the averaged velocity of specie i, $n(i)$ and n_d are concentration of specie i and dust. The sticking probability is assumed to be unity in the calculation of $R_{\rm acc}(i)$.

3.2.2. Reaction Rates

The rate coefficients for the gas phase reactions are given in the form of k=α(T/300)$^\beta$ e$^{-\gamma/T}$ (cm^{3}s $^{-1}$), as a function of temperature T.

Molecules on the grain surface require mobility to react. As the reaction rates, we used the formalism described in Hasegawa et al. (1992). The time scale $t_{\rm hop}$ for absorbed species to migrate one site to another is given by the equation:

$$t_{\rm hop} = \nu_0^{-1} \exp(E_b/kT_d), \tag{31}$$

$$\nu_0 = (2n_s E_D/\pi^2 m)^{1/2} \tag{32}$$

where E_b and E_D are respectively the potential energy barrier and absorption energy, which are different for each molecule, and T_d is the dust temperature. For lighter molecules like H or H_2, quantum tunneling is more rapid than thermal hopping, whose time scale is given by

$$t_q = \nu_0^{-1} \exp[(2a/\hbar)(2mE_b)^{1/2}], \tag{33}$$

where a is a thickness of potential barrier. The diffusion time $t_{\rm diff}$ which represent a timescale for absorbed species to sweep over all grain sites is given by

$$t_{\rm diff} = N_s t_{\rm hop} \ (t_{\rm hop} < t_{\rm q}) \tag{34}$$

$$t_{\rm diff} = N_s t_{\rm q} \ (t_{\rm hop} > t_{\rm q}), \tag{35}$$

where N_s is a total number of sites in one grain. A diffusion rate $R_{{\rm diff},i}$ is expressed as the inverse of $t_{\rm diff}$, and the reaction rate R_{ij} ($\rm cm^{-3}s^{-1}$) for species i and j to react with each other is given in the following equation.

$$R_{ij} = \kappa_{ij}(R_{{\rm diff},i} + R_{{\rm diff},j})N_i N_j n_d, \tag{36}$$

where κ_{ij} is the probability of reactions, N_i and N_j are the number of molecules, $n_{\rm d}$ is the dust grain number density. κ_{ij} is related to the activation energy $\rm E_A$ in the equation:

$$\kappa_{ij} = \exp(-2(a/\hbar)(2\mu E_A)^{1/2}), \tag{37}$$

where "a" is a rectangle barrier of thickness and μ is the reduced mass. "a" was taken as 1 Å. κ_{ij} is unity if there is no activation barrier. For lighter molecules, the timescales to sweep oner the grain surface are sometimes more shorter than accretion or evaporation rate, physically meaningful time period. In this case, $R_{\rm diff}$ is replaced by larger one of evaporation rate $k_{\rm des}$ ($\rm s^{-1}$) or accretion rate $k_{\rm acc}$ ($\rm s^{-1}$) (Caselli et al. 1998).

3.2.3. Desorption Energy

While both E_b and E_D are important parameters for the grain surface chemistry, their determinations are not easy. These values should be determined in terms of how tightly each species is adsorbed on the grain surface via the van der Waals interaction and the hydrogen bond interaction. Especially their interaction with major component of the grain surface, amorphous water, would be important. Since H_2O is a polar molecule, chemical species with larger polarity such as NH_3 would have larger E_D than non-polar species such as CO.

Collings et al. (2004) investigated the characteristics of thermal desorption for 16 species from laboratory analogue of icy mantle, and classified them into CO-like species, water-like species, and intermediate species. CO-like species showed volcano desorption: when a the low porosity amorphous water phase crystallizes, trapped molecules are desorbed before the desorption of water. Water-like species showed a single relevant desorption coincident with water. Intermediate species displayed several desorption phase, corresponding to the phase of both crystallizations and desorption of water. Garrod & Herbst (2006) determined E_D (and E_b) values based on the experiments by Collings et al. (2004). In Garrod & Herbst (2006) and other recent chemical simulations including those contained in this thesis, E_D values for other species are extrapolated by addition or subtraction of energies from members of the fragments, under an assumption that the

energies are the sum of fragments that compose the molecule. For example, it is known that NH_3 tends to have high E_D, 5534 K, and E_D for CH_3NH_2 (6584 K) is deduced as a sum of those of NH_3 (5534 K) and CH_2 (1050 K). I summarized the E_D values of some interested COMs in our simulations in Table 17, which were estimated in this way. With these E_D values, the timescales of evaporation for COMs are calculated using the equation (28). In this case, COMs are frozen on grains until the core is heated above 100 K.

Although it is difficult to determine accurate E_D values, it would be worth to evaluate the desorption temperatures of COMs qualitatively. One of ways to evaluate E_D values would be that E_D is higher for species with higher polarity, traced with larger permanent dipole moment. Such species would strongly interact with H_2O ice on grains. Therefore, we can quantitatively discuss an approximated desorption energy using the permanent dipole moments: $\mu = \sqrt{\mu_{\rm a}^2 + \mu_{\rm b}^2 + \mu_{\rm c}^2}$. In Table 17, I summarize dipole moments, and desorption energies used in our simulations. The dipole moments are 1.48 D for NH_3, 2.02 D for CH_2NH, 3.92 D for CH_2CHCN, 4.04 D for CH_3CH_2CN, 1.30 D for CH_3OCH_3, and 1.70 D for CH_3OH. Their larger dipole moments for N-bearing species imply that the interactions of these species with water ice would be strong, and they would not evaporate until the sources are sufficiently heated. Therefore, the extrapolated high E_D values for COMs in Table 17 would be not so bad.

The adsorption potential of the interaction with solid-phase H_2O can be presented as a function of the height from the surface. If a layer of H_2O is assumed, surface potential would vary not only perpendicular from surface, but also periodic in the direction of parallel to the surface (Watson 1976). E_D represents required energy to remove species toward perpendicular direction from the surface, while E_b represents energy necessary to overcome surface potential towards parallel direction to the surface. Since higher energy would be required to totally remove species towards the perpendicular direction than to move towards

the parallel direction, E_b values should be lower than E_D values. They are given assuming the ratio of "E_b/E_D", which is less than unity. In this work, "E_b/E_D" is fixed to 0.4 on the surface and 0.8 in the mantle as is employed in Ruaud et al. (2015).

3.2.4. The Photo-dissociation and Photo-ionization Processes by Interstellar UV Photons

In the diffuse cloud phase when external UV photons can penetrate, the photo-dissociation, or photo ionization process are important destruction processes of the species. In NAUTILUS, these rates are presented by the formula below with the visual extinction Av:

$$k = A \exp(-CAv)\ s^{-1}. \tag{38}$$

The coefficients A and C can be theoretically and/or experimentally obtained. The important wavelength for the photo-dissociation process is 5-13.6 eV, or 912 - 2500 $\mathring{A}$, since the intensity of UV vanishes above 13.6 eV due to the absorption by atomic hydrogen. The approximation formula of the standard interstellar UV radiation, of this range, with certain energy of E, is presented by Draine (1978) as shown below:

$$F(E) = \left[1.658 \times 10^6 (E/eV) - 2.152 \times 10^5 (E/eV)^2 + 6.919 \times 10^3 (E/eV)^3\right] photons\, cm^{-2}\, s^{-1}\, sr^{-1} eV^{-1} \tag{39}$$

The coefficients under the standard UV radiation are estimated from the cross sections of molecules and their potential energies (e.g., van Dishoeck. 1988).

3.2.5. The Effect of Cosmic-Rays

Cosmic-rays, usually protons and alpha particles with energies above 1 MeV can interact with gas phase species. These high energy particles directly ionize species "i" with a rate described below:

$$k_{\mathrm{CR},i} = A_i \zeta \tag{40}$$

where ζ (s^{-1}) represents the flux of cosmic rays.

Further, cosmic rays are important source of UV photons in the dense region with large Av, where interstellar UV photons cannot penetrate (Prasad & Tarafdar 1983). These processes are called as cosmic-ray induced photo-dissociation and photo-ionization processes, or sometimes referred to as the Prasad-Tarafdar mechanism. In this mechanism, UV photons are created in the interior of clouds through excitation of molecular hydrogen by secondary electrons generated by cosmic-ray ionization. This ionization rate for a certain species "i" is calculated by using the hydrogen ionization rate $\zeta(\mathrm{H_2})$ as below:

$$k_{\mathrm{CRP},i} = A_i \zeta(H_2) \tag{41}$$

The coefficient A_i depends on photo-dissociation cross section of the species (e.g. Gredel et al. 1989). This cross section is determined by considering energy distribution of generated secondary electrons from hydrogen, which has mean energy around 30 eV.

3.3. Reactions Contained in the Chemical Model

In this section, I summarize the initial abundance and chemical reactions used in our simulations. The chemical reactions summarized below are primarily based on the dataset of kida.uva.2014 (Wakelam et al. 2015) and Garrod (2013). The initial abundance and

important reactions in gas phase and on grains are summarized in Tables 16 through 19.

3.3.1. Initial Abundances

For the initial condition, I assume that the chemical evolution starts from atomic form except for H_2 as observed in the diffuse clouds. Elements with an ionization potential below 13.6 eV, corresponding to that of hydrogen, C, S, Si, Fe, Na, Mg, Cl, and P are initially singly ionized. For our simulations, I used the abundances from Ruaud et al. (2015). The initial abundance is listed in Table 16.

3.3.2. CH_3OH

It was thought that CH_3OH would be formed via two-step gas phase mechanism:

$CH_3^+ + H_2O \longrightarrow CH_3OH_2^+$

$CH_3OH_2^+ + e^- \longrightarrow CH_3OH + H$

However, Geppert et al. (2006) reported that a channel leading to H, CH_3 and OH is by far dominant one for dissociative recombination process of $CH_3OH_2^+$ and only 3 percent of total rates account for the formation of CH_3OH. The chemical modeling results in Geppert et al. (2006) claimed that observed CH_3OH abundance could not be explained by the "$CH_3OH_2^+ + e^-$" process with the newly measured branching ratio. In our simulations, it was assumed that 3 percent of the total rates for the dissociative recombination process of $CH_3OH_2^+$ produce CH_3OH and other 97 percent results in fragmentations of $CH_3OH_2^+$.

On the other hand, the importance of grain surface reactions were emphasized by both theoretical and experimental studies. Many theoretical studies implied the importance of hydrogenation process to CO (e.g., Tielens & Hagen 1982; Charnley et al. 1997).

$CO + H \longrightarrow HCO$

$HCO + H \longrightarrow H_2CO$

$H_2CO + H \longrightarrow CH_3O$

$CH_3O + H \longrightarrow CH_3OH$

The efficiency of these processes was confirmed by Watanabe et al. (2002). They conducted hydrogen beam experiments with H_2O-CO ice at 10 K, and demonstrated that formaldehyde and methanol can be efficiently produced.

Other possible formation processes on grains are also incorporated. Garrod (2008) suggested that complex organic molcules could be formed via reactions of radicals. In this case, a reaction of "CH_3 + OH" will form CH_3OH.

3.3.3. CH_3OCH_3 and $HCOOCH_3$

It was thought that COMs, like CH_3OCH_3 and $HCOOCH_3$, are formed via gas phase dissociative recombination processes of their protonated ions. These processes start with the evaporation of CH_3OH from grains. CH_3OH is protonated by H_3^+ to form $CH_3OH_2^+$, and react with other species:

$CH_3OH + H_3^+ \longrightarrow CH_3OH_2^+ + H_2$

For example, Charnley et al. (1992) suggested that the rection with H_2CO followed by an electron would lead to methyl formate:

$CH_3OH_2^+ + H_2CO \longrightarrow HC(OH)OCH_3^+ + H_2$, and then,

$HC(OH)OCH_3^+ + e^- \longrightarrow HCOOCH_3 + H$

They also suggested that the reaction with CH_3OH followed by an electron would lead

to dimethyl ether:

$CH_3OH_2^+ + CH_3OH \longrightarrow CH_3OCH_4^+ + H_2O$, and then,

$CH_3OCH_4^+ + e^- \longrightarrow CH_3OCH_3 + H$

However, Horn et al. (2004) claimed by quantum chemical calculations that the formation process of protonated methyl formate from methyl formate and protonated methanol has significant activation barrier. Furthermore, Geppert et al. (2006) claimed that the recombination processes of positive ions would cause fragmentation of ions, rather than subtraction of single proton. Thus, above similar formation process of CH_3OCH_3 would be also doubtful.

Garrod & Herbst (2006) suggested formation processes of $HCOOCH_3$ and CH_3OCH_3 via radical reactions below:

$CH_3O + CH_3 \longrightarrow CH_3OCH_3$, and

$HCO + CH_3O \longrightarrow HCOOCH_3$

Garrod & Herbst (2006) assumed that gas and grain temperatures in hot core would gradually rise, and found that above reactions can form $HCOOCH_3$ and CH_3OCH_3 efficietly under the temperature of 30 K.

In our simulations, both of the formation processes from via the recombination of positive ions and grain surface reactions are included.

3.3.4. CH_2CHCN and CH_3CH_2CN

Caselli et al. (1993) suggested formation processes of CH_2CHCN and CH_3CH_2CN, via the successive hydrogenation process to HC_3N:

$HC_3N + 2H \longrightarrow CH_2CHCN$, and

$CH_2CHCN + 2H \longrightarrow CH_3CH_2CN$.

In addition to the above, other grain surface reactions between radicals can form these species as discussed in Garrod (2008). For instance,

$CH_3 + CH_2CN \longrightarrow CH_3CH_2CN$.

On the other hand, the importance of gas phase reactions including CN radical was emphasized in previous experiments (Table 1 in (Choi et al. 2004)). In this case, CH_2CHCN is formed via a similar way to HC_3N:

$C_2H_2 + CN \longrightarrow HC_3N + H$,

$C_2H_4 + CN \longrightarrow CH_2CHCN + H$.

A similar process for C_2H_6 ($C_2H_6 + CN \longrightarrow CH_3CH_2CN + H$) is not included due to the lack of reliable data. Considering standard enthalpy of formation of C_2H_6, CN, CH_3CH_2CN, and H, respectively, -83, 438, 51, 217 kJ/mol, "$C_2H_6 + CN \longrightarrow CH_3CH_2CN + H$" is an exothermic reaction with heat of formation of 87 kJ/mol. It would be worth to investigate reaction rate of this process via experimental or theoretical studies. CH_2CHCN can also be formed via the dissociative recombination of positive ions, such as "$C_2H_4CN^+ + e^- \longrightarrow CH_2CHCN + H$".

3.3.5. CH_3COCH_3

The formation process of CH_3COCH_3 has been poorly discussed so far. Garrod (2008) assumed a formation process of CH_3COCH_3 from radicals:

$CH_3 + CO \longrightarrow CH_3CO$,

$CH_3CO + CH_3 \longrightarrow CH_3COCH_3$.

Otherwise, gas phase dissociative recombination process of $C_3H_6OH^+$ and $CH_3COCH_4^+$ would form CH_3COCH_3. In our simulations, both above processes are included.

3.3.6. NH_2CHO

Raunier et al. (2004) claimed the tentative detection of NH_2CHO in laboratory after the irradiation of UV on the HNCO ice, suggesting NH_2CHO would be a product of hydrogenation to isocyanic acid, HNCO:

$HNCO \xrightarrow{2H} NH_2CHO$.

This idea is supported by a correlation between observed HNCO and NH_2CHO abundances (Mendoza et al. 2014; López-Sepulcre et al. 2015)

However, more recent experiment by Noble et al. (2015) demonstrated that hydrogenation process to HNCO will form H_2NCO, and the subsequent hydrogenation will form HNCO again:

$HNCO \xrightarrow{H} H_2NCO$, and

$H_2NCO \xrightarrow{H} HNCO + H_2$.

Another grain surface formation path would be heavier radical reactions of NH_2 and HCO (Garrod 2008):

$NH_2 + HCO \longrightarrow NH_2CHO$.

A gas phase formation route is also suggested. Kahane et al. (2013) showed that a similar fractional abundance of NH_2CHO towards low-mass star-forming regions compared to high-mass star-forming regions, where the strength of the UV radiation field would be

weak. They suggested the formation process of NH_2CHO via gas phase reaction between NH_2 and H_2CO rather than the formation on ice surface:

$NH_2 + H_2CO \longrightarrow NH_2CHO + H.$

The importance of above formation process was emphasized by Barone et al. (2015). They conducted quantum chemical calculations, and reported its arrehnius reaction coefficients of α=2.6×10^{-12} cm^3 s^{-1}, β=-2.1, and γ=26.9 K. With these reaction coefficients, this reaction has the reaction rate of ∼7×10^{-11} cm^3s^{-1} at 50 K. They used a chemical modeling with predicted reaction rates, and succeeded to explain the observed NH_2CHO abundance in the envelope of a hot corino IRAS16293-2422 and the molecular shock region of L1157-B2.

Both above gas phase and grain surface formation route were incorporated in our simulations.

3.3.7. CH_2NH and CH_3NH_2

Both the experimental and theoretical studies implied that hydrogenation process to HCN on the dust surface might be essential for the formation process for CH_2NH and CH_3NH_2 (Woon 2002; Theule et al. 2011). These issues also have been discussed in details by Majumdar et al. (2013) where they identified CH_2NH_2 as another possible precursor for glycine formation:

$HCN \xrightarrow{H} HCNH,$

$HCNH \xrightarrow{H} CH_2NH,$

$CH_2NH \xrightarrow{H} CH_2NH_2,$

$CH_2NH_2 \xrightarrow{H} CH_3NH_2.$

Theule et al. (2011) mentioned that the hydrogenation process to CH_2NH might be much quicker compared to that of HCN. It is also suggested that CH_2NH may be formed in the gas phase reactions among radicals (Turner et al. 1999; Halfen et al. 2013). Halfen et al. (2013) showed that the excitation temperatures of CH_2NH and CH_3NH_2 are different, suggesting different formation paths for CH_2NH and CH_3NH_2. There are also other possible route to these species. Grain surface radical reactions such as "CH_2 + NH" or "CH_3 + N", which is based on the idea of Garrod (2008), and the gas phase dissociative recombinations of positive ions such as "$CH_2NH_2^+ + e^-$". If the main origin of CH_2NH is not the evaporation process from the grain, observed CH_2NH is not be a direct precursor to CH_3NH_2.

In the calculation in this thesis, all of above gas phase reactions and hydrogenation process to HCN were incorporated. For activation barriers of hydrogenation processes of HCN and CH_2NH, the theoretically predicted values (for HCN + H → H_2CN, HCN + H → HCNH, CH_2NH + H → CH_3NH, and CH_2NH + H → CH_2NH_2, respectively, 3647 K, 6440 K, 2134 K, and 3170 K) by Woon (2002) were employed.

3.4. The Physical Model

In the first the diffuse cloud phase, the gas density increases by gravitationally collapse. This phase is called collapsing phase. The initial gas density, n, was increased up to the peak density as a function of time, t, along with the modified free-fall differential equation shown below (Nejad et al. 1990):

$$\frac{\mathrm{d}n}{\mathrm{d}t} = B\left(\frac{n^4}{n_\mathrm{i}}\right)^{1/3}\left\{24\pi G m_H n_i\left[\left(\frac{n}{n_i}\right)^{1/3} - 1\right]\right\}^{1/2} \tag{42}$$

where n_i is the initial density, m_H is the mass of the hydrogen atom, and G is the

gravitational constant. However, the actual gravitational collapse would be somewhat slowed down than free-fall process due to the resistance of turbulent, thermal motion, or magnetic field. Thus, the collapsing speed is adjusted by a parameter of B. The factor B=1 corresponds to the usual free-fall case. The smaller values of B than unity is used to approximately assume the situation of non-free-fall cases, as Garrod (2013) employed B=0.7 assuming that internal physical processes would be against free-fall process.

While the gas kinetic temperature was fixed at 10 K in the collapsing phase, the dust temperature $T_{\rm dust}$ decreased from 19 K to 8 K depending on the visual extinction, which was calculated from the gas density of the cloud using the formula presented in Garrod (2011):

$$T_{\rm dust}(K) = 18.67 - 1.637A_{\rm v} + 0.07518A_{\rm v}^2 - 0.001492A_{\rm v}^3 \quad (43)$$

The visual extinction obeys the relationship $A_v=A_{v,0}(n/n_0)^{2/3}$, where $A_{v,0}$ and n_0 are the initial values of A_v and gas density n. $A_{v,0}$ was set to be 0.01 so that Av=10 is achieved at the dark cloud condition, $n=5\times10^4$ cm^{-3}. The evolution of the temperature and the density during collapsing phase is shown in Figures 16 (a) and (b).

Once the peak density was achieved, we fixed the density, and the gas and dust temperatures were raised from ∼10 K to their peak temperatures. This phase is called warm-up phase. Although the warm-up speed of hot cores are not well established, Garrod (2013) employed three warm-up speeds, named "fast" (7.12×10^4 years), "medium" (2.85×10^5 years), and "slow" (1.43×10^6 years) models in terms of the star-formation time scales of high, intermediate, and low-mass, star-forming regions, respectively. The physical conditions used as input to the chemical model are based on the "fast warm-up model" from Garrod (2013) to compare with our observation toward high-mass stars. The evolution of the temperature during warm-up phase is shown in Figure 16 (c). After that, chemical evolution continued with fixing their temperature and density to their peak values.

There are some uncertain parameters that may change the chemical evolution. The initial density, n_i, the parameter, B, change the timescale of the collapsing phase. While Garrod (2013) assumed the timescale of warm-up phase for high-mass stars to be 7.12×10^4 years, it is not well established. The peak density and the peak temperature of the cloud are other uncertain factors. If one of these factors largely contribute to difference of the chemical compositions of hot cores, they may be keys to explain the observed chemical difference. In the following section, the dependency on these parameters are discussed.

3.5. Parameter Dependence of the Chemical Network Simulations

One of the purposes for our chemical modeling is to discuss the hypothesis in Chapter 2 that different temperature or strength of UV radiation can contribute to the difference of observed COM abundances. It would be very important to see how other parameters can change the results of chemical evolution before the detailed test of the hypothesis. In this section, the different initial densities, warm-up speeds, peak densities, and collapsing speed will be compared to see the denepnency of chemical evolution on these parameters. The effect of different temperature and UV radiation will be discussed in detail in the following Discussion section (3.6).

3.5.1. Methodology

To discuss the difference in modeling results under different conditions, we computed "the degree of proximity" (hereafter DoP) at each time step using the following formula:

$$DoP(t) = \frac{1}{N_{total}} \sum_i |\log_{10} \frac{n_A(X)_i(t)}{n_B(X)_i(t)}|, \tag{44}$$

where $n_A(X)_i(t)$ and $n_B(X)_i(t)$ are the calculated abundance of species i at a certain

time step t, with different models A and B. N_{total} is the total number of species involved in the comparison. The smaller value of DoP means a better agreement between models A and B. If all the calculated species completely match with the models, DoP becomes 0. Since the simulated fractional abundances range up to 10^{-5} to less than 10^{-10}, the comparison using the squares of the difference tends to underestimate the importance of less abundant species. The comparison using logarithm in the above formula have an advantage in giving the same weight for both overestimated and underestimated by a factor k ($|\log_{10} k| = |\log_{10} k^{-1}|$), and sometimes employed in the past studies (e.g., Ruaud et al. 2015). Then observed species listed in Table 14 are used to calculate DoP.

3.5.2. Initial Density

First of all, I show the simulated results under different initial densities. Since I assumed the chemical evolution from the atomic form, it would be reasonable to start the physical evolution from the diffuse cloud phase. It is known that the well-known diffuse cloud ζ Oph, where atomic species are observed, shows the density between 0.1 and 1 cm^{-3} (Savage et al. 1977). Therefore, the initial density of the model should be close to this range. I performed simulations with the different initial densities of 0.1, 1, and 10 cm^{-3}. In these simulations, other parameters were fixed to be the same values: B=0.7, the timescale of the warm-up phase of 7.1×10^4 years, the peak density of 1×10^7 cm^{-3}, and the peak temperature of 200 K.

In Figure 17, the abundances of COMs are compared among three models. The time of zero years corresponds to the beginning of the warm-up phase. The black, red, and green lines, respectively represent the simulated abundances under the initial densities of 0.1, 1, and 10 cm^{-3}.

With these simulated abundances, I calculated DoPs to quantitatively discuss their difference. The DoPs of the initial density of 0.1 and 10 models are compared to the initial density of 1 cm^{-3} model in Figure 17. Since their DoP is less than unity after the warm-up phase, the difference in chemical evolution is small. Therefore, if the initial density is low enough, the initial density is not an important factor in the difference of the chemistry.

3.5.3. Warm-up Speed

The timescale of the warm-up phase of hot cores is not well known. Garrod (2013) employed the warm-up timescale of 7.1×10^4 years from theoretically predicted contraction timescale of high-mass stars (Bernasconi et al. 1996). However, we have to be careful that Bernasconi et al. (1996) did not calculate the evolution of temperature inside the cores. A one-dimensional radiation-hydrodynamics calculation for low-mass protostars by Aikawa et al. (2008) showed that the temperature at the radius of ∼100 AU rose from 10 K to ∼200 K in $\sim1\times10^4$ years. Since high-mass stars are predicted to evolve rapidly than low-mass stars, it would be reasonable to assume the timescale of 7×10^4 years to be an upper limit of the warm-up timescale for high-mass stars.

I performed simulations with the initial density of 1 cm^{-3}, B=0.7, the peak density of 1×10^7 cm^{-3}, and the peak temperature of 200 K. In Figure 18, the chemical evolution of COMs under the different warm-up timescales of 7.1×10^2, 7.1×10^3, and 7.1×10^4 years are compared. The time of zero years corresponds to the beginning of the warm-up phase. The black, red, and green lines, respectively, represent the simulated abundances under the timescale for the warm-up phase of 7.1×10^2, and 7.1×10^3, and 7.1×10^4 years.

With these simulated abundances, I calculated DoPs to quantitatively discuss their difference. DoPs of 7.1×10^2 and 7.1×10^3 years cases compared to 7.1×10^4 years case are

shown in Figure 18. As the results, the difference of these cases are so small that the warm-up speed would not affect the results of the chemical modeling.

3.5.4. Peak Density

I performed simulations with the initial density of 1 cm^{-3}, B=0.7, the warm-up timescale of 7.1×10^4 years, the peak temperature of 200 K. The different peak densities of 1×10^6, 1×10^7, and 1×10^8 cm^{-3} were considered.

In Figure 19, the abundances of COMs are compared among three densities. It is surprising that the difference in the simulated abundances are small among these densities while it is well known from the modeling of the dark cloud that chemical evolution tends to be accelerated under high-density condition (e.g., Suzuki et al. 2014).

This trend can be understood by different abundances of H_3O^+ depending on the density, which is the main destroyer of the gas phase species. If only H_3O^+ destructs gas phase species, the decreasing rate of species i can be expressed as follows:

$$\frac{\mathrm{d}X_i}{\mathrm{d}t} = -kX_iX[\mathrm{H_3O^+}]n, \tag{45}$$

where n is the gas density and X_i is the fractional abundance of certain species "i". In Figure 19, abundances of H_3O^+ under the different densities are shown. $X[H_3O^+]$ tends to decrease with density due to the high dissociative recombination rate with an electron. When $X[H_3O^+]$ is inversely proportional to n, a term of $X[H_3O^+]n$ does not depend on the density, and hence, the dependency of the destruction rate on density is canceled.

With these simulated abundances, I calculated DoPs to quantitatively discuss their difference. In Figure 19, the peak density of 1×10^6 and 1×10^8 cm^{-3} cases are compared

with that of 1×10^7cm^{-3} case to see the influence of the different peak density in hot core chemistry. The time of zero years corresponds to the beginning of the warm-up phase. DoP is less than unity before 1×10^6 years, suggesting that the dependence of the peak density is small. Longer timescale than 1×10^6 years is doubtful for the lifetime of hot cores (Wilner et al. 2001).

3.5.5. Collapsing Speed

The effect of turbulent, thermal, or magnetic resistance can be considered by choosing smaller B value in the free-fall equation (42) described in the section (3.4). To see how these resistances can contribute to the chemical evolution, simulations with B=1, B=0.7, B=0.2, and B=0.1 are compared. The other parameters were fixed to be the same values: the initial density of 1 cm^{-3}, the timescale of the warm-up phase of 7×10^4 years, the peak density of 1×10^7 cm^{-3}, and the peak temperature of 200 K.

In Figure 20, the abundances of COMs are compared among different B values. The time of zero years corresponds to the beginning of the warm-up phase. I found that some species showed notable difference in their abundances. For instance, the fractional abundance of CH_3OH is shown in Figure 20. CH_3OH abundances decrease under B=0.1 or 0.2, where collapsing speed is slower. This difference is explained by longer timescale of the collapsing phase. The conversion of CO to CH_3OH is almost completed in the end of collapsing phase with B=1. With B=0.2 and 0.1, the long timescale of the collapsing phase than B=1 leads to the fragmentation of CH_3OH to CH_3 and OH by cosmic rays.

With these simulated abundances, I calculated DoPs to quantitatively discuss their difference. DoPs of B=0.1, 0.2, and 1 cases compared to B=0.7 case are shown in Figure 20. DoPs are less than unity before 1×10^6 years for all cases. Longer timescale than 1×10^6 years

is doubtful for the lifetime of hot cores (Wilner et al. 2001). Thus, I exclude the possibility that different collapsing speed may contribute to the difference of the chemistry.

3.6. Discussion

3.6.1. Essential Formation Paths of the Observed Species

In the section (3.5), I showed that the contributions of initial density, the peak density, and the warm-up speed to the chemical evolution are relatively small. For the discussion of the origin of chemical difference in this section, it would be useful to discuss the major formation process of observed species under the standard parameters: the initial density of 1 cm^{-3}, B=0.7, the warm-up timescale of 7×10^4 years, the peak temperature of 200 K, the peak densities of 1×10^7 cm^{-3}. In Figure 21, I compared the abundances of interested species in the gas phase, on the grain surface and in the mantle setting the beginning of the warm-up phase to be "zero years". In these figures, fractional abundances just after the warm-up phase ($<4\times10^5$ years) are zoomed up to see the origin of interested species are gas phase or grain surface.

CH_3OH, $HCOOCH_3$ and CH_3OCH_3

Past studies showed that CH_3OH, $HCOOCH_3$ and CH_3OCH_3 would mainly formed on the grain surface rather than in the gas phase. Experimental and theoretical studies claimed that CH_3OH would be formed via the hydrogenation process to CO on grains (Watanabe et al. 2002; Tielens & Hagen 1982). The importance of radical-radical reactions were emphasized by Garrod & Herbst (2006) for $HCOOCH_3$ and CH_3OCH_3.

These trends can be clearly recognized from the trends that simulated fractional abundances in the mantle are completely converted into their gas phase abundances by the

evaporation process during the warm-up phase (Figure 21). In Figure 22, I compared the fractional abundances of CH_3OH, $HCOOCH_3$, and CH_3OCH_3 calculated without the grain surface reactions of "H_2CO + H", "HCO + CH_3O", and ""CH_3O + CH_3", respectively. The decrease of CH_3OH, $HCOOCH_3$, and CH_3OCH_3 without these processes show that these grain surface reactions are essential paths for CH_3OH, $HCOOCH_3$ and CH_3OCH_3.

CH_3NH_2 and CH_2NH

The fractional abundances of CH_3NH_2 and CH_2NH in the gas phase, on the grain surface and in the mantle are compared in Figure 21. The CH_3NH_2 abundance in the mantle is switched to that of gas phase abundance just before 1×10^5 years. The gas phase CH_3NH_2 is supplied by evaporation process from grains. On the other hand, apparently higher abundance of the gas phase CH_2NH than that of on the grain surface or in the mantle shows that CH_2NH should be newly formed in the gas phase. In Figure 22, I compare the CH_3NH_2 fractional abundance in the mantle excluding the reaction of "CH_2NH + H". In this case, CH_3NH_2 abundance is greatly decreased. This result indicates that CH_3NH_2 is a product of the hydrogenation process to CH_2NH, and that the grain surface CH_2NH becomes poor due to this rapid hydroganation process.

To reveal the major formation paths, formation rates for all gas phase reactions to form CH_2NH are compared in Figure 23. Formation rates are presented in terms of $k_{rate}(T, t) = k(T) \times n_1(t) \times n_2(t)$, where k(T) is the temperature-dependent rate constant (cm^3 s^{-1}) calculated with the Arrhenius equation, and $n_1(t)$ and $n_2(t)$ are the number densities (cm^{-3}) of reactant species in each time step. The black, red, and green lines, respectively, represent formation rates of CH_2NH via "CH + NH_3", "NH + CH_3" and sum of the reaction rates of the other gas phase processes. I found that the "NH + CH_3" prosess, shown in the red line, has the highest reaction rate at any time. In our simulations, NH and CH_3,

respectively, are produced by the destruction of NH_3 and COMs containing methyl-group such as CH_3OH. Therefore, CH_2NH is not a product of grain surface reactions but newly produced species in the gas phase chemistry after evaporations of other COMs.

NH_2CHO

The fractional abundances of NH_2CHO in the gas phase, on the grain surface and in the mantle are compared in Figure 21. The higher abundance in the gas phase than on the grain surface or in mantle shows gas phase origin of NH_2CHO. To reveal the major formation paths, the formation rates for all gas phase reactions to form NH_2CHO are compared in Figure 23. The black line represent the formation rate of NH_2CHO via gas phase process of "NH_2 + H_2CO". A sum of the reaction rates of other gas phase processes are presented by the red line. Since the "NH_2 + H_2CO" process has the higher formation rate of NH_2CHO than the sum of the other processes, this reaction would be the essential path for NH_2CHO, confirming the result of Barone et al. (2015).

CH_2CHCN

The fractional abundances of CH_2CHCN in the gas phase, on the grain surface and the in mantle are compared in Figure 21. Although CH_2CHCN is formed on grain via hydrogenation process to HC_3N, CH_2CHCN is quickly converted to CH_3CH_2CN due to further hydrogenation process. The higher abundance in the gas phase than on the grain surface or in mantle shows gas phase origin of CH_2CHCN. However, in my calculations, I assumed that there is no activation barrier in hydrogenation process to CH_2CHCN to form CH_3CH_2CN, due to lack of previous theoretical or experimental studies. It would be possible that CH_2CHCN would be increase on grain if there is a huge activation barrier and CH_2CHCN is not converted to CH_3CH_2CN. Since CH_2CHCN is quickly converted to

CH_3CH_2CN in our simulations, the abundance of CH_3CH_2CN on grain mantle would be the upper limit of possible CH_2CHCN abundance on grain mantle. The fractional abundance of CH_3CH_2CN is $\sim 7\times10^{-8}$ on grain mantle (Figure 21). In Figure 21, the gas phase abundance of CH_2CHCN is increasing at the time of 4×10^5 years, and its peak abundance is$\sim 1\times10^{-7}$ at 6×10^5 years. Therefore, gas phase production would be dominant even if we consider the upper limit of CH_2CHCN abundance on grains. To reveal the major formation paths in the gas phase, the formation rates for all gas phase reactions to form CH_2CHCN are compared in Figure 23. The black, red, and green lines, respectively, represent gas phase CH_2CHCN formation rates via "C_2H_4 + CN", "$C_2H_4CN^+$ + e^-", and the sum of the other processes The comparison of their formation rates suggests that the gas phase reaction of "C_2H_4 + CN", presented in the black line, is the essential path for CH_2CHCN in the gas phase.

While Caselli et al. (1993) suggested that both of CH_2CHCN and CH_3CH_2CN would be products of hydrogenation to HC_3N, gas phase synthesis processes were also investigated (e.g., Choi et al. 2004). However, their contributions to the gas phase abundance was not compared in the previous studies. In this thesis, I found that gas phase reaction of "C_2H_4 + CN" is the most dominant one to form CH_2CHCN compared to grain surface reactions for the first time.

CH_3CH_2CN

The fractional abundances of CH_3CH_2CN in the gas phase, on the grain surface and the mantle are compared in Figure 21. The comparable abundance of CH_3CH_2CN between in the gas phase and in grain mantle suggests that CH_3CH_2CN is originated from grains. Although I showed that gas phase CH_2CHCN is originated from the gas phase reaction, grain surface CH_2CHCN is important to for CH_3CH_2CN chemistry. Almost 90 % of grain

surface abundance of CH_2CHCN is due to the hydrogenation process to HC_3N. However, the abundance of CH_2CHCN on grains is low since the further hydrogenation process to CH_3CH_2CN is so rapid. In Figure 22, I compared the fractional abundance of CH_3CH_2CN calculated without the grain surface hydrogenation process to CH_2CHCN. Their decrease without hydrogenation process to CH_2CHCN shows that hydrogenation process is essential paths for CH_3CH_2CN in current simulations.

However, I note that there would be still room to discuss if CH_3CH_2CN is really originated from grains since some of possible important routes are not included in my simulations. If HCN is converted to CH_3NH_2, as I discussed, other hydrogenation processes to -CN bond are also likely.

The gas phase production of CH_3CH_2CN might be also important. Previous studies have suggested that CH_2CHCN and HC_3N would be formed via "C_2H_4 + CN" and "C_2H_2 + CN". Similarly, CH_3CH_2CN might be produced by the reaction of "C_2H_6 + CN".

It would be worth to conduct theoretical calculations or experimental studies for these processes.

CH_3COCH_3

The fractional abundances of CH_3COCH_3 in the gas phase, on the grain surface and in the mantle are compared in Figure 21. The higher abundance in the gas phase than on the grain surface or in mantle shows gas phase origin of CH_3COCH_3. To reveal the major formation paths, the formation rates for all gas phase reactions to form CH_3COCH_3 are compared in Figure 23. The black and red lines, respectively represent the formation rate of CH_3COCH_3 via "$C_3H_6OH^+ + e^-$" and "$CH_3COCH_4^+ + e^-$". The gas phase dissociative recombination reaction of "$C_3H_6OH^+ + e^-$", presented by the black line, is the essential path for CH_3COCH_3. A formation process of $C_3H_6OH^+$ is as follows: A part

of CH_3CH_2COOH is decomposed into CH_3CH_2CO and OH on the grains. CH_3CH_2CO is converted to CH_3CH_2CHO via grain surface hydrogenation process. After the evaporation of CH_3CH_2CHO, CH_3CH_2CHO and H_3O^+ form $C_3H_6OH^+$ and H_2O.

The previous simulation by Garrod (2008) assumed that CH_3COCH_3 is formed via the grain surface radical reactions, "CH_3CO + CH_3", and estimated its abundance to be less than 10^{-11}. This value is very low compared to our observed values. Our simulations suggested that, for the formation of CH_3COCH_3, the contribution of dissociative recombination process of protonated large COMs would be larger than grain surface reactions. However, the products and its reaction rates of "$C_3H_6OH^+ + e^-$" is not well established. Further theoretical/experimental studies would be required for further discussion of this path.

3.6.2. Comparison of Different Peak Temperature Models with Observed Data

Methodology

To compare the chemical simulation results with the observed abundances, I will utilize DoP with the following equation:

$$DoP(t) = \frac{1}{N_{obs}} \sum_i |\log_{10} \frac{n(X)_i(t)}{n(X)_{obs}}|, \tag{46}$$

where $n(X)_i(t)$ and $n(X)_{obs}$, respectively, are the calculated abundance of species i at a certain time step t, and the observed fractional abundance. As I will show in this section, while DoP is minimum between 5×10^5 and 1×10^6 years since the beginning of warm-up, the simulated fractional abundance of CH_3CH_2CN is more than 10 times lower than observed abundances towards G10.47+0.03. It means the essential formation path of this species

has not been established well. Since the inclusion of CH_3CH_2CN strongly increase DoP, I excluded CH_3CH_2CN in the following discussion. In addition, the very low excitation temperatures of CH_3CHO ($\sim$10 K) suggests that observed CH_3CHO would be originated from envelope component, CH_3CHO was excluded in this comparison.

3.6.3. Simulated Abundances under Different Temperatures

I performed simulations with the initial density of 1 cm^{-3}, B=0.7, the warm-up timescale of 7.1×10^4 years, the peak density of 1×10^7 cm^{-3}. The different peak temperatures of 120 K, 150 K, 200 K, 300 K and 400 K are compared. In Figure 24, the abundances of COMs are compared among the five different temperatures. In Figure 24, 120 K, 150 K, 300 K, and 400 K models are compared with the 200 K model to see how the peak temperature affects the result of the simulations. The horizontal dotted lines represent the highest and the lowest observed abundances obtained in Chapter 2. For CH_3NH_2, only one horizontal line corresponding to the observed abundance towards G10.47+0.03 is shown, since CH_3NH_2 is observed only towards G10.47+0.03 and NGC6334F and their fractional abundances of CH_3NH_2 are close. The time of zero years corresponds to the beginning of the warm-up phase.

In our simulations, CH_2NH and NH_2CHO were clearly overproduced than the observed highest value under a peak temperature of 200 K. On the other hand, I found that $HCOOCH_3$, CH_3NH_2, CH_2CHCN, NH_2CHO, and CH_2NH are depleted in the 120 K case. On the other hand, the temperature dependencies of O-bearing species, CH_3OH, CH_3OCH_3, CH_3COCH_3 are small. Among depleted species, the depletion of $HCOOCH_3$ and CH_3NH_2 is simply explained by their higher desorption energies, which makes their evaporation temperature higher than 120 K. However, I note that their desorption energies are uncertain and further experimental studies would be required.

On the other hand, the depletion of CH_2CHCN, NH_2CHO, and CH_2NH should be explained in the other way since in the previous subsection I showed that these species are gas phase origin. The difference of CH_2CHCN, NH_2CHO, and CH_2NH under different peak temperatures come from the conversion processes on grains. CH_2CHCN, NH_2CHO, and CH_2NH are mainly formed on the gas phase, and their grain surface abundances are not so high since they are quickly converted to other species on the grains (Theule et al. (2011) for CH_2NH, Caselli et al. (1993) for CH_2CHCN, and Noble et al. (2015) for NH_2CHO):

$$CH_2NH + H \longrightarrow CH_2NH_2$$

$$CH_2CHCN + H \longrightarrow CH_2CH_2CN$$

$$NH_2CHO + H \longrightarrow HNCHO + H_2$$

These species are formed in the gas phase for both 120 K and 200 K cases. After that, newly formed species are adsorbed on grains due to high density in hot cores. In the 200 K case, the temperature is so high that adsorbed species evaporate very quickly to gas phase again. In this case, the timescale to stay on grains is too short to react on the grain surface. However, in the 120 K case, CH_2CHCN, NH_2CHO, and CH_2NH, are converted into other species through the above grain surface reactions due to a longer residing time on grains. The abundances of O-bearing species such as CH_3OH and $HCOOCH_3$ do not decrease in this way, due to a lack of efficient destruction processes. While the simulated fractional abundances of NH_2CHO and CH_2NH tend to be overproduced under high temperature condition (T>150 K), their observed abundances are explained at 120 K case.

The increase of CH_3CH_2CN is due to the conversion of CH_2CHCN on grains. However, we found that the abundance of CH_3CH_2CN is also correlated with CH_2NH. Therefore, increase of CH_3CH_2CN contradict our observational results. While CH_3CH_2CN is not included in the comparison due to the lack of reliable reaction rates, the difference of

observed CH_3CH_2CN may be explained by assuming the hydrogenation process leading to finally $CH_3CH_2CH_2NH_2$, similar to hydrogenation to HCN to form finally CH_3NH_2. The detailed theoretical or experimental studies would be needed for further discussions for this species.

Comparison with Observed Data

I have shown that fractional abundances of some COMs tend to deplete for the 120 K case than 200 K case, due to destruction processes on the grains. In hot cores, there would be a temperature gradient from inner hot region to outer warm region. To approximately represent this temperature gradient, I assume that the temperature structure of the hot core can be modeled by using only two temperatures. I used a combination of 200 K and 120 K cases to discuss if the chemical difference among hot cores can be reconciled by temperature structures of hot cores. The ratio of volumes of 120 K region (V_{120K}) to 200 K region (V_{200K}), V_{120K}/V_{200K}, was employed as a parameter to represent the different temperature structure of hot cores. V_{120K}/V_{200K} was set to be 1, 10, 100, 1000 and chemical compositions are calculated as $\frac{X_{200K}V_{200K}+X_{120K}V_{120K}}{V_{200K}+V_{120K}}$. X_{120K} and X_{200K}, respectively, represent the simulated fractional abundances under temperatures of 120 K and 200 K. In the calculation of DoP, CH_3CHO and CH_3CH_2CN were excluded since CH_3CHO would exist envelope of hot cores and the formation process of CH_3CH_2CN is not established. DoP to the observations are presented in Figure 25, under different V_{120K}/V_{200K} values, 1, 10, 100, and 1000.

First of all, DoP for G10.47+0.03 is shown in Figure 25 (a). The minimum DoP is achieved under V_{120K}/V_{200K}=10 or 100. On the other hand, DoP for NGC6334F (Figure 25 (b)) is minimum under V_{120K}/V_{200K}=100 or 1000. DoP for W51 e1/e2 (Figure 25 (c)) is minimum under V_{120K}/V_{200K}=100. The smaller DoPs for NGC6334F and W51 e1/e2

under V_{120K}/V_{200K}=100 are due to the depletion of CH_2CHCN, CH_2NH, and NH_2CHO under 120 K regions. These results imply a possibility that high temperature region is dominant in G10.47+0.03 than NGC6334F and W51 e1/e2, which agree with the fact that high gas temperature was reported towards G10.47+0.03 than NGC6334F and W51 e1/e2 (Hernández-Hernández et al. 2014).

If the different abundances for N-bearing species can be explained by different temperature structures in hot cores, spatial distributions of N-bearing species would be compact compared to O-bearing species, since N-bearing species would trace inner high temperature region of hot cores. To confirm this hypothesis, future very high spatial resolution observations by ALMA would be necessary to sufficiently resolve the molecular spatial distributions in hot cores.

Comparison with Previous Studies

It would be useful to discuss the difference of this work from the previous study by Caselli et al. (1993). They investigated the chemical difference of Orion Hot Core, where N-bearing species are abundant, and Compact Ridge, where O-bearing species are abundant. They claimed that higher temperature for Hot Core than Compact Ridge may explain such chemical difference. They prepared a Hot Core and a Compact Ridge models, where chemical evolution starts from 40 K and 20 K, respectively. After the gravitational collapse, temperatures were suddenly raised to 200 K and 100 K, respectively. They found that N-bearing species such as CH_2CHCN and CH_3CH_2CN are abundant in the Hot Core model, since the higher temperature enables grain surface chemistry to efficiently form C_3N, followed by successive hydrogenation to form CH_2CHCN and CH_3CH_2CN. On the other hand, CH_2CHCN and CH_3CH_2CN are poor in the Compact Ridge model, where C_3N is formed in the gas phase rather than on grains.

Our simulations suggest the chemical difference between Hot Core and Compact Ridge might be reconciled by temperature in a different way from Caselli et al. (1993). We assumed that the evolution of the cloud starts from the diffuse cloud phase, where the temperature and the density are quite low. Therefore, there is no difference in physical conditions and chemical components among sources before the warm-up phase. I found that CH_2CHCN, NH_2CHO, and CH_2NH are not so abundant on the grains and they are rather formed in the gas phase. In this work, the difference of the chemical compositions is explained by the different temperatures after the warm-up phase. N-bearing species, such as CH_2CHCN, NH_2CHO, and CH_2NH, are formed in the gas phase with updated gas phase chemical reaction dataset than Caselli et al. (1993). Such N-bearing species are adsorbed and destructed on the grain before evaporating again if the temperature is not high enough. Therefore, the depletion of N-bearing species can be explained in Compact Ridge, due to adsorption and the following destruction process on grains under lower temperature environment than Hot Core.

3.6.4. The Effect of UV Radiation from a Central Star

Methodology

UV radiation from central stars may be another reason to explain the chemical difference among hot cores. In this subsection, I will discuss the effect of UV radiation to the chemistry. For simplicity, other physical parameters, than the intensity of UV radiation such as temperature and density were not changed. Their time dependencies are shown in Figure 16.

The radiation from the central star can be approximated as a black body radiation:

$$B_\nu(T)\mathrm{d}\nu = \frac{2h\nu^3}{c^2}\frac{d\nu}{\exp(\frac{h\nu}{kT})-1} \quad (47)$$

where T is the effective surface temperature of the star, ν is the frequency, c is the speed of light, h is the Planck constant. The number of photons between 5-13.6 eV can be counted by integrating $B_\nu(T)/h\nu$ over 5-13.6 eV (91.1-246 nm). UV radiation from the star is attenuated due to the effect of distance and visual extinction. The attenuation due to the distance is simply calculated by a factor of R^2/r^2, where the radius of star "R" and the distance from the star "r". Actually, the effective surface temperature of the star, T, and the stellar radius, R, would be simultaneously given by assuming the spectral type of the star. I will calculate two kinds of high-mass stars to determine these parameters: B0 type (R=8$M_\odot$ and T=30000K) and O5 type (R=20$M_\odot$ and T=45000K). Black body UV radiation between 5-13.6 eV at T=30000K and T=45000K, respectively, contain 3×10^{16} and 1×10^{17} times of photons compared to the standard UV radiation in the ISM, on the surface of stars.

Further, UV radiation from the star would be attenuated by interstellar dust particles. Since visual extinction is caused by interstellar dust particles, Av is a useful measure to estimate the attenuation of UV radiation. It is known that Av is proportional to the hydrogen column density: N[H] (cm^{-2}) $=2.21\times10^{21}$ Av (mag) (Güver et al. 2009). This equation is used to calculate the value of visual extinction from the star to a certain radius, r, under the given density profile of the hot cores. I employed the density profile based on the observations and theoretical studies of UCHII regions from Nomura & Millar (2004). They suggest that the hydrogen atom number densities (n_H) are not so different within 0.1 pc, which gradually drop from 0.1 pc. For simplicity, I assume that Av does not increase inside the HII region, where strong UV radiation would destroy dust. This situation is depicted in Figure 26 (a). Therefore, the distance in calculating the attenuation ($r_{attenuate}$)

can be obtained by subtracting the radius of HII region (r_{HII} from the distance to the center of the core "r"). Above discussion finally leads to the relationship of Av and the distance from the star, r, and hydrogen molecular column density, $n[H_2]$.

$$Av = 1.4 \times 10^{-3} \times n[H_2](cm^{-3}) \times r_{\rm attenuate}(pc), \tag{48}$$

,where

$$r_{\rm attenuate} = r - r_{HII} \tag{49}$$

The Region where UV Radiation is Dominant

First of all, it would be inevitable to investigate how UV radiation affects the chemical evolution depending on the distance ($r_{attenuate}$) from the HII region. Here, I assume an initial hydrogen density of 1 cm^{-3}, a timescale of the warm-up phase of 7×10^4 years, B=0.7, a peak density of 1×10^7 cm^{-3}, a peak temperature of 200 K and B0 type star. r_{HII} was assumed to be 0.003 pc, which corresponds to the size of hyper compact HII region of G10.47+0.03 (Cesaroni et al. 2010). DoPs for $r_{attenuate}$=0.001 and 0.002 pc cases compared to "without UV radiation from the star model" are shown in Figure 27. $r_{attenuate}$=0.001, and 0.002 pc cases, respectively, have Av values of 14, and 28 magnitudes. DoP compared to without UV model is almost zero at 0.002 pc, suggesting that strong attenuation by grain prohibited UV radiation from penetrating further outward of the cloud. This trend can also be seen if we assume O5 type star at r_{HII}=0.003 pc (Figure 28), which corresponds to the same situation with r_{HII}~0.015 pc under the B0 type star. In other words, attenuation by grain ($r_{attenuate}$) is a more important parameter than the type of the star or the size of HII region "r_{HII}". Since the effect UV radiation on chemical evolution is almost negligible at $r_{attenuate}$=0.002 pc, for the first approximation, it would be reasonable to fix $r_{attenuate}$=0.001 pc and chemical evolutions are affected by UV inside of this radius.

Comparison with Observed Data

It is useful to use an weighted volume $V_{ratio}=V_{noUV}/(V_{UV}+V_{noUV})$ as a parameter to compare our simulation results with observed data. V_{noUV} and V_{UV} are the volumes of the hot core where $r_{attenuate}$ is larger than 0.001 pc, and within 0.001 pc, respectively. The effect of UV radiation on chemical evolution is considered only in V_{UV}. When simulated abundances of certain species i are represented by X_{UV} and X_{noUV}, respectively, for at 0.001 pc and 0.002 pc from the star, weighted abundances are calculated as $X[i]_{weighted} = \frac{X[i]_{UV}V_{UV}+X[i]_{noUV}V_{noUV}}{V_{UV}+V_{noUV}}$, as this situation is depicted in Figure 26 (b). In Figure 29, $X_{weighted}[CH_2NH]$ under different V_{ratio} of 0, 0.5, 0.9, 1 are presented. $V_{ratio}=1$ corresponds to the situation without UV radiation from the star, while stronger UV radiation from evolved HII regions are assumed under smaller V_{ratio} values. The fractional abundance of CH_2NH is not close to the observed value unless V_{ratio} is larger than 0.9, corresponding to the situation when HII region gets well evolved.

Is this model able to explain other chemical difference of observed sources? In Figures 30 (a) and (b), DoP compared to the observed value towards (a) G10.47+0.03 and (b) NGC6334F are shown. DoP are quite large at $V_{ratio}=1$ for both cases, since most of organic species are destroyed. Therefore, although CH_2NH abundance is explained under $V_{ratio}=0.9$ or 1, such situation is not realistic.

3.7. Summary

The main results of this section can be summarized as follows:

1. I conducted the chemical modeling to investigate the chemical evolution of N-bearing species, especially glycine precursors. As the results, I found that CH_2NH would be efficiently produced via gas phase "CH_3 + NH" process rather than direct

evaporation from grains. The direct glycine precursor, CH_3NH_2 is efficiently formed from hydrogenation process to HCN and the following CH_2NH on grains. Since the hydrogenation process to CH_2NH is so fast that evaporation of CH_2NH is less important.

2. I found that gas phase CH_2CHCN can be efficiently formed from "C_2H_4 + CN" process rather than evaporation from grain surface. This is because grain surface CH_2CHCN is not so abundant due to the hydrogenation process to form CH_3CH_2CN.

3. CH_3CH_2CN was underproduced in the current chemical model by more than a factor of 10. It would be worth to investigate the efficiency of the "C_2H_6 + CN" process, a similar process with "C_2H_4 + CN" or "C_2H_2 + CN"process, which is suggested as the route to CH_2CHCN and HC_3N.

4. The link between the physical properties and chemical compositions of sources was discussed in terms of the different temperatures and UV radiation. The different UV radiation model could not well explain the chemical difference in the sources since all species are simultaneously destroyed. I found that different temperature can explain the depletion of some N-bearing species; if CH_2NH, CH_2CHCN, and NH_2CHO are adsorbed in the not so high temperature environment. They may be destructed by grain surface reactions before they evaporate again.

Chapter 4. Formation Process to Glycine

4. Formation Process to Glycine

4.1. Previous Studies about Chemical Evolution to Glycine

4.1.1. Processes in the Past Studies

In the final section, I discuss the formation process of the simplest amino acid, glycine. The formation paths to glycine both in the gas phase and on the grain surface have so far been discussed via theoretical and experimental studies.

For gas phase processes, Blagojevic et al. (2003) assumed that interstellar glycine would be synthesized via ion-molecule reactions. They prepared some combinations of positive ions and neutral species, and found that the reaction of "$NH_2OH^+ + CH_3COOH \longrightarrow NH_2CH_2COOH^+ + H_2O$" and "$NH_3OH^+ + CH_3COOH \longrightarrow NH_3CH_2COOH^+ + H_2O$"can efficiently form positive ions of glycine, which would be converted to the neutral form via dissociative recombination processes with an electron. Although NH_2OH (hydroxylamine) has not been detected in the ISM, it would be a plausible interstellar molecule since the ultraviolet laser irradiation of ice mixtures simulating interstellar grains produced hydroxylamine (Nishi et al. 1984). NH_2OH would be easily protonated in the gas phase chemistry due to its high proton affinity (Blagojevic et al. 2003). Charnley et al. (2006) conducted chemical modeling calculation assuming the physical condition of hot cores. They started their simulations from the observed or predicted abundances of CO, N_2, CH_4, H_2CO, C_2H_5OH, H_2S, C_2H_6, H_2O, CH_3OH, NH_3, HCOOH, and NH_2OH on interstellar ice, as is found in Rodgers & Charnley (2001) in detail. Assuming the constant density (10^7 cm^{-3}) and temperatures (100 K and 300 K) through the simulations, they found that the ion-neutral processes above can form glycine as much as 10^{-10} relative to molecular hydrogen.

The formation processes have also explored on the framework of grain surface chemistry.

Woon (2002) suggested that glycine would be built on the ice, under UV irradiation, from COOH and CH_2NH_2. He assumed that the UV irradiation on H_2O/CO ice would lead to abundant OH radical, which can react with CO to form COOH. CH_2NH_2 can be formed via hydrogenation process to abundant species HCN. Woon (2002) conducted quantum chemical calculations, and showed the activation barriers associated with "CO + OH", and hydrogenation processes to HCN, which finally lead to CH_3NH_2. Later, Theule et al. (2011) confirmed CH_3NH_2 after a UV irradiation experiment on ice containing HCN and H atoms, implying that these processes would valid in the ISM conditions.

Recently, Garrod (2013) conducted a systematic study, and investigated an effective formation route to glycine. He assumed that grain surface radical-radical reactions would form glycine, for instance,

$HOCO + CH_2NH_2 \longrightarrow NH_2CH_2COOH$, or

$NH_2 + CH_2COOH \longrightarrow NH_2CH_2COOH$

His model also included gas phase formation process of ionized glycine from CH_3COOH and NH_3OH^+ and NH_2OH^+, which were discovered by Blagojevic et al. (2003):

$NH_2OH^+ + CH_3COOH \longrightarrow NH_2CH_2COOH^+ + H_2O$

$NH_3OH^+ + CH_3COOH \longrightarrow NH_2CH_2COOH_2^+ + H_2O$

The dissociative recombination process of $NH_2CH_2COOH_2^+$ with an electron will form glycine.

Under the fast warm-up model, which assumed the environment of high-mass stars, he found that "$HOCO + CH_2NH_2 \longrightarrow NH_2CH_2COOH$" is the most dominant formation route to glycine, and the effect of gas phase formation routes is negligible. He claimed that HOCO is formed via a photodissociation process of or a chemical hydrogen subtraction from

HCOOH. In this case, the origin of HOCO was not "CO + OH" as previously suggested (Woon 2002). The origin of CH_2NH_2 is a photodissociation process of CH_3NH_2, or chemical hydrogen subtraction processes from CH_3NH_2.

However, the formation paths to glycine have been continuously updated by theoretical and experimental studies. In this section, I will investigate the importance of newly suggested formation paths to glycine, which was not incorporated into the network of Garrod (2013).

4.1.2. Newly Suggested Formation Paths to Glycine

Gas Phase Reactions

Based on the previous experiment by Blagojevic et al. (2003), Barrientos et al. (2012) conducted chemical network simulations to form glycine from protonated isomer of hydroxylamine, NH_3OH^+. They reported that the associated activation barriers for "NH_3OH^+ + CH_3COOH" and "NH_2OH^+ + CH_3COOH" are, respectively, 30.4 kcal/mol and 47.7 kcal/mol. Garrod (2013) has already concluded that these two paths are inefficient.

On the other hand, Barrientos et al. (2012) showed that "$NH_2OH_2^+$ + CH_3COOH" can produce glycine more efficiently with its low activation energy of 4.4 kcal/mol.

Radical-Radical Reactions

Singh et al. (2013) assumed that glycine can be synthesized from sequences of reactions with simple species, which are abundant in the ISM. They showed three possible routes to form glycine via quantum chemical calculations. Their assumed formation routes to glycine

are reactions (1-1) through (1-3) as shown below:

$CH_2 + NH_2 \longrightarrow CH_2NH_2$ (Reaction 1-1)

$CH_2NH_2 + CO \longrightarrow NH_2CH_2CO$ (Reaction 1-2)

$CH_2NH_2CO + OH \longrightarrow NH_2CH_2COOH$ (Reaction 1-3)

Singh et al. (2013) concluded that Reaction 1-1 and Reaction 1-3 are barrier-less reactions, while the Reaction 1-2 has an activation barrier of 7100 K.

Another sequences of reactions start from a combination of NH_2 and CH, as below:

$NH_2 + CH \longrightarrow NH_2CH$ (Reaction 2-1)

$NH_2CH + CO \longrightarrow NH_2CHCO$ (Reaction 2-2)

$NH_2CHCO + OH \longrightarrow NH_2CHCOOH$ (Reaction 2-3)

$NH_2CHCOOH + H \longrightarrow NH_2CH_2COOH$ (Reaction 2-4)

There are no activation barriers for Reaction 2-1, Reaction 2-2, and Reaction 2-3. However, Reaction 2-4 possesses an activation barrier of as high as $\sim$37000 K.

The third path starts from CH_2 and CO:

$CH_2 + CO \longrightarrow CH_2CO$ (Reaction 3-1)

$CH_2CO + OH \longrightarrow CH_2COOH$ (Reaction 3-2)

$CH_2COOH + NH_2 \longrightarrow NH_2CH_2COOH$ (Reaction 3-3)

Reaction 3-1, Reaction 3-2, and Reaction 3-3 are barrier-less reactions.

Among above reactions, Reaction 2-4 would never contribute to the chemical evolution with such a huge activation barrier. Since Reaction 1-2, Reaction 3-1, Reaction 3-2 were not included in the calculations by Garrod (2013), they may change the predicted glycine

abundance.

Reactions under UV or Cosmic-Ray Radiation

Munoz Caro et al. (2002) conducted laboratory experiments and confirmed 16 amino acids, including glycine, after UV irradiation on ice containing H_2O, CH_3OH, NH_3, CO and CO_2. Their experiments suggested that the formation of glycine is possible without HCN. However, the formation mechanism was unclear at that time. To deepen the understanding of formation path to glycine in this scheme, Holtom et al. (2005) conducted experiments assuming cosmic ray inducing environment on the interstellar ice analogue containing CH_3NH_2 and CO_2, under the assumption that CH_3NH_2 would have formed from CH_3 and NH_2 radicals during the experiments by Munoz Caro et al. (2002). As the results, they reported the confirmation of glycine. They claimed that this process starts from photo cleavages of C-H and N-H bonds in CH_3NH_2, and creates CH_2NH_2 and H. Although a process of "CO_2 + H $\longrightarrow$ HOCO" is not likely to occur due to its high activation barrier of 65.6 kJ/mol ($\sim$7900 K) (Zhu et al. 2001), the nascent H atom by strong UV photons would have extra energy to overcome this barrier (Holtom et al. 2005; Lee et al. 2009). Following reaction of "CH_2NH_2 and HOCO $\longrightarrow$ NH_2CH_2COOH" requires no entrance barrier (Holtom et al. 2005). Further, Lee et al. (2009) reported the formation of glycine from CH_3NH_2 and CO_2 on interstellar ice analog films under UV irradiation at 7.3-10 eV, corresponding to the effective energy range for interstellar UV radiation. I note that Garrod (2013) also claimed the importance of the reaction of "CH_2NH_2 + HOCO $\longrightarrow$ NH_2CH_2COOH". However, he assumed that HOCO was formed from the subtraction of H atom from HCOOH by radicals such as OH, rather then hydrogenation process to CO_2.

Despite its huge activation energy, the effect of UV may make this process efficient in the hot core condition. The external UV radiation in the ISM is strongly attenuated, and it

does not contribute to the chemical evolution inside the dense ($\sim 10^7$ cm^{-3}) hot cores. The main source of UV radiation inside a hot core would be black body radiation from newly born stars inside hot cores or the Prasad-Tarafdar mechanism.

4.1.3. Motivation of This Section

The chemical processes in the ISM are far from being completely understood. It would be worth to investigate formation process to glycine with newly suggested routes. The main difference of this work from Garrod (2013) is, first of all, that I will test newly suggested formation processes to glycine. Secondly, while chemical reactions in Garrod (2013) were based on the "osu" (Ohio State University) dataset, I employed the dataset of kida.uva.2014, in which gas phase chemical model was updated from the osu dataset with the latest suggestions by KIDA experts (Table 1 in Wakelam et al. (2015)). Especially, I will develop a chemical model with suprathermal hydrogen, H*, for the first time. For the H* chemistry, further discussions based on experimental and theoretical studies would be necessary. In the following subsections, I will indicate the importance of this process.

4.2. Modeling

4.2.1. Model 1: New Formation Processes of Glycine

Physical Processes

The same physical processes as the previous section is assumed in the simulations here. I write down again about the detail.

The physical conditions are based on the "fast warm-up model" presented in Garrod (2013), which modeled the physical evolution of high-mass stars. The initial gas density,

n, was increased up to the peak density as a function of time, t, along with the modified free-fall differential equation shown below (Nejad et al. 1990):

$$\frac{\mathrm{d}n}{\mathrm{d}t} = B\left(\frac{n^4}{n_\mathrm{i}}\right)^{1/3}\left\{24\pi G m_H n_i\left[\left(\frac{n}{n_i}\right)^{1/3} - 1\right]\right\}^{1/2} \tag{50}$$

where $\mathrm{n_i}$ is the initial density. However, the actual gravitational collapse would be somewhat slowed down than free-fall process due to the resistance of turbulent, thermal motion, or magnetic field. The collapsing speed is adjusted by a parameter of B. The factor B=1 corresponds to the usual free-fall case. The smaller values of B than unity is used to approximately assume the situation of non-free-fall cases, as Garrod (2013) employed B=0.7 assuming that internal physical processes would be against free-fall process.

While the gas temperature was fixed in the collapsing phase, the dust temperature decreased from 19 K to 8 K depending on the visual extinction, which was calculated from the gas density of the cloud using the formula presented in Garrod (2011):

$$T_\mathrm{dust} = 18.67 - 1.637A_\mathrm{v} + 0.07518A_\mathrm{v}^2 - 0.001492A_\mathrm{v}^3(K) \tag{51}$$

The visual extinction obeys the relationship $\mathrm{A_v}$=$\mathrm{A_{v,0}}(\mathrm{n_H}/\mathrm{n_{H,0}})^{2/3}$, where $\mathrm{A_{v,0}}$ and $\mathrm{n}_{H,0}$are the initial value of $\mathrm{A_v}$ and $\mathrm{n_H}$. $\mathrm{A_{v,0}}$ was set to be 0.01 so that Av=10 is achieved at the dark cloud condition, n=$5\times10^4\mathrm{cm}^{-3}$. Once the peak density were achieved, we fixed the density, and the gas and dust temperatures were raised from ∼10 K to their peak temperatures. After that, chemical evolution continued with fixing their temperature and density to their peak values.

As it was shown in the Chapter 3, the contribution to the chemical evolution from different initial densities, B, warm-up timescales, peak densities are small within our simulations. I conducted the calculations under an initial density of 1 cm^{-3}, B=0.7, a warm-up timescale of 7×10^4 years, a peak temperature of 200 K, and a peak density of

1×10^7 cm^{-3}.

The Chemical Processes

In addition to all the chemical processes in the Chapter 3, new possible paths to glycine were included. In the gas phase, $NH_2OH_2^+$ will form the positive ion of glycine with higher reaction rate than NH_3OH^+. Since Garrod (2013) employed the rate coefficient for "$NH_2OH_2^+$ + CH_3COOH" to be k=1.0×10^{-11} cm^{3}s^{-1}, I assumed higher value for NH_3OH^+ by a factor of 10:

$NH_2OH_2^+ + CH_3COOH \longrightarrow NH_2CH_2COOH_2^+ + H_2O$ (k=1.0×10^{-10} cm^{3}s^{-1}).

In addition to the above gas phase process, grain surface radical reactions were included. The following grain surface processes were newly added in Model 1 to investigate their importance:

$CH_2NH_2 + CO \longrightarrow NH_2CH_2CO$ (E_A=7100 K)

$CH_2 + CO \longrightarrow CH_2CO$ (E_A=0 K)

$CH_2CO + OH \longrightarrow CH_2COOH$ (E_A=0 K)

*4.2.2. Model 2: Suprathermal Hydrogen H**

In this subsection, I will develop the chemical model to discuss the importance of H* to the formation of glycine. H* was added in the modeling calculations for the first time. I call the model developed in this subsection as Model 2 to be distinguished from Model 1.

Basic physical model is the same as Model 1. I conducted the simulations with fixing the initial density of 1 cm^{-3}, B=0.7, the warm-up timescale of 7×10^4 years, and the peak density of 1×10^7 cm^{-3}.

Since all chemical processes except for H* reactions are the same as Model 1, processes below are included in Model 2 (Barrientos et al. 2012; Singh et al. 2013):

$NH_2OH_2^+ + CH_3COOH \longrightarrow NH_2CH_2COOH_2^+ + H_2O$ (gas phase reaction, k=1.0×10^{-10} cm^3s^{-1})

$CH_2NH_2 + CO \longrightarrow NH_2CH_2CO$ (grain surface reaction, E_A=7100 K)

$CH_2 + CO \longrightarrow CH_2CO$ (grain surface reaction, E_A=0 K)

$CH_2CO + OH \longrightarrow CH_2COOH$ (grain surface reaction, E_A=0 K)

*The Chemistry of H**

As it was mentioned in the previous section, the cosmic rays are the important source of UV flux in the dense region with large Av, where interstellar UV photons cannot penetrate (Prasad & Tarafdar 1983). For the modeling of H*, I simply assumed that H* is created by the dissociation process of any H-bearing species by UV field by the Prasad-Tarafdar mechanism. In Model 1, this process produced not H* but usual hydrogen atom.

For instance,

$CH_3NH_2 + h\nu \longrightarrow H^* + CH_2NH_2$, or

$NH_3 + h\nu \longrightarrow H^* + NH_2$

The activation energy of "$CO_2 + H \longrightarrow HOCO$" is ∼7900 K, corresponding to 0.68 eV. When UV photons of more than 5 eV react with CH_3NH_2, ∼4.3 eV is used to dissociate C-H bond, and extra energy is given to the dissociated hydrogen atoms than can sufficiently overcome the potential barrier associated with the "CO_2 + H" process. Since all grain surface reactions in my model have lower activation barriers than "$CO_2 + H \longrightarrow HOCO$" ($E_A$∼7900 K), H* would be able to overcome any activation barriers associated with grain

surface reactions. Therefore, in Model 2, I assumed that H* can lead to any hydrogenation process penetrating activation barriers (E_A=0 K). For instance, not only "CO_2 + H* $\longrightarrow$ HOCO", but also other grain surface hydrogenation processes such as "CO + H* $\longrightarrow$ HCO", are treated as barrierless reactions. I presented a diagram of formation paths of H* and HOCO in the above scenario in Figure 31.

For simplification, other chemical properties for H* were assumed to be the same as the usual H atoms. It was assumed that H* acts as a usual H atom in the gas phase chemistry after the evaporation process.

The inclusion of H* changes the reaction rates of hydrogenation processes dramatically. Recall that reaction rates on grain is proportional to κ_{ij}, as is given in the below formula using activation energy E_A:

$$\kappa_{ij} = \exp(-2(a/\hbar)(2\mu E_A)^{1/2}), \tag{52}$$

where "a" is the rectangle barrier of thickness (1 Å) and μ is the reduced mass. κ_{ij} is 2.7×10^{-16} for usual hydrogenation process to CO_2 (H + CO_2 $\longrightarrow$ HOCO), with its activation energy of $\sim$7900 K. With such a low reaction rate, usual hydrogenation process to CO_2 would be negligible even if CO_2 is abundant. However, κ_{ij} becomes unity for hydrogenation processes of H*, where E_A=0. The conversion of CO_2 to HOCO by the hydrogenation process of H* may strongly change the abundances of HOCO abundances on grains.

UV Radiation from Newly Born Stars

Very strong UV radiation from newly born stars would change the formation and destruction rates of glycine. I will also investigate this effect.

Basic physical and chemical models are the same as the previous subsection. However, the black body radiation from the newly born star is considered as a new source of UV radiation.

Basic modeling of black body radiation is the same as the one presented in subsection 3.6.4 in this thesis, which was devoted to the discussion of the destruction process under UV radiation. I conducted the calculation by fixing the initial density of 1 cm^{-3}, B=0.7, the warm-up timescale of 7×10^4 years, and the peak density of 1×10^7 cm^{-3}. B0 type star and r_{HII}= 0.003 pc were assumed. Recalling that the effect of UV radiation is dominant within the 0.001 pc from HII regions, and that dependency on the type of the star and the sizes of HII region are small, I investigated the chemical evolution to glycine at $r_{attenuate}$=0.001 pc. At the distance of $r_{attenuate}$=0.01 pc, the UV photon flux is $\sim3\times10^{13}$ photons cm^{-2} s^{-1}, which is comparable to the experimental condition in Lee et al. (2009), which confirmed glycine after the UV irradiation on CH_3NH_2 and CO_2 ice.

4.3. Results

4.3.1. Comparison of Garrod Model and Model 1

In this subsection, I will compare newly developed Model 1 and our previous model described in Chapter 3. In our previous model, included reactions related to glycine are same as Garrod (2013). Therefore, I call our previous model as "Garrod Model" in this section for the discussion of the formation process to glycine.

In Figure 32 (a), I will show the fractional abundances of glycine in the siulations with Model 1 and Garrod Model, both in the gas phase (red) and on grain (black). The solid lines and the dotted lines, respectively, represent the simulated fractional abundances with Model 1 and Garrod Model. Since the abundances of Garrod Model and Model 1 is very

close, I can conclude that the updated chemistry contained in KIDA does not change the abundance of glycine, and newly added formation paths are not so efficient compared to the previous paths modeled by Garrod.

Their peak abundances of gas phase are $\sim 1 \times 10^{-11}$ for both cases. On the other hand, Garrod (2013) reported the peak abundance of glycine to be $\sim 8 \times 10^{-11}$ under fast warm-up model. The difference would be due to the different peak temperature. While Garrod (2013) employed the peak temperature of 400 K, I performed simulations under the peak temperature of 200 K for both Model 1 and Garrod Model. In our models, glycine is not fully evaporated due to its high desorption energy (10100 K).

4.3.2. Implication of the Importance of H Chemistry*

UV Photons Generated by Prasad-Tarafdar Mechanism

In this subsection, I will discuss the importance of H* chemistry. First of all, I assume a region where UV radiation from stars are significantly attenuated and only the Prasad-Tarafdar mechanism produce H*. For comparison, chemical evolutions were simulated with both Model 1, where H* is not available, and Model 2. The glycine abundances in Model 1 (dotted line) and Model 2 (solid line) are shown in Figure 33 (a). The sum of the fractional abundance on grain surface and in mantle are shown in black the lines, while the gas phase abundance is shown in the red lines.

The gas phase fractional abundance of glycine is as high as $\sim 10^{-9}$ in Model 2, with the inclusion of H*. This value is almost 100 times higher than that of Model 1. This result implies that the fractional abundance of glycine can be strongly enhanced by adding the effect of H*.

The effects on other COMs

In this subsection, I present the effect of H* on the chemical evolutions of other COMs. In Figure 35, the abundances of COMs are compared between Garrod Model and Model 2. For both cases, physical parameters were fixed to be the same values: initial density of 1 cm^{-3}, B=0.7, the timescale of the warm-up phase of 7.1×10^4 years, the peak density of 1×10^7 cm^{-3}, and the peak temperature of 200 K. The time of zero years corresponds to the beginning of the warm-up phase and the chemical evolutions until 1×10^6 years are shown. The black and red lines, respectively, represent the simulated abundances with the Garrod Model and Model 2. I note that for COMs presented in Figure 35, there was almost no difference between the Garrod Model and Model 1. Therefore, the difference between the Garrod Model and Model 2 is due to the inclusion of H*.

Figure 35 suggests that the difference of interested COMs are not so large. While the difference of C_2H_5CN abundance is almost a factor of 10 around 1×10^6 years, the difference in abundances of other COMs is less than a factor of 10 anytime.

The DoP of the Model 2 model is compared to the Garrod Model in Figure 35. Since the DoP is less than 0.5 before 1×10^6 anytime, their chemical difference is small. This result indicates that while the inclusion of H* increase the abundance of glycine, it has small effect on the abundances of other interested COMs. Therefore, the inclusion of H* do not contradict the discussions in Chapter 3.

UV Radiation from Newly Born Stars

In the vicinity of HII regions, strong UV radiation would rapidly produce H*. In this subsection, glycine abundances will be compared under the condition of with and without UV radiation originated from stars.

In Figure 34 (a), the red and black lines respectively show the simulated glycine abundances in the gas phase and on grains. The solid line represents the calculation with UV radiation from the star, while the dotted line represents the simulation results under without UV radiation from the star. In the fpllowing discussions, I will use Model 2. Therefore, H* is included for both cases.

Surprisingly, the abundance of glycine on grains is as high as 10^{-6} if we consider the effect of UV from the star (red dotted line). The UV radiation from stars is too strong that rather destroy glycine on grains before evaporation.

4.4. Discussion

4.4.1. Formation Paths to Glycine in Model 1

According to Figure 32 (a), the gas phase abundance of glycine is comparable to that in grain mantle after evaporation process, suggesting that glycine originates from grains. In Figure 32 (b), I compared the formation rates ($cm^{-3}s^{-1}$) of glycine for all possible processes on the grains in both Garrod model and Model 1, to reveal which would be the essential one. The red lines represent the reaction rates of "CH_2NH_2 + HOCO" process, and the black lines represent the sum of the reaction rates for the other processes. For both cases, the most dominant formation path is "CH_2NH_2 + HOCO" at around 4-5$\times10^4$ years, when the temperature is 60-120 K. Another peak of black lines would be unimportant: in this peak, $HNCH_2COOH$ radical, which was produced via the destruction process of glycine, is used to reproduce glycine again via the reactions such as "$HNCH_2COOH$ + H". Therefore, major formation process to glycine would be "CH_2NH_2 + HOCO", which agrees with the results by Garrod (2013).

Therefore, the update of gas phase chemistry by KIDA does not change the chemistry

discussed by Garrod (2013). Further, this result indicate that newly investigated formation processes, gas phase reactions of "$NH_2OH_2^+$ + CH_3COOH" by Barrientos et al. (2012) and radical-radical reactions by Singh et al. (2013), would be unimportant compared to "CH_2NH_2 + HOCO" process.

4.4.2. Formation Paths to Glycine in Model 2

The reaction rates to form glycine are compared in Figure 33 (b). The red and black lines, respectively, represent the formation rates for "HOCO + CH_2NH_2" and a sum of the other paths. The reaction rate of "HOCO + CH_2NH_2" is nearly $\sim 10^{-12}$ cm^{-3} s^{-1} in Model 2 (solid lines), which is much higher than the cases in Model 1 (dotted lines). The dramatical increase of glycine in Model 2 is due to the efficient formation of HOCO radical on the grains via "H* + CO_2". The simulations indicate that it is possible that suprathermal H atoms can accelerate the formation of glycine much more efficiently than previously thought.

This result can be seen under the radiation of the central star. In Figure 34 (b), formation rates of glycine via "HOCO + CH_2NH_2" and the total reaction rate are shown in red and black lines, respectively. The solid and dotted lines, respectively, represent cases with and without UV radiation from the star. The total glycine formation rate is as high as 10^{-9} cm^{-3} s^{-1} under the UV flux from the star, where H* is quickly formed via destruction of saturated species and the reaction of "HOCO + CH_2NH_2" is so accelerated. However, the solid-phase glycine abundance quickly decreases before the evaporation at $\sim 7\times 10^4$ years.

4.5. Summary

I concluded that UV radiation from stars would decrease gas phase glycine abundance. HII regions would expand outward along with the evolution of hot cores, destroying surrounding hydrogen molecules by strong UV radiation. Thus, less evolved HII regions might be indicators of the sources where the effect of UV radiation is less dominant, where glycine would keep high abundance.

In addition, I confirmed that glycine is efficiently formed from "HOCO + CH_2NH_2", as suggested by Garrod (2013). However the most efficient formation path to the HOCO radical should be modified. I newly found that this reaction can be strongly accelerated by adding suprathermal hydrogen atoms, H*.

This result would provide us an important clue to prepare for future glycine surveys. Since CH_3NH_2 is a key species in the chemical evolution to glycine, CH_3NH_2 rich sources would be plausible glycine-rich sources. The most efficient way to form CH_3NH_2 is grain surface hydrogenation process to HCN and CH_2NH. On the other hand, I found that the most efficient formation process of CH_2NH is gas phase reaction of "CH_3 + NH", since grain surface CH_2NH is quickly converted to CH_3NH_2. If gas phase CH_2NH is independently formed from CH_3NH_2 via gas phase chemical reactions, CH_2NH would not be a good indicator of CH_3NH_2 rich sources. Therefore, CH_3NH_2 surveys should be conducted for future glycine surveys.

Chapter5. Conclusion

5. Conclusion

Origin of life is one of the oldest mysteries for the mankind. The latest theory suggests that comets would have provided prebiotic materials to the primordial Earth, leading to the chemical evolution to the origin of life. Based on this scenario, I investigated the evolution of N-bearing species in the ISM, in the context of the formation to glycine.

Based on the previous suggestions on the formation of glycine, I focused on possible glycine precursors, CH_2NH and CH_3NH_2. Although they were detected in the ISM, their detections were limited to the small number of sources. In addition, their formation processes in the actual interstellar medium were not established. To deepen our knowledge about the evolution of glycine precursors, I reported in this thesis the studies both from radio observations and theoretical simulations.

As the results of the CH_2NH surveys, I succeeded to detect CH_2NH towards eight star-forming regions including four new detections. CH_2NH would be ubiquitous species in the environment of high-mass star forming regions. Furthermore, I found the difference in CH_2NH abundances among sources, ranging from $\sim 10^{-8}$ to $\sim 10^{-9}$. CH_2NH was rich in the sources where other N-bearing species, such as CH_2CHCN and NH_2CHO were also abundant. The difference in chemical components is important clues to promote our knowledge about the evolution of N-bearing species.

The chemical evolution of high-mass stars was discussed with chemical modeling. This method enabled us to discuss how molecules get complexity from atomic initial form along with the evolution of high-mass stars. I found the new result that CH_2NH was not originated from grain surface, as has been commonly accepted for COMs, but newly formed through the gas phase reaction of "CH_3 + NH". This is because hydrogenation to HCN and CH_2NH is so efficient that CH_2NH on the grains was converted to CH_3NH_2. I also showed that CH_2CHCN can also be produced in the gas phase reactions of "C_2H_4 + CN",

and suggested the importance of CH_3CH_2CN formation via similar process"C_2H_6 + CN".

The connection of environment of observed sources and observed different abundances for N-bearing species was discussed by means of chemical simulations. The new hypothesis from this work is that N-bearing species might be depleted in the sources where temperature is not so high (less than 120 K). According to the chemical simulations, the depleted N-bearing species were formed in the gas-phase and they were converted to other species on grains. Therefore, they were destroyed on the grain surface reactions shortly after the adsorption. The chemical simulations suggested that it is possible to account for the different chemical properties of N-bearing species in terms of different temperature structures in the sources.

Finally, I discussed the formation process to glycine. The most effective path would be "CH_2NH_2 + HOCO" on the grains, as was suggested by Garrod (2013). With the first modeling of suprathermal hydrogen H*, I found that H* may strongly accelerate this process producing HOCO radical from a ubiquitous species, CO_2.

Since our theoretical study showed that CH_3NH_2 is abundant on grains, CH_2NH_2 would be sufficiently formed from CH_3NH_2. If HOCO can be provided from CO_2, the reaction of "CH_2NH_2 + HOCO" would form glycine efficiently on interstellar grains in any star-forming regions. In star-forming regions, comets will be formed via the aggregation of grains, which contain glycine inside. Such comets would have provided glycine to our primordial Earth and other exoplanets.

To further investigate this scenario, our next important step would be to achieve the first detection of interstellar glycine. Our simulations suggested that the UV photons from the central stars rather decreased glycine abundance since the destruction rates overcome the producing rates. It would be preferable to search for glycine in the regions where UV radiation from central stars is well attenuated. The chemical simulations predicted that

formation path of CH_2NH_2 would be hydrogen subtraction processes from CH_3NH_2, which would be abundant on the grains. Therefore, CH_3NH_2 would be a good compass to the first detection of glycine.

REFERENCES

Aikawa, Y., Wakelam, V., Garrod, R, T., & Herbst, E., ApJ, 674, 993 (2008)

Altwegg, K., Balsiger, H., Bar-Nun, A., et al. Sci, 2, id=e1600285 (2016)

Araya, E, D., Kurtz, S., Hofner, P., and Linz, H., ApJ, 138, 63 (2002)

Agúndez, M., Cernicharo, J., Pardo, J. R., et al. Astron. Space Sci., 313, 229 (2008)

Barone, V., Latouche, C., Skouteris, D., et al. arXiv:1507.03741v2 (2015)

Barrientos, C., Redondo, P., Largo, L., Rayón, V, M., & Largo, A., ApJ, 748, 99, (2012)

Bailey, J., Chrysostomou, A., Hough, J. H., et al. Sci, 281, 672 (1998)

Ball, J. A., Gottlieb, C. A., Lilley, A. E., & Radford, H. E. ApJ, 162, L203 (1970)

Belloche, A., Menten, K. M., & Comito, C., et al., A&A, 482 (2008)

Bernasconi, P. A., & Maeder, A., A&A, 307, 829 (1996)

Bisschop, S. E., Jørgensen, J, K., van Dishoeck, E, F., de Wachter, E, B, M., A&A, 465, 913 (2007)

Biver, N., Bockeleé-Morvan, D., Debout, V., et al.., A&A, 566, L5 (2014)

Blagojevic, V., Petrie, S., & Bohme, D. K. MNRAS, 339, L7 (2003)

Blake, G, A., Sutton, E, C., Masson, C, R., & Phillips, T, G., ApJ, 315, 621 (1978)

Blank J G & Miller G H Proc. 21st International Symp. on Shock Waves eds A Houwing et al (Panther Press, Australia) pp 1467, 72 (1998)

Bottinelli, S., Ceccarelli, C., Neri, R., et al., ApJ, 617, L69 (2004)

Brouillet, N., Despois, N., Baudry, A., et al, A&A, 550, A46 (2013)

Brown, R. D., et al., MNRAS, 186, 5P (1979)

Brown, R. D., Crofts, J. G., Godfrey, P. D., et al., ApJL, 197, L29 (1975)

Bonner, W, A., Orig. Life 21, 59 (1991)

Cazaux, S., Tielens, A. G. G. M., & Ceccarelli, C., et al., ApJ, 593, L51 (2003)

Caselli, P., Hasegawa, T. I., & Herbst, E., ApJ, 408, 548 (1998)

Caselli, P., Hasegawa, T. I., & Herbst, E., ApJ, 495, 3 (1998)

Cesaroni R., Hofner P., Araya E., Kurtz S., A&A, 509, A50, (2010)

Charnley, S, B., & Rodger, S, D., Proceedings IAU Symposium, 231, 2005, (2006)

Charnley, S. B., Tielens, A. G. G. M., & Millar, T. J. 1992, ApJ, 399, L71

Charnley, S, B., Tielens, A, G, G, M., & Rodgers, S, D., ApJ, 482, L203 (1997)

Churchwell, E., Walmsley, C. M., & Cesaroni, R., A&AS, 83, 119 (1990)

Choi, N., Blitz, M, A., McKee, K., Pilling, M, J., & Seakins P. W., Chemical Physics Letters, 384, 68 (2004)

Chyba, C, F., Thomas, P, J., Brookshaw, L., & Sagan, C. Science, 249, 366 (1990)

Chyba, C, F., & Sagan, C., Nature, 355, 125 (1992)

Chyba, C, F., & Sagan, C., Comets and the Origin and Evolution of Life ed P J Thomas, C F Chyba and CPMcKay, (New York, Berlin: Springer) pp 147, 73 (1997)

Collings, M. P., Anderson, M. A., Chen, R., et al., MNRAS, 354, 1133 (2004)

Codella, C., Beltrán, M, T., Cesaroni, R., et al., A&A, 550, A81 (2013)

Combes F., Gerin M., Wootten A., Wlodarczak G., Clausset F., Encrenaz P. J., A&A, 180, L13 (1987)

Combes, F., Nguyen-Q-Rieu, & Wlodarczak, G., A&A, 308, 618 (1996)

Cooper, G., Kimmich, N., Belisle, W., Sarinana, J., Brabham, K., & Garrel L.,

Danger, G., Borget, F., Chomat, M., et al. 2011, A&A, 535, A47 (2011)

Dickens, J. E., Irvine,W. M., Devries, C. H., & Ohishi, M., ApJ, 479, 312 (1997)

Demyk, K., Wlodarczak, G., & Carvajal, M., A&A, 489, 589 (2008)

Demyk, K., Mäder, H., Tercero, B., et al. A&A, 466, 255 (2007)

Draine, B, T., ApJS, 36, 595 (1978)

Ehrenfreund, P., et al., Rep. Prog. Phys. 65, 1427 (2002)

Elsila, J, E., Glavin, D, P., Dworkin, J, P., Sci. 44, 1323 (2009)

Elkins-tanton, L, T., Earth and Planetary Science Letters, 271, 181 (2008)

Engel, M, H., & Nagy, B.., Nature, 296, 837 (1982)

Engel, M, H., & Macko, S, A., Nature, 389, 265 (1997)

Favre, C., Despois, D., Brouillet, N., et al, A&A, 532, A32 (2011)

Favre, C., Carvajal, M., Field, D., et al. ApJS, 215, 25 (2014)

Fourikis, N., Takagi, K., & Morimoto, M., ApJL, 191, L139 (1974)

Friedel, D, N., Snyder, L, E., Remijan A, J., Turner, B, E., ApJ, 632, 95 (2005)

Gardner, F. F., & Winnewisser, G., ApJ, 195, L127 (1975)

Garrod, R, T. & Herbst, E., A&A, 457, 927 (2006)

Garrod, R, T., A&A...491..239G (2008)

Garrod, R, T., ApJ, 765, 60 (2013)

Garrod, R, T., & Pauly, T., ApJ, 735, 11 (2011)

Geppert, W, D., Hamberg, M., Thomas, R, D., et al., The Royal Society of Chemistry 2006, 133, 177 (2006)

Godfrey, P. D., Brown, R. D., Robinson, B. J., & Sinclair, M. W., Astrophys. Lett., 13, 119 (1973)

Gredel, R., Lepp, S., Dalgarno, A., & Herbst, E., ApJ, 347,289 (1989)

Güver, T., & Özel, F., arXiv:0903.2057v2 (2009)

Halfen, D. T., Iyushin, V. V., & Ziurys, L. M., ApJ, 767, 66 (2013)

Hasegawa, T. I., Herbst, E., & Leung, C. M., ApJS, 82, 167 (1992)

Hernández-Hernández, V., Zapata, L., Kurtz, S., & Garay, G., ApJ, 786, 38 (2014)

Hirota, T., Bushimata, T., Choi, Y. K., et al., PASJ, 60, 37 (2008)

Hirota, T., Kim, M. K., Kurono, Y., & Honma, M., ApJ, 801, 82 (2015)

Hofner, P., & Churchwell, E., A&AS, 120, 283 (1996)

Holtom, P. D., Bennett, C. J., Osamura, Y., Mason, N. J., & Kaiser, R. I., ApJ, 626, 940 (2005)

Horn, A., Møllendai, H., Sekiguchi, O, et al., ApJ, 611, 605 (2004)

Isokoski, K.,Bottinelli, S., & van Dishoeck, E. F., A&A, 554, A 100 (2013)

Ikeda, M., Ohishi, M., Nummelin, A., et al., ApJ, 560, 792 (2001)

Ikeda, M., Kawaguchi, K., Takakuwa, S., Sakamoto, A., Sunada, K., & Fuse, T., A&A, 390, 363 (2002)

Johnson, D. R., Lovas, F. J., Gottlieb, C. A., et al. ApJ, 218, 370 (1977)

Jiménez-Serra, I., Martín-Pintado, J., Báez-Rubio, A., Patel, N., & Thum, C., ApJL, 732, L27 (2011)

Jones, F, A., Cunningham, M, R., Godfrey, P, D., & Cragg, D, M., MNRAS, 347, 579 (2007)

Jørgensen, J. K., Favre, C., Bisschop, S, E., Bourke, T, L., van Dishoeck, E, F., & Schmalzl, M., ApJ, 757, L4 (2012)

Kahane C., Ceccarelli C., Faure A., Caux E., ApJ, 763, L38 (2013)

Kaifu, N., Morimoto, M., Nagane, K., et al., ApJL, 191, L135 (1974)

Kim, Y. S., & Kaiser, R. I., ApJ, 729, 68 (2011)

Kobayashi, K., Ogata, K., Tsunekawa, S., & Takano, S., ApJL, 657, L17 (2007)

Kwon. J., Tamura, M., Lucas. P. W., et al. ApJ, 765, L6 (2013)

Kuan Y., Charnley S.B., Huang H., Tseng W, Kisiel Z., ApJ, 593, 848 (2003)

Lee, C-W., Kim, J-K., Moon, E-S., Minh, Y-C., & Kang, H., ApJ, 697, 428, (2009)

Loinard L., Torres R. M., Mioduszewski A. J., & Rodríguez L. F., ApJ, 675, L29 (2008)

Loinard, L., Zapata, L. A., Rodríguez, L. F., et al., MNRAS,430, L10 (2013)

López-Sepulcre A., Jaber, Ali, A., Mendoza, E., et al., 2015, MNRAS 449, 2438

Majumdar, L., Das, A., Chakrabarti, S. K., & Chakrabarti, S. NewA, 20, 15 (2013)

Matthews, H, E., & Sears, T, J., ApJ, 272, 149 (1983)

McGuire, B, A.., Carroll, P, B., Loomis, R. A., et al. Sci, 352, 1449 (2016)

Mendoza, E., Lefloch, B., López-Seplcre, A., et al., MNRAS, 445, 151 (2014)

Menten, K. M., Reid, M. J., Forbrich, J., & Brunthaler, A., A&A, 474, 515 (2007)

Miller, S, L., Science, 117, 3046, 528 (1953)

Miller, S, L., Schlesinger, G., Advances in Space Research, 3, 47 (1983)

Minier, V., & Booth, R. S., A&A, 387, 176 (2002)

Munoz Caro, G. M., et al., Nature, 416, 403 (2002)

Müller, H. S. P., Belloche, A., Menten, K. M., et al. J. Mol. Spectr., 251, 319 (2008)

Nakajima, T., Kimura, K., Nishimura, A., et al., PASP, 125, 252 (2013)

Nejad, L, A, M., Williams, D, A., & Charnley, S, B., MNRAS,v246, 183 (1990)

Nishi, N., Shinohara, H., & Okuyama, T. J. Chem. Phys., 80, 3898 (1984)

Noble, J, A., Theule, P., Congiu, E., et al. A&A, 576, A91 (2015)

Nomura, H., & Millar, T, J., A&A, 414, 409 (2004)

Oró, P, J., Nature, 4774, 389 (1963)

Prasad, S, S., & Tarafdar, S, P., ApJ, 267, 603 (1983)

Peltzer, E. T., Bada, J. L., Schlesinger, G., & Miller, S. L., Advances in Space Research, 4, 69 (1984)

Peng, T.-C., Despois, D., Brouillet, N., Parise, B., & Baudry, A. A&A, 543, A152 (2012)

Peng T,-C., Despois, D., Brouillet, N, et al, A&A, 554, A78 (2013)

Rong, J., Qin, S, L., Zapata, L, A., et al, MNRAS, 455, 1428 (2016)

Pierazz, E., & Chyba, C, F., meteoritics & Planetary Science, 34, 909 (1999)

Plambeck, R. L., Bolatto, A. D., Carpenter, J. M., et al. ApJ, 765, 40 (2013)

Qin S.-L., Wu Y. F., Huang M. H., Zhao G., Li D., & Wang J.-J., Chen S., ApJ, 711, 399, (2010)

Reboussin L., Wakelam V., Guilloteau S., & Hersant F., MNRAS, 440, 3557 (2014)

Raunier, S., Chiavassa, T., Duvernay, F., et al., A&A, 416, 165 (2004)

Reid M. J., Menten K. M., Brunthaler A., et al., ApJ, 783, 130 (2014)

Rodgers, S.D. & Charnley, S.B. ApJ546, 324 (2001)

Ruaud, M., Loison, J, C., Hickoson, K, M., et al. MNRAS, 447 (2015)

Ruaud, M., Wakelam, V., & Hersant, F., MNRAS, 459, 3756 (2016)

Rubin, R. H., & Swenson, G, J., ApJ, 169, L39 (1971)

Sakai, N., Sakai, T., & Yamamoto, S., PASJ, 58, L15 (2006)

Sakai, N., Sakai. T., & Yamamoto. S., ApJ, 660, 363 (2007)

Savage, B, D., Bohlin, R, C., Drake, J, F., and Budich, W., ApJ, 216, 291 (1977)

Schilke, P., Groesbeck, T. D., Blake, G. A., & Philips, T. G. ApJS, 108, 301 (1997)

Semenov, D., Hersant, F., Wakelam, V., et al. A&A, 522, A42 (2010)

Sinclair M. W., Carrad G. J., Caswell J. L., Norris R. P., Whiteoak J. B., MNRAS, 256, 33 (1992)

Singh, A., Misra, S, A., & Tandon, P., Astron, 13, 8, 912 (2013)

Sridharan, T. K., Beuther, H., Schilke, P., Menten, K. M., & Wyrowski, F., ApJ, 566, 93, (2002)

Sridharan, T. K., Beuther, H., Saito, M., Wyrowski, F., & Schilke, P., ApJ, 634 L75 (2005)

Sandford, S, A., Allamandola, L, J., & Geballe, T., R., Science, 262, 400 (1993)

Sung, H., Bessell, M. S., & Lee, S.-W., AJ, 114, 2644 (1997)

Suzuki, T., Ohishi, M, Hirota, T., et al. ApJ, 788, 108 (2014)

Suzuki, T., Ohishi, M, Hirota, T., et al. ApJ, 825, 79 (2016)

Snyder, L. E., Buhl, D., Schwartz, P. R., et al. ApJ, 191 (1974)

Snyder, L. E., Hollis, J.M., Suenram, R. D., Lovas, F. J., Brown, L. W., & Buhl,D., ApJ, 268, 123 (1983)

Snyder L, E., Lovas F, J., Mehringer D. M., et al. ApJ, 578, 245 (2002)

Taquet, V., López-Sepulcre, A., Ceccarelli, C., et al. ApJ, 804, 81(2015)

Theule, P., Borget, F., Mispelaer, F., et al., A&A, 534, A64 (2011)

Tielens, A, G, G., & Hagen, W., Astron, 114, 245 (1982)

Tonks, W, B., & Melosh, H, J., journal of geophysical research, 98, 5393 (1993)

Trail, D., Watson, E, B., & Tailby, N, D., nature, 480, 79 (2011)

Turner, B. E, ApJS, 76, 617. (1991)

Turner, B. E., Terzieva, R., & Herbst, E., ApJ, 518, 699 (1999)

Urey, H, C., Natl. Acad. Sci. U. S., 38, 351(1952)

Val'tts, I. E., Larionov, G. M., & Bayandina, O. S., arXiv:1005.3715 (2012)

van Dishoeck, E, F., Rate Coefficients in Astrochemistry, 49-72 (1988)

Watanabe, N., & Kouichi, A., ApJ, 571, L173 (2002)

Watson, W, D., Rev. Mod. Phys., 48, 513 (1976)

Wakelam, V., Loison, J, C., Herbst, E, et al. ApJS, 217, 20 (2015)

Walsh, C., Loomis, R, A., Öberg, K, I., et al., ApJ, 823, L10 (2016)

J. C. G. Walker.,Evolution of the Atmosphere. Macmillan, New York. 179-208 (1977)

Wilner, D, J., De Pree, C, G., Welch, W, J., and Goss, W, M., ApJ, 550, L81 (2001)

Woon, D. E., ApJL, 571, L177 (2002)

Zhu, R. S., Diau, E. G. W., Lin, M. C., & Mebel, A. M., J. Phys. Chem. A, 105, 11249 (2001)

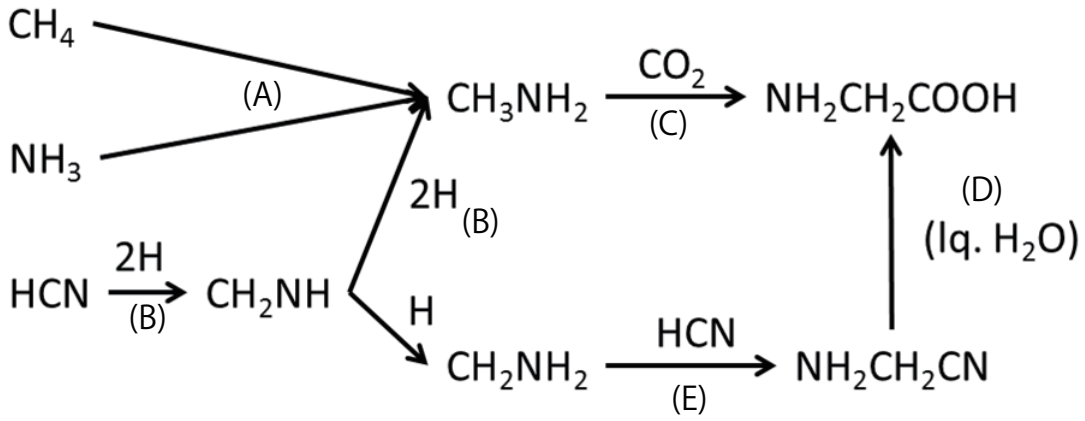

Fig. 1.— Assumed formation scenario to glycine. "lq" represents the hydrolysis process. References: (A)Kim & Kaiser (2011) (B)Theule et al. (2011) and Woon (2002) (C)Holtom et al. (2005) (D)Peltzer et al. (1984) (E) Danger et al. (2011)

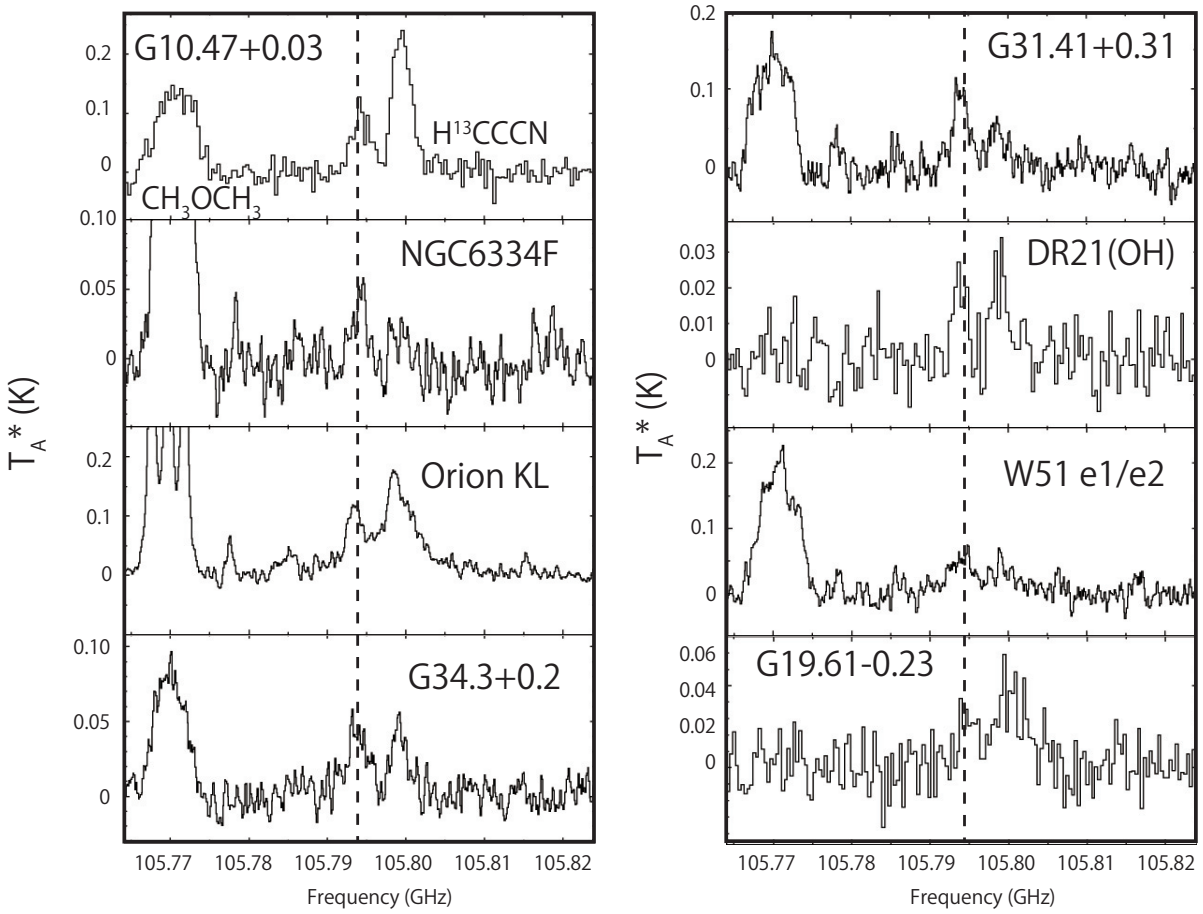

Fig. 2.— Observed CH_2NH 4_{04}-3_{13} transitions towards the detected sources. The vertical lines represent the rest frequency, 105.794062 GHz.

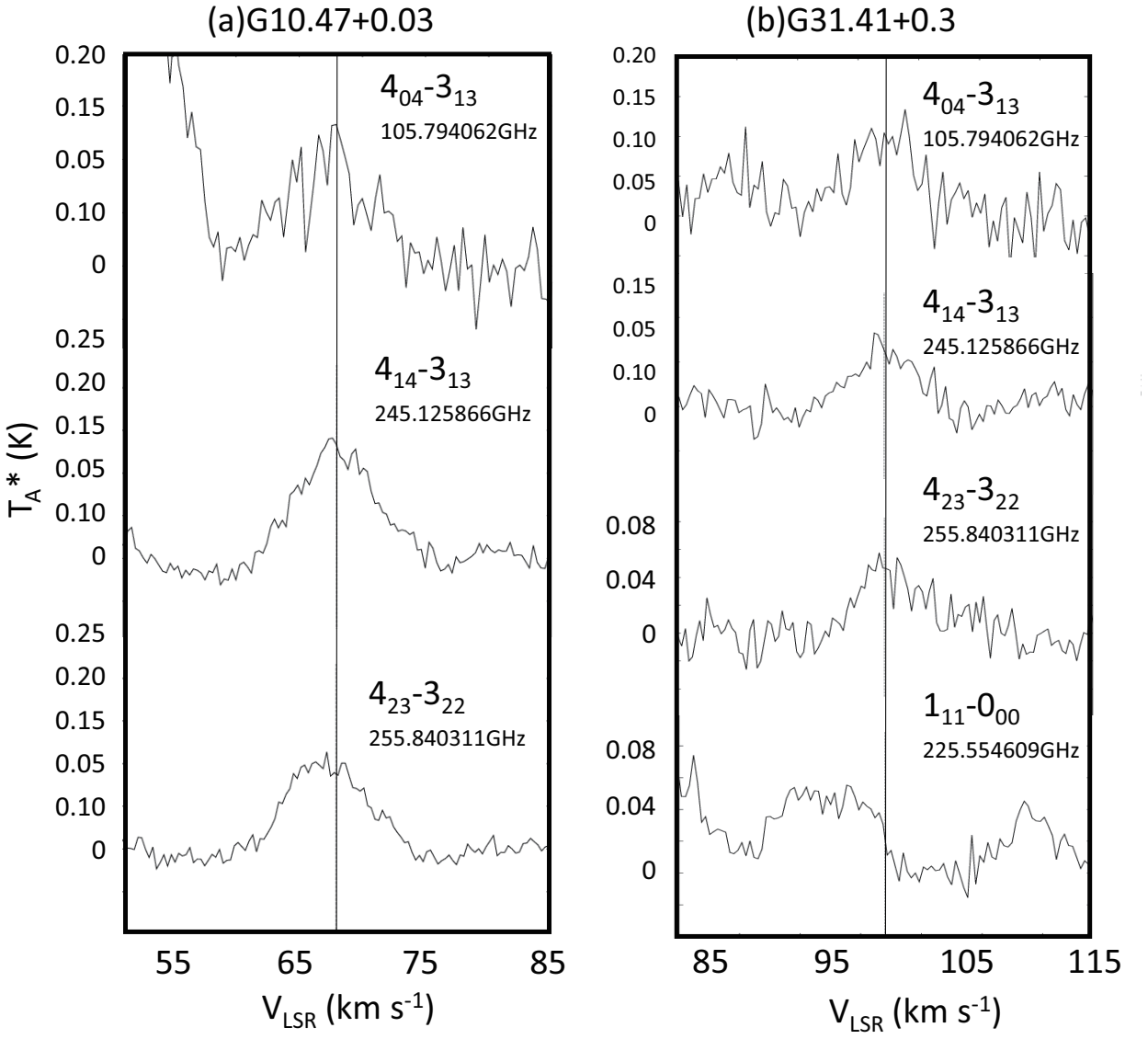

Fig. 3.— Comparison of radial velocities of CH_2NH lines observed with the NRO 45m telescope and the SMT telescope. The vertical solid lines represent the systematic radial velocities of individual sources, shown in Table 3.

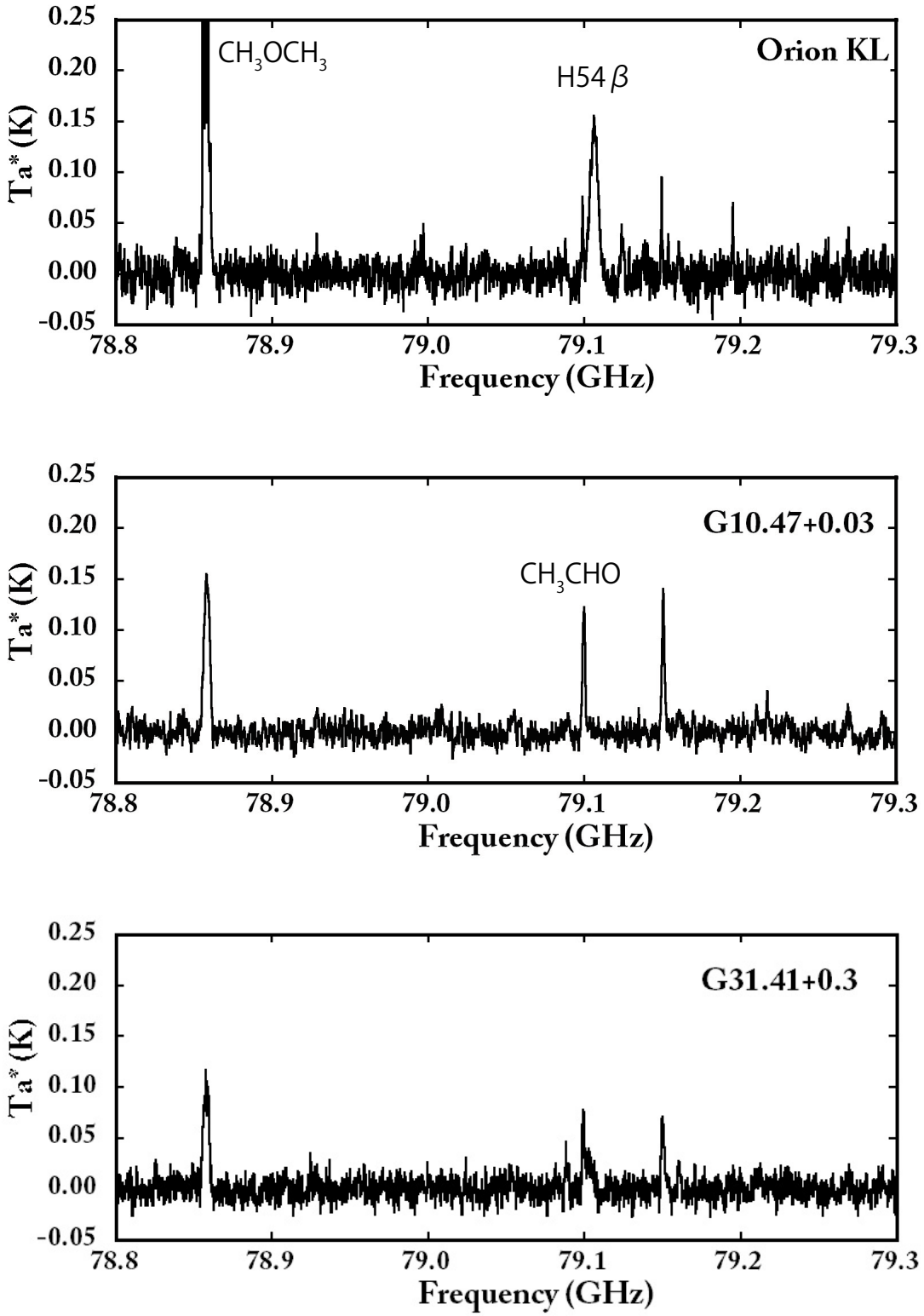

Fig. 4.— Observed Spectra. CH_3OCH_3 and CH_3CHO were detected.

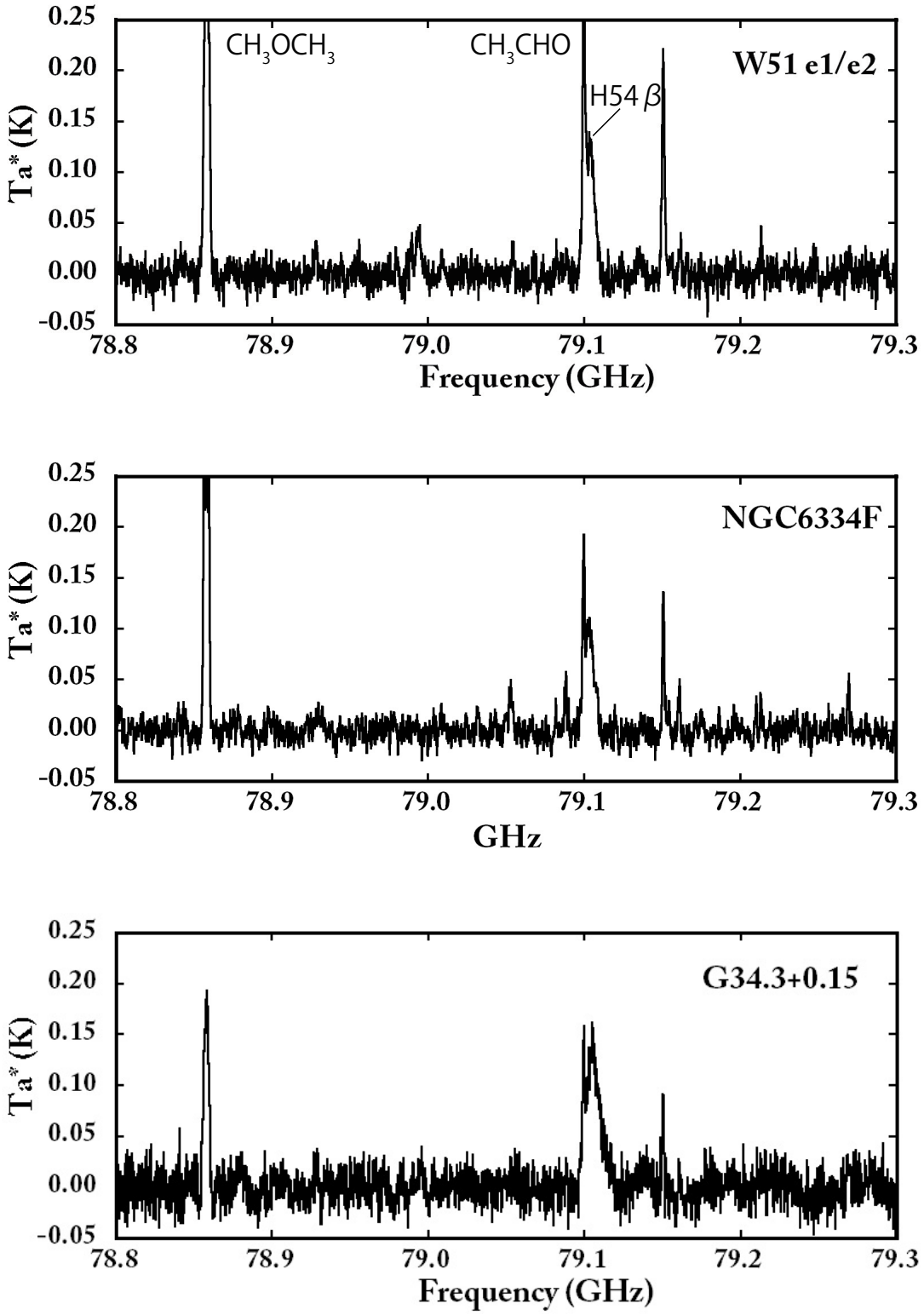

Fig. 4.— Observed Spectra. CH_3OCH_3 and CH_3CHO were detected.

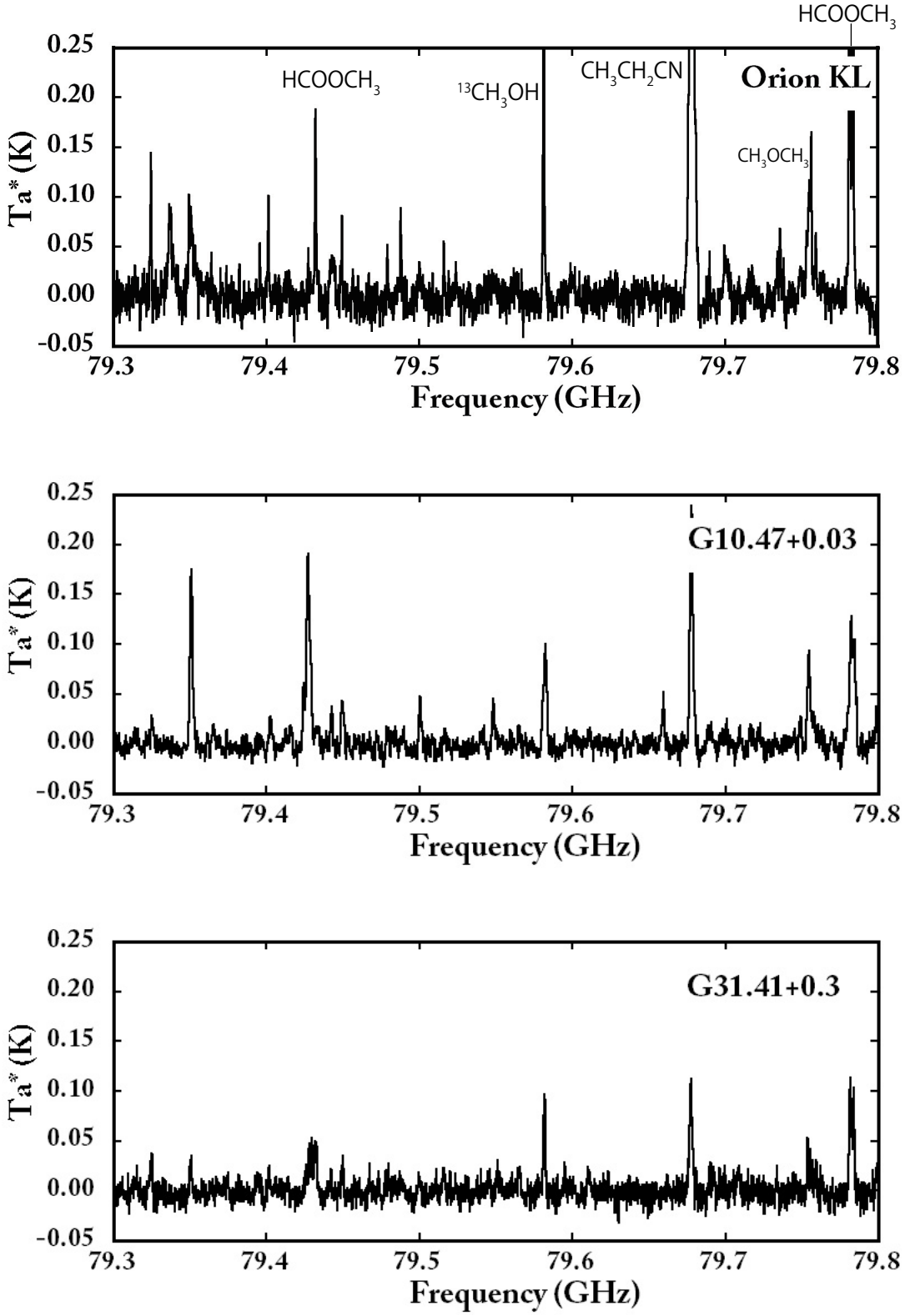

Fig. 4.— Observed Spectra. $HCOOCH_3$, CH_3CH_2CN, and CH_3OCH_3 were detected.

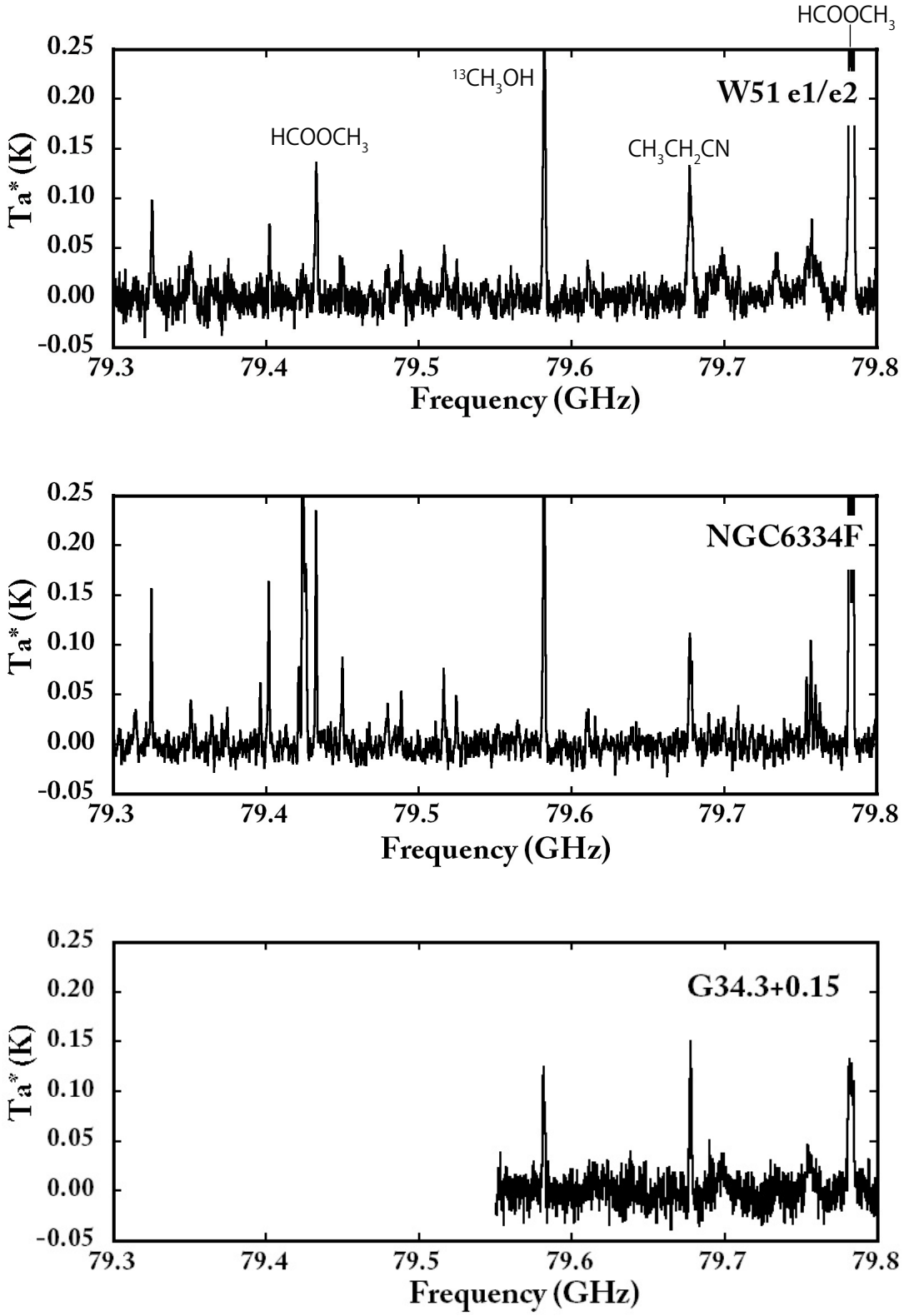

Fig. 4.— Observed Spectra. $HCOOCH_3$, CH_3CH_2CN, and CH_3OCH_3 were detected.

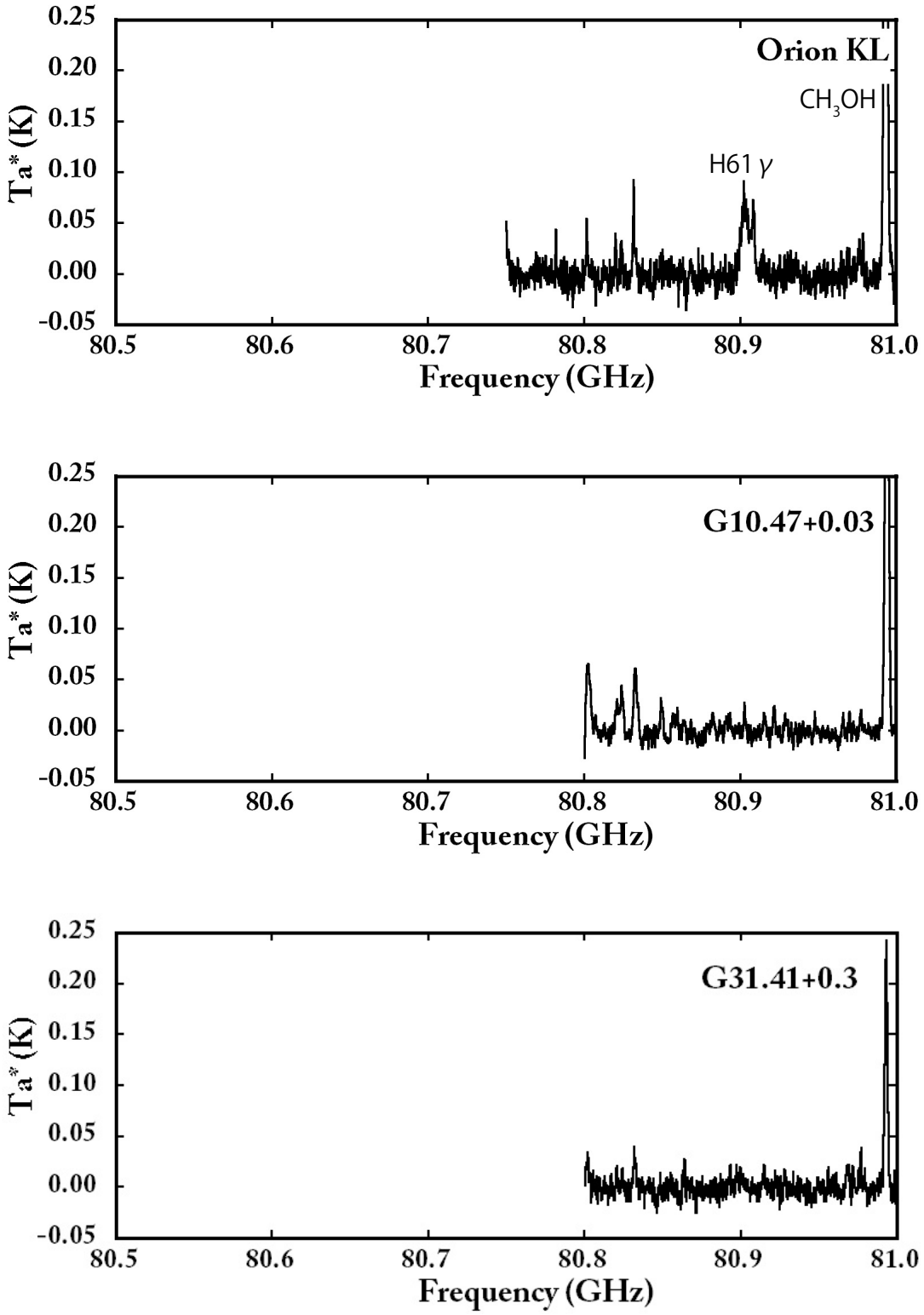

Fig. 4.— Observed Spectra. CH_3OH was detected.

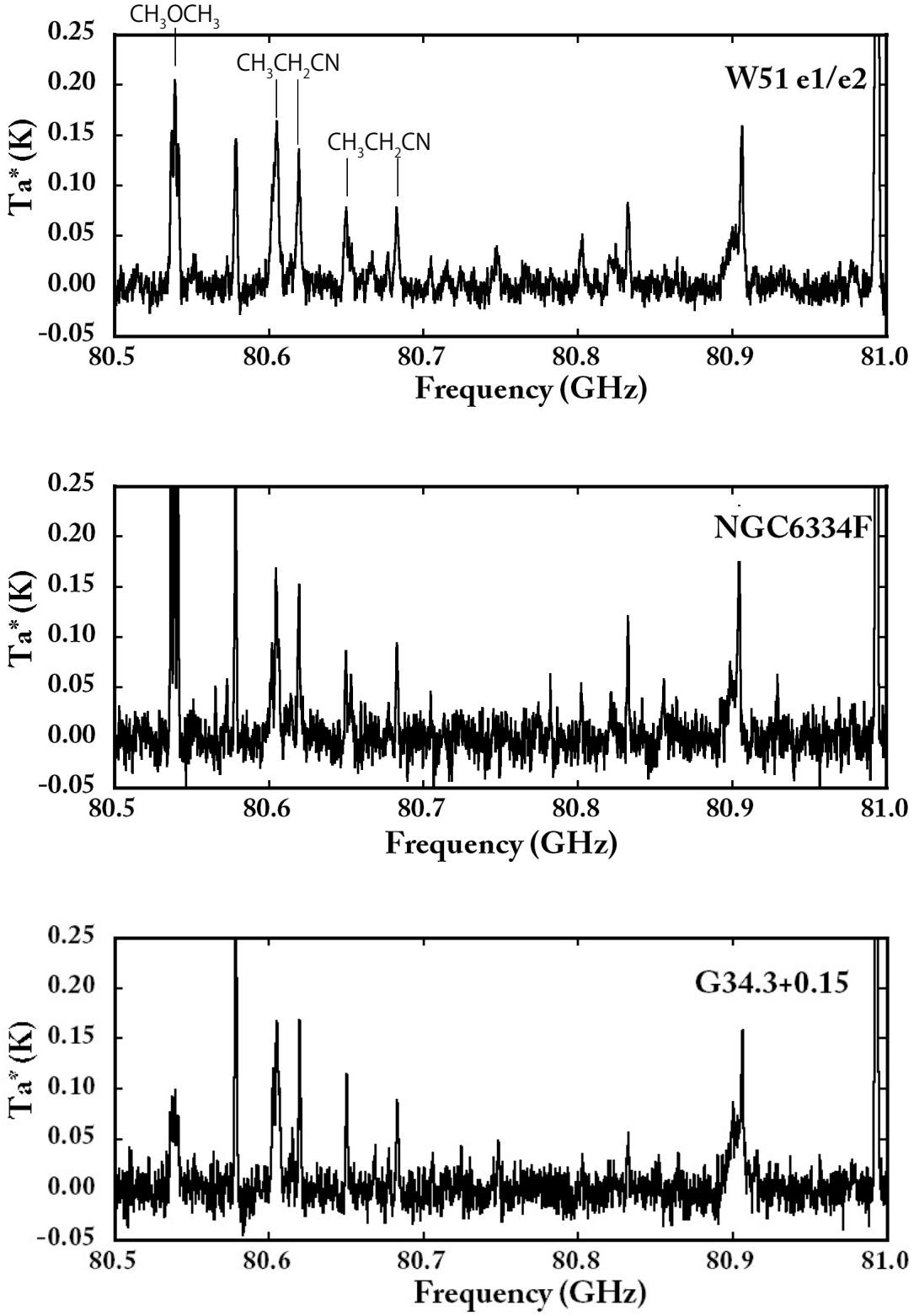

Fig. 4.— Observed Spectra. CH_3OCH_3, CH_3CH_2CN, and CH_3OH was detected.

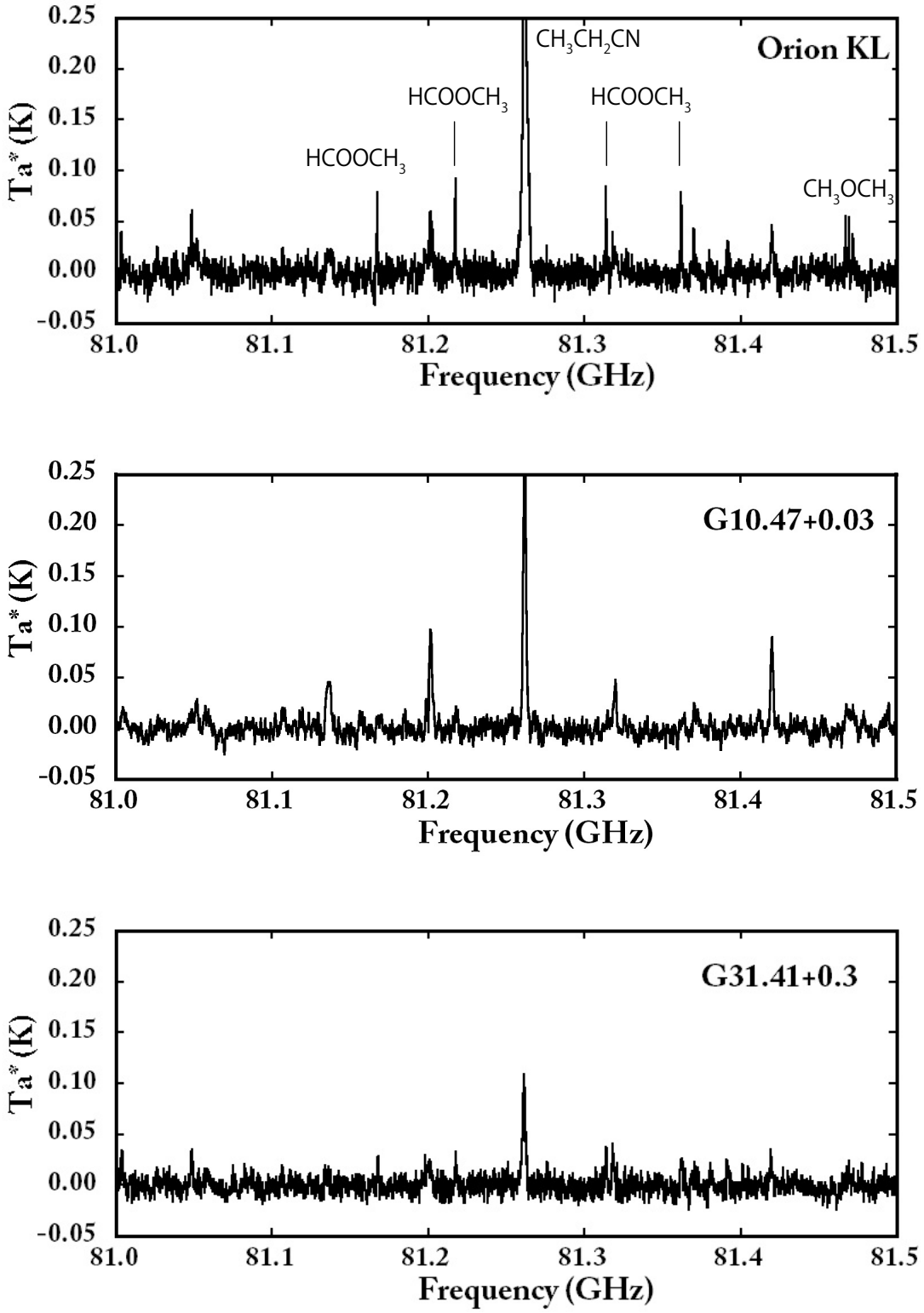

Fig. 4.— Observed Spectra. $HCOOCH_3$, CH_3CH_2CN, and CH_3OCH_3 were detected.

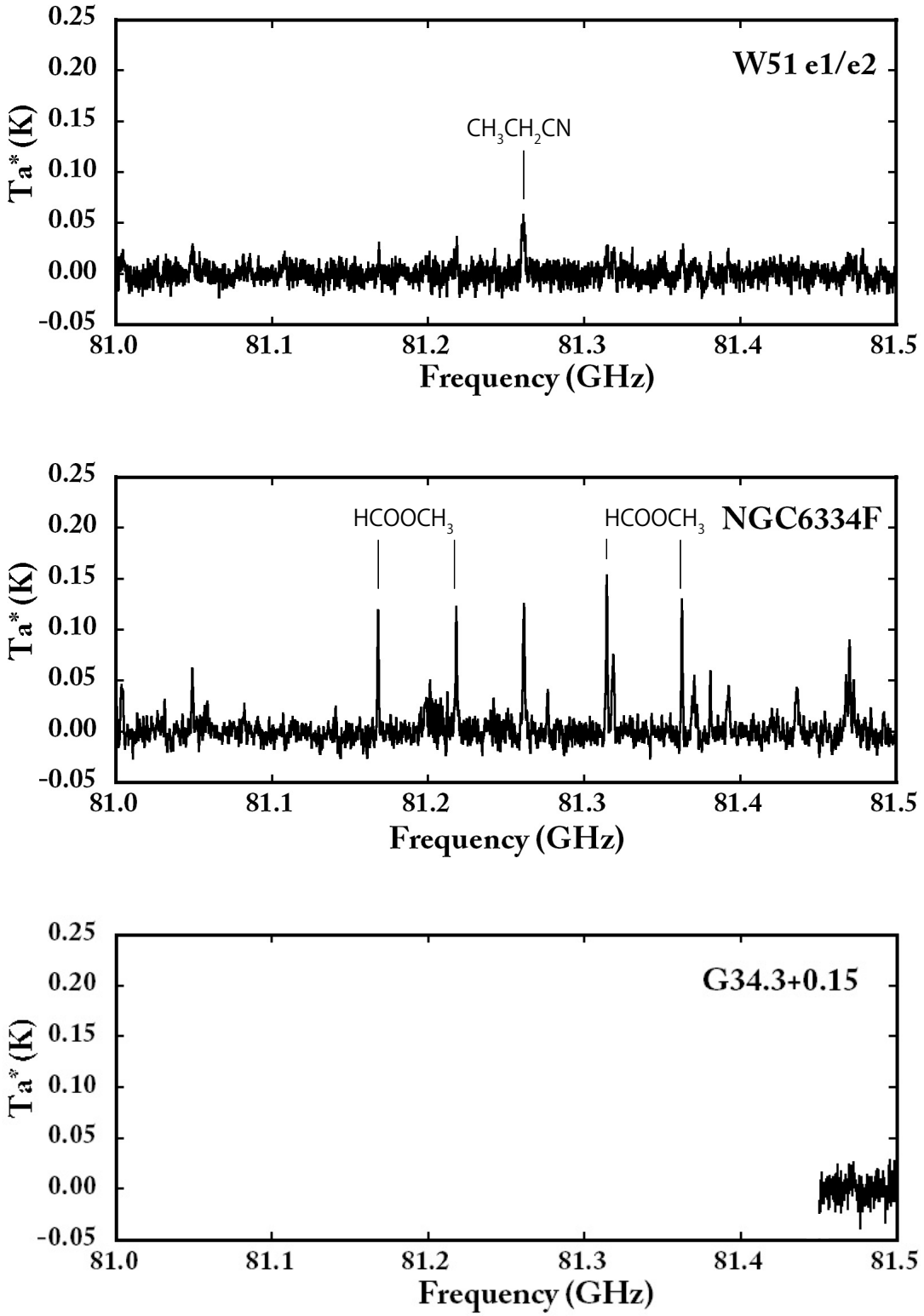

Fig. 4.— Observed Spectra.$HCOOCH_3$, CH_3CH_2CN, and CH_3OCH_3 were detected.

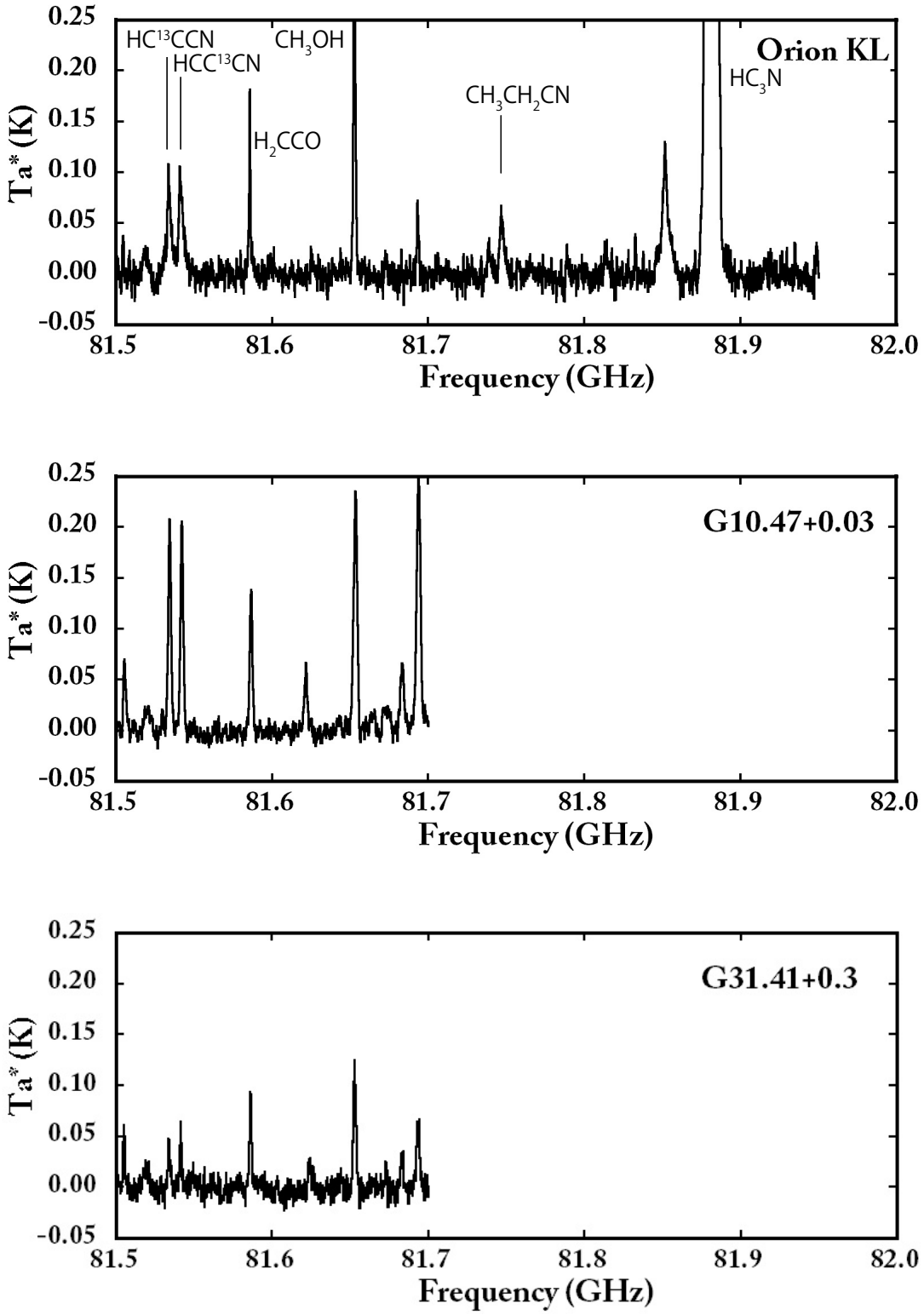

Fig. 4.— Observed Spectra. CH_3OH and CH_3CH_2CN were detected.

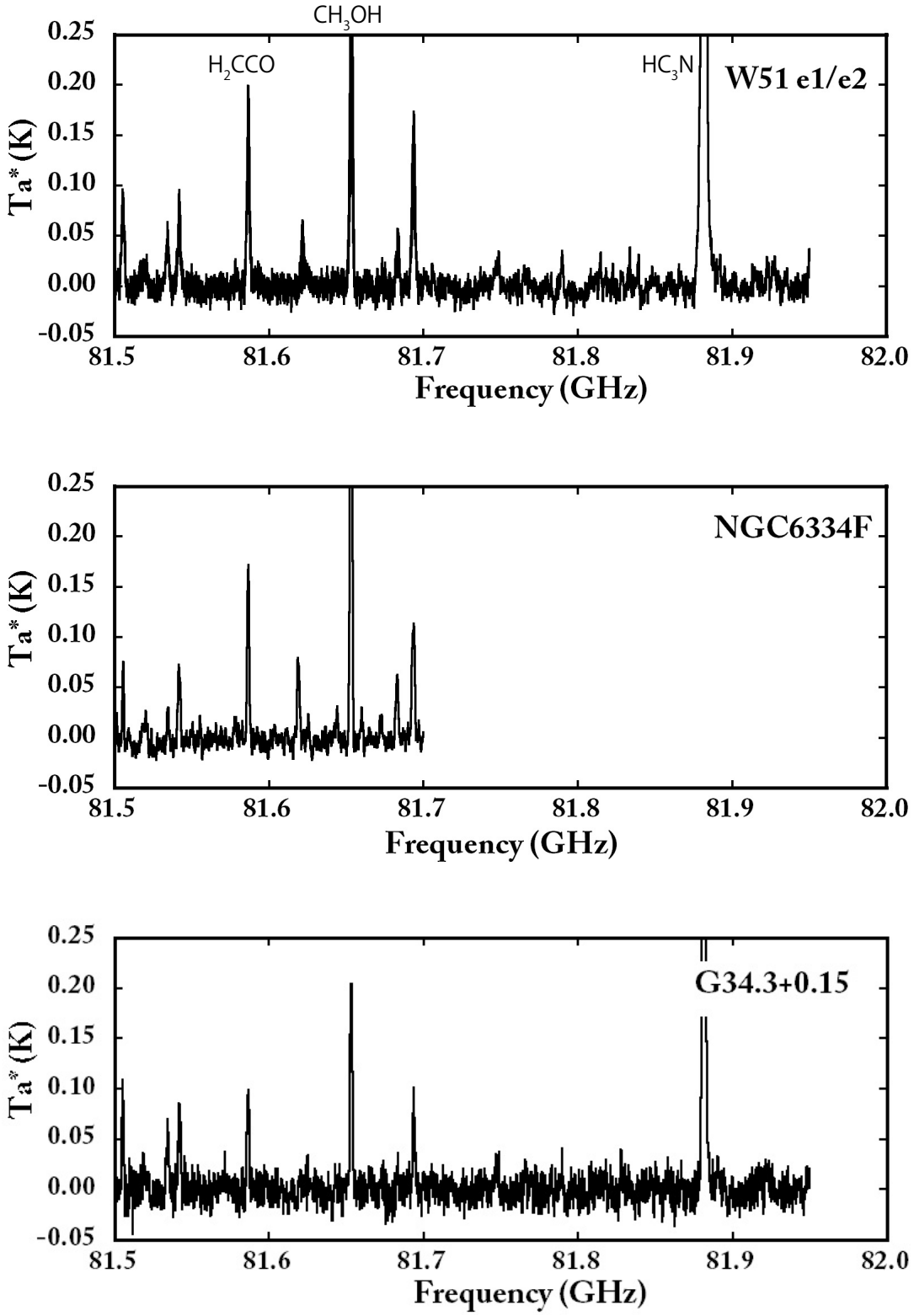

Fig. 4.— Observed Spectra. CH_3OH and CH_3CH_2CN were detected.

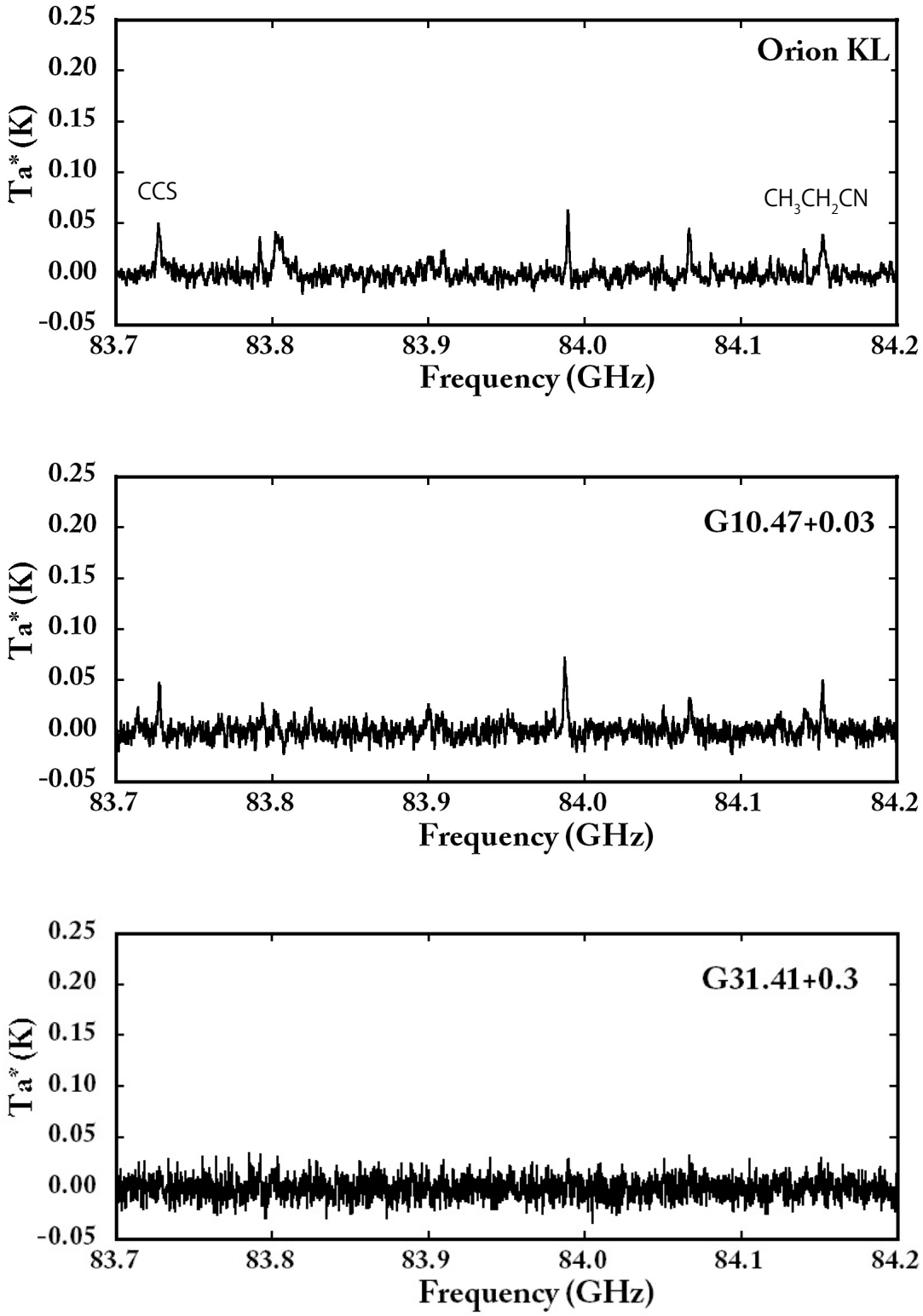

Fig. 4.— Observed Spectra. CH_3CH_2CN was detected.

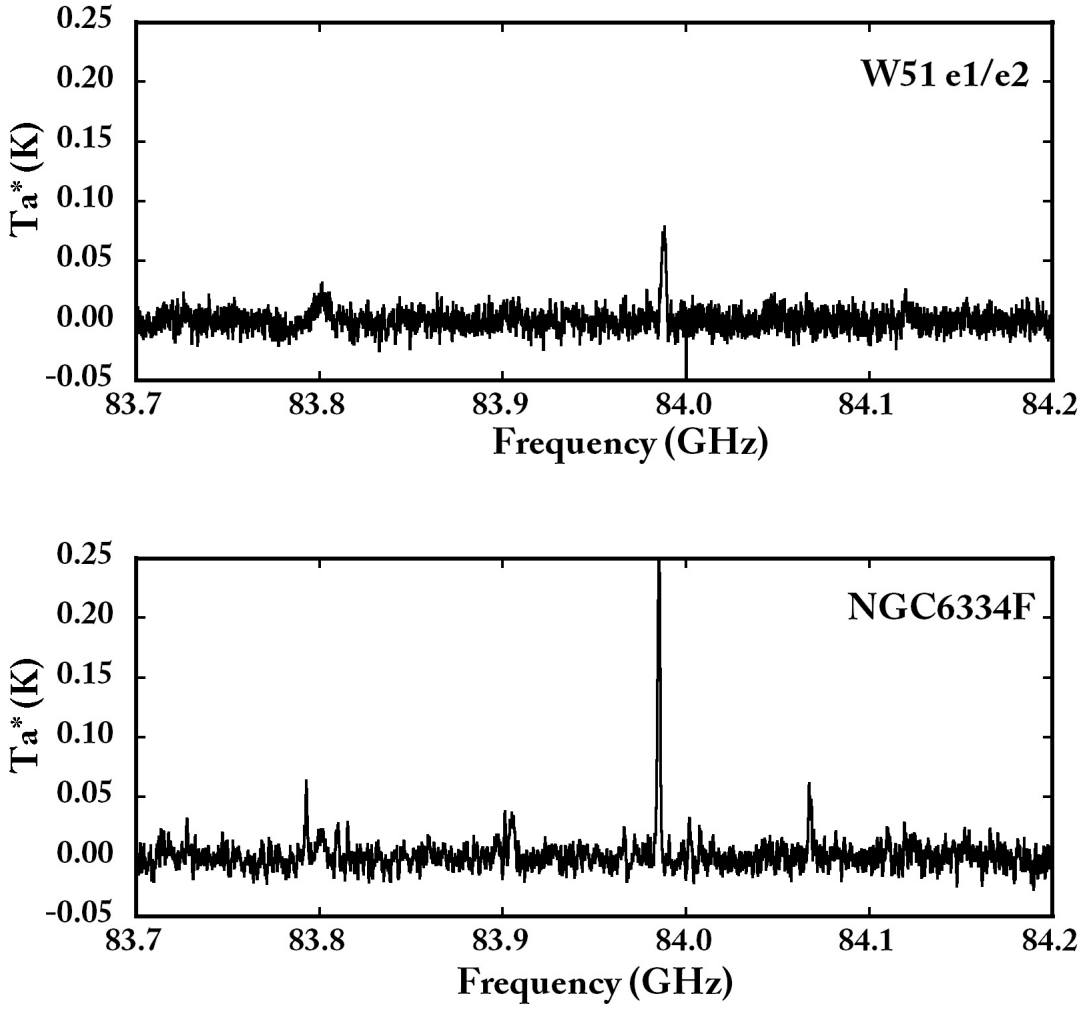

Fig. 4.— Observed Spectra.

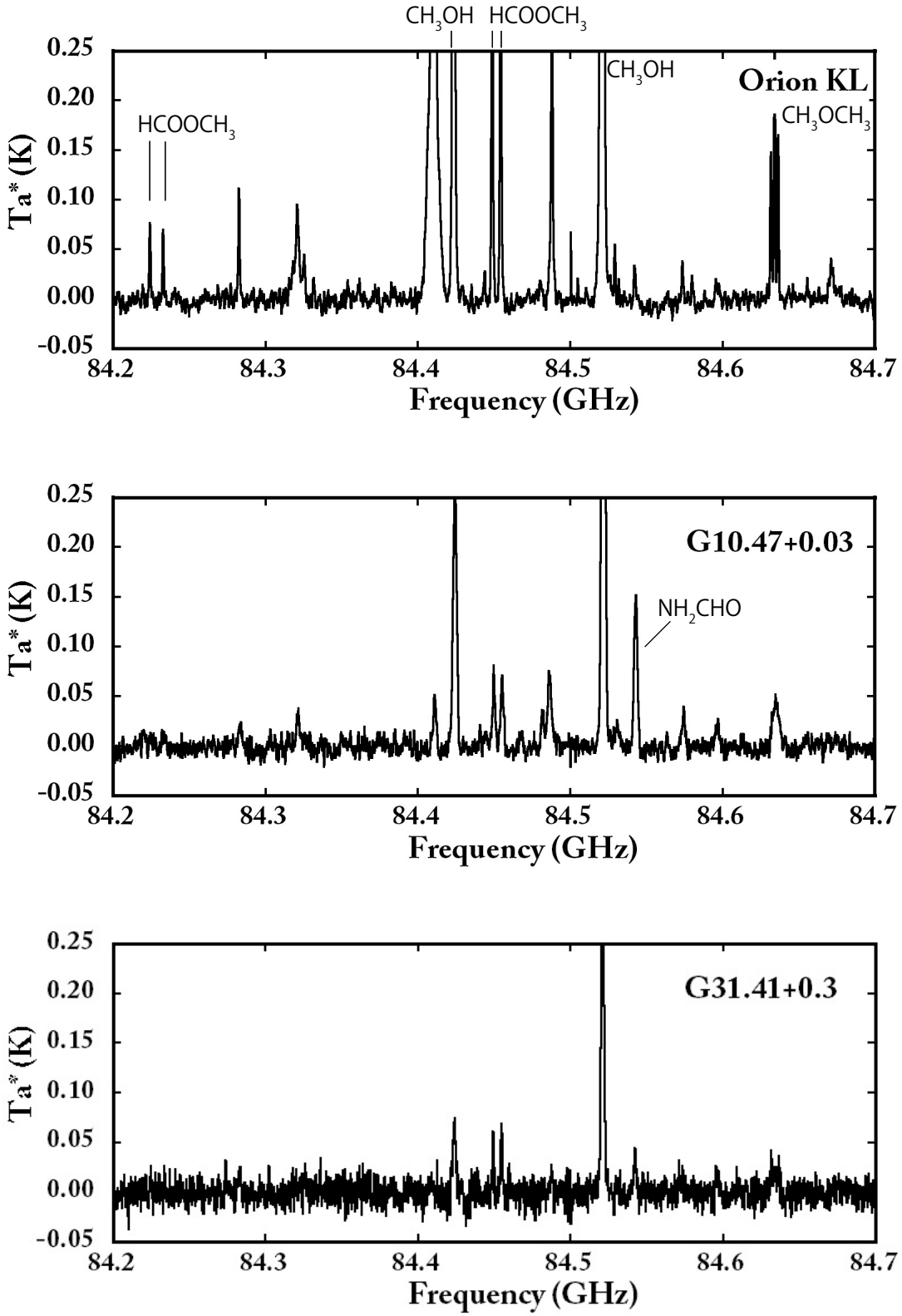

Fig. 4.— Observed Spectra. $HCOOCH_3$, CH_3OH, and CH_3OCH_3 were detected.

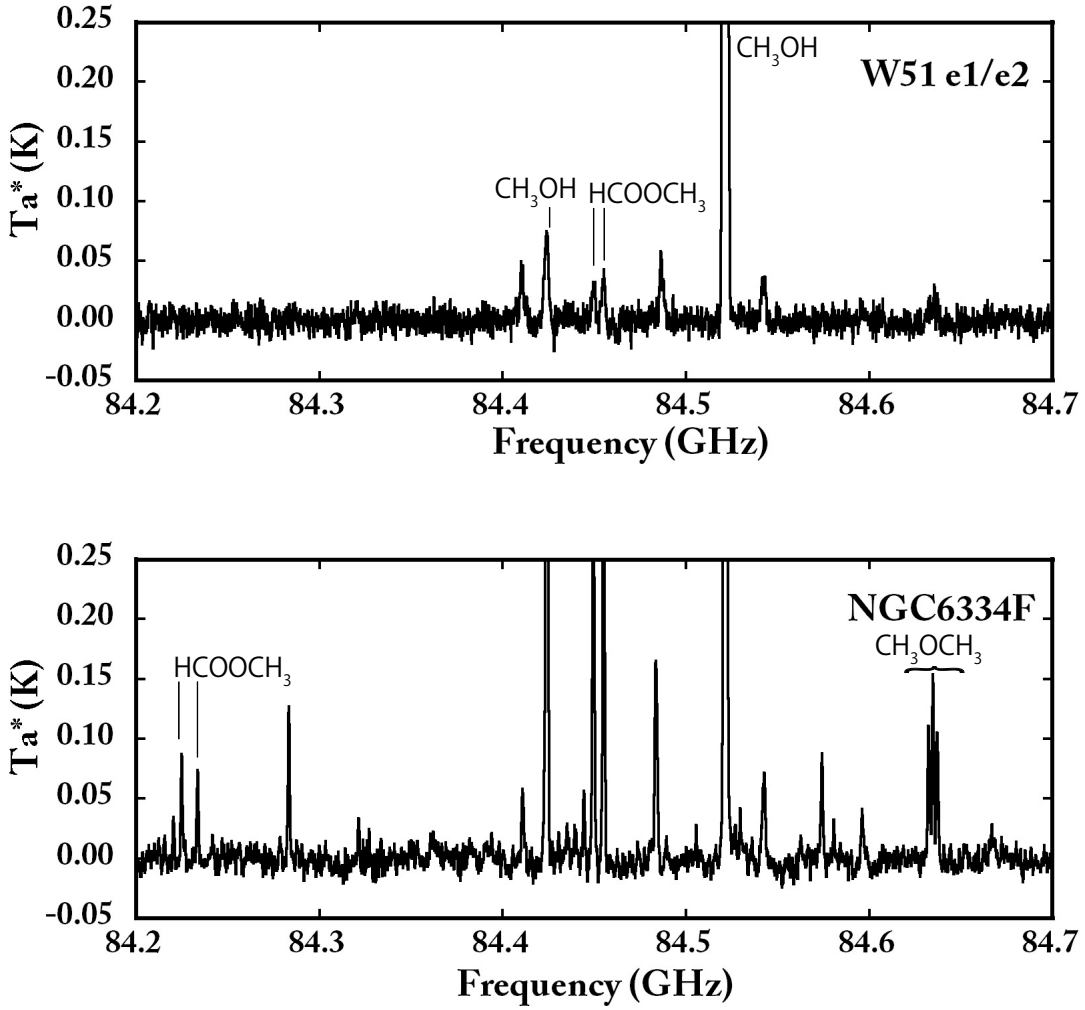

Fig. 4.— Observed Spectra. $HCOOCH_3$, CH_3OH, and CH_3OCH_3 were detected.

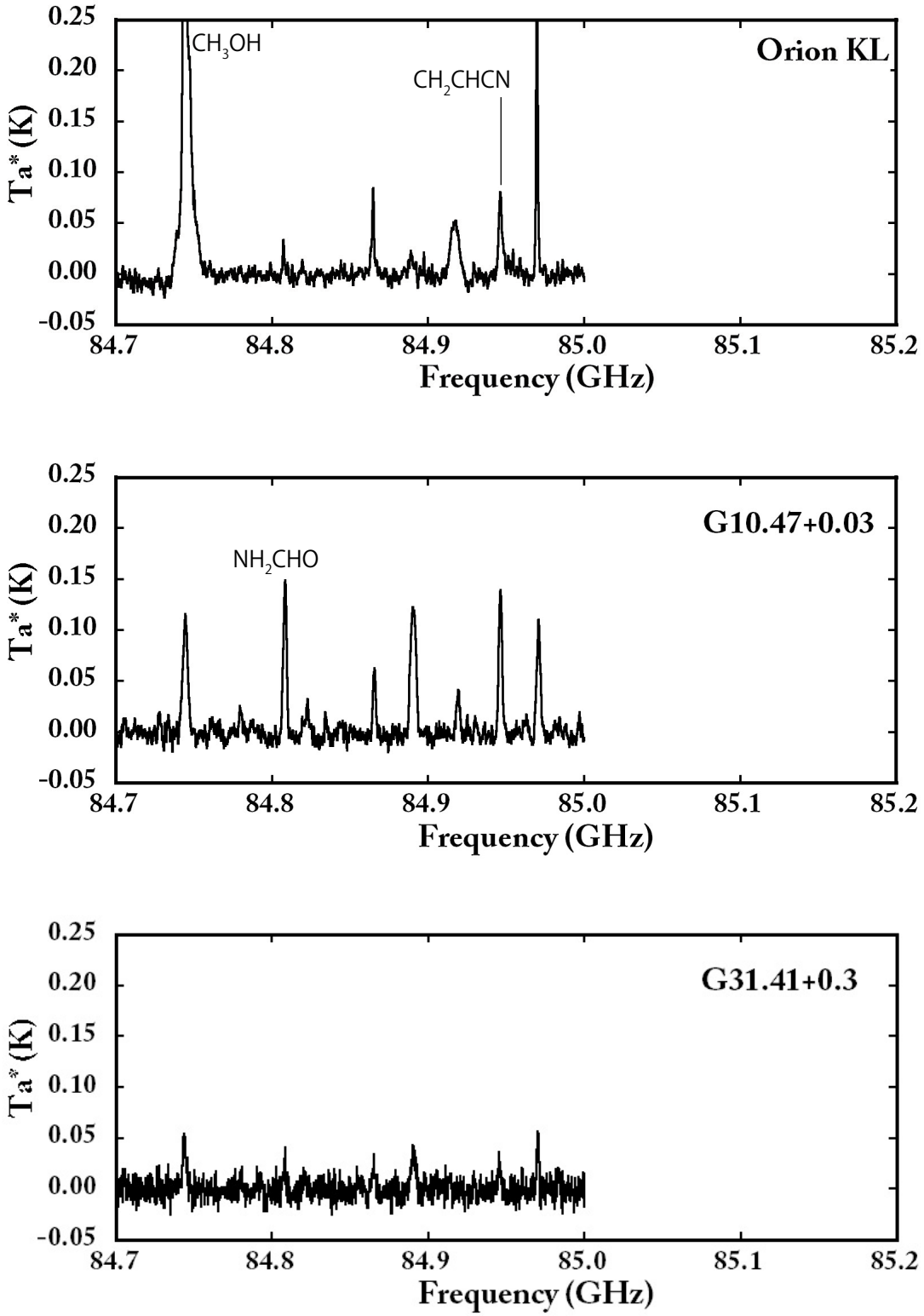

Fig. 4.— Observed Spectra. CH_3OH, NH_2CHO, and CH_2CHCN were detected.

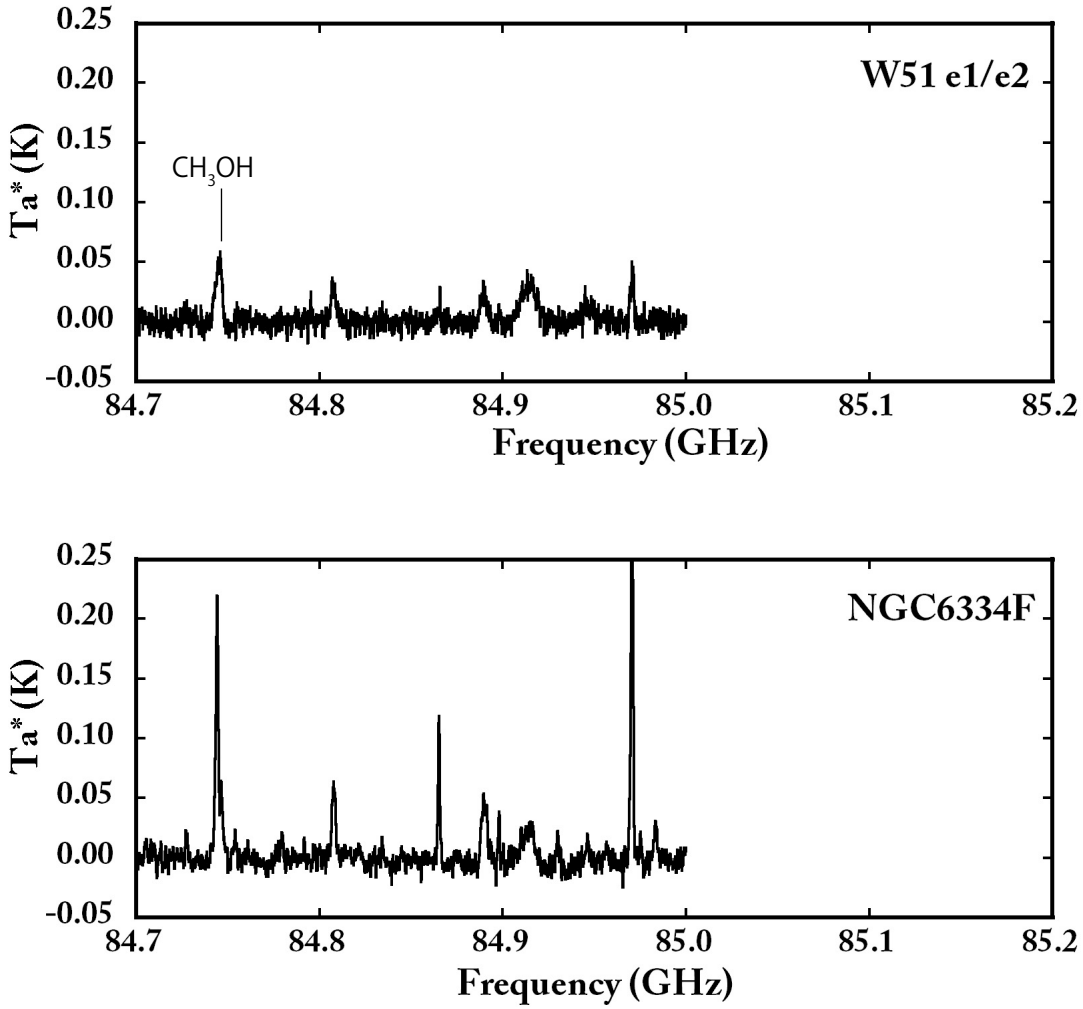

Fig. 4.— Observed Spectra.CH_3OH and NH_2CHO were detected.

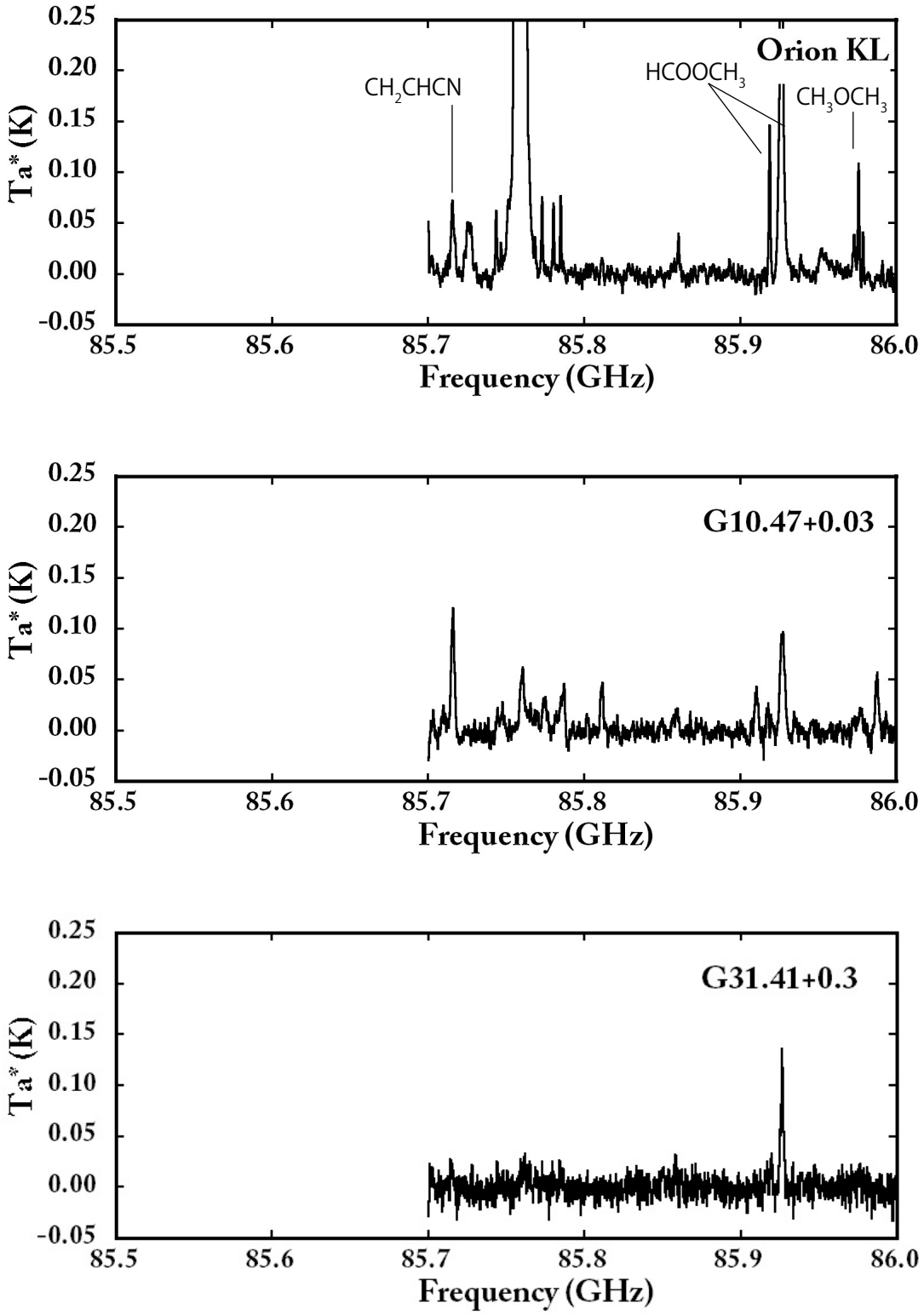

Fig. 4.— Observed Spectra. CH_2CHCN, $HCOOCH_3$, and CH_3OCH_3 were detected.

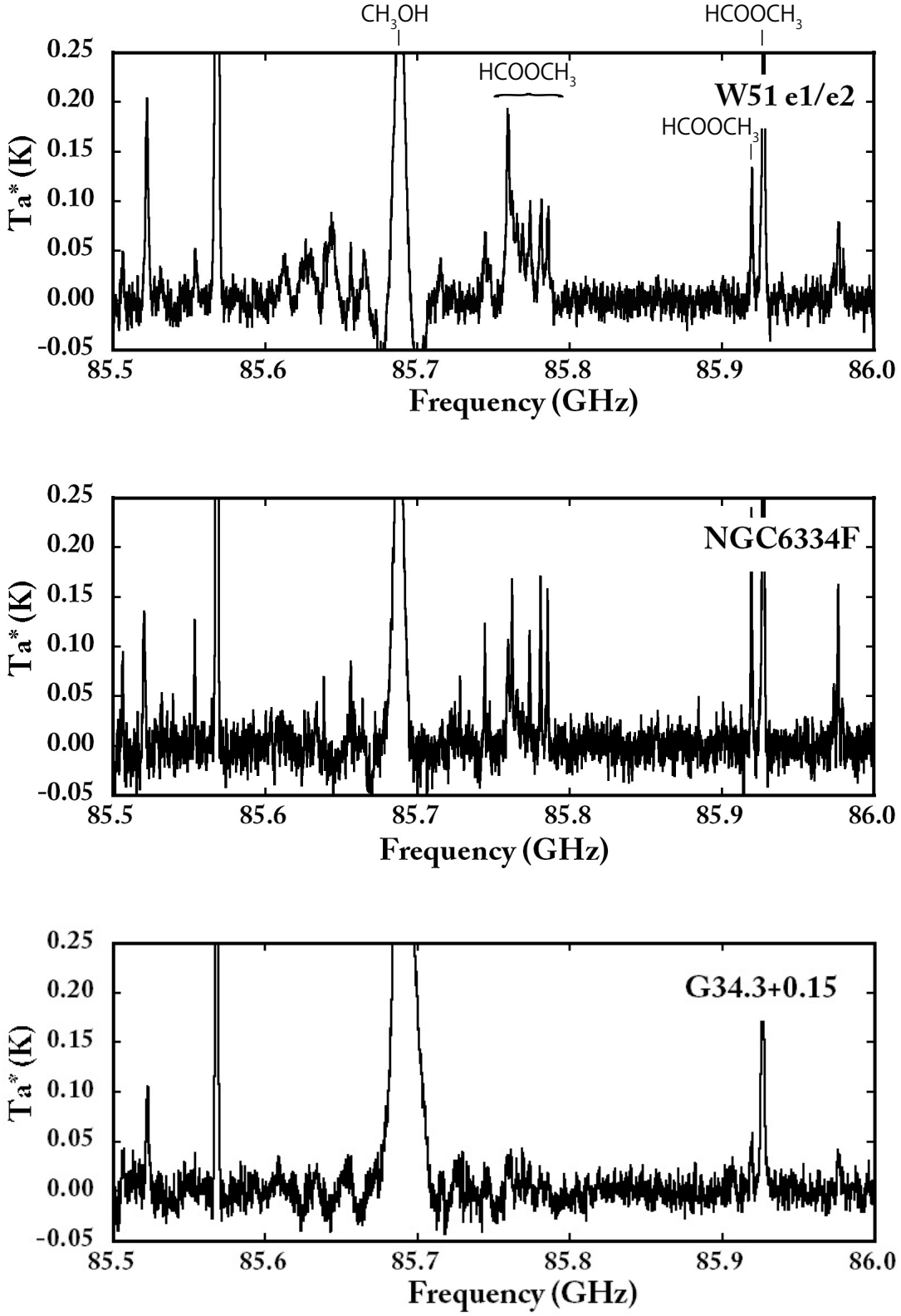

Fig. 4.— Observed Spectra. CH_3OH, $HCOOCH_3$, and CH_3OCH_3 were detected

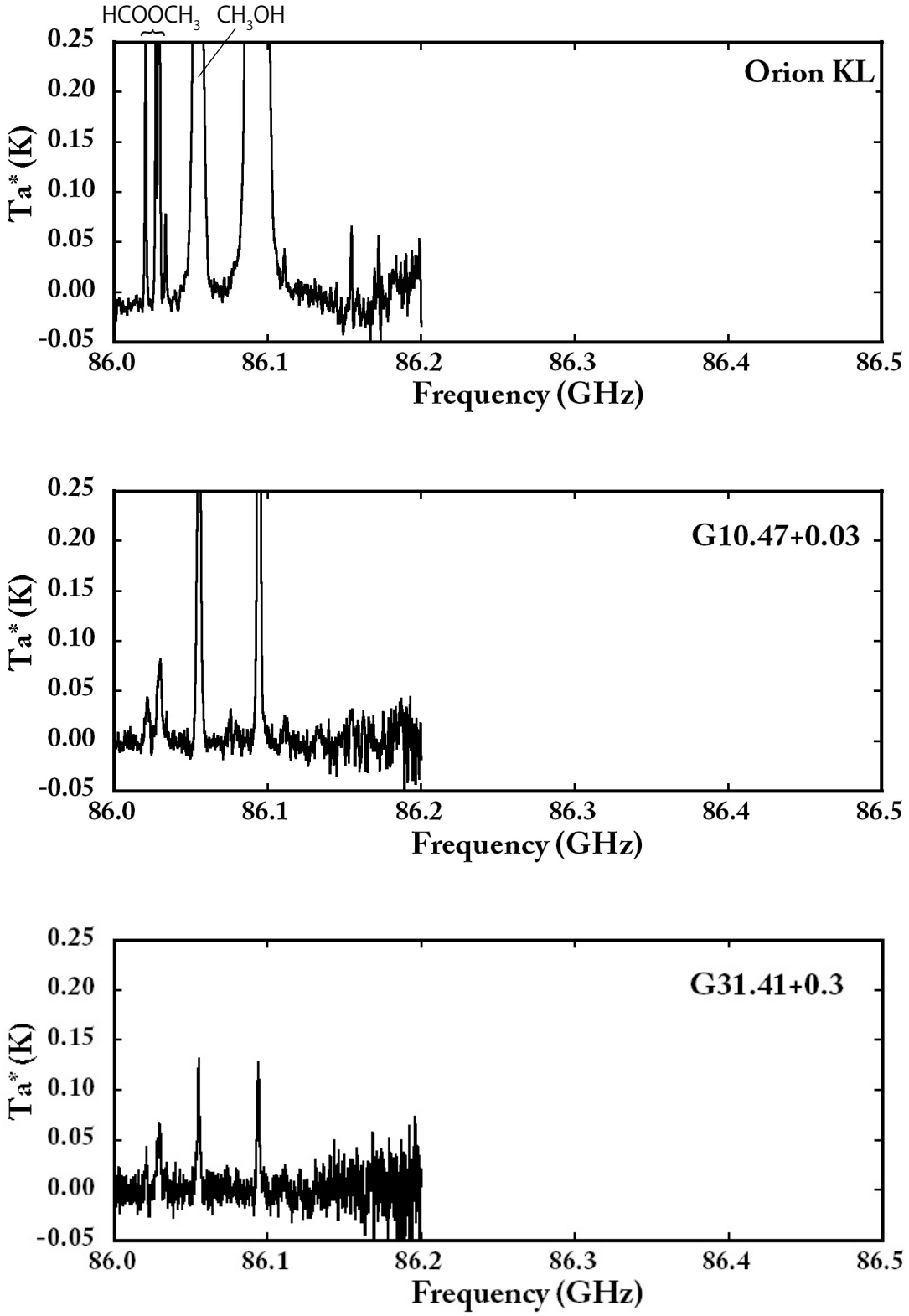

Fig. 4.— Observed Spectra. $HCOOCH_3$ and CH_3OH were detected.

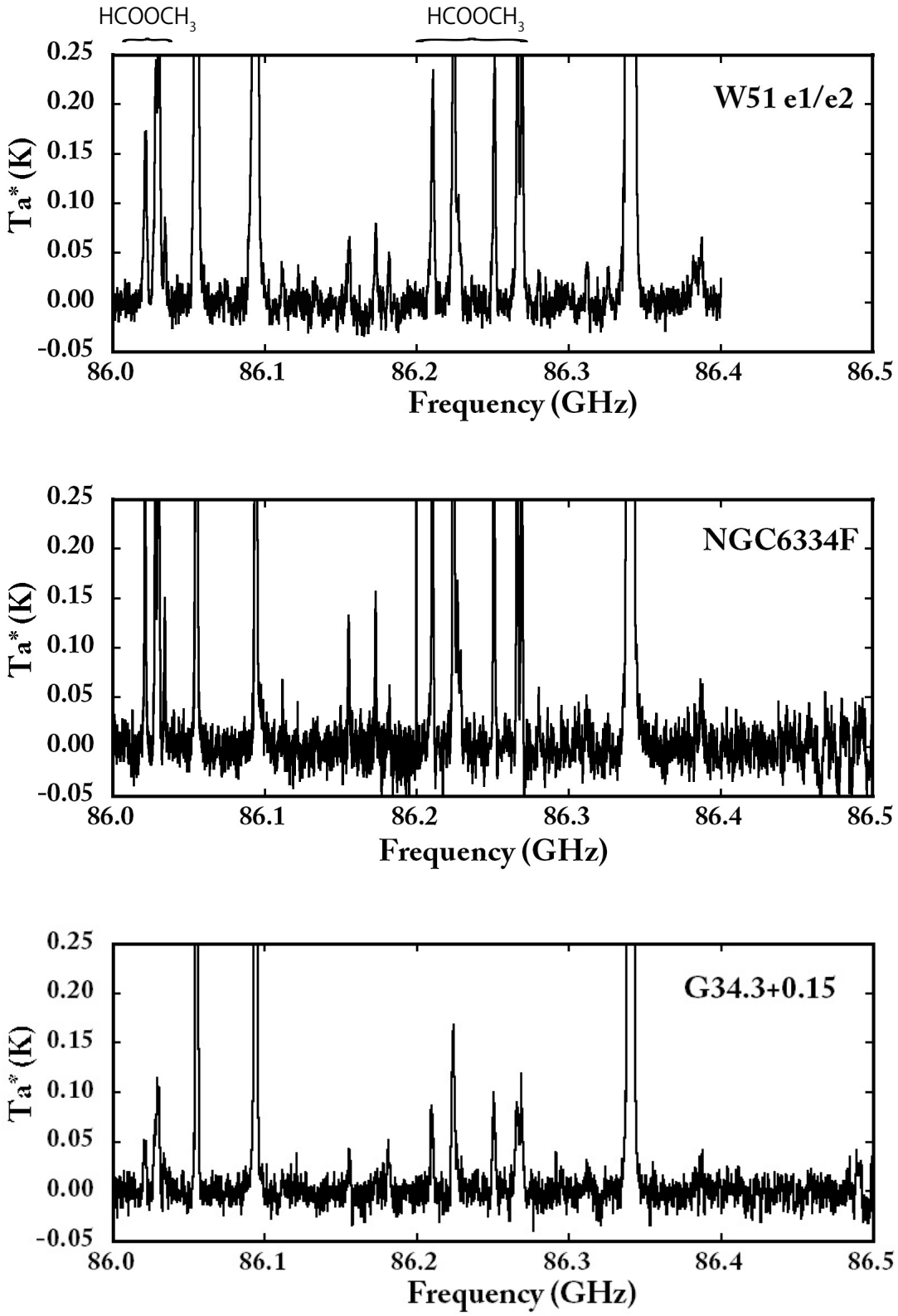

Fig. 4.— Observed Spectra. $HCOOCH_3$ and CH_3OH were detected.

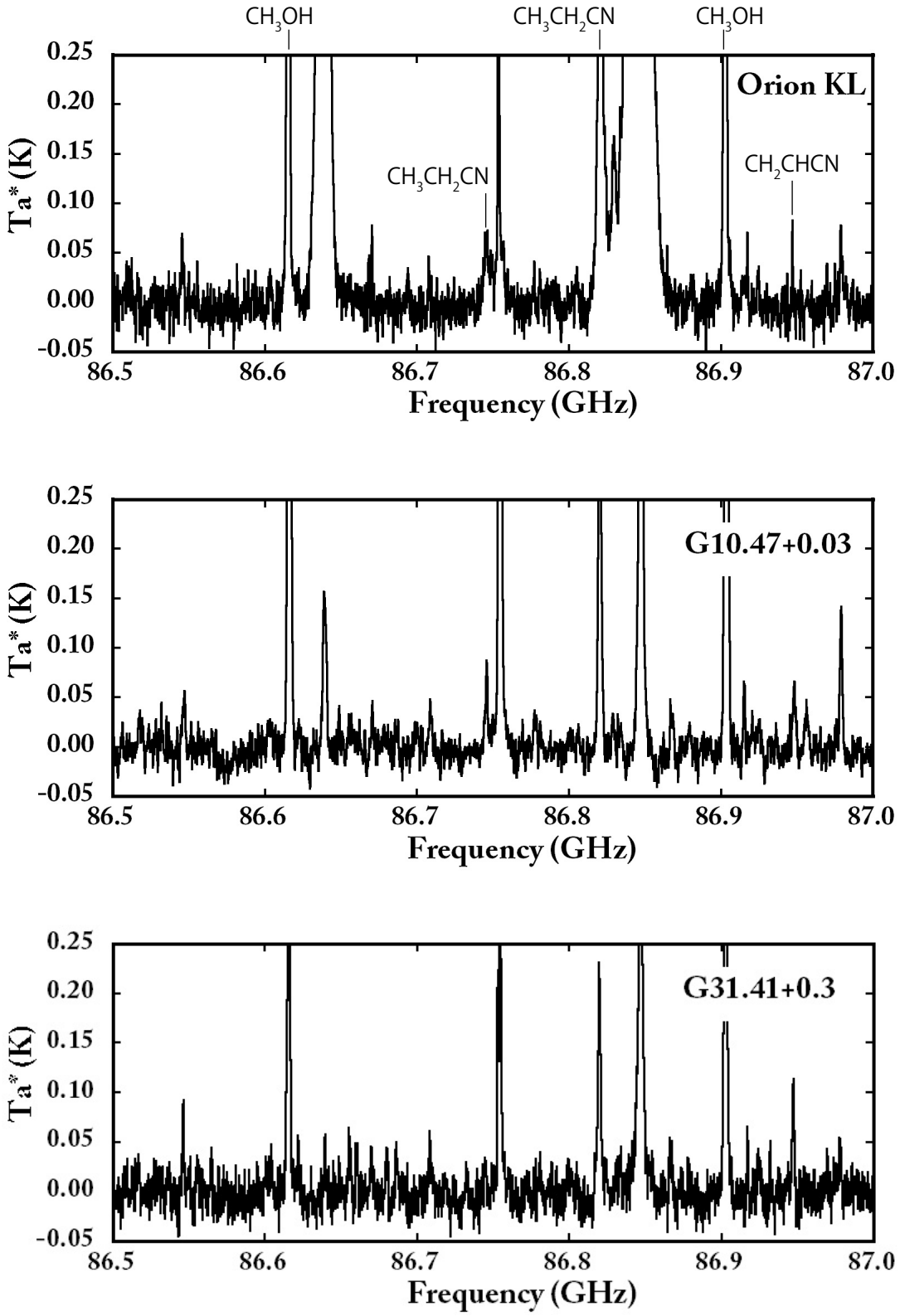

Fig. 4.— Observed Spectra. CH_3OH, CH_3CH_2CN and CH_2CHCN were detected.

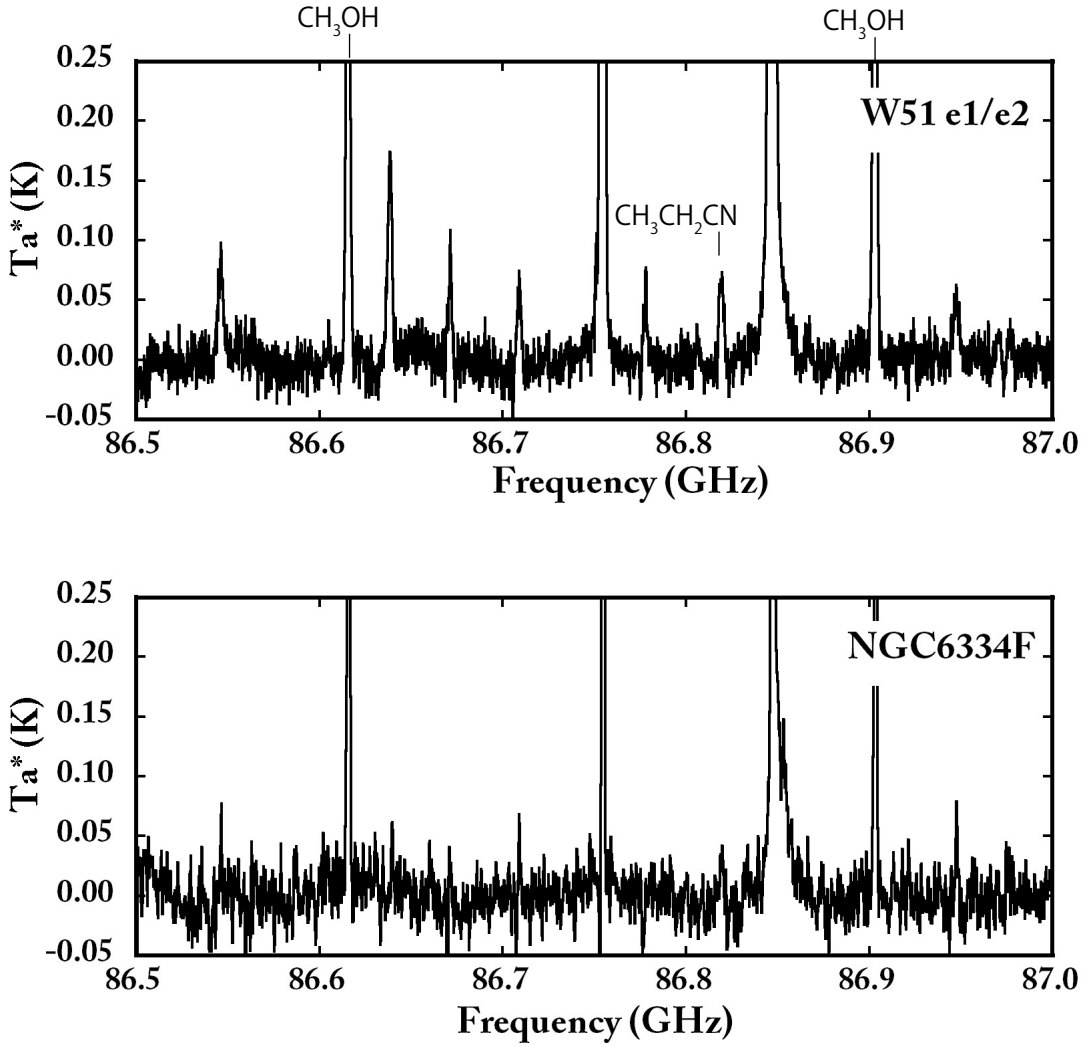

Fig. 4.— Observed Spectra. CH_3OH, CH_3CH_2CN and CH_2CHCN were detected.

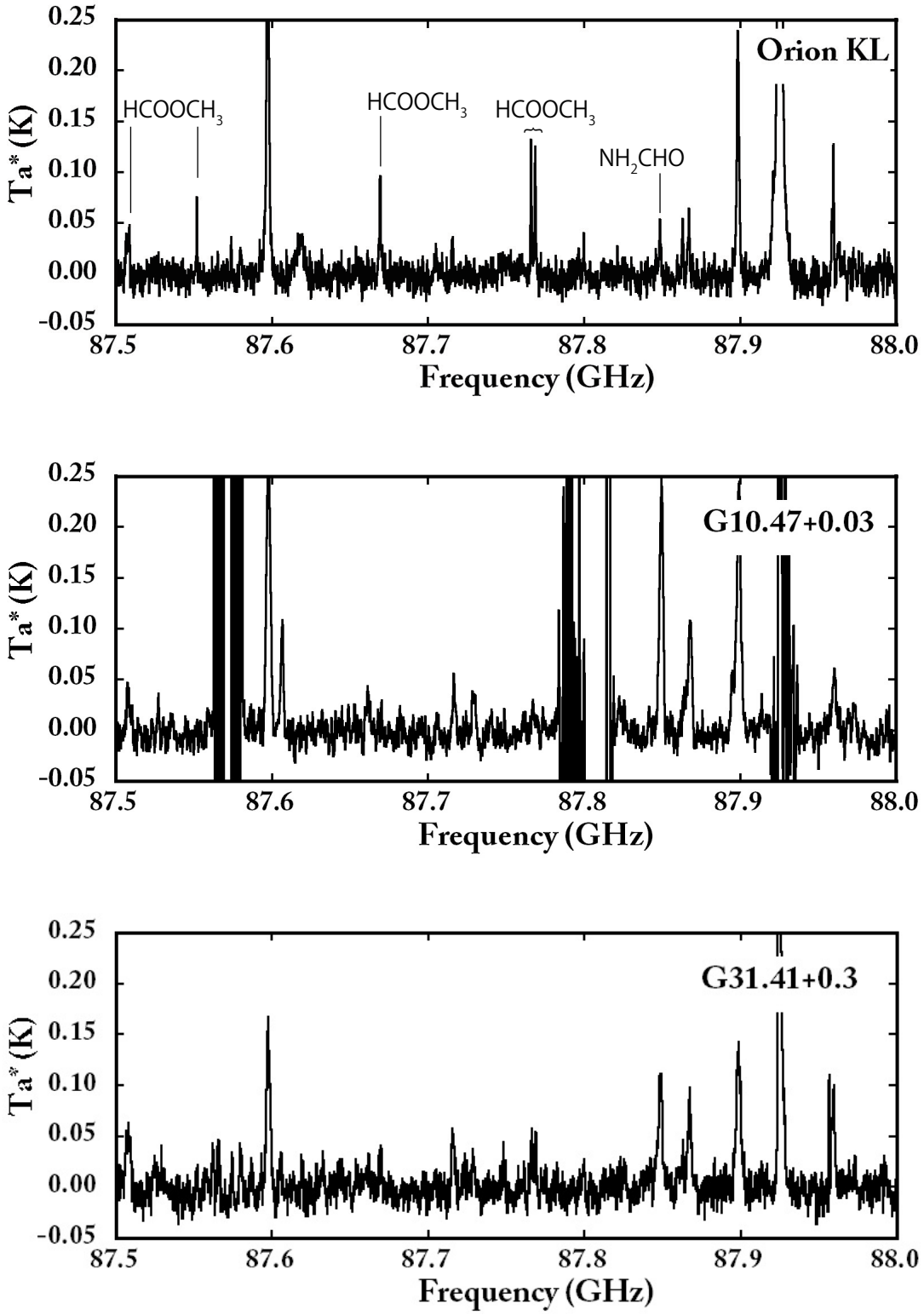

Fig. 4.— Observed Spectra. $HCOOCH_3$ and NH_2CHO were detected.

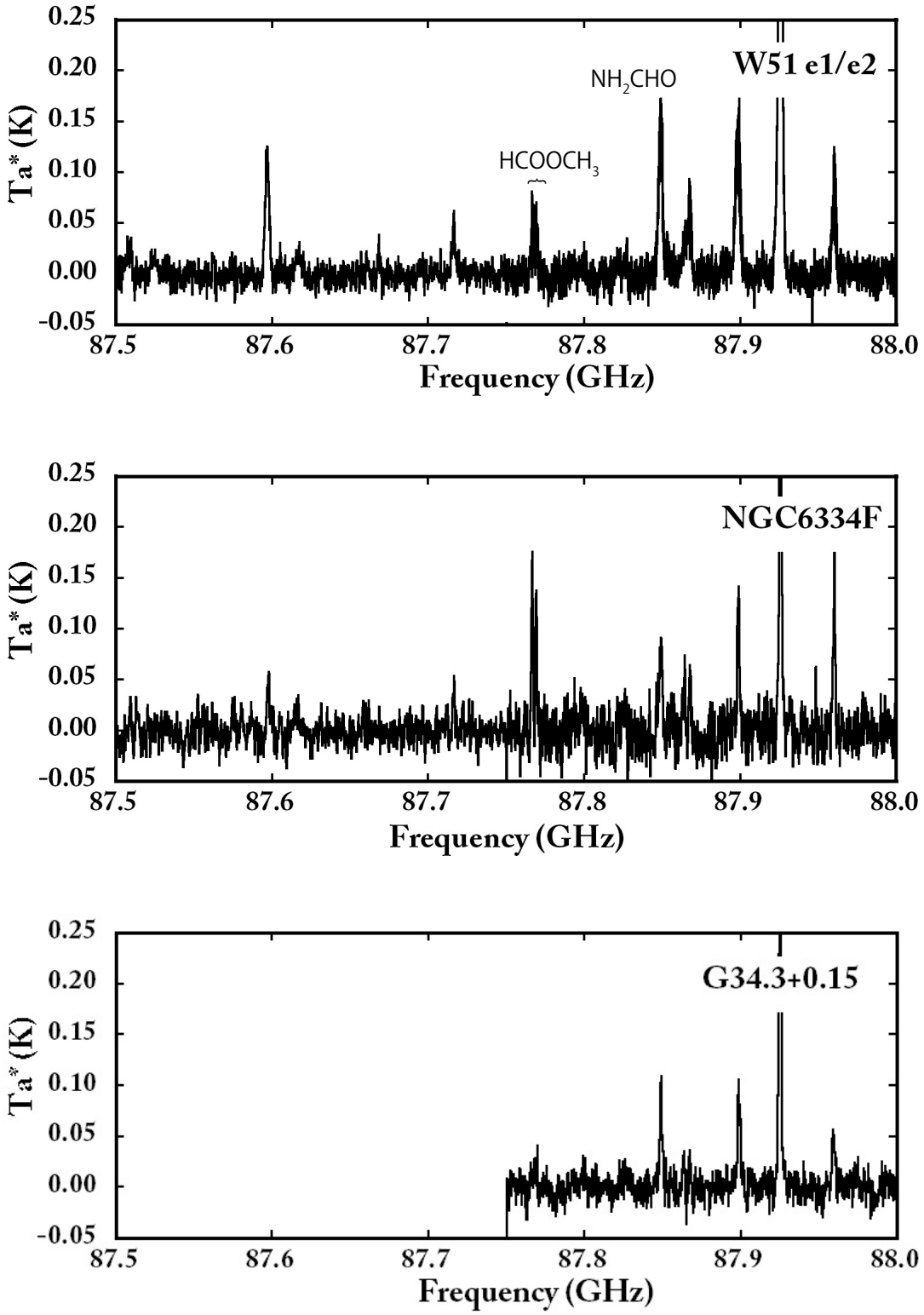

Fig. 4.— Observed Spectra. $HCOOCH_3$ and NH_2CHO were detected.

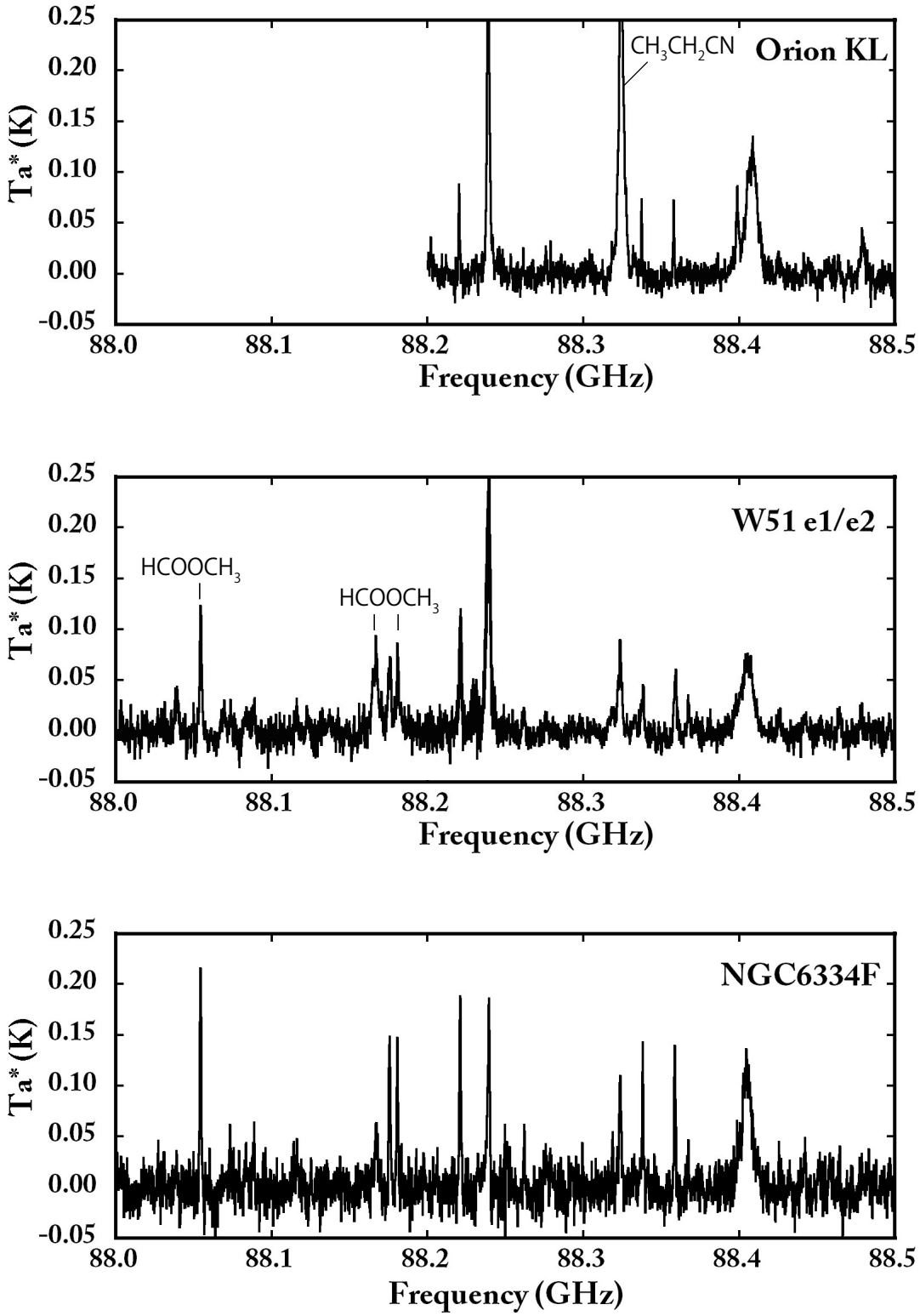

Fig. 4.— Observed Spectra. CH_3CH_2CN and $HCOOCH_3$ were detected.

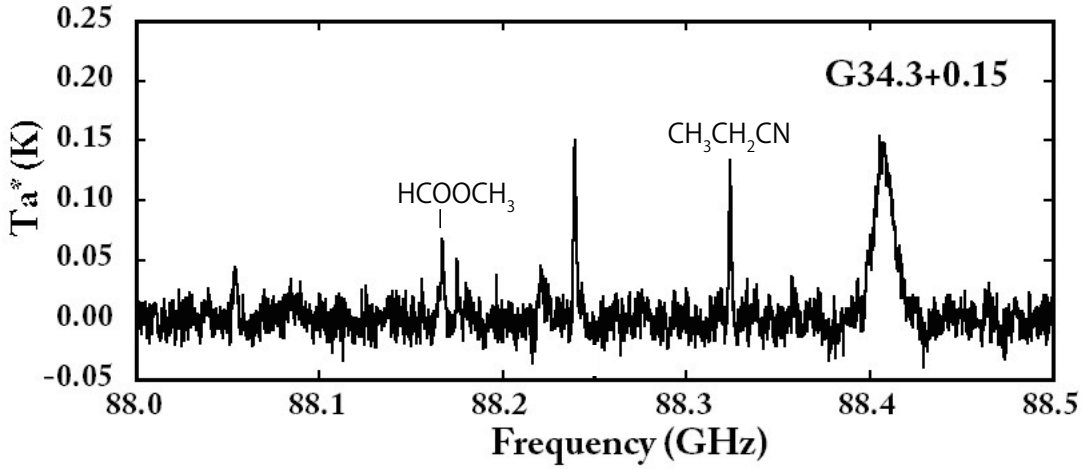

Fig. 4.— Observed Spectra. CH_3CH_2CN and $HCOOCH_3$ were detected.

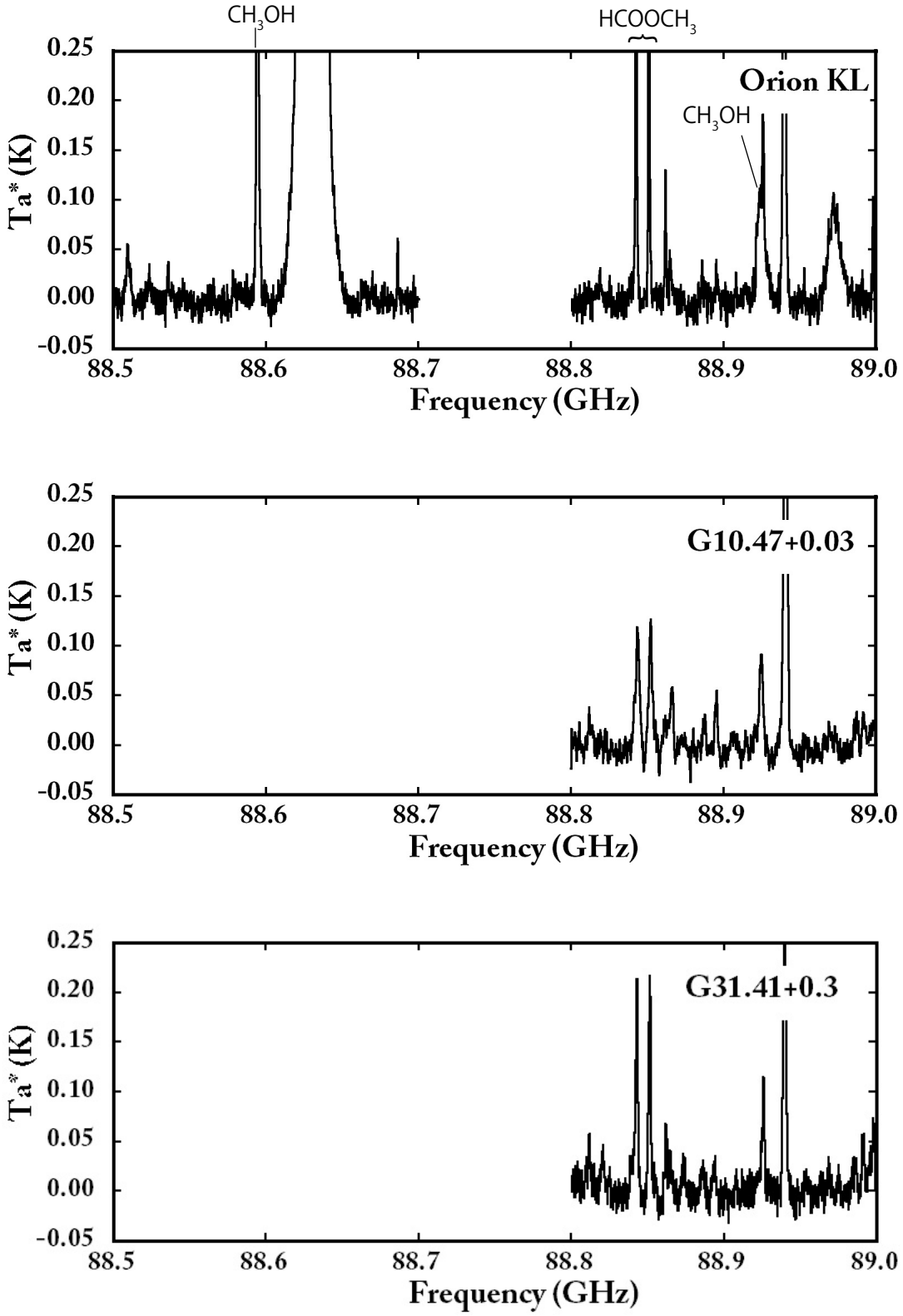

Fig. 4.— Observed Spectra. CH_3OH and $HCOOCH_3$ were detected.

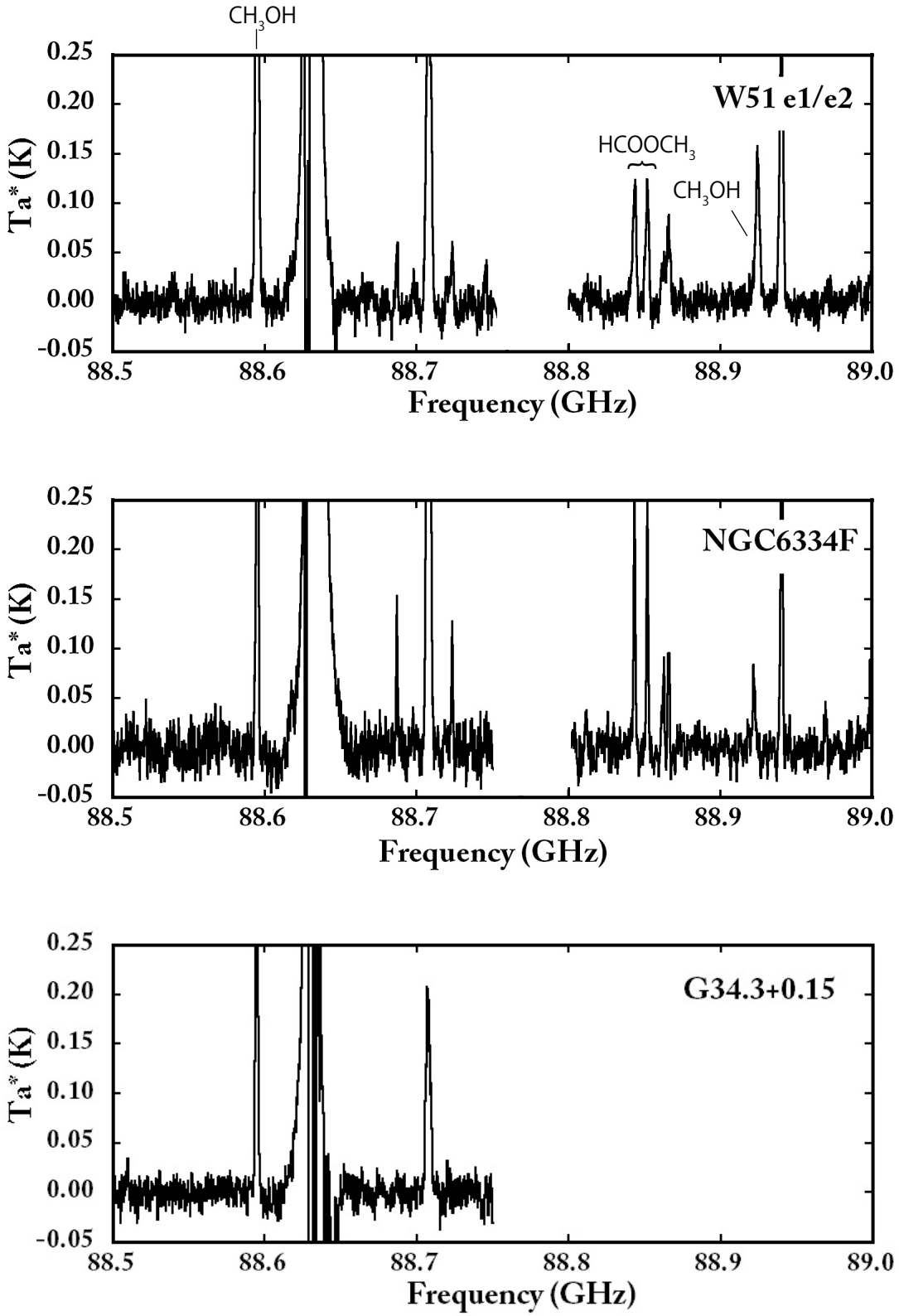

Fig. 4.— Observed Spectra. CH_3OH and $HCOOCH_3$ were detected.

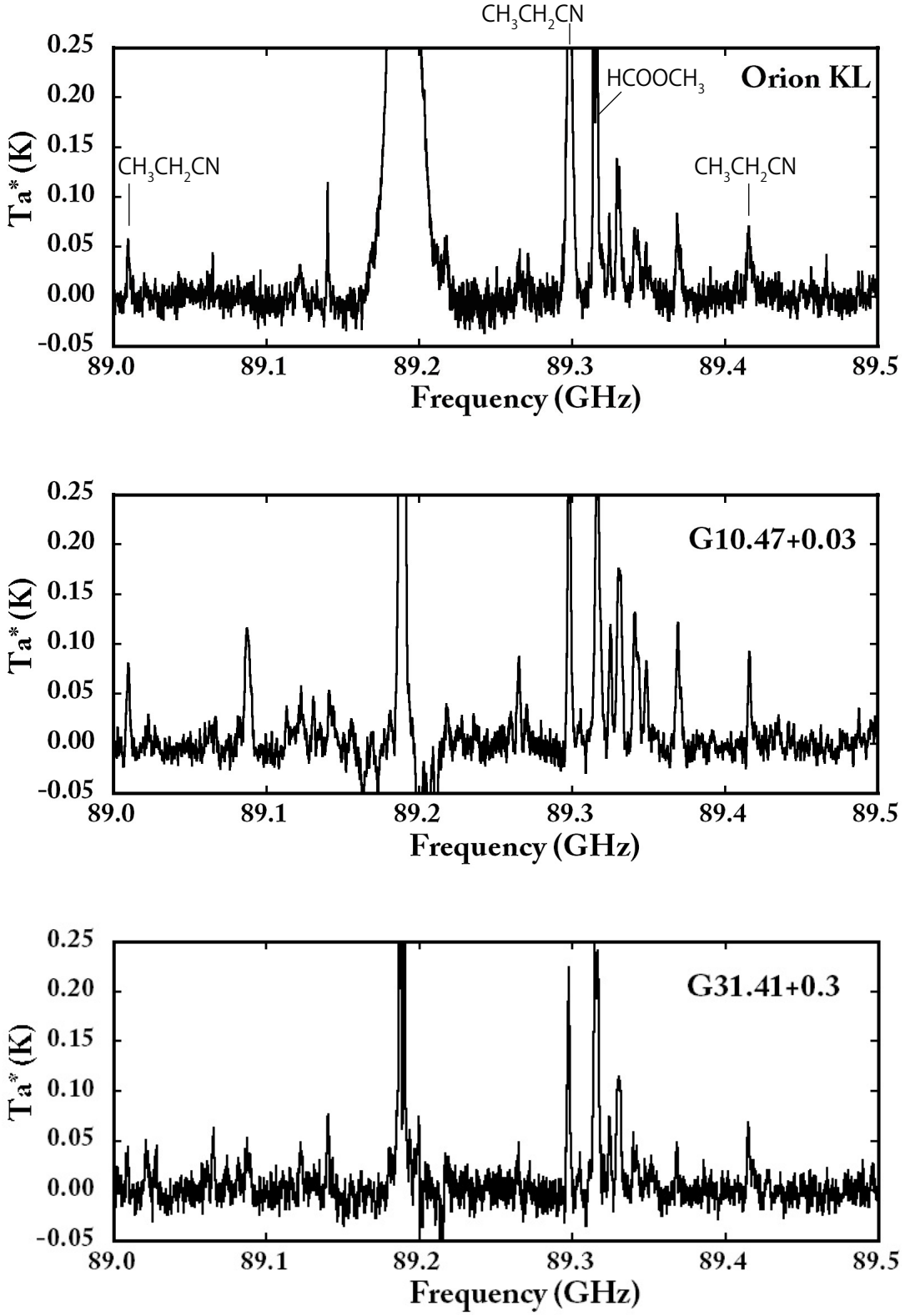

Fig. 4.— Observed Spectra. CH_3CH_2CN and $HCOOCH_3$ were detected.

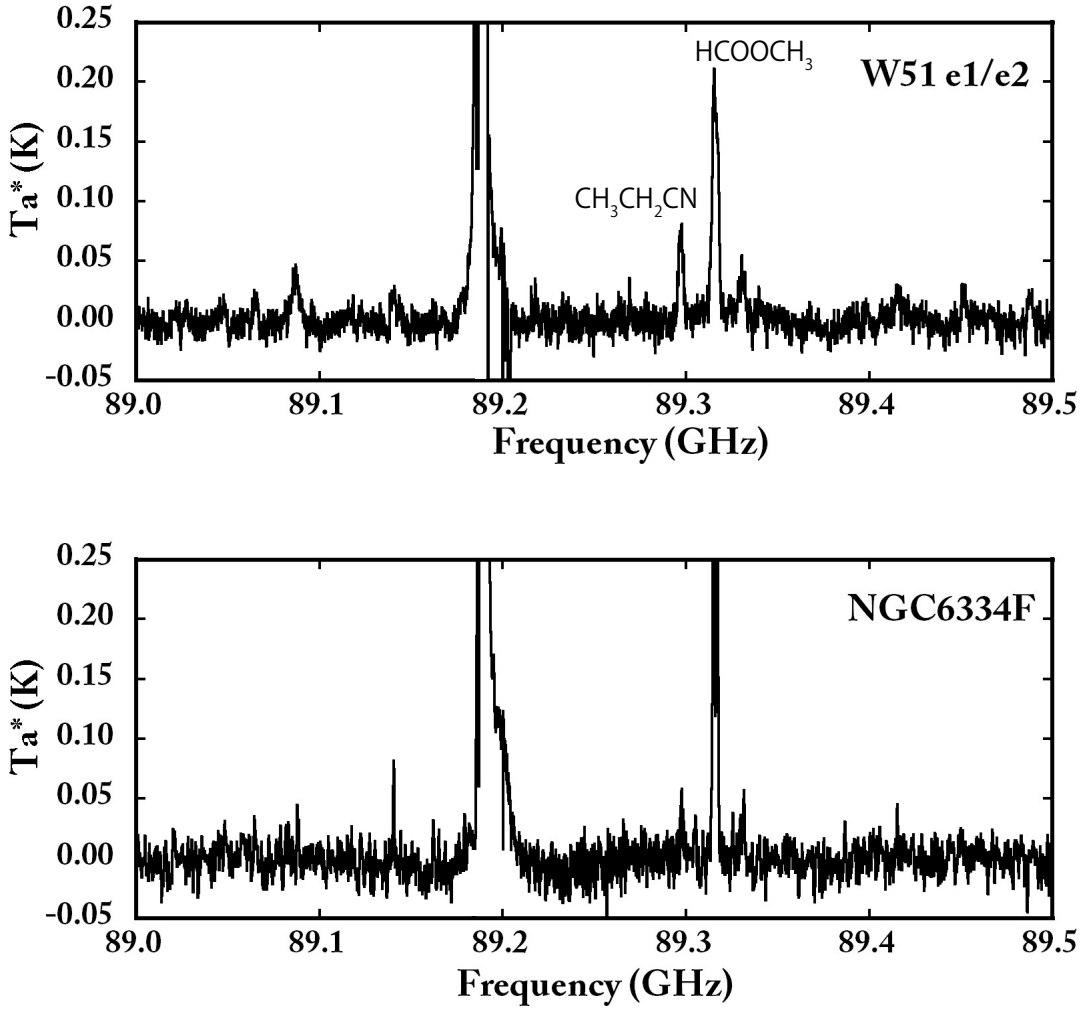

Fig. 4.— Observed Spectra. CH_3CH_2CN and $HCOOCH_3$ were detected.

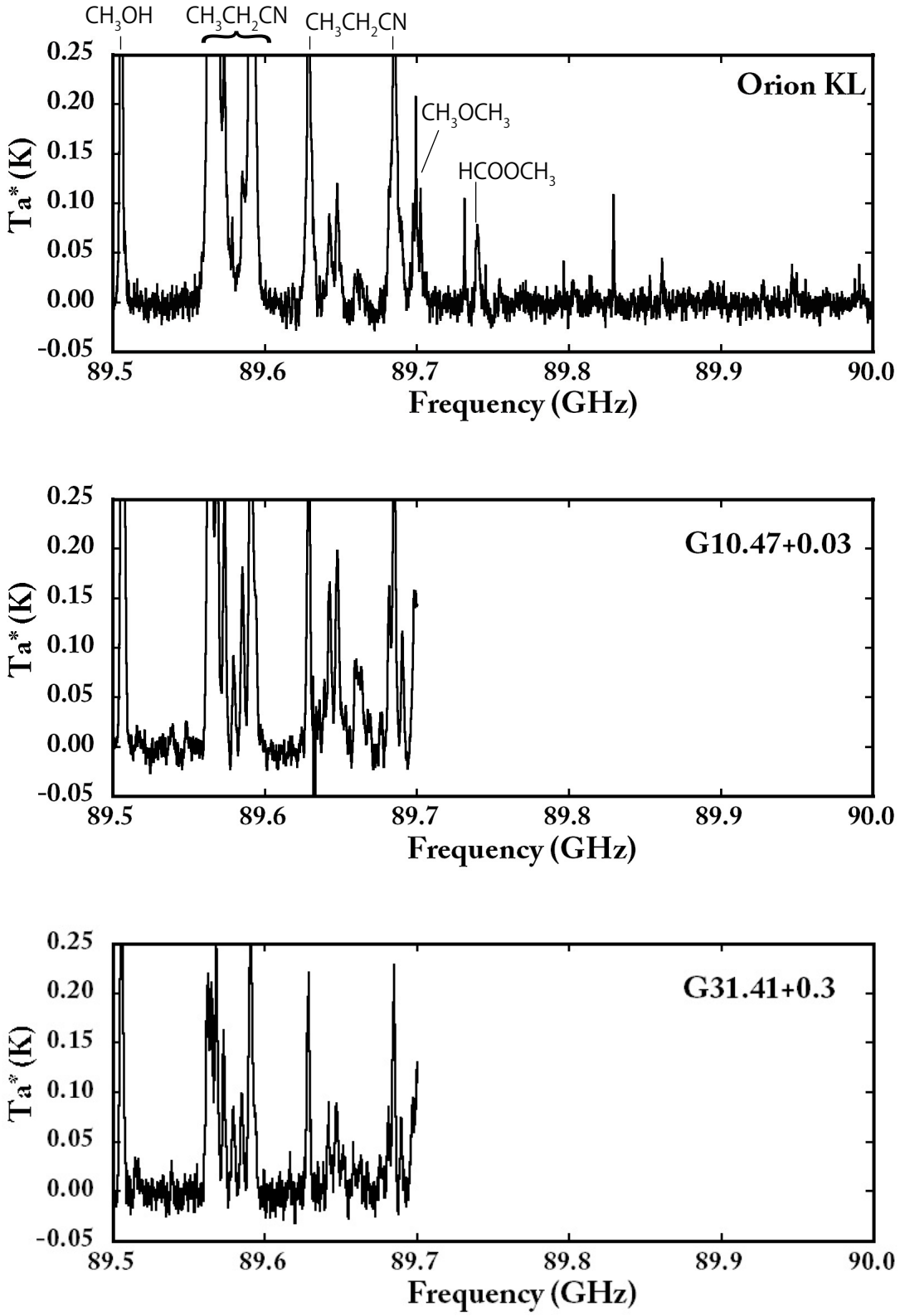

Fig. 4.— Observed Spectra. CH_3OH, CH_3CH_2CN, CH_3OCH_3, and $HCOOCH_3$ were detected.

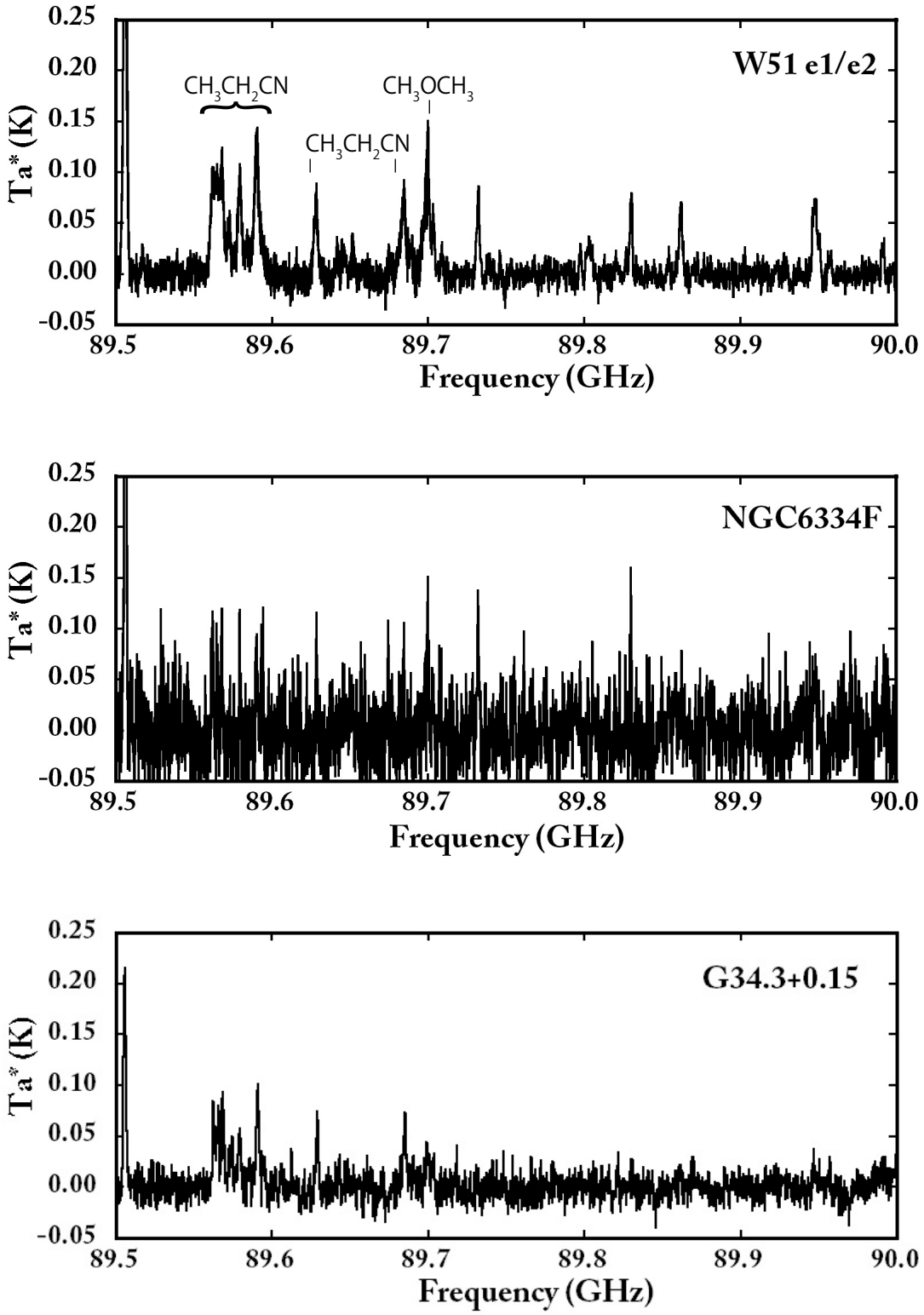

Fig. 4.— Observed Spectra. CH_3OH, CH_3CH_2CN, CH_3OCH_3, and $HCOOCH_3$ were detected.

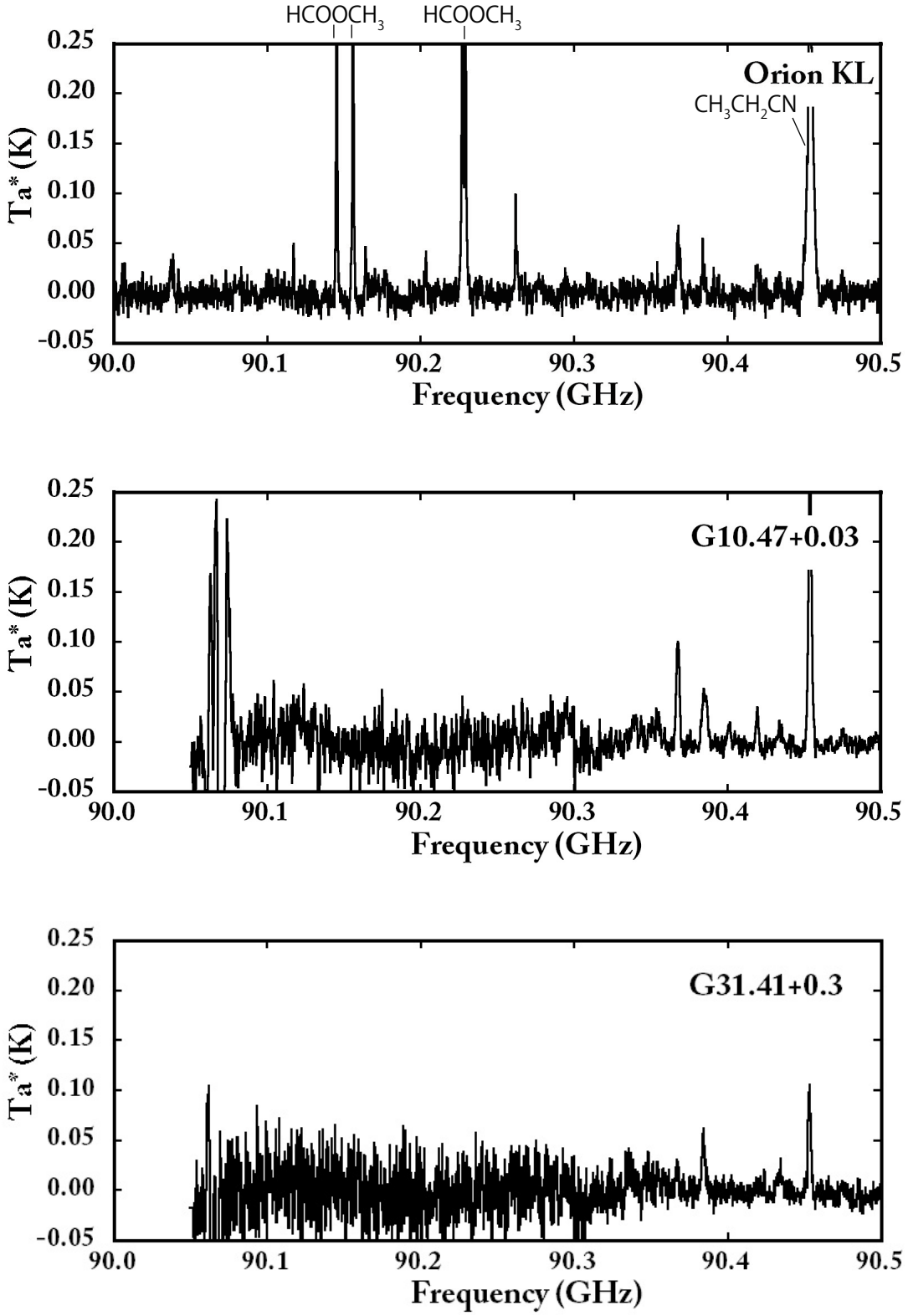

Fig. 4.— Observed Spectra. $HCOOCH_3$ and CH_3CH_2CN were detected.

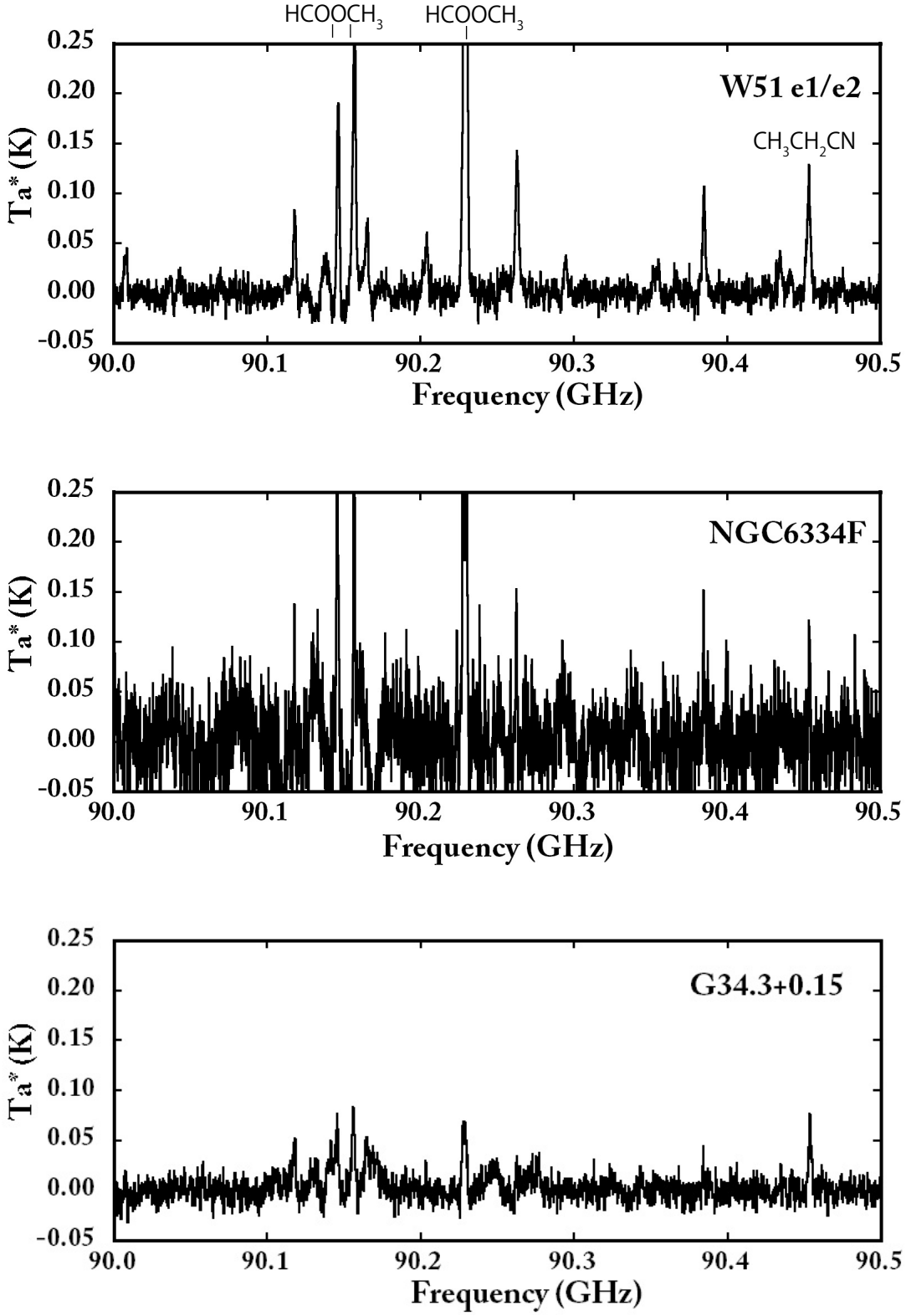

Fig. 4.— Observed Spectra. $HCOOCH_3$ and CH_3CH_2CN were detected.

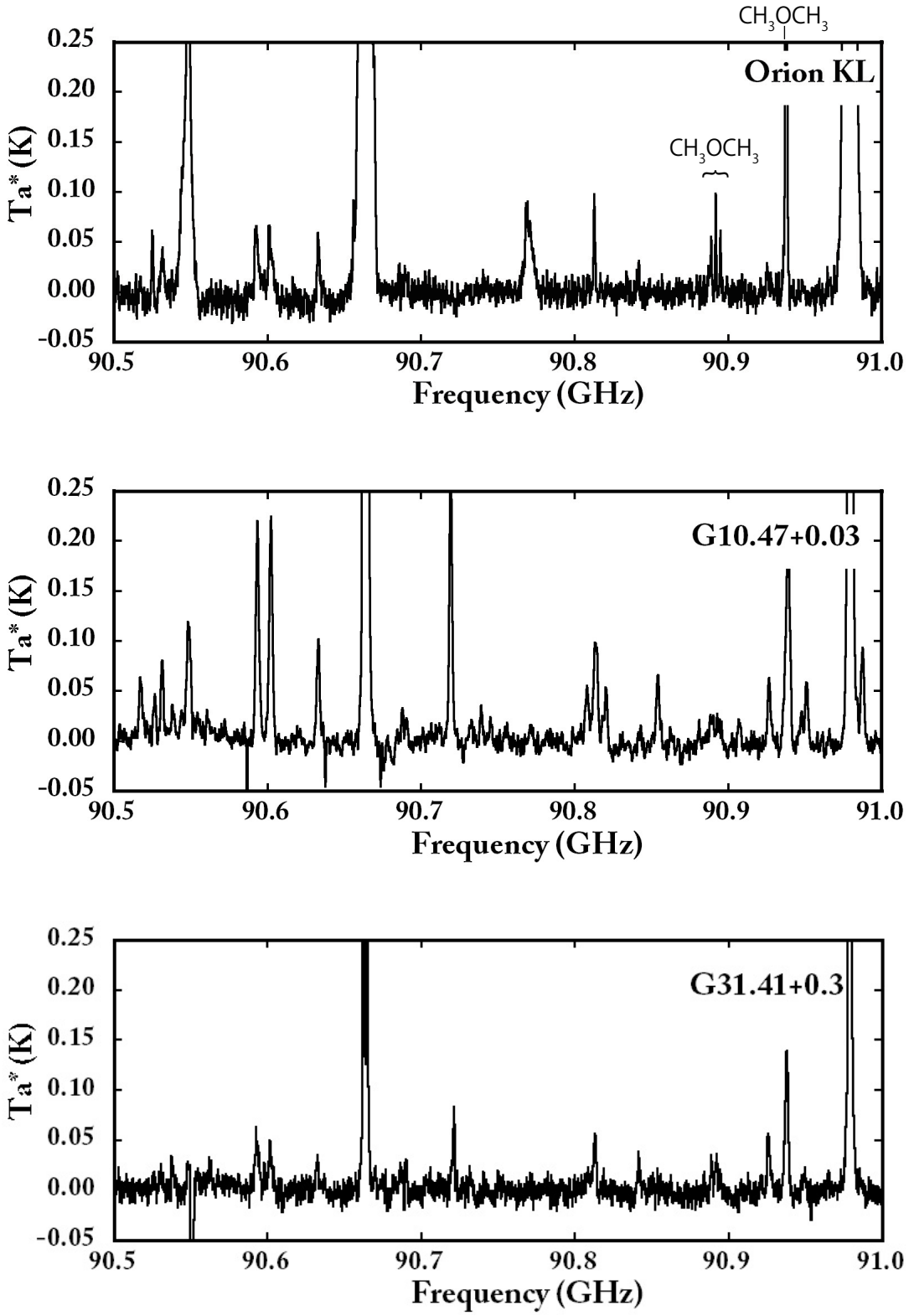

Fig. 4.— Observed Spectra. CH_3OCH_3 was detected.

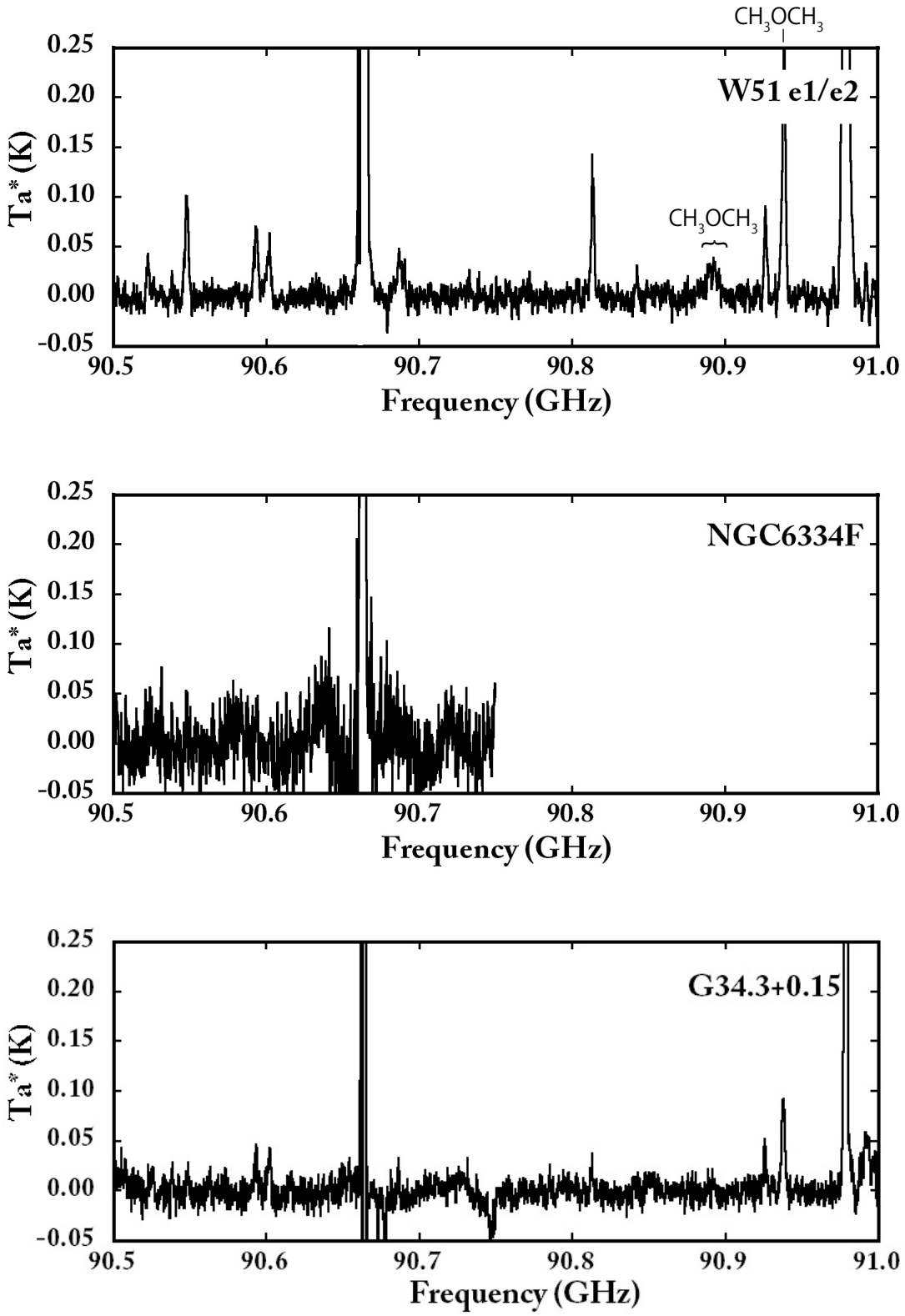

Fig. 4.— Observed Spectra. CH_3OCH_3 was detected.

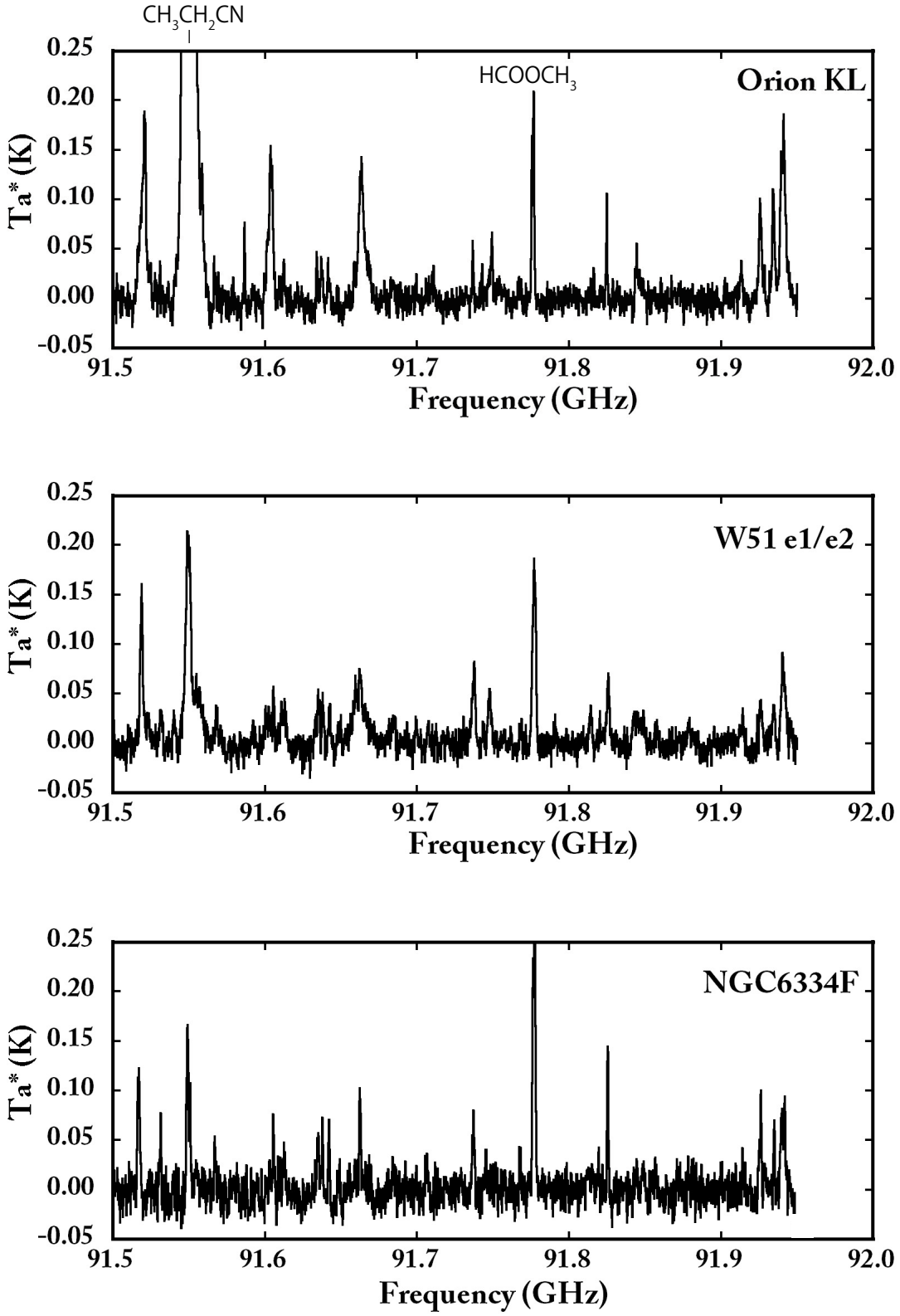

Fig. 4.— Observed Spectra. CH_3CH_2CN and $HCOOCH_3$ were detected.

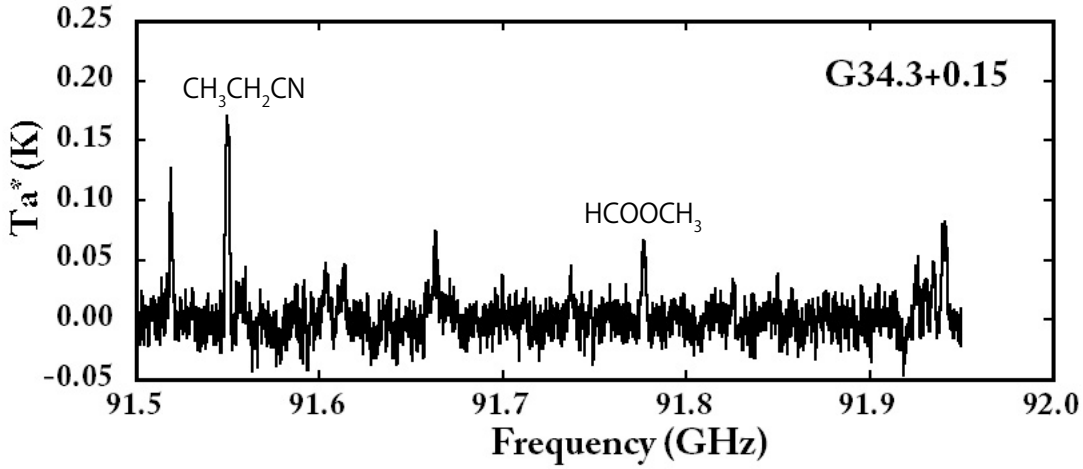

Fig. 4.— Observed Spectra. CH_3CH_2CN and $HCOOCH_3$ were detected.

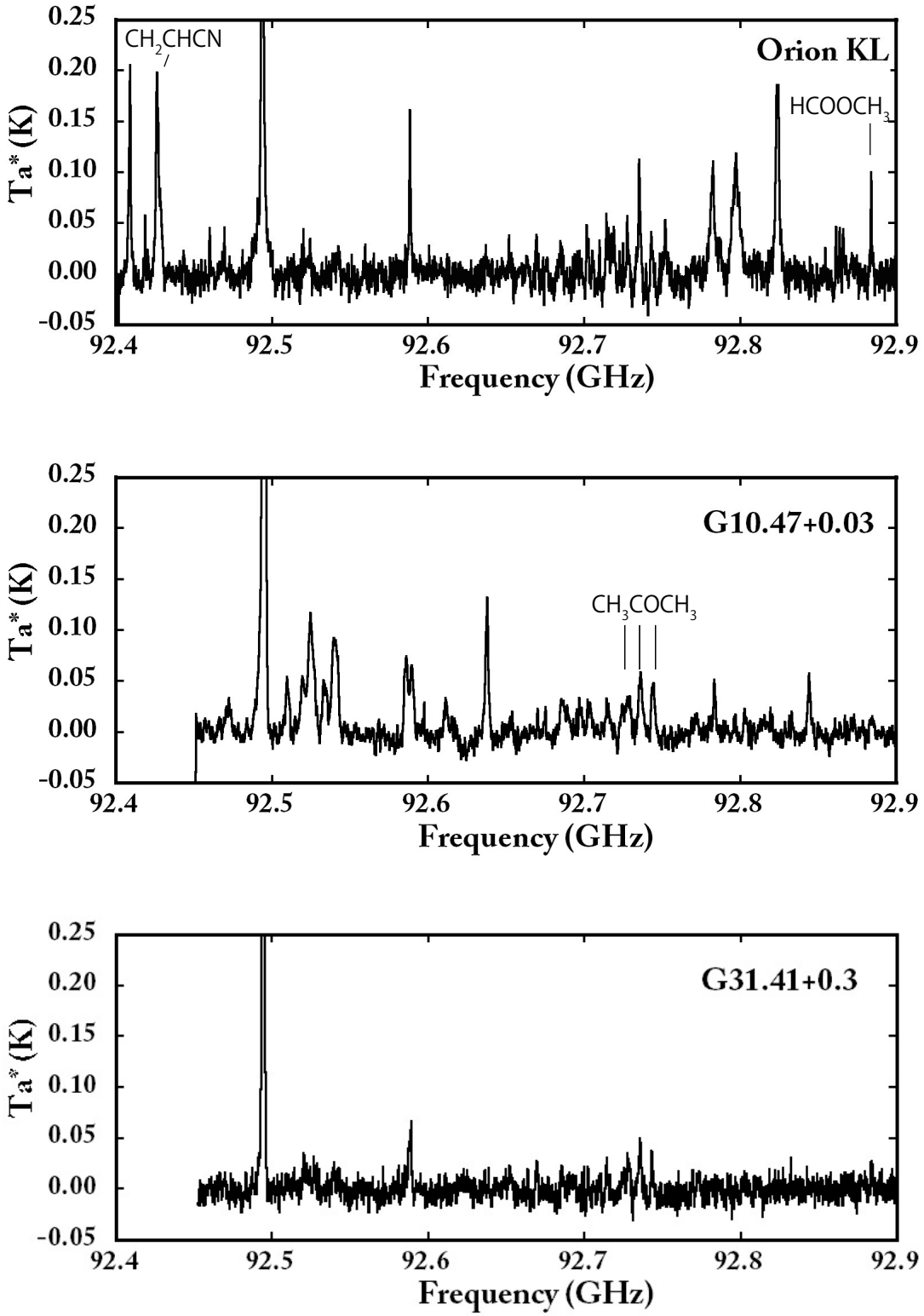

Fig. 4.— Observed Spectra. CH_2CHCN and $HCOOCH_3$ were detected.

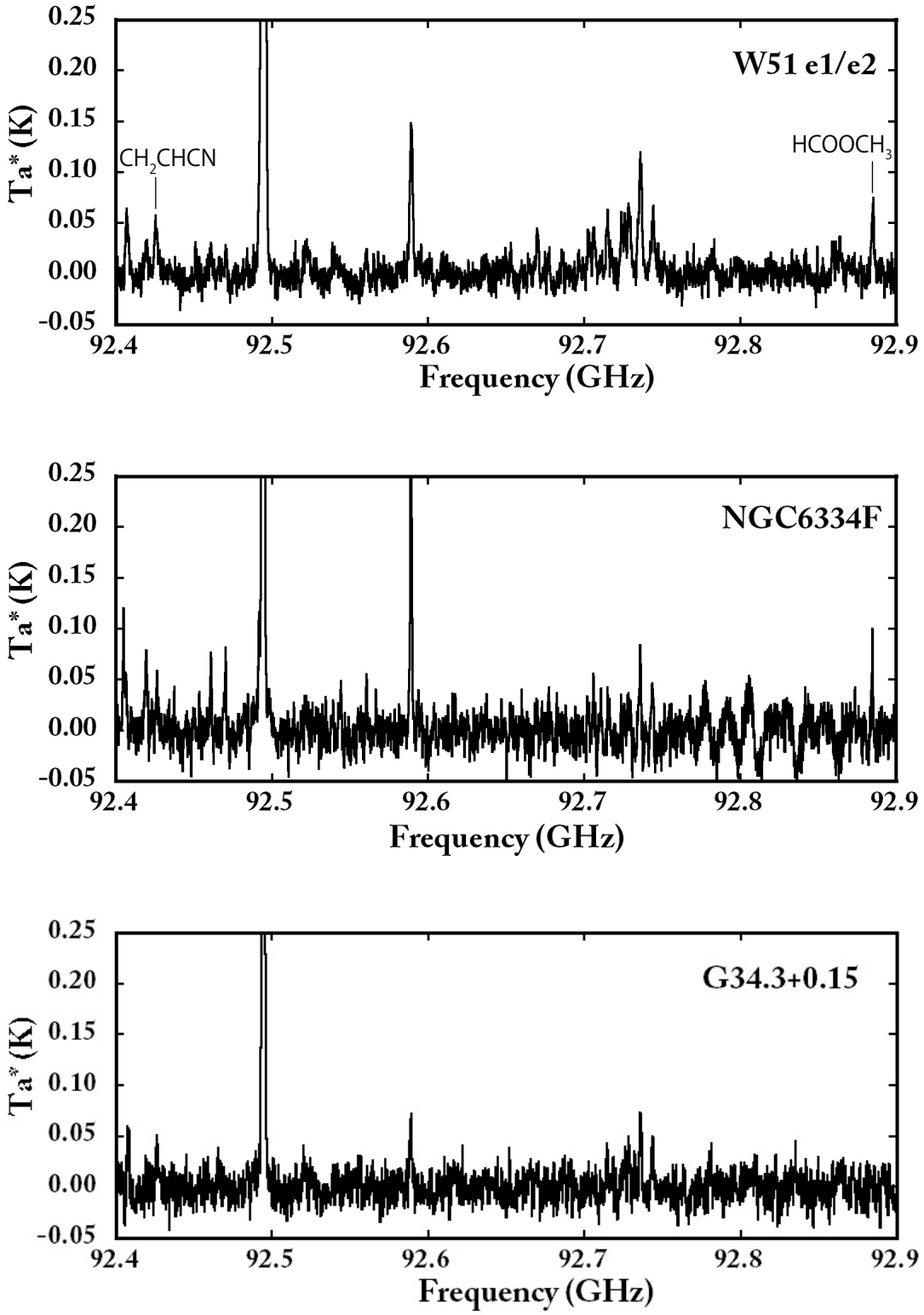

Fig. 4.— Observed Spectra. CH_2CHCN and $HCOOCH_3$ were detected.

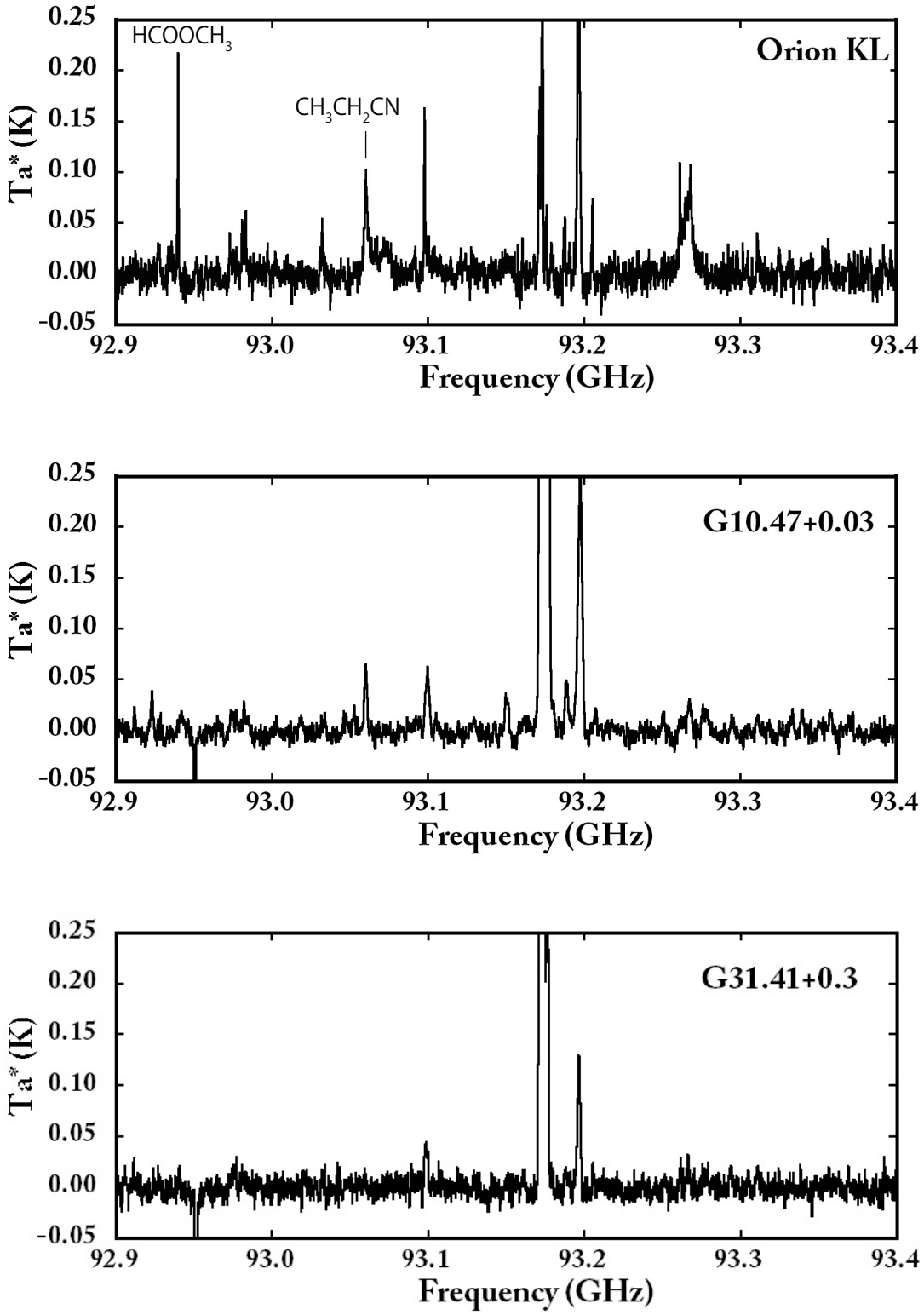

Fig. 4.— Observed Spectra. $HCOOCH_3$ and CH_3CH_2CN were detected.

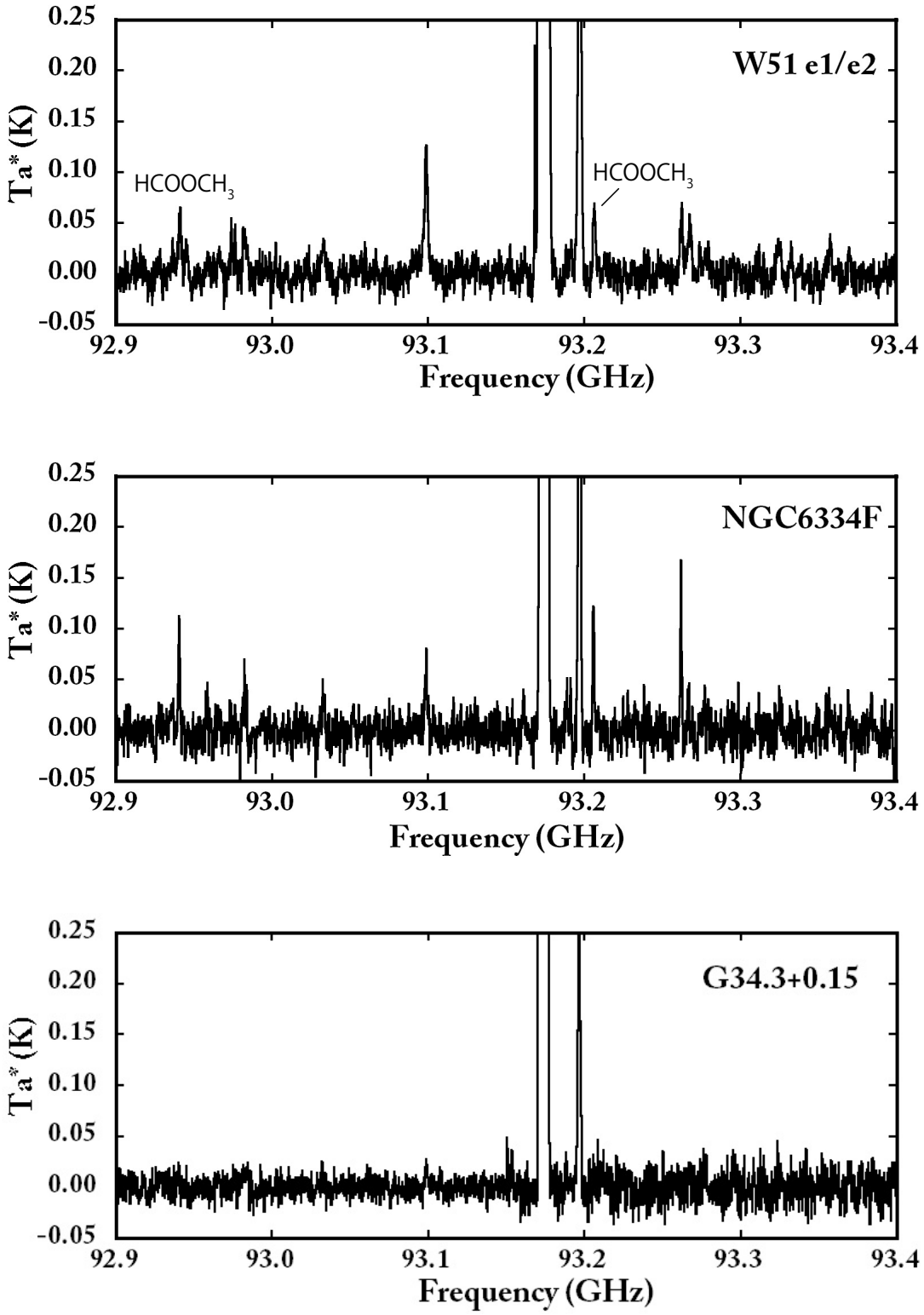

Fig. 4.— Observed Spectra. $HCOOCH_3$ and was detected.

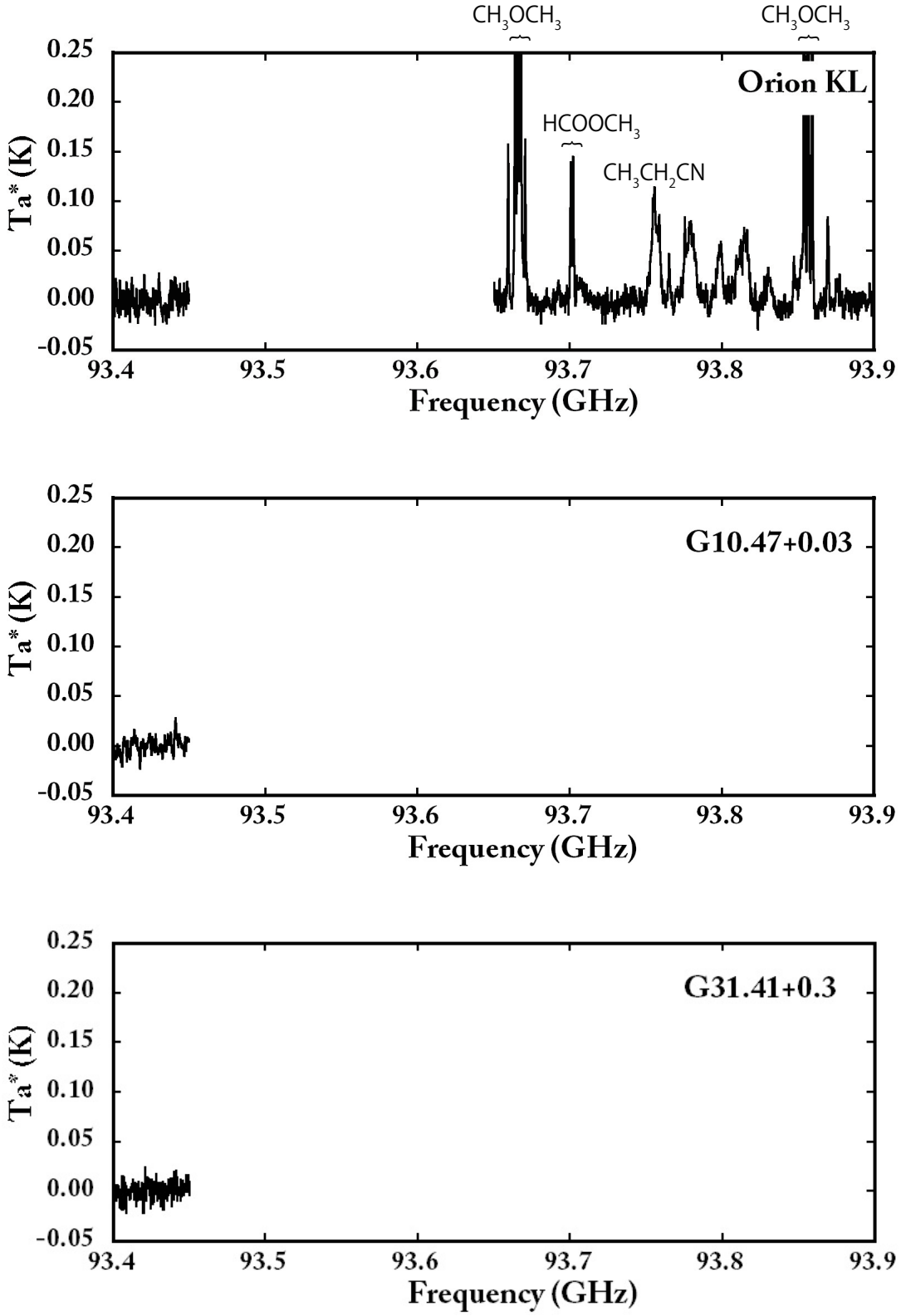

Fig. 4.— Observed Spectra. CH_3OCH_3, $HCOOCH_3$, and CH_3CH_2CN were detected.

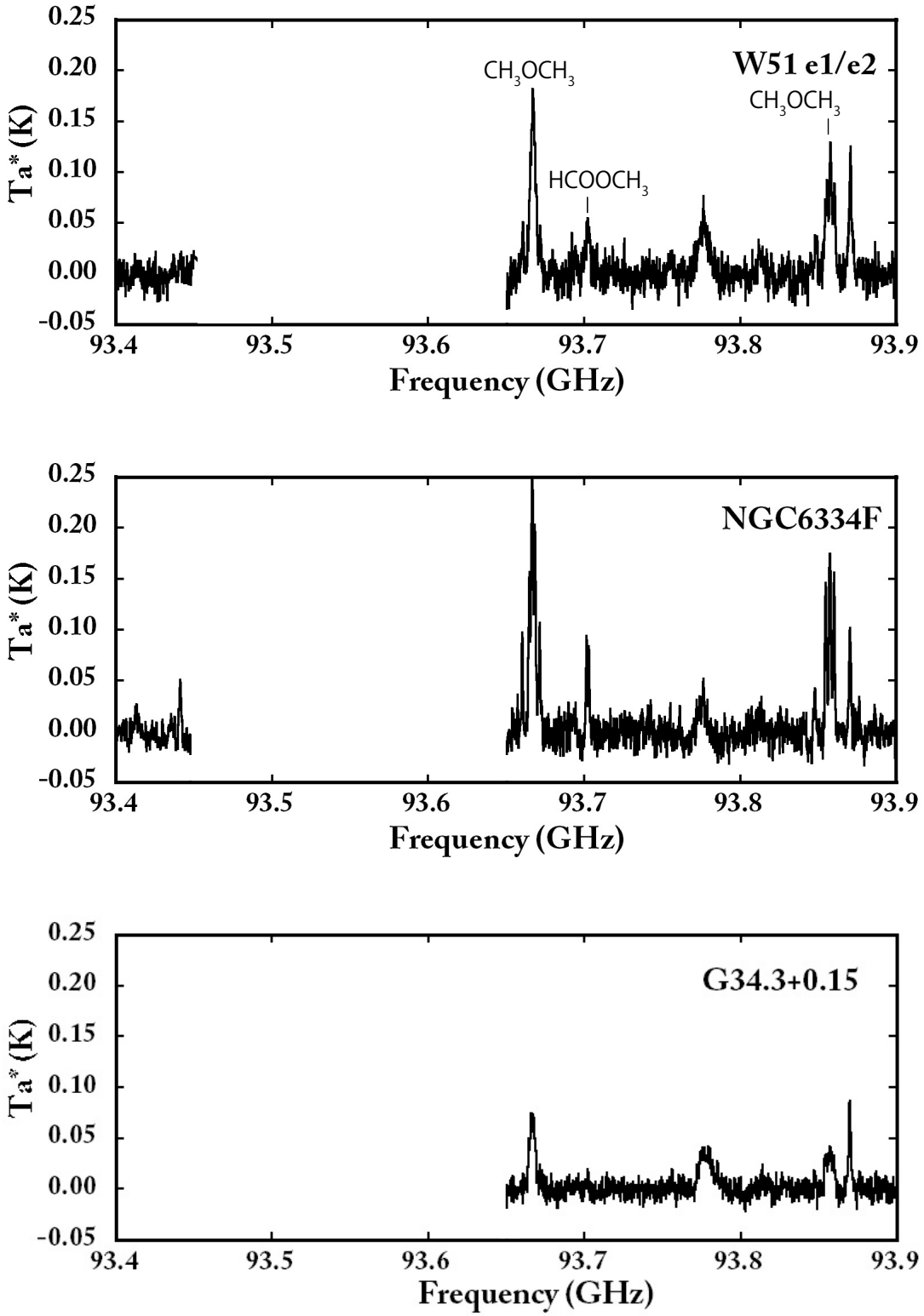

Fig. 4.— Observed Spectra.CH_3OCH_3 and $HCOOCH_3$ were detected.

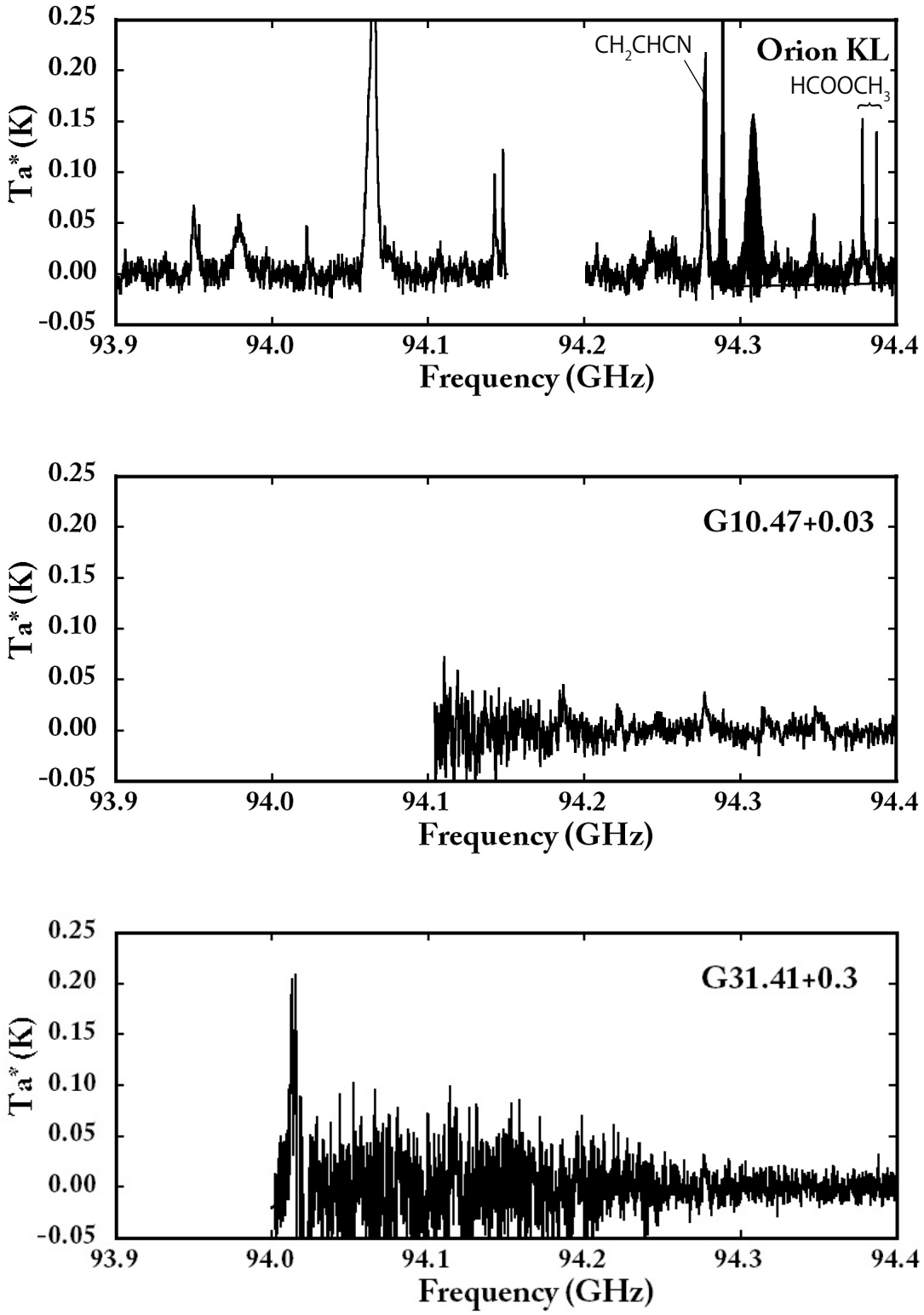

Fig. 4.— Observed Spectra. CH_2CHCN and $HCOOCH_3$ were detected.

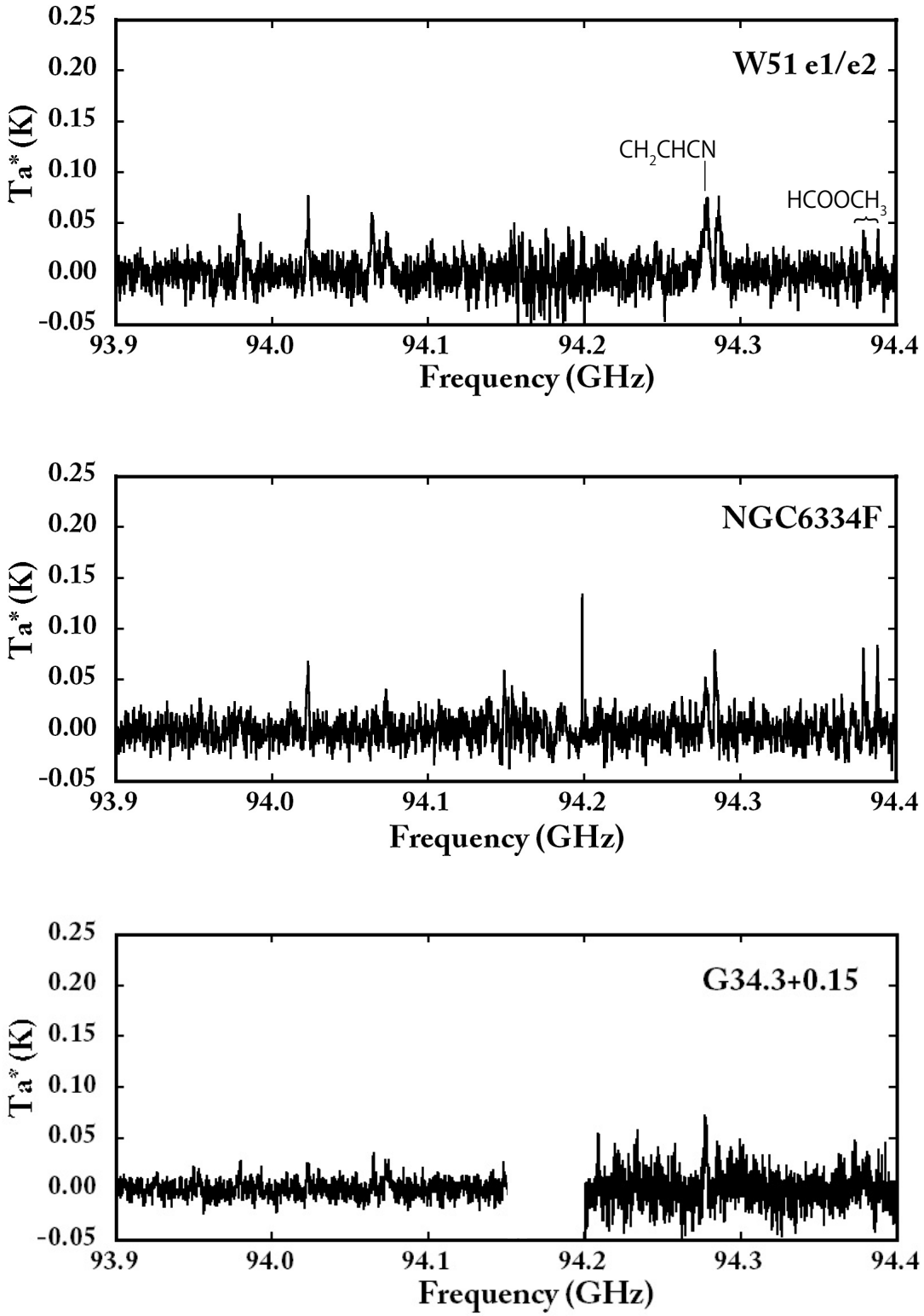

Fig. 4.— Observed Spectra. CH_2CHCN and $HCOOCH_3$ were detected.

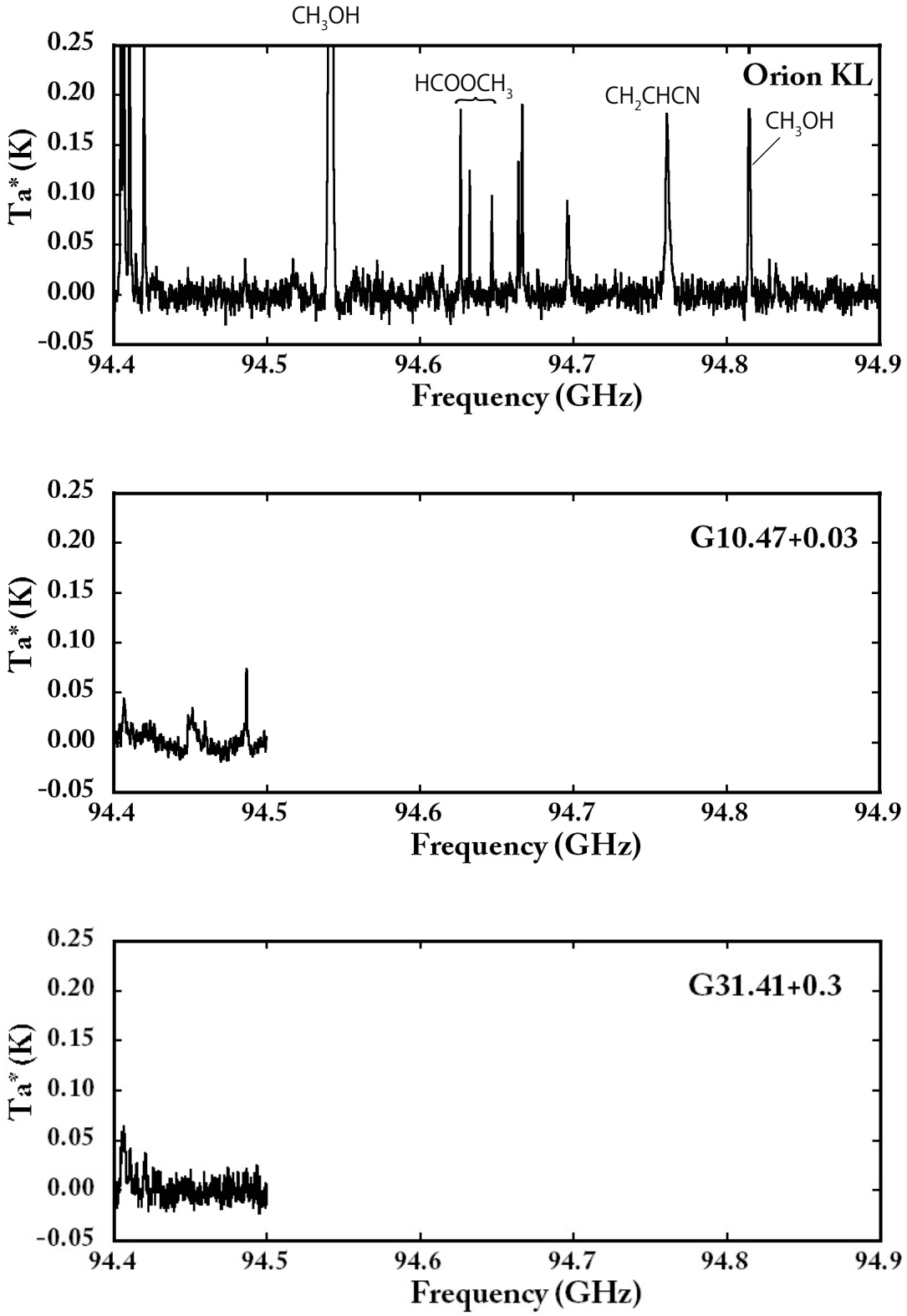

Fig. 4.— Observed Spectra. CH_3OH, $HCOOCH_3$, and CH_2CHCN were detected.

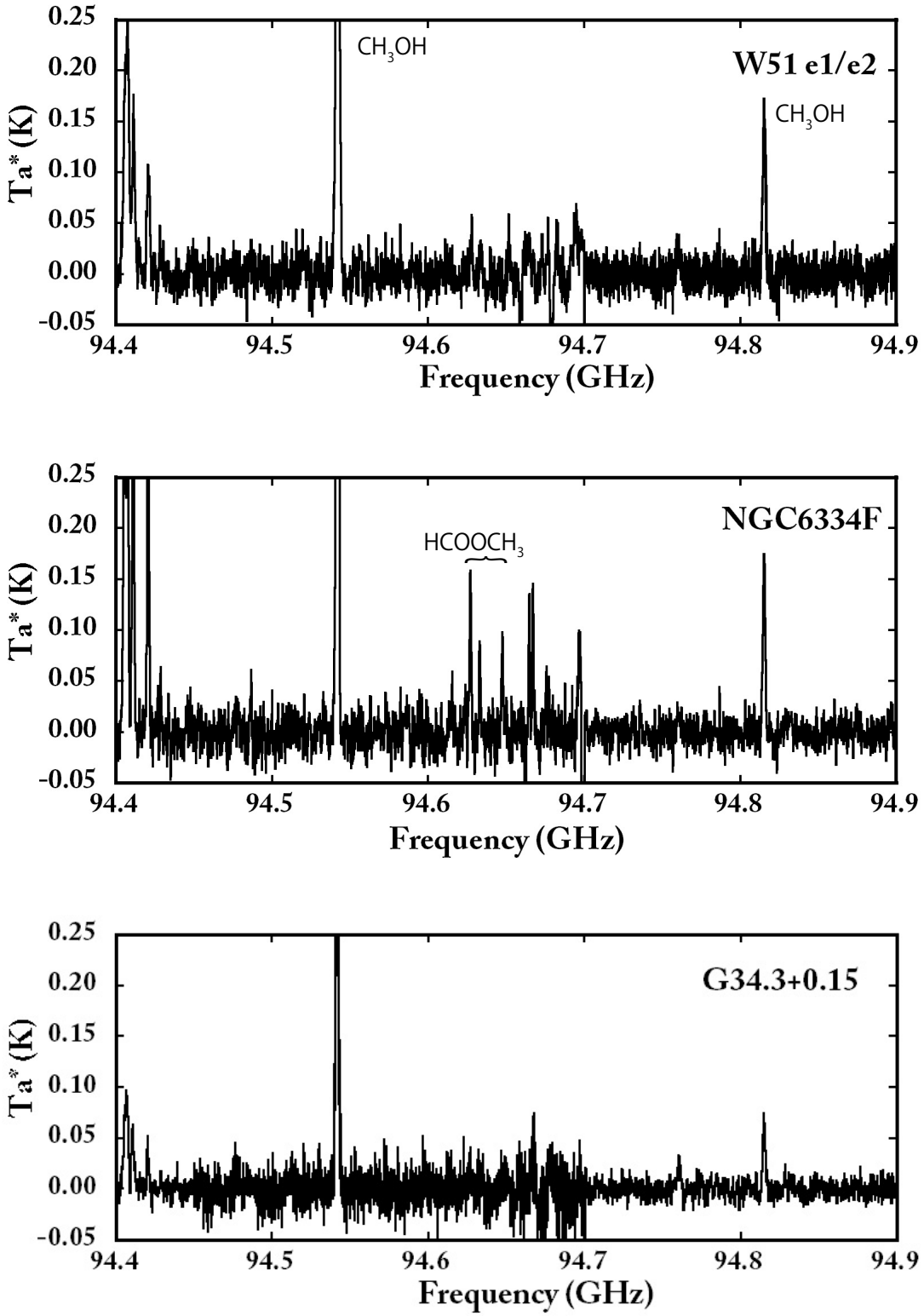

Fig. 4.— Observed Spectra. $HCOOCH_3$ and CH_3OH were detected

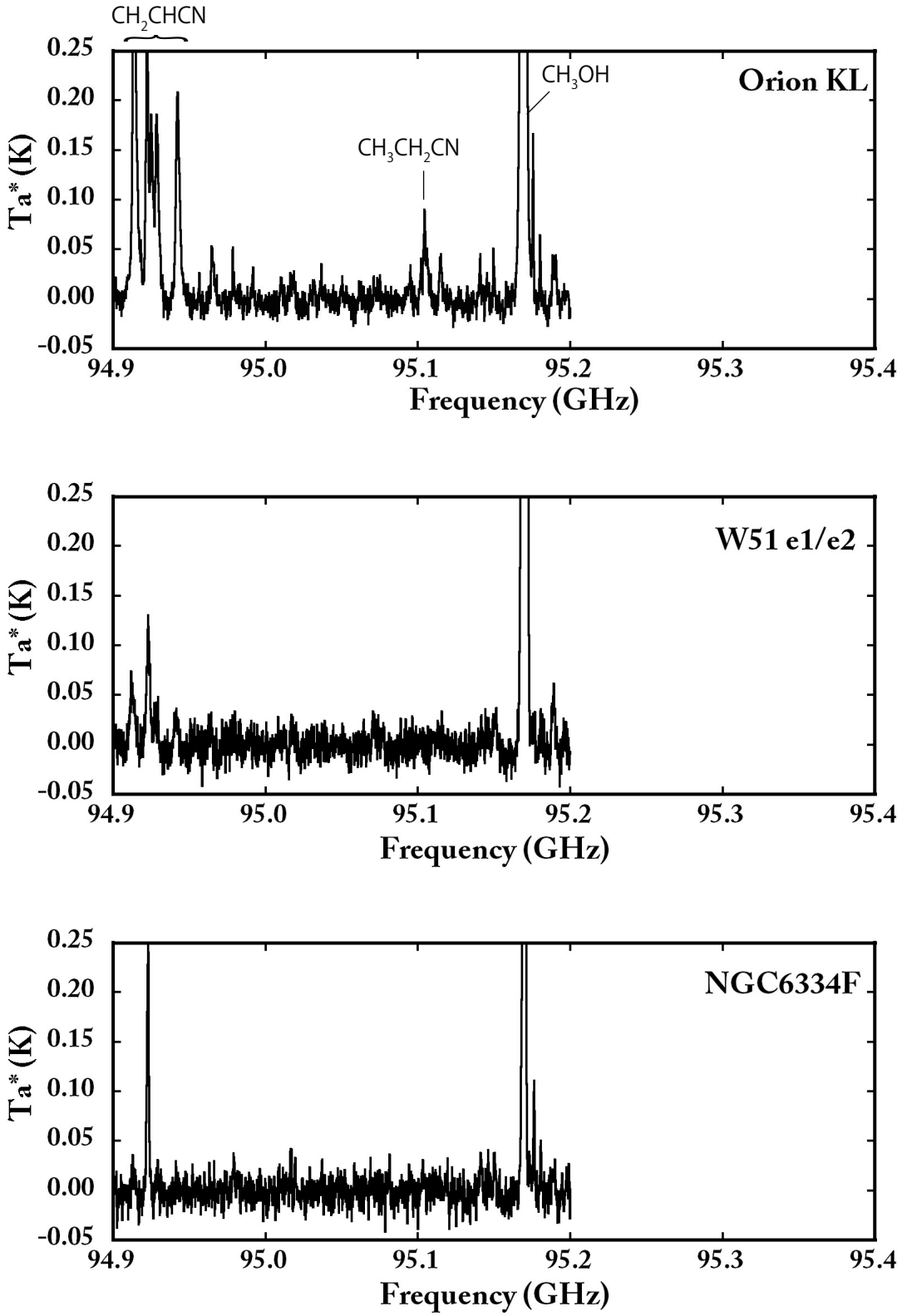

Fig. 4.— Observed Spectra. CH_2CHCN, CH_3CH_2CN, and CH_3OH were detected.

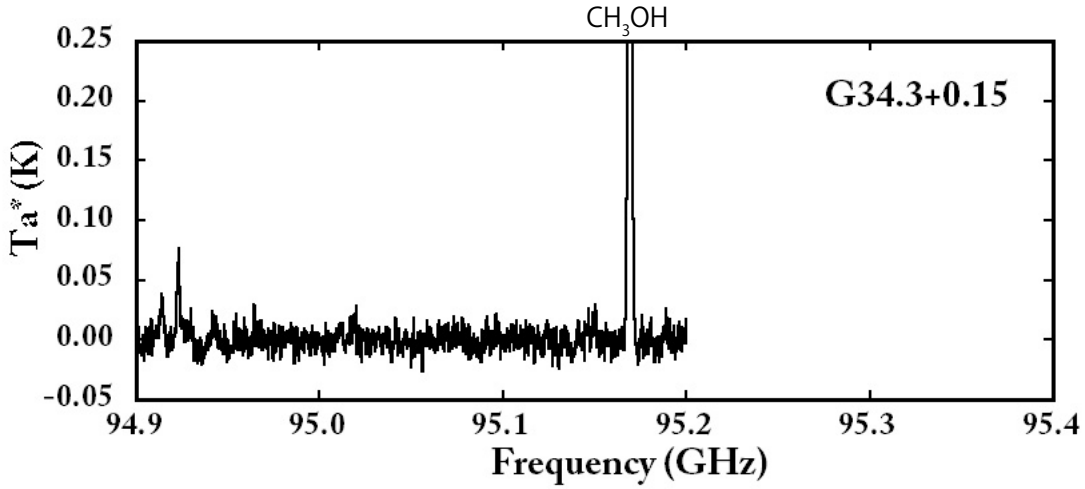

Fig. 4.— Observed Spectra. CH_3OH was detected

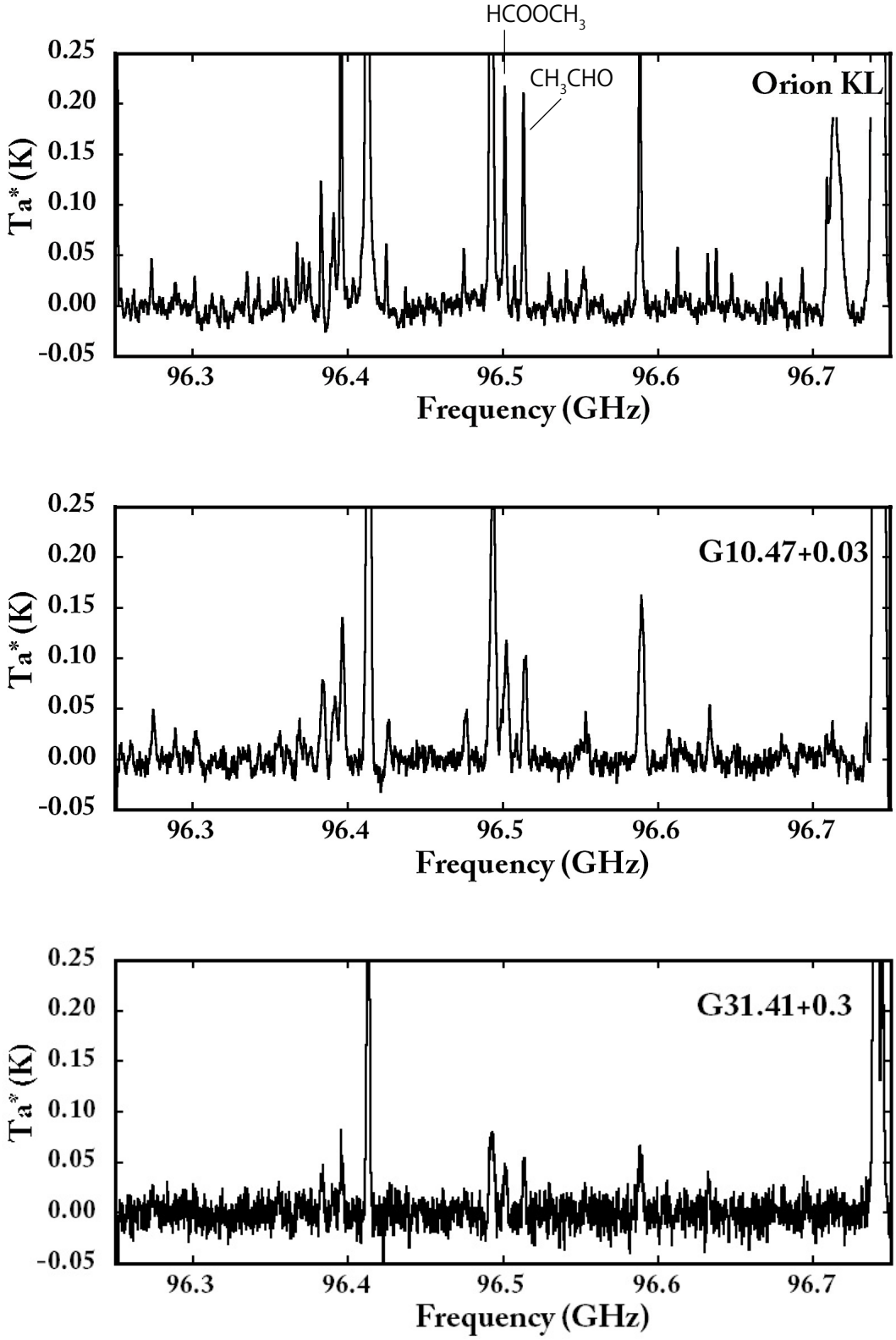

Fig. 4.— Observed Spectra. $HCOOCH_3$ and CH_3CHO were detected.

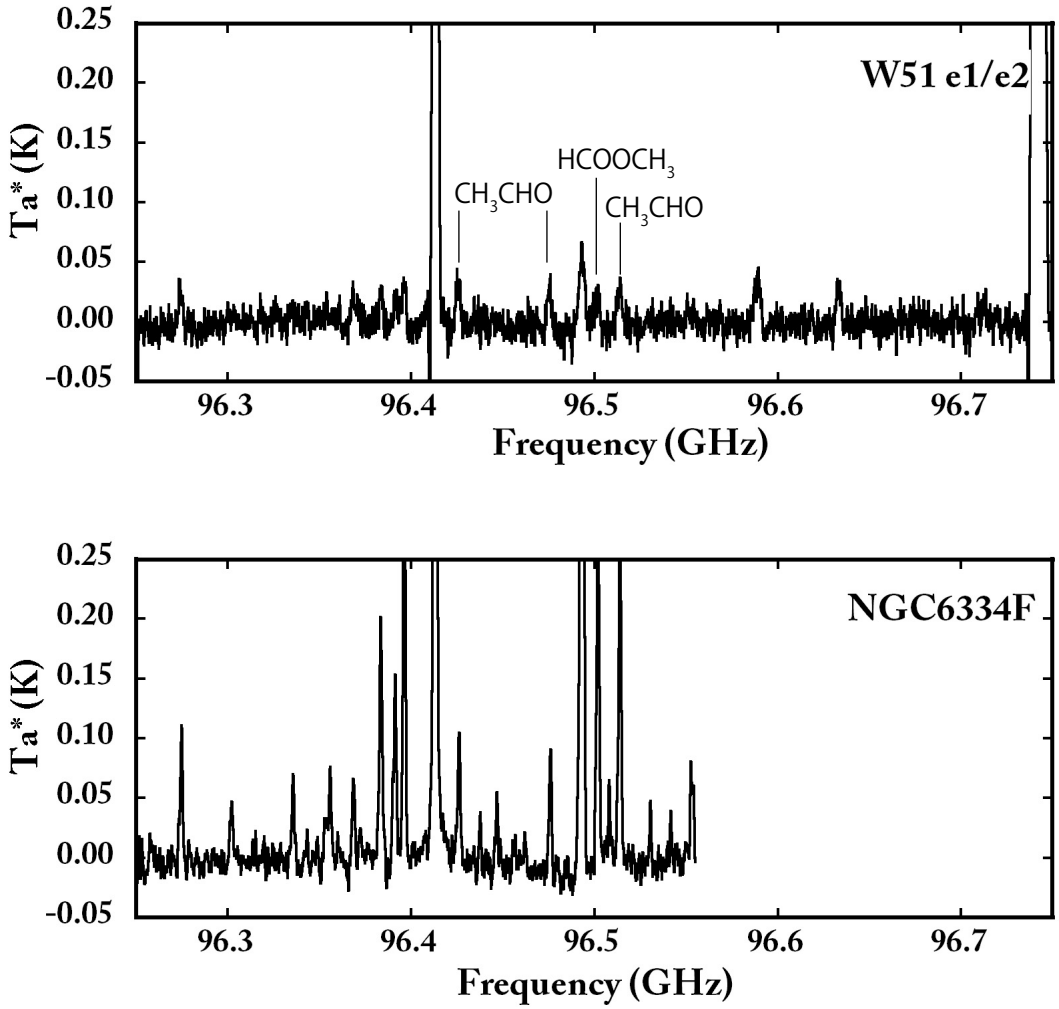

Fig. 4.— Observed Spectra. $HCOOCH_3$ and CH_3CHO were detected.

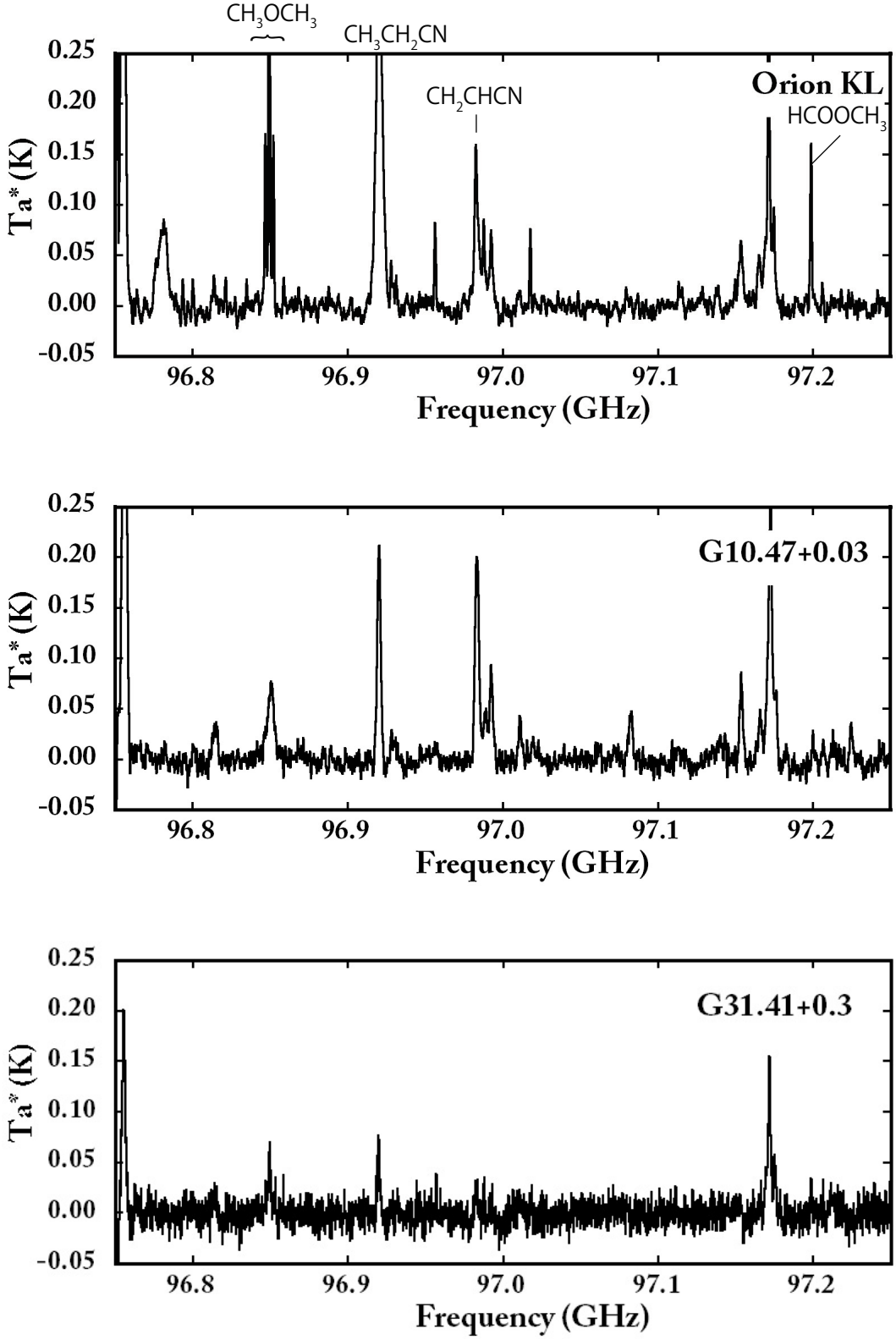

Fig. 4.— Observed Spectra. CH_3OCH_3, CH_3CH_2CN, CH_2CHCN, and $HCOOCH_3$ were detected.

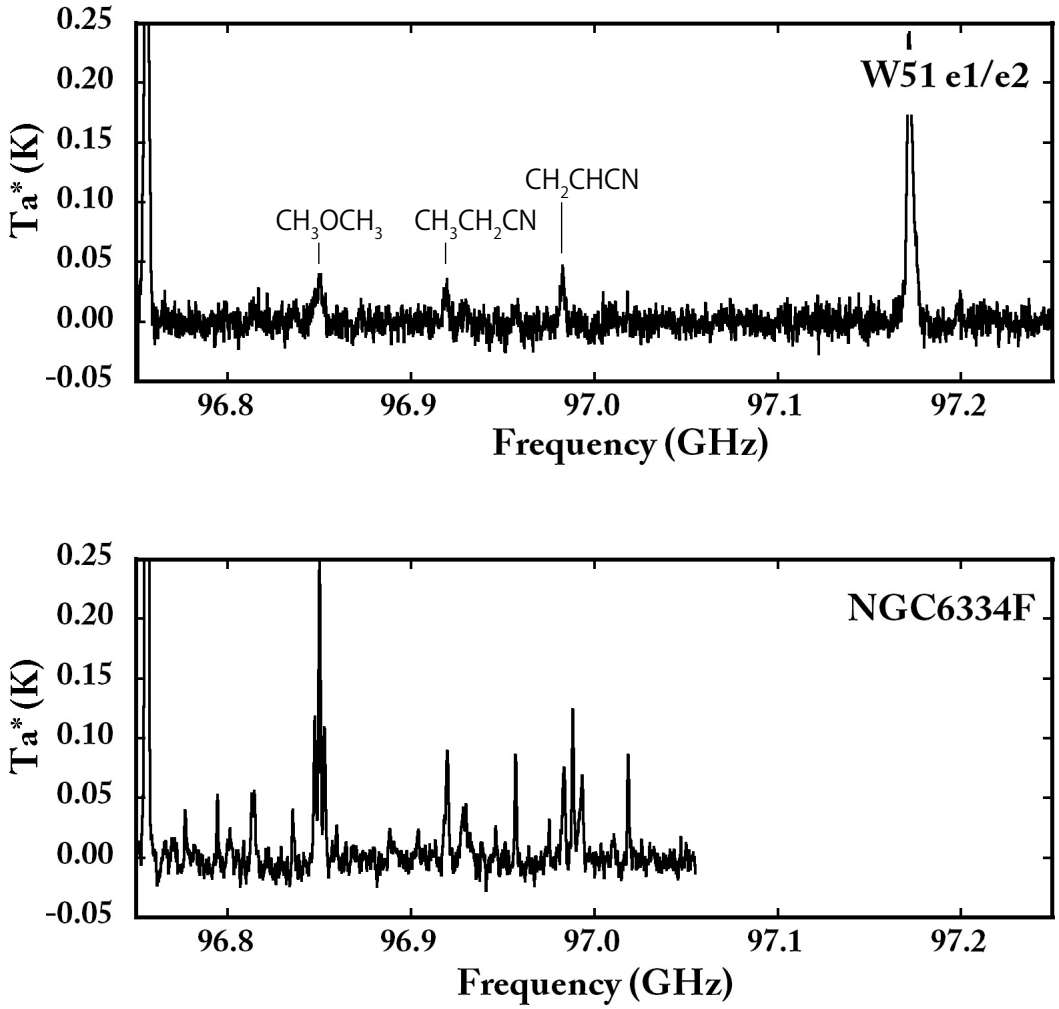

Fig. 4.— Observed Spectra. CH_3OCH_3, CH_3CH_2CN, and CH_2CHCN were detected.

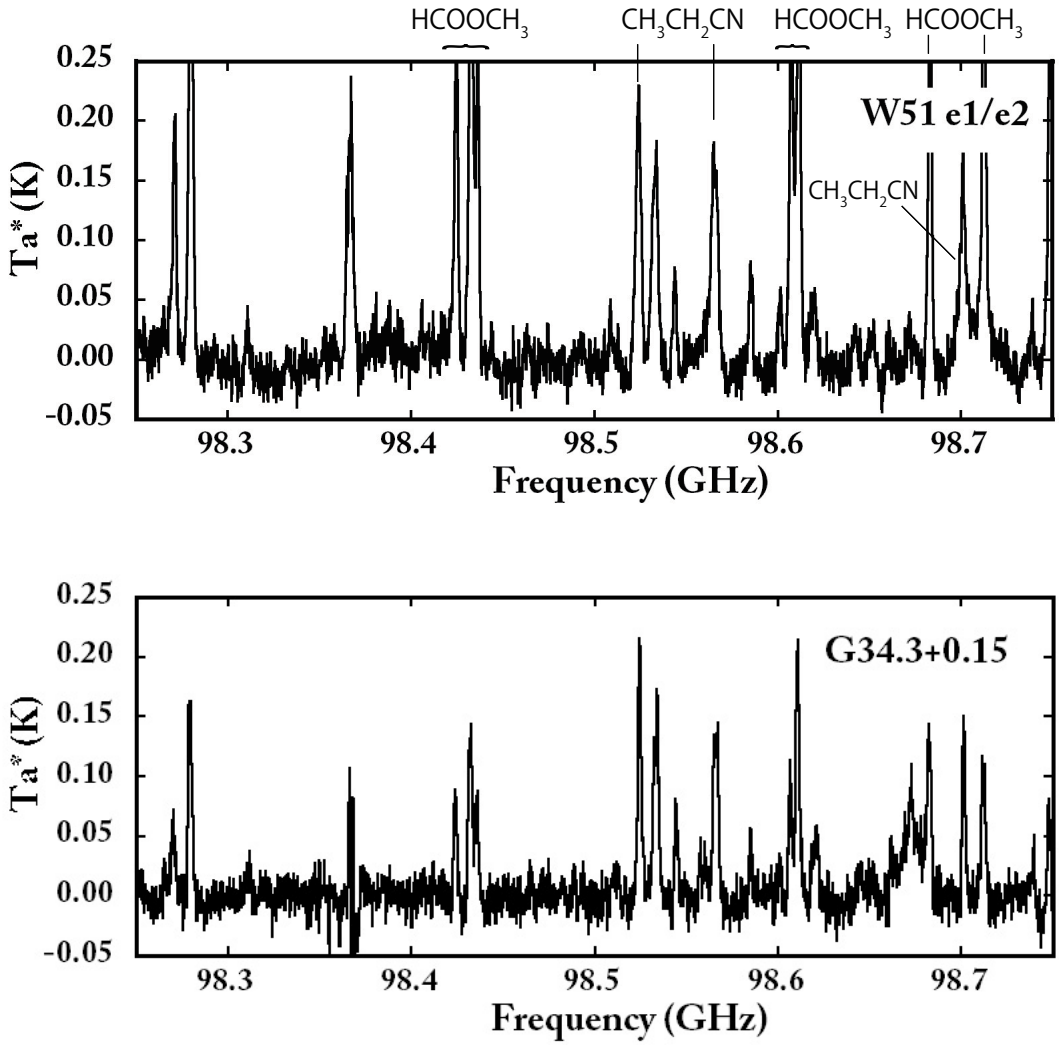

Fig. 4.— Observed Spectra. $HCOOCH_3$ and CH_3CH_2CN were detected.

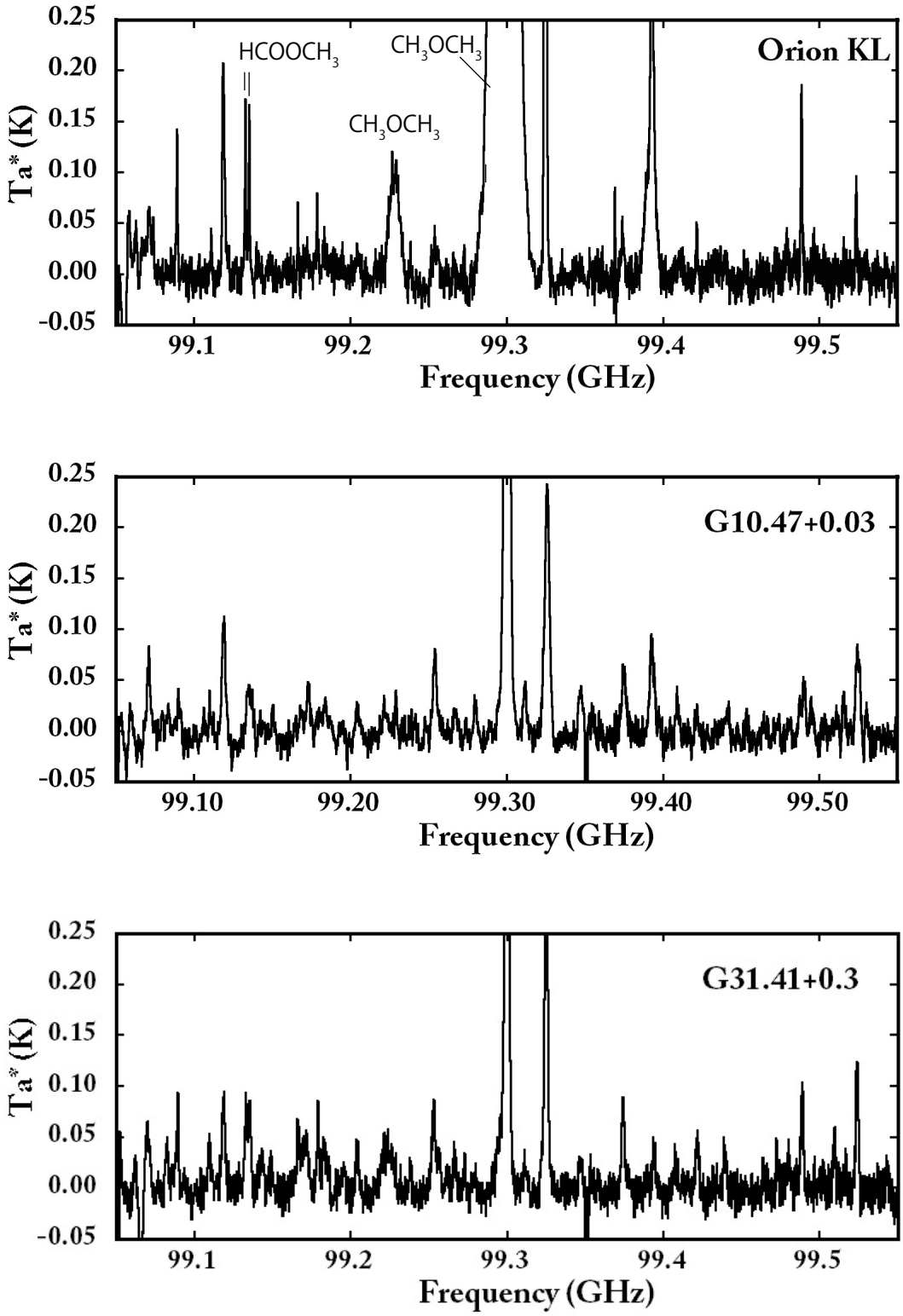

Fig. 4.— Observed Spectra. $HCOOCH_3$ and CH_3OCH_3 were detected.

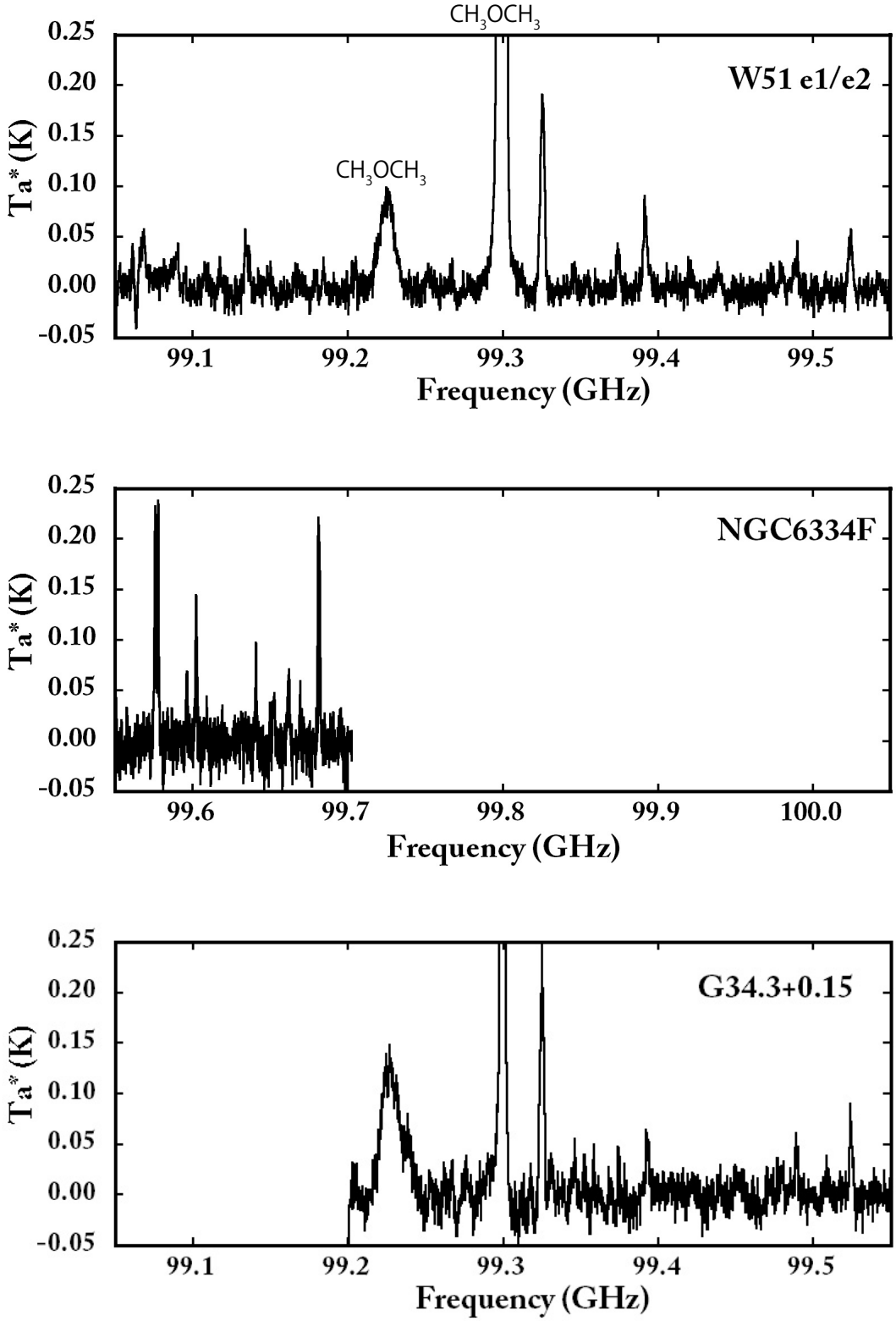

Fig. 4.— Observed Spectra. CH_3OCH_3 was detected.

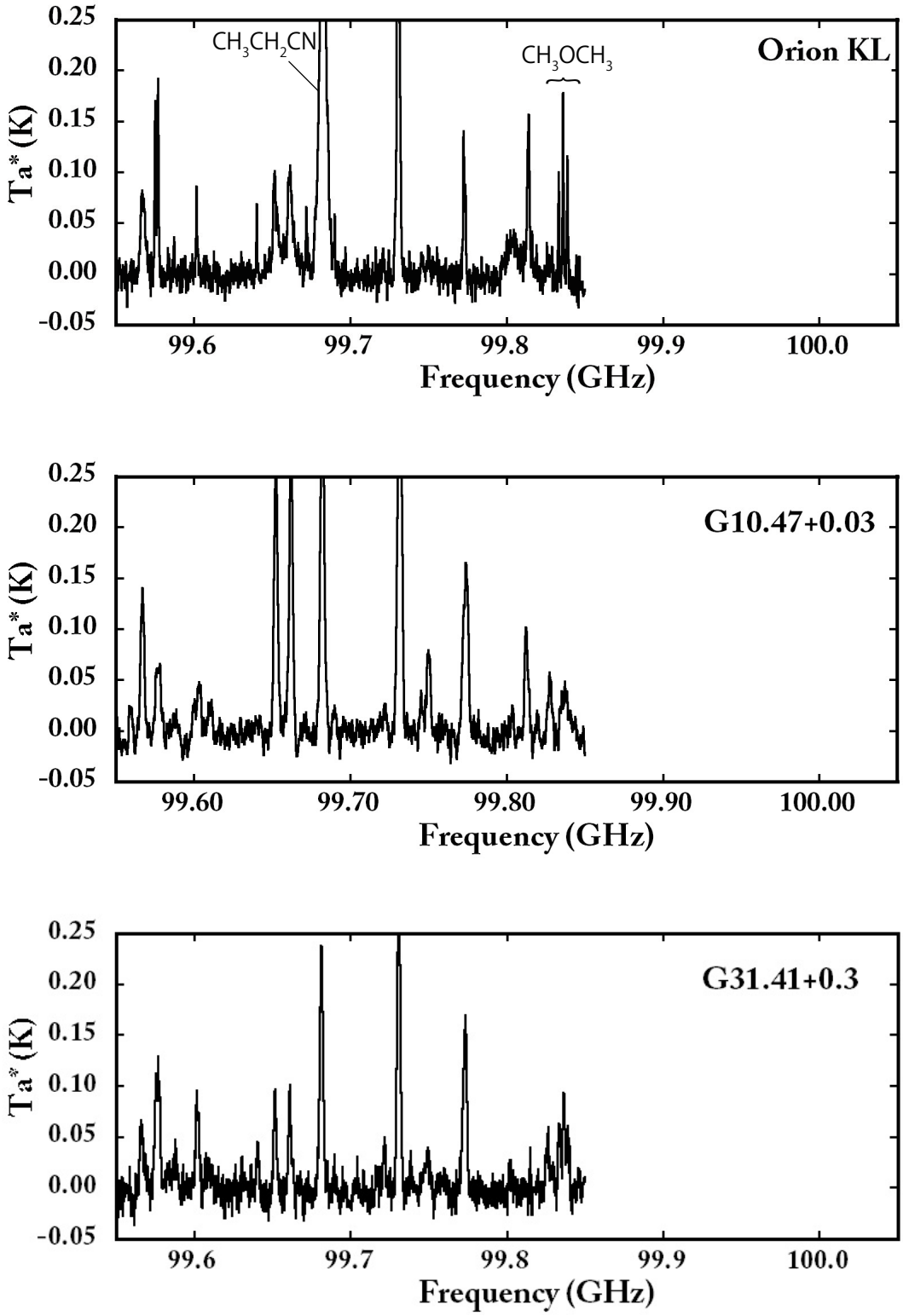

Fig. 4.— Observed Spectra. CH_3CH_2CN and CH_3OCH_3 was detected.

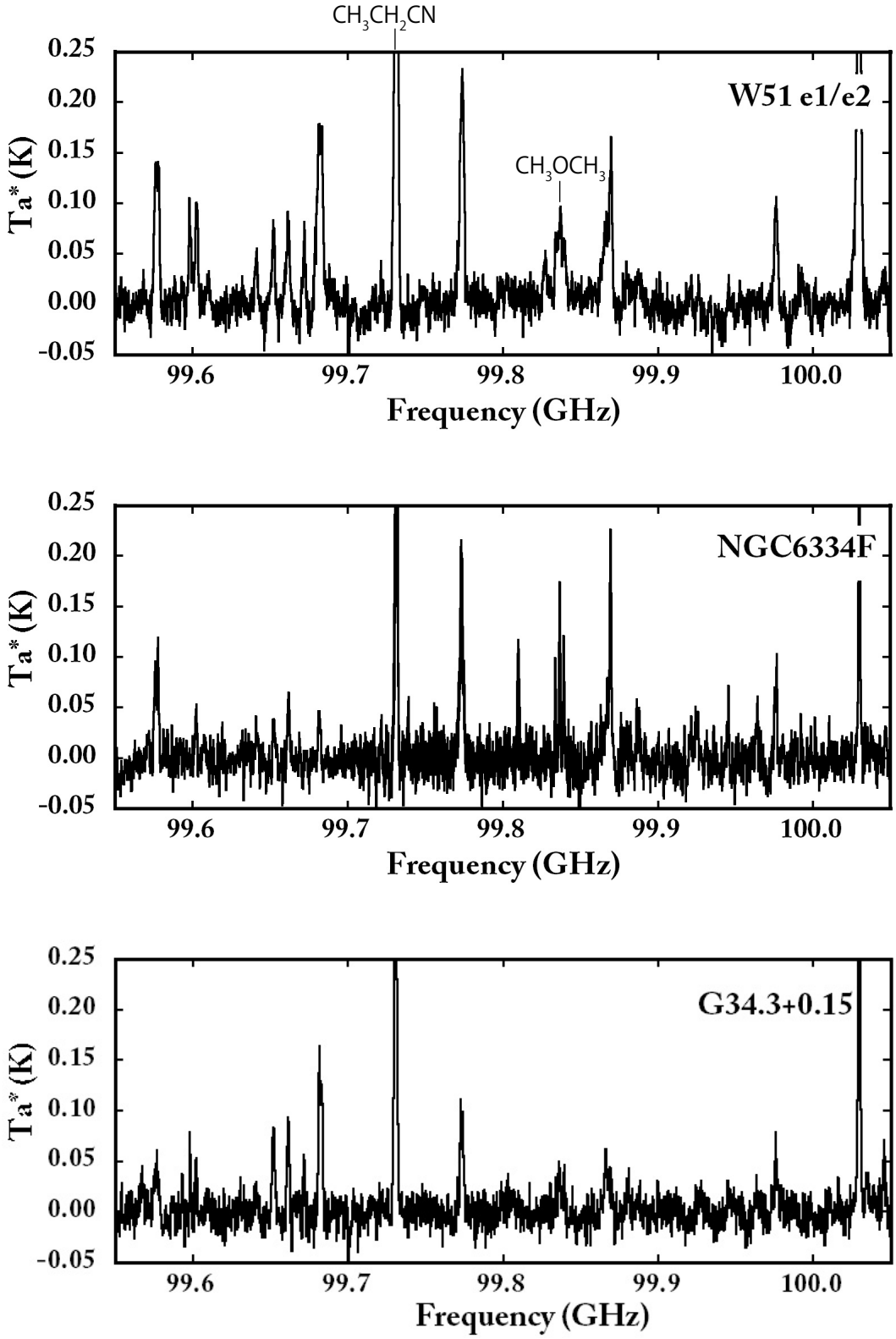

Fig. 4.— Observed Spectra. CH_3CH_2CN and CH_3OCH_3 was detected.

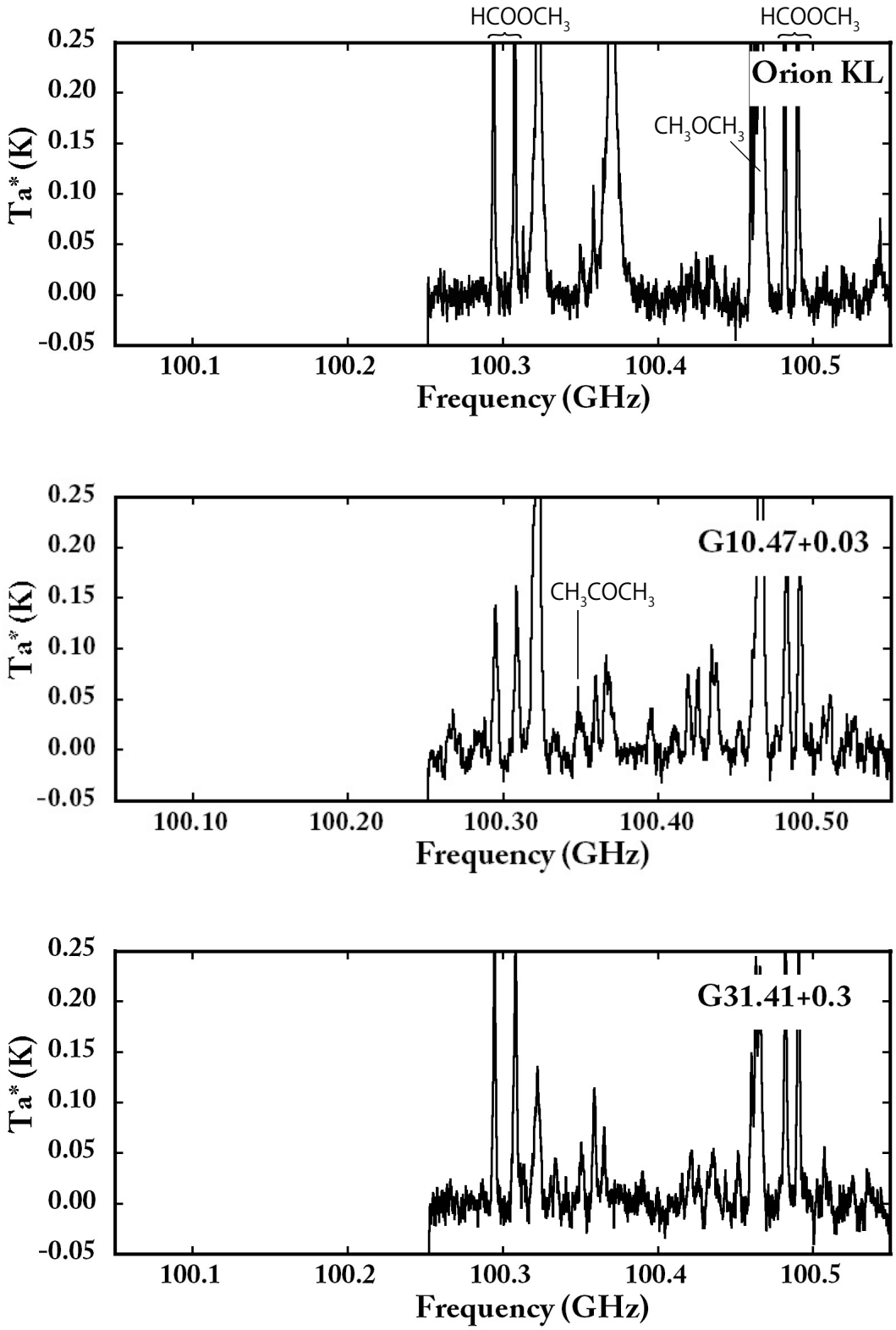

Fig. 4.— Observed Spectra. $HCOOCH_3$ and CH_3OCH_3 were detected.

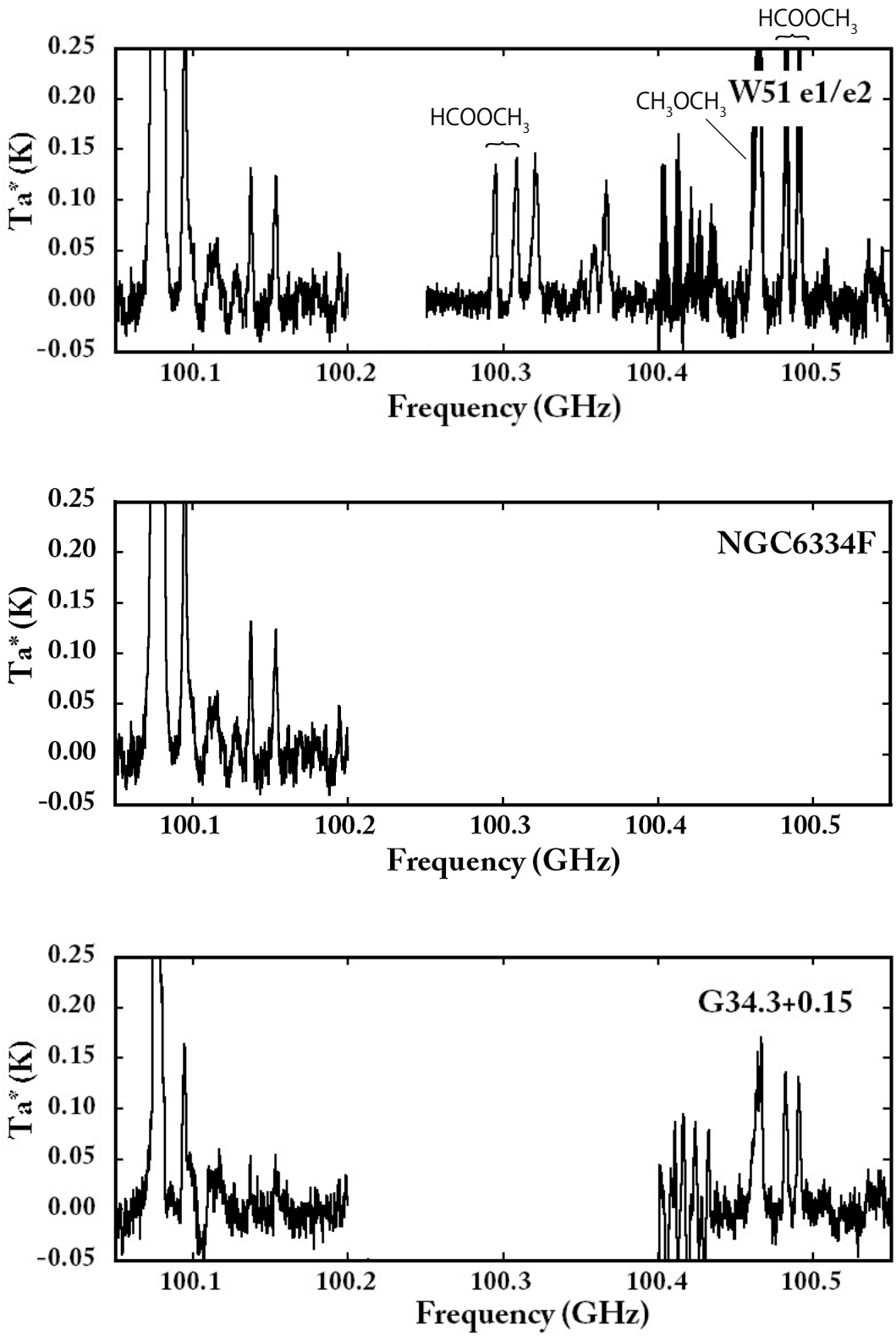

Fig. 4.— Observed Spectra. $HCOOCH_3$ and CH_3OCH_3 were detected.

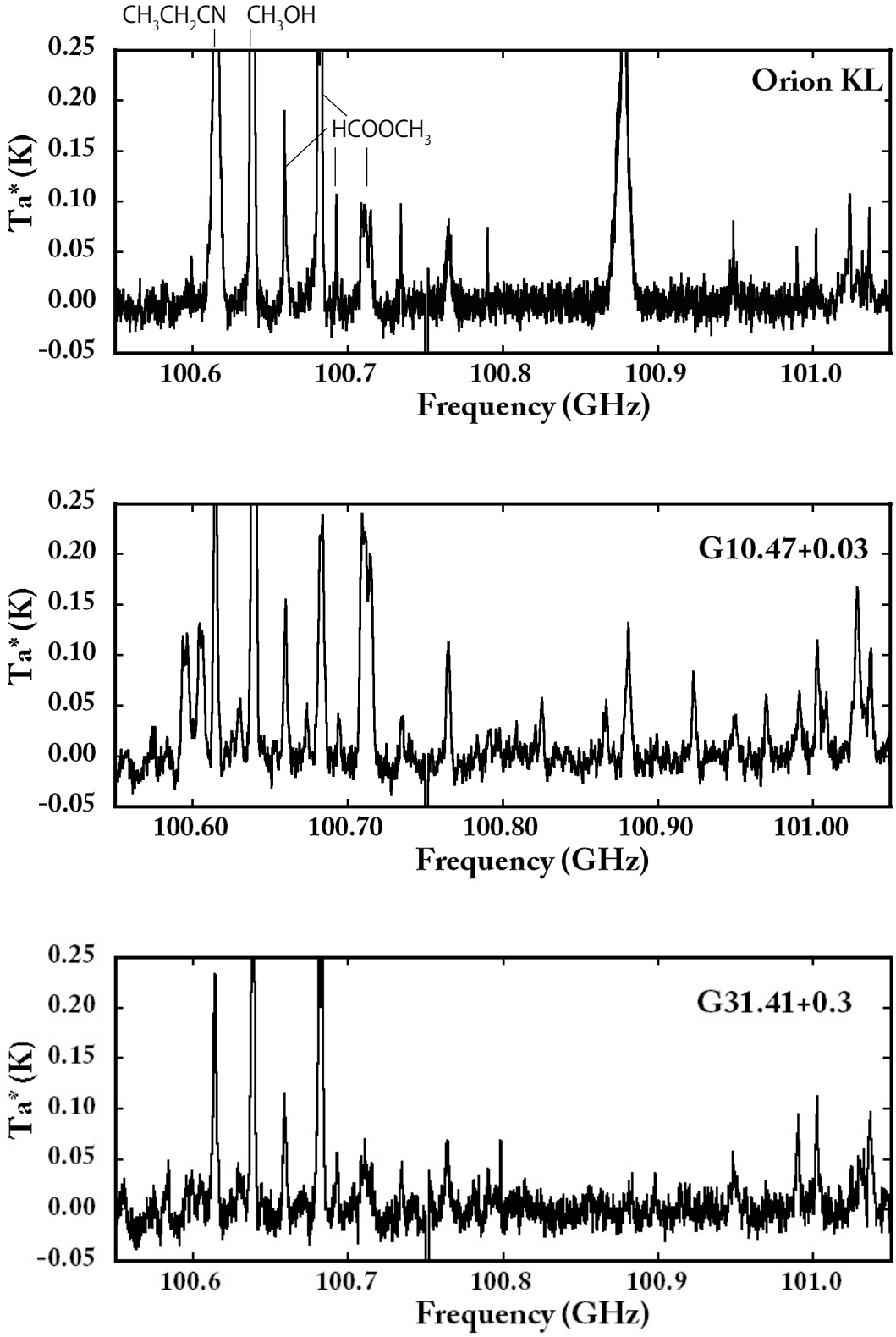

Fig. 4.— Observed Spectra. CH_3CH_2CN, CH_3OH, and $HCOOCH_3$ were detected.

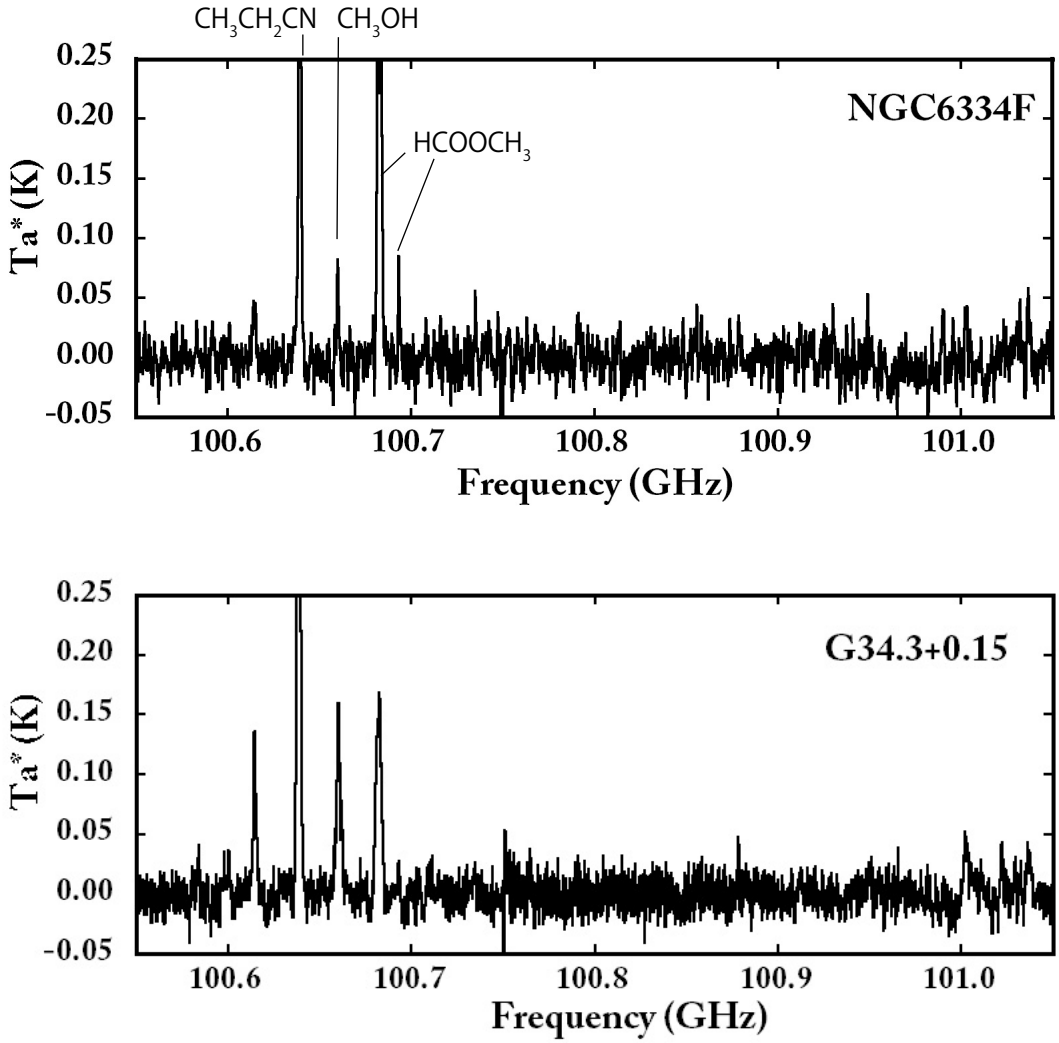

Fig. 4.— Observed Spectra. CH_3CH_2CN, CH_3OH, and $HCOOCH_3$ were detected.

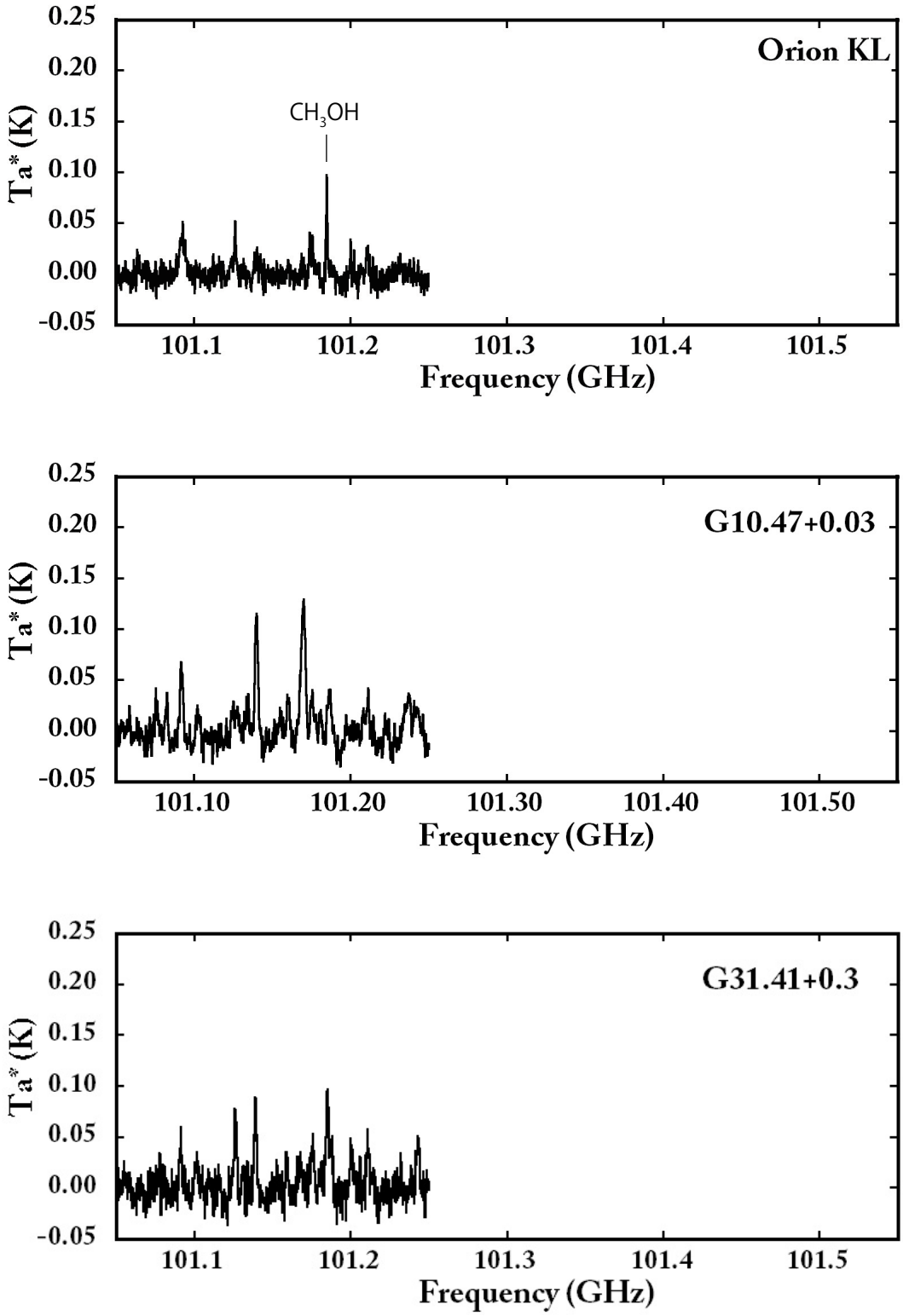

Fig. 4.— Observed Spectra. CH_3OH was detected.

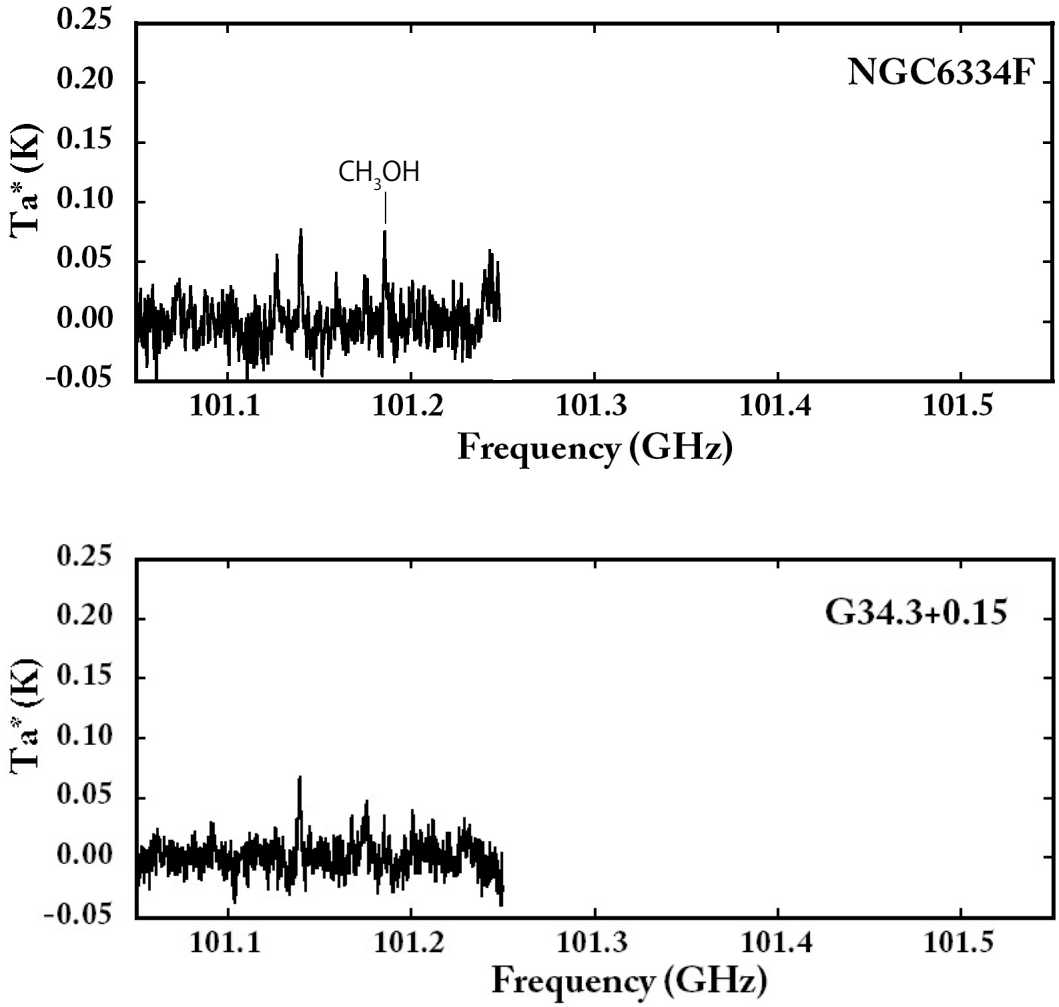

Fig. 4.— Observed Spectra. CH_3OH was detected.

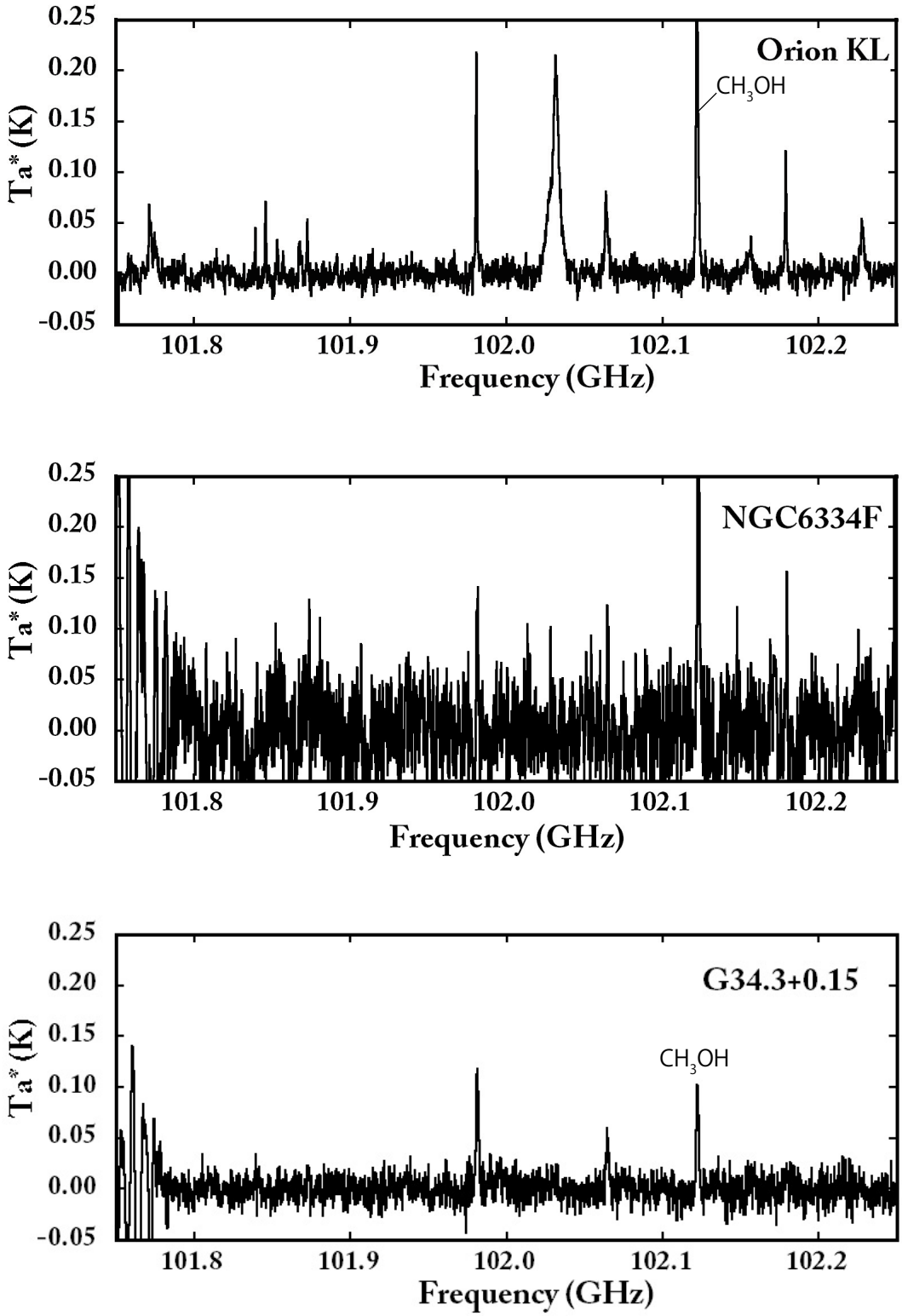

Fig. 4.— Observed Spectra. CH_3OH was detected.

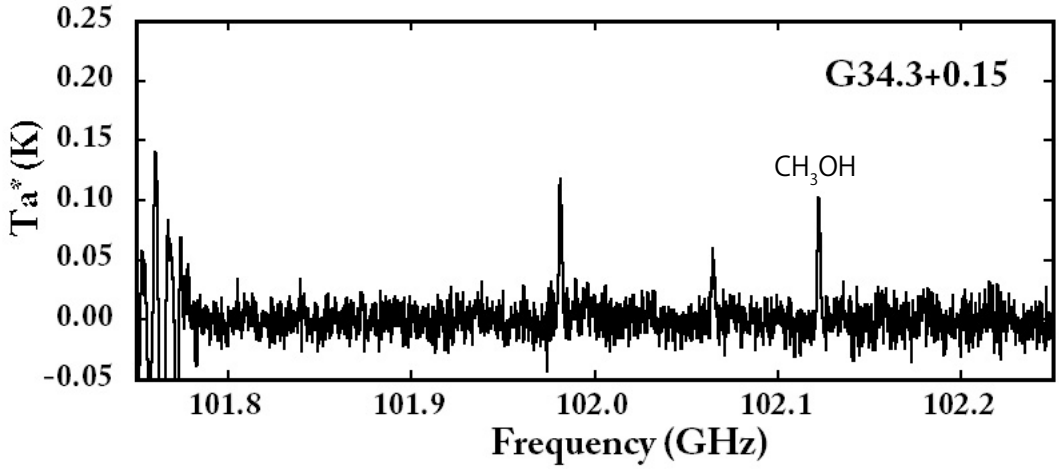

Fig. 4.— Observed Spectra. CH_3OH was detected.

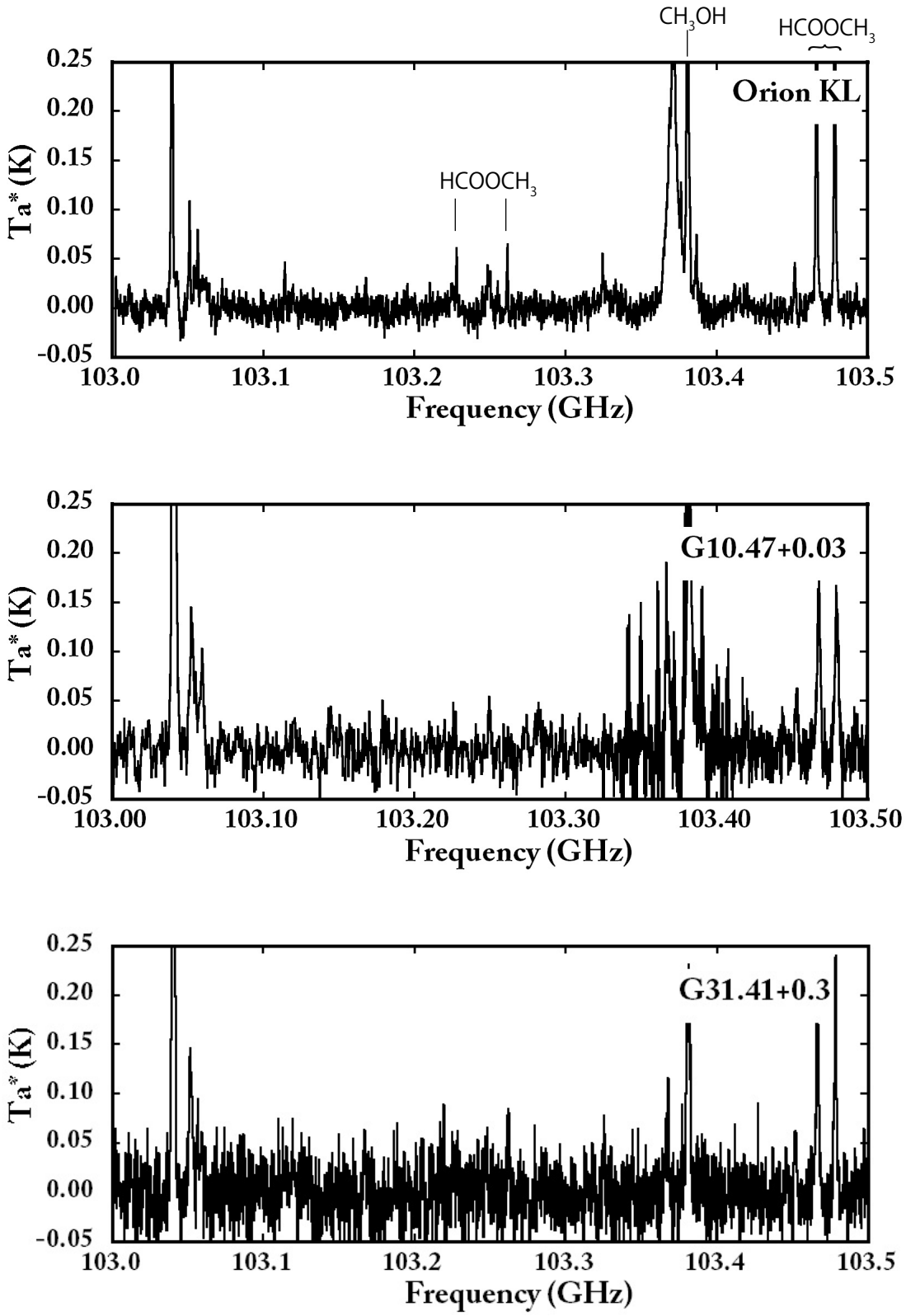

Fig. 4.— Observed Spectra. $HCOOCH_3$ and CH_3OH were detected.

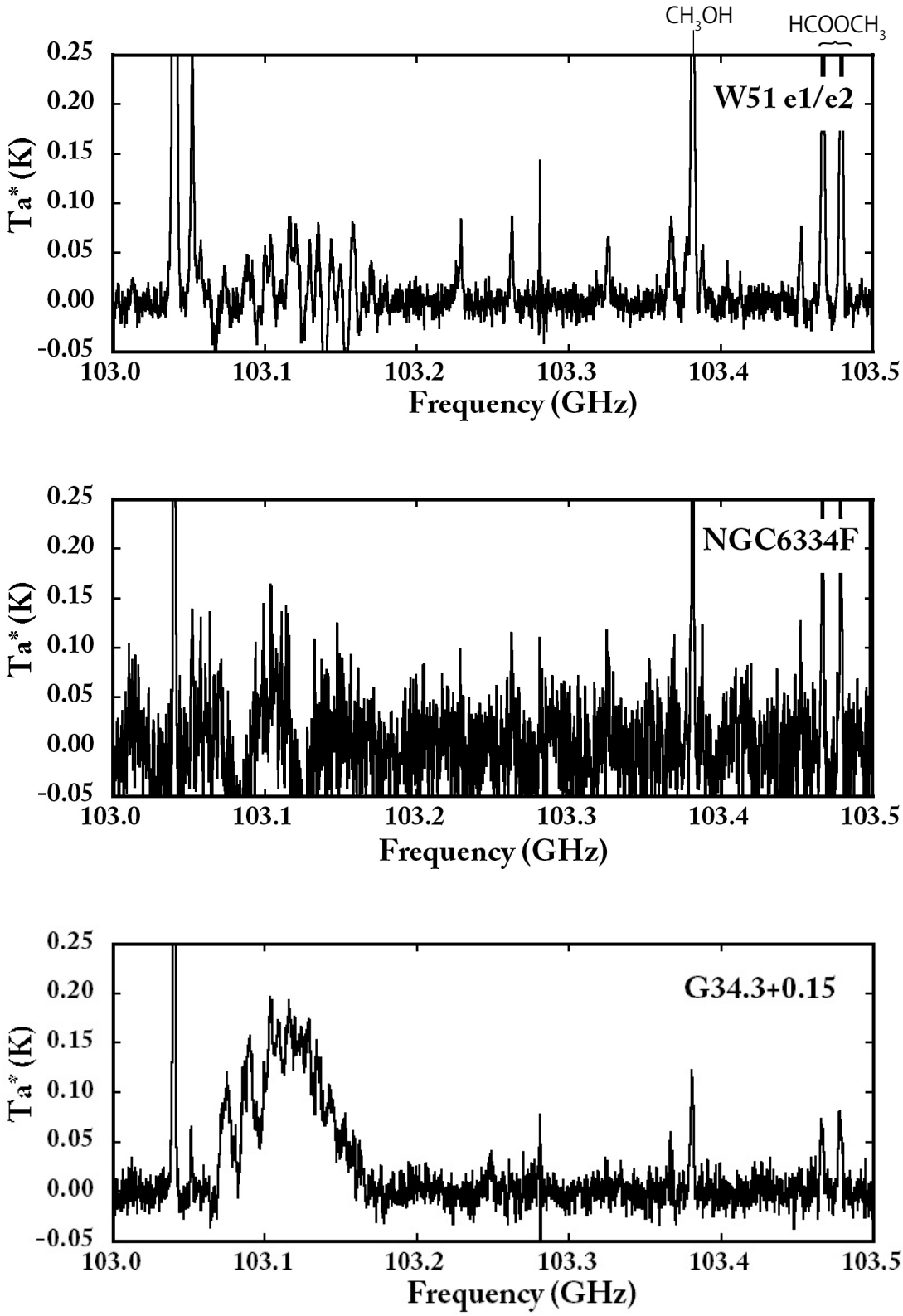

Fig. 4.— Observed Spectra.$HCOOCH_3$ and CH_3OH were detected.

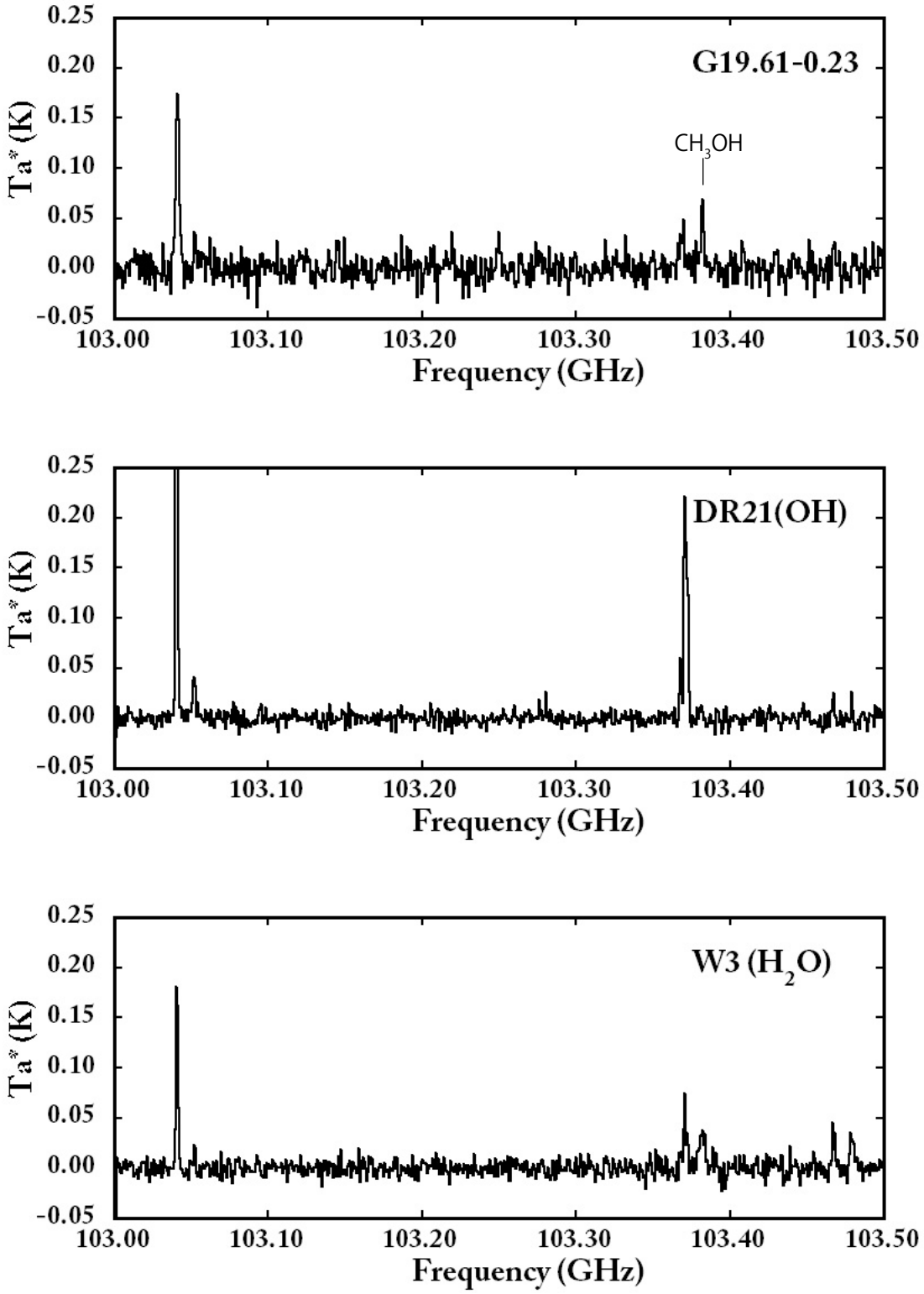

Fig. 4.— Observed Spectra. CH_3OH was detected.

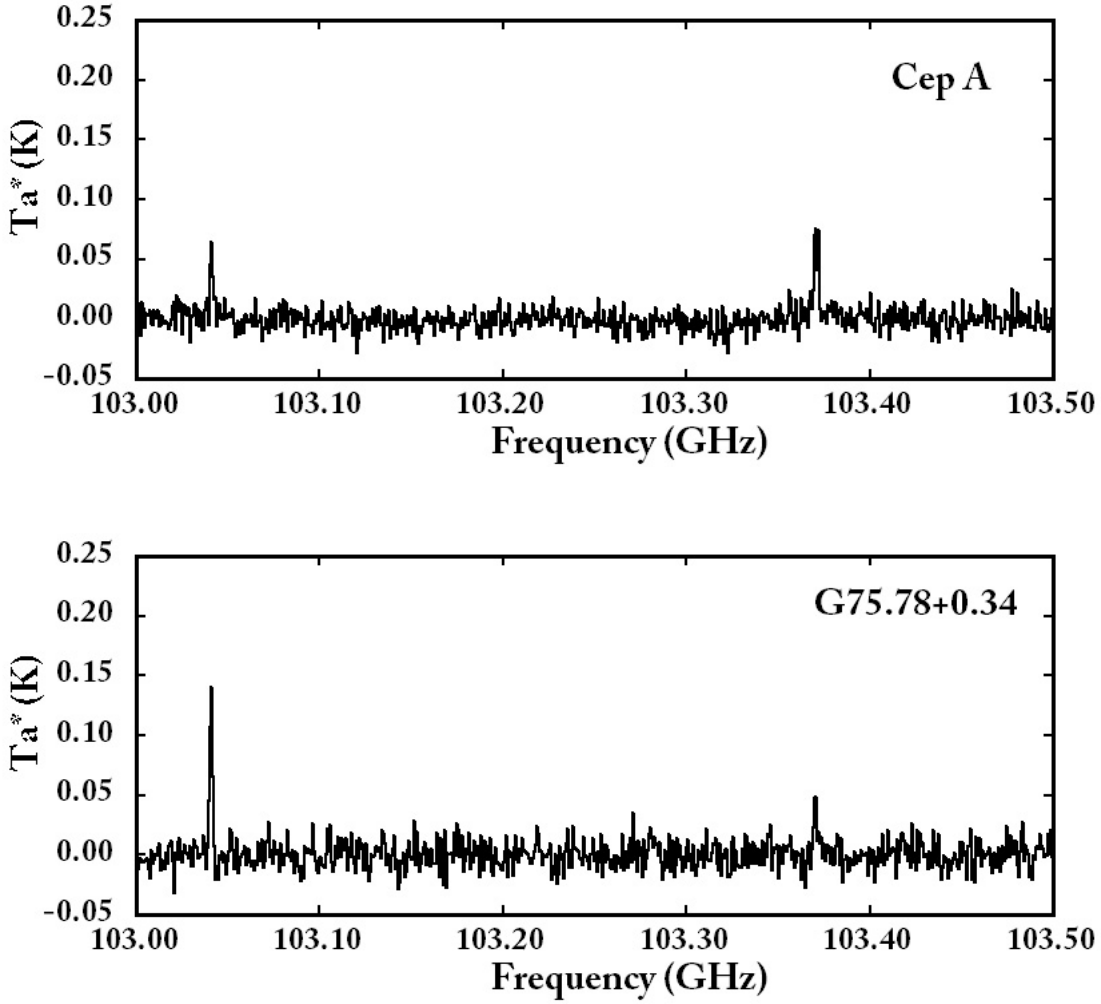

Fig. 4.— Observed Spectra. CH_3OH was detected.

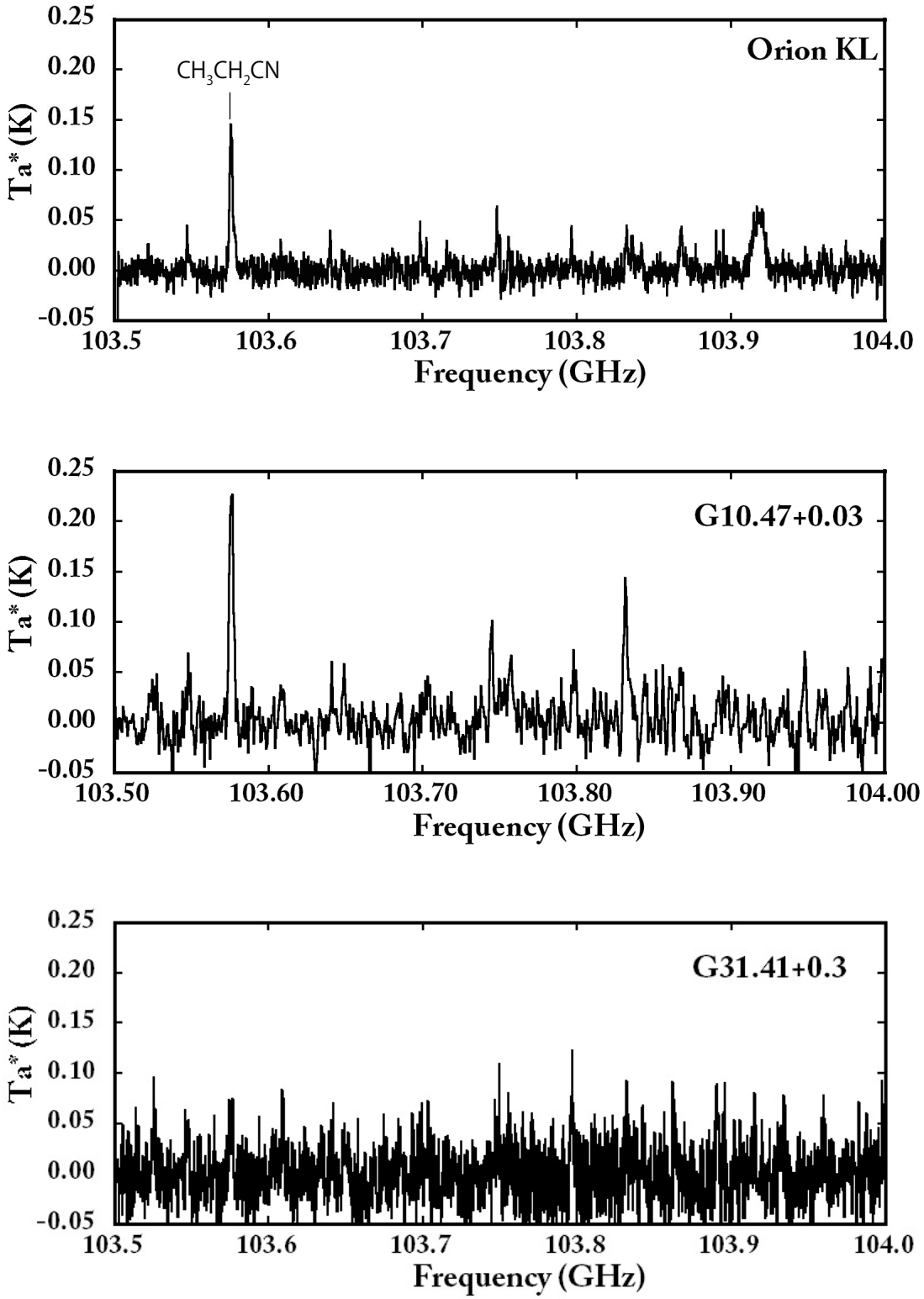

Fig. 4.— Observed Spectra. CH_3CH_2CN was detected.

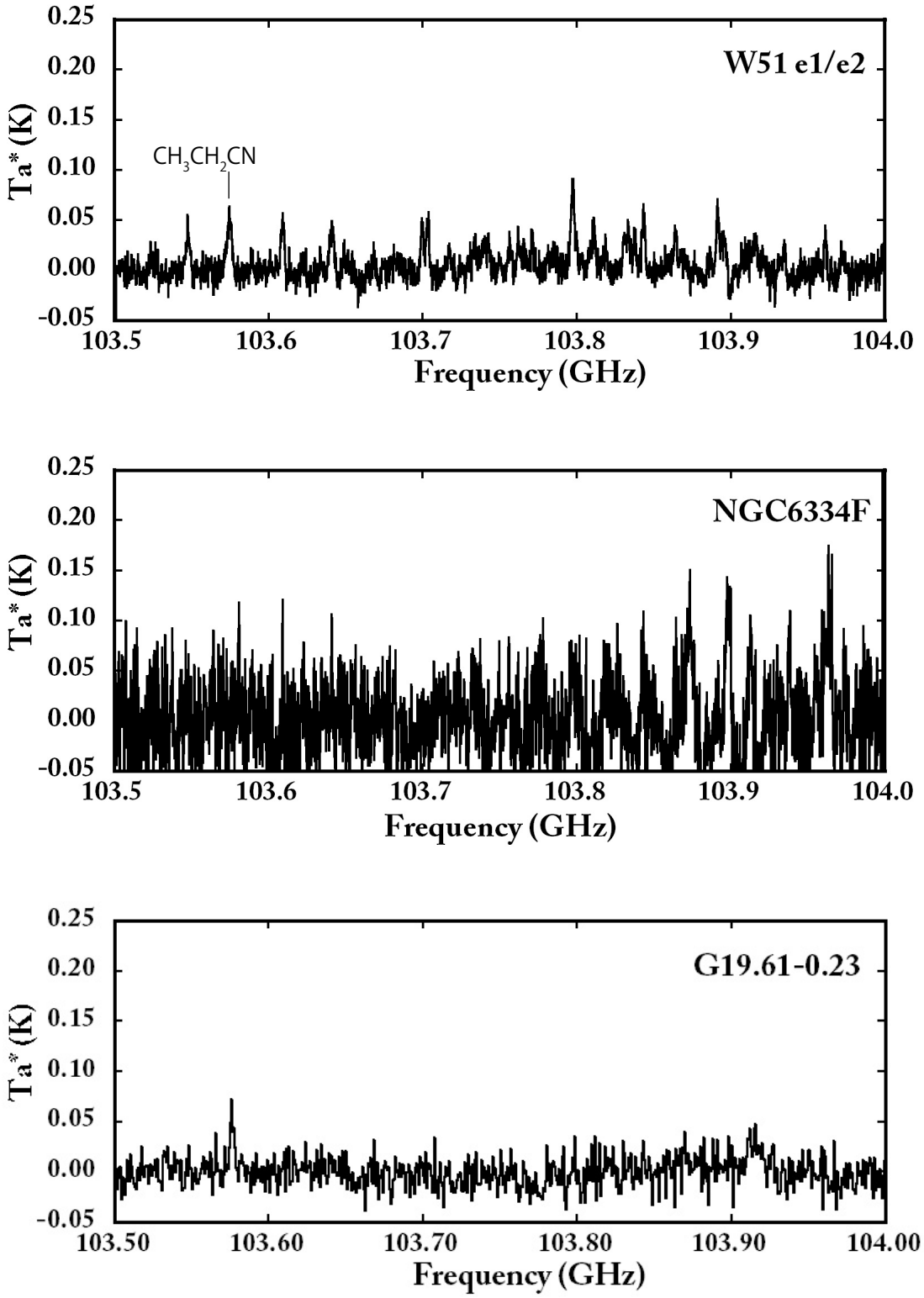

Fig. 4.— Observed Spectra. CH_3CH_2CN was detected.

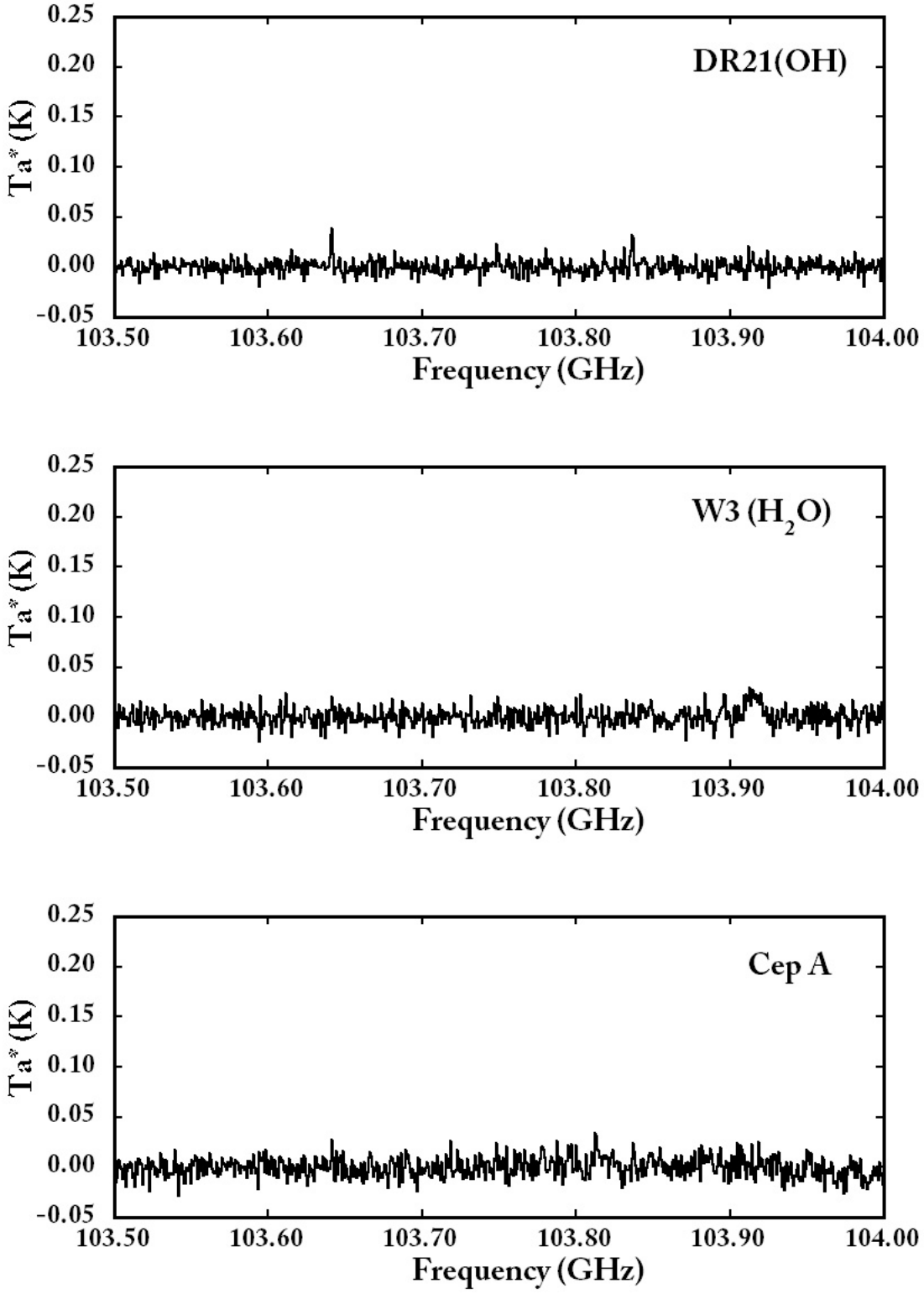

Fig. 4.— Observed Spectra.

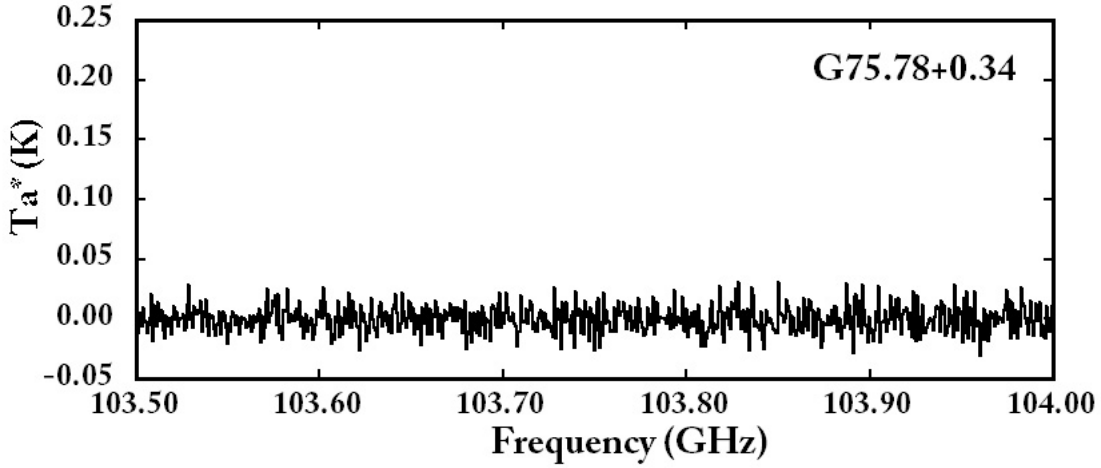

Fig. 4.— Observed Spectra.

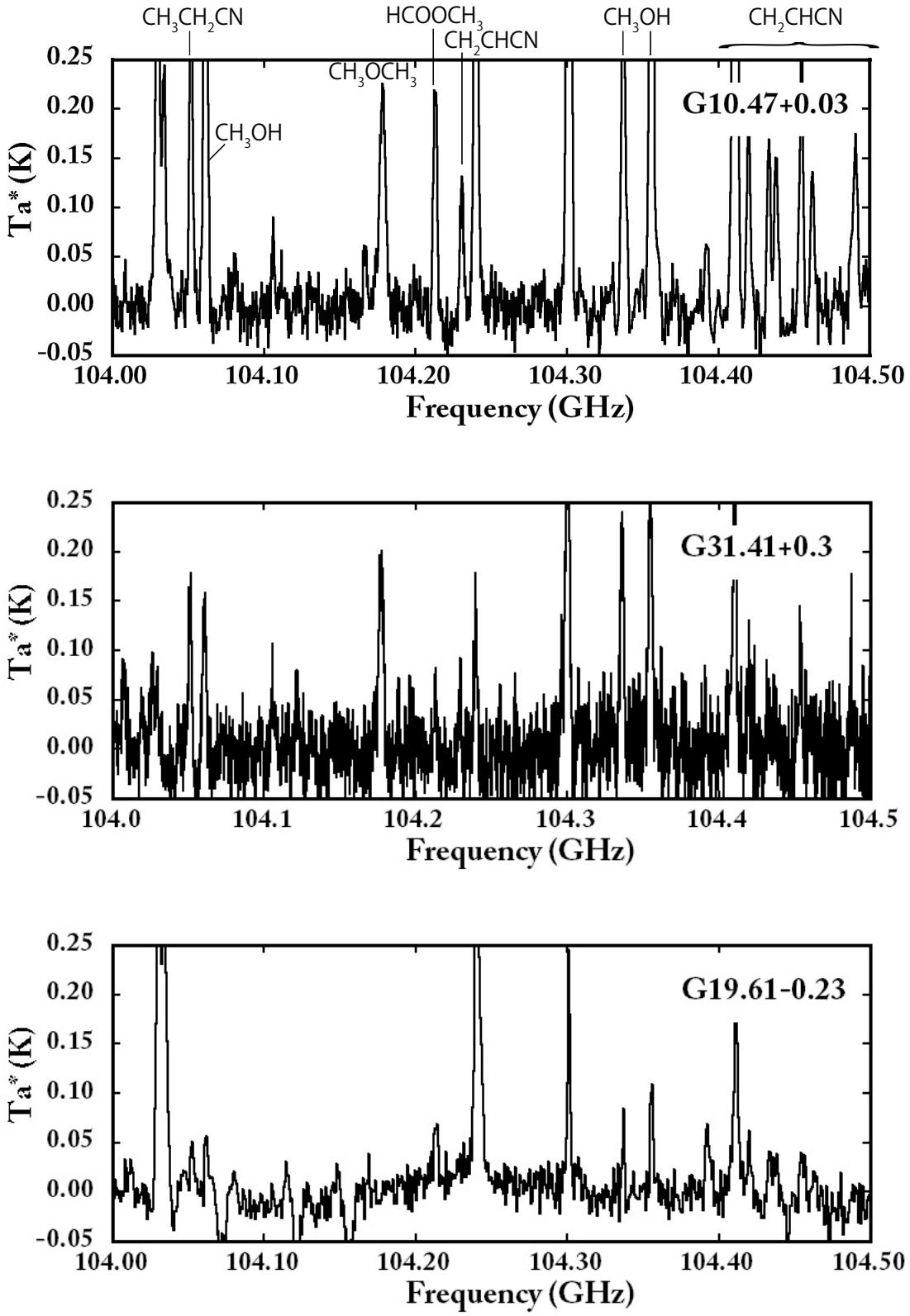

Fig. 4.— Observed Spectra. CH_3CH_2CN, CH_3OH, CH_3OCH_3, $HCOOCH_3$, and CH_2CHCN were detected.

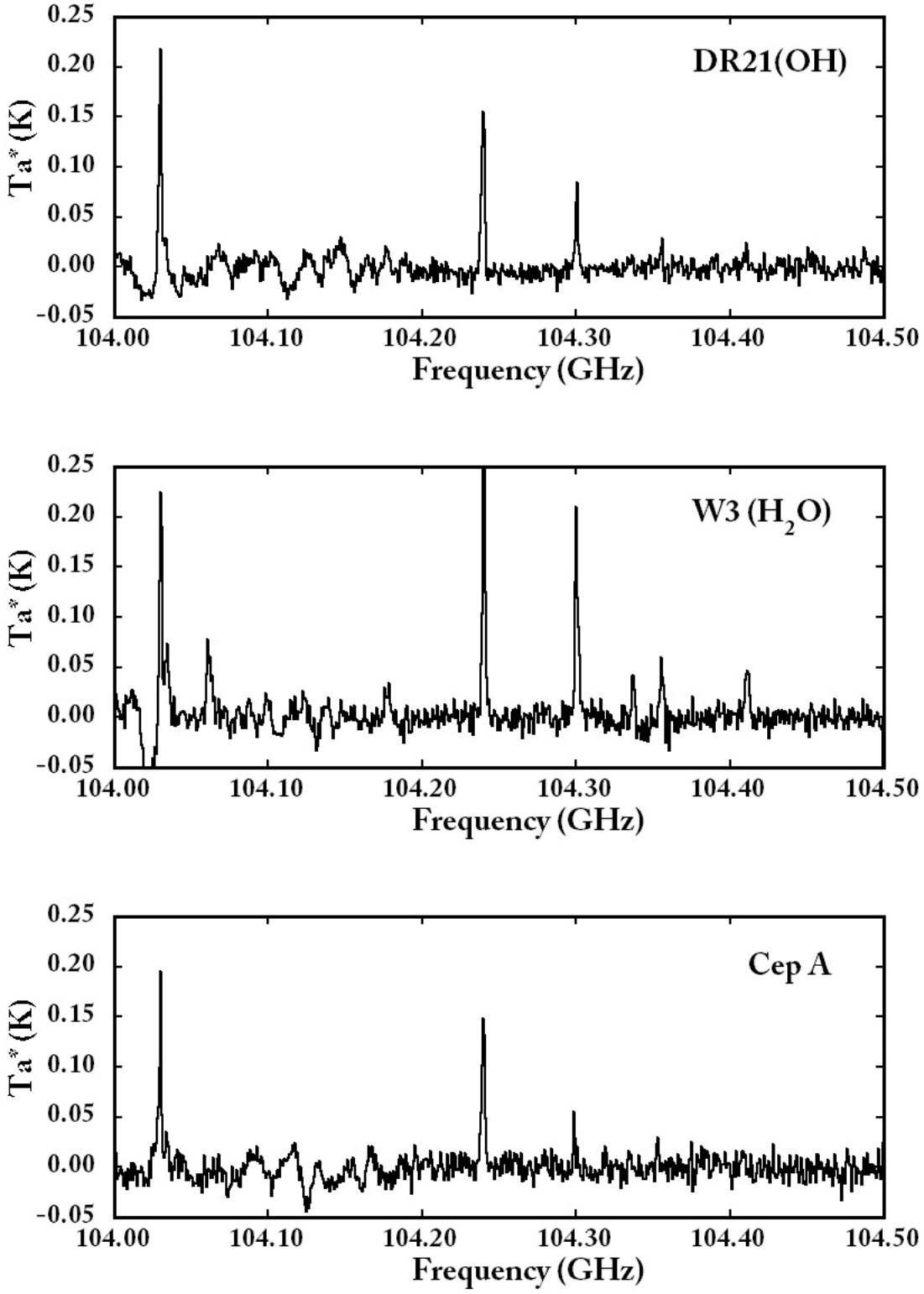

Fig. 4.— Observed Spectra.

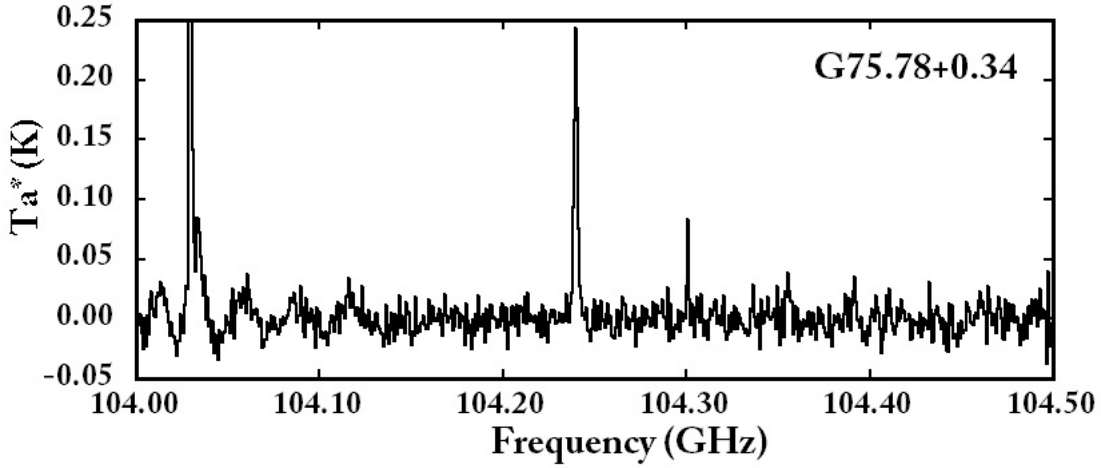

Fig. 4.— Observed Spectra.

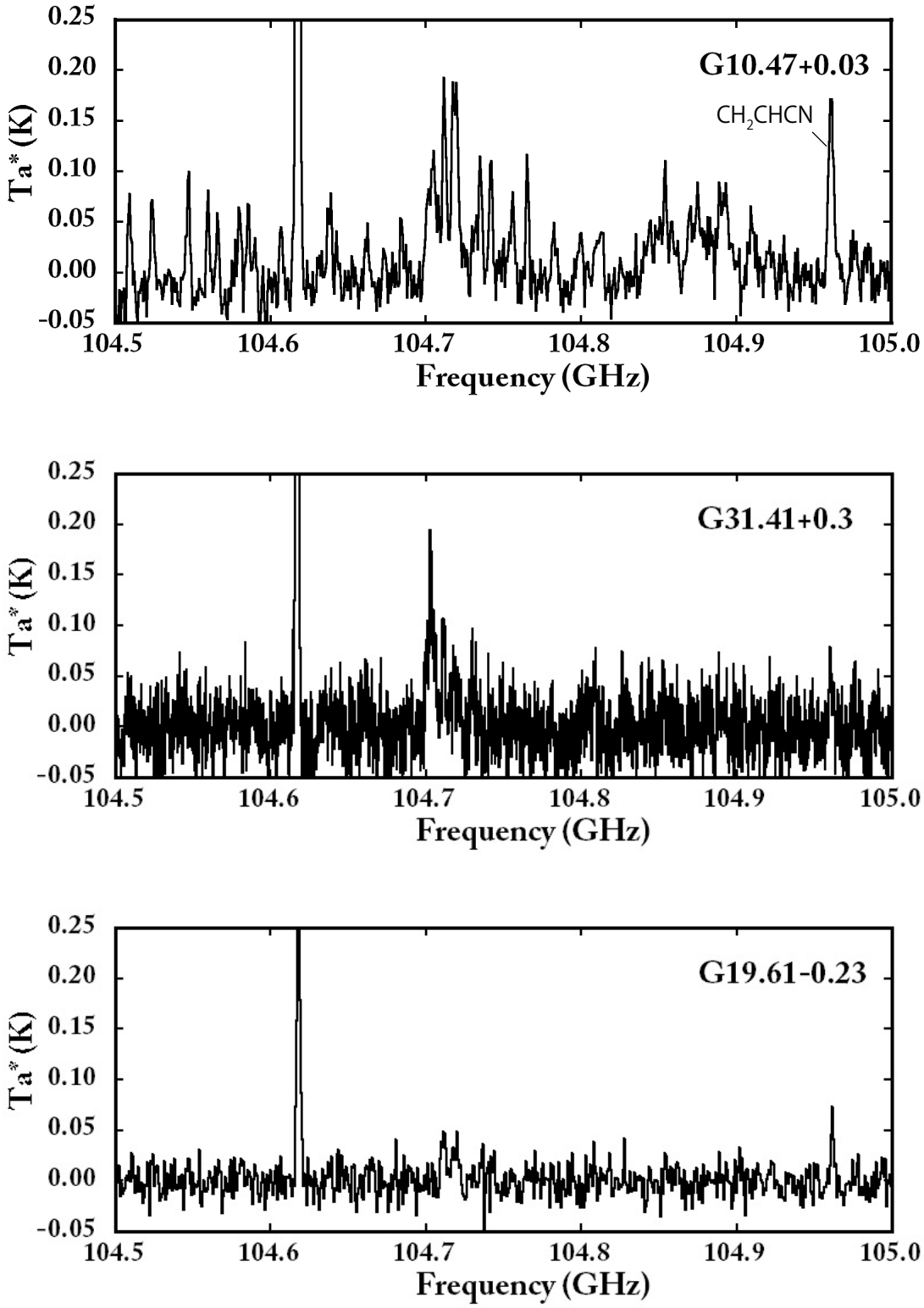

Fig. 4.— Observed Spectra. CH_2CHCN was detected.

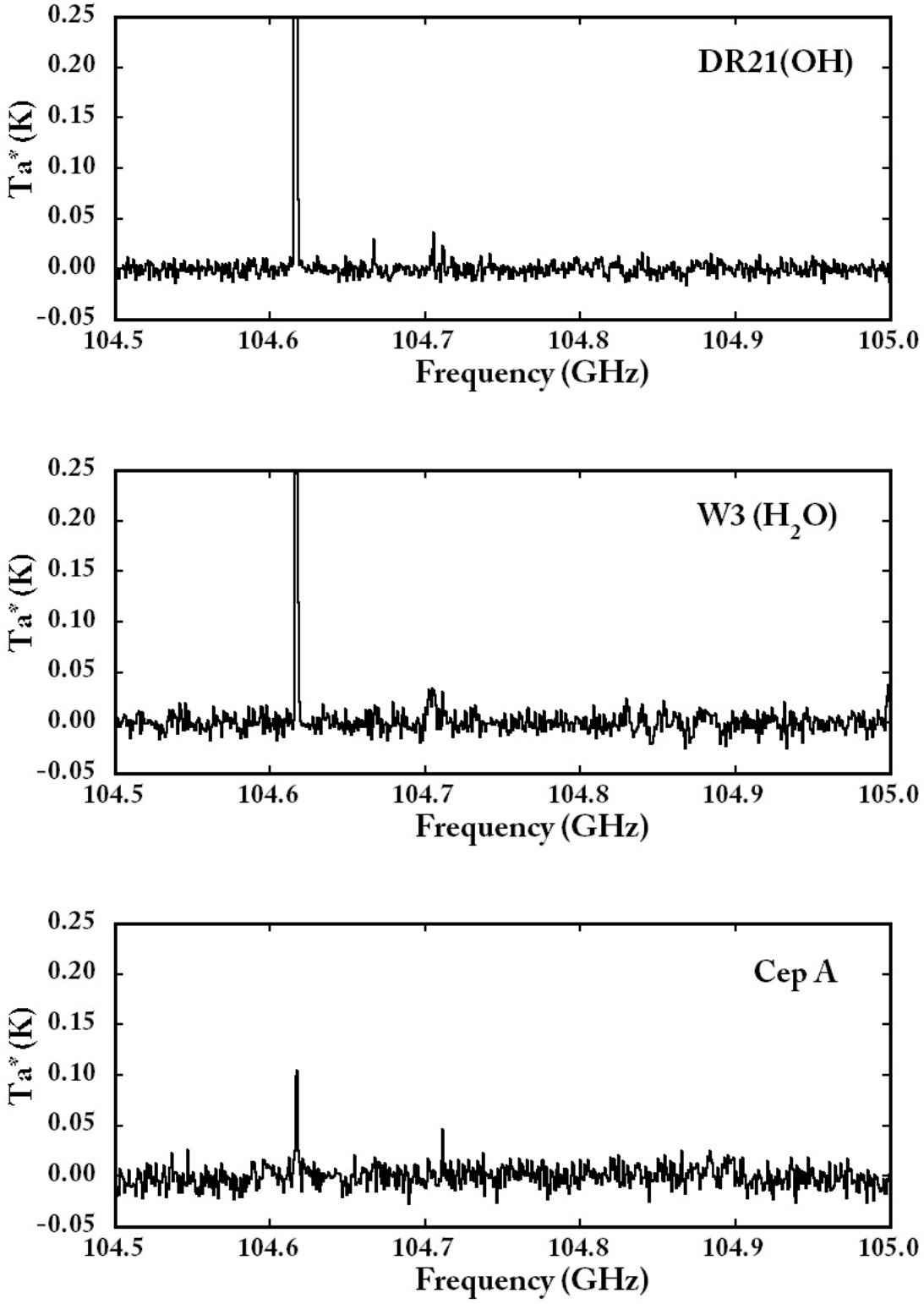

Fig. 4.— Observed Spectra.

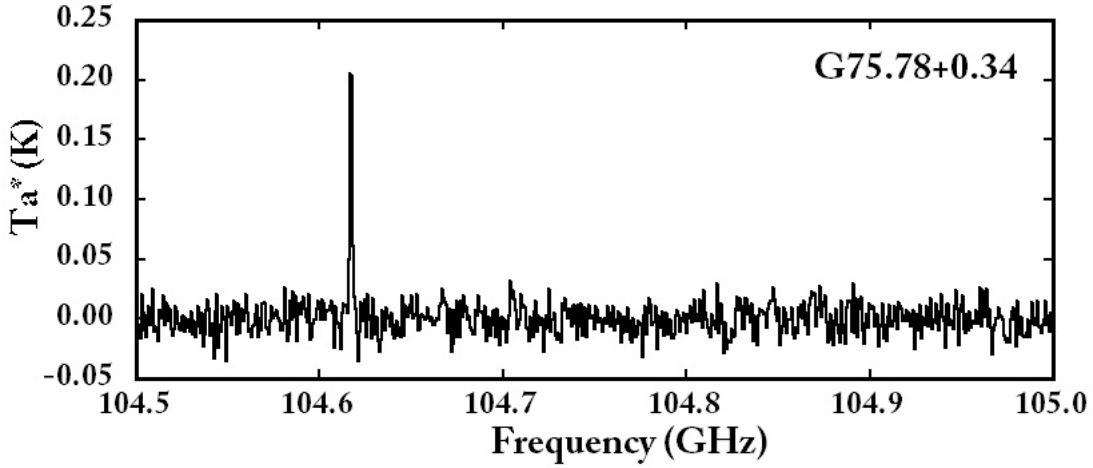

Fig. 4.— Observed Spectra.

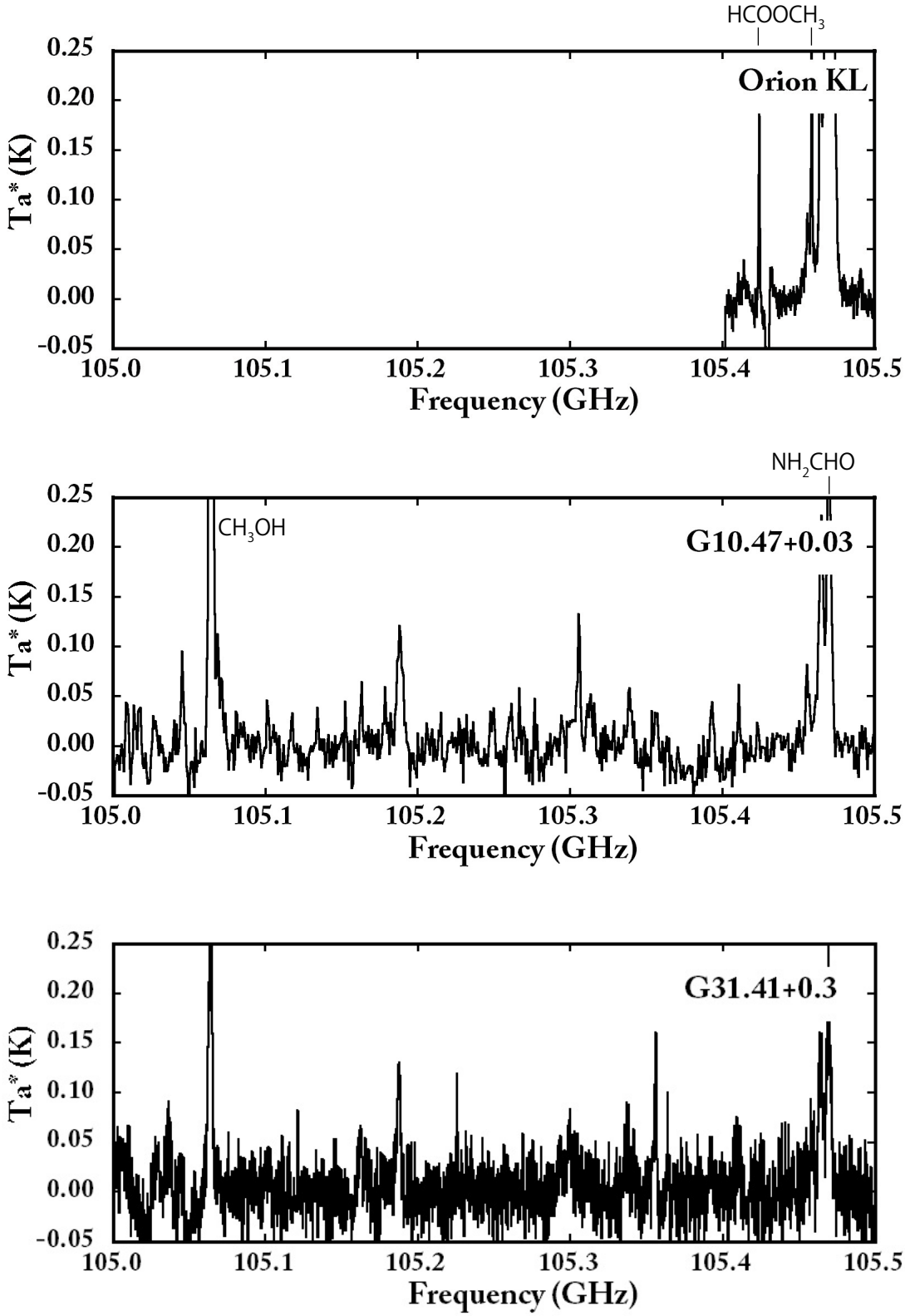

Fig. 4.— Observed Spectra. $HCOOCH_3$, NH_2CHO, and CH_3OH were detected.

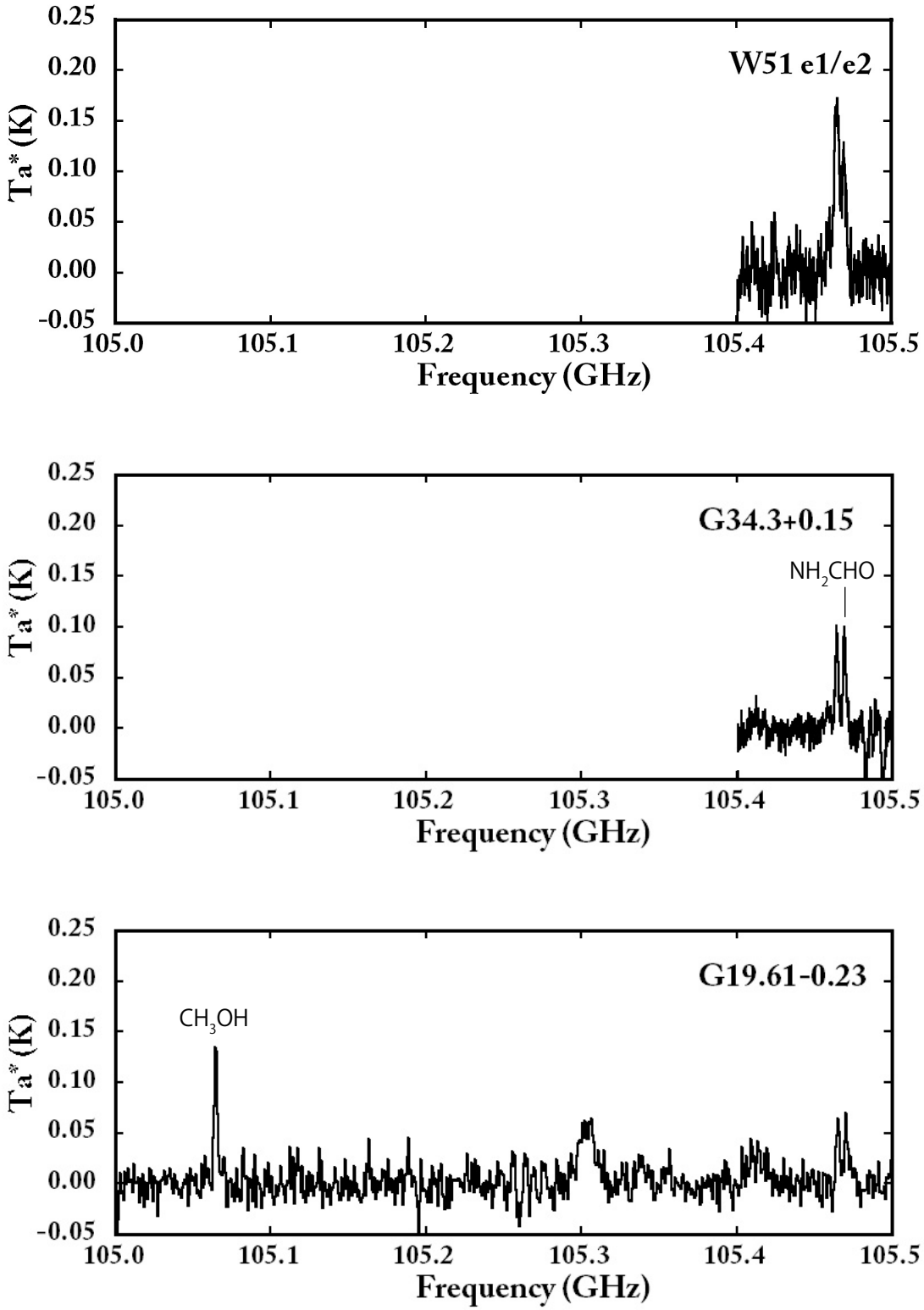

Fig. 4.— Observed Spectra. NH_2CHO, and CH_3OH were detected.

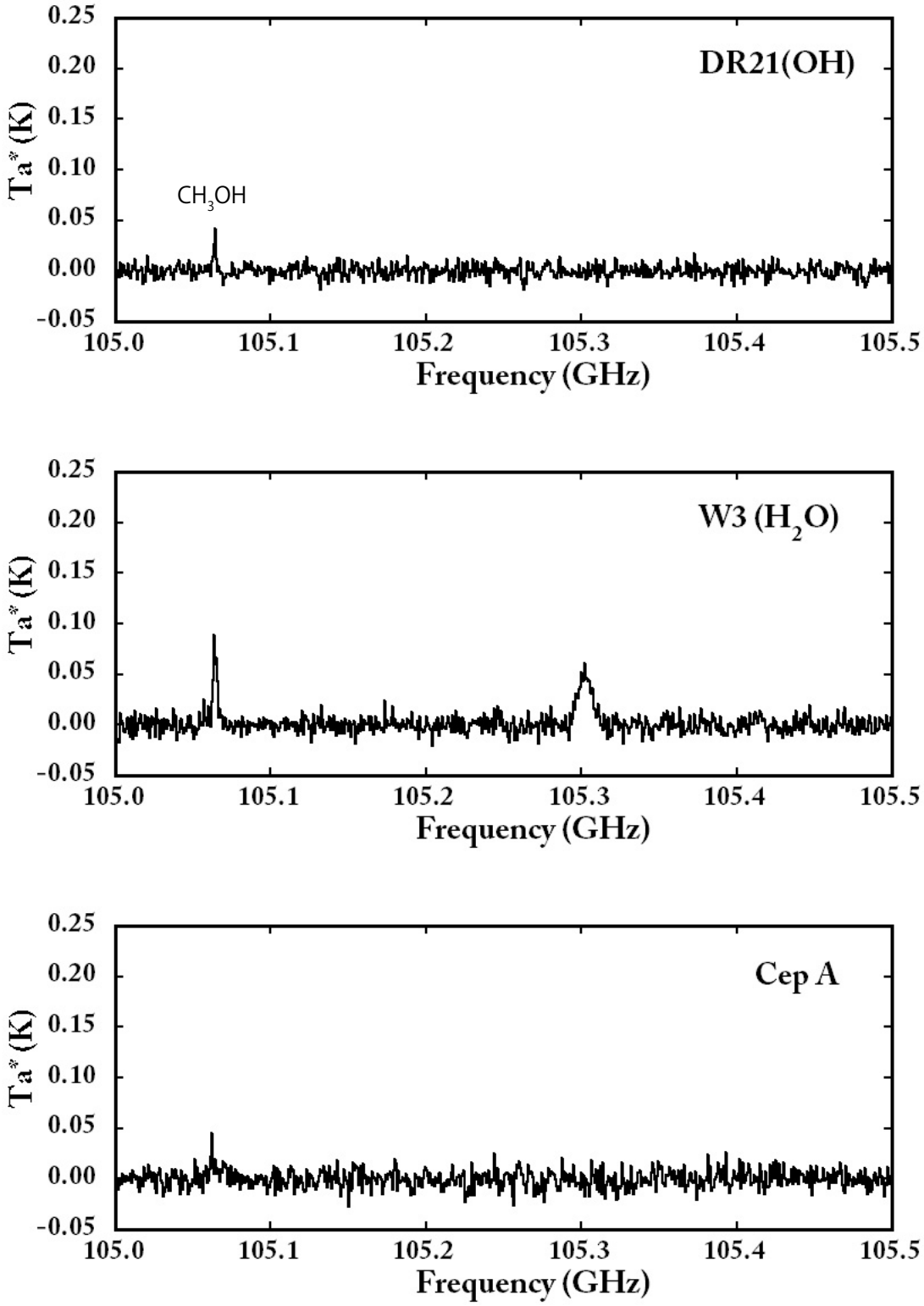

Fig. 4.— Observed Spectra. CH_3OH was detected.

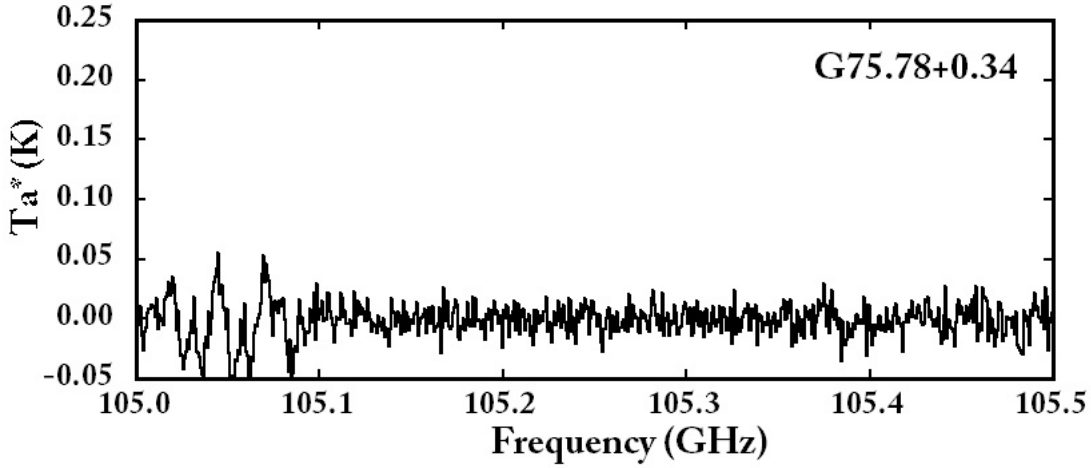

Fig. 4.— Observed Spectra.

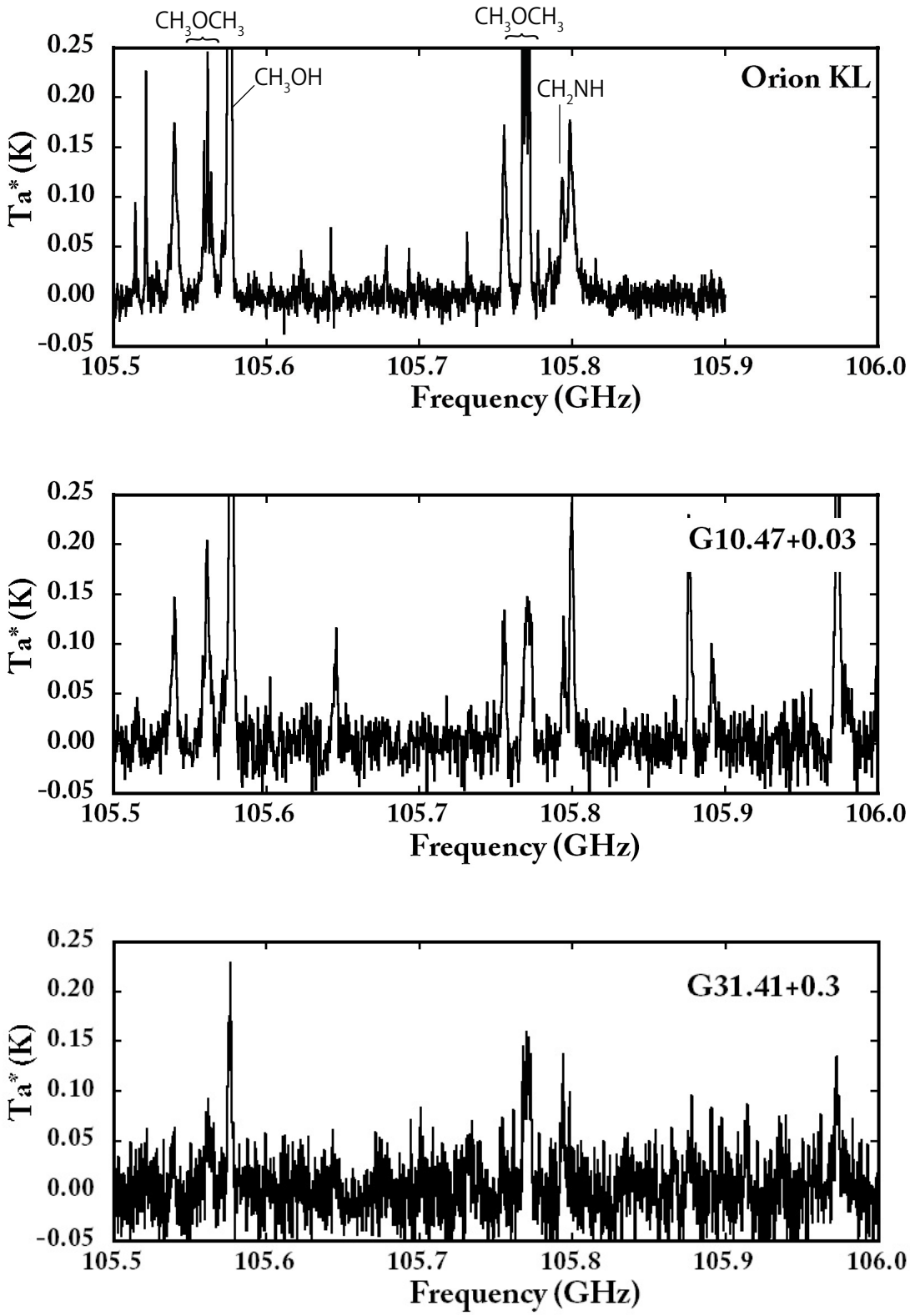

Fig. 4.— Observed Spectra. CH_3OCH_3, CH_3OH, and CH_2NH were detected.

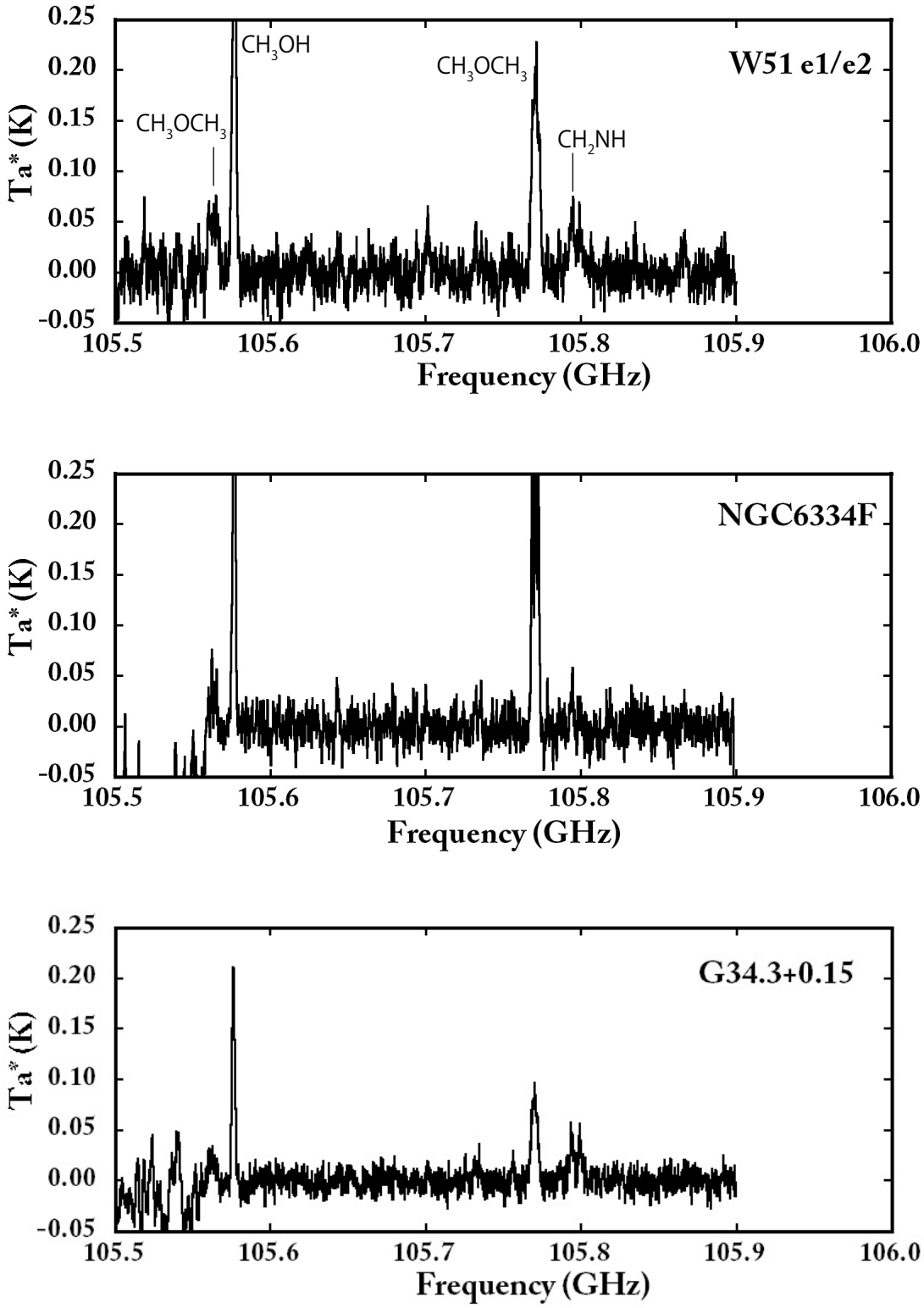

Fig. 4.— Observed Spectra. CH_3OCH_3, CH_3OH, and CH_2NH were detected.

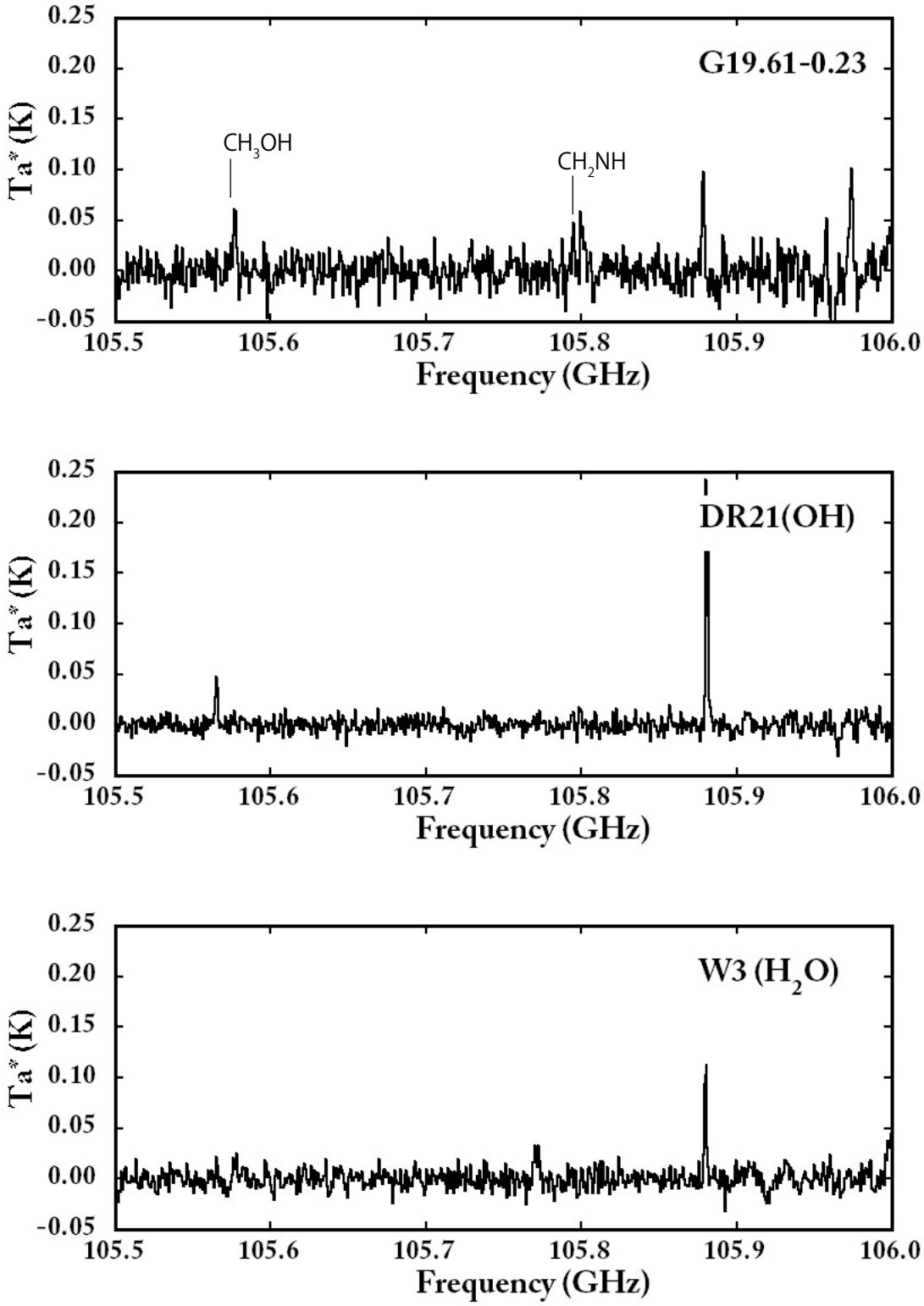

Fig. 4.— Observed Spectra. CH_3OH and CH_2NH were detected.

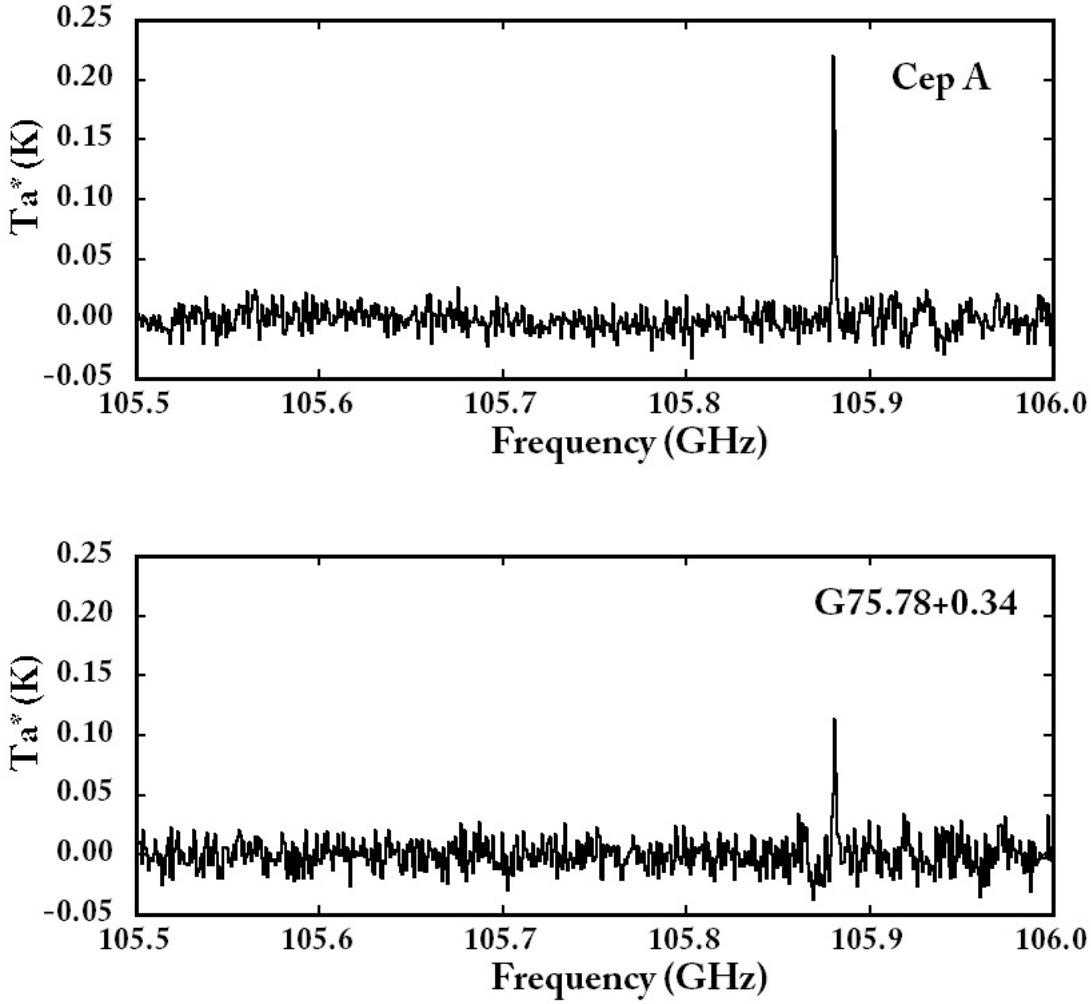

Fig. 4.— Observed Spectra.

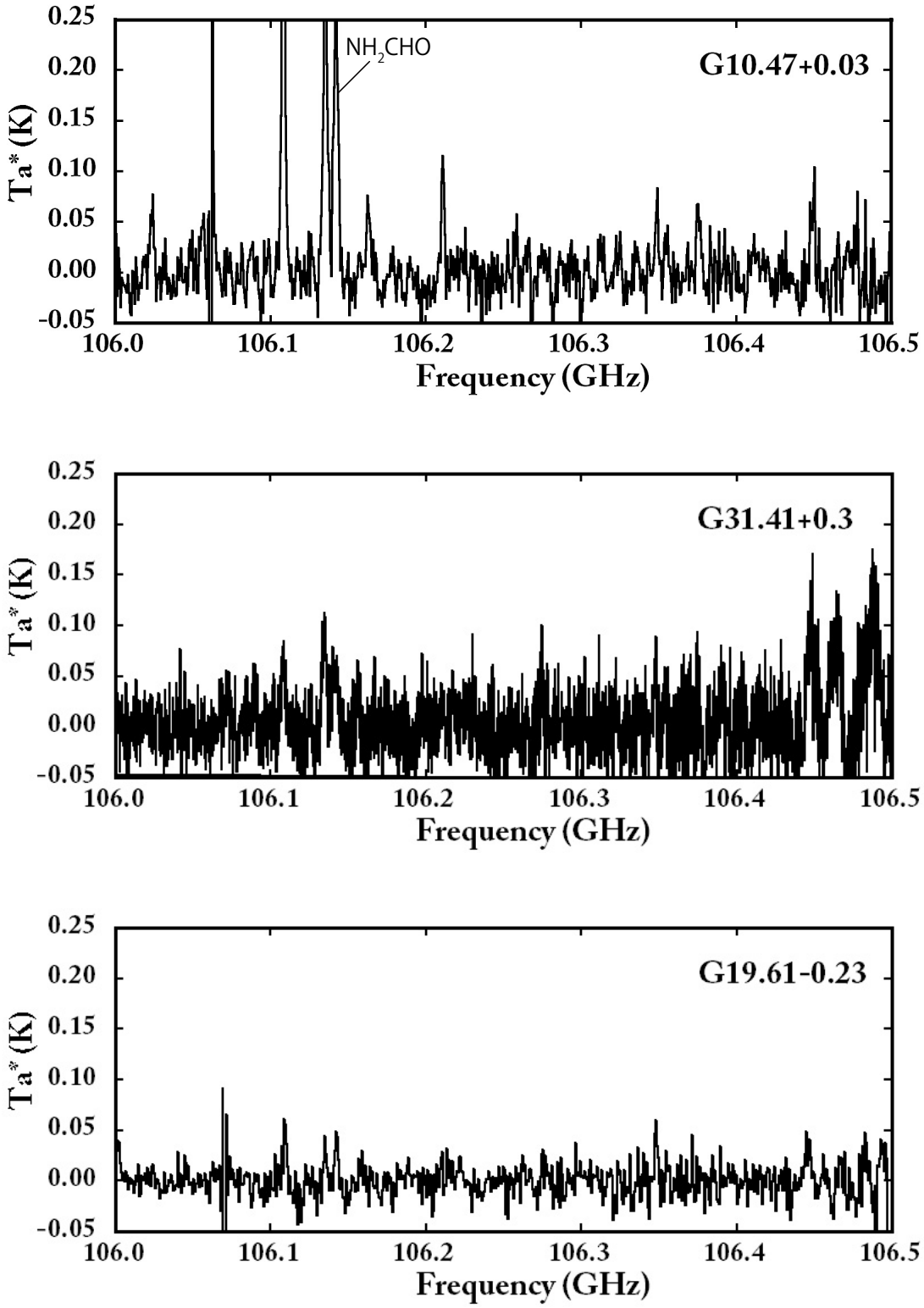

Fig. 4.— Observed Spectra. NH_2CHO was detected.

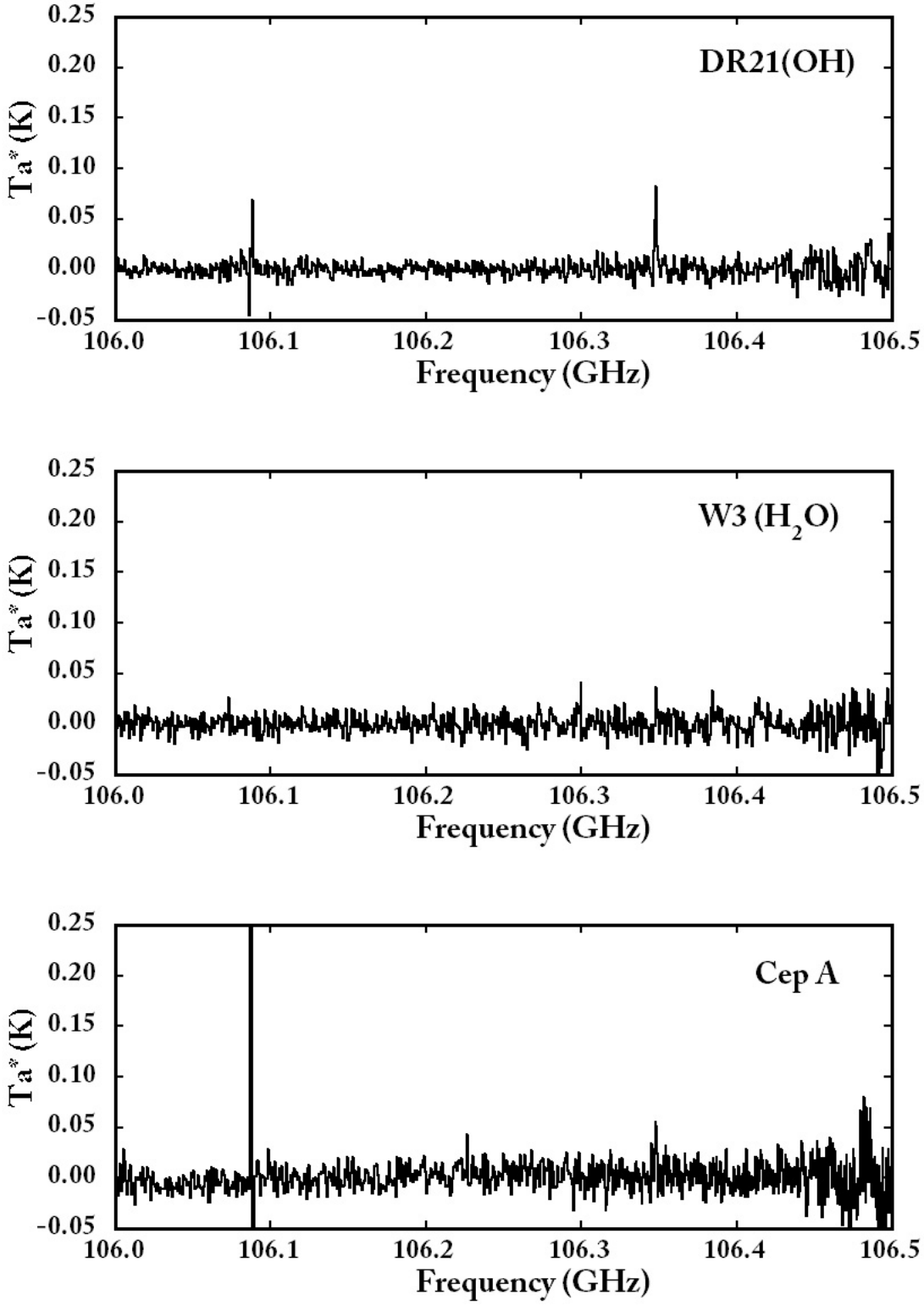

Fig. 4.— Observed Spectra.

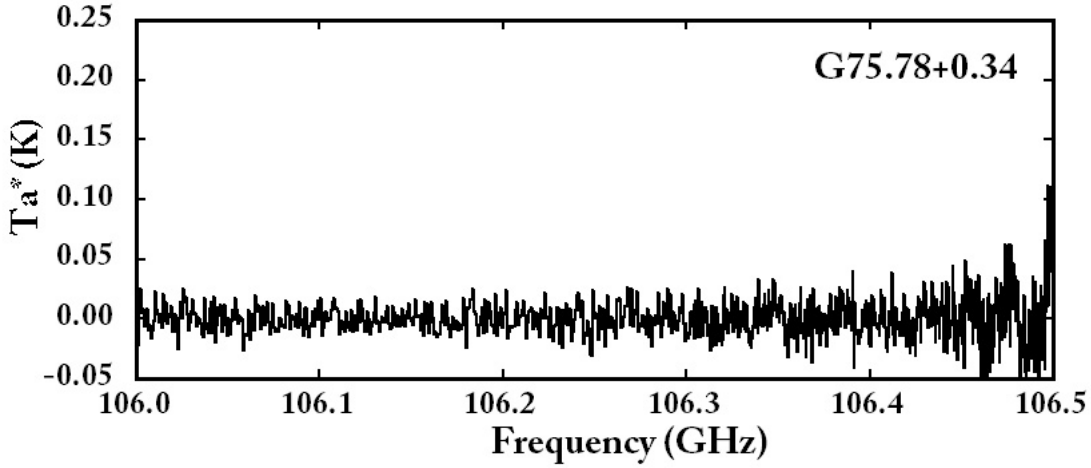

Fig. 4.— Observed Spectra.

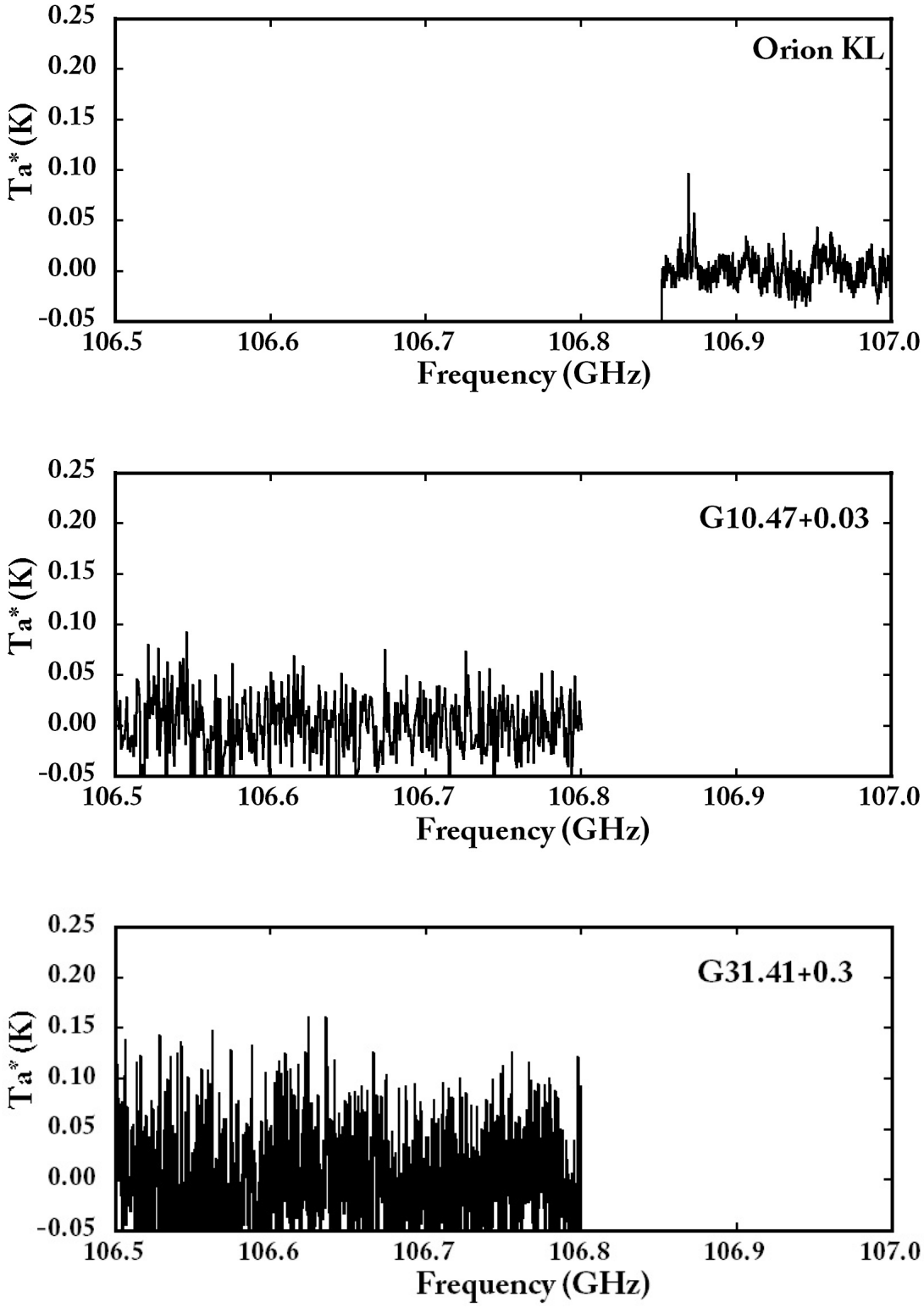

Fig. 4.— Observed Spectra.

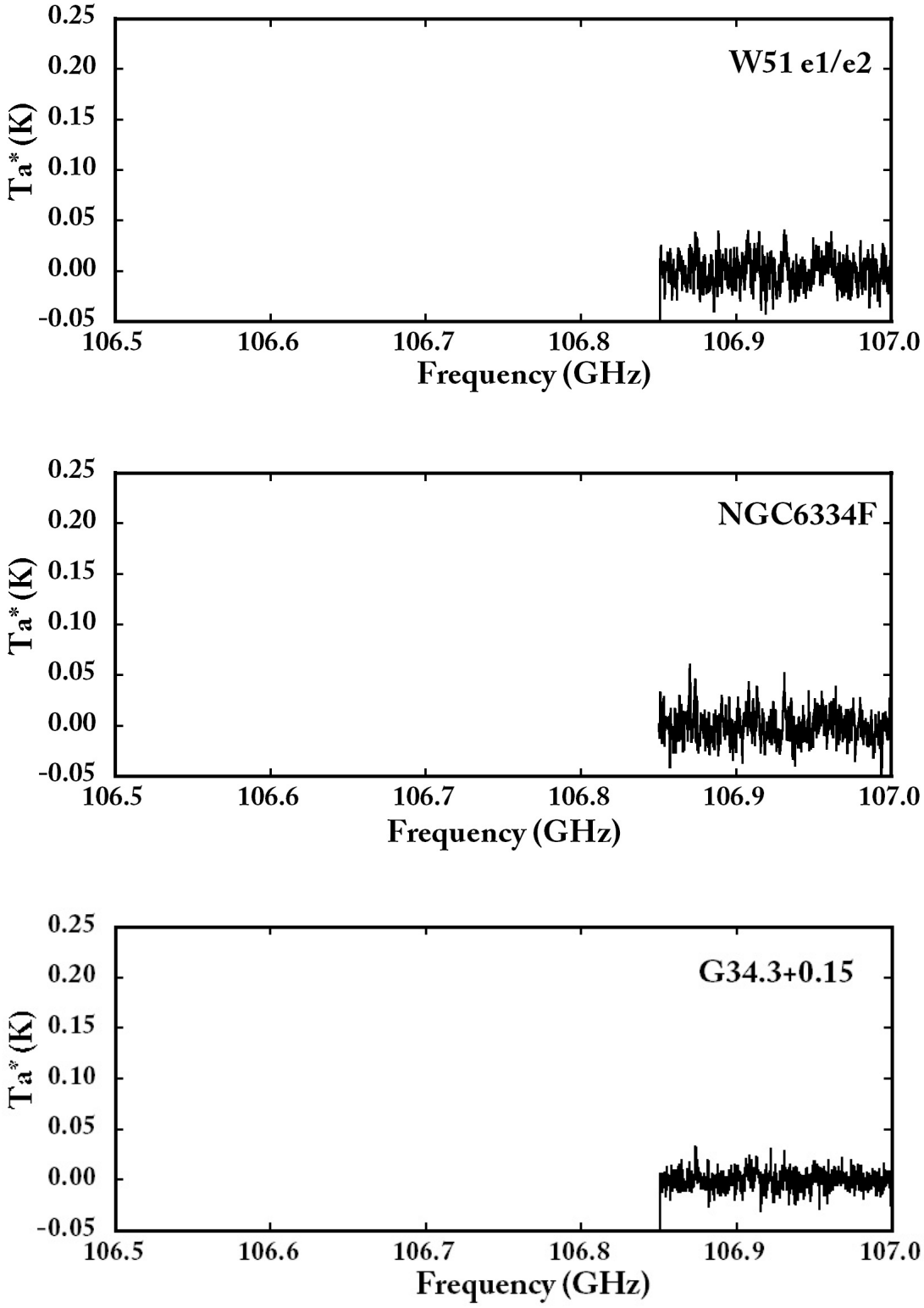

Fig. 4.— Observed Spectra.

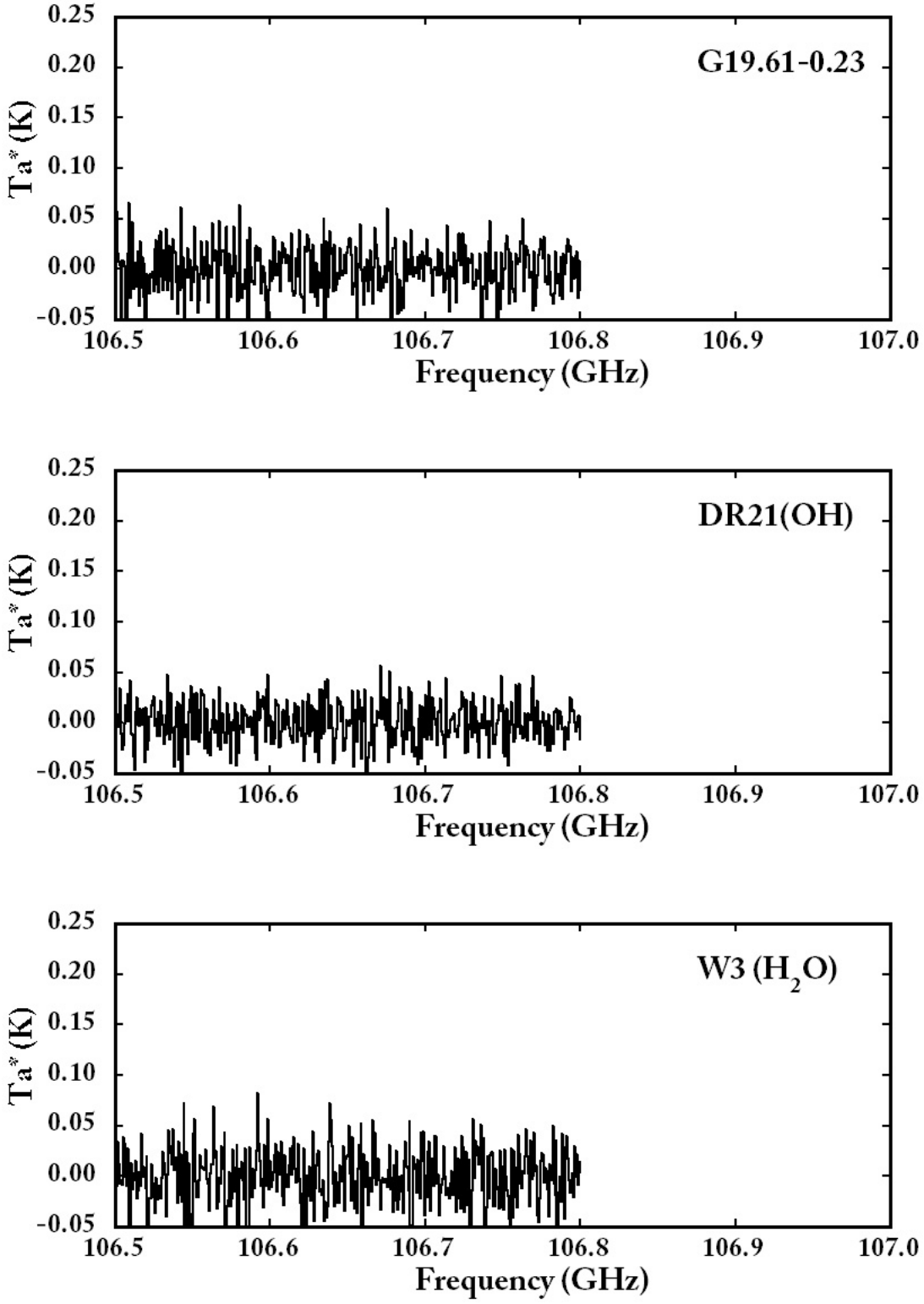

Fig. 4.— Observed Spectra.

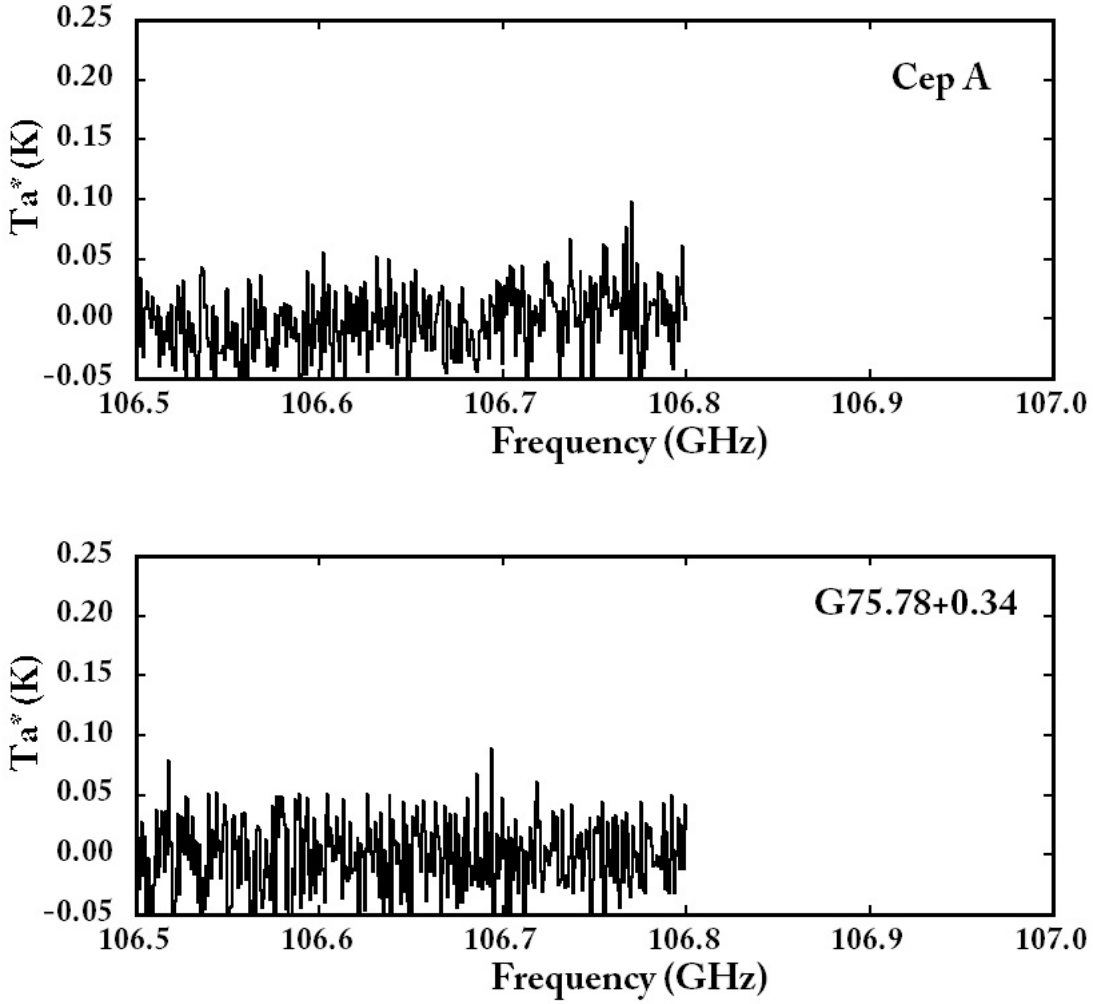

Fig. 4.— Observed Spectra.

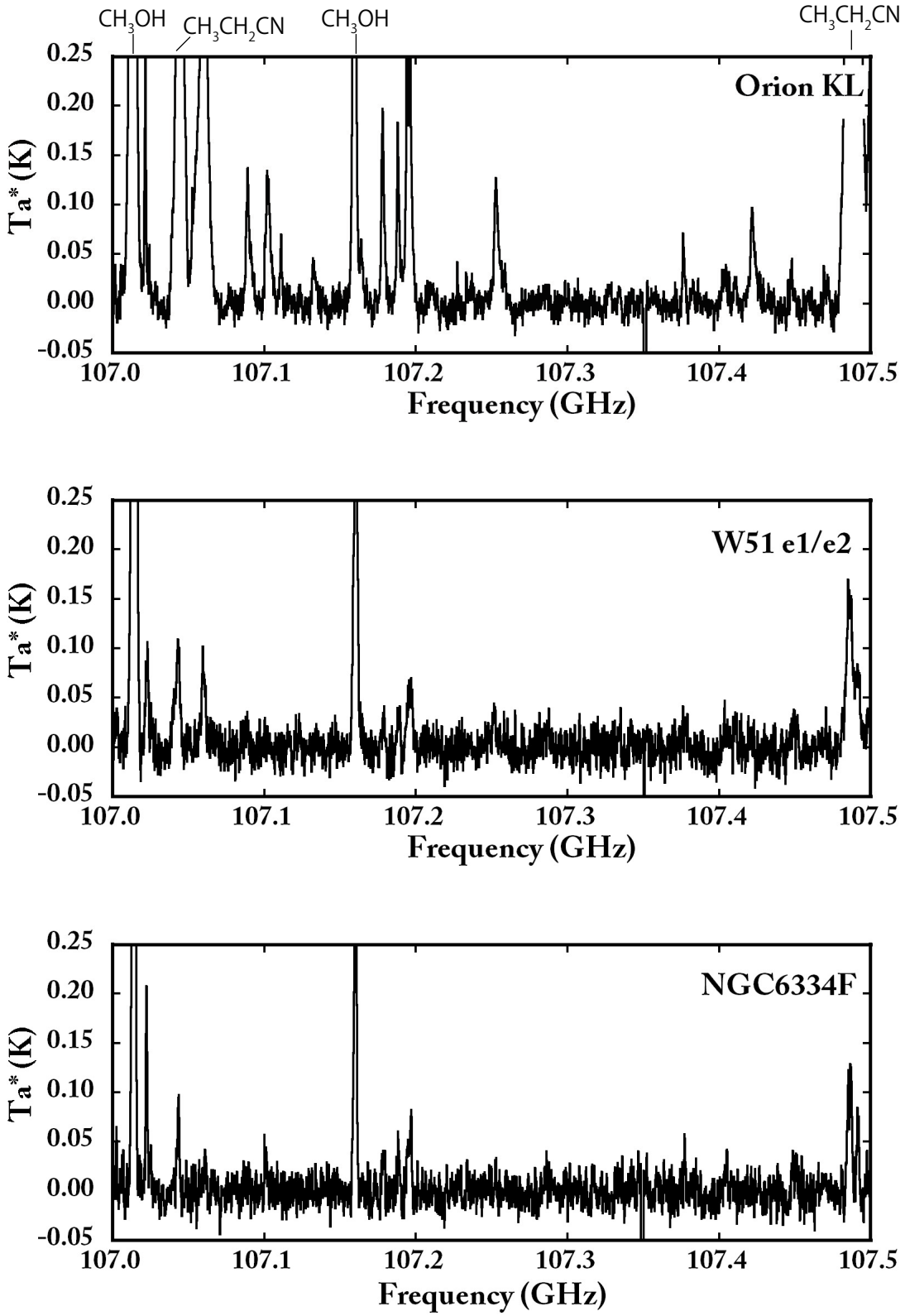

Fig. 4.— Observed Spectra. CH_3OH, CH_3CH_2CN, and CH_3OH were detected.

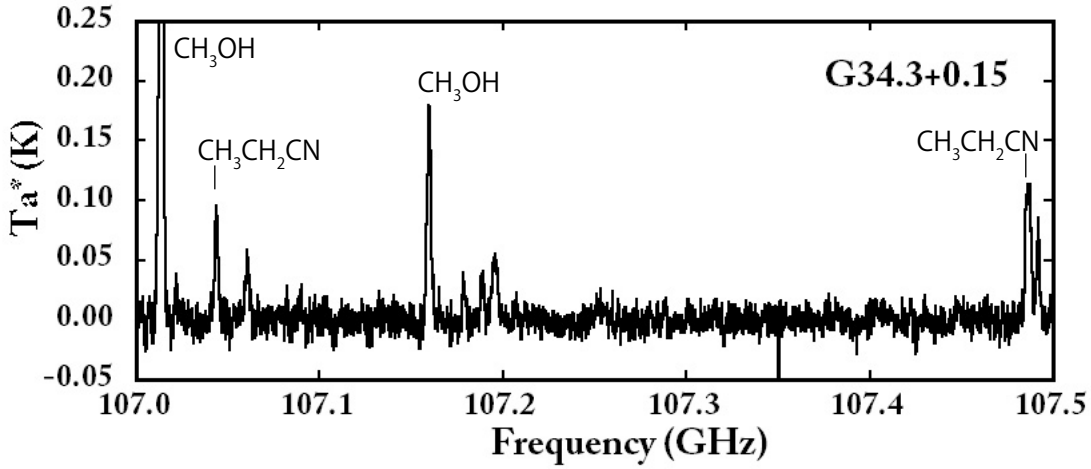

Fig. 4.— Observed Spectra. CH_3OH, CH_3CH_2CN, and CH_3OH were detected

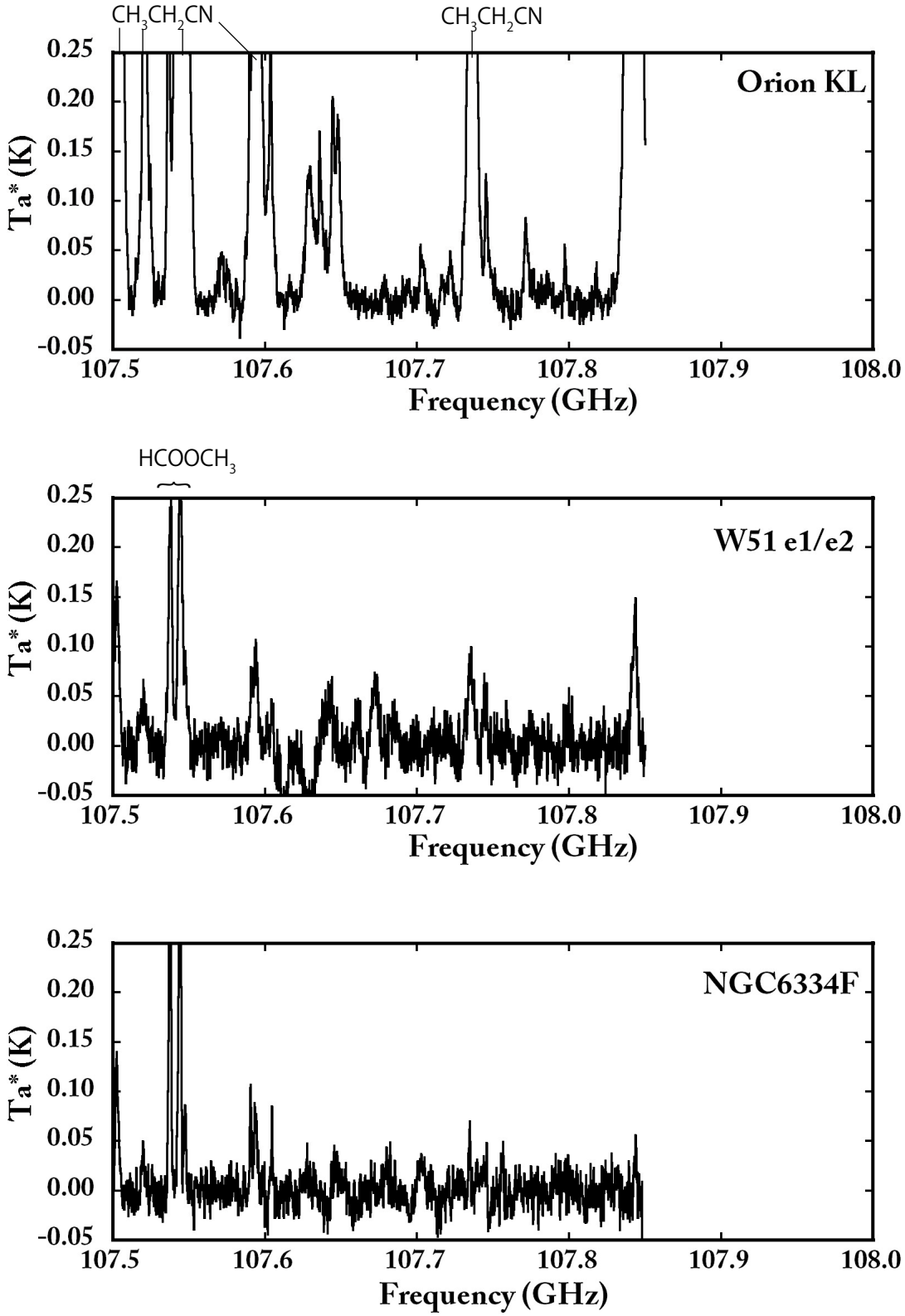

Fig. 4.— Observed Spectra. CH_3CH_2CN and $HCOOCH_3$ were detected.

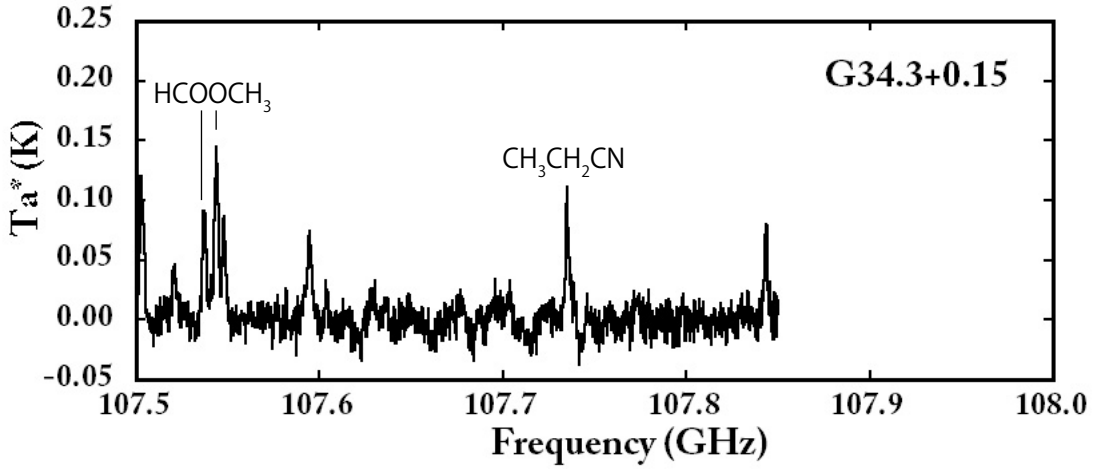

Fig. 4.— Observed Spectra. CH_3CH_2CN and $HCOOCH_3$ were detected.

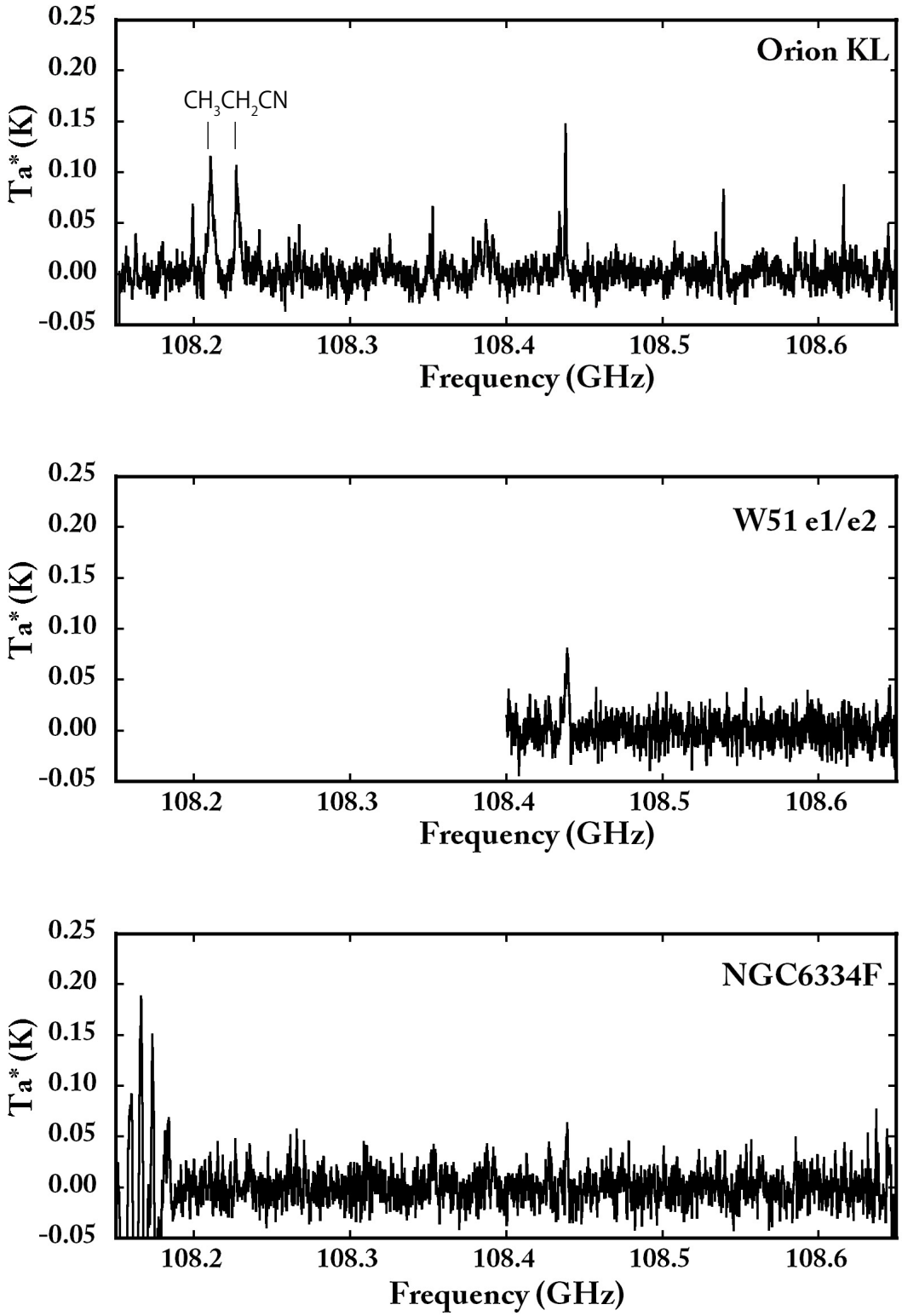

Fig. 4.— Observed Spectra. CH_3CH_2CN was detected

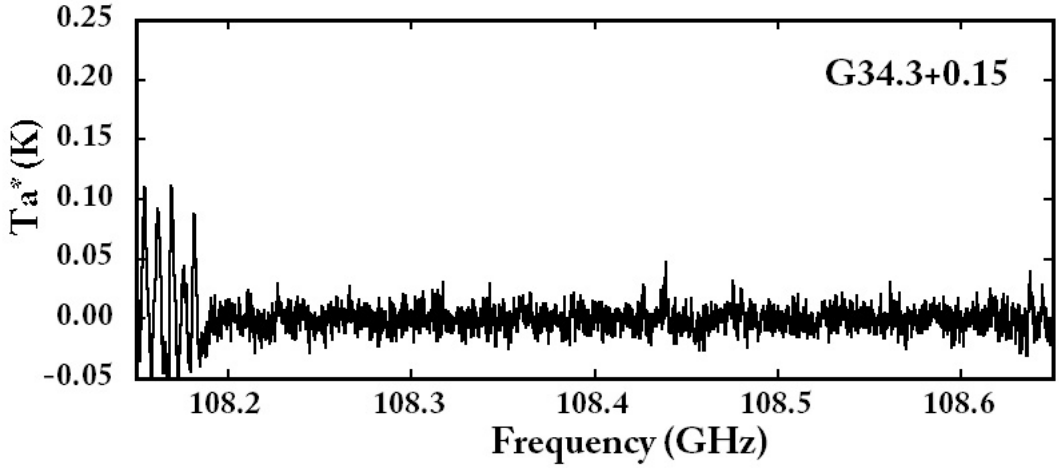

Fig. 4.— Observed Spectra.

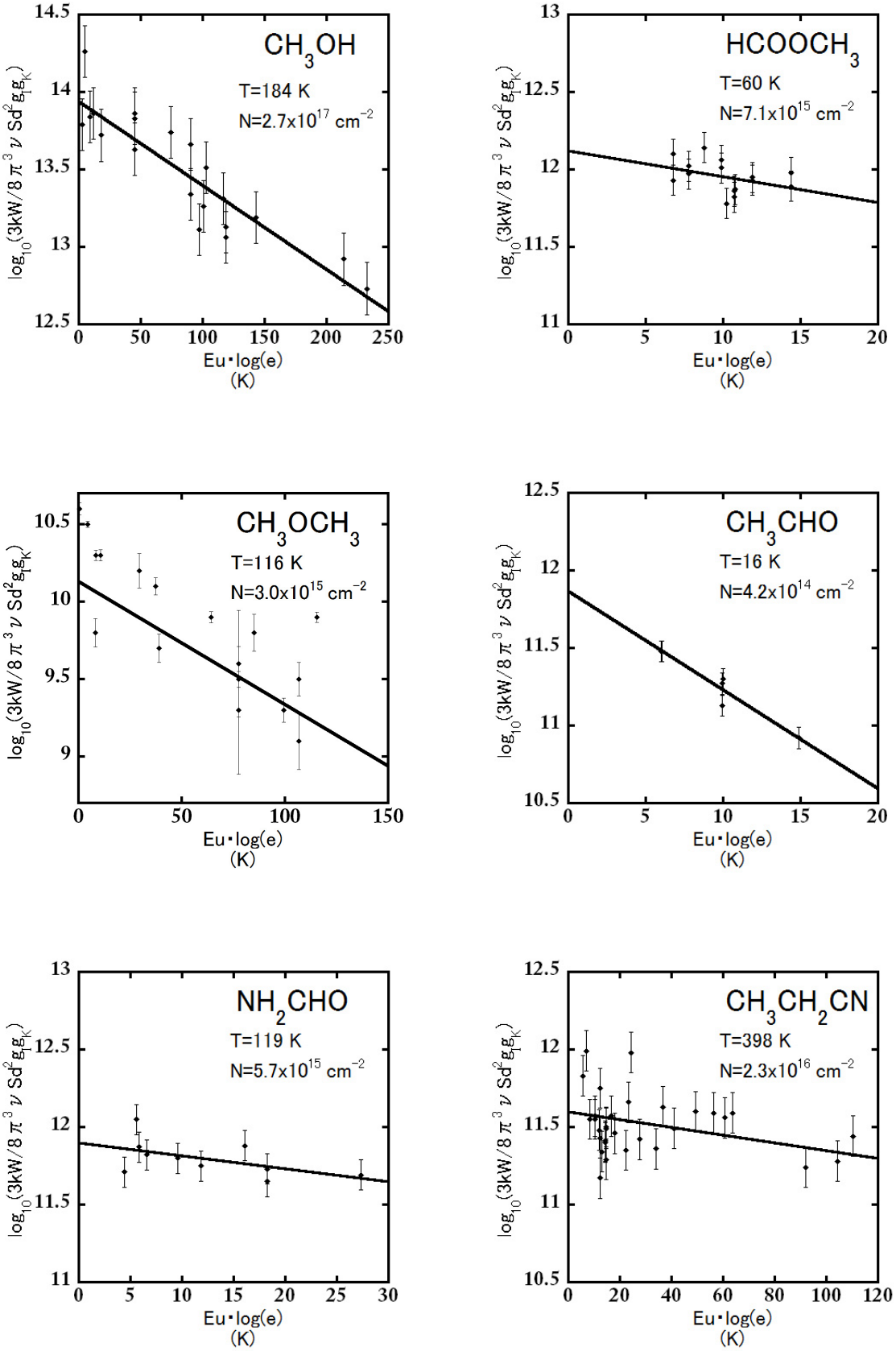

Fig. 5.— The rotation diagrams for G10.47+0.03.

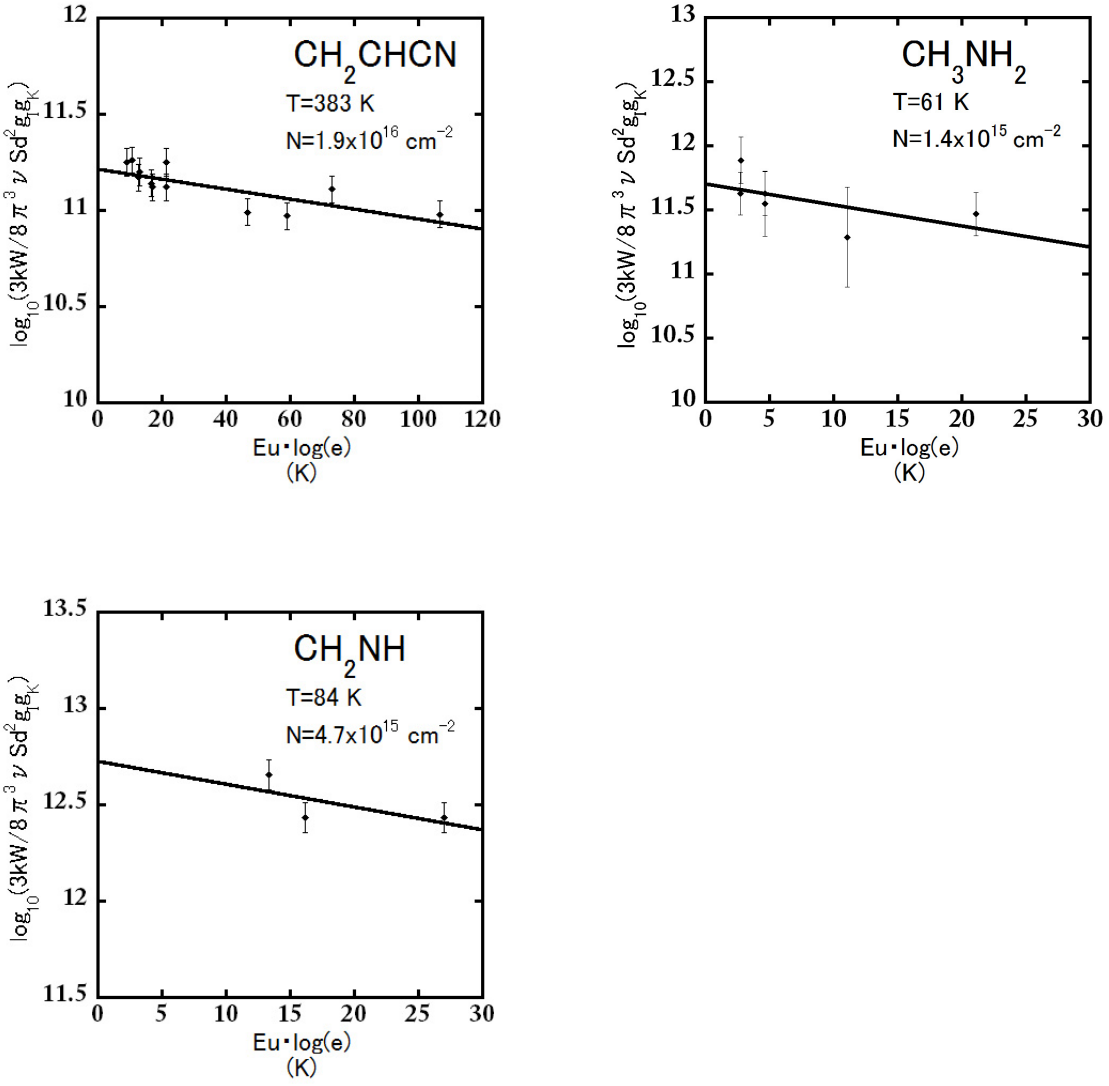

Fig. 5.— (continued) The rotation diagrams for G10.47+0.03.

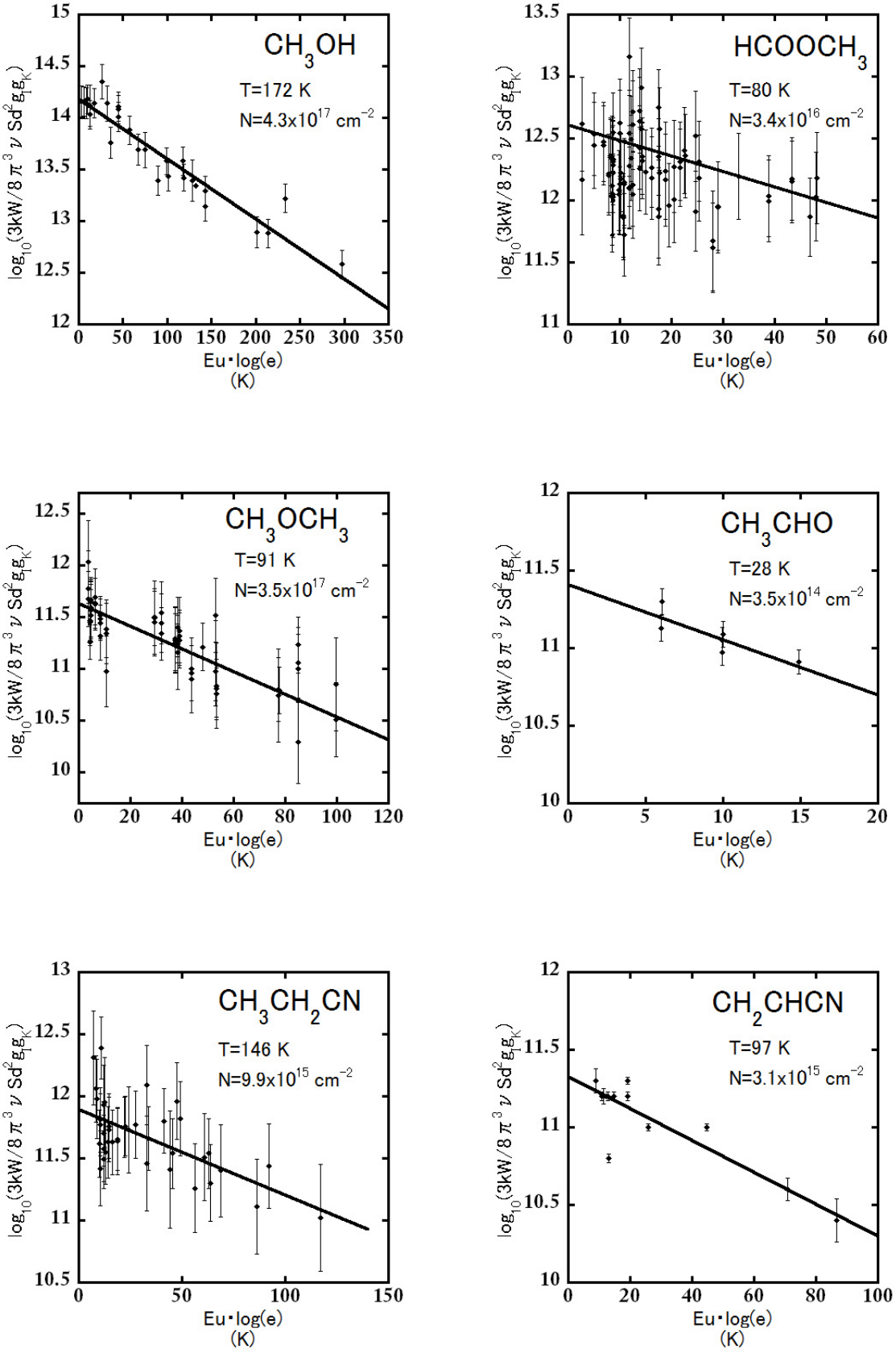

Fig. 6.— The rotation diagrams for Orion KL.

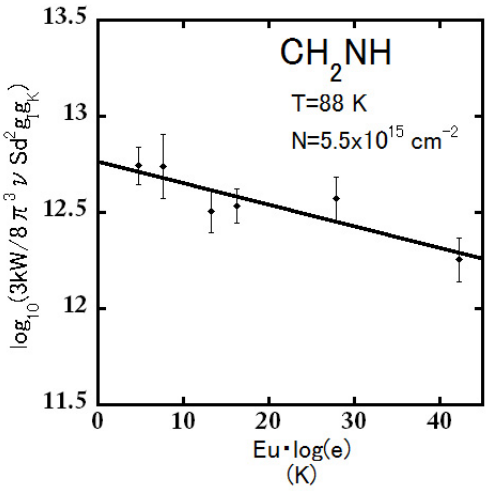

Fig. 6.— (continued) The rotation diagrams for Orion KL.

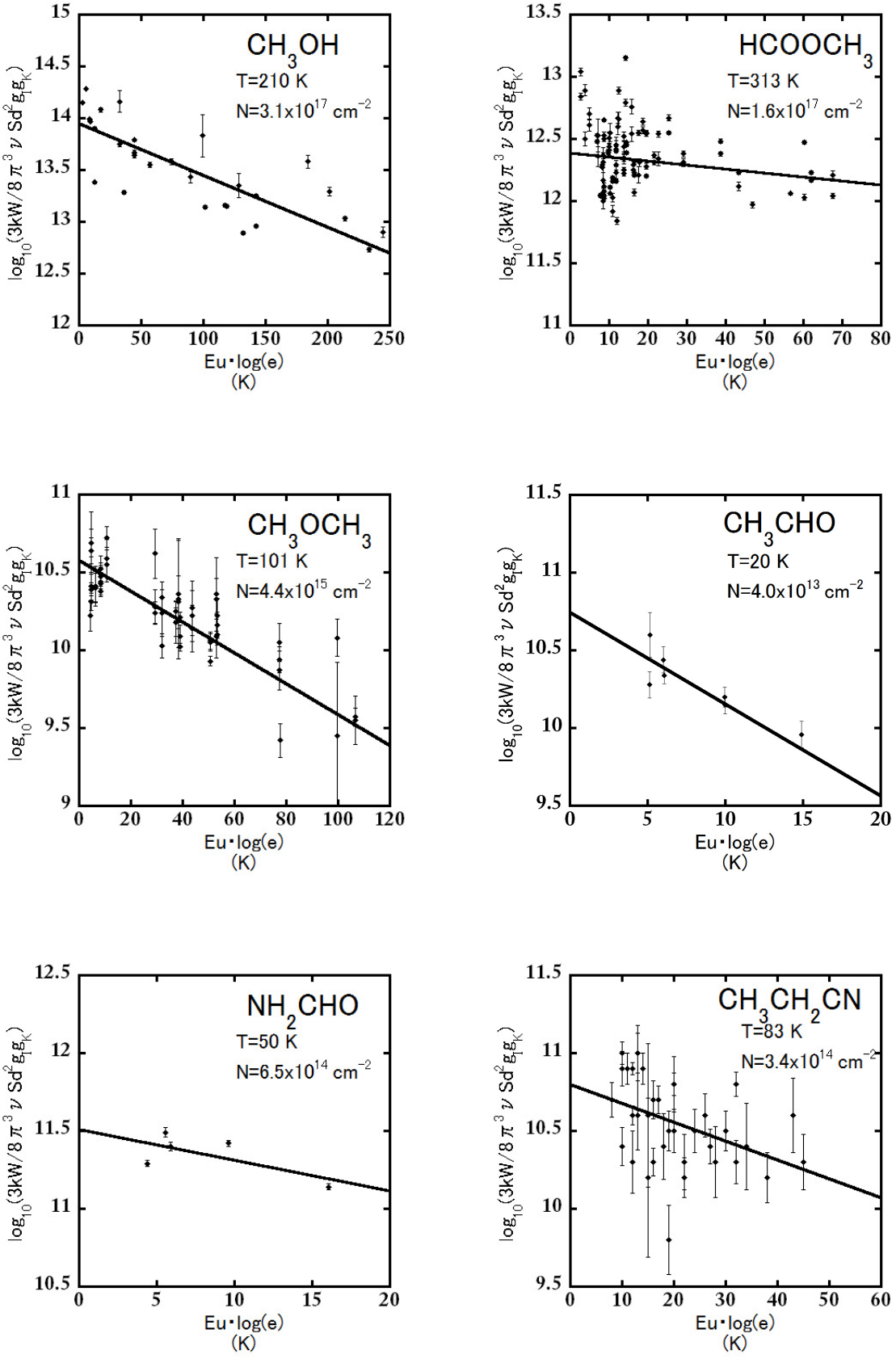

Fig. 7.— The rotation diagrams for NGC6334F.

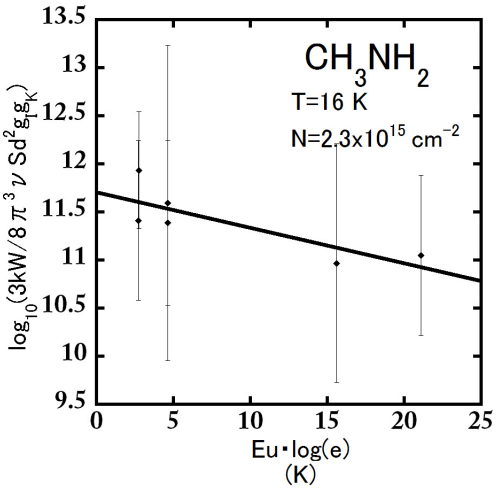

Fig. 7.— (continued) The rotation diagrams for NGC6334F

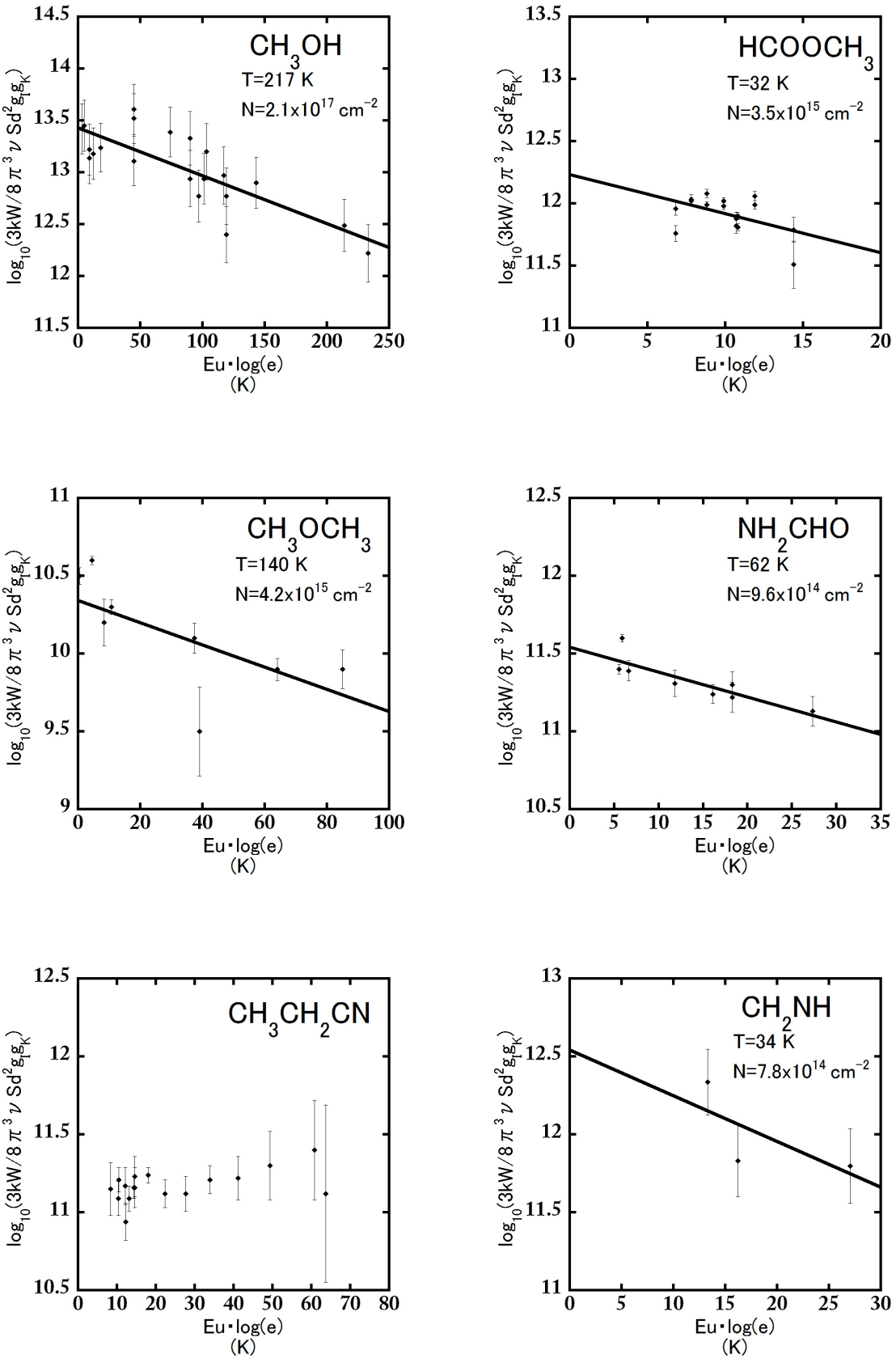

Fig. 8.— The rotation diagrams for G31.41+0.3.

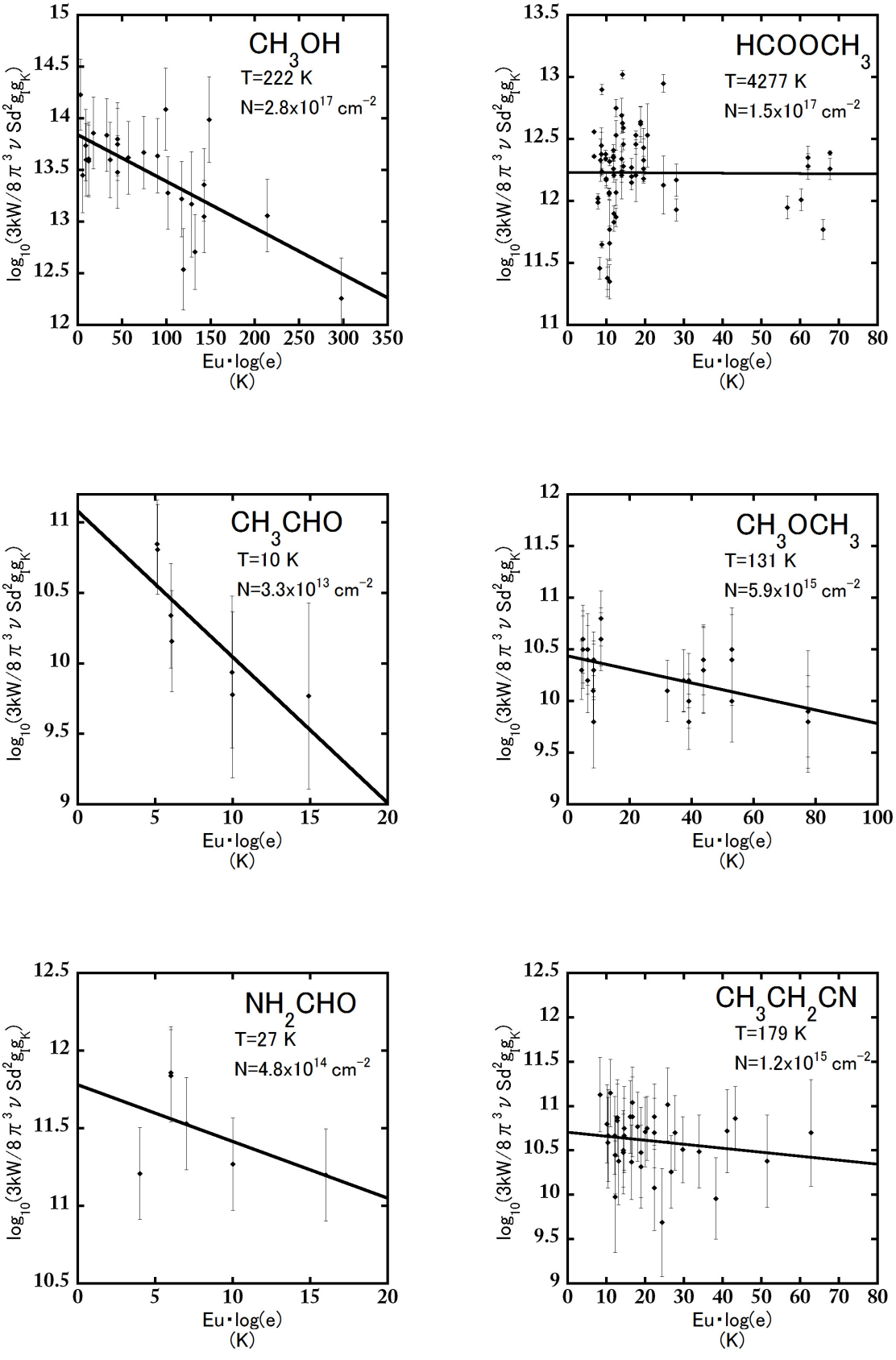

Fig. 9.— The rotation diagrams for W51 e1/e2.

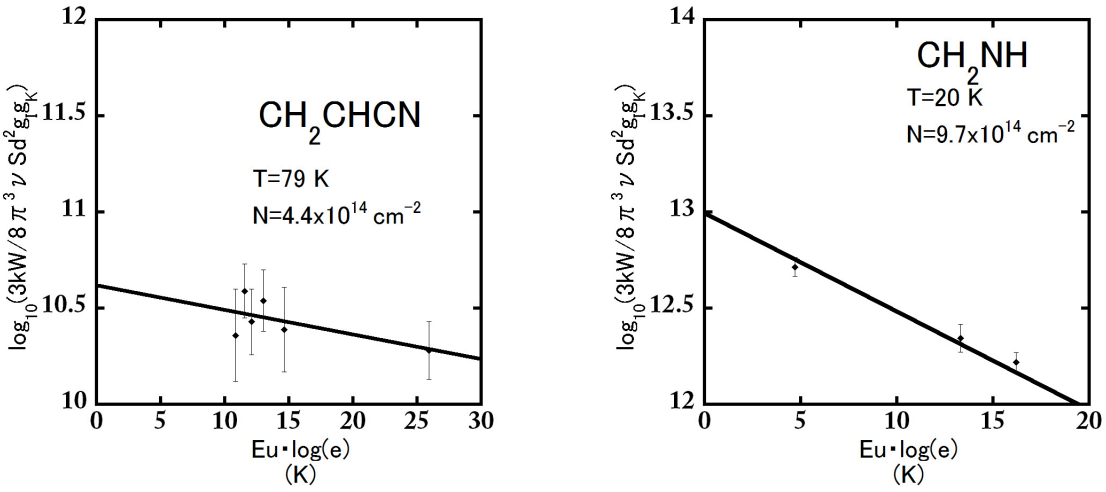

Fig. 9.— (continued) The rotation diagrams for W51 e1/e2.

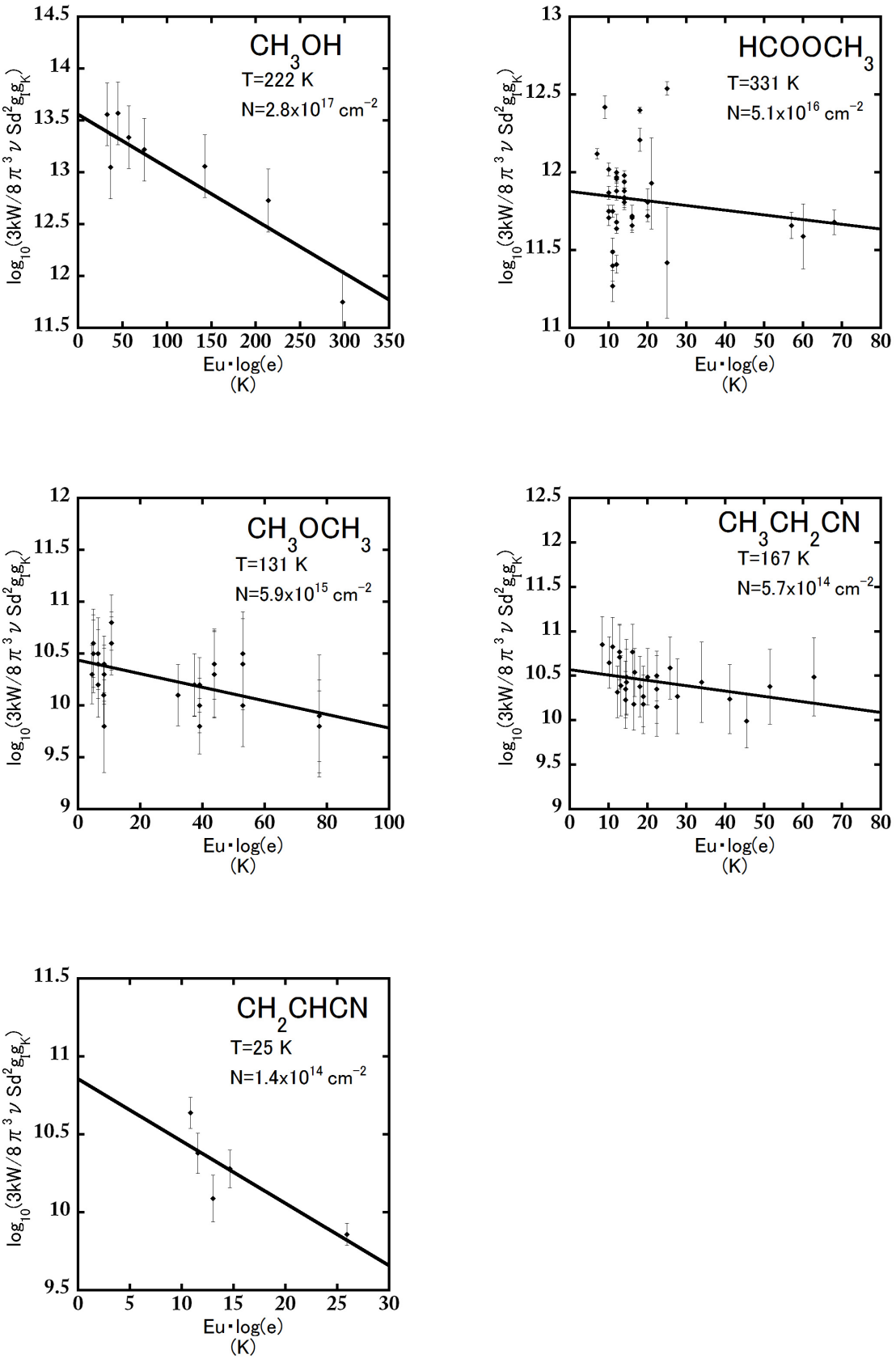

Fig. 10.— The rotation diagrams for G34.3+0.2.

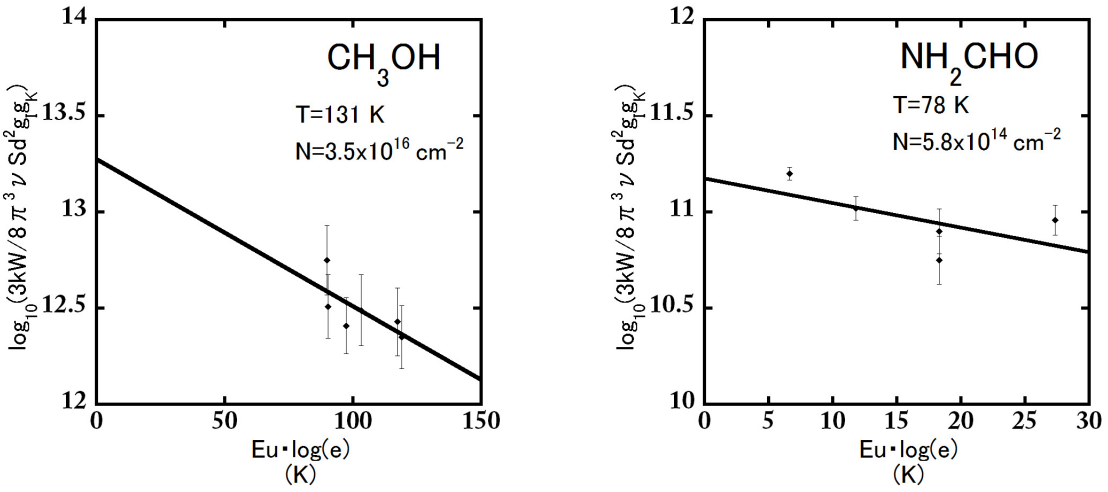

Fig. 11.— The rotation diagrams for G19.61-0.23.

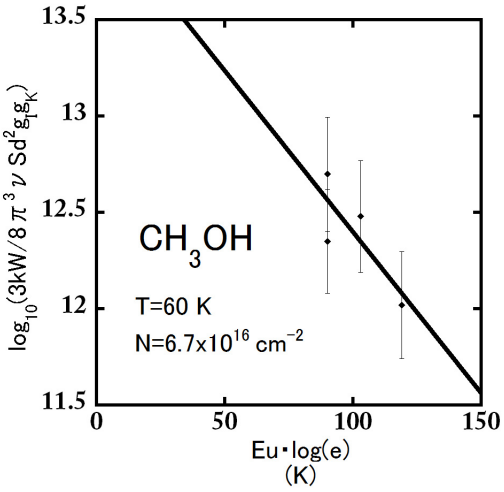

Fig. 12.— The rotation diagram for W3 (H_2O).

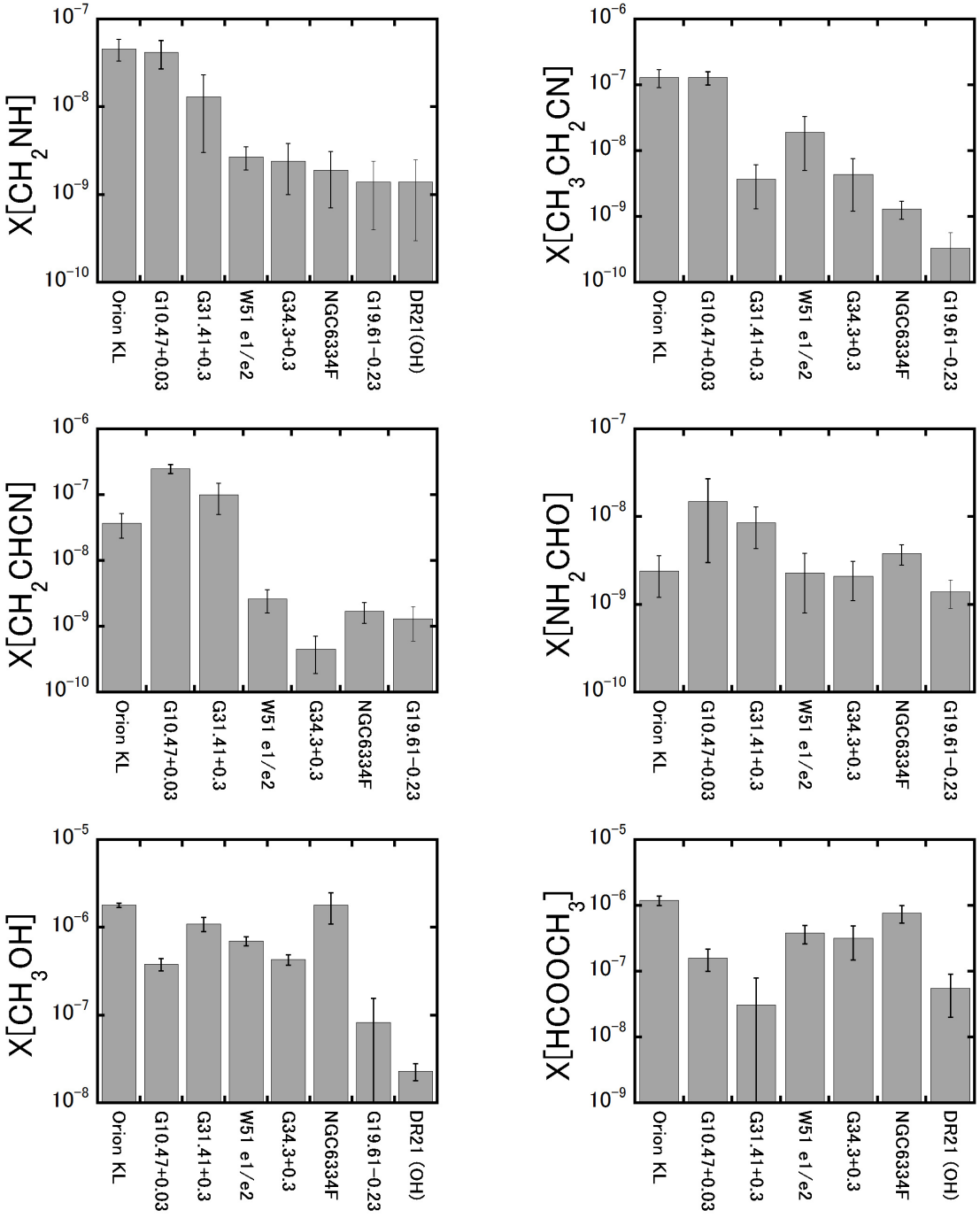

Fig. 13.— Histogram of fractional abundances for CH_2NH, CH_3CH_2CN, CH_2CHCN, NH_2CHO, CH_3OH, $HCOOCH_3$, CH_3OCH_3, and CH_3COCH_3. Basically, the fractional abundances under compact source sizes were assumed. For DR21(OH), fractional abundances under 10" source size was used due to lack of hydrogen column density derived by continuum emission.

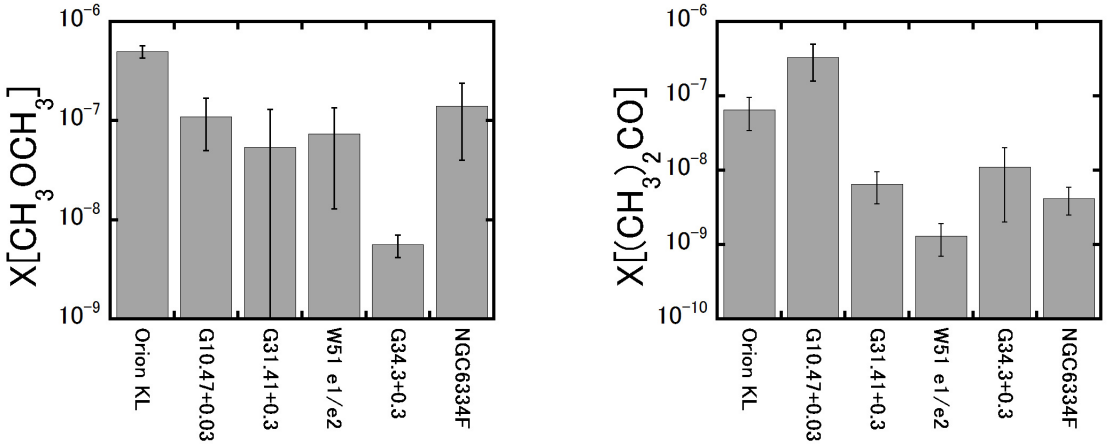

Fig. 13.— (continued) Histogram of fractional abundances for CH_2NH, CH_3CH_2CN, CH_2CHCN, NH_2CHO, CH_3OH, $HCOOCH_3$, CH_3OCH_3 and CH_3COCH_3. Basically, the fractional abundances under compact source sizes were assumed. For DR21(OH), fractional abundances under 10" source size was used due to lack of hydrogen column density derived by continuum emission.

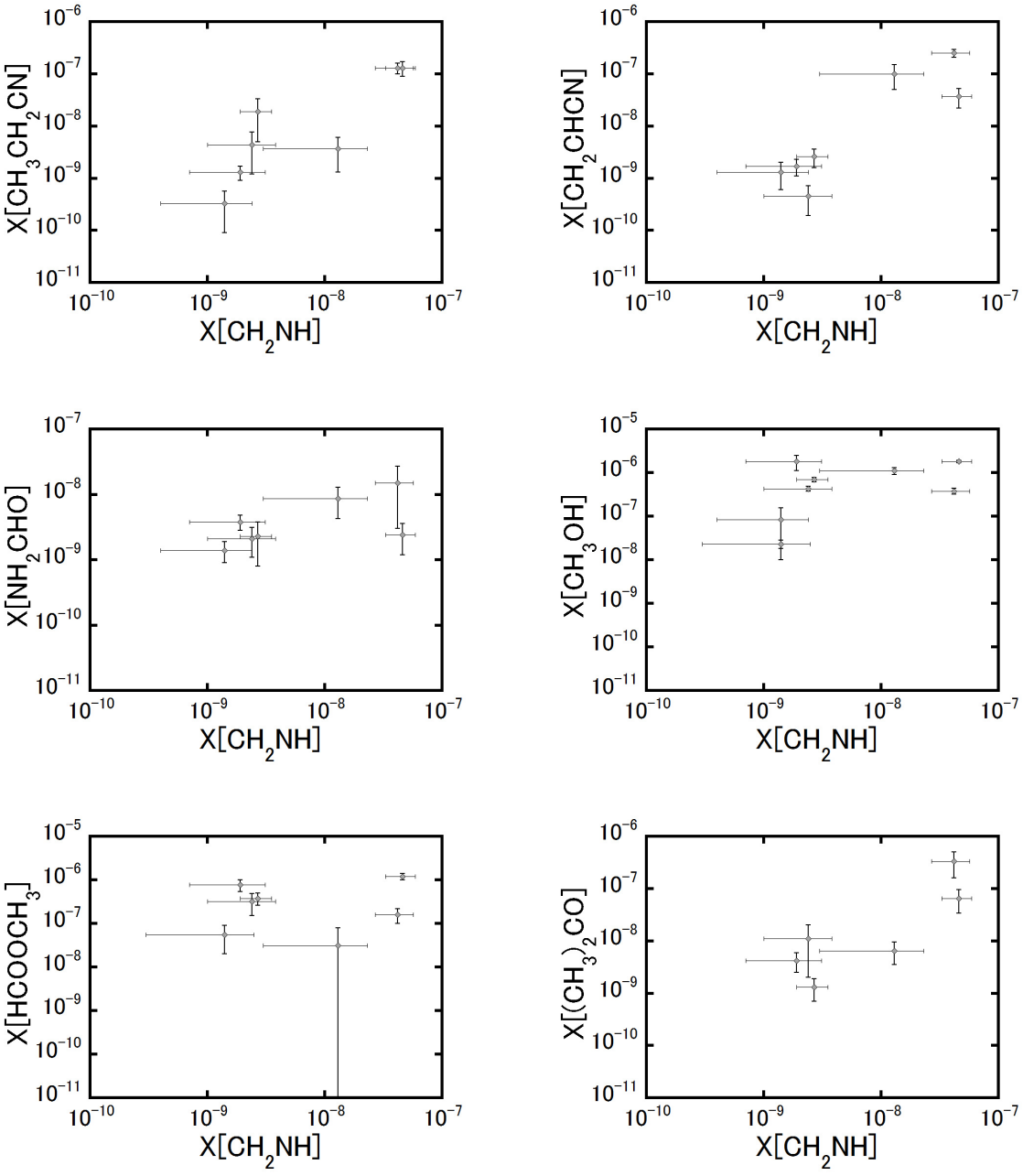

Fig. 14.— Correlation diagrams of fractional abundance between CH_2NH and other COMs.

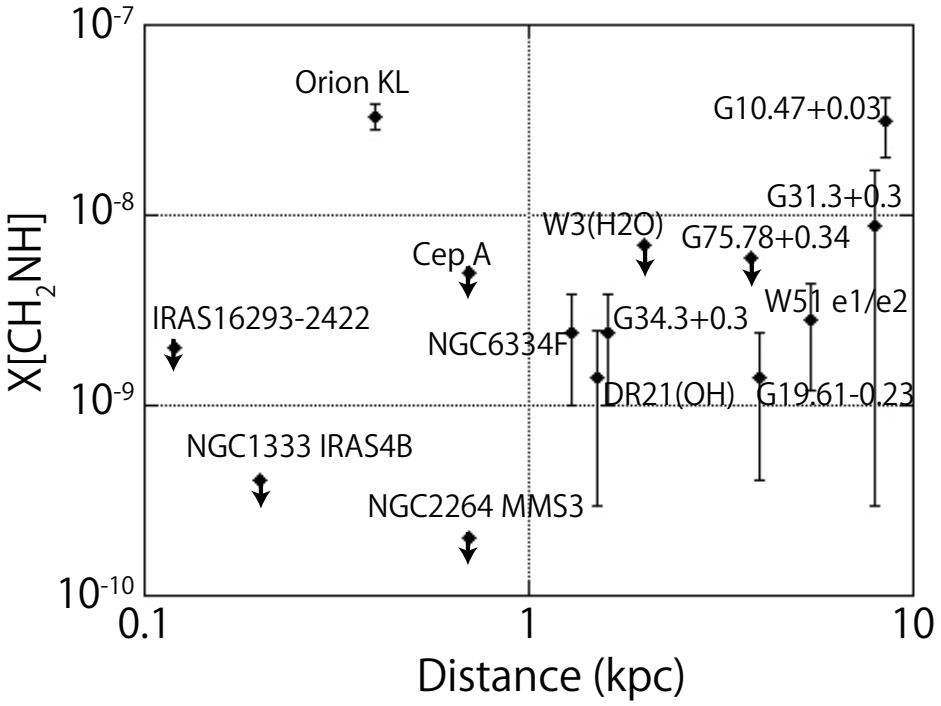

Fig. 15.— Plots of the distances to the sources against the CH_2NH fractional abundances. The upper limits of X[CH_2NH] are shown for sources where CH_2NH was not detected.

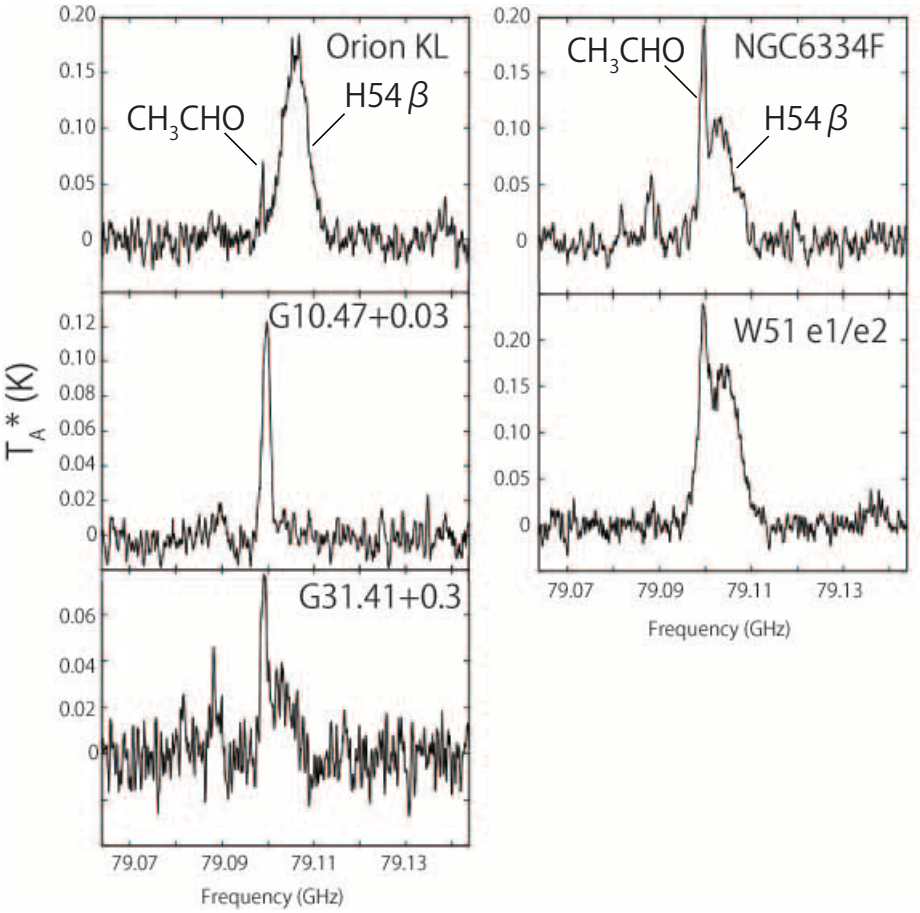

Fig. 16.— Observed recombination line "H54β" is shown next to narrow CH_3CHO transition. Its calculated frequency is 79.103866 GHz. Although Orion KL seems to have strong H54β line, it is known that the origin of this line is emitted from the other region in front of Orion Hot Core.

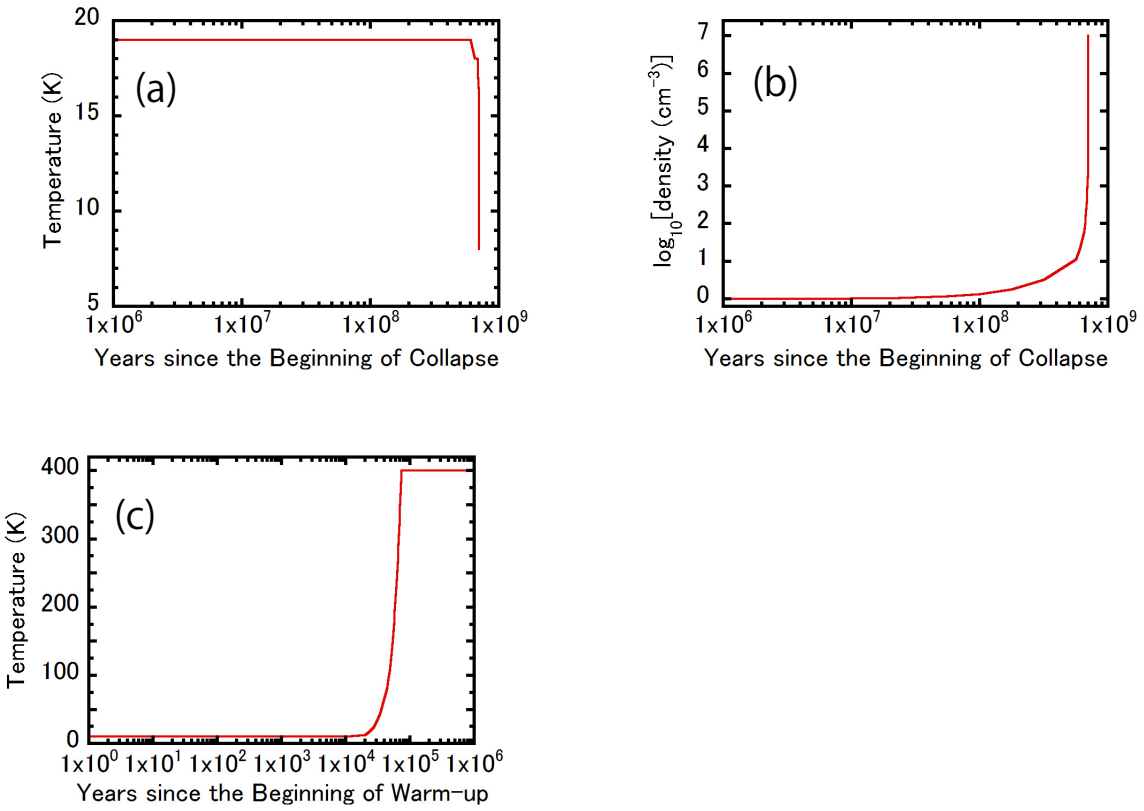

Fig. 17.— The evolution of the grain temperature and the density during the collapsing phase are shown in (a) and (b), respectively. In these figures, the parameter evolutions before 1×10^6 years are not shown, since both temperature and density were almost constant before 1×10^6 years. In this case, the gas density was assumed to rise to 1×10^7 cm^{-3}. The gas temperature in the proceeding warm-up phase is shown in (c). In this figure, the peak temperature was assumed to be 400 K. The density is fixed to the peak value achieved in the collapsing phase.

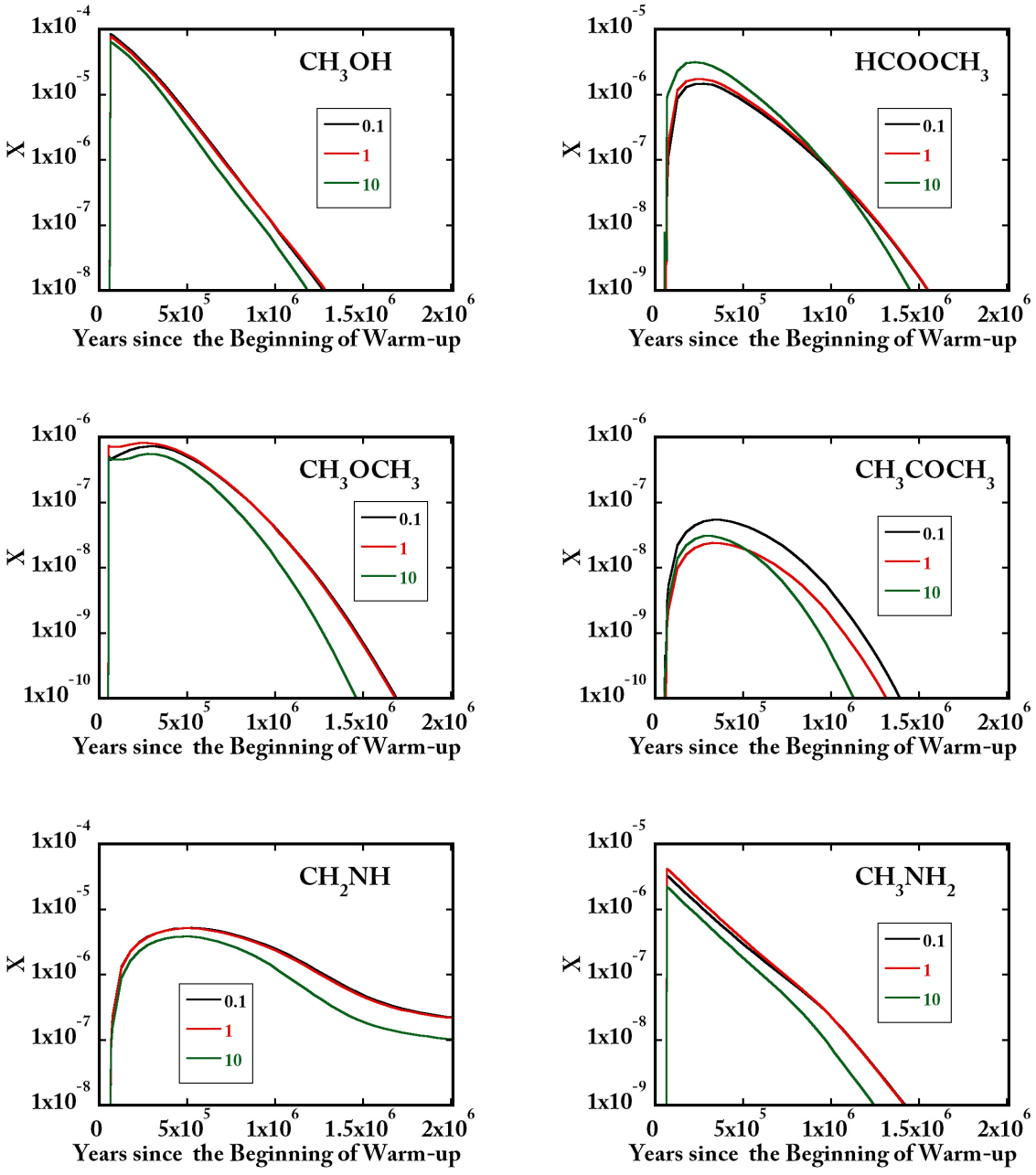

Fig. 18.— Comparison of abundances of COMs simulated under different initial densities of 0.1, 1, and 10 cm^{-3}.

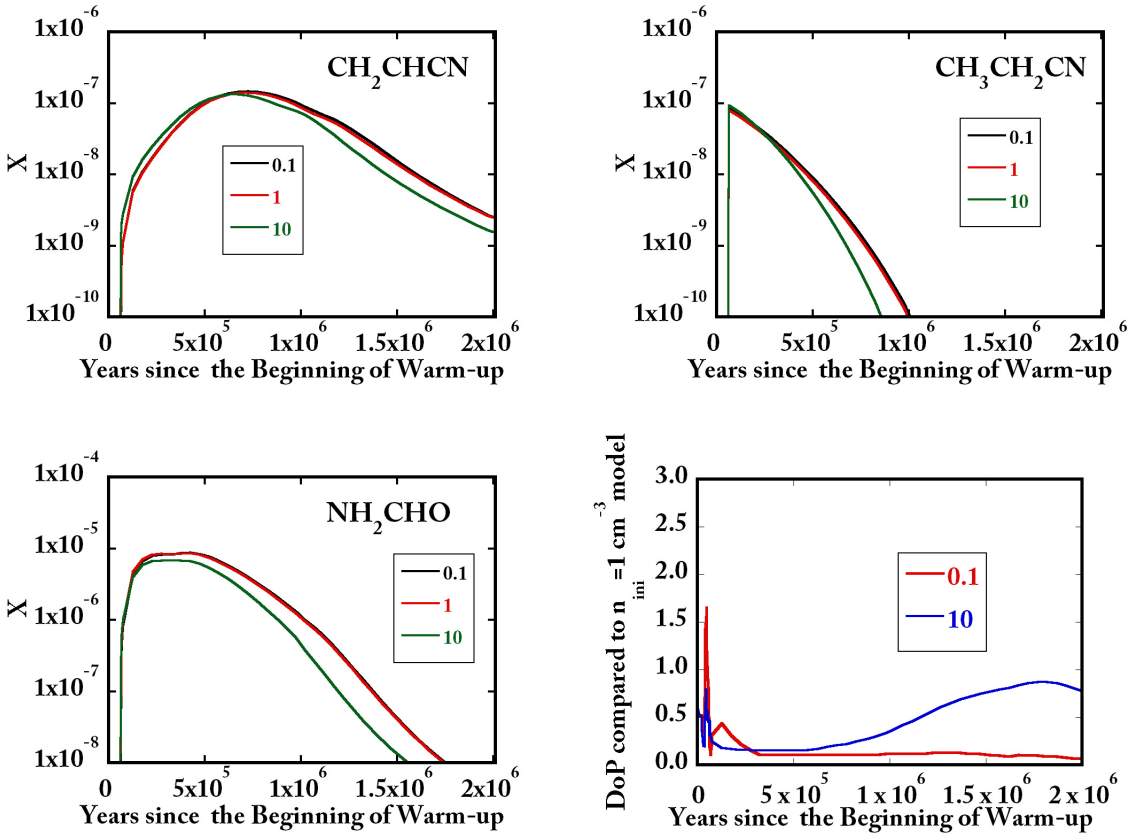

Fig. 18.— (continued) Comparison of abundances of COMs simulated under different initial densities of 0.1, 1, and 10 cm^{-3}. DoPs of initial density of 0.1 and 10 cm^{-3} models compared to that of 1 cm^{-3} model is also shown.

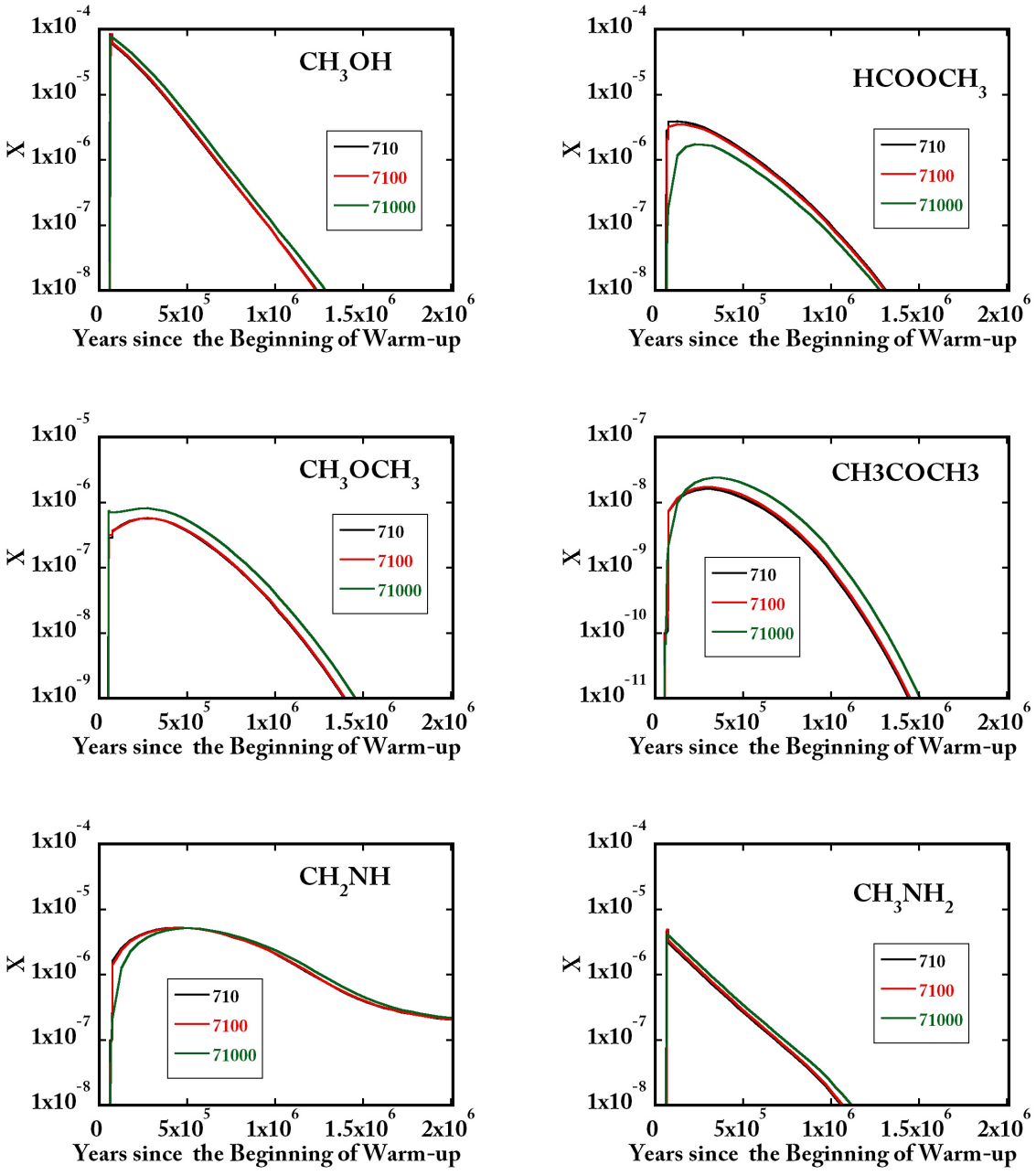

Fig. 19.— Comparison of abundances of COMs simulated under the different warm-up timescales of 710, 7100, and 71000 years.

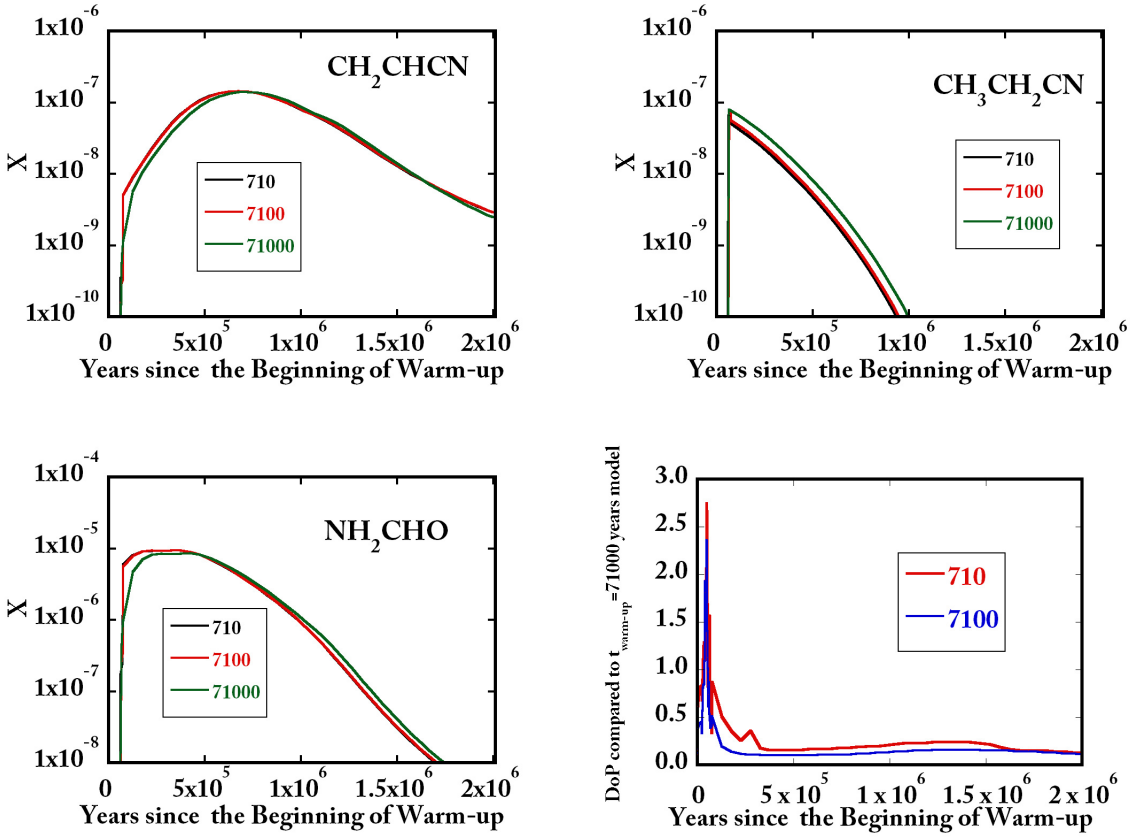

Fig. 19.— Comparison of abundances of COMs simulated under the different warm-up timescales of 710, 7100, and 71000 years. DoPs of warm-up timescale of 710 and 7100 models compared to 71000 model are also shown.

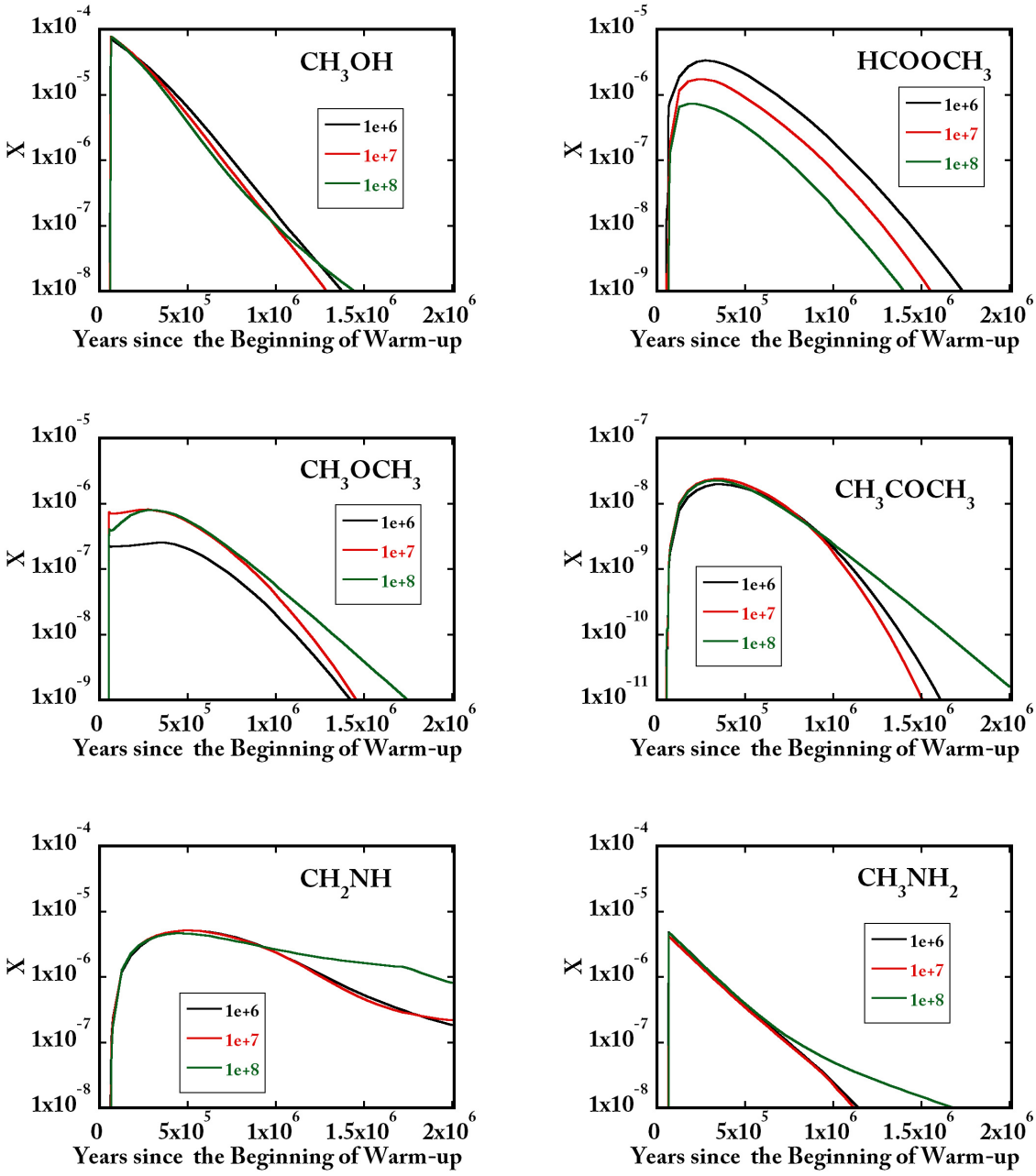

Fig. 20.— Comparison of abundances of COMs simulated under the different peak densities, 1×10^6, 10^7, and 10^8 cm^{-3}.

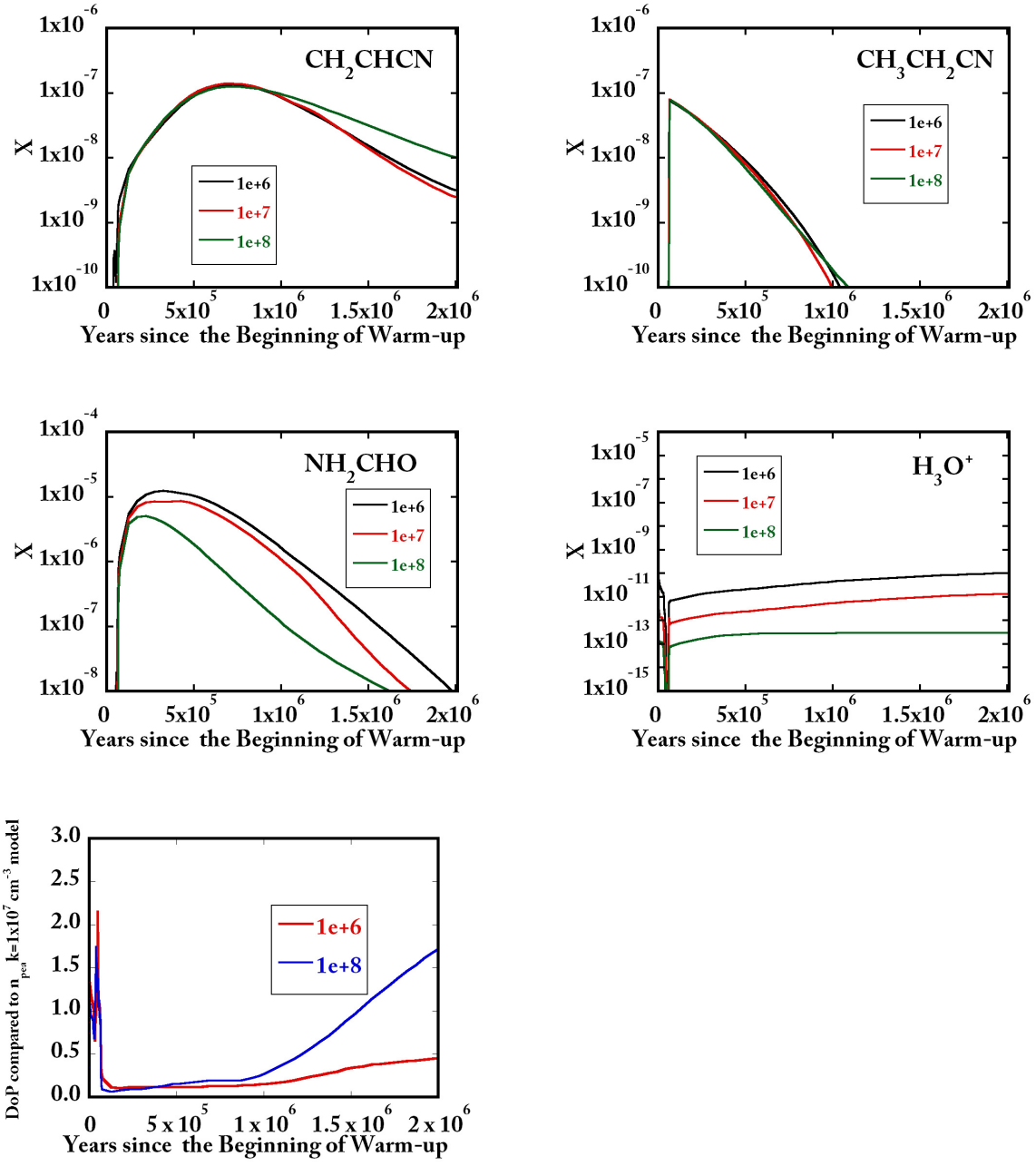

Fig. 20.— (continued) Comparison of abundances of COMs simulated under the different peak densities, 1×10^6, 10^7, and 10^8 cm^{-3}. DoPs of 1×10^6 and 10^8 cm^{-3} models compared to 10^7 cm^{-3} is also shown.

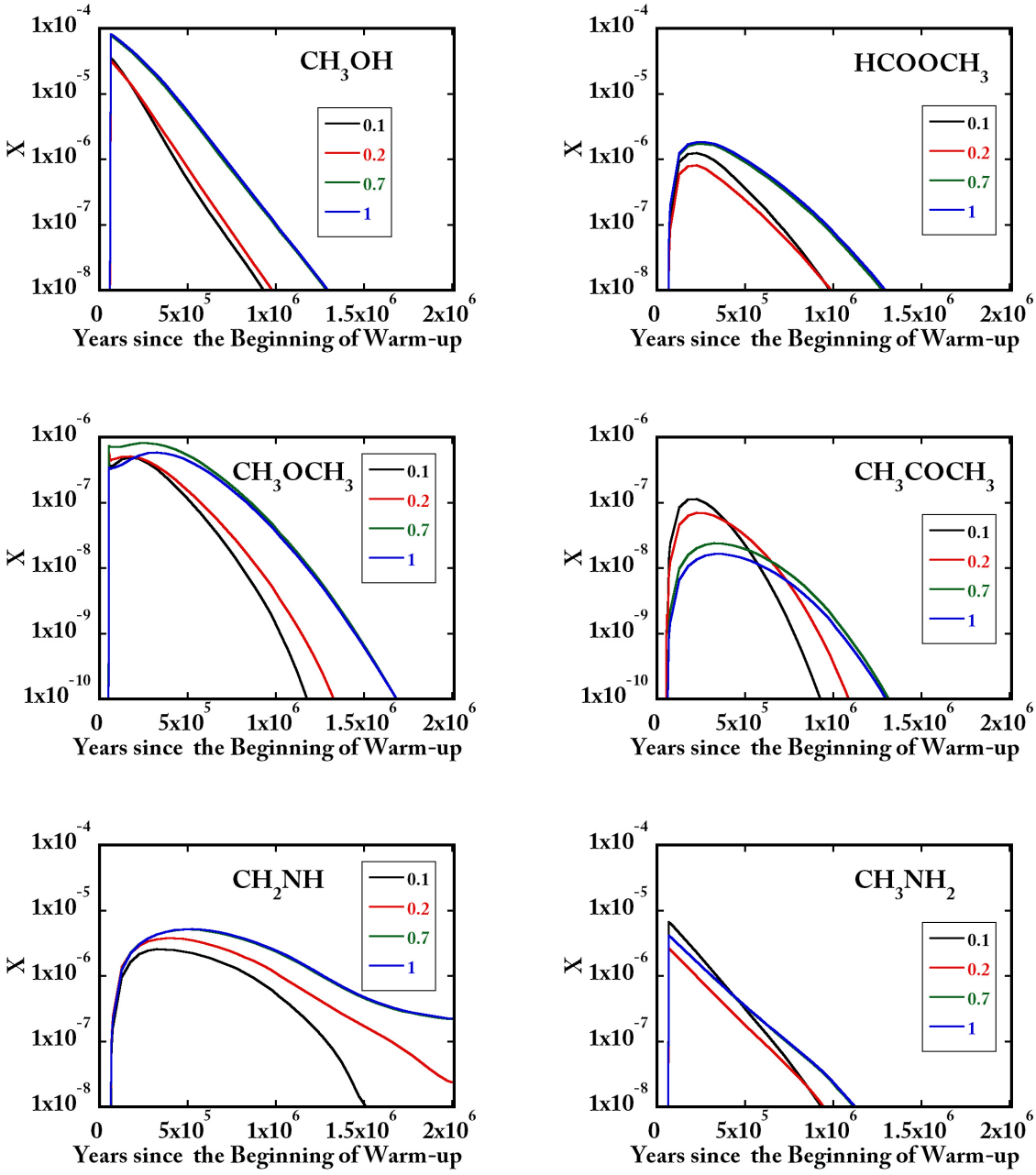

Fig. 21.— Comparison of abundances of COMs simulated under the different collapsing speed determined by the factor of B, 0.1, 0.2, 0.7, and 1. B=1 is a case for free-fall.

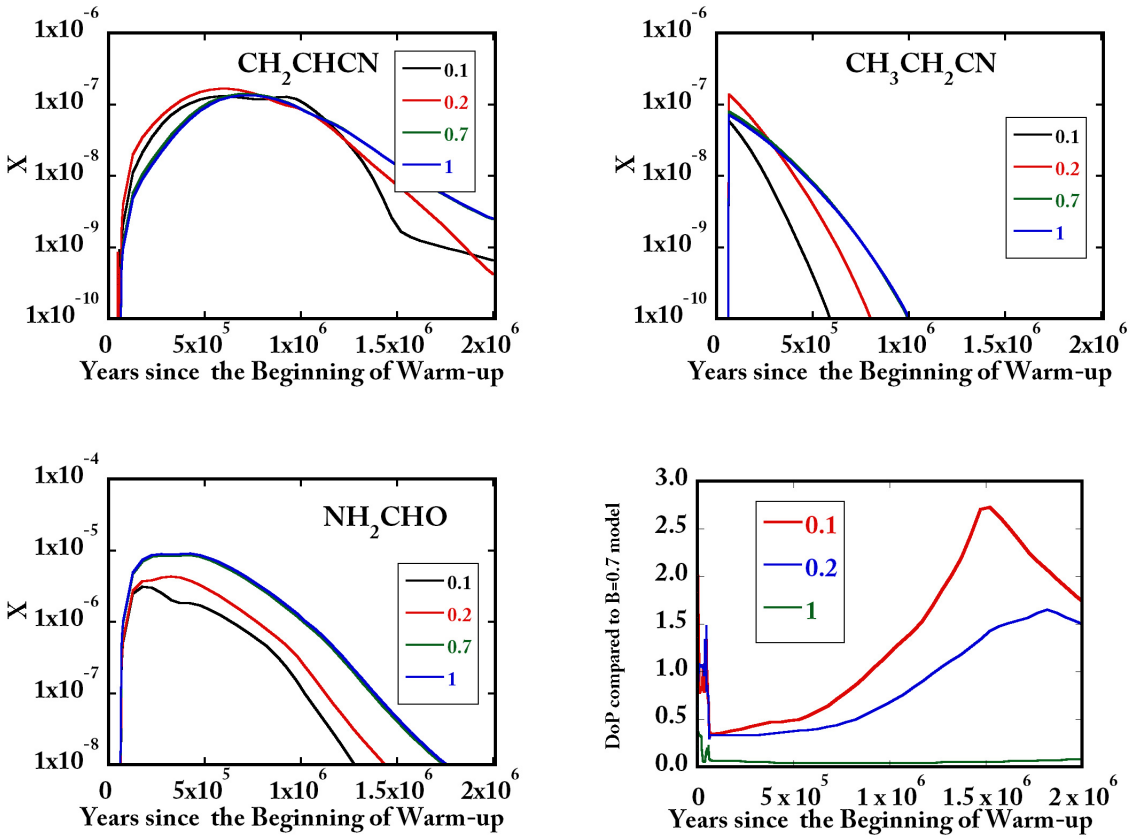

Fig. 21.— (continued) Comparison of abundances of COMs simulated under the different collapsing speed determined by the factor of B, 0.1, 0.2, 0.7, and 1. B=1 is a case for free-fall. DoPs of B=0.1, 0.2, and 1 models to B=0.7 model are also shown.

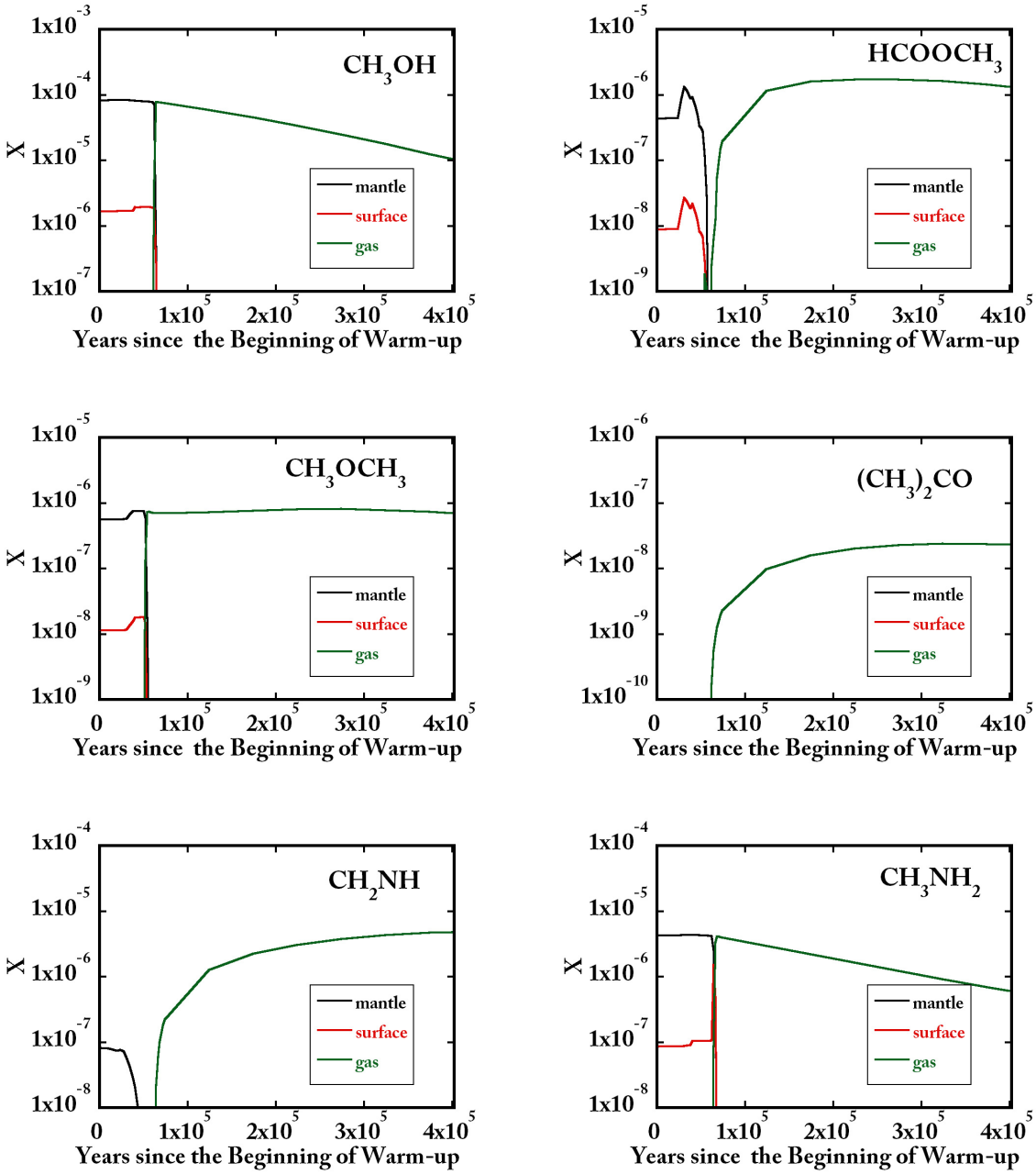

Fig. 22.— Abundances of interested species in the gas, in the mantle, and on the surface are shown just before and after evaporation process. Higher abundances in the gas phase than mantle and surface indicate that origin of the species are gas phase reactions rather than evaporation from the grain.

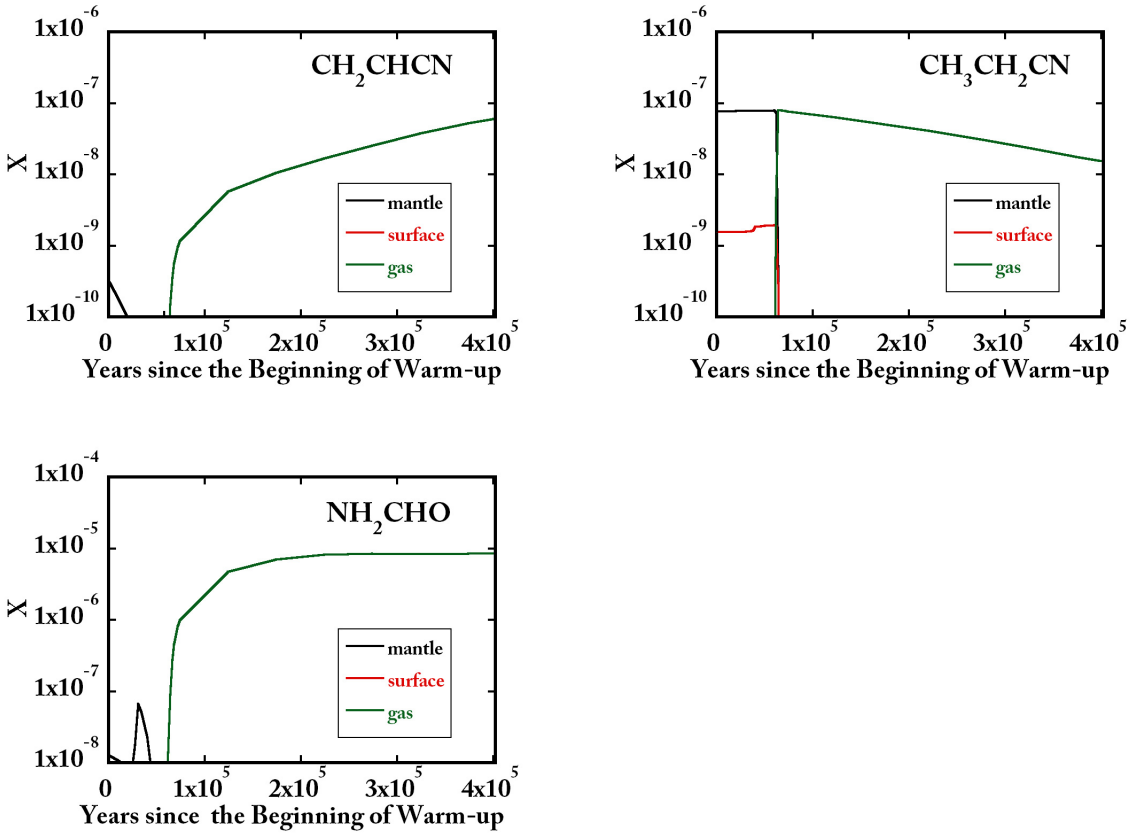

Fig. 22.— (continued) Abundances of interested species in the gas, in the mantle, and on the surface are shown just before and after evaporation process. Higher abundances in the gas phase than mantle and surface indicate that origin of the species are gas phase reactions rather than evaporation from the grain.

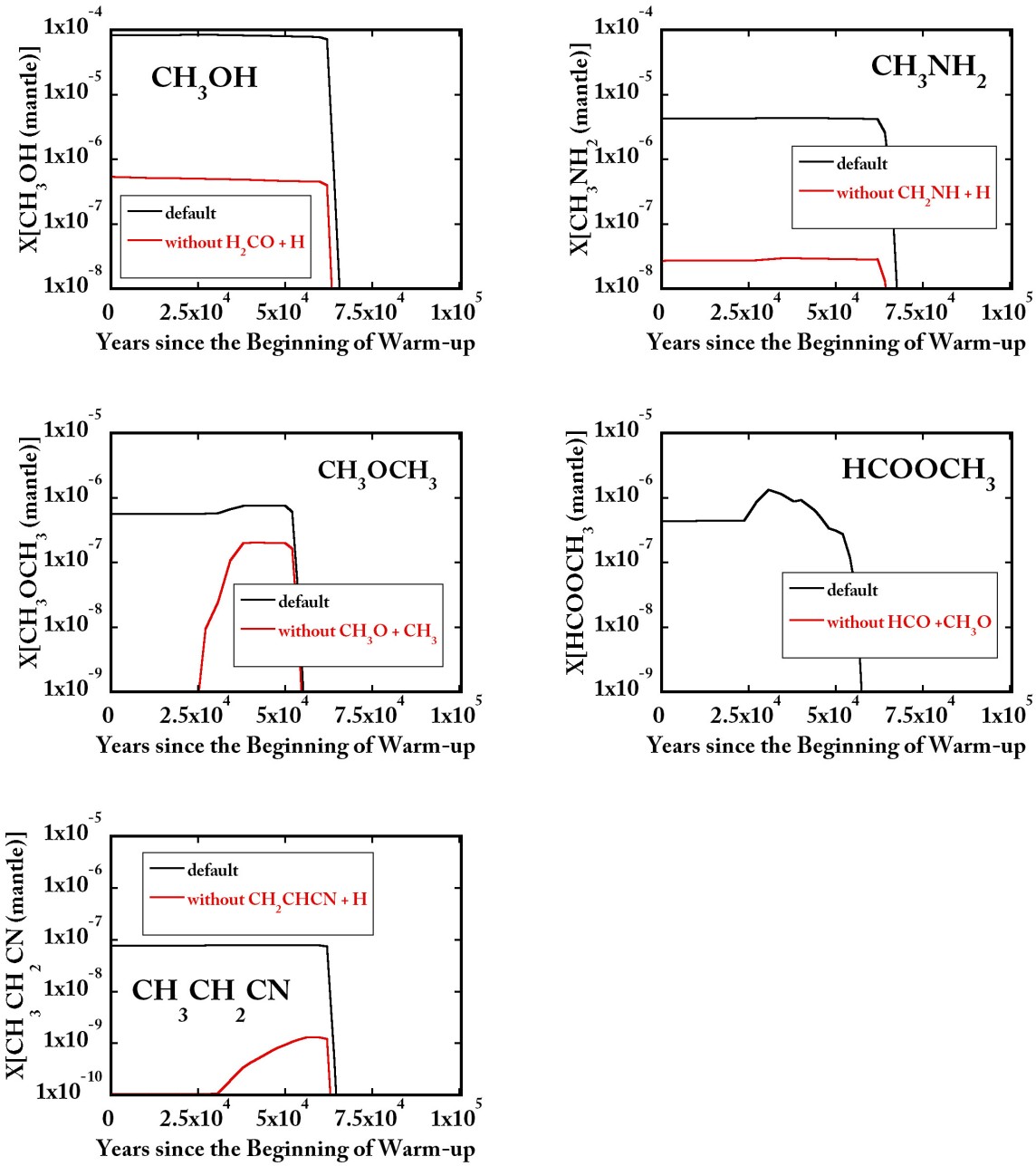

Fig. 23.— Simulated fractional abundances of CH_3OH, CH_3NH_2, CH_3OCH_3, $HCOOCH_3$ and CH_3CH_2CN in mantle are shown. They are evaporated from the grain during warm-up phase ($<7.5\times10^4$years). We can see the decreasement of CH_3OH, CH_3NH_2, CH_3OCH_3, $HCOOCH_3$, and CH_3CH_2CN abundances if the reactions of "H_2CO + H", "CH_2NH + H", "$CH_3O + CH_3$", "$HCO + CH_3O$", "CH_2CHCN + H" are excluded. These paths are essential ones for CH_3OH, CH_3NH_2, CH_3OCH_3, $HCOOCH_3$, and CH_3CH_2CN formations, as discussed in past modeling studies.

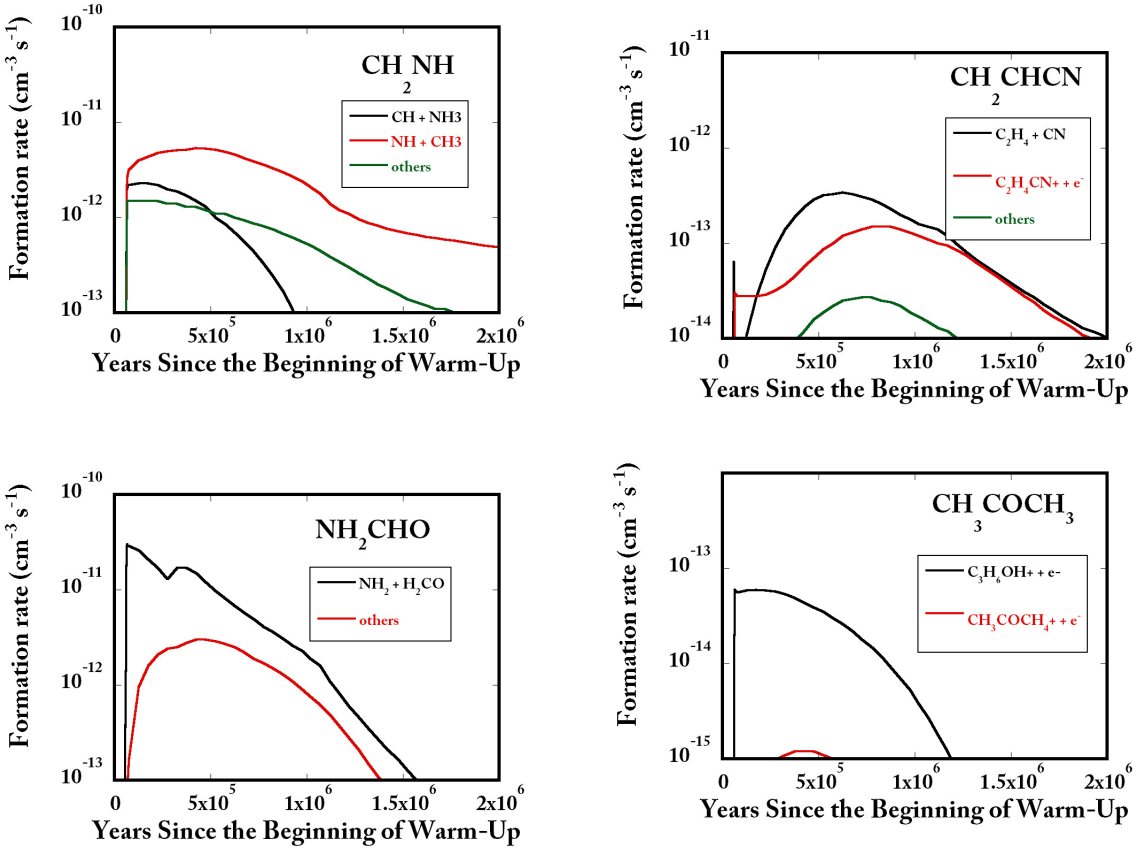

Fig. 24.— The gas phase formation rates (cm^{-3} s^{-1}) of reactions to form CH_2NH, CH_2CHCN, NH_2CHO, and CH_3COCH_3 are compared. The major formation paths for CH_2NH, CH_2CHCN, NH_2CHO, and CH_3COCH_3 are NH + CH_3, CH + NH_3, NH_2 + H_2CO, and $C_3H_6OH^+$ + e^-, respectively.

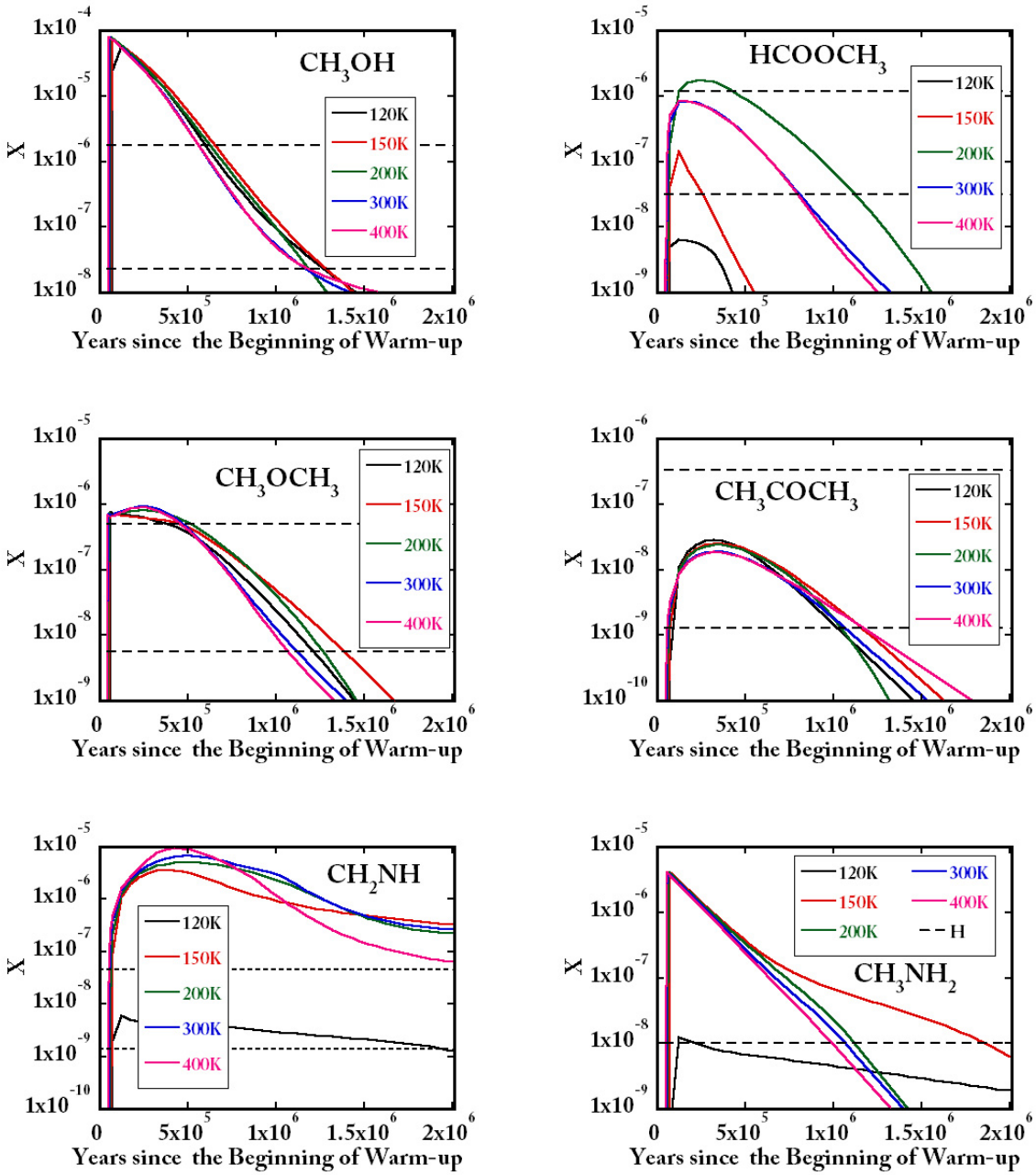

Fig. 25.— Comparison of abundances of COMs simulated under the different peak temperatures, 120, 150, 200, 300, and 400 K. The horizontal dotted lines represent the highest and the lowest observed abundances obtained in Chapter 2. For CH_3NH_2, only one horizontal dotted line corresponding to the observed abundance towards G10.47+0.03 is shown, since CH_3NH_2 is observed only towards G10.47+0.03 and NGC6334F and their fractional abundances of CH_3NH_2 is close.

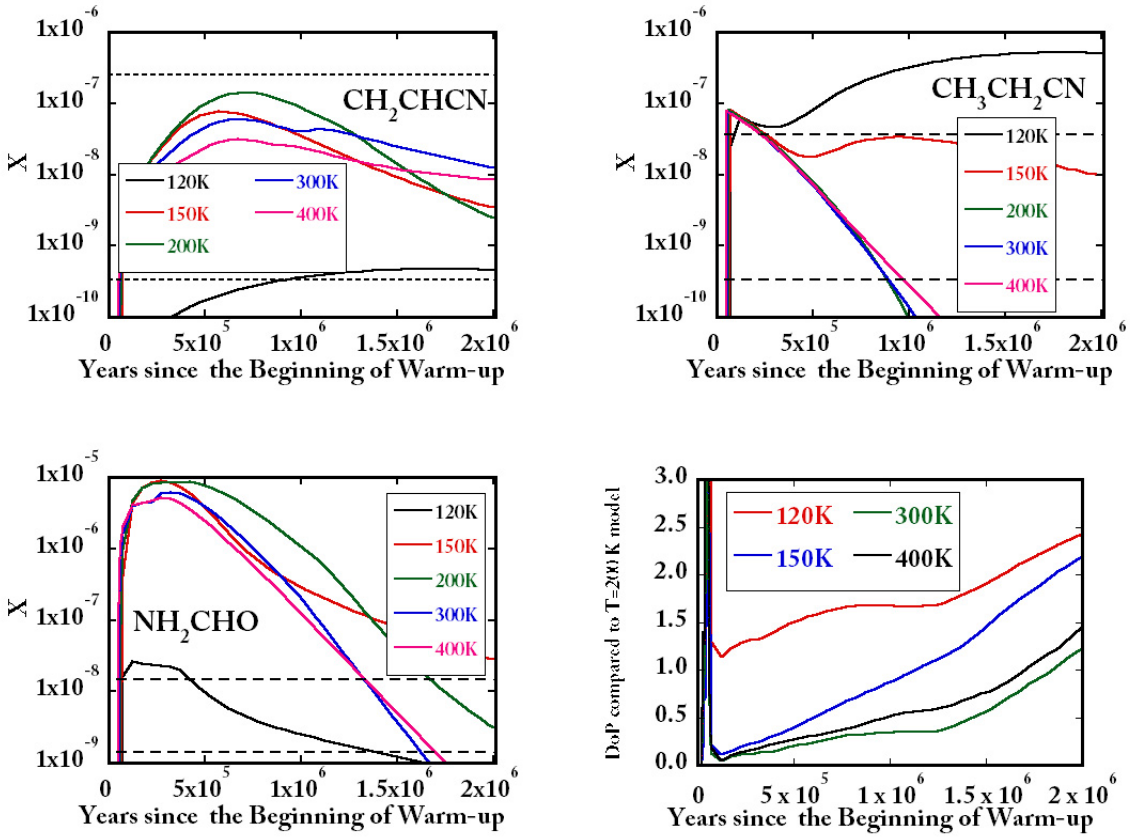

Fig. 25.— (continued) Comparison of abundances of COMs simulated under the different peak temperatures, 120, 150, 200, 300, and 400 K. The horizontal lines represent the highest and the lowest observed abundances obtained in Chapter 2. DoPs of 120, 150, 300, and 400 K models compared to 200 K model are also shown.

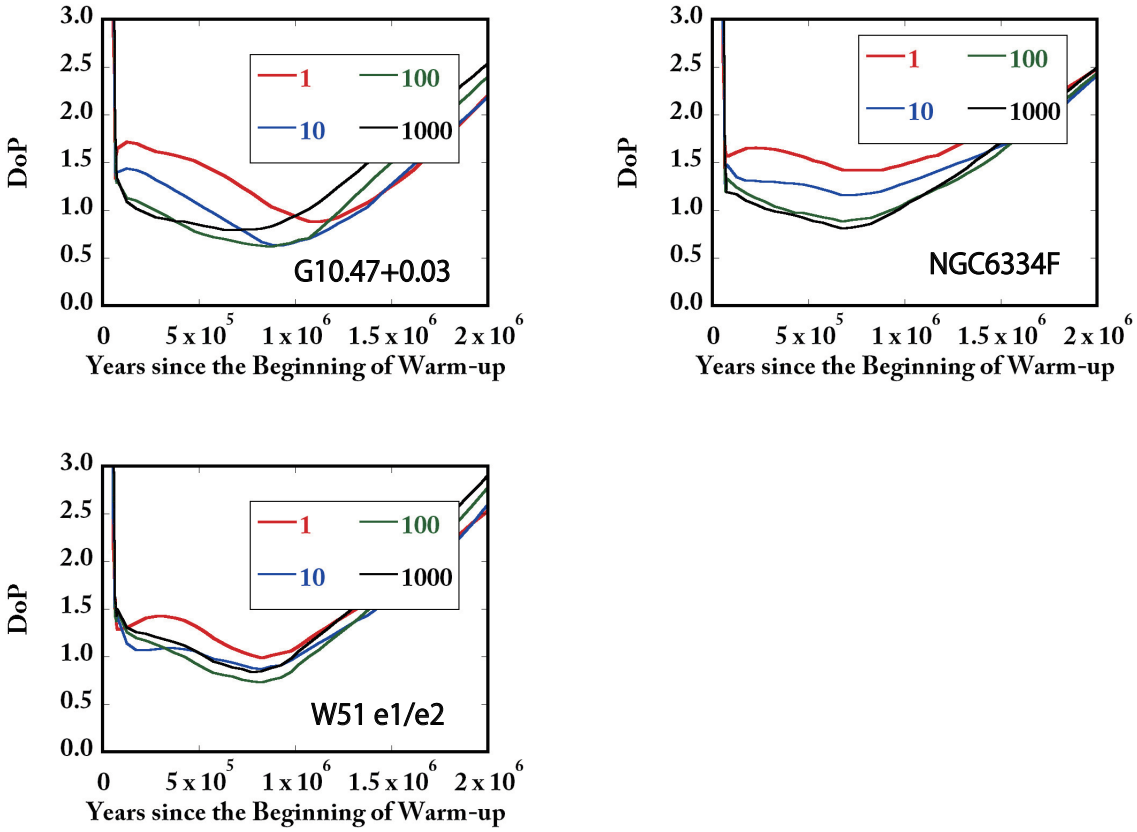

Fig. 26.— DoPs under V_{120K}/V_{200K}=1, 10, 100, and 1000 were calculated for G10.47+0.03, NGC6334F, and W51 e1/e2. Smaller V_{120K}/V_{200K} represent a core where high temperature region is dominant.

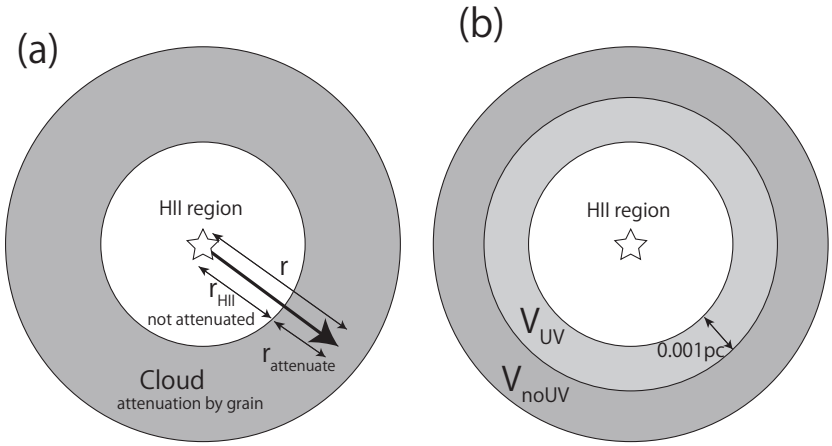

Fig. 27.— (a) Assumed structure of HII region and the cloud are shown. (b) Assumed structure of HII region, an area affected by UV, and an area where UV is not dominant, are shown. Observed fractional abundances are compared with modeling results assuming this structure.

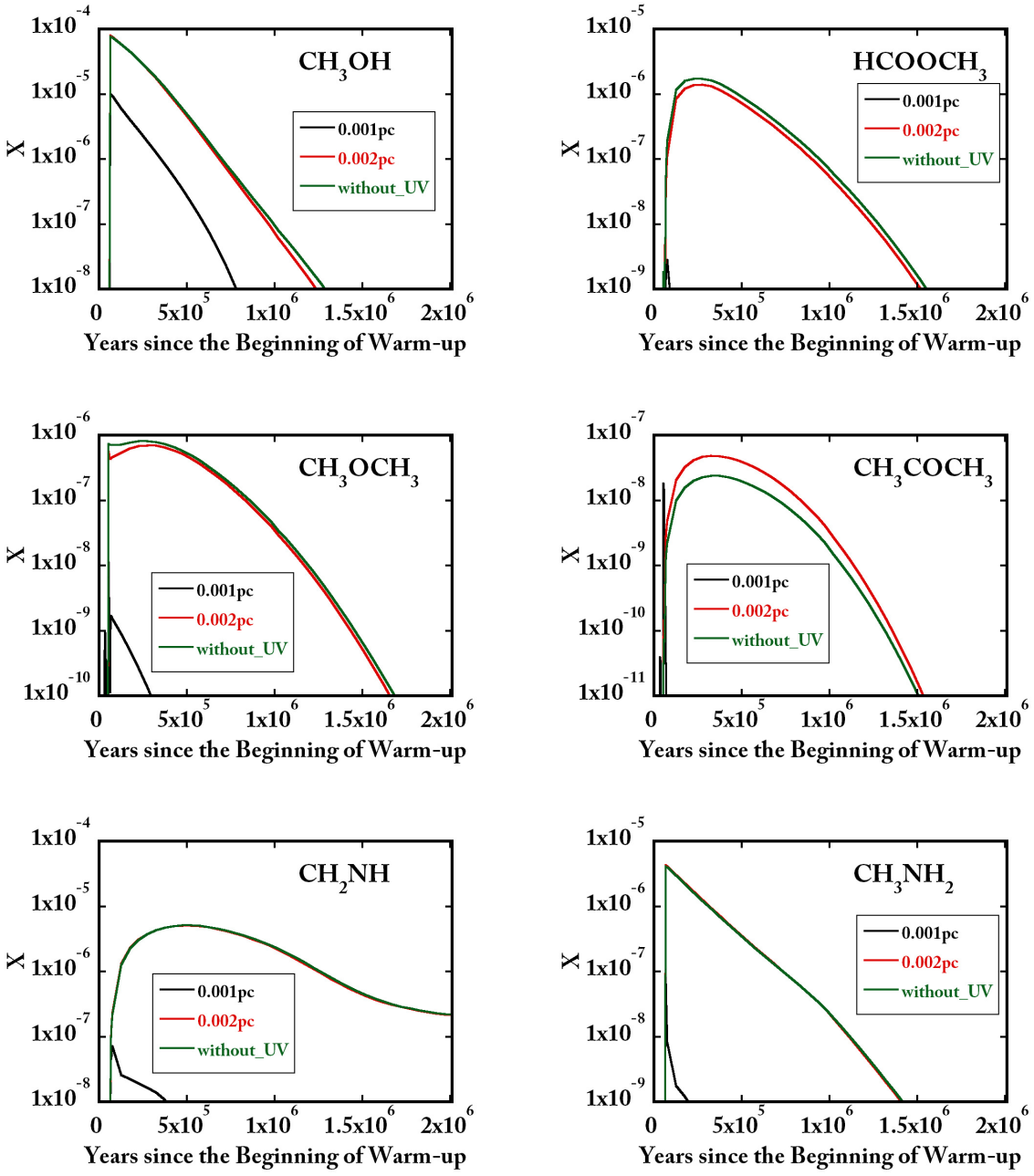

Fig. 28.— Comparison of abundances of COMs simulated under UV radiation from B0 type star in the different distance from the edge of HII region ($r_{attenuate}$=0.001 pc, 0.002 pc).

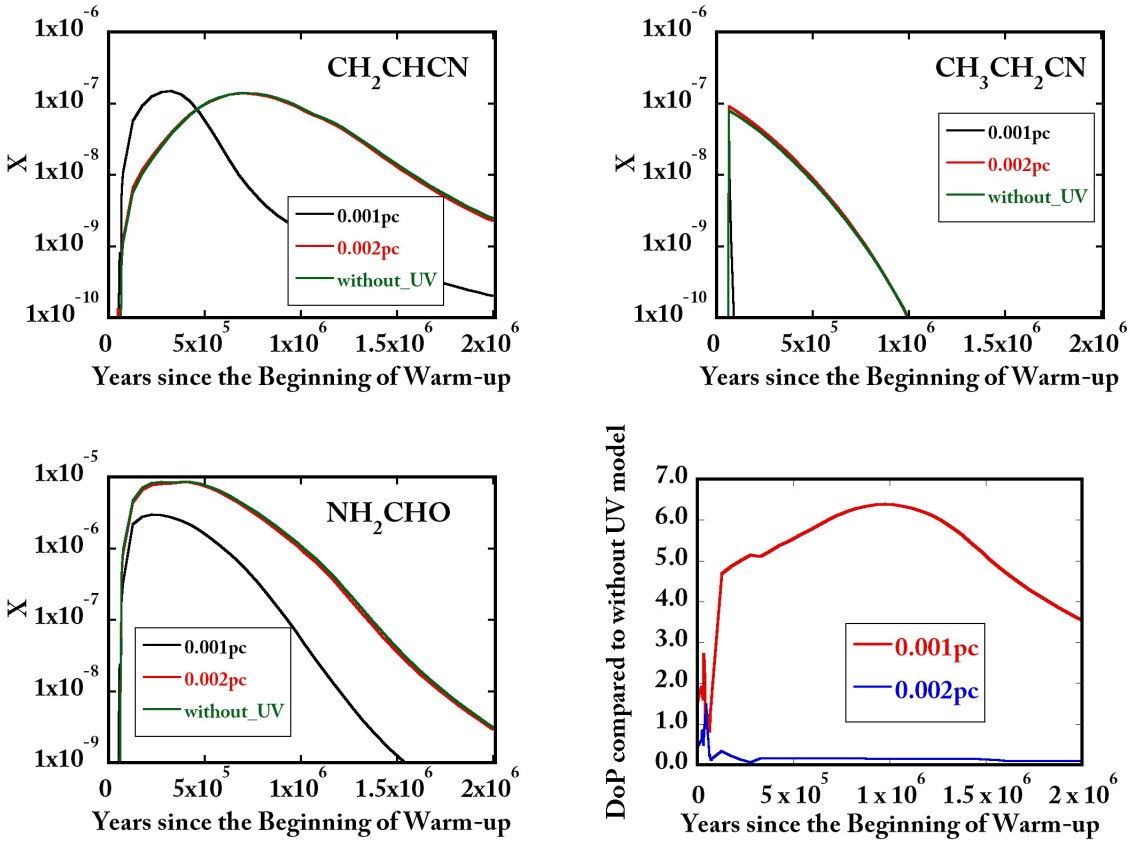

Fig. 28.— (continued) Comparison of abundances of COMs simulated under UV radiation from B0 type star in the different distance from the edge of HII region ($r_{attenuate}$=0.001 pc, 0.002 pc). DoP of $r_{attenuate}$=0.001 pc, 0.002 pc models compared to without UV model are also shown.

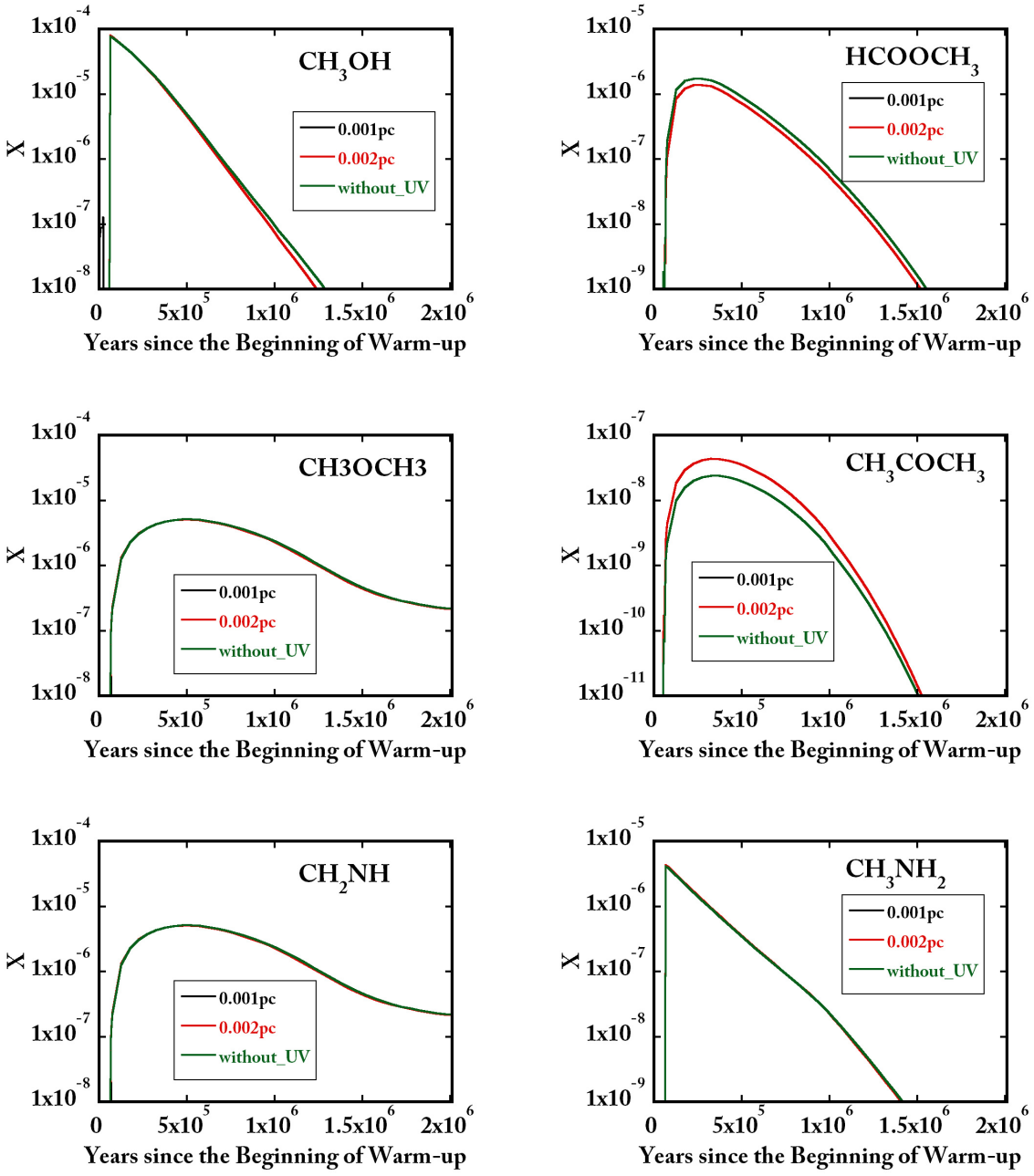

Fig. 29.— Comparison of abundances of COMs simulated under UV radiation from O5 type star in the different distance from the edge of HII region ($r_{attenuate}$=0.001 pc, 0.002 pc)..

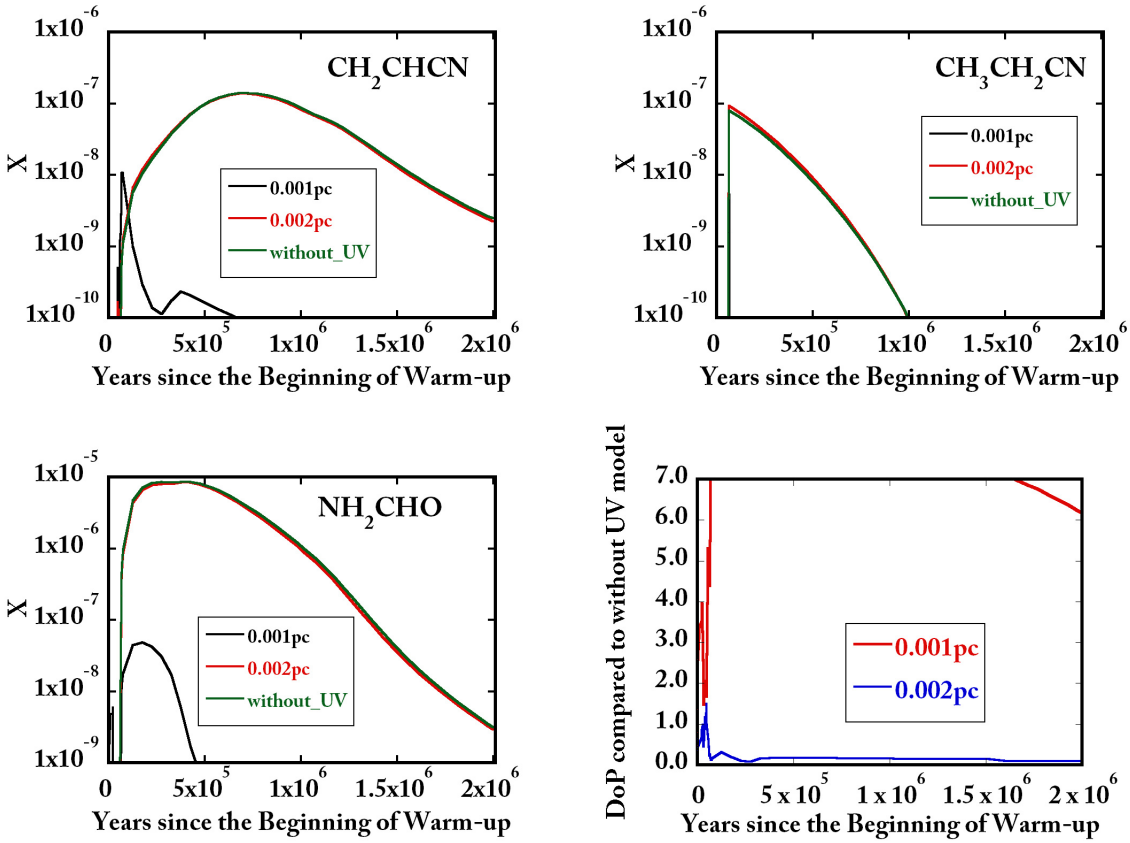

Fig. 29.— (continued) Comparison of abundances of COMs simulated under UV radiation from O5 type star in the different distance from the edge of HII region ($r_{attenuate}$=0.001 pc, 0.002 pc). DoP of $r_{attenuate}$=0.001 pc, 0.002 pc models compared to without UV model are also shown.

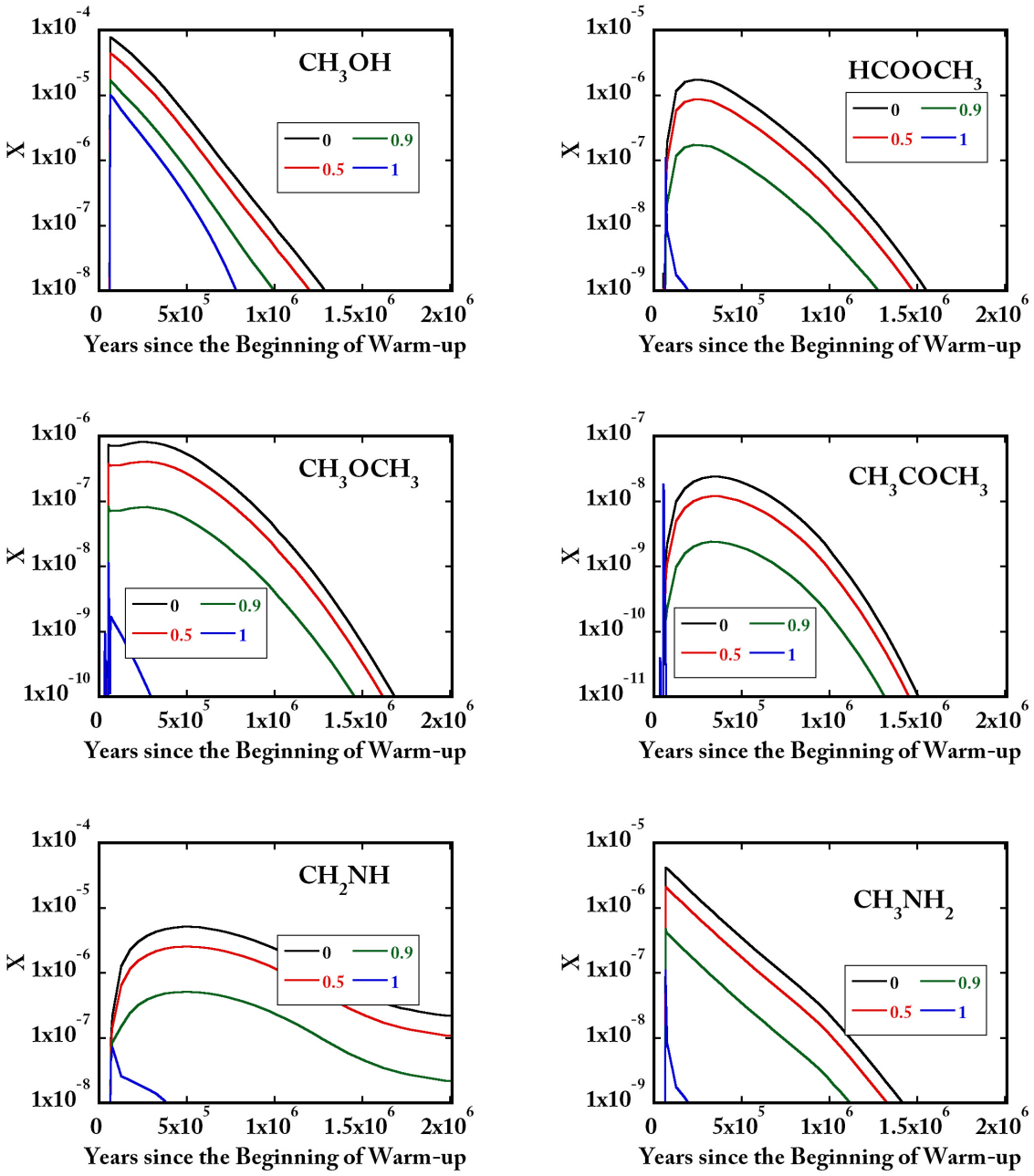

Fig. 30.— Comparison of abundances of COMs simulated under $V_{UV}/(V_{UV}+V_{noUV})$=0, 0.5, 0.9, and 1. A structure depicted in Figure 26 with central B0 type star is assumed. These calculatins are made under the assumption that I observed both inner side of the cloud, where UV is dominant, and outer part of the cloud, where the effect of UV is negligible.

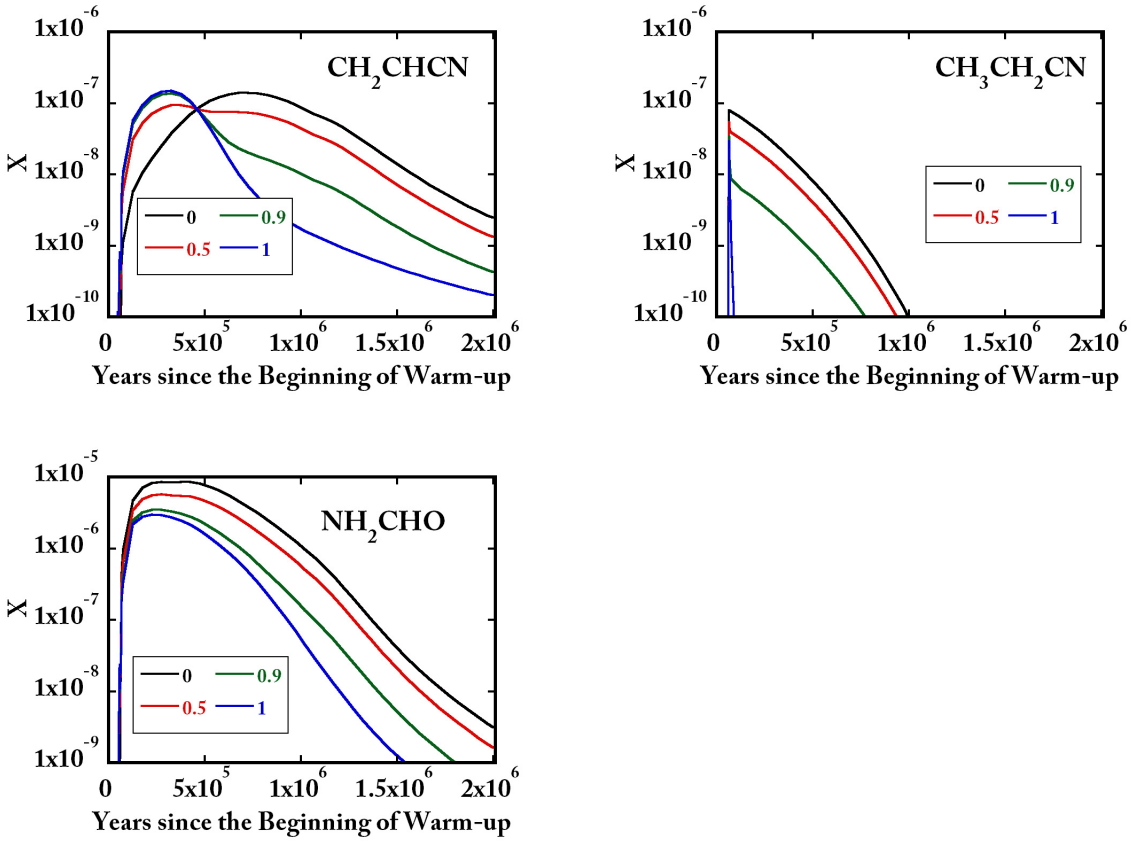

Fig. 30.— (continued) Fractional abundances under $V_{UV}/(V_{UV}+V_{noUV})$=0, 0.5, 0.9, and 1 are shown. A structure depicted in Figure 26 with central B0 type star is assumed. These calculatins are made under the assumption that I observed both inner side of the cloud, where UV is dominant, and outer part of the cloud, where the effect of UV is negligible.

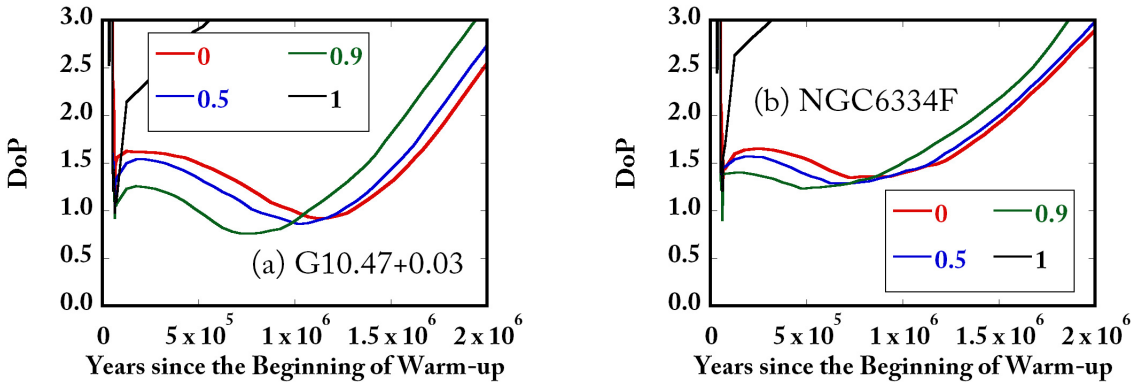

Fig. 31.— DoPs compared to observations toward (a)G10.47+0.03 and (b)NGC6334F under $V_{UV}/(V_{UV}+V_{noUV})$=0, 0.5, 0.9, and 1 are shown. A structure depicted in Figure 26 with central B0 type star is assumed. These simulations are made under the assumption that both inner side of the cloud, where UV is dominant, and outer part of the cloud, where the effect of UV is negligible, are observed by a single beam.

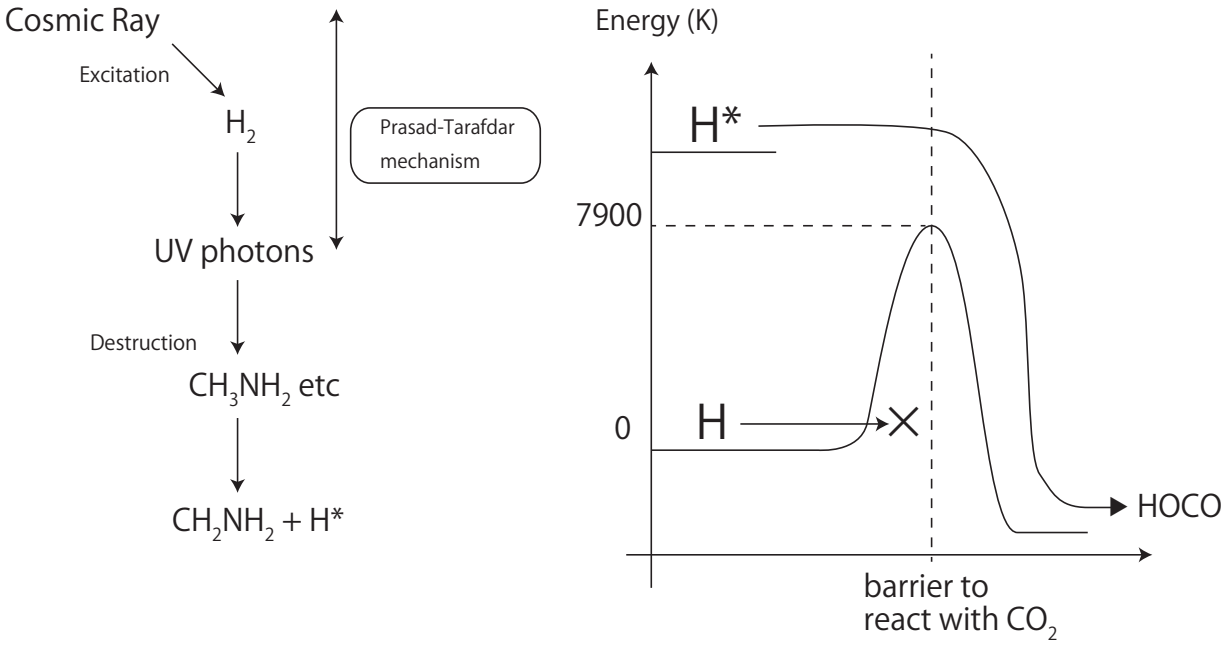

Fig. 32.— It was assumed that suprathermal hydrogen is formed via UV radiation field. In dense cores, UV radiation field would be formed by Prasad-Tarafdar mechanism, starting from the destruction of H_2 by cosmic rays. When such UV ratiation field destroy molecules, dissociated hydrogen atoms would have extra energy and referred to as "suprathermal hydrogen" H*. Although it is unlikely for usual H atoms to react with CO_2, the extra energy of H* make it possible to overcome the activation barrier.

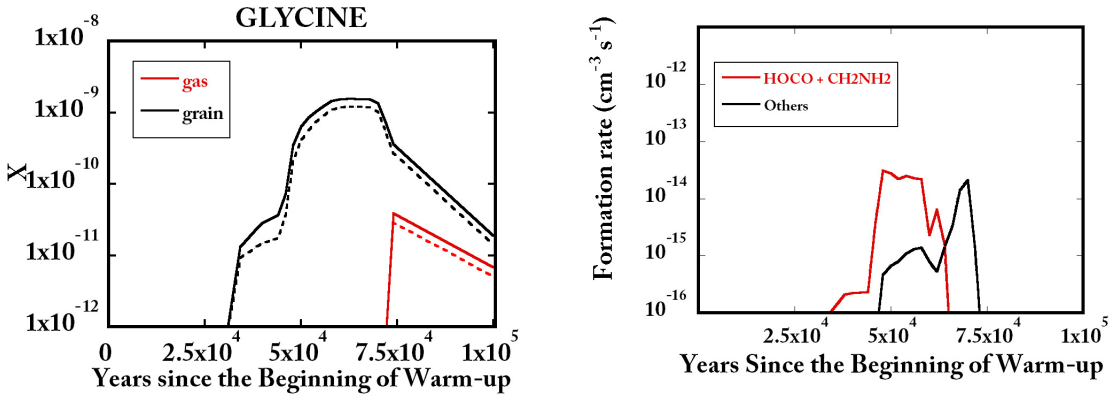

Fig. 33.— (a) Glycine abundances of Garrod (dotted line) model and Model 1 (solid line) are compared. The black lines and red lines, respectively, represent gas phase and grain surface glycine abundances. (b) The formation rates (cm^{-3} s^{-1}) of glycine are compared. The red lines are corresponding to "CH_2NH_2 + HOCO" process, while the black lines represent the sum of reaction rates for the other processes.

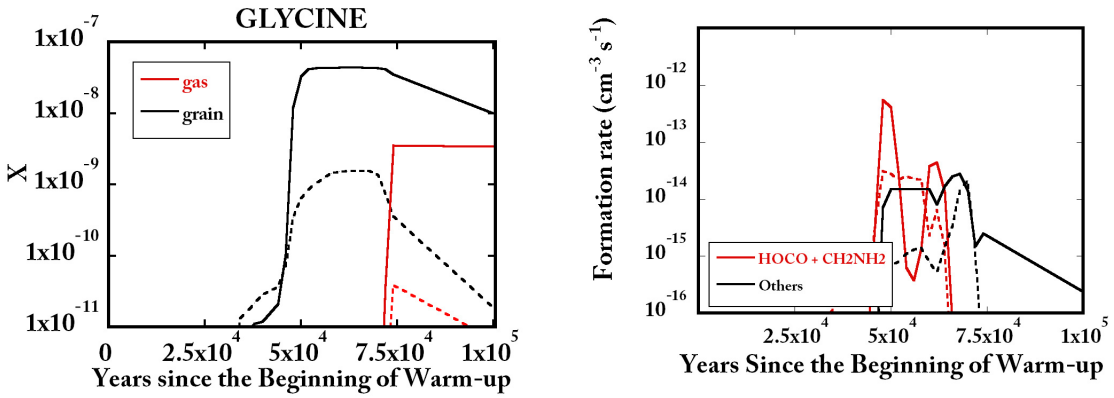

Fig. 34.— (a) Glycine abundances of Model 1 (dotted lines) and Model 2 (solid lines) are compared. In Model 2, H* chemistry is added to Model 1. The black lines and red lines, respectively, represent gas phase and grain surface glycine abundances. (b) The formation rates (cm^{-3} s^{-1}) of glycine are compared. The red lines are corresponding to "CH_2NH_2 + HOCO" process, while the black lines represent the sum of reaction rates for the other processes.

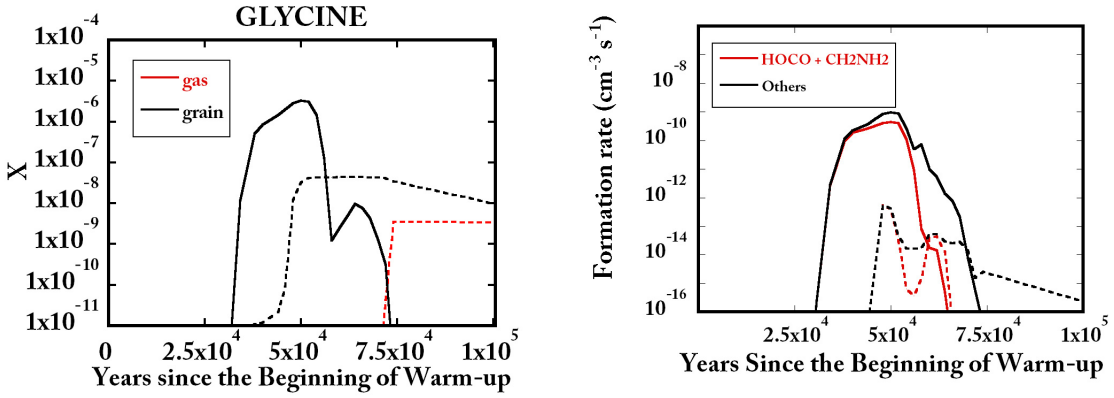

Fig. 35.— (a) With Model 2, glycine abundances are compared under the condition of with (solid lines) and without (dotted lines) UV flux from a star. The black lines and red lines, respectively, represent gas phase and grain surface glycine abundances. The gas phase glycine abundance is lower than 10^{-10} under UV radiation from a star. (b) The formation rates (cm^{-3} s^{-1}) of glycine are compared under the condition of with (solid lines) and without (dotted lines) UV radiation from a star. The red lines represents the rate of "CH_2NH_2 + HOCO" reaction, while the black lines represent total formation rates.

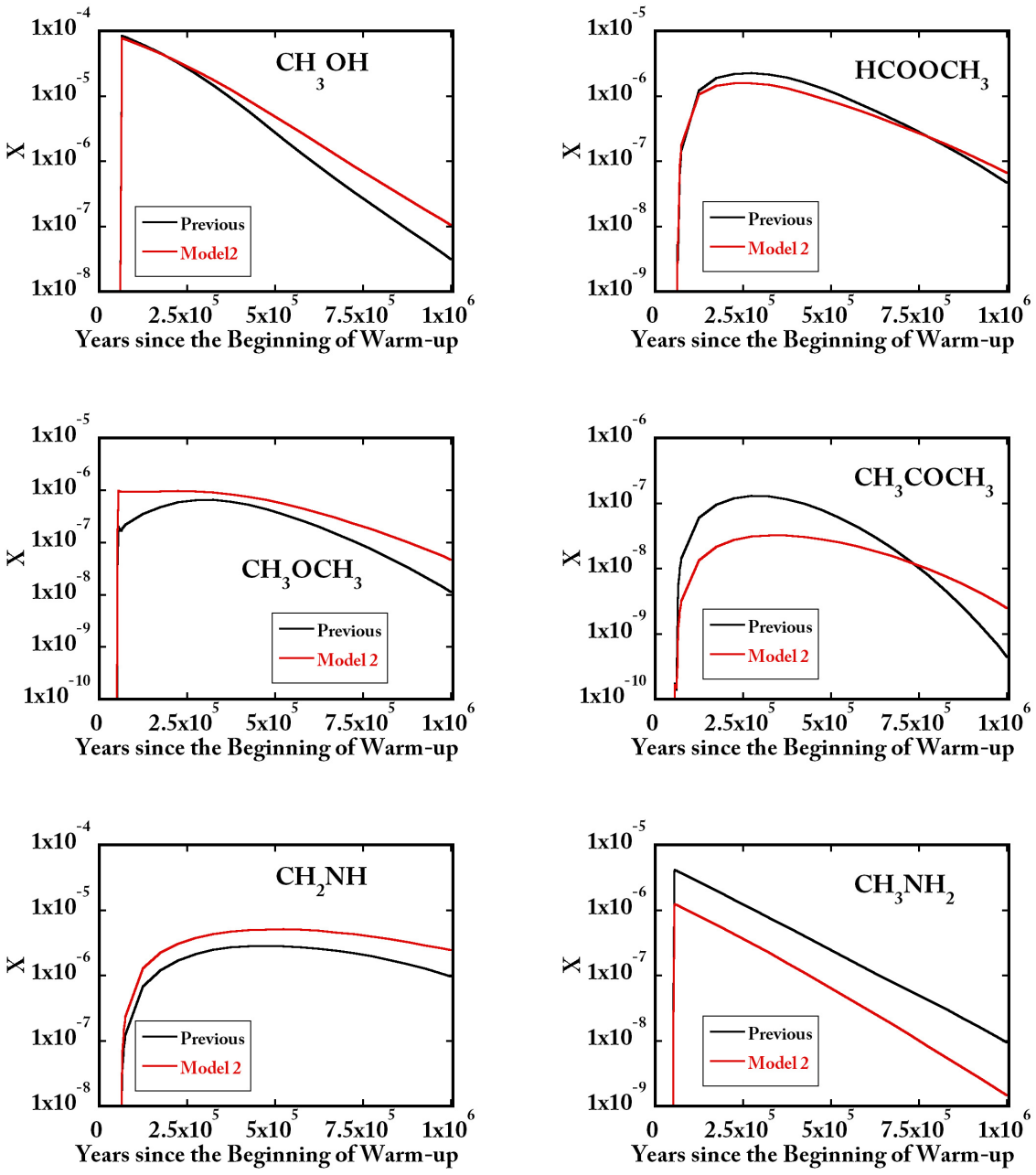

Fig. 36.— Comparison of abundances of COMs simulated under the Garrod Model and Model 2.

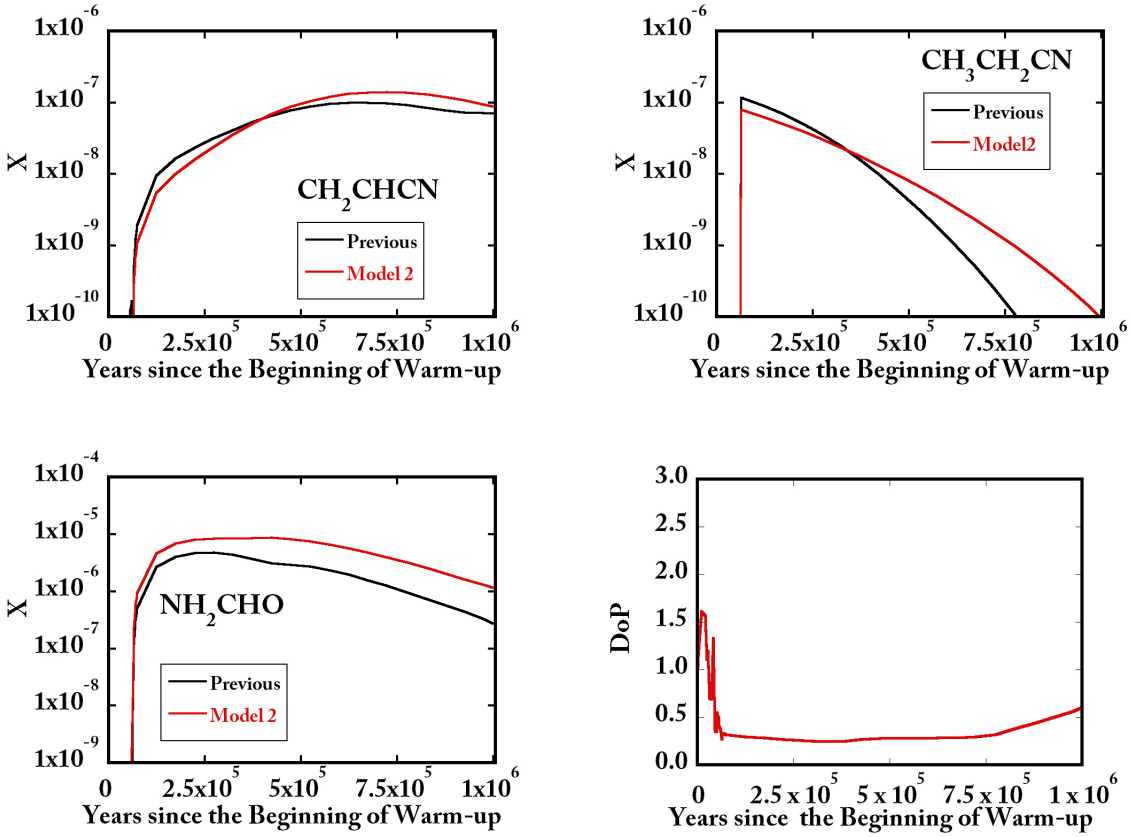

Fig. 36.— (continued) Comparison of abundances of COMs simulated under the previous model and Model 2. The DoP is also shown.

Table 1. Detected CH_2NH Lines in the Past Survey

Source	transitions	ν (MHz)	reference
Sagittarius B2*			(1)
Orion KL	2_{11}-2_{02}	172267.113	(2)
	1_{10}-1_{11}	225554.692	(2)
	4_{14}-3_{13}	245125.974	(2)
	7_{16}-7_{07}	250161.865	(2)
	6_{06}-5_{15}	251421.379	(2)
W51 e1/e2	1_{11}-0_{00}	225554.692	(2)
	4_{14}-3_{13}	245125.974	(2)
	6_{06}-5_{15}	251421.379	(2)
	4_{23}-3_{22}	255840.431	(2)
G34.3+0.2	4_{14}-3_{13}	245125.974	(2)
G19.61-0.23	3_{13}-2_{02}	340354.315	(3)

Note. — *27 transitions were reported by Halfen et al. (2013) towards Sagittarius B2. References. (1) Halfen et al. (2013) and references therein (2) Dickens et al. (1997) (3) Qin et al. (2010)

Table 2. Observed CH_2NH Lines

Transition	ν (MHz)	E_u (K)	$S\mu^2$ (D^2)	Telescope
4_{04}-3_{13}	105794.062	30.6	3.93	NRO
1_{11}-0_{00}	225554.609	10.8	2.34	SMT
4_{14}-3_{13}	245125.866	37.3	6.58	SMT
4_{23}-3_{22}	255840.311	62.2	5.27	SMT

Table 3. List of Observed Sources

Source	α(J2000) h m s	δ(J2000) ° ′ ″	V_{LSR} (km s $^{-1}$)	distance (kpc)	Masers	Mass High/Low	Detection	reference
W3(H_2O)	02 27 04.6	+61 52 25	-47	2.0	M	H	no	1, 6
NGC1333 IRAS4B	03 29 11.99	+31 13 08.9	6.8	0.2		L	no	3, 7
Orion KL	05 35 14.5	-05 22 30.6	6	0.4	M	H	confirm	1, 8
NGC2264 MMS3	06 41 12.3	+09 29 11.9	8	0.7		H	no	4, 9
IRAS16293-2422	16 32 22.63	-24 28 31.8	2.7	0.12		L	no	5, 10
NGC6334F	17 26 42.8	-36 09 17.0	-7	1.3	M	H	new	1, 6
G10.47+0.03	18 08 38.13	-19 51 49.4	68	8.5	M	H	new	1, 6
G19.61-0.23	18 27 38.0	-11 56 42	41.9	4.0	M	H	confirm	1, 11
G31.41+0.3	18 47 34.6	-01 12 43	97	7.9	M	H	new	1, 12
G34.3+0.2	18 53 18.54	+01 14 57.0	58	1.6	M	H	confirm	1, 6
W51 e1/e2	19 23 43.77	+14 30 25.9	58	5.4	M	H	confirm	1, 6
G75.78+0.34	20 21 44.1	+37 26 40	-0.1	3.8	M	H	no	2, 6
DR21 (OH)	20 39 01.1	+42 22 50.2	-3	1.5	M	H	new	1, 6
Cep A	22 56 17.9	+62 01 49	-10.5	0.7	M	H	no	2, 6

Note. — "M" represents CH_3OH maser sources reported in Minier & Booth (2002). "H" and "L" respectively shows high-mass and low-mass star-forming regions. In the column of detection, "no","confirm", and "new", respectively, represent non-detection sources, confirmations of the past CH_2NH surveys, and new CH_2NH detections. References. (1) Ikeda et al. (2001) (2) Minier & Booth (2002) (3) Sakai et al. (2006) (4) Sakai et al. (2007) (5)Cauzax et al. (2003) (6)Reid et al. (2014) (7)Hirota et al. (2008) (8)Menten et al. (2007) (9) Sung et al. (1997) (10)Loinard et al. (2008) (11)Hofner & Churchwell (1996) (12)Churchwell et al. (1990)

Table 4. Observed Lines towards G10.47+0.03

Species	Obs. freq (GHz)	Rest freq (GHz)	Transition	Eu (K)	Sd^2 (D^2)	T_A* (mK)	Δv (km s^{-1})	V_{LSR} (km s^{-1})	rms noise (mK)
CH_3OH	80.99371	80.99324	7(2,6)-8(1,7)–	103	2.5	488	9.9	66.3	9
	81.65344	81.65293	18(4,14)-19(3,16)	493	5.9	228	9.9	66.1	8
	84.42421	84.42378	13(-3,11)-14(-2,13)	274	4.3	262	9.7	66.5	6
	84.52160	84.52117	5(-1,5)-4(0,4)	40	3.1	1022	8.0	66.5	16
	84.74446	84.74390	19(4,15)-18(5,14)E	537	5.2	111	13.0	66.0	11
	86.61607	86.61560	7(2,6)-6(3,3)–	103	1.4	515	9.8	66.4	15
	86.90346	86.90295	7(2,5)-6(3,4)++	103	1.4	560	9.8	66.2	14
	88.94051	88.93999	15(3,12)-14(4,11)A–	328	4.2	404	9.5	66.3	13
	89.50643	89.50581	8(-4,5)-9(-3,7)	171	1.6	514	10.2	65.9	10
	95.91483	95.91431	2(1,2)-1(1,1)A++	21	1.2	682	8.3	66.4	13
	96.74019	96.73936	2(-1,2)-1(-1,1)	13	1.2	1690	9.0	65.4	16
	96.74222	96.74138	2(0,2)-1(0,1)++	7	1.6	1264	5.5	65.4	12
	96.74507	96.74455	2(0,2)-1(0,1)	20	1.6	992	7.8	66.4	18
	96.75602	96.75551	2(1,1)-1(1,0)	28	1.2	707	8.8	66.4	16
	100.63947	100.63890	13(2,11)-12(3,9)	234	3.8	552	9.8	66.3	13
	103.38174	103.38115	12(-2,11)-12(1,11)	207	0.8	279	10.7	66.3	18
	104.06116	104.06066	13(-3,11)-12(-4,9)	274	3.3	378	10.1	66.5	15
	104.33701	104.33656	13(-2,12)-13(1,12)	237	1.2	329	10.2	66.7	19
	104.35542	104.35482	10(4,7)-11(3,8)–	208	2.5	446	10.5	66.3	17
	105.06433	105.06369	13(1,13)-12(2,10)++	224	4.3	491	10.0	66.2	15
	105.57686	105.57629	14(-2,13)-14(1,13)	270	1.8	361	9.0	66.4	15
$HCOOCH_3$	79.78208	79.78227	7(0,7)-6(0,6)E	16	18.4	114	8.7	68.7	7
	79.78432	79.78391	7(0,7)-6(0,6)A	16	18.4	95	7.1	66.5	5
	86.02165	86.02165	7(5,2)-6(5,1)E	33	9.2	41	9.5	68.0	5
	86.02965	86.02966	7(5,2)-6(5,1)A	33	9.2	79	11.9	68.1	7
	blended	86.03021	7(5,3)-6(5,2)A	33	9.2				
	88.84352	88.84349	7(1,6)-6(1,5)E	18	18.2	108	10.6	67.9	9
	88.85214	88.85208	7(1,6)-6(1,5)A	18	18.2	114	8.8	67.8	10
	89.31643	89.31459	8(1,8)-7(1,7)E	20	21	268	13.1	61.8	11
	blended	89.31667	8(1,8)-7(1,7)A	20	21				
	96.07718	96.07726	8(2,7)-7(2,6)A	24	20	92	9.9	68.2	10
	100.29514	100.29514	8(3,5)-7(3,4)E	27	18.4	137	8.8	68.0	9

Table 4—Continued

Species	Obs. freq (GHz)	Rest freq (GHz)	Transition	Eu (K)	Sd^2 (D^2)	T_A* (mK)	Δv (km s^{-1})	V_{LSR} (km s^{-1})	rms noise (mK)
	100.30879	100.30879	8(3,5)-7(3,4)A	27	18.4	142	9.0	68.0	9
	100.48265	100.48265	8(1,7)-7(1,6)E	23	20.8	206	8.9	68.0	10
	100.49149	100.49150	8(1,7)-7(1,6)A	23	20.8	193	8.4	68.0	7
	100.68295	100.68148	9(0,9)-8(0,8)A	25	23.7	239	11.6	63.6	11
	blended	100.68339	9(0,9)-8(0,8)E	25	23.7				
	103.46729	103.46729	8(2,6)-7(2,5)E	25	20.2	152	7.5	68.0	13
	103.47927	103.47927	8(2,6)-7(2,5)A	25	20.2	141	8.8	68.0	16
CH_3OCH_3	78.85820	78.85627	13(2,11)-13(1,12)EA	90	73.2	155	15.9	60.7	7
	blended	78.85627	13(2,11)-13(1,12)AE	90	109.9				
	blended	78.85782	13(2,11)-13(1,12)EE	90	293				
	blended	78.85937	13(2,11)-13(1,12)AA	90	183.1				
	81.37050	81.36897	21(5,16)-20(6,15)AA	246	47.4	26	4.5	62.4	7
	blended	81.37051	21(5,16)-20(6,15)EE	246	75.6				
	81.37255	81.37191	21(5,16)-20(6,15)AE	246	28.4	15	6.8	65.7	7
	blended	81.37217	21(5,16)-20(6,15)EA	246	18.7				
	81.46997	81.46762	18(4,15)-17(5,12)AA	178	41.5	18	8.5	59.4	6
	blended	81.46992	18(4,15)-17(5,12)EE	178	66.4				
	81.47159	81.47207	18(4,15)-17(5,12)EA	178	16.5	16	8.6	69.8	5
	blended	81.47239	18(4,15)-17(5,12)AE	178	24.9				
	84.53055	84.52710	18(4,14)-17(5,13)AA	179	25	19	17.0	55.8	9
	blended	84.52959	18(4,14)-17(5,13)EE	179	66.6				
	blended	84.53193	18(4,14)-17(5,13)AE	179	8.3				
	blended	84.53225	18(4,14)-17(5,13)EA	179	16.6				
	84.63472	84.63190	3(2,1)-3(1,2)AE	19	32.3	45	16.7	58.0	5
	blended	84.63227	3(2,1)-3(1,2)EA	19	86.1				
	blended	84.63441	3(2,1)-3(1,2)EE	19	10.8				
	blended	84.63674	3(2,1)-3(1,2)AA	19	21.5				
	90.93867	90.93751	6(0,6)-5(1,5)AA	1	19	198	10.4	64.2	10
	blended	90.93810	6(0,6)-5(1,5)EE	3	19				
	blended	90.93870	6(0,6)-5(1,5)AE	0	19				
	blended	90.93870	6(0,6)-5(1,5)EA	1	19				
	92.70223	92.69614	8(5,4)-9(4,5)AE	68	5.7	27	11.0	48.3	4

Table 4—Continued

Species	Obs. freq (GHz)	Rest freq (GHz)	Transition	Eu (K)	Sd^2 (D^2)	T_A* (mK)	Δv (km s^{-1})	V_{LSR} (km s^{-1})	rms noise (mK)
	blended	92.69897	8(5,3)-9(4,5)EA	68	3.5				
	blended	92.70196	8(5,3)-9(4,5)EE	68	12				
	blended	92.70307	8(5,4)-9(4,5)AA	68	9.6				
	96.85040	96.84724	5(2,4)-5(1,5)EA	19	16.4	72	16.8	58.2	5
	blended	96.84729	5(2,4)-5(1,5)AE	19	8.2				
	blended	96.84988	5(2,4)-5(1,5)EE	19	65.6				
	blended	96.85250	5(2,4)-5(1,5)AA	19	24.6				
	96.92934	96.92805	17(8,10)-18(7,12)EE	229	40.7	20	9.9	64.0	11
	blended	96.92927	17(8,10)-18(7,11)AA	229	15.7				
	blended	96.92937	17(8,9)-18(7,12)AA	229	26.2				
	blended	96.92979	17(8,10)-18(7,11)AE	229	5.2				
	blended	96.92989	17(8,9)-18(7,12)AE	229	15.7				
	blended	96.93111	17(8,9)-18(7,11)EE	229	40.7				
	blended	96.93291	17(8,9)-18(7,11)EA	229	10.4				
	99.32577	99.32436	4(1,4)-3(0,3)EA	10	17.5	241	10.9	63.7	7
	blended	99.32436	4(1,4)-3(0,3)AE	10	26.2				
	blended	99.32521	4(1,4)-3(0,3)EE	10	69.8				
	blended	99.32606	4(1,4)-3(0,3)AA	10	43.6				
	100.43443	100.43420	22(5,18)-21(6,15)AA	266	50.9	102	8.2	67.3	5
	blended	100.43548	22(5,18)-21(6,15)EE	266	81.4				
	blended	100.43671	22(5,18)-21(6,15)EA	266	20.3				
	blended	100.43682	22(5,18)-21(6,15)AE	266	30.6				
	100.46361	100.46041	6(2,5)-6(1,6)EA	25	19.2	146	14.1	58.5	10
	blended	100.46044	6(2,5)-6(1,6)AE	25	28.8				
	blended	100.46307	6(2,5)-6(1,6)EE	25	76.9				
	blended	100.46571	6(2,5)-6(1,6)AA	25	48.1				
	100.94935	100.94684	19(4,16)-18(5,13)AA	196	27	35	11.8	60.5	7
	blended	100.94900	19(4,16)-18(5,13)EE	196	71.9				
	blended	100.95109	19(4,16)-18(5,13)EA	196	18				
	blended	100.95125	19(4,16)-18(5,13)AE	196	9				
	104.17791	104.17587	17(2,15)-17(1,16)EA	148	79.6	216	13.7	62.1	16
	blended	104.17587	17(2,15)-17(1,16)AE	148	119.3				

Table 4—Continued

Species	Obs. freq (GHz)	Rest freq (GHz)	Transition	Eu (K)	Sd^2 (D^2)	T_A* (mK)	Δv (km s^{-1})	V_{LSR} (km s^{-1})	rms noise (mK)
	blended	104.17738	17(2,15)-17(1,16)EE	148	318.3				
	blended	104.17889	17(2,15)-17(1,16)AA	148	198.9				
	105.77078	105.76828	13(1,12)-13(0,13)EA	86	36.7	146	14.6	60.9	18
	blended	105.76828	13(1,12)-13(0,13)AE	86	55				
	blended	105.77034	13(1,12)-13(0,13)EE	86	146.7				
	blended	105.77240	13(1,12)-13(0,13)AA	86	91.7				
CH_3CHO	79.09965	79.09931	4(1,3)-3(1,2)E	12	23.7	127	7.0	66.7	10
	79.15052	79.15017	4(1,3)-3(1,2)A–	12	23.7	134	7.1	66.7	12
	95.94796	95.94744	5(0,5)-4(0,4)E	14	31.6	93	7.0	66.4	5
	95.96395	95.96347	5(0,5)-4(0,4)A++	14	31.6	94	6.9	66.5	6
	96.36871	96.36779	5(3,3)-4(3,3)A++	34	20.2	34	6.8	65.1	8
	blend	96.36838	5(3,2)-4(3,2)E	34	20.3				
	96.42627	96.42562	5(-2,4)-4(-2,3)E	23	26.4	39	6.1	66.0	5
	96.47602	96.47552	5(2,3)-4(2,2)E	23	26.4	49	7.4	66.5	6
	96.63339	96.63267	5(2,3)-4(2,2)A++	23	26.6	47	7.0	65.8	5
CH_3COCH_3	92.72787	92.72790	9(0,9)-8(1,8)AE	23	72	34	12.5	68.1	5
	blend	92.72791	9(1,9)-8(0,8)AE	23	72				
	blend	92.72795	9(0,9)-8(1,8)EA	23	72				
	blend	92.72795	9(1,9)-8(0,8)EA	23	72				
	92.73603	92.73567	9(0,9)-8(1,8)EE	23	72	54	9.7	66.8	10
	blend	92.73567	9(1,9)-8(0,8)EE	23	72				
	92.74398	92.74336	9(0,9)-8(1,8)AA	23	72	50	7.3	66.0	6
	100.34931	100.35030	8(2,6)-7(3,5)EE	25	43.4	38	12.6	71.0	11
	99.26684	99.26643	5(5,0)-4(4,1)AA	14	34.3	19	7.5	66.8	6
NH_2CHO	81.69384	81.69345	4(1,4)-3(1,3)	13	49	249	10.2	66.5	6
	84.54279	84.54233	4(0,4)-3(0,3)	10	52.3	153	8.9	66.4	8
	84.80825	84.80779	4(2,3)-3(2,2)	22	39.2	150	8.5	66.4	6
	84.89041	84.88899	4(3,2)-3(3,1)	37	22.9	129	13.9	63.0	7
	blended	84.89098	4(3,1)-3(3,0)	37	22.9				
	87.84931	87.84887	4(1,3)-3(1,2)	14	49	241	8.6	66.5	12
	105.46468	105.46422	5(0,5)-4(0,4)	15	65.3	333	11.5	66.7	16
	105.97343	105.97260	5(2,4)-4(2,3)	27	54.9	280	10.1	65.6	16

Table 4—Continued

Species	Obs. freq (GHz)	Rest freq (GHz)	Transition	Eu (K)	Sd^2 (D^2)	T_A* (mK)	Δv (km s^{-1})	V_{LSR} (km s^{-1})	rms noise (mK)
	106.10827	106.10786	5(4,2)-4(4,1)	63	23.5	240	8.7	66.8	17
	blended	106.10788	5(4,1)-4(4,0)	63	23.5				
	106.13511	106.13442	5(3,3)-4(3,2)	42	41.8	209	9.8	66.1	15
	106.14198	106.14139	5(3,2)-4(3,1)	42	41.8	189	9.0	66.3	17
CH_2CHCN	84.94625	84.94625	9(0,9)-8(0,8)	20	130.9	143	8.5	68.0	6
	85.71571	85.71570	9(2,7)-8(2,6)	29	124.5	116	8.5	68.0	6
	96.98319	96.98244	10(1,9)-9(1,8)	25	145.5	208	8.9	65.7	7
	103.57570	103.57570	11(0 11)-10(0 10)	30	160	241	9.0	68.0	17
	104.21291	104.21291	11(2 10)-10(2 9)	39	154.8	234	7.9	68.0	20
	104.41963	104.41928	11(6,5)-10(6,4)	108	112.5	220	8.6	67.0	15
	blend	104.41928	11(6,6)-10(6,5)	108	112.5				
	104.43302	104.43302	11(3 9)-10(3 8)	50	148.2	197	8.6	68.0	9
	104.43784	104.43748	11(7,4)-10(7,3)	136	95.3	178	8.6	67.0	10
	blend	104.43748	11(7,5)-10(7,4)	136	95.3				
	104.45423	104.45423	11(3 8)-10(3 7)	50	148.2	224	10.3	68.0	16
	104.46177	104.46147	11(8,4)-10(8,3)	168	75.4	160	10.5	67.1	12
	blend	104.46147	11(8,3)-10(8,2)	168	75.4				
	104.52381	104.52351	11(10,2)-10(10,1)	245	27.8	79	5.9	67.2	13
	blend	104.52351	11(10,1)-10(10,0)	245	27.8				
	104.96147	104.96147	11(2,9)-10(2,8)	39	154.8	149	12.0	68.0	26
CH_3CH_2CN	79.44246	79.44246	7(1,7)-6(0,6)	13	6.5	35	5.3	66.9	6
	79.67780	79.67780	9(0,9)-8(0,8)	19	133.1	233	8.8	66.9	7
	81.26173	81.26173	9(2,7)-8(2,6)	24	126.8	259	7.9	66.5	5
	84.15223	84.15223	11(0,11)-10(1,10)	28	10.3	40	7.4	66.6	6
	86.82016	86.82016	10(1,10)-9(1,9)	24	146.7	352	8.5	66.9	10
	88.89511	88.89511	19(1,18)-19(0,19)	84	11.2	52	5.5	67.1	8
	89.00957	89.00957	25(2,23)-25(1,24)	147	24.4	77	7.3	67.1	8
	89.29798	89.29798	10(2,9)-9(2,8)	28	142.3	310	8.3	66.9	9
	89.41584	89.41584	24(3,21)-24(2,22)	140	27.8	91	6.7	66.5	8
	89.56272	89.56272	10(6,4)-9(6,3)	64	94.9	337	9.0	66.6	6
	blended		10(6,5)-9(6,4)	64	94.9				
	89.56544	89.56544	10(7,3)-9(7,2)	78	75.6	294	7.2	66.6	7

Table 4—Continued

Species	Obs. freq (GHz)	Rest freq (GHz)	Transition	Eu (K)	Sd^2 (D^2)	T_A* (mK)	Δv (km s^{-1})	V_{LSR} (km s^{-1})	rms noise (mK)
	blended		10(7,4)-9(7,3)	78	75.6				
	89.56845	89.56845	10(5,6)-9(5,5)	51	111.2	345	8.8	66.8	6
	blended		10(5,5)-9(5,4)	51	111.2				
	89.57341	89.57341	10(8,2)-9(8,1)	95	53.4	247	8.1	66.8	9
	blended		10(8,3)-9(8,2)	95	53.4				
	89.58524	89.58524	10(9,1)-9(9,0)	114	28.2	173	8.0	66.9	5
	blended		10(9,2)-9(9,1)	114	28.2				
	89.59098	89.59098	10(4,7)-9(4,6)	41	124.5	400	11.0	64.8	15
	blended		10(4,6)-9(4,5)	41	124.5				
	89.62876	89.62876	10(3,8)-9(3,7)	34	134.9	314	8.2	67.1	9
	89.68500	89.68500	10(3,7)-9(3,6)	34	134.9	318	7.9	67.0	6
	90.41925	90.41925	15(1,14)-14(2,13)	54	6.8	34	5.3	66.9	5
	90.45368	90.45368	10(2,8)-9(2,7)	28	142.3	270	8.1	66.9	6
	90.53132	90.53132	23(3,20)-23(2,21)	129	26	81	7.0	66.8	5
	93.06001	93.06001	30(3,27)-30(2,28)	212	36.2	64	6.0	67.4	3
	96.92010	96.92010	11(0,11)-10(0,10)	28	162.6	211	8.0	66.9	7
	99.07084	99.07084	32(3,29)-32(2,30)	240	37.3	75	7.1	67.3	10
	99.68190	99.68190	11(2,9)-10(2,8)	33	157.6	360	8.5	66.7	8
	100.61463	100.61463	11(1,10)-10(1,9)	30	161.6	341	8.0	66.7	10
	103.05920	103.05920	33(3 30)-33(2 31)	254	37.5	88	9.9	68.4	12
	104.10603	104.10603	13(0 13)-12(1 12)	39	13.2	76	5.5	66.8	16
	105.46983	105.46983	12(0 12)-11(0 11)	33	177.4	446	9.0	66.5	16
CH_2NH	105.79406	105.79429	4(0,4)-3(1,3)	31	3.9	101	10.0	68.7	7
	245.12579	245.12587	4(1,4)-3(1,3)	37	6.6	140	10.1	68.1	7
	255.84021	255.84031	4(2,3)-3(2,2)	62	5.3	120	9.8	68.1	6
CH_3NH_2	78.92875	78.92870	2(1)E1-1-2(0)E1+1	11	2.9	20	7.8	67.8	8
	79.00877	79.00870	1(1)B1-1(0)B2	6	2.4	26	4.8	67.7	8
	79.21031	79.21030	1(1)E1-1-1(0)E1+1	6	1.4	26	5.2	67.9	9
	86.07498	86.07473	4(1)A2-4(0)A1	25	7.3	21	3.6	67.1	11
	89.08145	89.08146	2(1)A2-2(0)A1	11	4	27	3.1	68.0	8
	81.52081	81.52108	6(1)A2 - 6(0)A1	49	10.8	24	6.1	69.0	8

Table 5. Observed Lines towards Orion KL

Species	Obs. freq (GHz)	Rest freq (GHz)	Transition	Eu (K)	Sd^2 (D^2)	T_A* (mK)	Δv (km s^{-1})	V_{LSR} (km s^{-1})	rms noise (mK)
CH_3OH	80.99277	80.99326	7(2,6)-8(1,7)–	103	2.5	2450	4.3	7.8	15
	81.65268	81.65293	18(4,14)-19(3,16)	493	5.9	439	4.2	6.9	20
	84.42337	84.42371	13(-3,11)-14(-2,13)	274	4.3	888	5.8	7.2	24
	84.52058	84.52121	5(-1,5)-4(0,4)	40	3.1	6136	2.5	8.2	14
	84.57350	84.57402	19(2,17)-18(-3,16)	463	0.4	48	3.0	7.8	12
	84.74384	84.74390	19(4,15)-18(5,14)	537	5.2	409	9.8	6.2	24
	86.61514	86.61560	7(2,6)-6(3,3)–	103	1.4	1606	5.0	7.6	21
	86.90250	86.90295	7(2,5)-6(3,4)++	103	1.4	1787	4.9	7.6	18
	88.59442	88.59481	15(3,13)-14(4,10)++	328	4.2	711	4.4	7.3	13
	88.93962	88.93999	15(3,12)-14(4,11)–	328	4.2	877	5.0	7.3	13
	89.50534	89.50578	8(-4,5)-9(-3,7)	171	1.6	1073	3.9	7.5	12
	94.54129	94.54181	8(3,5)-9(2,7)	131	2.2	2325	5.2	7.7	13
	94.81459	94.81507	19(7,13)-20(6,14)++	685	4.6	309	4.0	7.5	14
	blend	94.81508	19(7,12)-20(6,15)–	685	4.6				
	95.16877	95.16952	8(0,8)-7(1,7)++	84	7.2	8569	3.0	8.4	13
	95.91365	95.91431	2(1,2)-1(1,1)++	21	1.2	3986	2.7	8.1	14
	96.73871	96.73936	2(-1,2)-1(-1,1)	13	1.2	4067	2.9	8.0	15
	96.74070	96.74138	2(0,2)-1(0,1)++	7	1.6	4518	3.1	8.1	15
	96.74389	96.74455	2(0,2)-1(0,1)	20	1.6	4235	3.0	8.0	15
	96.75484	96.75551	2(1,1)-1(1,0)	28	1.2	3418	2.8	8.1	16
	99.60153	99.60195	15(1,14)-15(1,15)-+	295	0.1	75	2.6	7.3	8
	100.63845	100.63887	13(2,11)-12(3,9)	234	3.8	1847	4.8	7.3	14
	101.12623	101.12677	5(-2,4)-5(1,4)	61	0.01	44	4.0	7.6	5
	101.18483	101.18537	6(-2,5)-6(1,5)	75	0.02	88	2.9	7.6	7
	102.12211	102.12270	10(-2,9)-10(1,9)	154	0.3	354	3.6	7.7	20
	103.32452	103.32525	12(3,9)-13(0,13)	229	0.04	51	2.5	8.1	5
	103.38059	103.38121	12(-2,11)-12(1,11)	207	0.8	512	3.5	7.8	14
	105.57579	105.57638	14(-2,13)-14(1,13)	270	1.8	1386	4.8	7.7	12
	107.01313	107.01377	3(1,3)-4(0,4)++	28	3	8145	3.3	7.8	15
	107.15932	107.15991	15(-2,14)-15(1,14)	305	2.6	1244	4.7	7.7	12
$HCOOCH_3$	79.40120	79.40177	9(3,7)-9(2,8)E	33	2.1	96	3.1	8.1	11
	79.43210	79.43272	9(3,7)-9(2,8)A	33	2.1	175	3.7	8.3	10

Table 5—Continued

Species	Obs. freq (GHz)	Rest freq (GHz)	Transition	Eu (K)	Sd^2 (D^2)	T_A* (mK)	Δv (km s^{-1})	V_{LSR} (km s^{-1})	rms noise (mK)
	79.44927	79.44981	9(2,8)-9(1,9)E	29	1.3	67	2.9	8.1	12
	79.48779	79.48829	9(2,8)-9(1,9)A	29	1.3	80	3.2	7.9	8
	79.78123	79.78165	7(0,7)-6(0,6)E	16	18.4	579	3.4	7.6	15
	79.78336	79.78391	7(0,7)-6(0,6)A	16	18.4	583	3.6	8.1	15
	81.16729	81.16769	13(2,11)-13(1,12)E	59	2.8	76	2.3	7.5	10
	81.21731	81.21781	13(2,11)-13(1,12)A	59	2.8	83	2.9	7.9	6
	81.31373	81.31410	16(3,13)-16(2,14)E	89	4.6	78	2.6	7.3	6
	81.36188	81.36230	16(3,13)-16(2,14)A	89	4.6	75	2.5	7.5	7
	81.38003	81.38058	3(2,1)-2(1,2)E	6	0.6	23	1.6	8.0	7
	81.39162	81.39228	3(2,1)-2(1,2)A	6	0.6	26	4.0	8.4	7
	84.22411	84.22480	11(4,7)-11(3,8)E	50	3	76	3.7	8.5	12
	84.23282	84.23326	11(4,7)-11(3,8)A	50	3	72	3.5	7.6	12
	84.44863	84.44910	7(2,6)-6(2,5)E	19	17.2	453	3.9	7.7	10
	84.45423	84.45479	7(2,6)-6(2,5)A	19	17.2	465	3.9	8.0	11
	85.91865	85.91909	7(6,1)-6(6,0)E	40	5	146	3.7	7.5	5
	85.92630	85.92651	7(6,2)-6(6,1)E	40	5	546	7.5	6.7	8
	blend	85.92723	7(6,2)-6(6,1)A	40	5				
	blend	85.92724	7(6,1)-6(6,0)A	40	5				
	86.02058	86.02101	7(5,2)-6(5,1)E	33	9.2	263	3.6	7.5	8
	86.02718	86.02767	7(5,3)-6(5,2)E	33	9.2	271	3.5	7.7	7
	86.02926	86.02945	7(5,3)-6(5,2)A	33	9.2	373	5.5	6.7	14
	00.00000	86.03021	7(5,2)-6(5,1)A	33	9.2	0	0.0	0.0	0
	87.55188	87.55242	10(2,9)-10(1,10)A	34	1.3	72	1.6	7.9	6
	87.76589	87.76630	8(0,8)-7(1,7)E	20	2.8	126	2.5	7.4	6
	87.76854	87.76907	8(0,8)-7(1,7)A	20	2.8	115	2.7	7.8	10
	88.68634	88.68691	11(3,9)-11(2,10)E	45	2.4	60	1.9	7.9	5
	88.84264	88.84312	7(1,6)-6(1,5)E	18	18.2	518	3.1	7.6	14
	88.85107	88.85164	7(1,6)-6(1,5)A	18	18.2	507	3.0	7.9	19
	89.31413	89.31459	8(1,8)-7(1,7)E	20	21	587	3.3	7.5	14
	89.31606	89.31667	8(1,8)-7(1,7)A	20	21	636	3.7	8.0	14
	89.74516	89.74566	11(1,10)-11(0,11)E	40	1.3	40	1.4	7.7	6
	89.79648	89.79699	11(1,10)-11(0,11)A	40	1.3	39	1.6	7.7	7

Table 5—Continued

Species	Obs. freq (GHz)	Rest freq (GHz)	Transition	Eu (K)	Sd^2 (D^2)	T_A* (mK)	Δv (km s^{-1})	V_{LSR} (km s^{-1})	rms noise (mK)
	90.14518	90.14563	7(2,5)-6(2,4)E	20	17.3	394	2.9	7.5	14
	90.15593	90.15651	7(2,5)-6(2,4)A	20	17.3	391	3.0	7.9	17
	90.22714	90.22760	8(0,8)-7(0,7)E	20	21.1	437	3.4	7.5	12
	90.22906	90.22965	8(0,8)-7(0,7)A	20	21	431	3.2	8.0	12
	91.77540	91.77588	8(1,8)-7(0,7)E	20	2.9	156	2.3	7.6	6
	91.77656	91.77725	8(1,8)-7(0,7)A	20	2.9	212	3.1	8.2	7
	92.88371	92.88412	17(3,14)-17(2,15)E	100	4.4	185	2.3	7.3	10
	92.93981	92.94028	17(3,14)-17(2,15)A	100	4.4	197	2.3	7.5	12
	93.20521	93.20566	14(2,12)-14(1,13)E	67	2.8	66	2.6	7.4	8
	93.26127	93.26176	14(2,12)-14(1,13)A	67	2.8	82	2.1	7.6	8
	93.65952	93.66003	8(4,4)-8(3,5)A	32	1.8	146	2.3	7.6	9
	93.67064	93.70128	8(4,4)-8(3,5)E	32	1.4	138	3.1	104.0	17
	94.37810	94.37849	9(1,8)-8(2,7)E	28	1.7	137	2.7	7.2	11
	94.38708	94.38765	9(1,8)-8(2,7)A	28	1.7	134	2.0	7.8	9
	94.62630	94.62687	12(3,10)-12(2,11)E	52	2.5	170	2.4	7.8	11
	94.63216	94.63272	5(2,4)-4(1,3)E	11	1	120	2.0	7.8	6
	94.64673	94.64732	5(2,4)-4(1,3)A	11	1	91	2.2	7.9	7
	94.66641	94.66693	12(3,10)-12(2,11)A	52	2.5	168	2.7	7.7	15
	95.17539	95.17592	7(4,3)-7(3,4)A	27	1.5	152	2.5	7.7	13
	96.05836	96.05907	11(2,10)-11(1,11)E	41	1.3	58	6.5	8.2	6
	96.07018	96.07065	8(2,7)-7(2,6)E	24	20	544	4.1	7.5	13
	96.07627	96.07688	8(2,7)-7(2,6)A	24	20	573	4.4	7.9	18
	96.08642	96.08666	6(4,2)-6(3,3)A	23	1.1	55	5.4	6.7	6
	96.10670	96.10722	11(2,10)-11(1,11)A	41	1.3	50	3.3	7.6	14
	96.16716	96.16764	6(4,2)-6(3,3)E	23	0.8	38	4.6	7.5	9
	96.50123	96.50799	7(4,4)-7(3,5)E	27	1	212	5.0	27.0	8
	96.55208	96.55255	6(4,3)-6(3,4)E	23	0.8	32	7.7	7.5	5
	96.61255	96.61316	8(4,5)-8(3,6)E	32	1.4	62	3.1	7.9	14
	96.63743	96.63777	7(4,4)-7(3,5)A	27	1.5	61	3.5	7.1	15
	96.64746	96.64810	5(4,1)-5(3,2)E	19	0.7	32	3.5	8.0	14
	96.67035	96.67090	5(4,2)-5(3,3)E	19	0.7	26	2.6	7.7	8
	96.69290	96.69352	6(4,3)-6(3,4)A	23	1.1	37	3.2	7.9	8

Table 5—Continued

Species	Obs. freq (GHz)	Rest freq (GHz)	Transition	Eu (K)	Sd^2 (D^2)	T_A* (mK)	Δv (km s^{-1})	V_{LSR} (km s^{-1})	rms noise (mK)
	96.70911	96.70921	8(4,5)-8(3,6)A	32	1.8	119	6.0	6.3	12
	96.79359	96.79409	5(4,2)-5(3,3)A	19	0.8	28	2.5	7.5	8
	96.95627	96.95687	9(4,6)-9(3,7)E	37	2	84	3.3	7.8	14
	97.01759	97.01807	9(4,6)-9(3,7)A	37	2.1	79	3.1	7.5	5
	97.19862	97.19913	17(5,12)-17(4,13)A	108	5.2	162	3.7	7.6	5
	blend	97.19922	17(5,12)-17(4,13)E	108	5.2				
	99.13272	99.13319	9(0,9)-8(1,8)E	25	3.3	155	2.5	7.4	12
	99.13518	99.13579	9(0,9)-8(1,8)A	25	3.3	153	2.5	7.8	13
	99.16626	99.16652	11(2,9)-10(3,8)E	43	1.1	60	2.3	6.8	6
	99.17866	99.17936	11(2,9)-10(3,8)A	43	1.2	71	2.3	8.1	9
	100.29401	100.29451	8(3,5)-7(3,4)E	27	18.4	631	3.1	7.5	12
	100.30756	100.30821	8(3,5)-7(3,4)A	27	18.4	628	3.2	7.9	12
	100.48163	100.48217	8(1,7)-7(1,6)E	23	20.8	654	3.1	7.6	13
	100.49007	100.49071	8(1,7)-7(1,6)A	23	20.8	673	3.2	7.9	13
	100.65938	100.65969	12(4,9)-12(3,10)E	57	3	152	5.5	6.9	17
	100.68095	100.68148	9(0,9)-8(0,8)E	25	23.7	680	3.2	7.6	17
	100.68275	100.68339	9(0,9)-8(0,8)A	25	23.7	696	0.0	0.0	17
	100.69258	100.69305	12(4,9)-12(3,10)A	57	3	106	2.0	7.4	17
	100.73416	100.73477	12(1,11)-12(0,12)E	47	1.4	84	2.6	7.8	17
	100.79015	100.79077	12(1,11)-12(0,12)A	47	1.4	75	1.6	7.9	13
	103.22784	103.22841	13(4,10)-13(3,11)E	65	3.2	55	2.2	7.7	8
	103.26144	103.26201	13(4,10)-13(3,11)A	65	3.2	60	2.4	7.7	8
	103.46598	103.46648	8(2,6)-7(2,5)E	25	20.2	429	3.2	7.5	11
	103.47803	103.47870	8(2,6)-7(2,5)A	25	20.2	431	3.3	7.9	11
	105.42404	105.42464	15(2,13)-15(1,14)A	76	2.8	185	2.3	7.7	11
	105.45846	105.45897	18(3,15)-18(2,16)E	111	4.3	243	2.7	7.4	15
	105.52120	105.52175	18(3,15)-18(2,16)A	111	4.3	197	2.4	7.6	14
	107.53662	107.53719	9(2,8)-8(2,7)E	29	22.8	1141	2.8	7.6	9
	107.54312	107.54375	9(2,8)-8(2,7)A	29	22.8	952	2.8	7.8	9
CH_3OCH_3	78.85586	78.85627	13(2,11)-13(1,12)AE	90	109.9	441	3.2	7.6	12
	blend	78.85627	13(2,11)-13(1,12)EA	90	73.2				
	78.85737	78.85782	13(2,11)-13(1,12)EE	90	293	667	3.1	7.7	12

Table 5—Continued

Species	Obs. freq (GHz)	Rest freq (GHz)	Transition	Eu (K)	Sd^2 (D^2)	T_A* (mK)	Δv (km s^{-1})	V_{LSR} (km s^{-1})	rms noise (mK)
	78.85892	78.85937	13(2,11)-13(1,12)AA	90	183.1	458	3.5	7.7	12
	79.75310	79.75370	15(3,13)-14(4,10)AA	122	21.1	38	2.5	8.2	5
	79.75617	79.75661	15(3,13)-14(4,10)EE	122	56.2	109	1.9	7.6	6
	79.75905	79.75945	15(3,13)-14(4,10)EA	122	14	55	4.9	7.5	7
	81.46711	81.46762	18(4,15)-17(5,12)AA	178	41.5	39	2.4	7.9	5
	81.46941	81.46992	18(4,15)-17(5,12)EE	178	66.4	59	3.0	7.9	5
	84.52910	84.52959	18(4,14)-17(5,13)EE	179	66.6	56	3.4	7.7	14
	84.63156	84.63190	3(2,1)-3(1,2)AE	11	16.4	146	3.9	7.2	5
	blend	84.63227	3(2,1)-3(1,2)EA	11	10.9				
	84.63389	84.63441	3(2,1)-3(1,2)EE	11	43.7	260	3.5	7.8	7
	84.63621	84.63674	3(2,1)-3(1,2)AA	11	27.3	169	3.5	7.9	5
	85.97270	85.97325	13(2,12)-12(3,9)AA	88	16.8	36	5.7	7.9	12
	85.97562	85.97613	13(2,12)-12(3,9)EE	88	44.9	111	3.4	7.8	12
	85.97850	85.97900	13(2,12)-12(3,9)EA	88	11.2	46	2.6	7.7	5
	89.69763	89.69774	2(2,1)-2(1,2)AE	8	8.5	86	5.9	6.4	15
	89.69930	89.69980	2(2,1)-2(1,2)EE	8	22.3	186	3.1	7.7	12
	89.70245	89.70281	2(2,1)-2(1,2)AA	8	14.1	94	4.9	7.2	13
	90.88871	90.88925	15(3,12)-14(4,11)AA	123	36.2	48	3.3	7.8	7
	90.89177	90.89225	15(3,12)-14(4,11)EE	123	57.9	99	2.1	7.6	7
	90.89471	90.89518	15(3,12)-14(4,11)AE	123	21.7	57	2.6	7.5	7
	blend	90.89533	15(3,12)-14(4,11)EA	123	14.5				
	90.93755	90.93751	6(0,6)-5(1,5)AA	19	32.3	409	4.9	5.9	14
	blend	90.93810	6(0,6)-5(1,5)EE	19	86.1				
	blend	90.93870	6(0,6)-5(1,5)AE	19	10.8				
	blend	90.93870	6(0,6)-5(1,5)EA	19	21.5				
	91.47334	91.47376	3(2,2)-3(1,3)EA	11	9.7	105	3.5	7.4	9
	blend	91.47414	3(2,2)-3(1,3)AE	11	4.9				
	91.47608	91.47660	3(2,2)-3(1,3)EE	11	38.9	317	2.6	7.7	15
	91.47873	91.47924	3(2,2)-3(1,3)AA	11	14.6	141	2.4	7.7	7
	92.70142	92.70196	8(5,3)-9(4,5)EE	68	12	105	2.4	7.7	10
	92.70247	92.70307	8(5,4)-9(4,5)AA	68	9.6	92	2.0	7.9	6
	92.70977	92.71029	8(5,4)-9(4,6)EE	68	12	126	2.0	7.7	7

Table 5—Continued

Species	Obs. freq (GHz)	Rest freq (GHz)	Transition	Eu (K)	Sd^2 (D^2)	T_A* (mK)	Δv (km s^{-1})	V_{LSR} (km s^{-1})	rms noise (mK)
	93.66408	93.66460	12(1,11)-12(0,12)EA	74	37.6	400	2.7	7.7	12
	blend	93.66460	12(1,11)-12(0,12)AE	74	18.8				
	93.66590	93.66646	12(1,11)-12(0,12)EE	74	150.2	905	2.5	7.8	12
	93.66772	93.66832	12(1,11)-12(0,12)AA	74	56.3	452	3.0	7.9	12
	93.85395	93.85444	4(2,3)-4(1,4)EA	15	13.3	471	2.4	7.6	10
	blend	93.85456	4(2,3)-4(1,4)AE	15	19.9				
	93.85654	93.85710	4(2,3)-4(1,4)EE	15	53.1	670	2.4	7.8	10
	93.85913	93.85971	4(2,3)-4(1,4)AA	15	33.2	452	2.2	7.8	19
	94.14797	94.14845	11(6,5)-12(5,7)EE	111	23.2	120	2.2	7.5	7
	96.84679	96.84724	5(2,4)-5(1,5)EA	19	16.4	169	3.7	7.4	17
	blend	96.84729	5(2,4)-5(1,5)AE	19	8.2				
	96.84936	96.84988	5(2,4)-5(1,5)EE	19	65.6	409	3.4	7.6	17
	96.85195	96.85250	5(2,4)-5(1,5)AA	19	24.6	170	3.4	7.7	17
	96.93120	96.93111	17(8,9)-18(7,11)EE	229	40.7	24	4.3	5.7	14
	99.32384	99.32436	4(1,4)-3(0,3)EA	10	17.5	449	2.4	7.6	10
	blend	99.32436	4(1,4)-3(0,3)AE	10	26.2				
	99.32466	99.32521	4(1,4)-3(0,3)EE	10	69.8	585	1.8	7.7	5
	99.32546	99.32606	4(1,4)-3(0,3)AA	10	43.6	421	2.4	7.8	15
	99.83309	99.83366	14(2,13)-13(3,10)AA	101	28.9	97	2.0	7.7	7
	99.83589	99.83645	14(2,13)-13(3,10)EE	101	46.2	173	2.0	7.7	9
	99.83869	99.83924	14(2,13)-13(3,10)EA	101	11.5	111	2.2	7.7	7
	blend	99.83925	14(2,13)-13(3,10)AE	101	17.3				
	100.45988	100.46041	6(2,5)-6(1,6)EA	25	19.2	372	2.7	7.6	16
	blend	100.46044	6(2,5)-6(1,6)AE	25	28.8				
	100.46245	100.46307	6(2,5)-6(1,6)EE	25	76.9	532	2.7	7.9	16
	100.46517	100.46571	6(2,5)-6(1,6)AA	25	48.1	242	1.6	7.6	17
	100.94845	100.94900	19(4,16)-18(5,13)EE	196	71.9	44	2.7	7.6	5
	105.55919	105.55979	19(4,15)-18(5,14)AA	196	45.2	128	4.0	7.7	14
	105.56150	105.56207	19(4,15)-18(5,14)EE	196	72.3	214	3.4	7.6	11
	105.56371	105.56427	19(4,15)-18(5,14)AE	196	27.1	113	4.1	7.6	8
	105.76769	105.76828	13(1,12)-13(0,13)AE	86	55	665	2.7	7.7	12
	blend	105.76828	13(1,12)-13(0,13)EA	86	36.7				

Table 5—Continued

Species	Obs. freq (GHz)	Rest freq (GHz)	Transition	Eu (K)	Sd^2 (D^2)	T_A* (mK)	Δv (km s^{-1})	V_{LSR} (km s^{-1})	rms noise (mK)
	105.76972	105.77034	13(1,12)-13(0,13)EE	86	146.7	981	2.7	7.8	12
	105.77178	105.77240	13(1,12)-13(0,13)AA	86	91.7	701	2.5	7.8	12
CH_3CHO	79.09887	79.09931	4(1,3)-3(1,2)E	12	23.7	64	3.5	7.7	7
	79.14952	79.15017	4(1,3)-3(1,2)A–	12	23.7	83	3.3	8.5	8
	95.94700	95.94744	5(0,5)-4(0,4)E	14	31.6	85	5.5	7.4	7
	95.96292	95.96346	5(0,5)-4(0,4)A++	14	31.6	82	3.9	7.7	9
	96.27351	96.27426	5(2,4)-4(2,3)	23	26.6	46	4.1	8.3	12
	96.36735	96.36779	5(3,3)-4(3,2)A++	34	20.2	63	3.9	7.4	11
	blend	96.36838	5(3,2)-4(3,1)E	34	20.3				
	96.42484	96.42562	5(-2,4)-4(-2,3)E	23	26.4	62	3.5	8.4	11
	96.47484	96.47552	5(2,3)-4(2,2)E	23	26.4	53	4.6	8.1	11
	96.63202	96.63267	5(2,3)-4(2,2)A++	23	26.6	55	2.9	8.0	13
CH_3COCH_3	81.78887	81.78900	7(1,6)-6(2,5)AE	18	44.8	24	4.3	6.5	10
	blend	81.78927	7(1,6)-6(2,5)EA	18	44.8				
	81.81309	81.81373	7(1,6)-6(2,5)EE	17	44.8	31	2.7	8.3	9
	81.83269	81.83305	7(2,6)-6(1,5)EE	17	44.8	38	3.3	7.3	6
	81.83782	81.83824	7(1,6)-6(2,5)AA	17	44.8	23	1.8	7.5	9
	91.63413	91.63464	8(1,7)-7(2,6)EE	22	53.4	45	2.8	7.7	8
	91.63722	91.63746	8(2,7)-7(1,6)EE	22	53.4	34	5.0	6.8	7
	91.65876	91.65911	8(1,7)-7(2,6)AA	22	53.3	39	3.4	7.2	5
	92.72744	92.72790	9(0,9)-8(1,8)AE	23	72	97	2.5	7.5	5
	blend	92.72791	9(1,9)-8(0,8)AE	23	72				
	blend	92.72795	9(0,9)-8(1,8)EA	23	72				
	blend	92.72795	9(1,9)-8(0,8)EA	23	72				
	92.73531	92.73567	9(0,9)-8(1,8)EE	23	72	171	4.4	7.2	14
	blend	92.73567	9(1,9)-8(0,8)EE	23	72				
	92.74299	92.74336	9(0,9)-8(1,8)AA	23	72	87	3.8	7.2	10
	blend	92.74336	9(1,9)-8(0,8)AA	23	72				
	100.35006	100.35030	8(2,6)-7(3,5)EE	25	43.4	45	4.7	6.7	9
	108.38706	108.38759	8(3,5)-7(4,4)EE	27	32.5	53	4.0	7.5	12
NH_2CHO	81.69326	81.69345	4(1,4)-3(1,3)	13	49	62	5.1	6.7	9
	84.54213	84.54233	4(0,4)-3(0,3)	10	52.3	35	4.4	6.7	11

Table 5—Continued

Species	Obs. freq (GHz)	Rest freq (GHz)	Transition	Eu (K)	Sd^2 (D^2)	T_A* (mK)	Δv (km s^{-1})	V_{LSR} (km s^{-1})	rms noise (mK)
	84.80731	84.80779	4(2,3)-3(2,2)	22	39.2	32	4.1	7.7	11
	87.84847	87.84887	4(1,3)-3(1,2)	14	49	43	4.1	7.4	6
	102.06409	102.06427	5(1,5)-4(1,4)	18	62.8	69	7.0	6.5	8
	105.46416	105.46422	5(0,5)-4(0,4)	15	65.3	229	6.3	6.2	15
CH_2CHCN	84.94625	84.94600	9(0,9)-8(0,8)	20	131	143	8.5	5.1	6
	85.71570	85.71542	9(2,7)-8(2,6)	29	125	116	8.5	5.0	8
	92.42667	92.42625	10(1,10)-9(1,9)	27	144	167	9.4	4.6	20
	94.27727	94.27663	10(0,10)-9(0,9)	25	145	204	8.6	4.0	13
	94.76119	94.76078	10(2,9)-9(2,8)	34	140	158	9.4	4.7	13
	94.91399	94.91312	10(4,7)-9(4,6)	60	122	333	10.0	3.2	17
	blend	94.91323	10(4,6)-9(4,5)	60	122				
	blend	94.91396	10(5,5)-9(5,4)	79	109				
	blend	94.91396	10(5,6)-9(5,5)	79	109				
	94.92508	94.92501	10(6,5)-9(6,4)	103	93	176	7.2	5.8	8
	blend	94.92501	10(6,4)-9(6,3)	103	93				
	94.92874	94.92861	10(3,8)-9(3,7)	45	132	173	9.0	5.6	11
	94.94241	94.94163	10(3,7)-9(3,6)	45	132	198	9.3	3.5	10
	94.96523	94.96491	10(8,3)-9(8,2)	163	52	46	7.2	5.0	8
	blend	94.96491	10(8,2)-9(8,1)	163	52				
	94.99163	94.99155	10(9,2)-9(9,1)	200	28	29	3.1	5.7	6
	blend	94.99155	10(9,1)-9(9,0)	200	28				
	96.98320	96.98244	10(1,9)-9(1,8)	28	144	207	9.1	3.6	7
	103.57574	103.57540	11(0,11)-10(0,10)	30	160	136	7.5	5.0	9
CH_3CH_2CN	79.67784	79.67750	9(0,9)-8(0,8)	19	133	690	8.5	4.7	15
	81.26172	81.26143	9(2,7)-8(2,6)	24	127	389	7.9	4.9	10
	81.74705	81.74648	18(1,17)-18(0,18)	76	11	57	10.2	3.9	5
	84.15244	84.15184	11(0,11)-10(1,10)	28	10	33	12.2	3.9	9
	86.74552	86.74531	8(1,8)-7(0,7)	16	8	60	12.8	5.3	10
	86.82017	86.81984	10(1,10)-9(1,9)	24	147	566	8.4	4.9	16
	88.32406	88.32375	10(0,10)-9(0,9)	23	148	388	8.3	5.0	15
	89.00948	89.00930	25(2,23)-25(1,24)	147	24	56	4.7	5.4	13
	89.29796	89.29764	10(2,9)-9(2,8)	28	142	460	8.5	4.9	14

Table 5—Continued

Species	Obs. freq (GHz)	Rest freq (GHz)	Transition	Eu (K)	Sd^2 (D^2)	T_A* (mK)	Δv (km s^{-1})	V_{LSR} (km s^{-1})	rms noise (mK)
	89.41532	89.41537	24(3,21)-24(2,22)	140	28	66	7.6	6.2	7
	89.56279	89.56231	10(6,4)-9(6,3)	64	95	589	10.5	4.4	16
	blend	89.56231	10(6,5)-9(6,4)	64	95				
	89.56540	89.56503	10(7,3)-9(7,2)	78	76	551	6.9	4.8	18
	blend	89.56503	10(7,4)-9(7,3)	78	76				
	89.56831	89.56809	10(5,6)-9(5,5)	51	111	728	9.6	5.3	13
	blend	89.56810	10(5,5)-9(5,4)	51	111				
	89.57309	89.57305	10(8,2)-9(8,1)	95	53	299	12.4	5.9	12
	blend	89.57305	10(8,3)-9(8,2)	95	53				
	89.58582	89.58491	10(9,1)-9(9,0)	114	28	158	13.1	3.0	12
	blend	89.58491	10(9,2)-9(9,1)	114	28				
	blend	89.59101	10(4,6)-9(4,5)	41	125				
	blend	89.59367	28(3,25)-28(2,26)	186	34				
	89.62879	89.62844	10(3,8)-9(3,7)	34	135	481	8.3	4.8	16
	89.68501	89.68471	10(3,7)-9(3,6)	34	135	484	8.8	5.0	16
	90.45363	90.45335	10(2,8)-9(2,7)	28	142	401	8.4	5.1	18
	90.53156	90.53095	23(3,20)-23(2,21)	129	26	38	7.7	4.0	8
	91.01877	91.01826	29(3,26)-29(2,27)	199	35	52	5.6	4.3	5
	91.55011	91.54911	10(1,9)-9(1,8)	25	147	1601	14.7	2.7	15
	93.06026	93.05981	30(3,27)-30(2,28)	212	36	86	8.0	4.6	9
	93.75563	93.75508	21(3,18)-21(2,19)	110	22	101	14.1	4.3	9
	93.94993	93.94931	9(1,9)-8(0,8)	20	9	60	9.7	4.0	5
	95.10428	95.10405	26(2,24)-26(1,25)	158	24	80	5.5	5.3	8
	96.92002	96.91975	11(0,11)-10(0,10)	28	163	396	9.9	5.2	6
	99.68198	99.68150	11(2,9)-10(2,8)	33	158	542	10.3	4.6	15
	100.61463	100.61428	11(1,10)-10(1,9)	30	162	571	8.6	5.0	19
	101.09135	101.09166	10(1,10)-9(0,9)	24	10	33	6.8	6.9	6
	102.22785	102.22741	17(3,14)-17(2,15)	76	16	45	9.2	4.7	6
	103.86766	103.86725	21(1,20)-21(0,21)	102	11	38	6.9	4.8	7
	107.04385	107.04351	12(2,11)-11(2,10)	38	173	800	9.6	5.0	22
	blend	107.48518	12(7,6)-11(7,5)	88	117				
	blend	107.48696	12(6,6)-11(6,5)	74	133				

Table 5—Continued

Species	Obs. freq (GHz)	Rest freq (GHz)	Transition	Eu (K)	Sd^2 (D^2)	T_A* (mK)	Δv (km s^{-1})	V_{LSR} (km s^{-1})	rms noise (mK)
	blend	107.48696	12(6,7)-11(6,6)	74	133				
	107.49199	107.49157	12(8,4)-11(8,3)	105	99	653	10.9	4.8	13
	blend	107.49157	12(8,5)-11(8,4)	105	99				
	blend	107.50247	12(5,7)-11(5,6)	61	147				
	blend	107.50360	12(9,3)-11(9,2)	124	78				
	blend	107.50360	12(9,4)-11(9,3)	124	78				
	107.52086	107.51994	12(10,2)-11(10,1)	145	54	353	11.3	3.4	13
	blend	107.51994	12(10,3)-11(10,2)	145	54				
	107.54761	107.54759	12(4,8)-11(4,7)	51	158	819	11.6	5.9	13
	107.59458	107.59404	12(3,10)-11(3,9)	44	167	748	10.5	4.5	13
	107.70327	107.70217	34(3,31)-34(2,32)	269	37	44	9.4	2.9	8
	107.73525	107.73473	12(3,9)-11(3,8)	44	167	713	10.8	4.6	15
	108.21091	108.21038	11(1,11)-10(0,10)	29	11	93	11.2	4.5	12
	108.22752	108.22711	14(3,11)-14(2,12)	55	12	91	7.6	4.9	9
CH_2NH	105.79352	105.79406	4(0,4)-3(1,3)	31	3.9	116	7.8	7.5	9

Table 6. Observed Lines towards NGC6334F

Species	Obs. freq (GHz)	Rest freq (GHz)	Transition	Eu (K)	Sd^2 (D^2)	T_A* (mK)	Δv (km s^{-1})	V_{LSR} (km s^{-1})	rms noise (mK)
CH_3OH	80.99346	80.99326	7(2,6)-8(1,7)–	103	2.5	1086	5.9	-6.7	7
	81.65317	81.65293	18(4,14)-19(3,16)	493	5.9	506	5.2	-6.9	21
	83.79289	83.79265	18(-2,17)-18(2,16)	423	0.2	54	4.9	-6.9	7
	84.42402	84.42371	13(-3,11)-14(-2,13)	274	4.3	522	5.4	-7.1	15
	84.52163	84.52121	5(-1,5)-4(0,4)	40	3.1	4014	4.3	-7.5	8
	84.57398	84.57402	19(2,17)-18(-3,16)	463	0.4	80	4.7	-5.9	6
	84.74419	84.74390	19(4,15)-18(5,14)	537	5.2	204	6.4	-7.0	9
	85.56844	85.56807	6(-2,5)-7(-1,7)	75	2	974	5.5	-7.3	18
	86.61591	86.61560	7(2,6)-6(3,3)–	103	1.4	549	5.7	-7.1	19
	86.90334	86.90295	7(2,5)-6(3,4)++	103	1.4	571	5.3	-7.3	17
	88.59515	88.59481	15(3,13)-14(4,10)++	328	4.2	794	5.0	-7.1	17
	88.94029	88.93999	15(3,12)-14(4,11)–	328	4.2	390	5.3	-7.0	12
	89.50609	89.50578	8(-4,5)-9(-3,7)	171	1.6	619	5.3	-7.1	33
	94.54212	94.54181	8(3,5)-9(2,7)	131	2.2	1036	5.5	-7.0	16
	94.81507	94.81507	19(7,13)-20(6,14)++	685	4.6	180	5.5	-6.0	11
	blend	94.81508	19(7,12)-20(6,15)–	685					
	95.16963	95.16952	8(0,8)-7(1,7)++	84	7.2	1787	5.7	-6.4	15
	95.91472	95.91431	2(1,2)-1(1,1)++	21	1.2	1685	5.0	-7.3	7
	96.44680	96.44660	21(-2,20)-21(2,19)	563	0.3	57	3.2	-6.6	8
	96.73986	96.73936	2(-1,2)-1(-1,1)	13	1.2	3270	5.4	-7.5	8
	96.74188	96.74138	2(0,2)-1(0,1)++	7	1.6	3867	4.6	-7.6	8
	96.74498	96.74455	2(0,2)-1(0,1)	20	1.6	2244	5.4	-7.3	8
	96.75591	96.75551	2(1,1)-1(1,0)	28	1.2	1520	5.0	-7.3	9
	99.60220	99.60195	15(1,14)-15(1,15)-+	295	0.1	51	3.4	-6.8	9
	100.63927	100.63887	13(2,11)-12(3,9)	234	3.8	868	5.2	-7.2	14
	101.18563	101.18537	6(-2,5)-6(1,5)	75	0	73	3.7	-6.8	12
	103.32483	103.32525	12(3,9)-13(0,13)	229	0	129	1.7	-4.8	30
	103.38133	103.38121	12(-2,11)-12(1,11)	207	0.8	362	5.4	-6.3	36
	105.57650	105.57638	14(-2,13)-14(1,13)	270	1.8	472	5.5	-6.3	17
	107.01407	107.01377	3(1,3)-4(0,4)++	28	3	1310	5.7	-6.8	13
	107.16006	107.15991	15(-2,14)-15(1,14)	305	2.6	423	5.0	-6.4	12
$HCOOCH_3$	79.40195	79.40177	9(3,7)-9(2,8)E	33	2.1	115	4.3	-6.7	12

Table 6—Continued

Species	Obs. freq (GHz)	Rest freq (GHz)	Transition	Eu (K)	Sd^2 (D^2)	T_A* (mK)	Δv (km s^{-1})	V_{LSR} (km s^{-1})	rms noise (mK)
	79.43270	79.43272	9(3,7)-9(2,8)A	33	2.1	277	4.0	-5.9	17
	79.45003	79.44981	9(2,8)-9(1,9)E	29	1.3	92	4.1	-6.8	10
	79.48834	79.48829	9(2,8)-9(1,9)A	29	1.3	97	2.3	-6.2	14
	79.78191	79.78165	7(0,7)-6(0,6)E	16	18.4	523	4.6	-7.0	19
	79.78405	79.78391	7(0,7)-6(0,6)A	16	18.4	516	4.2	-6.5	14
	80.56526	80.56497	10(2,8)-9(3,7)E	36	0.9	51	2.4	-7.1	8
	80.57267	80.57268	10(2,8)-9(3,7)A	36	0.9	56	3.6	-6.0	11
	81.16795	81.16769	13(2,11)-13(1,12)E	59	2.8	119	3.5	-6.9	5
	81.21802	81.21781	13(2,11)-13(1,12)A	59	2.8	108	5.0	-6.8	9
	81.31431	81.31410	16(3,13)-16(2,14)E	89	4.6	145	4.0	-6.8	9
	81.36249	81.36230	16(3,13)-16(2,14)A	89	4.6	126	3.6	-6.7	8
	81.38070	81.38058	3(2,1)-2(1,2)E	6	0.6	61	2.8	-6.5	5
	81.39219	81.39228	3(2,1)-2(1,2)A	6	0.6	40	6.9	-5.7	6
	84.22483	84.22480	11(4,7)-11(3,8)E	50	3	85	3.7	-6.1	6
	84.23358	84.23326	11(4,7)-11(3,8)A	50	3	74	3.8	-7.1	6
	84.44942	84.44910	7(2,6)-6(2,5)E	19	17.2	338	4.5	-7.1	8
	84.45498	84.45479	7(2,6)-6(2,5)A	19	17.2	332	4.4	-6.7	7
	85.63848	85.63835	4(2,3)-3(1,2)E	9	0.8	71	1.8	-6.5	8
	85.65604	85.65580	4(2,3)-3(1,2)A	9	0.8	84	3.8	-6.8	11
	85.76211	85.76188	21(5,16)-21(4,17)E	156	7.9	147	4.2	-6.8	14
	85.77360	85.77332	21(5,16)-21(4,17)A	156	7.9	115	3.6	-7.0	7
	85.78086	85.78070	20(5,15)-20(4,16)E	143	7.3	160	3.7	-6.6	6
	85.78548	85.78526	20(5,15)-20(4,16)A	143	7.3	151	3.5	-6.8	8
	85.91937	85.91909	7(6,1)-6(6,0)E	40	5	224	3.9	-7.0	13
	85.92704	85.92651	7(6,2)-6(6,1)E	40	5	500	6.0	-7.8	19
	blended	85.92723	7(6,2)-6(6,1)A	40	5				
	blended	85.92724	7(6,1)-6(6,0)A	40	5				
	86.02129	86.02101	7(5,2)-6(5,1)E	33	9.2	311	4.2	-7.0	11
	86.02786	86.02767	7(5,3)-6(5,2)E	33	9.2	317	3.5	-6.7	13
	86.02995	86.02945	7(5,3)-6(5,2)A	33	9.2	426	5.9	-7.8	13
	blended	86.03021	7(5,2)-6(5,1)A	33	9.2				
	86.21024	86.21008	7(4,4)-6(4,3)A	27	12.7	390	4.2	-6.6	18

Table 6—Continued

Species	Obs. freq (GHz)	Rest freq (GHz)	Transition	Eu (K)	Sd^2 (D^2)	T_A* (mK)	Δv (km s^{-1})	V_{LSR} (km s^{-1})	rms noise (mK)
	86.22413	86.22355	7(4,3)-6(4,2)E	27	12.6	613	5.1	-8.0	13
	blended	86.22411	7(4,4)-6(4,3)E	27	12.6				
	86.25074	86.25058	7(4,3)-6(4,2)A	27	12.7	418	3.9	-6.6	18
	86.26600	86.26583	7(3,5)-6(3,4)A	23	15.3	432	4.4	-6.6	13
	86.26896	86.26866	7(3,5)-6(3,4)E	23	15.2	451	4.1	-7.0	18
	87.76653	87.76630	8(0,8)-7(1,7)E	20	2.8	171	3.8	-6.8	5
	87.76909	87.76907	8(0,8)-7(1,7)A	20	2.8	144	3.4	-6.1	9
	88.05443	88.05403	19(5,14)-19(4,15)E	130	6.6	216	3.7	-7.4	8
	blended	88.05437	19(5,14)-19(4,15)A	130	6.6				
	88.17566	88.17563	10(4,6)-10(3,7)E	43	2.5	149	3.9	-6.1	11
	88.18063	88.18036	10(4,6)-10(3,7)A	43	2.5	139	3.5	-6.9	9
	88.68704	88.68691	11(3,9)-11(2,10)E	45	2.4	144	3.1	-6.4	6
	88.72344	88.72324	11(3,9)-11(2,10)A	45	2.4	115	3.8	-6.7	6
	88.84342	88.84312	7(1,6)-6(1,5)E	18	18.2	247	4.4	-7.0	9
	88.85181	88.85164	7(1,6)-6(1,5)A	18	18.2	238	4.5	-6.6	8
	89.31491	89.31459	8(1,8)-7(1,7)E	20	21	272	4.6	-7.1	10
	89.31693	89.31667	8(1,8)-7(1,7)A	20	21	286	4.2	-6.9	6
	90.14579	90.14563	7(2,5)-6(2,4)E	20	17.3	270	4.7	-6.5	24
	90.15668	90.15651	7(2,5)-6(2,4)A	20	17.3	301	3.6	-6.6	24
	90.22783	90.22760	8(0,8)-7(0,7)E	20	21.1	364	4.7	-6.8	25
	90.22980	90.22965	8(0,8)-7(0,7)A	20	21	344	4.5	-6.5	20
	91.77605	91.77588	8(1,8)-7(0,7)E	20	2.9	202	2.9	-6.5	7
	91.77727	91.77679	20(4,16)-20(3,17)E	139	6.4	315	3.9	-7.6	10
	blended	91.77725	8(1,8)-7(0,7)A	20	2.9				
	91.82536	91.82518	20(4,16)-20(3,17)A	139	6.4	145	3.1	-6.6	7
	92.88439	92.88412	17(3,14)-17(2,15)E	100	4.4	143	3.6	-6.9	9
	92.94048	92.94028	17(3,14)-17(2,15)A	100	4.4	108	3.7	-6.6	8
	93.20590	93.20566	14(2,12)-14(1,13)E	67	2.8	118	3.9	-6.8	6
	93.26191	93.26176	14(2,12)-14(1,13)A	67	2.8	122	3.2	-6.5	8
	93.66019	93.66003	8(4,4)-8(3,5)A	32	1.8	99	2.8	-6.5	5
	93.70138	93.70128	8(4,4)-8(3,5)E	32	1.4	89	3.1	-6.3	7
	94.37880	94.37849	9(1,8)-8(2,7)E	28	1.7	113	4.2	-7.0	17

Table 6—Continued

Species	Obs. freq (GHz)	Rest freq (GHz)	Transition	Eu (K)	Sd^2 (D^2)	T_A* (mK)	Δv (km s^{-1})	V_{LSR} (km s^{-1})	rms noise (mK)
	94.38786	94.38765	9(1,8)-8(2,7)A	28	1.7	137	4.0	-6.7	13
	94.62706	94.62687	12(3,10)-12(2,11)E	52	2.5	154	4.0	-6.6	8
	94.63298	94.63272	5(2,4)-4(1,3)E	11	1	90	3.2	-6.8	8
	94.64753	94.64732	5(2,4)-4(1,3)A	11	1	87	4.0	-6.7	9
	94.66712	94.66693	12(3,10)-12(2,11)A	52	2.5	141	2.8	-6.6	14
	95.17615	95.17592	7(4,3)-7(3,4)A	27	1.5	102	2.9	-6.7	6
	96.05927	96.05907	11(2,10)-11(1,11)E	41	1.3	55	3.6	-6.6	7
	96.07099	96.07065	8(2,7)-7(2,6)E	24	20	410	4.2	-7.1	7
	96.07705	96.07688	8(2,7)-7(2,6)A	24	20	396	4.9	-6.5	13
	96.08724	96.08666	6(4,2)-6(3,3)A	23	1.1	58	4.7	-7.8	6
	96.10746	96.10722	11(2,10)-11(1,11)A	41	1.3	42	3.8	-6.8	6
	96.16775	96.16764	6(4,2)-6(3,3)E	23	0.8	49	3.2	-6.3	7
	96.50803	96.50799	7(4,4)-7(3,5)E	27	1	64	3.3	-6.1	7
	96.61325	96.61316	8(4,5)-8(3,6)E	32	1.4	72	3.2	-6.3	5
	96.63799	96.63777	7(4,4)-7(3,5)A	27	1.5	58	3.7	-6.7	4
	96.64809	96.64810	5(4,1)-5(3,2)E	19	0.7	37	2.8	-6.0	5
	96.67098	96.67090	5(4,2)-5(3,3)E	19	0.7	35	2.2	-6.3	9
	96.69378	96.69352	6(4,3)-6(3,4)A	23	1.1	58	3.8	-6.8	7
	96.70961	96.70921	8(4,5)-8(3,6)A	32	1.8	101	4.5	-7.2	8
	96.77688	96.77676	7(4,3)-7(3,5)E	24	0.5	39	3.4	-6.4	5
	96.79433	96.79409	5(4,2)-5(3,3)A	19	0.8	54	2.6	-6.7	6
	96.83545	96.83528	4(4,0)-4(3,1)A	17	0.4	38	2.9	-6.5	9
	96.85933	96.85939	4(4,0)-4(3,1)E	17	0.4	27	2.7	-5.8	8
	96.95700	96.95687	9(4,6)-9(3,7)E	37	2	89	3.3	-6.4	5
	97.01839	97.01807	9(4,6)-9(3,7)A	37	2.1	89	3.3	-7.0	7
	97.19943	97.19913	17(5,12)-17(4,13)A	108	5.2	183	4.1	-6.9	9
	blended	97.19922	17(5,12)-17(4,13)E	108	5.2				
	98.27076	98.27037	8(6,2)-7(6,1)E	45	9.4	372	3.8	-7.2	18
	98.27970	98.27887	8(6,3)-7(6,2)E	45	9.4	626	5.7	-8.5	15
	blended	98.27975	8(6,3)-7(6,2)A	45	9.4				
	blended	98.27979	8(6,2)-7(6,1)A	45	9.4				
	98.42442	98.42408	8(5,3)-7(5,2)E	38	13.1	430	4.0	-7.0	15

Table 6—Continued

Species	Obs. freq (GHz)	Rest freq (GHz)	Transition	Eu (K)	Sd^2 (D^2)	T_A* (mK)	Δv (km s^{-1})	V_{LSR} (km s^{-1})	rms noise (mK)
	98.43183	98.43175	8(5,4)-7(5,3)E	38	13.1	334	3.7	-6.2	16
	98.43288	98.43277	8(5,4)-7(5,3)A	38	13.1	450	4.9	-6.3	19
	98.43603	98.43582	8(5,3)-7(5,2)A	38	13.1	449	4.0	-6.6	17
	98.60709	98.60677	8(3,6)-7(3,5)E	27	18.4	497	4.3	-7.0	16
	98.61133	98.61120	8(3,6)-7(3,5)A	27	18.4	500	5.1	-6.4	16
	98.68281	98.68263	8(4,5)-7(4,4)A	32	16.1	545	4.2	-6.6	16
	98.71228	98.71193	8(4,5)-7(4,4)E	32	15.6	483	4.4	-7.1	20
	99.13338	99.13319	9(0,9)-8(1,8)E	25	3.3	78	2.9	-6.6	5
	99.13595	99.13579	9(0,9)-8(1,8)A	25	3.3	74	4.0	-6.5	5
	100.07879	100.07853	9(1,9)-8(1,8)E	25	23.6	684	4.6	-6.8	13
	100.08080	100.08057	9(1,9)-8(1,8)A	25	23.6	612	4.8	-6.7	18
	100.29486	100.29451	8(3,5)-7(3,4)E	27	18.4	250	4.4	-7.0	13
	100.30848	100.30821	8(3,5)-7(3,4)A	27	18.4	275	4.2	-6.8	10
	100.48252	100.48217	8(1,7)-7(1,6)E	23	20.8	574	4.4	-7.1	20
	100.49095	100.49071	8(1,7)-7(1,6)A	23	20.8	572	4.4	-6.7	17
	100.54375	100.54378	12(1,11)-12(1,12)E	47	0.8	60	2.5	-5.9	14
	100.60018	100.60000	12(1,11)-12(1,12)A	47	0.8	71	2.7	-6.5	9
	100.65963	100.65969	12(4,9)-12(3,10)E	57	3	256	4.9	-5.8	19
	100.68183	100.68148	9(0,9)-8(0,8)E	25	23.7	544	4.7	-7.0	7
	100.68370	100.68339	9(0,9)-8(0,8)A	25	23.7	537	4.1	-6.9	13
	100.69341	100.69305	12(4,9)-12(3,10)A	57	3	131	3.7	-7.1	9
	100.73506	100.73477	12(1,11)-12(0,12)E	47	1.4	114	3.2	-6.8	11
	100.79081	100.79077	12(1,11)-12(0,12)A	47	1.4	105	2.1	-6.1	9
	103.26241	103.26201	13(4,10)-13(3,11)A	65	3.2	115	3.3	-7.2	19
	103.46674	103.46648	8(2,6)-7(2,5)E	25	20.2	326	4.1	-6.8	27
	103.47879	103.47870	8(2,6)-7(2,5)A	25	20.2	328	3.9	-6.3	27
	107.53752	107.53719	9(2,8)-8(2,7)E	29	22.8	399	4.6	-6.9	16
	107.54397	107.54375	9(2,8)-8(2,7)A	29	22.8	414	4.8	-6.6	12
CH_3CHO	79.09963	79.09931	4(1,3)-3(1,2)E	12	23.7	149	5.6	-7.2	14
	79.15059	79.15017	4(1,3)-3(1,2)A–	12	23.7	98	4.2	-7.6	5
	95.94798	95.94744	5(0,5)-4(0,4)E	14	31.6	227	4.5	-7.7	7
	95.96393	95.96346	5(0,5)-4(0,4)A++	14	31.6	252	5.0	-7.5	13

Table 6—Continued

Species	Obs. freq (GHz)	Rest freq (GHz)	Transition	Eu (K)	Sd^2 (D^2)	T_A* (mK)	Δv (km s^{-1})	V_{LSR} (km s^{-1})	rms noise (mK)
	96.27480	96.27426	5(2,4)-4(2,3)A–	23	26.6	109	4.3	-7.7	8
	96.36855	96.36779	5(3,3)-4(3,2)A++	34	20.2	68	5.0	-8.4	10
	blend	96.36838	5(3,2)-4(3,1)E	34	20.3				
	96.42612	96.42562	5(-2,4)-4(-2,3)E	23	26.4	105	4.9	-7.5	8
CH_3OCH_3	78.85641	78.85627	13(2,11)-13(1,12)AE	90	109.9	472	4.5	-6.5	8
	blend	78.85627	13(2,11)-13(1,12)EA	90					
	78.85794	78.85782	13(2,11)-13(1,12)EE	90	293	547	4.0	-6.4	5
	78.85947	78.85937	13(2,11)-13(1,12)AA	90	183.1	366	4.4	-6.4	14
	79.75388	79.75370	15(3,13)-14(4,10)AA	122	21.1	67	4.7	-6.7	9
	79.75667	79.75661	15(3,13)-14(4,10)EE	122	56.2	126	3.9	-6.2	9
	79.75952	79.75945	15(3,13)-14(4,10)EA	122	14	77	3.0	-6.3	9
	80.53652	80.53635	5(2,3)-5(1,4)AE	19	32.2	299	3.9	-6.6	18
	blend	80.53641	5(2,3)-5(1,4)EA	19					
	80.53877	80.53865	5(2,3)-5(1,4)EE	19	85.9	391	4.3	-6.4	20
	80.54099	80.54091	5(2,3)-5(1,4)AA	19	53.7	292	4.0	-6.3	10
	81.36906	81.36897	21(5,16)-20(6,15)AA	246	47.4	31	3.8	-6.3	7
	81.37046	81.37051	21(5,16)-20(6,15)EE	246	75.6	53	3.7	-5.8	7
	81.37214	81.37191	21(5,16)-20(6,15)AE	246	28.4	25	2.8	-6.9	7
	blend	81.37217	21(5,16)-20(6,15)EA	246					
	81.46765	81.46762	18(4,15)-17(5,12)AA	178	41.5	50	4.4	-6.1	10
	81.46986	81.46992	18(4,15)-17(5,12)EE	178	66.4	84	4.8	-5.8	10
	81.47243	81.47239	18(4,15)-17(5,12)AE	178	24.9	49	4.0	-6.1	10
	84.52956	84.52959	18(4,14)-17(5,13)EE	179	66.6	42	2.8	-5.9	5
	84.63219	84.63190	3(2,1)-3(1,2)AE	11	16.4	109	4.4	-7.0	5
	blend	84.63227	3(2,1)-3(1,2)EA	11					
	84.63458	84.63441	3(2,1)-3(1,2)EE	11	43.7	149	4.0	-6.6	5
	84.63689	84.63674	3(2,1)-3(1,2)AA	11	27.3	104	4.4	-6.5	5
	85.97344	85.97325	13(2,12)-12(3,9)AA	88	16.8	46	5.5	-6.7	10
	85.97621	85.97613	13(2,12)-12(3,9)EE	88	44.9	147	4.1	-6.3	14
	85.97915	85.97900	13(2,12)-12(3,9)EA	88	11.2	47	3.3	-6.5	9
	88.70928	88.70622	15(2,13)-15(1,14)EA	117	78.8	348	4.1	-16.3	10
	blend	88.70622	15(2,13)-15(1,14)AE	117					

Table 6—Continued

Species	Obs. freq (GHz)	Rest freq (GHz)	Transition	Eu (K)	Sd^2 (D^2)	T_A* (mK)	Δv (km s^{-1})	V_{LSR} (km s^{-1})	rms noise (mK)
	88.70788	88.70770	15(2,13)-15(1,14)EE	117	315.4	456	3.7	-6.6	6
	88.70927	88.70918	15(2,13)-15(1,14)AA	117	197.1	349	4.1	-6.3	10
	90.88927	90.88925	15(3,12)-14(4,11)AA	123	36.2	107	3.8	-6.1	9
	90.89238	90.89225	15(3,12)-14(4,11)EE	123	57.9	133	3.8	-6.4	9
	90.89528	90.89518	15(3,12)-14(4,11)AE	123	21.7	97	3.8	-6.3	9
	blend	90.89533	15(3,12)-14(4,11)EA	123					
	90.93823	90.93751	6(0,6)-5(1,5)AA	19	32.3	589	5.9	-8.4	9
	blend	90.93810	6(0,6)-5(1,5)EE	19					
	blend	90.93870	6(0,6)-5(1,5)AE	19					
	blend	90.93870	6(0,6)-5(1,5)EA	19					
	91.47412	91.47376	3(2,2)-3(1,3)EA	11	9.7	102	4.9	-7.2	12
	blend	91.47414	3(2,2)-3(1,3)AE	11					
	91.47673	91.47660	3(2,2)-3(1,3)EE	11	38.9	290	4.0	-6.4	13
	91.47933	91.47924	3(2,2)-3(1,3)AA	11	14.6	130	3.8	-6.3	6
	92.70199	92.70196	8(5,3)-9(4,5)EE	68	12	61	2.3	-6.1	8
	92.70295	92.70307	8(5,4)-9(4,5)AA	68	9.6	47	3.3	-5.6	8
	92.71031	92.71029	8(5,4)-9(4,6)EE	68	12	61	2.5	-6.0	8
	92.71469	92.71611	8(5,3)-9(4,6)AA	68	5.7	47	3.4	-1.4	8
	93.66479	93.66460	12(1,11)-12(0,12)EA	74	37.6	139	4.7	-6.6	12
	blend	93.66460	12(1,11)-12(0,12)AE	74					
	93.66657	93.66646	12(1,11)-12(0,12)EE	74	150.2	287	3.7	-6.4	11
	93.66833	93.66832	12(1,11)-12(0,12)AA	74	56.3	198	4.2	-6.0	11
	93.85463	93.85444	4(2,3)-4(1,4)EA	15	13.3	145	4.0	-6.6	10
	blend	93.85456	4(2,3)-4(1,4)AE	15					
	93.85721	93.85710	4(2,3)-4(1,4)EE	15	53.1	204	4.3	-6.4	11
	93.85983	93.85971	4(2,3)-4(1,4)AA	15	33.2	146	3.9	-6.4	7
	96.84749	96.84724	5(2,4)-5(1,5)EA	19	16.4	112	4.2	-6.8	9
	blend	96.84729	5(2,4)-5(1,5)AE	19					
	96.85010	96.84988	5(2,4)-5(1,5)EE	19	65.6	245	4.2	-6.7	9
	96.85268	96.85250	5(2,4)-5(1,5)AA	19	24.6	110	3.9	-6.6	9
	96.92848	96.92805	17(8,10)-18(7,12)EE	229	40.7	36	8.8	-7.3	9
	96.93006	96.92937	17(8,9)-18(7,12)AA	229	26.2	27	1.8	-8.1	9

Table 6—Continued

Species	Obs. freq (GHz)	Rest freq (GHz)	Transition	Eu (K)	Sd^2 (D^2)	T_A* (mK)	Δv (km s^{-1})	V_{LSR} (km s^{-1})	rms noise (mK)
	99.32542	99.32436	4(1,4)-3(0,3)EA	10	17.5	248	6.6	-9.2	16
	blend	99.32436	4(1,4)-3(0,3)AE	10					
	blend	99.32521	4(1,4)-3(0,3)EE	10					
	blend	99.32606	4(1,4)-3(0,3)AA	10					
	99.83381	99.83366	14(2,13)-13(3,10)AA	101	28.9	96	2.6	-6.4	6
	99.83663	99.83645	14(2,13)-13(3,10)EE	101	46.2	157	3.5	-6.5	14
	99.83926	99.83924	14(2,13)-13(3,10)EA	101	11.5	109	2.8	-6.1	8
	blend	99.83925	14(2,13)-13(3,10)AE	101					
	100.46061	100.46041	6(2,5)-6(1,6)EA	25	19.2	280	4.2	-6.6	19
	blend	100.46044	6(2,5)-6(1,6)AE	25					
	100.46329	100.46307	6(2,5)-6(1,6)EE	25	76.9	365	4.7	-6.7	23
	100.46591	100.46571	6(2,5)-6(1,6)AA	25	48.1	306	5.1	-6.6	13
	105.76844	105.76828	13(1,12)-13(0,13)AE	86	55	262	3.7	-6.4	7
	blend	105.76828	13(1,12)-13(0,13)EA	86					
	105.77053	105.77034	13(1,12)-13(0,13)EE	86	146.7	332	4.0	-6.5	16
	105.77251	105.77240	13(1,12)-13(0,13)AA	86	91.7	235	3.5	-6.3	16
CH_3COCH_3	81.78928	81.78900	7(1,6)-6(2,5)AE	18	44.8	62	3.1	-7.0	9
	blended	81.78927	7(1,6)-6(2,5)EA	18					
	90.53815	90.53790	13(3,10)-13(2,11)AE	60	28.4	60	3.2	-6.8	5
	blended	90.53795	13(4,10)-13(3,11)AE	60					
	blended	90.53799	13(3,10)-13(2,11)EA	60					
	blended	90.53804	13(4,10)-13(3,11)EA	60					
	91.63448	91.63464	8(1,7)-7(2,6)EE	22	53.4	47	3.0	-5.5	11
	91.63777	91.63746	8(2,7)-7(1,6)EE	22	53.4	68	2.7	-7.0	11
	91.66245	91.66203	8(2,7)-7(1,6)AA	22	53.4	103	3.8	-7.4	11
	92.72882	92.72790	9(0,9)-8(1,8)AE	23	72	49	8.2	-9.0	8
	blended	92.72791	9(1,9)-8(0,8)AE	23					
	blended	92.72795	9(0,9)-8(1,8)EA	23					
	blended	92.72795	9(1,9)-8(0,8)EA	23					
	92.73591	92.73567	9(0,9)-8(1,8)EE	23	72	67	2.3	-6.8	8
	blended	92.73567	9(1,9)-8(0,8)EE	23					
	92.74359	92.74336	9(0,9)-8(1,8)AA	23	72	73	3.2	-6.8	8

Table 6—Continued

Species	Obs. freq (GHz)	Rest freq (GHz)	Transition	Eu (K)	Sd^2 (D^2)	T_A* (mK)	Δv (km s^{-1})	V_{LSR} (km s^{-1})	rms noise (mK)
	blended	92.74336	9(1,9)-8(0,8)AA	23					
NH_2CHO	81.69341	81.69345	4(1,4)-3(1,3)	13	49	92	6.9	-5.9	13
	84.54235	84.54233	4(0,4)-3(0,3)	10	52.3	69	6.8	-6.1	5
	84.80777	84.80779	4(2,3)-3(2,2)	22	39.2	61	7.8	-5.9	5
	84.89116	84.89098	4(3,1)-3(3,0)	37	22.9	38	3.9	-6.6	7
	87.84896	87.84887	4(1,3)-3(1,2)	14	49	88	7.2	-6.3	11
CH_3CH_2CN	79.67737	79.67750	9(0,9)-8(0,8)	19	133.1	121	4.7	-5.5	8
	80.60199	80.60213	9(6,4)-8(6,3)	59	74.1	95	5.2	-5.5	8
	blended	80.60213	9(6,3)-8(6,2)	59					
	80.60447	80.60457	9(5,5)-8(5,4)	47	92.2	165	5.3	-5.6	8
	blended	80.60457	9(5,4)-8(5,3)	47					
	80.60623	80.60621	9(7,3)-8(7,2)	74	52.7	90	5.5	-6.1	5
	blended	80.60621	9(7,2)-8(7,1)	74					
	80.61931	80.61923	9(4,6)-8(4,5)	37	107.1	140	6.3	11.6	12
	blended	80.61968	9(4,5)-8(4,4)	37				11.6	
	80.64973	80.64987	9(3,7)-8(3,6)	29	118.6	80	5.3	-5.5	10
	80.68278	80.68280	9(3,6)-8(3,5)	29	118.6	92	5.0	-5.9	7
	81.26127	81.26143	9(2,7)-8(2,6)	24	126.8	115	5.0	-5.4	5
	86.81971	86.81984	10(1,10)-9(1,9)	24	146.7	38	4.9	-5.6	14
	88.32358	88.32375	10(0,10)-9(0,9)	23	147.9	108	5.1	-5.4	7
	89.29752	89.29764	10(2,9)-9(2,8)	28	142.3	47	3.3	-5.6	5
	89.56191	89.56231	10(6,4)-9(6,3)	64	94.9	53	4.2	-4.7	7
	blended	89.56231	10(6,5)-9(6,4)	64					
	89.56483	89.56503	10(7,3)-9(7,2)	78	75.6	44	4.3	-5.3	7
	blended	89.56503	10(7,4)-9(7,3)	78					
	89.56813	89.56809	10(5,6)-9(5,5)	51	111.2	49	5.4	-6.1	6
	blended	89.56810	10(5,5)-9(5,4)	51					
	89.59047	89.59003	10(4,7)-9(4,6)	41	124.5	52	7.2	-7.5	8
	blended	89.59101	10(4,6)-9(4,5)	41					
	89.62884	89.62844	10(3,8)-9(3,7)	34	134.9	48	2.7	-7.4	11
	89.68438	89.68471	10(3,7)-9(3,6)	34	134.9	107	2.5	-4.9	22
	90.45320	90.45335	10(2,8)-9(2,7)	28	142.3	126	5.0	-5.5	5

Table 6—Continued

Species	Obs. freq (GHz)	Rest freq (GHz)	Transition	Eu (K)	Sd^2 (D^2)	T_A* (mK)	Δv (km s^{-1})	V_{LSR} (km s^{-1})	rms noise (mK)
	91.54908	91.54911	10(1,9)-9(1,8)	25	146.7	165	5.0	-5.9	10
	96.91967	96.91975	11(0,11)-10(0,10)	28	162.6	91	5.0	-5.8	3
	98.52413	98.52388	11(6,6)-10(6,5)	68	114.5	166	6.5	-6.8	15
	blended	98.52388	11(6,5)-10(6,4)	68					
	blended	98.52466	11(7,5)-10(7,4)	83					
	blended	98.52466	11(7,4)-10(7,3)	83					
	98.53206	98.53207	11(8,3)-10(8,2)	99	76.8	102	4.5	-6.0	15
	blended	98.53207	11(8,4)-10(8,3)	99					
	98.53393	98.53397	11(5,7)-10(5,6)	56	129.4	159	4.2	-5.9	13
	blended	98.53399	11(5,6)-10(5,5)	56					
	98.56479	98.56483	11(4,8)-10(4,7)	46	141.5	118	5.8	-5.9	14
	98.56674	98.56679	11(4,7)-10(4,6)	46	141.5	101	3.6	-5.9	8
	98.70091	98.70110	11(3,8)-10(3,7)	38	150.9	116	4.8	-5.4	7
	99.68137	99.68150	11(2,9)-10(2,8)	33	157.6	222	4.9	-5.6	14
	100.61410	100.61428	11(1,10)-10(1,9)	30	161.6	107	5.5	-5.5	16
	107.04341	107.04351	12(2,11)-11(2,10)	38	172.9	95	4.0	-5.7	5
	107.48491	107.48518	12(7,5)-11(7,4)	88	117.3	108	3.6	-5.3	9
	blended	107.48518	12(7,6)-11(7,5)	88					
	107.48670	107.48696	12(6,6)-11(6,5)	74	133.4	125	4.6	-5.3	11
	blended	107.48696	12(6,7)-11(6,6)	74					
	107.49134	107.49157	12(8,4)-11(8,3)	105	98.8	83	4.5	-5.4	9
	blended	107.49157	12(8,5)-11(8,4)	105					
	107.50261	107.50242	12(5,8)-11(5,7)	61	147	129	6.4	-6.5	10
	blended	107.50247	12(5,7)-11(5,6)	61					
	107.54759	107.54759	12(4,8)-11(4,7)	51	158.1	84	3.4	-6.0	5
	107.59379	107.59404	12(3,10)-11(3,9)	44	166.7	82	6.3	-5.3	8
	107.73408	107.73473	12(3,9)-11(3,8)	44	166.7	43	2.6	-4.2	8
CH_2CHCN	92.42618	92.42625	10(1,10)-9(1,9)	27	144.1	53	3.7	-5.8	16
CH_3NH_2	78.92837	78.92873	2(1)E1-1-2(0)E1+1	11	2.9	26	3.1	-4.6	11
	79.00842	79.00870	1(1)B1-1(0)B2	6	2.4	32	2.2	-4.9	11
	79.21007	79.21030	1(1)E1-1-1(0)E1+1	6	1.4	42	3.3	-5.1	13
	81.52124	81.52108	6(1)A2-6(0)A1	49	10.8	23	2.2	-6.6	8

Table 6—Continued

Species	Obs. freq (GHz)	Rest freq (GHz)	Transition	Eu (K)	Sd^2 (D^2)	T_A* (mK)	Δv (km s^{-1})	V_{LSR} (km s^{-1})	rms noise (mK)
	83.97923	83.97894	5(1)A1-5(0)A2	36	9	26	1.5	-7.0	11
	89.08183	89.08150	2(1)A2-2(0)A1	11	4	32	2.6	-7.1	24
CH_2NH	105.79420	105.79406	4(0,4)-3(1,3)	31	3.9	47	1.8	-5.6	19

Table 7. Observed Lines towards W51 e1/e2

Species	Obs. freq (GHz)	Rest freq (GHz)	Transition	Eu (K)	Sd^2 (D^2)	T_A* (mK)	Δv (km s^{-1})	V_{LSR} (km s^{-1})	rms noise (mK)
CH_3OH	79.51672	79.51629	16(-2,15)-16(2,14)	342	0.1	45	6.7	55.4	8
	80.99335	80.99326	7(2,6)-8(1,7)–	103	2.5	326	9.6	56.7	11
	81.65328	81.65293	18(4,14)-19(3,16)	493	5.9	349	8.1	55.7	11
	84.42384	84.42371	13(-3,11)-14(-2,13)	274	4.3	73	9.4	56.6	10
	84.52135	84.52121	5(-1,5)-4(0,4)	40	3.1	1262	8.2	56.5	24
	85.56834	85.56807	6(-2,5)-7(-1,7)	75	2	690	9.7	56.0	20
	86.61561	86.61560	7(2,6)-6(3,3)–	103	1.4	417	9.2	57.0	13
	86.90293	86.90295	7(2,5)-6(3,4)++	103	1.4	438	9.7	57.1	16
	88.59507	88.59481	15(3,13)-14(4,10)++	328	4.2	575	8.8	56.1	15
	88.94004	88.93999	15(3,12)-14(4,11)–	328	4.2	267	9.6	56.8	8
	89.50606	89.50578	8(-4,5)-9(-3,7)	171	1.6	453	8.9	56.1	12
	94.54200	94.54181	8(3,5)-9(2,7)	131	2.2	702	9.4	56.4	22
	94.81528	94.81507	19(7,13)-20(6,14)++	685	4.6	152	7.8	56.3	19
	blend	94.81508	19(7,12)-20(6,15)–	685	4.6				
	95.16997	95.16952	8(0,8)-7(1,7)++	84	7.2	2613	8.0	55.6	12
	95.91446	95.91431	2(1,2)-1(1,1)++	21	1.2	435	8.4	56.5	12
	96.73945	96.73936	2(-1,2)-1(-1,1)	13	1.2	550	4.8	56.7	25
	96.74143	96.74138	2(0,2)-1(0,1)++	7	1.6	1892	11.1	56.8	26
	96.74471	96.74455	2(0,2)-1(0,1)	20	1.6	830	8.3	56.5	13
	96.75570	96.75551	2(1,1)-1(1,0)	28	1.2	466	8.3	56.4	14
	99.60230	99.60195	15(1,14)-15(1,15)-+	295	0.1	22	5.5	56.0	7
	100.63915	100.63887	13(2,11)-12(3,9)	234	3.8	677	9.3	56.2	17
	103.32567	103.32525	12(3,9)-13(0,13)	229	0	61	6.6	55.8	8
	103.38148	103.38121	12(-2,11)-12(1,11)	207	0.8	371	8.5	56.2	20
	105.57660	105.57638	14(-2,13)-14(1,13)	270	1.8	350	8.5	56.4	22
	107.01423	107.01377	3(1,3)-4(0,4)++	28	3	1402	8.7	55.7	26
	107.16018	107.15991	15(-2,14)-15(1,14)	305	2.6	315	8.7	56.2	18
$HCOOCH_3$	79.40220	79.40177	9(3,7)-9(2,8)E	33	2.1	74	4.5	55.4	10
	79.43289	79.43272	9(3,7)-9(2,8)A	33	2.1	126	6.6	56.4	10
	79.45040	79.44981	9(2,8)-9(1,9)E	29	1.3	35	4.8	54.8	8
	79.48858	79.48829	9(2,8)-9(1,9)A	29	1.3	42	6.6	55.9	7
	79.78219	79.78165	7(0,7)-6(0,6)E	16	18.4	337	7.7	55.0	5

Table 7—Continued

Species	Obs. freq (GHz)	Rest freq (GHz)	Transition	Eu (K)	Sd^2 (D^2)	T_A* (mK)	Δv (km s^{-1})	V_{LSR} (km s^{-1})	rms noise (mK)
	79.78440	79.78391	7(0,7)-6(0,6)A	16	18.4	295	5.5	55.2	5
	84.44941	84.44910	7(2,6)-6(2,5)E	19	17.2	29	7.9	55.9	5
	85.76220	85.76188	21(5,16)-21(4,17)E	156	7.9	103	8.9	55.9	4
	85.77376	85.77332	21(5,16)-21(4,17)A	156	7.9	84	8.1	55.5	14
	85.78098	85.78070	20(5,15)-20(4,16)E	143	7.3	83	9.4	56.0	17
	85.78556	85.78526	20(5,15)-20(4,16)A	143	7.3	78	8.5	55.9	17
	85.91958	85.91909	7(6,1)-6(6,0)E	40	5	121	5.8	55.3	16
	85.92719	85.92651	7(6,2)-6(6,1)E	40	5	292	8.3	54.6	21
	blended	85.92723	7(6,2)-6(6,1)A	40	5				
	blended	85.92724	7(6,1)-6(6,0)A	40	5				
	86.02140	86.02101	7(5,2)-6(5,1)E	33	9.2	174	7.5	55.6	15
	86.02829	86.02767	7(5,3)-6(5,2)E	33	9.2	224	7.9	54.8	16
	86.03046	86.02945	7(5,3)-6(5,2)A	33	9.2	266	6.5	53.5	17
	blended	86.03021	7(5,2)-6(5,1)A	33	9.2				
	86.21039	86.21008	7(4,4)-6(4,3)A	27	12.7	222	7.1	55.9	18
	86.22430	86.22355	7(4,3)-6(4,2)E	27	12.6	362	7.7	54.4	23
	blended	86.22411	7(4,4)-6(4,3)E	27	12.6				
	86.25095	86.25058	7(4,3)-6(4,2)A	27	12.7	248	5.6	55.7	12
	86.26627	86.26583	7(3,5)-6(3,4)A	23	15.3	280	6.5	55.5	16
	86.26917	86.26866	7(3,5)-6(3,4)E	23	15.2	269	6.0	55.2	7
	87.76680	87.76630	8(0,8)-7(1,7)E	20	2.8	77	5.3	55.3	16
	87.76942	87.76907	8(0,8)-7(1,7)A	20	2.8	62	5.7	55.8	17
	88.05453	88.05403	19(5,14)-19(4,15)E	130	6.6	118	5.2	55.3	16
	blended	88.05437	19(5,14)-19(4,15)A	130	6.6				
	88.17579	88.17563	10(4,6)-10(3,7)E	43	2.5	67	8.6	56.5	15
	88.18085	88.18036	10(4,6)-10(3,7)A	43	2.5	61	9.1	55.3	17
	88.68713	88.68691	11(3,9)-11(2,10)E	45	2.4	60	4.5	56.2	14
	88.72335	88.72324	11(3,9)-11(2,10)A	45	2.4	53	6.4	56.6	13
	88.84338	88.84312	7(1,6)-6(1,5)E	18	18.2	119	8.7	56.1	9
	88.85179	88.85164	7(1,6)-6(1,5)A	18	18.2	115	8.2	56.5	11
	89.31536	89.31459	8(1,8)-7(1,7)E	20	21	201	9.8	54.4	10
	89.31755	89.31667	8(1,8)-7(1,7)A	20	21	99	5.1	54.1	4

Table 7—Continued

Species	Obs. freq (GHz)	Rest freq (GHz)	Transition	Eu (K)	Sd^2 (D^2)	T_A* (mK)	Δv (km s^{-1})	V_{LSR} (km s^{-1})	rms noise (mK)
	89.79756	89.79699	11(1,10)-11(0,11)A	40	1.3	26	4.7	55.1	7
	91.77705	91.77588	8(1,8)-7(0,7)E	20	2.9	181	8.1	53.2	11
	blended	91.77679	20(4,16)-20(3,17)E	139	6.4				
	blended	91.77725	8(1,8)-7(0,7)A	20	2.9				
	91.82561	91.82518	20(4,16)-20(3,17)A	139	6.4	63	6.8	55.6	7
	93.66059	93.66003	8(4,4)-8(3,5)A	32	1.8	40	5.3	55.2	9
	93.70226	93.70128	8(4,4)-8(3,5)E	32	1.4	46	10.5	53.9	10
	96.07070	96.07065	8(2,7)-7(2,6)E	24	20	38	9.4	56.8	8
	96.07699	96.07688	8(2,7)-7(2,6)A	24	20	40	9.1	56.7	5
	96.58738	96.58662	5(4,1)-5(3,2)A	19	0.8	32	4.0	54.6	5
	98.27093	98.27037	8(6,2)-7(6,1)E	45	9.4	207	6.6	55.3	21
	98.27990	98.27887	8(6,3)-7(6,2)E	45	9.4	411	8.3	53.9	15
	blended	98.27975	8(6,3)-7(6,2)A	45	9.4				
	blended	98.27979	8(6,2)-7(6,1)A	45	9.4				
	98.42452	98.42408	8(5,3)-7(5,2)E	38	13.1	265	7.4	55.7	21
	98.43278	98.43175	8(5,4)-7(5,3)E	38	13.1	388	8.7	53.9	18
	blended	98.43277	8(5,4)-7(5,3)A	38	13.1				
	98.43635	98.43582	8(5,3)-7(5,2)A	38	13.1	262	5.7	55.4	15
	98.60746	98.60677	8(3,6)-7(3,5)E	27	18.4	316	7.7	54.9	20
	98.61139	98.61120	8(3,6)-7(3,5)A	27	18.4	339	8.0	56.4	26
	98.68304	98.68263	8(4,5)-7(4,4)A	32	16.1	319	6.7	55.8	18
	98.71244	98.71193	8(4,5)-7(4,4)E	32	15.6	329	8.5	55.5	22
	98.74838	98.74780	8(4,4)-7(4,3)E	32	15.6	320	6.9	55.2	16
	99.13382	99.13319	9(0,9)-8(1,8)E	25	3.3	52	3.1	55.1	8
	99.13649	99.13579	9(0,9)-8(1,8)A	25	3.3	39	3.2	54.9	4
	100.29476	100.29451	8(3,5)-7(3,4)E	27	18.4	130	8.2	56.3	10
	100.30834	100.30821	8(3,5)-7(3,4)A	27	18.4	136	9.3	56.6	10
	100.48266	100.48217	8(1,7)-7(1,6)E	23	20.8	353	7.4	55.6	22
	100.49113	100.49071	8(1,7)-7(1,6)A	23	20.8	360	7.6	55.7	20
	100.66013	100.65969	12(4,9)-12(3,10)E	57	3	218	10.5	55.7	18
	100.68258	100.68148	9(0,9)-8(0,8)E	25	23.7	411	10.3	53.7	16
	100.68431	100.68339	9(0,9)-8(0,8)A	25	23.7	121	3.8	54.3	12

Table 7—Continued

Species	Obs. freq (GHz)	Rest freq (GHz)	Transition	Eu (K)	Sd^2 (D^2)	T_A* (mK)	Δv (km s^{-1})	V_{LSR} (km s^{-1})	rms noise (mK)
	100.69360	100.69305	12(4,9)-12(3,10)A	57	3	76	4.5	55.4	14
	100.73509	100.73477	12(1,11)-12(0,12)E	47	1.4	62	6.4	56.1	15
	103.05777	103.05705	21(4,17)-21(3,18)E	152	6.2	57	5.9	54.9	4
	103.22912	103.22841	13(4,10)-13(3,11)E	65	3.2	80	3.2	54.9	4
	103.26245	103.26201	13(4,10)-13(3,11)A	65	3.2	78	5.7	55.7	8
	103.46707	103.46648	8(2,6)-7(2,5)E	25	20.2	316	7.0	55.3	9
	103.47913	103.47870	8(2,6)-7(2,5)A	25	20.2	317	6.8	55.7	12
	107.53775	107.53719	9(2,8)-8(2,7)E	29	22.8	241	7.4	55.4	14
	107.54437	107.54375	9(2,8)-8(2,7)A	29	22.8	272	10.3	55.3	26
CH_3CHO	79.09962	79.09931	4(1,3)-3(1,2)E	12	23.7	213	6.5	56.8	10
	79.15052	79.15017	4(1,3)-3(1,2)A–	12	23.7	208	7.2	56.7	8
	95.94758	95.94744	5(0,5)-4(0,4)E	14	31.6	92	7.2	57.6	7
	95.96383	95.96346	5(0,5)-4(0,4)A++	14	31.6	98	10.2	56.9	10
	96.27416	96.27426	5(2,4)-4(2,3)A–	23	26.6	30	6.5	58.3	7
	96.36893	96.36779	5(3,3)-4(3,2)A++	34	20.2	20	10.9	54.5	8
	blend	96.36838	5(3,2)-4(3,1)E	34	20.3				
	96.42562	96.42562	5(-2,4)-4(-2,3)E	23	26.4	34	8.1	58.0	8
CH_3OCH_3	78.85819	78.85627	13(2,11)-13(1,12)AE	90	109.9	340	14.1	49.7	18
	blend	78.85627	13(2,11)-13(1,12)EA	90	73.2				
	blend	78.85782	13(2,11)-13(1,12)EE	90	293				
	blend	78.85937	13(2,11)-13(1,12)AA	90	183.1				
	79.75413	79.75370	15(3,13)-14(4,10)AA	122	21.1	42	9.5	55.4	8
	79.75700	79.75661	15(3,13)-14(4,10)EE	122	56.2	63	6.0	55.5	7
	79.76030	79.75945	15(3,13)-14(4,10)EA	122	14	33	13.9	53.8	6
	blend	79.75960	15(3,13)-14(4,10)AE	122	7				
	80.53685	80.53635	5(2,3)-5(1,4)AE	19	32.2	155	6.7	55.1	5
	blend	80.53641	5(2,3)-5(1,4)EA	19	21.5				
	80.53916	80.53865	5(2,3)-5(1,4)EE	19	85.9	206	6.6	55.1	5
	80.54138	80.54091	5(2,3)-5(1,4)AA	19	53.7	139	5.4	55.3	5
	81.46805	81.46762	18(4,15)-17(5,12)AA	178	41.5	34	6.1	55.4	8
	81.47024	81.46992	18(4,15)-17(5,12)EE	178	66.4	45	6.1	55.8	8
	81.47263	81.47239	18(4,15)-17(5,12)AE	178	24.9	28	3.9	56.1	8

Table 7—Continued

Species	Obs. freq (GHz)	Rest freq (GHz)	Transition	Eu (K)	Sd^2 (D^2)	T_A* (mK)	Δv (km s^{-1})	V_{LSR} (km s^{-1})	rms noise (mK)
	90.93825	90.93751	6(0,6)-5(1,5)AA	19	32.3	134	8.8	54.6	9
	blend	90.93810	6(0,6)-5(1,5)EE	19	86.1				
	blend	90.93870	6(0,6)-5(1,5)AE	19	10.8				
	blend	90.93870	6(0,6)-5(1,5)EA	19	21.5				
	91.47466	91.47376	3(2,2)-3(1,3)EA	11	9.7	66	4.9	54.1	10
	blend	91.47414	3(2,2)-3(1,3)AE	11	4.9				
	91.47707	91.47660	3(2,2)-3(1,3)EE	11	38.9	142	6.5	55.5	10
	91.47972	91.47924	3(2,2)-3(1,3)AA	11	14.6	62	5.8	55.4	10
	93.66705	93.66460	12(1,11)-12(0,12)EA	74	37.6	162	12.7	49.2	11
	blend	93.66460	12(1,11)-12(0,12)AE	74	18.8				
	blend	93.66646	12(1,11)-12(0,12)EE	74	150.2				
	blend	93.66832	12(1,11)-12(0,12)AA	74	56.3				
	93.85516	93.85444	4(2,3)-4(1,4)EA	15	13.3	80	8.8	54.7	8
	blend	93.85456	4(2,3)-4(1,4)AE	15	19.9				
	93.85766	93.85710	4(2,3)-4(1,4)EE	15	53.1	113	4.6	55.2	5
	93.85995	93.85971	4(2,3)-4(1,4)AA	15	33.2	87	6.0	56.2	6
	96.84981	96.84724	5(2,4)-5(1,5)EA	19	16.4	31	15.3	49.1	7
	blend	96.84729	5(2,4)-5(1,5)AE	19	8.2				
	blend	96.84988	5(2,4)-5(1,5)EE	19	65.6		0.0		
	blend	96.85250	5(2,4)-5(1,5)AA	19	24.6		0.0		
	99.32543	99.32436	4(1,4)-3(0,3)EA	10	17.5	189	9.4	53.8	9
	blend	99.32436	4(1,4)-3(0,3)AE	10	26.2				
	blend	99.32521	4(1,4)-3(0,3)EE	10	69.8				
	blend	99.32606	4(1,4)-3(0,3)AA	10	43.6				
	99.83409	99.83366	14(2,13)-13(3,10)AA	101	28.9	63	5.5	55.7	8
	99.83681	99.83645	14(2,13)-13(3,10)EE	101	46.2	88	7.8	55.9	7
	99.83973	99.83924	14(2,13)-13(3,10)EA	101	11.5	59	6.5	55.5	8
	blend	99.83925	14(2,13)-13(3,10)AE	101	17.3				
	100.46107	100.46041	6(2,5)-6(1,6)EA	25	19.2	176	7.0	55.0	10
	blend	100.46044	6(2,5)-6(1,6)AE	25	28.8				
	100.46383	100.46307	6(2,5)-6(1,6)EE	25	76.9	320	6.7	54.7	10
	100.46440	100.46571	6(2,5)-6(1,6)AA	25	48.1	311	18.5	60.9	10

Table 7—Continued

Species	Obs. freq (GHz)	Rest freq (GHz)	Transition	Eu (K)	Sd^2 (D^2)	T_A* (mK)	Δv (km s^{-1})	V_{LSR} (km s^{-1})	rms noise (mK)
	blend	105.76828	13(1,12)-13(0,13)AE	86	55				
	blend	105.76828	13(1,12)-13(0,13)EA	86	36.7				
	105.77091	105.77034	13(1,12)-13(0,13)EE	86	146.7	211	6.1	55.4	10
	105.77316	105.77240	13(1,12)-13(0,13)AA	86	91.7	126	4.9	54.8	10
CH_3COCH_3	81.78966	81.78900	7(1,6)-6(2,5)AE	18	44.8	33	4.5	55.6	7
	blended	81.78927	7(1,6)-6(2,5)EA	18	44.8				
	90.53840	90.53790	13(3,10)-13(2,11)AE	60	28.4	22	3.3	56.4	5
	blended	90.53795	13(4,10)-13(3,11)AE	60	28.4				
	blended	90.53799	13(3,10)-13(2,11)EA	60	28.4				
	blended	90.53804	13(4,10)-13(3,11)EA	60	28.4				
	91.63513	91.63464	8(1,7)-7(2,6)EE	22	53.4	48	5.5	56.4	7
	91.63795	91.63746	8(2,7)-7(1,6)EE	22	53.4	45	4.2	56.4	9
	91.66291	91.66203	8(2,7)-7(1,6)AA	22	53.4	49	6.5	55.1	8
	92.73563	92.73567	9(0,9)-8(1,8)EE	23	72	40	9.1	58.1	9
	blended	92.73567	9(1,9)-8(0,8)EE	23	72				
	92.74359	92.74336	9(0,9)-8(1,8)AA	23	72	27	4.7	57.3	9
	blended	92.74336	9(1,9)-8(0,8)AA	23	72				
NH_2CHO	81.69355	81.69345	4(1,4)-3(1,3)	13	49	169	8.8	57.6	7
	84.54226	84.54233	4(0,4)-3(0,3)	10	52.3	32	12.2	58.3	5
	84.80763	84.80779	4(2,3)-3(2,2)	22	39.2	28	12.1	58.6	6
	84.88950	84.88899	4(3,2)-3(3,1)	37	22.9	24	14.2	56.2	5
	blended	84.89098	4(3,1)-3(3,0)	37	22.9				
	87.84887	87.84887	4(1,3)-3(1,2)	14	49	170	10.3	58.0	11
	105.46470	105.46422	5(0,5)-4(0,4)	15	65.3	171	11.5	56.6	19
CH_3CH_2CN	79.67754	79.67750	9(0,9)-8(0,8)	19	133.1	112	12.5	56.9	11
	80.60253	80.60213	9(6,4)-8(6,3)	59	74.1	94	13.2	55.5	8
	blended	80.60213	9(6,3)-8(6,2)	59	74.1				
	80.60525	80.60457	9(5,5)-8(5,4)	47	92.2	138	9.4	54.5	5
	blended	80.60457	9(5,4)-8(5,3)	47	92.2				
	blended	80.60621	9(7,3)-8(7,2)	74	52.7				
	blended	80.60621	9(7,2)-8(7,1)	74	52.7				
	80.61921	80.61923	9(4,6)-8(4,5)	37	107.1	112	11.7	57.1	9

Table 7—Continued

Species	Obs. freq (GHz)	Rest freq (GHz)	Transition	Eu (K)	Sd^2 (D^2)	T_A* (mK)	Δv (km s^{-1})	V_{LSR} (km s^{-1})	rms noise (mK)
	blended	80.61968	9(4,5)-8(4,4)	37	107.1				
	80.64964	80.64987	9(3,7)-8(3,6)	29	118.6	74	9.4	57.9	7
	80.68270	80.68280	9(3,6)-8(3,5)	29	118.6	70	9.4	57.4	5
	81.26083	81.26143	9(2,7)-8(2,6)	24	126.8	49	8.3	59.2	7
	86.81917	86.81984	10(1,10)-9(1,9)	24	146.7	73	9.4	59.3	12
	88.32352	88.32375	10(0,10)-9(0,9)	23	147.9	112	8.8	57.8	11
	89.29707	89.29764	10(2,9)-9(2,8)	28	142.3	73	10.0	58.9	8
	89.56230	89.56231	10(6,4)-9(6,3)	64	94.9	101	10.4	57.0	9
	blended	89.56231	10(6,5)-9(6,4)	64	94.9				
	89.56492	89.56503	10(7,3)-9(7,2)	78	75.6	71	7.3	57.4	5
	blended	89.56503	10(7,4)-9(7,3)	78	75.6				
	89.56784	89.56809	10(5,6)-9(5,5)	51	111.2	108	11.4	57.8	7
	blended	89.56810	10(5,5)-9(5,4)	51	111.2				
	89.57253	89.57305	10(8,2)-9(8,1)	95	53.4	51	12.0	58.7	7
	blended	89.57305	10(8,3)-9(8,2)	95	53.4				
	89.59029	89.59003	10(4,7)-9(4,6)	41	124.5	136	12.0	56.1	9
	blended	89.59101	10(4,6)-9(4,5)	41	124.5				
	89.62823	89.62844	10(3,8)-9(3,7)	34	134.9	77	8.9	57.7	7
	89.68427	89.68471	10(3,7)-9(3,6)	34	134.9	75	11.3	58.5	10
	90.45286	90.45335	10(2,8)-9(2,7)	28	142.3	48	10.4	58.6	5
	91.54958	91.54911	10(1,9)-9(1,8)	25	146.7	206	13.0	55.5	11
	96.91901	96.91975	11(0,11)-10(0,10)	28	162.6	27	8.8	59.3	7
	98.52398	98.52388	11(6,6)-10(6,5)	68	114.5	216	10.2	56.7	9
	blended	98.52388	11(6,5)-10(6,4)	68	114.5				
	blended	98.52466	11(7,5)-10(7,4)	83	97				
	blended	98.52466	11(7,4)-10(7,3)	83	97				
	blended	98.53207	11(8,4)-10(8,3)	99	76.8				
	blended	98.53397	11(5,7)-10(5,6)	56	129.4				
	blended	98.53399	11(5,6)-10(5,5)	56	129.4				
	98.54377	98.54415	11(9,2)-10(9,1)	118	53.9	69	6.1	58.1	9
	blended	98.54415	11(9,3)-10(9,2)	118	53.9				
	98.56548	98.56483	11(4,8)-10(4,7)	46	141.5	170	13.9	55.0	11

Table 7—Continued

Species	Obs. freq (GHz)	Rest freq (GHz)	Transition	Eu (K)	Sd^2 (D^2)	T_A* (mK)	Δv (km s^{-1})	V_{LSR} (km s^{-1})	rms noise (mK)
	blended	98.56679	11(4,7)-10(4,6)	46	141.5				
	98.61138	98.61010	11(3,9)-10(3,8)	38	150.9	338	8.0	53.1	22
	98.70097	98.70110	11(3,8)-10(3,7)	38	150.9	137	13.6	57.4	18
	99.68083	99.68150	11(2,9)-10(2,8)	33	157.6	74	11.4	59.0	6
	100.61338	100.61428	11(1,10)-10(1,9)	30	161.6	69	9.6	59.7	10
	105.46914	105.46929	12(0,12)-11(0,11)	33	177.4	113	9.5	57.4	14
	107.04306	107.04351	12(2,11)-11(2,10)	38	172.9	100	8.5	58.3	8
	107.49020	107.48518	12(7,5)-11(7,4)	88	117.3	73	18.4	43.0	12
	blended	107.48518	12(7,6)-11(7,5)	88	117.3				
	blended	107.48696	12(6,6)-11(6,5)	74	133.4				
	blended	107.48696	12(6,7)-11(6,6)	74	133.4				
	blended	107.49157	12(8,4)-11(8,3)	105	98.8				
	blended	107.49157	12(8,5)-11(8,4)	105	98.8				
	107.50233	107.50242	12(5,8)-11(5,7)	61	147	148	11.7	57.3	12
	blended	107.50247	12(5,7)-11(5,6)	61	147				
	blended	107.50360	12(9,3)-11(9,2)	124	77.8				
	blended	107.50360	12(9,4)-11(9,3)	124	77.8				
	107.51987	107.51994	12(10,2)-11(10,1)	145	54.4	44	13.1	57.2	12
	107.54425	107.54392	12(4,9)-11(4,8)	51	158.1	291	8.6	56.1	11
	107.54780	107.54759	12(4,8)-11(4,7)	51	158.1	73	5.5	56.4	7
	107.59400	107.59404	12(3,10)-11(3,9)	44	166.7	93	7.9	57.1	11
	107.73520	107.73473	12(3,9)-11(3,8)	44	166.7	75	14.0	55.7	15
CH_2CHCN	92.42566	92.42625	10(1,10)-9(1,9)	27	144.1	47	7.9	58.9	5
	94.27723	94.27663	10(0,10)-9(0,9)	25	145.5	15	15.7	55.1	7
	94.75991	94.76078	10(2,9)-9(2,8)	34	139.7	30	8.4	59.7	9
	94.91261	94.91312	10(4,7)-9(4,6)	60	122.3	58	11.1	58.6	9
	blended	94.91323	10(4,6)-9(4,5)	60	122.3				
	blended	94.91396	10(5,5)-9(5,4)	79	109.2				
	blended	94.91396	10(5,6)-9(5,5)	79	109.2				
	96.98259	96.98244	10(1,9)-9(1,8)	28	144.1	38	7.9	56.5	6
	103.57455	103.57540	11(0,11)-10(0,10)	30	160	51	10.3	59.5	8
CH_2NH	105.79420	105.79406	4(0,4)-3(1,3)	31	3.9	54	11.6	58.4	9

Table 7—Continued

Species	Obs. freq (GHz)	Rest freq (GHz)	Transition	Eu (K)	Sd^2 (D^2)	T_A* (mK)	Δv (km s^{-1})	V_{LSR} (km s^{-1})	rms noise (mK)

Table 8. Observed Lines towards G31.41+0.3

Species	Obs. freq (GHz)	Rest freq (GHz)	Transition	Eu (K)	Sd^2 (D^2)	T_A* (mK)	Δv (km s^{-1})	V_{LSR} (km s^{-1})	rms noise (mK)
CH_3OH	80.99327	80.99324	7(2,6)-8(1,7)–	103	2.5	241	6.1	96.9	9
	81.65291	81.65293	18(4,14)-19(3,16)	493	5.9	114	7.3	97.1	11
	84.42373	84.42378	13(-3,11)-14(-2,13)	274	4.3	70	7.9	97.2	12
	84.52089	84.52117	5(-1,5)-4(0,4)	40	3.1	481	5.7	98.0	15
	84.74390	84.74390	19(4,15)-18(5,14)E	537	5.2	51	8.7	97.0	11
	86.61558	86.61560	7(2,6)-6(3,3)–	103	1.4	387	6.4	97.1	16
	86.90297	86.90295	7(2,5)-6(3,4)++	103	1.4	449	6.9	96.9	22
	88.93988	88.93999	15(3,12)-14(4,11)A–	328	4.2	276	7.2	97.4	15
	89.50577	89.50581	8(-4,5)-9(-3,7)	171	1.6	435	5.3	97.1	13
	95.91428	95.91431	2(1,2)-1(1,1)A++	21	1.2	206	6.5	97.1	12
	96.73946	96.73936	2(-1,2)-1(-1,1)	13	1.2	486	4.9	96.7	21
	96.74148	96.74138	2(0,2)-1(0,1)++	7	1.6	568	5.2	96.7	20
	96.74460	96.74455	2(0,2)-1(0,1)	20	1.6	252	6.2	96.8	15
	96.75546	96.75551	2(1,1)-1(1,0)	28	1.2	199	6.5	97.2	11
	100.63886	100.63890	13(2,11)-12(3,9)	234	3.8	428	6.1	97.1	16
	103.38084	103.38115	12(-2,11)-12(1,11)	207	0.8	230	6.1	97.9	17
	104.06051	104.06066	13(-3,11)-12(-4,9)	274	3.3	200	8.3	97.4	24
	104.33627	104.33656	13(-2,12)-13(1,12)	237	1.2	195	8.4	97.8	24
	104.35479	104.35482	10(4,7)-11(3,8)–	208	2.5	249	7.5	97.1	28
	105.06374	105.06369	13(1,13)-12(2,10)++	224	4.3	292	7.6	96.9	16
	105.57613	105.57629	14(-2,13)-14(1,13)	270	1.8	215	7.1	97.4	25
$HCOOCH_3$	79.78164	79.78227	7(0,7)-6(0,6)E	16	18.4	107	6.7	99.4	12
	79.78386	79.78391	7(0,7)-6(0,6)A	16	18.4	102	4.5	97.2	12
	86.02102	86.02165	7(5,2)-6(5,1)E	33	9.2	37	4.4	99.2	12
	86.02906	86.02966	7(5,2)-6(5,1)A	33	9.2	57	10.9	99.1	16
	blended	86.03021	7(5,3)-6(5,2)A	33	9.2				
	88.84302	88.84349	7(1,6)-6(1,5)E	18	18.2	222	5.1	98.6	12
	88.85147	88.85208	7(1,6)-6(1,5)A	18	18.2	208	5.6	99.1	18
	89.31463	89.31459	8(1,8)-7(1,7)E	20	21	235	6.4	96.9	18
	89.31660	89.31667	8(1,8)-7(1,7)A	20	21	227	5.5	97.2	10
	96.07659	96.07726	8(2,7)-7(2,6)A	24	20	67	5.6	99.1	14
	100.29450	100.29514	8(3,5)-7(3,4)E	27	18.4	258	5.4	98.9	17

Table 8—Continued

Species	Obs. freq (GHz)	Rest freq (GHz)	Transition	Eu (K)	Sd^2 (D^2)	T_A* (mK)	Δv (km s^{-1})	V_{LSR} (km s^{-1})	rms noise (mK)
	100.30797	100.30879	8(3,5)-7(3,4)A	27	18.4	233	7.1	99.5	19
	100.48211	100.48265	8(1,7)-7(1,6)E	23	20.8	266	5.8	98.6	15
	100.49057	100.49150	8(1,7)-7(1,6)A	23	20.8	276	6.1	99.8	16
	100.68146	100.68148	9(0,9)-8(0,8)A	25	23.7	266	5.5	97.0	15
	100.68340	100.68339	9(0,9)-8(0,8)E	25	23.7	256	4.7	97.0	14
	103.46638	103.46729	8(2,6)-7(2,5)E	25	20.2	197	5.7	99.6	23
	103.47848	103.47927	8(2,6)-7(2,5)A	25	20.2	216	6.0	99.3	23
CH_3CHO	79.09925	79.09931	4(1,3)-3(1,2)E	12	23.7	74	7.0	97.2	12
	79.15018	79.15017	4(1,3)-3(1,2)A–	12	23.7	70	7.2	97.0	12
	95.94745	95.94744	5(0,5)-4(0,4)E	14	31.6	31	6.5	97.0	15
	95.96363	95.96347	5(0,5)-4(0,4)A++	14	31.6	42	7.0	96.5	16
CH_3OCH_3	78.85766	78.85627	13(2,11)-13(1,12)EA	90	73.2	105	15.9	91.7	15
	blended	78.85627	13(2,11)-13(1,12)AE	90	109.9				
	blended	78.85782	13(2,11)-13(1,12)EE	90	293				
	blended	78.85937	13(2,11)-13(1,12)AA	90	183.1				
	90.93794	90.93751	6(0,6)-5(1,5)AA	1	19	142	10.4	95.6	10
	blended	90.93810	6(0,6)-5(1,5)EE	3	19				
	blended	90.93870	6(0,6)-5(1,5)AE	0	19				
	blended	90.93870	6(0,6)-5(1,5)EA	1	19				
	96.84943	96.84724	5(2,4)-5(1,5)EA	19	16.4	58	16.8	90.2	17
	blended	96.84729	5(2,4)-5(1,5)AE	19	8.2				
	blended	96.84988	5(2,4)-5(1,5)EE	19	65.6				
	blended	96.85250	5(2,4)-5(1,5)AA	19	24.6				
	99.32505	99.32436	4(1,4)-3(0,3)EA	10	17.5	299	10.9	94.9	13
	blended	99.32436	4(1,4)-3(0,3)AE	10	26.2				
	blended	99.32521	4(1,4)-3(0,3)EE	10	69.8				
	blended	99.32606	4(1,4)-3(0,3)AA	10	43.6				
	100.43523	100.43420	22(5,18)-21(6,15)AA	266	50.9	47	8.2	93.9	11
	blended	100.43548	22(5,18)-21(6,15)EE	266	81.4				
	blended	100.43671	22(5,18)-21(6,15)EA	266	20.3				
	blended	100.43682	22(5,18)-21(6,15)AE	266	30.6				
	100.46035	100.46041	6(2,5)-6(1,6)EA	25	19.2	141	14.1	97.2	13

Table 8—Continued

Species	Obs. freq (GHz)	Rest freq (GHz)	Transition	Eu (K)	Sd^2 (D^2)	T_A* (mK)	Δv (km s^{-1})	V_{LSR} (km s^{-1})	rms noise (mK)
	blended	100.46044	6(2,5)-6(1,6)AE	25	28.8				
	blended	100.46307	6(2,5)-6(1,6)EE	25	76.9				
	blended	100.46571	6(2,5)-6(1,6)AA	25	48.1				
	100.94847	100.94684	19(4,16)-18(5,13)AA	196	27	51	11.8	92.2	11
	blended	100.94900	19(4,16)-18(5,13)EE	196	71.9				
	blended	100.95109	19(4,16)-18(5,13)EA	196	18				
	blended	100.95125	19(4,16)-18(5,13)AE	196	9				
	104.17709	104.17587	17(2,15)-17(1,16)EA	148	79.6	203	13.7	93.5	29
	blended	104.17587	17(2,15)-17(1,16)AE	148	119.3				
	blended	104.17738	17(2,15)-17(1,16)EE	148	318.3				
	blended	104.17889	17(2,15)-17(1,16)AA	148	198.9				
	105.77016	105.76828	13(1,12)-13(0,13)EA	86	36.7	148	14.6	91.7	31
	blended	105.76828	13(1,12)-13(0,13)AE	86	55				
	blended	105.77034	13(1,12)-13(0,13)EE	86	146.7				
	blended	105.77240	13(1,12)-13(0,13)AA	86	91.7				
CH_3COCH_3	92.72799	92.72790	9(0,9)-8(1,8)AE	23	72	28	8.0	96.7	12
	blend	92.72791	9(1,9)-8(0,8)AE	23	72				
	blend	92.72795	9(0,9)-8(1,8)EA	23	72				
	blend	92.72795	9(1,9)-8(0,8)EA	23	72				
	92.73555	92.73567	9(0,9)-8(1,8)EE	23	72	46	6.0	97.4	10
	blend	92.73567	9(1,9)-8(0,8)EE	23	72				
	92.74321	92.74336	9(0,9)-8(1,8)AA	23	72	36	3.5	97.5	12
	99.26641	99.26643	5(5,0)-4(4,1)AA	14	34.3	41	4.9	97.0	12
	100.35073	100.35030	8(2,6)-7(3,5)EE	25	43.4	54	7.9	95.7	11
NH_2CHO	81.69346	81.69345	4(1,4)-3(1,3)	13	49	63	9.0	96.9	10
	84.89044	84.88899	4(3,2)-3(3,1)	37	22.9	34	12.3	91.9	10
	blended	84.89098	4(3,1)-3(3,0)	37	22.9				
	87.84870	87.84887	4(1,3)-3(1,2)	14	49	114	9.8	97.6	13
	105.46447	105.46422	5(0,5)-4(0,4)	15	65.3	139	10.3	96.3	28
	105.97273	105.97260	5(2,4)-4(2,3)	27	54.9	106	9.6	96.6	26
	106.10800	106.10786	5(4,2)-4(4,1)	63	23.5	63	9.1	96.6	17
	blended	106.10788	5(4,1)-4(4,0)	63	23.5				

Table 8—Continued

Species	Obs. freq (GHz)	Rest freq (GHz)	Transition	Eu (K)	Sd^2 (D^2)	T_A* (mK)	Δv (km s^{-1})	V_{LSR} (km s^{-1})	rms noise (mK)
	106.13460	106.13442	5(3,3)-4(3,2)	42	41.8	101	7.6	96.5	22
	106.14127	106.14139	5(3,2)-4(3,1)	42	41.8	62	10.2	97.4	18
CH_3CH_2CN	79.67739	79.67751	9(0,9)-8(0,8)	19	133.1	99	8.2	97.4	13
	81.26127	81.26133	9(2,7)-8(2,6)	24	126.8	101	7.1	97.2	8
	86.81976	86.81985	10(1,10)-9(1,9)	24	146.7	229	5.7	97.3	12
	89.00898	89.00931	25(2,23)-25(1,24)	147	24.4	37	5.2	98.1	13
	89.29745	89.29766	10(2,9)-9(2,8)	28	142.3	188	6.7	97.7	16
	89.41513	89.41539	24(3,21)-24(2,22)	140	27.8	66	6.4	97.9	15
	89.56206	89.56231	10(6,4)-9(6,3)	64	94.9	208	7.3	97.9	17
	blended	89.56231	10(6,5)-9(6,4)	64	94.9				
	89.56472	89.56503	10(7,3)-9(7,2)	78	75.6	212	7.0	98.0	14
	blended	89.56503	10(7,4)-9(7,3)	78	75.6				
	89.56792	89.56809	10(5,6)-9(5,5)	51	111.2	240	7.4	97.6	16
	blended	89.56810	10(5,5)-9(5,4)	51	111.2				
	89.57280	89.57305	10(8,2)-9(8,1)	95	53.4	154	7.0	97.8	16
	blended	89.57305	10(8,3)-9(8,2)	95	53.4				
	89.58472	89.58491	10(9,1)-9(9,0)	114	28.2	92	7.3	97.6	15
	blended	89.58491	10(9,2)-9(9,1)	114	28.2				
	89.59044	89.59003	10(4,7)-9(4,6)	41	124.5	260	10.0	95.6	12
	blended	89.59101	10(4,6)-9(4,5)	41	124.5				
	89.62834	89.62848	10(3,8)-9(3,7)	34	134.9	208	6.7	97.5	20
	89.68460	89.68471	10(3,7)-9(3,6)	34	134.9	220	5.4	97.4	18
	90.45318	90.45335	10(2,8)-9(2,7)	28	142.3	103	6.7	97.6	9
	99.07015	99.07060	32(3,29)-32(2,30)	240	37.3	57	9.7	98.4	12
	99.68134	99.68146	11(2,9)-10(2,8)	33	157.6	231	7.4	97.3	12
	100.61417	100.61420	11(1,10)-10(1,9)	30	161.6	226	6.8	97.1	13
CH_2CHCN	84.94559	84.94625	9(0,9)-8(0,8)	20	130.9	26	6.1	99.3	12
	96.98260	96.98244	10(1,9)-9(1,8)	25	145.5	27	6.0	96.5	17
	103.57528	103.57570	11(0 11)-10(0 10)	30	160	63	7.7	98.2	21
	104.21254	104.21291	11(2 10)-10(2 9)	39	154.8	48	9.9	98.1	20
	104.45388	104.45423	11(3 8)-10(3 7)	50	148.2	86	5.6	98.0	17
	104.96034	104.96147	11(2,9)-10(2,8)	39	154.8	68	5.2	100.2	14

Table 8—Continued

Species	Obs. freq (GHz)	Rest freq (GHz)	Transition	Eu (K)	Sd^2 (D^2)	T_A* (mK)	Δv (km s^{-1})	V_{LSR} (km s^{-1})	rms noise (mK)
CH_2NH	105.79404	105.79420	4(0,4)-3(1,3)	31	3.9	98	2.4	97.5	9

Table 9. Observed Lines towards G34.3+0.2

Species	Obs. freq (GHz)	Rest freq (GHz)	Transition	Eu (K)	Sd^2 (D^2)	T_A* (mK)	Δv (km s^{-1})	V_{LSR} (km s^{-1})	rms noise (mK)
CH_3OH	80.99306	80.99326	7(2,6)-8(1,7)–	103	2.5	539	7.1	59.4	12
	81.65298	81.65293	18(4,14)-19(3,16)	493	5.9	210	6.3	58.4	9
	85.56790	85.56807	6(-2,5)-7(-1,7)	75	2	495	7.0	59.2	10
	88.59464	88.59481	15(3,13)-14(4,10)++	328	4.2	369	7.0	59.2	11
	89.50548	89.50578	8(-4,5)-9(-3,7)	171	1.6	206	6.9	59.6	6
	94.54160	94.54181	8(3,5)-9(2,7)	131	2.2	511	6.8	59.3	16
	94.81494	94.81507	19(7,13)-20(6,14)++	685	4.6	71	5.2	59.0	6
	blend	94.81508	19(7,12)-20(6,15)–	685	4.6				
	95.16931	95.16952	8(0,8)-7(1,7)++	84	7.2	827	7.1	59.3	17
	99.60181	99.60195	15(1,14)-15(1,15)-+	295	0.1	50	4.0	59.0	9
	100.63866	100.63887	13(2,11)-12(3,9)	234	3.8	399	7.1	59.2	11
	103.32509	103.32525	12(3,9)-13(0,13)	229	0	31	2.5	59.1	9
	103.38091	103.38121	12(-2,11)-12(1,11)	207	0.8	110	6.4	59.5	10
	105.57602	105.57638	14(-2,13)-14(1,13)	270	1.8	192	6.5	59.6	10
	107.01371	107.01377	3(1,3)-4(0,4)++	28	3	664	6.7	58.8	22
	107.15965	107.15991	15(-2,14)-15(1,14)	305	2.6	170	7.1	59.3	9
$HCOOCH_3$	79.78253	79.78165	7(0,7)-6(0,6)E	16	18.4	127	14.9	55.3	15
	blended	79.78391	7(0,7)-6(0,6)A	16	18.4		0.0	299851.1	
	85.76141	85.76188	21(5,16)-21(4,17)E	156	7.9	40	4.5	60.3	6
	85.91923	85.91909	7(6,1)-6(6,0)E	40	5	49	8.1	58.1	9
	85.92656	85.92651	7(6,2)-6(6,1)E	40	5	198	9.3	58.4	10
	blended	85.92723	7(6,2)-6(6,1)A	40	5				
	blended	85.92724	7(6,1)-6(6,0)A	40	5				
	86.02094	86.02101	7(5,2)-6(5,1)E	33	9.2	50	6.7	58.9	8
	86.02738	86.02767	7(5,3)-6(5,2)E	33	9.2	57	5.3	59.6	7
	86.02960	86.02945	7(5,3)-6(5,2)A	33	9.2	110	7.8	58.1	8
	blended	86.03021	7(5,2)-6(5,1)A	33	9.2				
	86.20987	86.21008	7(4,4)-6(4,3)A	27	12.7	81	7.1	59.3	10
	86.22384	86.22355	7(4,3)-6(4,2)E	27	12.6	167	7.5	57.6	11
	blended	86.22411	7(4,4)-6(4,3)E	27	12.6				
	86.25030	86.25058	7(4,3)-6(4,2)A	27	12.7	87	5.5	59.6	10
	86.26583	86.26583	7(3,5)-6(3,4)A	23	15.3	86	9.3	58.6	9

Table 9—Continued

Species	Obs. freq (GHz)	Rest freq (GHz)	Transition	Eu (K)	Sd^2 (D^2)	T_A* (mK)	Δv (km s^{-1})	V_{LSR} (km s^{-1})	rms noise (mK)
	86.26866	86.26866	7(3,5)-6(3,4)E	23	15.2	100	5.5	58.6	8
	88.05400	88.05403	19(5,14)-19(4,15)E	130	6.6	40	7.9	58.7	8
	blended	88.05437	19(5,14)-19(4,15)A	130	6.6				
	91.77684	91.77588	8(1,8)-7(0,7)E	20	2.9	64	7.8	55.5	9
	blended	91.77679	20(4,16)-20(3,17)E	139	6.4				
	blended	91.77725	8(1,8)-7(0,7)A	20	2.9				
	91.82536	91.82518	20(4,16)-20(3,17)A	139	6.4	29	5.6	58.0	10
	98.27009	98.27037	8(6,2)-7(6,1)E	45	9.4	55	9.0	59.4	8
	98.27932	98.27887	8(6,3)-7(6,2)E	45	9.4	161	7.3	57.2	10
	blended	98.27975	8(6,3)-7(6,2)A	45	9.4				
	blended	98.27979	8(6,2)-7(6,1)A	45	9.4				
	98.42400	98.42408	8(5,3)-7(5,2)E	38	13.1	88	6.2	58.8	10
	98.43222	98.43175	8(5,4)-7(5,3)E	38	13.1	139	7.0	57.2	10
	blended	98.43277	8(5,4)-7(5,3)A	38	13.1				
	98.43560	98.43582	8(5,3)-7(5,2)A	38	13.1	79	7.0	59.3	9
	98.60672	98.60677	8(3,6)-7(3,5)E	27	18.4	103	7.0	58.8	8
	98.61070	98.61120	8(3,6)-7(3,5)A	27	18.4	210	6.6	60.1	10
	98.68238	98.68263	8(4,5)-7(4,4)A	32	16.1	143	8.0	59.4	10
	98.70134	98.71193	8(4,5)-7(4,4)E	32	15.6	146	5.7	90.8	7
	98.71199	98.74780	8(4,4)-7(4,3)E	32	15.6	111	7.9	167.3	9
	100.48206	100.48217	8(1,7)-7(1,6)E	23	20.8	127	8.0	58.9	8
	100.49062	100.49071	8(1,7)-7(1,6)A	23	20.8	122	7.5	58.9	10
	100.66030	100.65969	12(4,9)-12(3,10)E	57	3	158	5.6	56.8	4
	100.68095	100.68148	9(0,9)-8(0,8)E	25	23.7	67	5.7	60.2	5
	100.68273	100.68339	9(0,9)-8(0,8)A	25	23.7	149	7.7	60.6	9
	100.69326	100.69305	12(4,9)-12(3,10)A	57	3	23	3.0	58.0	8
	100.73459	100.73477	12(1,11)-12(0,12)E	47	1.4	21	4.8	59.1	8
	103.46628	103.46648	8(2,6)-7(2,5)E	25	20.2	70	6.9	59.2	10
	103.47836	103.47870	8(2,6)-7(2,5)A	25	20.2	79	7.4	59.6	10
	107.53713	107.53719	9(2,8)-8(2,7)E	29	22.8	88	7.0	58.8	7
	107.54374	107.54375	9(2,8)-8(2,7)A	29	22.8	134	7.9	58.6	6
CH_3CHO	79.09948	79.09931	4(1,3)-3(1,2)E	12	23.7	85	4.8	58.0	9

Table 9—Continued

Species	Obs. freq (GHz)	Rest freq (GHz)	Transition	Eu (K)	Sd^2 (D^2)	T_A* (mK)	Δv (km s^{-1})	V_{LSR} (km s^{-1})	rms noise (mK)
	79.15031	79.15017	4(1,3)-3(1,2)A–	12	23.7	93	4.4	58.1	14
CH_3OCH_3	78.85781	78.85627	13(2,11)-13(1,12)AE	90	109.9	189	13.5	52.8	17
	blend	78.85627	13(2,11)-13(1,12)EA	90	73.2				
	blend	78.85782	13(2,11)-13(1,12)EE	90	293				
	blend	78.85937	13(2,11)-13(1,12)AA	90	183.1				
	79.75542	79.75370	15(3,13)-14(4,10)AA	122	21.1	35	15.7	52.1	8
	blend	79.75661	15(3,13)-14(4,10)EE	122	56.2				
	blend	79.75945	15(3,13)-14(4,10)EA	122	14				
	blend	79.75960	15(3,13)-14(4,10)AE	122	7				
	80.53827	80.53635	5(2,3)-5(1,4)AE	19	32.2	80	22.2	51.4	13
	blend	80.53641	5(2,3)-5(1,4)EA	19	21.5				
	blend	80.53865	5(2,3)-5(1,4)EE	19	85.9				
	blend	80.54091	5(2,3)-5(1,4)AA	19	53.7				
	90.93778	90.93751	6(0,6)-5(1,5)AA	19	32.3	89	8.5	57.7	6
	blend	90.93810	6(0,6)-5(1,5)EE	19	86.1				
	blend	90.93870	6(0,6)-5(1,5)AE	19	10.8				
	blend	90.93870	6(0,6)-5(1,5)EA	19	21.5				
	93.66664	93.66460	12(1,11)-12(0,12)EA	74	37.6	71	13.5	52.1	8
	blend	93.66460	12(1,11)-12(0,12)AE	74	18.8				
	blend	93.66646	12(1,11)-12(0,12)EE	74	150.2				
	blend	93.66832	12(1,11)-12(0,12)AA	74	56.3				
	93.85423	93.85444	4(2,3)-4(1,4)EA	15	13.3	30	4.8	59.3	6
	blend	93.85456	4(2,3)-4(1,4)AE	15	19.9				
	93.85723	93.85710	4(2,3)-4(1,4)EE	15	53.1	38	9.9	58.2	4
	93.85995	93.85971	4(2,3)-4(1,4)AA	15	33.2	21	4.3	57.8	6
	99.32507	99.32436	4(1,4)-3(0,3)EA	10	17.5	232	8.4	56.5	17
	blend	99.32436	4(1,4)-3(0,3)AE	10	26.2				
	blend	99.32521	4(1,4)-3(0,3)EE	10	69.8				
	blend	99.32606	4(1,4)-3(0,3)AA	10	43.6				
	100.46462	100.46041	6(2,5)-6(1,6)EA	25	19.2	134	18.4	46.0	20
	blend	100.46044	6(2,5)-6(1,6)AE	25	28.8				
	blend	100.46307	6(2,5)-6(1,6)EE	25	76.9				

Table 9—Continued

Species	Obs. freq (GHz)	Rest freq (GHz)	Transition	Eu (K)	Sd^2 (D^2)	T_A* (mK)	Δv (km s^{-1})	V_{LSR} (km s^{-1})	rms noise (mK)
	blend	100.46571	6(2,5)-6(1,6)AA	25	48.1				
	105.76988	105.76828	13(1,12)-13(0,13)AE	86	55	84	13.3	54.1	7
	blend	105.76828	13(1,12)-13(0,13)EA	86	36.7				
	blend	105.77034	13(1,12)-13(0,13)EE	86	146.7				
	blend	105.77240	13(1,12)-13(0,13)AA	86	91.7				
CH_3COCH_3	81.78954	81.78900	7(1,6)-6(2,5)AE	18	44.8	40	2.1	56.6	10
	blended	81.78927	7(1,6)-6(2,5)EA	18	44.8				
	91.66311	91.66203	8(2,7)-7(1,6)AA	22	53.4	59	8.1	55.1	9
	92.73597	92.73567	9(0,9)-8(1,8)EE	23	72	69	4.8	57.6	9
	blended	92.73567	9(1,9)-8(0,8)EE	23	72				
	92.74367	92.74336	9(0,9)-8(1,8)AA	23	72	39	5.3	57.6	9
	blended	92.74336	9(1,9)-8(0,8)AA	23	72				
NH_2CHO	81.69370	81.69345	4(1,4)-3(1,3)	13	49	87	6.3	57.7	10
	87.84910	87.84887	4(1,3)-3(1,2)	14	49	83	7.0	57.8	11
	105.46458	105.46422	5(0,5)-4(0,4)	15	65.3	94	6.0	57.6	7
CH_3CH_2CN	79.67779	79.67750	9(0,9)-8(0,8)	19	133.1	147	4.9	57.5	10
	80.60228	80.60213	9(6,4)-8(6,3)	59	74.1	94	4.9	58.0	8
	blended	80.60213	9(6,3)-8(6,2)	59	74.1				
	80.60520	80.60457	9(5,5)-8(5,4)	47	92.2	152	12.0	56.3	14
	blended	80.60457	9(5,4)-8(5,3)	47	92.2				
	blended	80.60621	9(7,3)-8(7,2)	74	52.7				
	blended	80.60621	9(7,2)-8(7,1)	74	52.7				
	80.61977	80.61923	9(4,6)-8(4,5)	37	107.1	167	6.0	56.6	12
	blended	80.61968	9(4,5)-8(4,4)	37	107.1				
	80.65015	80.64987	9(3,7)-8(3,6)	29	118.6	111	5.0	57.6	7
	80.68298	80.68280	9(3,6)-8(3,5)	29	118.6	83	5.8	57.9	9
	88.32400	88.32375	10(0,10)-9(0,9)	23	147.9	126	5.5	57.8	7
	89.56257	89.56231	10(6,4)-9(6,3)	64	94.9	68	5.7	57.7	10
	blended	89.56231	10(6,5)-9(6,4)	64	94.9				
	89.56531	89.56503	10(7,3)-9(7,2)	78	75.6	67	6.6	57.7	12
	blended	89.56503	10(7,4)-9(7,3)	78	75.6				
	89.56842	89.56809	10(5,6)-9(5,5)	51	111.2	82	6.7	57.5	10

Table 9—Continued

Species	Obs. freq (GHz)	Rest freq (GHz)	Transition	Eu (K)	Sd^2 (D^2)	T_A* (mK)	Δv (km s^{-1})	V_{LSR} (km s^{-1})	rms noise (mK)
	blended	89.56810	10(5,5)-9(5,4)	51	111.2				
	89.57417	89.57305	10(8,2)-9(8,1)	95	53.4	46	4.4	54.8	5
	blended	89.57305	10(8,3)-9(8,2)	95	53.4				
	89.59066	89.59003	10(4,7)-9(4,6)	41	124.5	91	7.2	56.5	9
	blended	89.59101	10(4,6)-9(4,5)	41	124.5				
	89.62881	89.62844	10(3,8)-9(3,7)	34	134.9	70	5.8	57.4	8
	89.68486	89.68471	10(3,7)-9(3,6)	34	134.9	59	7.8	58.1	10
	90.45363	90.45335	10(2,8)-9(2,7)	28	142.3	69	5.4	57.7	4
	91.54978	91.54911	10(1,9)-9(1,8)	25	146.7	180	7.1	56.4	17
	98.52447	98.52388	11(6,6)-10(6,5)	68	114.5	203	7.1	56.8	11
	blended	98.52388	11(6,5)-10(6,4)	68	114.5				
	blended	98.52466	11(7,5)-10(7,4)	83	97				
	blended	98.52466	11(7,4)-10(7,3)	83	97				
	98.53359	98.53207	11(8,4)-10(8,3)	99	76.8	156	9.9	54.0	15
	blended	98.53397	11(5,7)-10(5,6)	56	129.4				
	blended	98.53399	11(5,6)-10(5,5)	56	129.4				
	98.54452	98.54415	11(9,2)-10(9,1)	118	53.9	69	6.0	57.5	10
	blended	98.54415	11(9,3)-10(9,2)	118	53.9				
	98.56609	98.56483	11(4,8)-10(4,7)	46	141.5	143	9.9	54.8	14
	blended	98.56679	11(4,7)-10(4,6)	46	141.5				
	98.61069	98.61010	11(3,9)-10(3,8)	38	150.9	209	6.7	56.8	10
	98.70133	98.70110	11(3,8)-10(3,7)	38	150.9	144	5.9	57.9	6
	99.68159	99.68150	11(2,9)-10(2,8)	33	157.6	148	4.0	58.3	10
	100.61452	100.61428	11(1,10)-10(1,9)	30	161.6	125	5.5	57.9	11
	105.46955	105.46929	12(0,12)-11(0,11)	33	177.4	93	6.4	57.9	7
	107.04366	107.04351	12(2,11)-11(2,10)	38	172.9	90	6.0	58.2	5
	107.48648	107.48518	12(7,5)-11(7,4)	88	117.3	118	9.5	55.0	11
	blended	107.48518	12(7,6)-11(7,5)	88	117.3				
	blended	107.48696	12(6,6)-11(6,5)	74	133.4				
	blended	107.48696	12(6,7)-11(6,6)	74	133.4				
	107.49191	107.49157	12(8,4)-11(8,3)	105	98.8	76	5.4	57.6	5
	blended	107.49157	12(8,5)-11(8,4)	105	98.8				

Table 9—Continued

Species	Obs. freq (GHz)	Rest freq (GHz)	Transition	Eu (K)	Sd^2 (D^2)	T_A* (mK)	Δv (km s^{-1})	V_{LSR} (km s^{-1})	rms noise (mK)
	107.50297	107.50242	12(5,8)-11(5,7)	61	147	116	7.4	57.1	8
	blended	107.50247	12(5,7)-11(5,6)	61	147				
	blended	107.50360	12(9,3)-11(9,2)	124	77.8				
	blended	107.50360	12(9,4)-11(9,3)	124	77.8				
	107.52083	107.51994	12(10,2)-11(10,1)	145	54.4	39	9.0	56.1	8
	107.54372	107.54392	12(4,9)-11(4,8)	51	158.1	134	7.8	59.2	7
	107.54793	107.54759	12(4,8)-11(4,7)	51	158.1	73	6.4	57.7	6
	107.59448	107.59404	12(3,10)-11(3,9)	44	166.7	67	8.0	57.4	7
	107.73515	107.73473	12(3,9)-11(3,8)	44	166.7	86	7.6	57.4	9
CH_2CHCN	92.42646	92.42625	10(1,10)-9(1,9)	27	144.1	35	6.6	57.9	10
	94.27761	94.27663	10(0,10)-9(0,9)	25	145.5	61	7.4	55.5	15
	94.76073	94.76078	10(2,9)-9(2,8)	34	139.7	26	7.5	58.8	7
	94.91395	94.91312	10(4,7)-9(4,6)	60	122.3	33	7.3	56.0	6
	blended	94.91323	10(4,6)-9(4,5)	60	122.3				
	blended	94.91396	10(5,5)-9(5,4)	79	109.2				
	blended	94.91396	10(5,6)-9(5,5)	79	109.2				
	103.57602	103.57540	11(0,11)-10(0,10)	30	160	25	7.6	56.8	9
CH_2NH	105.79420	105.79406	4(0,4)-3(1,3)	31	3.9	42	9.7	59.0	14

Table 10. Observed Lines towards G19.61-0.23

Species	Obs. freq (GHz)	Rest freq (GHz)	Transition	Eu (K)	Sd^2 (D^2)	T_A* (mK)	Δv (km s^{-1})	V_{LSR} (km s^{-1})	rms noise (mK)
CH_3OH	103.38181	103.38115	12(-2,11)-12(1,11)	207	0.8	69	5.3	37.4	15
	104.06136	104.06066	13(-3,11)-12(-4,9)	274	3.3	91	6.9	37.3	17
	104.33730	104.33656	13(-2,12)-13(1,12)	237	1.2	67	4.7	37.2	15
	104.35532	104.35482	10(4,7)-11(3,8)–	208	2.5	96	7.2	37.9	18
	105.06443	105.06369	13(1,13)-12(2,10)++	224	4.3	146	6.6	37.2	17
	105.57686	105.57629	14(-2,13)-14(1,13)	270	1.8	95	4.6	37.7	18
NH_2CHO	105.46481	105.46422	5(0,5)-4(0,4)	15	65.3	101	9.1	37.6	14
	105.97357	105.97260	5(2,4)-4(2,3)	27	54.9	84	6.2	36.5	18
	106.10866	106.10786	5(4,2)-4(4,1)	63	23.5	64	6.1	37.0	17
	blended	106.10788	5(4,1)-4(4,0)	63	23.5				
	106.13468	106.13442	5(3,3)-4(3,2)	42	41.8	47	4.6	38.6	18
	106.14198	106.14139	5(3,2)-4(3,1)	42	41.8	54	5.6	37.6	21
CH_3CH_2CN	104.05127	104.05127	12(1 12)-11(1 11)	34	176.5	78	7.1	39.3	20
	105.46999	105.46999	12(0 12)-11(0 11)	33	177.4	102	7.4	37.3	12
CH_2CHCN	103.57601	103.57570	11(0 11)-10(0 10)	30	160	63	8.3	38.4	19
	104.21317	104.21291	11(2 10)-10(2 9)	39	154.8	61	9.1	38.5	14
	104.42009	104.41928	11(6,5)-10(6,4)	108	112.5	89	7.4	37.0	18
	blend	104.41928	11(6,6)-10(6,5)	108	112.5				
	104.43312	104.43302	11(3 9)-10(3 8)	50	148.2	50	9.0	39.0	19
	104.96110	104.96147	11(2,9)-10(2,8)	39	154.8	72	5.4	40.3	16
CH_2NH	105.79406	105.79429	4(0,4)-3(1,3)	31	3.9	31	8.5	40.0	12

Table 11. Observed Lines towards DR21(OH)

Species	Obs. freq (GHz)	Rest freq (GHz)	Transition	Eu (K)	Sd^2 (D^2)	T_A* (mK)	Δv (km s^{-1})	V_{LSR} (km s^{-1})	rms noise (mK)
CH_3OH	105.06372	105.06369	13(1,13)-12(2,10)++	224	4.3	41	4.4	-03.1	8
$HCOOCH_3$	103.46663	103.46729	8(2,6)-7(2,5)E	25	20.2	22	3.9	-01.1	9
	103.47894	103.47927	8(2,6)-7(2,5)A	25	20.2	27	2.9	-02.0	8
CH_2NH	105.79406	105.79429	4(0,4)-3(1,3)	31	3.9	24	5.4	-02.3	7

Table 12. Observed Lines towards W3 (H_2O)

Species	Obs. freq (GHz)	Rest freq (GHz)	Transition	Eu (K)	Sd^2 (D^2)	T_A* (mK)	Δv (km s^{-1})	V_{LSR} (km s^{-1})	rms noise (mK)
CH_3OH	103.38174	103.38115	12(-2,11)-12(1,11)	207	0.8	35	9.3	-48.7	14
	104.06069	104.06066	13(-3,11)-12(-4,9)	274	3.3	48	6.2	-47.1	12
	104.33696	104.33656	13(-2,12)-13(1,12)	237	1.2	42	7.6	-48.2	14
	104.35520	104.35482	10(4,7)-11(3,8)–	208	2.5	62	7.8	-48.1	16
$HCOOCH_3$	103.46686	103.46729	8(2,6)-7(2,5)E	25	20.2	22	9.4	-45.8	9
	103.47887	103.47927	8(2,6)-7(2,5)A	25	20.2	26	7.5	-45.8	9

Table 13. Abundances Assuming 10" source size

Source	N[H_2] (10^{23} cm^{-2})	Species	N (cm^{-2})	Tex (K)	X
G10.47+0.03	1.3	CH_3OH	2.7±0.4 (17)	184±20	2.1±0.3 (-6)
		$HCOOCH_3$	7.1±1.9 (15)	60±39	5.5±1.4 (-8)
		CH_3OCH_3	3.0±0.8 (15)	126±21	2.3±0.6 (-8)
		CH_3CHO	4.2±0.9 (14)	16±2	4.4±1.5 (-9)
		NH_2CHO	5.7±0.8 (15)	119±61	4.4±0.6 (-8)
		CH_3CH_2CN	2.3±0.3 (16)	398±209	4.2±0.4 (-7)
		CH_2CHCN	1.9±0.1 (16)	383±104	1.4±0.1 (-7)
		CH_2NH	4.7±1.6 (15)	84±54	3.6±1.3 (-8)
		CH_3NH_2	1.2±0.4 (14)	61±42	1.0±0.3 (-8)
		$(CH_3)_2CO$	3.8±1.9 (16)	[170]	2.9±1.5 (-7)
Orion KL	1.0	CH_3OH	4.3±0.3 (17)	172±8	3.1±0.3 (-6)
		$HCOOCH_3$	3.4±1.0 (16)	80±43	1.2±0.2 (-6)
		CH_3OCH_3	4.3±0.3 (16)	91±7	3.3±0.2 (-7)
		CH_3CHO	3.5±0.1 (14)	28±8	2.4±0.5 (-9)
		$(CH_3)_2CO$	6.6±3.2 (15)	[100]	1.0±0.8 (-7)
		NH_2CHO	3.8±1.9 (14)	[100]	2.9±1.5 (-9)
		CH_3CH_2CN	9.9±1.2 (15)	146±28	7.6±1.0 (-8)
		CH_2CHCN	3.1±0.2 (15)	97±7	2.4±0.2 (-8)
		CH_2NH	5.5±0.7 (15)	88±18	4.2±0.5 (-8)
NGC6334F	2.0	CH_3OH	3.1±0.5 (17)	201±24	1.6±0.3 (-6)
		$HCOOCH_3$	1.5±0.4 (17)	313±575	7.7±2.3 (-7)
		CH_3OCH_3	4.4±1.0 (15)	101±21	2.2±0.5 (-8)
		CH_3CHO	1.5±0.4 (15)	28±11	7.4±2.1 (-10)
		$(CH_3)_2CO$	7.2±3.0 (14)	[80]	3.6±1.5 (-9)
		NH_2CHO	6.5±1.7 (14)	50±30	3.3±0.8 (-9)
		CH_3CH_2CN	3.4±0.7 (14)	83±30	1.7±0.4 (-9)
		CH_2CHCN	2.9±1.0 (14)	[80]	1.5±0.5 (-9)
		CH_3NH_2	2.3±1.1 (15)	27±13	8.6±3.8 (-9)
		CH_2NH	3.3±2.0 (14)	[40]	1.7±1.0 (-9)
W51 e1/e2	3.6	CH_3OH	2.8±0.7 (17)	222±46	7.8±1.8 (-7)
		$HCOOCH_3$	5.3±3.6 (16)	4277±48777	1.5±0.2 (-5)
		CH_3OCH_3	5.9±0.9 (15)	131±24	1.4±0.2 (-8)

Table 13—Continued

Source	N[H_2] (10^{23} cm^{-2})	Species	N (cm^{-2})	Tex (K)	X
		CH_3CHO	9.1±4.9 (14)	11±3	2.5±1.4 (-9)
		$(CH_3)_2CO$	2.6±1.3 (14)	26±11	7.3±3.6 (-10)
		NH_2CHO	4.8±3.2 (14)	27±23	1.3±0.9 (-9)
		CH_3CH_2CN	1.2±0.3 (15)	179±140	3.0±0.6 (-9)
		CH_2CHCN	5.6±2.0 (14)	79±48	1.5±0.6 (-9)
		CH_2NH	9.7±2.7 (14)	20±2	2.7±0.8 (-9)
G31.41+0.3	1.6	CH_3OH	1.1±0.2 (17)	217±37	6.6±1.2 (-7)
		$HCOOCH_3$	3.6±1.4 (15)	33±18	2.2±0.8 (-8)
		CH_3OCH_3	6.6±3.0 (14)	140±44	2.6±0.8 (-8)
		CH_3CHO	4.0±2.0 (14)	[10]	2.5±1.3 (-9)
		NH_2CHO	9.6±0.1 (14)	62±15	6.0±0.8 (-9)
		CH_2CHCN	3.7±2.4 (14)	[60]	2.3±1.5 (-9)
		CH_2NH	8.5±8.2 (14)	34±20	4.9±3.8 (-9)
		$(CH_3)_2CO$	3.6±1.4 (15)	[60]	4.1±1.9 (-9)
G34.3+0.2	3.0	CH_3OH	1.2±0.3 (17)	196±42	4.1±1.3 (-7)
		$HCOOCH_3$	5.2±0.9 (16)	331±362	1.7±0.3 (-7)
		CH_3OCH_3	1.7±0.4 (15)	117±72	5.6±1.4 (-9)
		CH_3CHO	5.2±2.0 (14)	[10]	1.7±0.7 (-9)
		$(CH_3)_2CO$	3.2±2.6 (15)	[60]	1.1±0.9 (-8)
		NH_2CHO	6.2±3.0 (14)	[60]	2.1±1.0 (-9)
		CH_3CH_2CN	5.7±1.0 (14)	167±83	1.9±3.4 (-9)
		CH_2CHCN	1.4±0.8 (14)	25±10	4.5±2.6 (-10)
		CH_2NH	7.1±4.2 (14)	[40]	2.4±1.4 (-9)
G19.61-0.23		CH_3OH	3.5±3.3 (16)	131±68	
		NH_2CHO	5.8±2.2 (14)	78±57	
		CH_3CH_2CN	1.4±1.0 (14)	[60]	
		CH_2CHCN	5.3±3.0 (14)	[60]	
		CH_2NH	3.8±2.6 (14)	[40]	
DR21(OH)	2.0	CH_3OH	4.6 (15)	[150]	2.3±0.5 (-8)
		$HCOOCH_3$	1.1 (15)	[150]	5.5±3.5 (-8)
		CH_2NH	2.7 (14)	[40]	1.4±1.1 (-9)
W3(H_2O)	1.0	CH_3OH	6.7±9.6 (17)	60±22	6.7±9.6 (-7)

Table 13—Continued

Source	N[H_2] (10^{23} cm^{-2})	Species	N (cm^{-2})	Tex (K)	X
		$HCOOCH_3$	2.7±2.0 (15)	[150]	2.7±2.0 (-8)

Note. — a (b) means a× 10^b. 10" source size was assumed. Hydrogen column densities of these sources were summarized in (Ikeda et al. 2001). A reliable data for hydrogen column density under extended source was not available for G19.61-0.23.

Table 14. Abundances in Compact Source Size

Source	Species	Θ initial (sec)	N initial (cm^{-2})	Tex initial (K)	Θ (sec)	N (cm^{-2})	Tex (K)	X
G10.47+0.03	CH_3OH	1.3	6.8 (18)	184	3.2±0.2	2.6±0.4 (18)	106±20	3.8±0.6 (-7)
	$HCOOCH_3$	1.3	4.2 (17)	60	1.6±0.3	1.1±0.4 (18)	151±78	1.6±0.6 (-7)
	CH_3OCH_3	1.3	1.8 (17)	116	1.9±0.4	7.6±0.4 (17)	94±17	1.1±0.6 (-7)
	NH_2CHO	1.3	1.8 (17)	119	2.1±0.4	7.6±4.1 (17)	63±39	1.5±1.2 (-8)
	CH_3CH_2CN	1.3	1.4 (18)	398	1.3±0.1	8.5±2.2 (17)	169±26	1.3±0.3 (-7)
	CH_2CHCN	1.3	1.1 (18)	383	1±0.1	1.7±0.3 (18)	230±47	2.5±0.4 (-7)
	CH_2NH				[1.3]	2.8±1.0 (17)	84±54	4.2±1.5 (-8)
	CH_3NH_2				[1.3]	8.0±2.1 (16)	[61]	1.2±0.3 (-8)
	$(CH_3)_2CO$				[1.3]	2.2±1.1 (18)	[170]	3.3±1.7 (-7)
Orion KL	CH_3OH		6.8 (18)	183	[5.2]	2.3±0.1 (18)	192±18	1.8±0.1 (-6)
	$HCOOCH_3$		2.7 (17)	80	[3.5]	1.5±0.2 (17)	44±3	1.2±0.2 (-6)
	CH_3OCH_3		3.4 (17)	91	[3.5]	6.5±0.9 (17)	178±24	5.0±0.7 (-7)
	$(CH_3)_2CO$				[2.8]	8.4±4.1 (16)	[100]	6.5±3.1 (-8)
	NH_2CHO				[3.5]	3.1±1.6 (15)	[100]	2.4±1.2 (-9)
	CH_3CH_2CN		1.2 (17)	146	[2.8]	1.7±0.6 (17)	63±6	1.3±0.4 (-7)
	CH_2CHCN		1.1 (18)	97	[2.8]	4.8±2.0 (16)	122±50	3.7±1.5 (-8)
	CH_2NH		4.6 (16)	88	[3.5]	6.0±1.7 (16)	88±18	4.6±1.3 (-8)
NGC6334F	CH_3OH	3.5	6.8 (18)	201	3.8±0.5	2.6±0.4 (18)	116±37	1.8±0.7 (-6)
	$HCOOCH_3$	3.5	4.2 (17)	313	1.9±0.1	1.1±0.4 (18)	101±10	9.3±1.6 (-7)
	CH_3OCH_3	3.5	1.8 (17)	101	4.5±1.5	7.6±0.4 (17)	82±14	1.4±1.0 (-7)
	$(CH_3)_2CO$				[3.5]	5.9±2.4 (15)	[80]	4.2±1.7 (-9)
	NH_2CHO				[3.5]	5.3±1.3 (15)	[50]	3.8±1.0 (-9)
	CH_3CH_2CN		1.4 (18)	83	[3.5]	8.5±2.2 (17)	58±23	1.3±0.4 (-9)
	CH_2CHCN				[3.5]	2.4±0.8 (15)	[80]	1.7±0.6 (-9)
	CH_3NH_2				[3.5]	1.4±0.6 (16)	[27]	1.0±0.4 (-8)
	CH_2NH				[3.5]	2.7±1.6 (15)	[40]	1.9±1.2 (-9)
W51 e1/e2	CH_3OH	2	7.1 (18)	222	3.1±0.3	3.7±0.4 (18)	246±50	7.0±0.8 (-7)
	$HCOOCH_3$	2	1.3 (18)	200	1.6±0.2	2.0±0.6 (18)	69±16	3.8±1.2 (-7)
	CH_3OCH_3	2	1.3 (17)	131	2.8±0.8	3.9±3.2 (17)	95±28	7.4±6.1 (-8)
	$(CH_3)_2CO$				[2.0]	6.6±3.3 (15)	[27]	1.3±0.6 (-9)
	NH_2CHO				[2.0]	1.2±0.8 (16)	[26]	2.3±1.5 (-9)
	CH_3CH_2CN	2	2.7 (16)	179	1.6±1.0	9.8±7.5 (16)	39±37	1.9±1.4 (-8)

Table 14—Continued

Source	Species	Θ initial (sec)	N initial (cm^{-2})	Tex initial (K)	Θ (sec)	N (cm^{-2})	Tex (K)	X
	CH_2CHCN				[2.0]	1.4±0.5 (16)	[20]	2.6±1.0 (-9)
G31.41+0.3	CH_3OH	1.7	3.5 (18)	217	1.8±0.1	3.8±0.6 (18)	185±51	1.1±0..2 (-6)
	$HCOOCH_3$	1.7	1.3 (17)	33	2.6±1.1	1.1±1.7 (17)	41±35	3.1±4.9 (-8)
	CH_3OCH_3	1.7	1.5 (17)	140	3.4±2.2	1.9±2.7 (17)	76±12	5.4±7.7 (-8)
	NH_2CHO	1.7	3.3 (16)	62	1.8±0.3	3.0±1.5 (16)	41±18	8.6±4.3 (-9)
	CH_3CH_2CN	1.7	3.5 (17)	100	1.7±0.6	3.5±1.7 (17)	62±44	3.7±2.4 (-9)
	CH_2CHCN		1.3 (16)		[1.7]	1.3 (16)	[60]	1.0±0.5 (-7)
	CH_2NH				[1.7]	4.6 (16)	[34]	1.3±1.0 (-8)
	$(CH_3)_2CO$				[1.7]	2.3 (16)	[60]	6.5±3.0 (-9)
G34.3+0.2	CH_3OH	2	3.0 (18)	196	2.3±0.3	3.2±0.5 (18)	98±27	4.3±0.6 (-7)
	$HCOOCH_3$	2	1.3 (18)	200	1.3±0.4	2.4±1.3 (18)	48±29	3.2±1.7 (-7)
	CH_3OCH_3				[2.0]	4.2±1.1 (16)	[117]	5.6±1.4 (-9)
	$(CH_3)_2CO$				[2.0]	8.1±6.5 (16)	[60]	1.1±0.9 (-8)
	NH_2CHO				[2.0]	1.6±0.8 (16)	[60]	2.1±1.0 (-9)
	CH_3CH_2CN	2	1.4 (16)	167	1.4±0.4	3.3±2.4 (16)	49±30	4.4±3.2 (-9)
	CH_2CHCN				[2.0]	3.4±1.9 (15)	[25]	4.5±2.6 (-10)
	CH_2NH				[2.0]	1.8±1.1 (16)	[40]	2.4±1.4 (-9)
G19.61-0.23	CH_3OH				[2.5]	5.6±5.3 (17)	131±68	8.3±7.9 (-8)
	NH_2CHO				[2.5]	9.2±3.6 (15)	78±57	1.4±0.5 (-9)
	CH_3CH_2CN				[2.5]	2.2±1.6 (15)	[60]	3.3±2.4 (-10)
	CH_2CHCN				[2.5]	8.5±4.8 (15)	[60]	1.3±0.7 (-9)
	CH_2NH				[2.5]	9.4±6.5 (15)	[40]	1.4±1.0 (-9)

Note. — a (b) means a× 10^b. Fractional abundances were calculated from the H_2 column densities are: 6.69×10^{24} cm^{-2} for G10.47+0.03, 1.35×10^{24} cm^{-2} for NGC6334F, 5.27×10^{24} cm^{-2} (Hernández-Hernández et al. 2014), and 1.3×10^{24} cm^{-2} (Hirota et al. 2015).

Table 15. Observed Parameters of H54β

Source	Tb (mK)	Δv (kms^{-1})	W (mK·kms^{-1})	X[CH_2NH] $\times 10^{-8}$
Orion KL	Not detected*			3.3(±0.5)
G10.47+0.3	<24	[30]	<72	3.1(±1.1)
G31.41+0.03	131	23.6	1018	0.89(±0.85)
NGC6334F	383	29.7	3762	0.24(±0.17)

Note. — Observed recombination line parameters, brightness temperatures Tb (mK), line width Δv (kms^{-1}), and integrated intensities W (mK·kms^{-1}) are shown. The upper limit was calculated for G10.47+0.03, with 3 σ noise level and line width of 30 kms^{-1}. We also showed the observed fractional abundances of CH_2NH. *Reference: Plambeck et al. (2013).

Table 16. Initial Elemental Abundances Compared to Total Hydrogen Atoms

Element	Abundance	Element	Abundance
H_2	0.5	Si^+	8.0 (-9)
He	0.09	Fe^+	3.0 (-9)
N	6.2 (-5)	Na^+	2.0 (-9)
O	2.4 (-4)	Mg^+	7.0 (-9)
C^+	1.7 (-4)	P^+	2.0 (-10)
S^+	8.0 (-9)	Cl^+	1.0 (-9)

Note. — Elemental abundance used in our chemical reaction model. This table is referred from Ruaud et al. (2015).

Table 17. Desorption Energies and Dipole Moments

Species	μ (D)	E_D (K)
CH_3OH	1.70	5534
$HCOOCH_3$	1.77	6295
CH_3OCH_3	1.30	3151
CH_3COCH_3	2.93	3500
CH_2NH	2.02	5534
CH_3NH_2	1.29	6584
CH_2CHCN	3.92	5484
CH_3CH_2CN	4.04	5540
NH_2CHO	3.72	5556

Note. — Desorption energies used our chemical reaction model and dipole moments cited from splatalogue.

Table 18. Important Gas Phase Reactions Related to Interested COMs

Reaction	α	β	γ
$CH_3OH_2^+ + e^- \longrightarrow H + H_2 + H_2CO$	9.1 (-8)	-6.7 (-1)	0
$CH_3OH_2^+ + e^- \longrightarrow H_2O + CH_3$	8.19 (-8)	-6.7 (-1)	0
$CH_3OH_2^+ + e^- \longrightarrow H + OH + CH_3$	4.64 (-7)	-6.7 (-1)	0
$CH_3OH_2^+ + e^- \longrightarrow H + CH_2 + H_2O$	1.91 (-7)	-6.7 (-1)	0
$CH_3OH_2^+ + e^- \longrightarrow H + CH_3OH$	2.73 (-8)	-6.7 (-1)	0
$HC(OH)OCH_3^+ + e^- \longrightarrow HCOOCH_3 + CH_3OH$	1.5 (-7)	-5 (-1)	0
$HC(OH)OCH_3^+ + e^- \longrightarrow HCOOCH_3 + H$	1.5 (-7)	-5 (-1)	0
$CH_3OCH_4^+ + e^- \longrightarrow O{+}CH_3 + CH_4$	7.48 (-7)	-7 (-1)	0
$CH_3OCH_4^+ + e^- \longrightarrow CH_3 + CH_3OH$	8.33 (-7)	-7 (-1)	0
$CH_3OCH_4^+ + e^- \longrightarrow H + CH_3OCH_3+$	1.19 (-7)	-7 (-1)	0
$C_2H_4{+}CN \longrightarrow H + CH_2CHCN$	2.67 (-10)	-6.9 (-1)	3.1 (1)
$C_2H_4{+}CN \longrightarrow HCN + C_2H_3$	2.14 (-10)	-6.9 (-1)	3.1 (1)
$C_2H_4CN^+ + e^- \longrightarrow H_2 + H_2$	1.5 (-7)	-5 (-1)	0
$C_2H_4CN^+ + e^- \longrightarrow H + H_2$	1 (-6)	-3 (-1)	0
$C_2H_4CN^+ + e^- \longrightarrow H + CH_2CHCN$	1 (-6)	-3 (-1)	0
$C_3H_6OH^+ + e^- \longrightarrow CH_3 + CH_3CHO$	1.5 (-7)	-5 (-1)	0
$C_3H_6OH^+ + e^- \longrightarrow H + CH_3COCH_3$	1.5 (-7)	-5 (-1)	0
$CH_3COCH_4^+ + e^- \longrightarrow CH_3CO + CH_3{+}H$	6.75 (-8)	-5 (-1)	0
$CH_3COCH_4^+ + e^- \longrightarrow H_2CCO + CH_4{+}H$	6.75 (-8)	-5 (-1)	0
$CH_3COCH_4^+ + e^- \longrightarrow CH_3CO + CH_4$	1.5 (-8)	-5 (-1)	0
$CH_3COCH_4^+ + e^- \longrightarrow CH_3COCH_3 + H$	1.5 (-8)	-5 (-1)	0

Table 18—Continued

Reaction	α	β	γ
$CH_3COCH_4^+ + e^- \longrightarrow CH_3 + CO + CH_4$	6.75 (-8)	-5 (-1)	0
$H_2CO + NH_2 \longrightarrow H + NH_2CHO$	2.6 (-12)	-2.1 (0)	2.69 (1)
$NH + CH_3 \longrightarrow CH_2NH + H$	1.3 (-10)	1.7 (-1)	0
$CH + NH_3 \longrightarrow CH_2NH + H$	1.52 (-10)	-5 (-2)	0
$CH_2NH_2^+ + e^- \longrightarrow CH_2NH + H$	1.5 (-7)	-5 (-1)	0
$CH_3NH_3^+ + e^- \longrightarrow CH_2NH + H_2 + H$	1.5 (-7)	-5 (-1)	0
$CH_3NH_2^+ + e^- \longrightarrow CH_2NH + H_2$	1.5 (-7)	-5 (-1)	0

Note. — a (b) means a$\times$ 10^b. α, β, and γ represent the coefficients for the Arrhenius equation.

Table 19. Dust Surface Reactions Related to Interested COMs

Reaction	E_A (K)
$CO + H \longrightarrow HCO$	2.5 (3)
$HCO + H \longrightarrow H_2CO$	0
$H_2CO + H \longrightarrow CH_3O$	2.2 (3)
$H_2CO + H \longrightarrow CH_2OH$	5.4 (3)
$CH_3O + H \longrightarrow CH_3OH$	0
$CH_2OH + H \longrightarrow CH_3OH$	0
$CH_3 + OH \longrightarrow CH_3OH$	0
$CH_3O + CH_3 \longrightarrow CH_3OCH_3$	0
$HCO + CH_3O \longrightarrow HCOOCH_3$	0
$HC_3N + H \longrightarrow CH_2CCN$	0
$CH_2CCN + H \longrightarrow CH_2CHCN$	0
$CH_2CHCN + H \longrightarrow CH_3CHCN$	0
$CH_3CHCN + H \longrightarrow CH_3CH_2CN$	0
$CH_2 + CHCN \longrightarrow CH_2CHCN$	0
$C_2H_5 + CN \longrightarrow CH_3CH_2CN$	0
$CH_3 + CH_2CN \longrightarrow CH_3CH_2CN$	0
$CH_3CO + CH_3 \longrightarrow CH_3COCH_3$	0
$H + NH_2CHO \longrightarrow H_2 + H_2NCO$	0
$H + H_2NCO \longrightarrow NH_2CHO$	0
$NH_2 + CHO \longrightarrow NH_2CHO$	0
$HCN + H \longrightarrow HCNH$	6.44 (3)

Table 19—Continued

Reaction	E_A (K)
$HCN + H \longrightarrow H_2CN$	3.65 (3)
$HCNH + H \longrightarrow CH_2NH$	0
$H_2CN + H \longrightarrow CH_2NH$	0
$CH_2NH + H \longrightarrow CH_3NH$	2.13 (3)
$CH_2NH + H \longrightarrow CH_2NH_2$	3.17 (3)
$CH_3NH + H \longrightarrow CH_3NH_2$	0
$CH_2NH_2 + H \longrightarrow CH_3NH_2$	0
$N + CH_3 \longrightarrow CH_2NH$	0
$NH + CH_2 \longrightarrow CH_2NH$	0
$NH_2 + CH \longrightarrow CH_2NH$	0
$NH_2 + CH_3 \longrightarrow CH_3NH_2$	0

Note. — The dust surface reactions related to CH_2NH are shown. E_A represents the value of the activation barrier. Since radical species are so reactive, radical-radical reactions would have no activation barriers. The activation barriers for HCN and CH_2NH were cited from

the theoretical study by Woon (2002).